

**SULPHUR-COORDINATED
IRON AND COPPER COMPLEXES
RELEVANT TO FERREDOXINS AND
BLUE-COPPER-PROTEINS**

a thesis by

Peter Beardwood

submitted for the degree of Doctor of Philosophy of the
University of London and for the Diploma of Membership of
Imperial College.

Chemistry Department
Imperial College
LONDON SW7 2AY

JANUARY 1983

ABSTRACT

SULPHUR-COORDINATED IRON AND COPPER COMPLEXES RELEVANT TO FERREDOXINS AND BLUE-COPPER-PROTEINS.

EPR, Mössbauer and vibrational studies are reported for some iron-sulphur protein model complexes of the type $[\text{Fe}(\text{SR})_4]^-$, $[\text{Fe}_2\text{S}_2(\text{SR})_4]^{2-/3-}$, $[\text{Fe}_4\text{S}_4(\text{SR})_4]^{2-/3-}$, and for their selenium homologues.

The unstable trianion $[\text{Fe}_2\text{S}_2(\text{S}_2\text{-o-xylyl})_2]^{3-}$ is identified by EPR and Mössbauer as the product from chemical reduction of the corresponding dianion and is found to have similar properties to some $[2\text{Fe-2S}]^{1+}$ ferredoxins. EPR spectra for other reduced $[\text{Fe}_2\text{X}_2(\text{YR})_4]^{2-}$ ($\text{X}, \text{Y} = \text{S}, \text{Se}$) complexes having monodentate aryl-chalcogenide ligands show solvent-dependent behaviour which is analysed in terms of their varying g-tensors.

Broadening of the low field peaks in the EPR spectra of $[\text{Fe}_2\text{X}_2(\text{S}_2\text{-o-xylyl})_2]^{3-}$ ($\text{X} = \text{S}, \text{Se}$) and $[\text{Fe}_2\text{S}_2(\text{SC}_6\text{H}_4\text{Cl})_4]^{3-}$ is interpreted as originating from a dominant Orbach spin-lattice relaxation mechanism involving the first excited state of the antiferromagnetic exchange-interaction spin manifold at energies ranging $600\text{-}900\text{ cm}^{-1}$.

X- and Q-band EPR spectra are described for frozen solutions of $[\text{Fe}(\text{S}_2\text{-o-xylyl})_2]^-$ and are interpreted in terms of a high D value ($\sim 2\text{cm}^{-1}$) and a distribution in \underline{D} symmetries centered at $\lambda \approx 0.13$ and ranging over $\lambda \approx \pm 0.05$ in half-width. Comparison is made with spectra for rubredoxins and desulforedoxin.

The three groups of complexes (1-Fe, 2-Fe and 4-Fe) and their selenium homologues have been studied by resonance Raman and infra-red spectroscopy. Many of the observed bands have been assigned to normal vibrations and correlations have been made between the efficiency in resonance enhancement of some Raman totally symmetric modes and deconvoluted electronic absorption profiles. Some reassessment of previously reported iron-sulphur protein Raman spectra is made possible by comparison with the model complexes.

An extensive series of $\text{Cu}(\text{II})\text{N}_2\text{S}_2$ substituted- β -aminothione complexes with systematically variable stereochemistry have been prepared at low temperatures as models for the type 1 centre in blue-copper-proteins. Spectroscopic and redox measurements on these complexes are consistent with pseudo-tetrahedral coordination geometry in which the degree of tetrahedral distortion is dependent upon the steric bulk of the amino substituent. Small parallel copper-hyperfine splitting in the EPR and intense "blue" $\text{S} \rightarrow \text{Cu}$ charge transfer bands in the electronic spectra of the model complexes correlate with similar features in the type 1 protein spectra and further confirm the general pseudo-tetrahedral CuN_2S_2 coordination of the latter.

ACKNOWLEDGEMENTS

I am grateful to my supervisor, Dr JOHN GIBSON, for his patient, friendly and helpful supervision over the period of this work.

I thank Dr BILL GRIFFITH for his supervision and encouragement during my time of responsibility for operation of the Raman spectrometer. In this respect I am also indebted to Mr BRIAN O'HARE for his excellent tuition in running and maintaining this machine.

I would like to thank Dr HENRY RZEPA for his help with several aspects of computing.

I gladly and appreciatively acknowledge the work of Prof. CHARLES JOHNSON and Dr JIM RUSH, of the university of Liverpool physics department, in measuring and simulating the Mössbauer spectra described in this thesis.

I would like to thank those of the technical staff in the department who have performed constructional, analytical or other general work on my behalf. I am grateful also to Mrs ELSIE WILSON for so pleasantly restoring order each week to the chaos of dirty glassware in our laboratory.

My thanks go to MOIRA SHANAHAN for her typing of this manuscript.

I thank those with whom I have shared lab space over the past six years: NANI, ANA, DAPHNE, DOUG, VIVIENE and MALCOLM; not least for enduring (*mostly* without complaint) the malodour of thiols etc.

This work was supported in part by the Science Research Council, to which body I express my thanks.

Against the 'lone and level sands' of these pages,
and in praise of Him from whom nothing is hidden.

**"Let not the wise man glory in his wisdom, let not
the mighty man glory in his might, let not the rich
man glory in his riches; but let him who glories
glory in this, that he understands and knows me,
that I am the LORD who practise steadfast love,
justice, and righteousness in the earth; for in these
things I delight, says the LORD."**

Jeremiah 9

*To my parents
with much affection*

CONTENTS

	<u>PAGE:</u>
ABSTRACT	2
ACKNOWLEDGEMENTS	3
CONTENTS	6
LIST OF FIGURES	9
LIST OF TABLES	16
ABBREVIATIONS AND NOMENCLATURE	20
0. <u>INTRODUCTION</u>	22
1. <u>EPR IN $[\text{Fe}_2\text{S}_2(\text{SR})_4]^{3-}$.</u>	27
1.1. EPR in 2Fe2S Ferredoxins	31
1.2. 2Fe2S Ferredoxin Model Complexes: $[\text{Fe}_2\text{S}_2(\text{SR})_4]^{2-}$	33
1.3. $[\text{Fe}_2\text{S}_2(\text{S}_2\text{-o-xylyl})_2]^{3-}$	35
1.4. Reduced $[\text{Fe}_2\text{S}_2(\text{SC}_6\text{H}_4\text{Y})_4]^{2-}$ (Y = Cl, H, Me)	56
1.5. Discussion	73
1.6. Reduction of Selenium-Substituted Dimers	82
1.7. Concluding Remarks	89
1.8. Experimental	90
2. <u>SPIN-LATTICE RELAXATION IN $[\text{Fe}_2\text{X}_2(\text{SR})_4]^{3-}$ (X = S, Se).</u>	96
2.1. Introduction: Spin-Lattice Relaxation in Ferredoxins	99
2.2. Relaxation Mechanisms	100
2.3. Deduction of T_1 from Homogeneous Broadening	102
2.4. Spin-Lattice Relaxation in 2Fe Synthetic Complexes	106
2.5. Discussion	115
2.6. Conclusion	122
2.7. Experimental	124

3.	<u>COMMENTS ON THE EPR SPECTRUM OF $[\text{Fe}(\text{S}_2\text{-o-xylyl})_2]^-$ IN FROZEN SOLUTION.</u>	126
3.1.	Introduction: EPR in High-Spin Fe(III) S_4	129
3.2.	EPR of $[\text{Fe}(\text{S}_2\text{-o-xylyl})_2]^-$; Determination of λ	133
3.3.	EPR at Q-Band	147
3.4.	Determination of D	150
3.5.	Origin of the Sharp $g' = 4.3$ Resonance	155
3.6.	Conclusion	160
3.7.	Experimental	162
4.	<u>RESONANCE RAMAN OF IRON-SULPHUR COMPLEXES.</u>	164
4.1.	Introduction: RR in Iron-Sulphur Proteins	168
4.2.	Mononuclear Iron-Sulphur Complex; Analogue of Rubredoxins	171
4.3.	Binuclear Iron-Sulphur Complexes; Analogues of 2Fe2S Ferredoxins	184
4.4.	Tetranuclear Iron-Sulphur Complexes; Analogues of 4Fe4S Proteins	221
4.5.	Experimental - Sample Preparation	245
5.	<u>TYPE 1 COPPER IN BLUE-COPPER-PROTEINS; β-AMINOTHIONE MODEL COMPLEXES.</u>	251
5.1.	Introduction: Proteins and Models	255
5.2.	Cu(II) β -Aminothione Complexes	260
5.3.	Electronic Spectra	265
5.4.	Electron Paramagnetic Resonance	277
5.5.	Vibrational Spectra	306
5.6.	Electrochemistry	315
5.7.	Concluding Remarks and Summary	323
5.8.	Experimental	324

6. <u>EXPERIMENTAL</u>	337
6.1. Preparative Chemistry of Iron-Sulphur Complexes	338
6.2. Instrumentation	340
6.3. "EPRPOW" ; EPR Powder Simulation Program for $S = 1/2$	340
APPENDIX A: An interactive spectral manipulation program	349
APPENDIX B: A variable temperature cryostat for rapidly- rotating Raman samples	360
REFERENCES	364

FIGURES

<u>No.</u>		<u>PAGE:</u>
0.1.	Iron-sulphur bonding arrangements in four types of protein centres.	24
0.2	Synthesis of some 1-Fe, 2-Fe and 4-Fe sulphur complexes and their chemical-electrochemical inter-relationships.	25
1.1.	Typical EPR for 2Fe-Fe _{red} ; and the model for the 2Fe-Fd centre.	31
1.2.	EPR of [Fe ₂ S ₂ (S ₂ -o-xylyl) ₂] ³⁻ in DMF (0.1 M nBuNCℓO ₄) at 100 K.	36
1.3.	EPR of [Fe ₂ S ₂ (S ₂ -o-xylyl) ₂] ³⁻ in DMSO.	38
1.4.	Power saturation in EPR of [Fe ₂ S ₂ (S ₂ -o-xylyl) ₂] ³⁻ .	38
1.5.	⁵⁷ Fe hyperfine splitting in the low field EPR of [Fe ₂ S ₂ (S ₂ -o-xylyl) ₂] ³⁻ .	41
1.6.	Mössbauer spectra of [Fe ₂ S ₂ (S ₂ -o-xylyl) ₂] ²⁻ .	44
1.7.	Mössbauer spectra of [Fe ₂ S ₂ (S ₂ -o-xylyl) ₂] ²⁻ and its reduction product.	47
1.8.	Mössbauer spectra of reduced [Fe ₂ S ₂ (S ₂ -o-xylyl) ₂] ²⁻ .	49
1.9.	EPR of [Fe ₂ S ₂ (SC ₆ H ₄ Y) ₄] ²⁻ (Y = Cl, H, Me) reduced in NMP.	57
1.10.	EPR of [Fe ₂ S ₂ (SC ₆ H ₄ Y) ₄] ²⁻ (Y = Cl, H, Me) reduced in DMF.	58
1.11.	EPR of reduced [Fe ₂ S ₂ (SC ₆ H ₄ Y) ₄] ²⁻ .	59
1.12.	EPR of reduced [Fe ₂ S ₂ (SC ₆ H ₄ Y) ₄] ²⁻ .	64
1.13.	EPR of [Fe ₂ S ₂ (SPh) ₄] ²⁻ reduced in varying concentrations of CH ₂ Cl ₂ /DMF.	65
1.14.	EPR of [Fe ₂ S ₂ (SC ₆ H ₄ Y) ₄] ²⁻ reduced in 2% v/v CH ₂ Cl ₂ /DMF.	66
1.15.	EPR of [Fe ₂ S ₂ (SR) ₄] ²⁻ + tBuSH, after reduction.	70
1.16.	Power saturation in the EPR signal from [Fe ₂ S ₂ (S ₂ -o-xylyl) ₂] ²⁻ reduced in the presence of excess tBuSH.	72

1.17.	Plot of g-values vs $(g_y - g_x)$ for $2\text{Fe Fd}_{\text{red}}$ and reduced analogue complexes.	75
1.18.	EPR of $[\text{Fe}_2\text{X}_2(\text{S}_2\text{-o-xylyl})_2]^{3-}$ (X = S, Se) in DMF.	83
1.19.	EPR of $[\text{Fe}_2\text{X}_2(\text{YPh})_4]^{2-}$ (X, Y = S, Se) reduced in DMF.	84
1.20.	EPR of $[\text{Fe}_2\text{X}_2(\text{YPh})_4]^{2-}$ (X, Y = S, Se) reduced in 0.2 M $n\text{Bu}_4\text{NClO}_4/\text{DMF}$.	85
1.21.	Plot of g-values vs. $(g_y - g_x)$ for reduced selenium derivatives of 2Fe-Fd and analogue complexes.	87
2.1.	Spin-state manifolds for antiferromagnetic coupling of two irons in ferric-ferric and ferrous-ferric oxidation levels.	99
2.2.	Three relaxation mechanisms of an EPR spin system and their temperature dependence.	101
2.3.	Convolution of theoretical EPR absorption spectrum with Gaussian and Lorentzian functions.	103
2.4.	Errors inherent in deconvolution of Lorentzian broadening for an outlying EPR peak.	105
2.5.	Temperature dependent broadening of the $[\text{Fe}_2\text{S}_2(\text{S}_2\text{-o-xylyl})_2]^{3-}/\text{DMSO}$ EPR lineshape.	108
2.6.	T_1 -broadening with temperature at H_2 in $[\text{Fe}_2\text{S}_2(\text{S}_2\text{-o-xylyl})_2]^{3-}$ EPR.	109
2.7.	T_1 -broadening with temperature at H_2 in $[\text{Fe}_2\text{Se}_2(\text{S}_2\text{-o-xylyl})_2]^{3-}/\text{DMF}$ EPR.	112
2.8.	T_1 -broadening with temperature at H_2 in $[\text{Fe}_2\text{S}_2(\text{SC}_6\text{H}_4\text{Cl})_4]^{3-}/\text{DMF}$ EPR.	114
2.9.	T_1 variation with temperature for $[\text{Fe}_2\text{S}_2(\text{S}_2\text{-o-xylyl})_2]^{3-}$ in (1:1) DMSO/DMF .	116

- 3.1. Splitting of the three Kramers doublets for $S = 5/2$ 132
under axial and fully rhombic symmetries.
- 3.2. X-band EPR spectra for $\text{Et}_4\text{N}[\text{Fe}(\text{S}_2\text{-o-xylyl})_2]$ in frozen 135
solution.
- 3.3. Predicted principal-axis resonance fields for $D = 2.0 \text{ cm}^{-1}$, 137
 $\nu = 9.12 \text{ GHz}$, $\lambda = 0$ to $1/3$.
- 3.4. Additive powder spectra for lowest and middle doublets 138
resulting from fields predicted at $\lambda = 0.13$.
- 3.5. Representations of the λ -field-intensity relationships 143
used for the lowest doublet in the λ -distribution
simulation procedure.
- 3.6. Representations of the λ -field-intensity relationships 144
used for the middle doublet in the λ -distribution
simulation procedure.
- 3.7. Trial simulations involving five different λ -distribution 145
centrings ($\Delta\lambda_{\frac{1}{2}} = 0.05$) and three linewidth formulae.
- 3.8. Trial simulations involving three different λ -distribution 146
half-widths ($\lambda_0 = 0.13$).
- 3.9. Predicted principal-axis resonance fields for $D = 2.0 \text{ cm}^{-1}$, 148
 $\nu = 36 \text{ GHz}$ and $\lambda = 0$ to $1/3$ compared with experimental
Q-band spectrum for a frozen solution of $\text{Et}_4\text{N}[\text{Fe}(\text{S}_2\text{-o-xylyl})_2]$.
- 3.10. λ -Dependence of zero-field splitting between lowest and 152
middle and between middle and upper Kramers doublets.
- 3.11. Temperature dependence of the fractional populations for 153
the three $S = 5/2$ doublets with $D = 2.0 \text{ cm}^{-1}$ and $\lambda = 0.13$
compared with experimental normalised intensities for the
 $g' = 8.4$ peak of $[\text{Fe}(\text{S}_2\text{-o-xylyl})_2]^{+}$.

3.12.	Temperature dependence of the fractional doublet populations for the three $S = 5/2$ doublets with $D = 13.5 \text{ cm}^{-1}$ and $\lambda = 0.1$ compared with experimental normalised intensities of the sharp $g' = 4.3$ resonance for $[\text{Fe}(\text{S}_2\text{-o-xylyl})_2]^-$.	155
4.1.	Crystallographically determined structural data for the FeS_4 site in Rd from <u><i>C. pasteurianum</i></u> .	171
4.2.	Raman spectra for Rd from <u><i>C. pasteurianum</i></u> with 488 nm excitation.	171
4.3.	Crystallographically determined structural data for the FeS_4 sites in $[\text{Et}_4\text{N}][\text{Fe}(\text{S}_2\text{-o-xylyl})_2]$.	174
4.4.	Solid-state Raman spectra for $[\text{Et}_4\text{N}][\text{Fe}(\text{S}_2\text{-o-xylyl})_2]$ with three excitation frequencies.	177
4.5.	Raman spectrum for $[\text{Et}_4\text{N}][\text{Fe}(\text{S}_2\text{-o-xylyl})_2]$ in acetone with 568.2 nm excitation.	178
4.6.	Electronic spectrum of $[\text{Fe}(\text{S}_2\text{-o-xylyl})_2]^-$ in acetone and resonance enhancement of several Raman peaks.	181
4.7.	Raman spectra for S and Se bridged adrenodoxin with 488 nm excitation.	184
4.8.	Approximate descriptions of the normal modes of vibration for the bridged dimer M_2X_6 .	187
4.9.	Crystal structures for three $[2\text{Fe}-2\text{S}]^{2+}$ complexes.	190
4.10.	Solid state Raman spectra of $[\text{Et}_4\text{N}]_2[\text{Fe}_2\text{X}_2(\text{S}_2\text{-o-xylyl})_2]$ ($\text{X} = \text{S}, \text{Se}$) with 530.9 nm excitation.	198
4.11.	Solid state infrared absorption spectra for several dimer complexes.	199
4.12.	Solid state Raman spectra of $[\text{Et}_4\text{N}]_2[\text{Fe}_2\text{X}_2(\text{SPh})_4]$ ($\text{X} = \text{S}, \text{Se}$) with 482.5 nm excitation.	200
4.13.	Solid state Raman spectra of $[\text{Et}_4\text{N}]_2[\text{Fe}_2\text{X}_2(\text{SePh})_4]$ with 482.5 nm ($\text{X} = \text{S}$) and 530.9 nm ($\text{X} = \text{Se}$) excitation.	201

4.14.	Solid state Raman Spectra of $[\text{Et}_4\text{N}]_2[\text{Fe}_2\text{X}_2(\text{STol})_4]$ (X = S, Se) with 482.5 nm excitation.	202
4.15.	Electronic absorption spectra for $[\text{Fe}_2\text{X}_2(\text{YPh})_4]^{2-}$ (X, Y = S, Se) in DMF.	212
4.16.	$[\text{Fe}_2\text{X}_2(\text{YR})_4]^{2-}$ (X, Y, = S, Se: R = Ph, pClPh) in acetone. Electronic spectra and Raman excitation profiles.	214
4.17.	Electronic reflectance spectra and Raman excitation profiles for $[\text{Et}_4\text{N}]_2[\text{Fe}_2\text{X}_2(\text{S}_2\text{-o-xylyl})_2]$ (X = S, Se).	216
4.18.	Raman spectra for three 4Fe-4S centres (488 nm excitation).	221
4.19.	Solid state Raman spectra of $[\text{Et}_4\text{N}]_2[\text{Fe}_4\text{X}_4(\text{SPh})_4]$ (X = S, Se) with 530.9 nm excitation.	228
4.20.	Solid state infrared absorption spectra for the tetramer complexes.	229
4.21.	Solid state Raman spectra of $[\text{Et}_4\text{N}]_2[\text{Fe}_4\text{X}_4(\text{SePh})_4]$ (X = S, Se) with 482.5 nm excitation.	230
4.22.	Solid state Raman spectra of $[\text{Et}_4\text{N}]_2[\text{Fe}_4\text{X}_4(\text{SBz})_4]$ (X = S, Se) with 482.5 nm excitation.	231
4.23.	Electronic spectrum of $[\text{Fe}_4\text{S}_4(\text{SPh})_4]^{2-}$ in acetone and resonance enhancement of several Raman peaks.	240
4.24.	Details of Raman spectrometer (SPEX RAMALOG V) sample-compartment arrangement for spinning samples in an inert atmosphere.	246
5.1.	Electronic spectra of $\text{Cu(II)}(\text{RN-MeMeS})_2$ in THF or DMF.	266
5.2.	Reflectance spectra of $\text{Cu(II)}(\text{RN-MeMeS})_2$.	267
5.3.	Correlation of d-orbital energies for tetrahedral and square-planar Cu(II) related by a compression along the z-axis.	270

5.4.	X-band EPR spectra of $^{63}\text{Cu(II)}(\text{iBuN-MeMeS})_2$ and $^{63}\text{Cu(II)}(\text{sBuN-MeMeS})_2$ in MeOH at 100 K.	281
5.5.	X-band EPR spectra of $^{64}\text{Cu(II)}(1\text{NaphthylN-MeMeS})_2$ and $^{63}\text{Cu(II)}(\text{pMeOPhN-MeMeS})_2$ in MeOH at 100 K.	282
5.6.	EPR spectra for $\text{Cu(II)}(\text{RN-R}_2\text{R}_1\text{S})_2$ in mobile toluene.	283
5.7.	$A_{ }$ vs. $g_{ }$ plot for EPR of $\text{Cu(II)}(\text{RN-R}_2\text{R}_1\text{S})_2$ in solution.	286
5.8.	EPR of $^{63}\text{Cu(II)}$ doped $\text{Zn(II)}(\text{RN-MeMeS})_2$ (R = CH _x and Et) at 100 K.	290
5.9.	EPR of $^{63}\text{Cu(II)}$ doped $\text{Zn(II)}(\text{RN-MeMeS})_2$ (R = pMeOPh and 2,6-Me ₂ Ph) at 100 K.	291
5.10.	EPR of $^{63}\text{Cu(II)}$ doped $\text{M(II)}(\text{MeN-MeMeS})_2$ (M = Zn and Cd) at 100 K.	292
5.11.	EPR of $^{63}\text{Cu(II)}$ doped $\text{Zn(II)}[(\text{CH}_2)_n(\text{N-MeMeS})_2]$ (n = 2,3) at 100 K.	293
5.12.	X and Q band EPR of $^{63}\text{Cu(II)}$ doped $\text{Ni(II)}[(\text{CH}_2)_2(\text{N-MeMeS})_2]$ at 100 K.	294
5.13.	EPR of Cu(II) doped $\text{Ni(II)}(\text{RN-MeMeS})_2$ (R = C ₁₈ H ₃₇ and pClPh) at 100 K.	295
5.14.	$A_{ }$ vs. $g_{ }$ plot for EPR of Cu(II) doped $\text{M(II)}(\text{RN-MeMeS})_2$ (M = Zn, Ni, Cd).	297
5.15.	$A_{ }$ vs. $g_{ }$ plot for EPR of Cu(II) 2N2S complexes and the blue-copper-proteins.	298
5.16.	Raman spectra of solid $\text{Cu(II)}(\text{MeN-MeMeS})_2$ at -140°C .	308
5.17.	Cyclic voltammograms of $\text{Cu(II)}(\text{MeN-MeMeS})_2$ in DMF.	316

5.18.	Polarogram of $\text{Cu(II)(nOctN-MeMeS)}_2$ in DMF at a RDME	319
5.19.	Low temperature filtration apparatus.	329
6.1.	Relations between the \underline{g} and \underline{A} tensor coordinate systems.	341
B.1.	Cryostat, solution sample spinner and refrigeration method	361
B.2.	Cross sectional view of cryostat and solid-sample spinner	362
B.3.	Pyrex cryostat body	363
B.4.	Details of solid and solution sample spinners	363

TABLES

<u>No.</u>		<u>PAGE:</u>
1.1.	EPR parameters for $[\text{Fe}_2\text{S}_2(\text{S}_2\text{-o-xylyl})_2]^{3-}$.	39
1.2.	Parameters used to fit Mössbauer spectra of $[\text{Fe}_2\text{S}_2(\text{S}_2\text{-o-xylyl})_2]^{2-}$ in DMF at 4.2 K.	43
1.3.	Mössbauer spectral parameters for $2\text{Fe-Fd}_{\text{ox}}$ and $[\text{Fe}_2\text{S}_2(\text{SR})_4]^{2-}$ salts at 4.2 K.	45
1.4.	Parameters used to fit Mössbauer spectra of $[\text{Fe}_2\text{S}_2(\text{S}_2\text{-o-xylyl})_2]^{3-}$ in DMF at 4.2 K.	48
1.5.	Mössbauer spectral parameters for $2\text{Fe Fd}_{\text{red}}$ at 4.2 K.	51
1.6.	EPR data for reduced $[\text{Fe}_2\text{S}_2(\text{SC}_6\text{H}_4\text{Y})_4]^{2-}$.	60
1.7.	EPR data for two-iron ferredoxins.	76
1.8.	EPR data for reduced $[\text{Fe}_2\text{X}_2(\text{YR})_4]^{2-}$ (X, Y = S, Se).	86
1.9.	EPR data for selenium-bridged ferredoxins.	88
2.1.	Antiferromagnetic coupling parameter, J, for $[2\text{Fe-2S}]^{(1+,2+)}$ centres in ferredoxins and synthetic analogues.	123
3.1.	Transition probabilities derived from the programs "EPR" and "EPRPOW" using the parameters $\lambda = 0.13$, $D = 2.0 \text{ cm}^{-1}$, $\nu = 9.12 \text{ GHz}$.	141
4.1.	Vibrational frequencies for iron-sulphur proteins and related synthetic complexes.	169
4.2.	Correlations between the point group T_d and sub-groups.	172

4.3.	RR and IR data for $\text{Et}_4\text{N}[\text{Fe}(\text{III})(\text{S}_2\text{-o-xylyl})_2]$.	176
4.4.	RR spectrum of FeS_4 core in $[\text{Fe}(\text{S}_2\text{-o-xylyl})_2]^-$ - assignments.	181
4.5.	Symmetry distributions of the normal vibrational modes for five M_2X_6 structures.	190
4.6.	RR and IR data for $[\text{Et}_4\text{N}]_2[\text{Fe}_2\text{X}_2(\text{S}_2\text{-o-xylyl})_2]$ ($\text{X} = \text{S}, \text{Se}$).	192
4.7.	RR and IR data for $[\text{Et}_4\text{N}]_2[\text{Fe}_2\text{X}_2(\text{SPh})_4]$ ($\text{X} = \text{S}, \text{Se}$).	193
4.8.	RR and IR data for $[\text{Et}_4\text{N}]_2[\text{Fe}_2\text{X}_2(\text{SePh})_4]$ ($\text{X} = \text{S}, \text{Se}$).	194
4.9.	RR and IR data for $[\text{Et}_4\text{N}]_2[\text{Fe}_2\text{X}_2(\text{STol})_4]$ ($\text{X} = \text{S}, \text{Se}$).	195
4.10.	RR and IR data for $[\text{Et}_4\text{N}]_2[\text{Fe}_2\text{S}_2(\text{SC}_6\text{H}_4\text{Cl})_4]$.	196
4.11.	RR and IR data for $[\text{Et}_4\text{N}]_2[\text{Fe}_2\text{X}_2\text{Cl}_4]$ ($\text{X} = \text{S}, \text{Se}$) and $[\text{Et}_4\text{N}]_2[\text{Fe}_2\text{S}_2\text{Br}_4]$.	196
4.12.	$[\text{Fe}_2\text{X}_2(\text{S}_2\text{-o-xylyl})_2]^{2-}$ ($\text{X} = \text{S}, \text{Se}$) vibrational assignments.	206
4.13.	$[\text{Fe}_2\text{X}_2(\text{YPh})_4]^{2-}$ ($\text{X}, \text{Y}, = \text{S}, \text{Se}$) vibrational assignments.	208
4.14.	$[\text{Fe}_2\text{X}_2(\text{STol})_4]^{2-}$ ($\text{X} = \text{S}, \text{Se}$) vibrational assignments.	210
4.15.	$[\text{Fe}_2\text{S}_2(\text{SC}_6\text{H}_4\text{Cl})_4]^{2-}$ vibrational assignments	210
4.16.	$[\text{Fe}_2\text{X}_2\text{Y}_4]^{2-}$ ($\text{X} = \text{S}, \text{Se}; \text{Y} = \text{Cl}, \text{Br}$) vibrational assignments.	211
4.17.	Electronic spectra of $[\text{Fe}_2\text{X}_2(\text{YR})_4]^{2-}$ ($\text{X}, \text{Y} = \text{S}, \text{Se}$).	211
4.18.	Reflectance spectra of $[\text{Fe}_2\text{X}_2(\text{SR})_4]^{2-}$ ($\text{X} = \text{S}, \text{Se}$).	215
4.19.	Correlation of vibrational assignments for dimer complexes.	218
4.20.	Normal vibrations of $\text{M}_4(\text{X}_b)_4(\text{X}_t)_4$ in T_d and D_{2d} symmetries.	224
4.21.	RR and IR data for $[\text{Et}_4\text{N}]_2[\text{Fe}_4\text{X}_4(\text{PhS})_4]$ ($\text{X} = \text{S}, \text{Se}$).	225

4.22.	RR and IR data for $[\text{Et}_4\text{N}]_2[\text{Fe}_4\text{X}_4(\text{SePh})_4]$ (X = S, Se).	226
4.23.	RR and IR data for $[\text{Et}_4\text{N}]_2[\text{Fe}_4\text{X}_4(\text{SBz})_4]$ (X = S, Se).	227
4.24.	$[\text{Fe}_4\text{X}_4(\text{YPh})_4]^{2-}$ (X, Y = S, Se) vibrational assignments.	235
4.25.	$[\text{Fe}_4\text{X}_4(\text{BzS})_4]^{2-}$ (X = S, Se) vibrational assignments.	239
5.1.	Visible absorption band maxima of $\text{Cu(II)}(\text{RN-R}_2\text{R}_1\text{S})_2$ in solution.	265
5.2.	Solid state reflectance spectra of $\text{Cu(II)}(\text{RN-R}_2\text{R}_1\text{S})_2$; band maxima at room temperature.	268
5.3.	Electronic spectral parameters for some blue-copper-proteins and their assignment.	272
5.4.	Electronic spectral parameters for $\text{Ni(II)}(\text{RN-MeMeS})_2$ complexes in CH_2Cl_2 .	276
5.5.	EPR parameters for $\text{Cu(II)}(\text{RN-R}_2\text{R}_1)_2$ in solution at 100 K.	278
5.6.	EPR parameters used in simulating $^{63}\text{Cu(II)}(\text{RN-MeMeS})_2$ solution spectra.	280
5.7.	EPR parameters for $^{63}\text{Cu(II)}$ doped $\text{Zn(II)}(\text{RN-MeMeS})_2$ at 100 K.	288
5.8.	EPR parameters for Cu(II) doped $\text{Ni(II)}(\text{RN-MeMeS})_2$ at 100 K.	289
5.9.	EPR parameters for Cu(II) doped $\text{Cd(II)}(\text{RN-MeMeS})_2$ at 100 K.	289
5.10.	EPR parameters used in simulating spectra of $^{63}\text{Cu(II)}$ doped $\text{M(II)}(\text{RN-MeMeS})_2$ (M = Zn, Ni).	296
5.11.	$g_{ }$ and $ A_{ } $ parameters for previously reported 2N2S copper(II) complexes.	299

5.12.	EPR parameters for blue-copper-proteins.	300
5.13.	Raman spectral parameters for $\text{Cu(II)(MeN-MeMeS)}_2$ at -140°C (KBr disc).	306
5.14.	Raman spectral parameters for $\text{Cu(II)(iBuN-MeMeS)}_2$ at -140°C (KBr disc).	307
5.15.	Low frequency IR data for $\text{Cu(II)(RN-MeMeS)}_2$ (R = Me, iBu).	307
5.16.	Symmetries and selection rules for normal modes of CuN_2S_2 .	309
5.17.	Raman spectral data for blue-copper-proteins.	312
5.18.	Electrochemical data for $\text{Cu(II)(RN-MeMeS)}_2$ (R = Me, Et, nOct, iPr and en/2) at <u>ca.</u> -35°C .	315
5.19.	PMR data for β -aminothione ligands - $(\text{RN-R}_2\text{R}_1\text{S})$.	326
5.20.	Elemental microanalyses for β -aminothione ligands - $(\text{RN-R}_2\text{R}_1\text{S})$.	327
5.21.	Elemental microanalyses for cupric β -aminothione complexes - $\text{Cu(II)(RN-R}_2\text{R}_1\text{S)}_2$.	330
5.22.	Elemental microanalyses for zinc, nickel and cadmium β -aminothione complexes - M(II)(RN-MeMeS)_2 .	334

Extra information relating to some Figures and Tables can be found at the end of each section under Experimental.

Abbreviations, Nomenclature and Symbols

ACN ⁻	Acenaphthylenide radical anion
Ar	Aryl substituent
Bz	Benzyl substituent
CT	Charge transfer
D	Axial component of <u>D</u> tensor
DMF	N,N-dimethylformamide
DMSO	Dimethylsulphoxide
$E_{\frac{1}{2}}$	Half-wave potential
EDTA	Ethylene diamine tetraacetic acid
en	1,2-diaminoethane
ENDOR	Electron nuclear double resonance
EPR	Electron paramagnetic resonance
EXAFS	Extended X-ray absorption fine structure
Fd _{ox/red}	Ferredoxin (oxidised/reduced)
H	Magnetic field
HMDE	Hanging mercury drop electrode
IR	Infrared absorption spectroscopy
LMCT	Ligand to metal charge transfer
J	Antiferromagnetic exchange constant
NMP	N-Methyl pyrrolidinone
NMR	Nuclear magnetic resonance
Ph	Phenyl substituent
PTFE	Polytetrafluoroethylene
R	Organic substituent
Rd	Rubredoxin
RDME	Rapid dropping mercury electrode

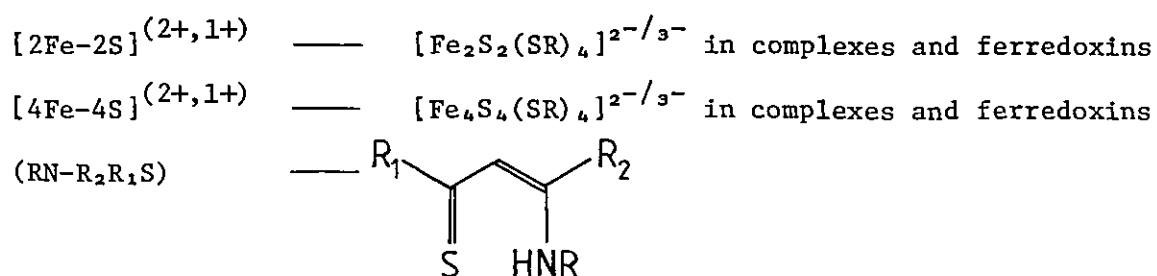
RR	Resonance Raman spectroscopy
S ₂ -o-xylyl	α,α'-dithio-o-xylene (also S ₂ -o-xyl)
T ₁	Electron spin-lattice relaxation time
THF	Tetrahydrofuran
Tol	Tolyl substituent

As per context:-

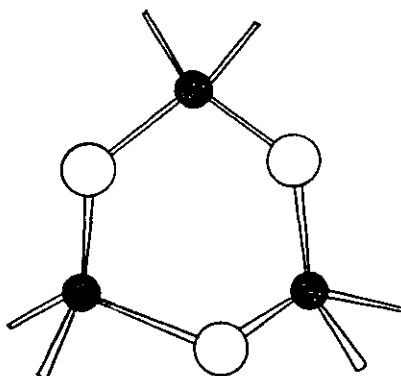
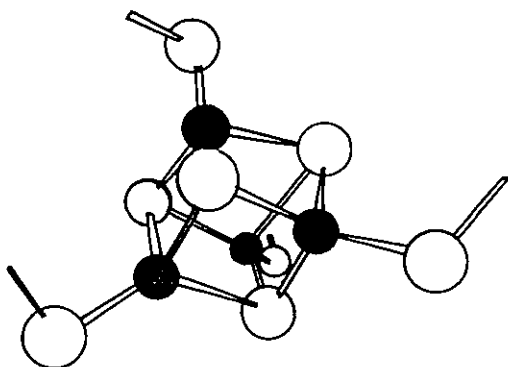
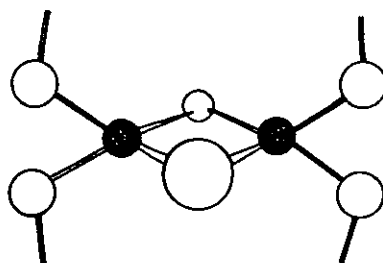
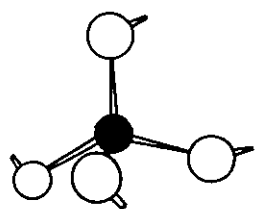
δ	—	isomer shift
		deformation vibration
		NMR shift
λ	—	Wavelength (visible)
		Rhombic component of <u>D</u> tensor
		Spin orbit coupling constant
ν	—	Stretching vibration
		microwave frequency

In describing spectral bands:-

w	weak	pr	poorly resolved
m	medium	dl	double
s	strong	mlt	multiplet
v	very	ρ	depolarisation ratio
sh	shoulder	p	polarised
br	broad	dp	depolarised
n	narrow		



INTRODUCTION



0. INTRODUCTION.

Many metal-containing biomolecules have been discovered in the last few decades. The most prominent metals involved are Mg, Mn, Fe, Co, Cu, Zn and Mo. In order to achieve some particular function the metal ions are often coordinated in an unusual manner and lead to physico-chemical properties not previously encountered in synthetic chemistry. Study of the similarities and differences between metalloproteins and model metal complexes has proven to be of considerable use in understanding their structure and function. The bulk of such investigation has centred around iron-heme complexes, iron-sulphur complexes and model-complexes for the blue copper proteins.¹ A brief description of progress in mimicking the coordination and properties of Type 1 blue copper proteins may be found in Section 5.1. Development of model complexes for iron-sulphur proteins has been dominated by R.H. Holm and co-workers.

Three types of iron-sulphur centres in proteins are well established, involving 1Fe, [2Fe-2S] and [4Fe-4S], coordinated, in general, to four cysteinyl sulphurs, Figures 0.1.1 to 0.1.3. In the rhombic FeS₄ coordination characteristic of rubredoxins (Rd) the iron may be ferric or ferrous. The two-iron ferredoxins (Fd) contain a [2Fe-2S] cluster in which the two irons are bridged by two sulphides and may take up oxidation states Fe(III)Fe(III) = [2Fe-2S]²⁺ and Fe(III)Fe(II) = [2Fe-2S]¹⁺. A cubane [4Fe-4S] unit, consisting of interpenetrating 4Fe and 4S approximate tetrahedra, is found in the four-iron ferredoxins. In nature, nearly all [4Fe-4S] proteins divide into two groups of two oxidation levels,

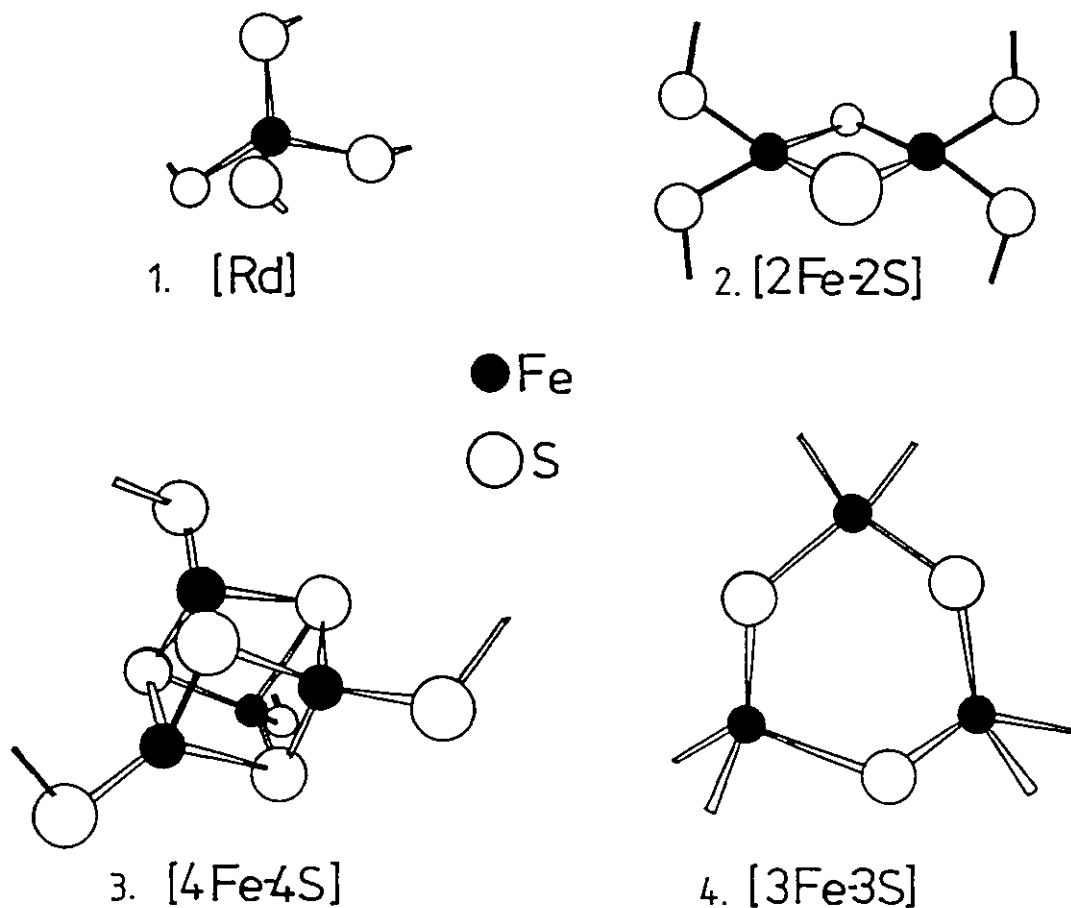
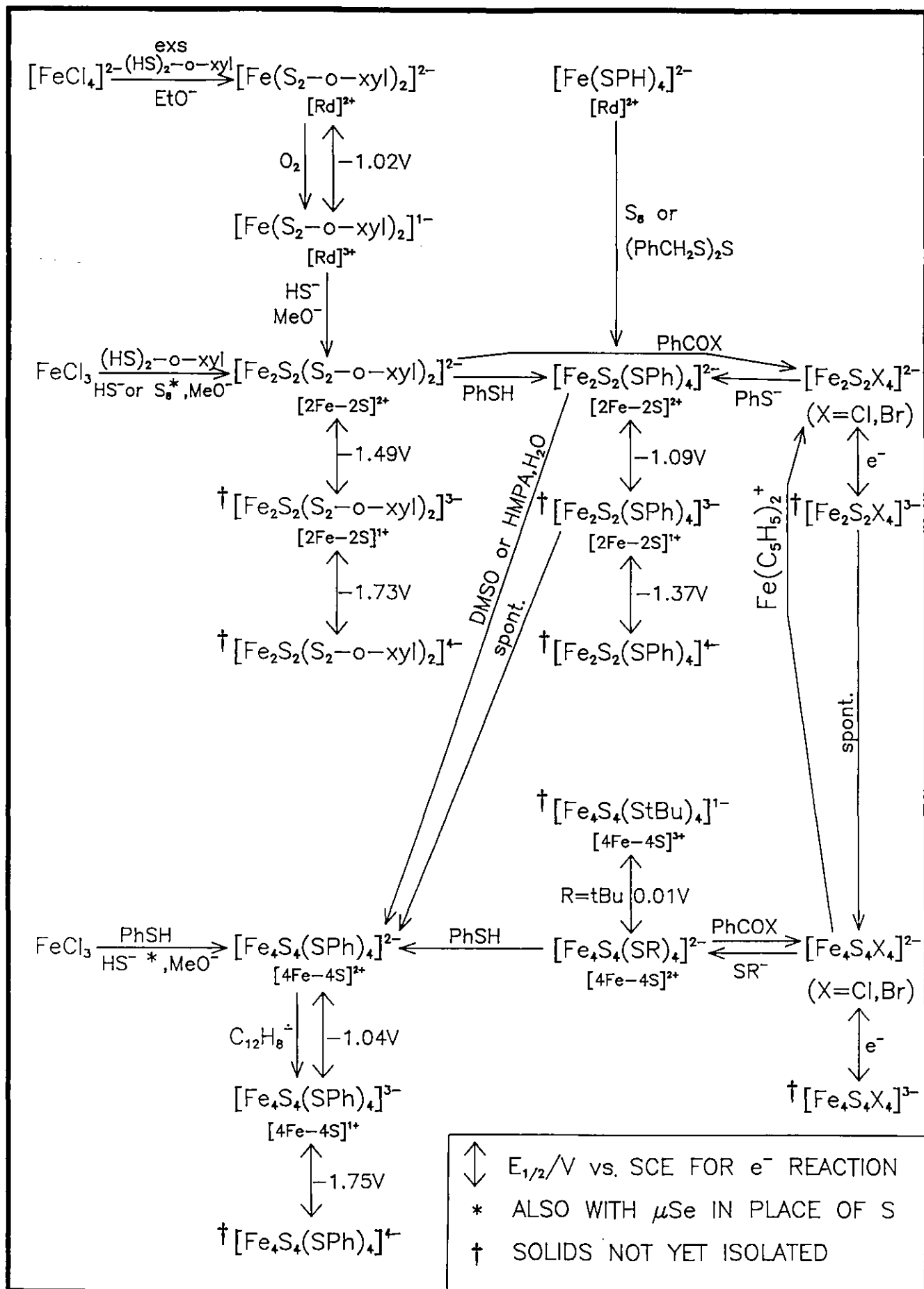


Figure 0.1. Iron-sulphur bonding arrangements in (1) 1-Fe(rubredoxin, Rd), (2) 2-Fe and (3) 4-Fe (ferredoxin, Fd) protein centres and (4) in the proposed 3-Fe centre.

firstly, $[4\text{Fe}-4\text{S}]^{(2+, 1+)}$ [i.e., $2\text{Fe(III)}2\text{Fe(II)}$ and $\text{Fe(III)}3\text{Fe(II)}$] and secondly, $[4\text{Fe}-4\text{S}]^{(3+, 2+)}$ [i.e., $3\text{Fe(III)}\text{Fe(II)}$ and $2\text{Fe(III)}2\text{Fe(II)}$]. A fourth type of centre involving $[3\text{Fe}-3\text{S}]$ has recently been recognised, Figure 0.1.4, but this cluster together with its structure and properties are not yet well established.²

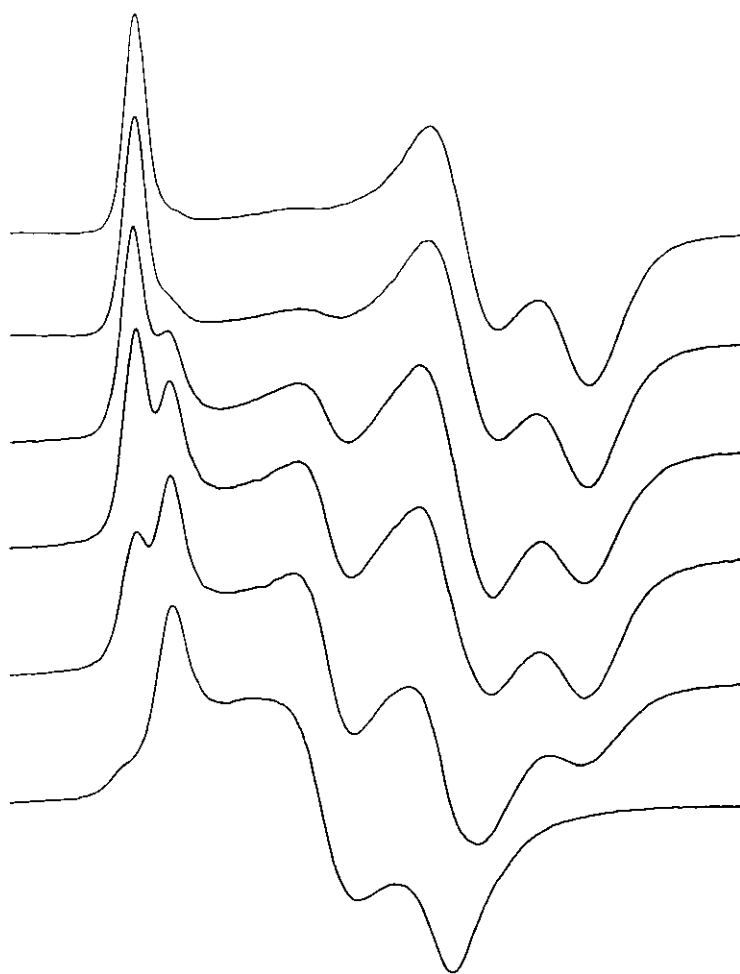
Some of the terms and symbols used here are taken from the nomenclature recommendations of the NC-IUB.³ These will not always be strictly adhered to in this thesis as the nomenclature recommended may have confusing connotations in the context of inorganic chemistry. Iron-

FIG. 0.2 SYNTHESIS OF SOME 1-Fe, 2-Fe AND 4-Fe SULPHUR COMPLEXES & THEIR CHEMICAL-ELECTROCHEMICAL INTER-RELATIONSHIPS



sulphur proteins and their properties have been very widely reviewed.³⁻¹⁰ $[\text{Fe}(\text{SR})_4]^{1-}, 2-$, $[\text{Fe}_2\text{S}_2(\text{SR})_4]^{2-}, 3-, 4-$ and $[\text{Fe}_4\text{S}_4(\text{SR})_4]^{1-}, 2-, 3-, 4-$ synthetic species have been prepared and characterised or detected spectroscopically or electrochemically by Holm and others.^{1,11-13} These complexes have been demonstrated to be excellent analogues for the three major iron-sulphur centres found in proteins. The scheme in Figure 0.2 shows some of the reaction chemistry for the interrelated 1Fe, 2Fe and 4Fe compounds and the correspondence with the oxidation levels found for rubredoxins and ferredoxins.

In this present work some further, mainly spectroscopic, investigation is undertaken into the properties of several of the iron-sulphur complexes in Figure 0.2. EPR and Raman are used as the main means of study and the results are compared with corresponding protein characteristics. Some new 2Fe-complexes involving ligation by selenium are examined also. Lastly, a number of 2N2S coordinated cupric complexes with non-planar geometry are described as model complexes for blue copper proteins.

SECTION 1**EPR IN $[\text{Fe}_2\text{S}_2(\text{SR})_4]^{3-}$** 

1. EPR in $[\text{Fe}_2\text{S}_2(\text{SR})_4]^{3-}$.

ABSTRACT	30
1.1. <u>EPR in 2Fe2S Ferredoxins.</u>	31
1.2. <u>2Fe2S Ferredoxin Model Complexes: $[\text{Fe}_2\text{S}_2(\text{SR})_4]^{2-}$.</u>	33
1.3. <u>$[\text{Fe}_2\text{S}_2(\text{S}_2\text{-o-xylyl})_2]^{3-}$.</u>	35
1.3.1. EPR	35
1.3.2. ^{57}Fe EPR	40
1.3.3. Mössbauer of $[\text{Fe}_2\text{S}_2(\text{S}_2\text{-o-xylyl})_2]^{2-,3-}$.	42
1.3.3.1. Mössbauer for the dianion.	43
1.3.3.2. Mössbauer for the trianion.	46
1.3.4. Addendum.	54
1.4. <u>Reduced $[\text{Fe}_2\text{S}_2(\text{SC}_6\text{H}_4\text{Y})_4]^{2-}$, (Y = Cl, H, Me).</u>	56
1.4.1. Effect of solvent vitrification.	56
1.4.1.1. Spectral types and simulations	56
1.4.1.2. Vitreous samples.	63
1.4.1.3. Devitrified samples.	67
1.4.2. Stability.	68
1.4.3. Effect of added thiols.	68
1.4.4. Summary.	71
1.5. <u>Discussion.</u>	73
1.5.1. Analysis of g -tensor principal values.	73
1.5.2. Further discussion of spectral solvent-dependency.	78

1.6.	<u>Reduction of Selenium Substituted Dimers.</u>	82
1.7.	<u>Concluding Remarks.</u>	89
1.8.	<u>Experimental.</u>	90
1.8.1.	One electron reduction of $[\text{Fe}_2\text{X}_2(\text{YR})_4]^{2-}$ (X,Y = S,Se)	90
1.8.2.	^{57}Fe enriched $[\text{Fe}_2\text{S}_2(\text{S}_2\text{-o-xylyl})_2]^{2-}$.	92
1.8.3.	Experimental details for Figures.	93

ABSTRACT

$[\text{Et}_4\text{N}]_2[\text{Fe}_2\text{S}_2(\text{S}_2\text{-o-xylyl})_2]$ may be reduced in DMF using sodium acenaphthylenide to give paramagnetic solutions containing 60-80% of the trianion $[\text{Fe}_2\text{S}_2(\text{S}_2\text{-o-xylyl})_2]^{3-}$. The EPR spectrum is characteristic of reduced ferredoxins, having g -values of 2.007, 1.940 and 1.922. An ^{57}Fe enriched sample shows splittings from two iron atoms, with mean hyperfine interactions of ca. 14 G.

Mössbauer spectra for $[\text{Fe}_2\text{S}_2(\text{S}_2\text{-o-xylyl})_2]^{2-}$ in solution are found to be more compatible with $[2\text{Fe-2S}]^{2+}$ ferredoxin spectra than are similar spectra obtained for solid samples, and a slight inequivalence between the two irons is observed. Mössbauer spectra of the reduced dimer give clear evidence of antiferromagnetically coupled components of a paramagnetic species, closely resembling those found in $[2\text{Fe-2S}]^{1+}$ ferredoxins.

Other sulphur-bridged diferric complexes with monodentate aryl-thiolate ligands, $[\text{Fe}_2\text{S}_2(\text{SC}_6\text{H}_4\text{Y})_4]^{2-}$ ($\text{Y} = \text{Cl}, \text{H}, \text{Me}$), may also be reduced to yield 20-60% of the corresponding paramagnetic trianion, as evidenced by EPR. The signals observed are found to be highly solvent-dependent and also to be affected by the presence of excess thiol. Some preliminary interpretation of these effects is attempted by analysis of the g -tensor. EPR spectra of the reduction products of related selenium-bridged and selenium terminally-ligated diferric complexes are also reported.

1. EPR IN $[\text{Fe}_2\text{S}_2(\text{SR})_4]^{3-}$.

1.1. EPR in 2Fe2S Ferredoxins.

EPR has proven to be of considerable use in the characterisation of iron-sulphur proteins and in elucidation of their metal-site structures.^{6,14-16}

Figure 1.1.1 shows spectra typical of 2Fe ferredoxins (Fd) isolated from three different natural sources. In each case the lineshape can be attributed to a ground-state doublet having two principal g-values below 2.0. The signals saturate easily at low temperatures and broaden rapidly at higher temperatures. This unusual form and behaviour of the spectra is now well understood in terms of the classic interpretation of Gibson and Thornley *et al.*,^{17,18} involving antiferromagnetic coupling between ferric and ferrous irons via two bridging sulphide ligands,

Figure 1.1.1. Typical EPR spectra for 2Fe-Fd_{red},

Figure 1.1.2. Model for the 2Fe-Fd centre.

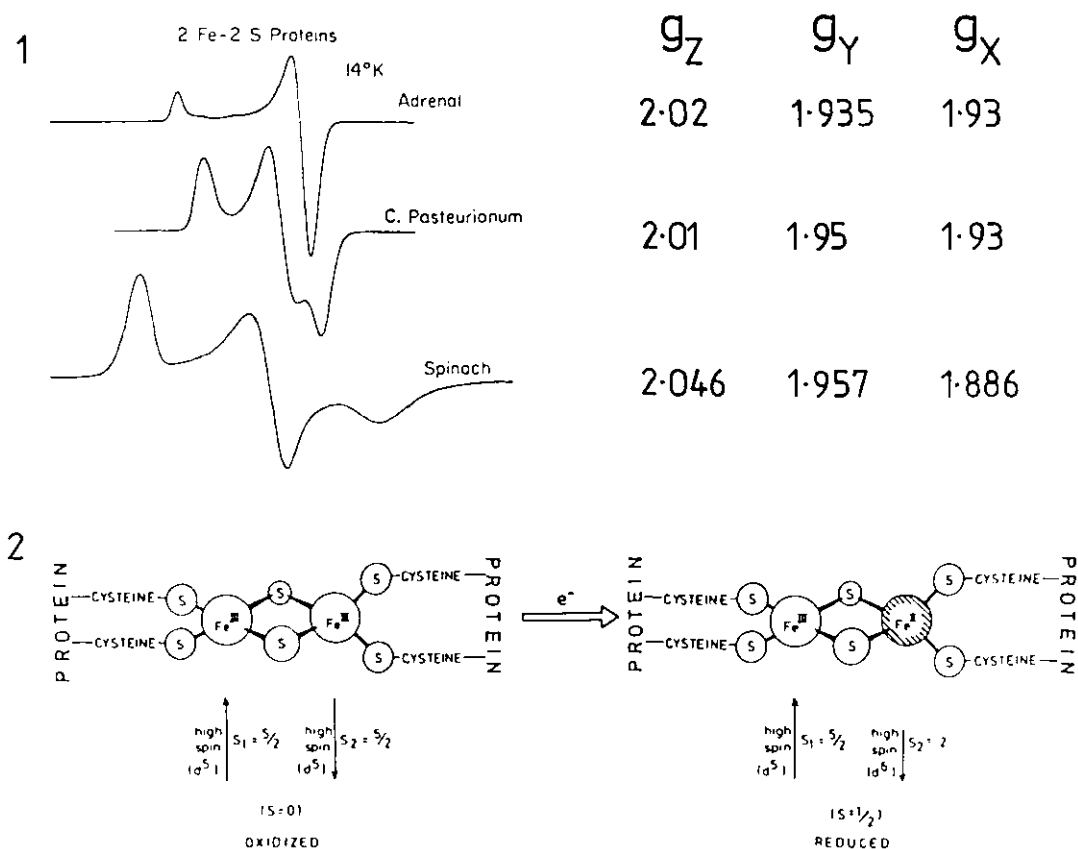


(Figure 1.1.2.). The appropriate spin Hamiltonian for such coupling of two different spins, S_1 and S_2 , is given in equation El.1; J is the exchange constant and takes by convention negative values for an

$$\hat{\mathcal{H}}_s = \beta H. (\underline{g}_1 \cdot \hat{S}_1 + \underline{g}_2 \cdot \hat{S}_2) - 2J\hat{S}_1 \cdot \hat{S}_2 \quad (\text{El.1})$$

antiferromagnetic interaction. Defining $\hat{S} = \hat{S}_1 + \hat{S}_2$, $\underline{g}\hat{S} = \underline{g}_1\hat{S}_1 + \underline{g}_2\hat{S}_2$ and rearranging gives equation El.2, and for ferric ($S_1 = 5/2$,

$$\underline{g} = \left(\frac{\hat{S}^2 + \hat{S}_1^2 - \hat{S}_2^2}{2\hat{S}^2} \right) \underline{g}_1 + \left(\frac{\hat{S}^2 - \hat{S}_1^2 + \hat{S}_2^2}{2\hat{S}^2} \right) \underline{g}_2 \quad (\text{El.2})$$

$\hat{S}_1^2 = 35/4$) and ferrous ($S_2 = 2$, $\hat{S}_2^2 = 24/4$) equation El.3.

$$\underline{g} = \frac{7}{3} \underline{g}_1 - \frac{4}{3} \underline{g}_2 \quad (\text{El.3})$$

Assuming tetrahedral sulphur coordination, a reasonable value for g_1 is 2.02, whilst for the ferrous ion admixture of two excited orbital states (d_{xz} and d_{yz}) into the ground state (d_{z^2}) can lead to its g_2 being considerably greater than 2.0 in the x and y directions. Thus, for the coupled pair, two g-values are expected to be below the free spin value (g_e).

The $J\hat{S}_1 \cdot \hat{S}_2$ Hamiltonian term results in spin states characterised by S ranging from $(S_1 - S_2)$ to $(S_1 + S_2)$ ($1/2, 3/2, 5/2, 7/2, 9/2$) at energies 0, $-3J$, $-8J$, $-15J$ and $-24J$. A two-phonon resonant relaxation process involving the higher spin states was postulated to explain the

anomalous temperature dependence of the EPR signal from the ground state.¹⁷ This interpretation was later demonstrated to be correct.¹⁹ The different temperature ranges over which broadening occurs for the various ferredoxins, can be understood in terms of variation in the strength of exchange coupling.

When both irons are ferric the anti-ferromagnetic coupling results in a singlet ground-state and hence the oxidised ferredoxin is found experimentally to be devoid of EPR.

The electronic model proposed by Gibson et al. has subsequently been amply borne out by experiments of many kinds. ENDOR and Mössbauer techniques demonstrate that the ferric and ferrous ions are indeed distinct, being non-equivalent.²⁰⁻²³ Coordination of the irons is considered to be tetrahedral, with the 2Fe2S unit ligated in general by four cysteinyl residues (Figure 1.1), as originally proposed by Brintzinger²⁴ et al. X-ray diffraction data for Spirulina platensis at 2.8 Å resolution confirms such a chelate structure.^{25,26}

1.2. 2Fe2S Ferredoxin Model Complexes: $[\text{Fe}_2\text{S}_2(\text{SR})_4]^{2-}$.

The first well-defined synthetic analogue of the oxidised form of 2Fe2S proteins was reported in 1973 by Holm and coworkers.²⁷ This involved coordination of a coupled 2Fe2S unit by two terminal o-xylyl- α - α' -dithiolate (S_2 -o-xylyl) ligands.

Whilst the synthesis of other alkyl-mercaptide coordinated 2Fe2S species has not yet been achieved, $[\text{Fe}_2\text{S}_2(\text{SC}_6\text{H}_4\text{Y})_4]^{2-}$, (Y = H, Me, Cl) complexes have been prepared by ligand substitution²⁸ or more recently by direct synthesis.²⁹ Two further species involving the same type of

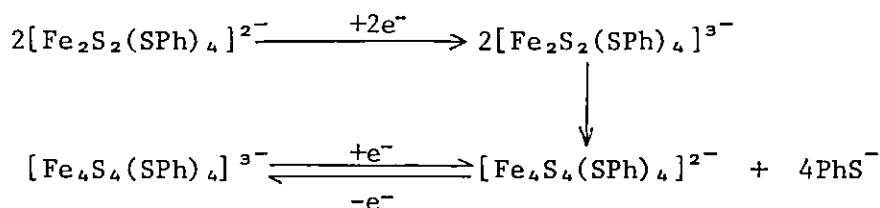
2Fe6S metal centre have been isolated: $[(\text{PhS})_2\text{FeS}_2\text{FeS}_2\text{MoS}_2]^{3-}$ ³⁰ and the novel $[\text{S}_5\text{FeS}_2\text{FeS}_5]^{2-}$.³¹ Iron-sulphur complexes with cysteine-containing synthetic peptides have been reported to show visible solution spectra comparable with $2\text{Fe-Fd}_{\text{ox}}$ but could not be isolated.³² Other potential 2Fe-Fd analogues have either been prepared only in solution and are consequently of indeterminate structure^{33,34} and refs. therein or involve decidedly non-physiological ligands.³⁵⁻³⁷

The $[\text{Fe}_2\text{S}_2(\text{SR})_4]^{2-}$ complexes, and in particular that involving the chelating o-xylyl ligand, have been extensively studied by Holm and his associates^{27,28,38} using X-ray crystallography, electronic spectroscopy, Mössbauer, magnetic susceptibility, NMR and voltammetry. Additionally, Teo and Shulman *et al.*³⁹ have made an EXAFS investigation comparing $[\text{Fe}_2\text{S}_2(\text{S}_2\text{-o-xylyl})_2]^{2-}$ with 2Fe-Fd , and a vibrational study for several of the complexes is reported in Section 4 of this thesis.

$[\text{Fe}_2\text{S}_2(\text{S}_2\text{-o-xylyl})_2]^{2-}$ is considered to be a suitable minimal structural and electronic representation of $2\text{Fe-Fd}_{\text{ox}}$ sites confirming the μ_2 -sulphido structure $[\text{Fe}_2\text{S}_2(\text{S-Cys})_4]$ proposed for the proteins.

From their discovery the ferredoxins have been characterised, when reduced, by the unusual EPR signal described in the previous section. Several model iron-complexes have been proposed on the grounds that they reproduce some feature of the Fd_{red} spectra.^{40-42,37,34,33} None of these are known to possess tetramercapto coordination of a coupled μ_2 -sulphido-diron unit. Reduction of $[\text{Fe}_2\text{S}_2(\text{S}_2\text{-o-xylyl})_2]^{2-}$ to a stable trianion species has on the other hand proven elusive,^{43,44} and thiol-extrusion of the metal centre of reduced spinach Fd yields mainly only the dianion.

This instability is in keeping with the quasi-reversibility of the reduction process as observed by cyclic voltammetry.²⁸ $[\text{Fe}_2\text{S}_2(\text{SR})_4]^{2-}$ itself is found to convert spontaneously in protic media to $[\text{Fe}_4\text{S}_4(\text{SR})_4]^{2-}$, and the non-redox process $[\text{Fe}_2\text{S}_2(\text{SR})_4]^{3-} \rightarrow [\text{Fe}_4\text{S}_4(\text{SR})_4]^{2-}$ involving reactant ($2[\text{Fe}_2\text{S}_2]^{1+}$) and product ($[\text{Fe}_4\text{S}_4]^{2+}$) cores in the same oxidation level is facile even in aprotic solvents. Thus, prolonged electrolysis of dimer dianion solutions at a potential above that for the first one-electron reduction yields $[\text{Fe}_4\text{S}_4(\text{SR})_4]^{3-}$ from further reduction of the initially formed tetramer dianion⁴⁵:-

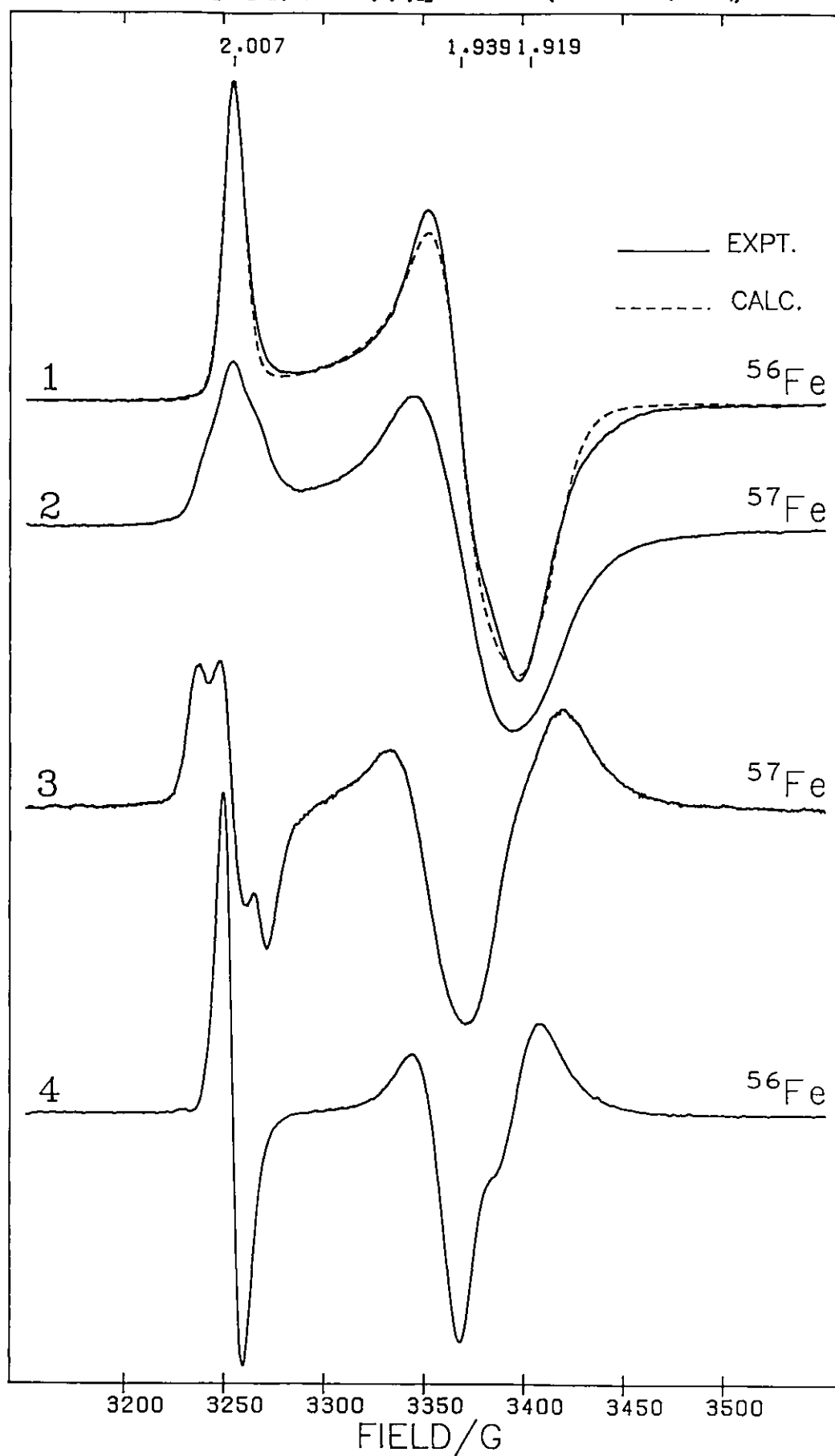


In this present work it has been found that chemical reduction of $[\text{Fe}_2\text{S}_2(\text{SR})_4]^{2-}$, followed by the rapid quenching of further reactions with low temperature solvent glassification, enables EPR signals of the dimer trianion to be observed.

1.3. $[\text{Fe}_2\text{S}_2(\text{S}_2\text{-o-xylyl})_2]^{3-}$.

1.3.1. EPR.

Figure 1.2 shows the first (1.2.1) and second (1.2.4) derivative EPR signals for a sample resulting from the reduction of a DMF solution of $[\text{Fe}_2\text{S}_2(\text{S}_2\text{-o-xylyl})_2]^{2-}$ with just over one equivalent of acenaphthylenide radical anion ($\text{ACN}^{\cdot-}$). $n\text{-Bu}_4\text{NClO}_4$ (0.1 M) has been added to the solution to increase the solubility of the iron complex and to ensure

Fig. 1. 2 EPR of $[\text{Fe}_2\text{S}_2(\text{S}_2\text{-o-xylyl})_2]^{2-}$ in DMF(0.1M $n\text{Bu}_4\text{NClO}_4$) at 100K

glassification on freezing. Similar spectra are obtained when, for example, CH_2Cl_2 ($\sim 2\text{M}$), H_2O ($\sim 2\text{M}$) or DMSO (50/50) is added in order to obtain a vitreous sample. A non-glassy sample results from the use of pure DMF, and the EPR spectrum then has a larger linewidth. Comparable lineshapes are found when pure DMSO is used as solvent (Figure 1.3.1). These non-vitreous samples demonstrate a reversible broadening of the signal in the temperature range 100 — 200 K (Figure 1.3.1-2).

At liquid nitrogen temperatures the signals are only slightly power saturated at 200 mW, on the instrument used, as can be seen from Figure 1.4. Spectra measured at ~ 12 K show very similar lineshapes to those observed at 100 K but could easily be extensively saturated at powers above 0.2 mW.

The g -values measured from these spectra at maximum, crossover and minimum are 2.007, 1.940 and 1.922. These are invariant to ± 0.001 for the various solvent systems used. Simulation of the lineshape does not lead to significantly different values; neither can this technique be considered more accurate in view of the difficulty in fitting the high field part of the spectrum. On the whole, low temperature spectra are better simulated with a Gaussian rather than Lorentzian lineshape; however, neither is entirely adequate, and it has been found necessary to use a convolution of these two functions to get acceptable results.

The least-squares fitted calculated lines in Figures 1.2.1 and 1.3.1 result from the use of such a mixed Gaussian-Lorentzian convolution product. Despite giving, as might be anticipated, a closer match to the experimental

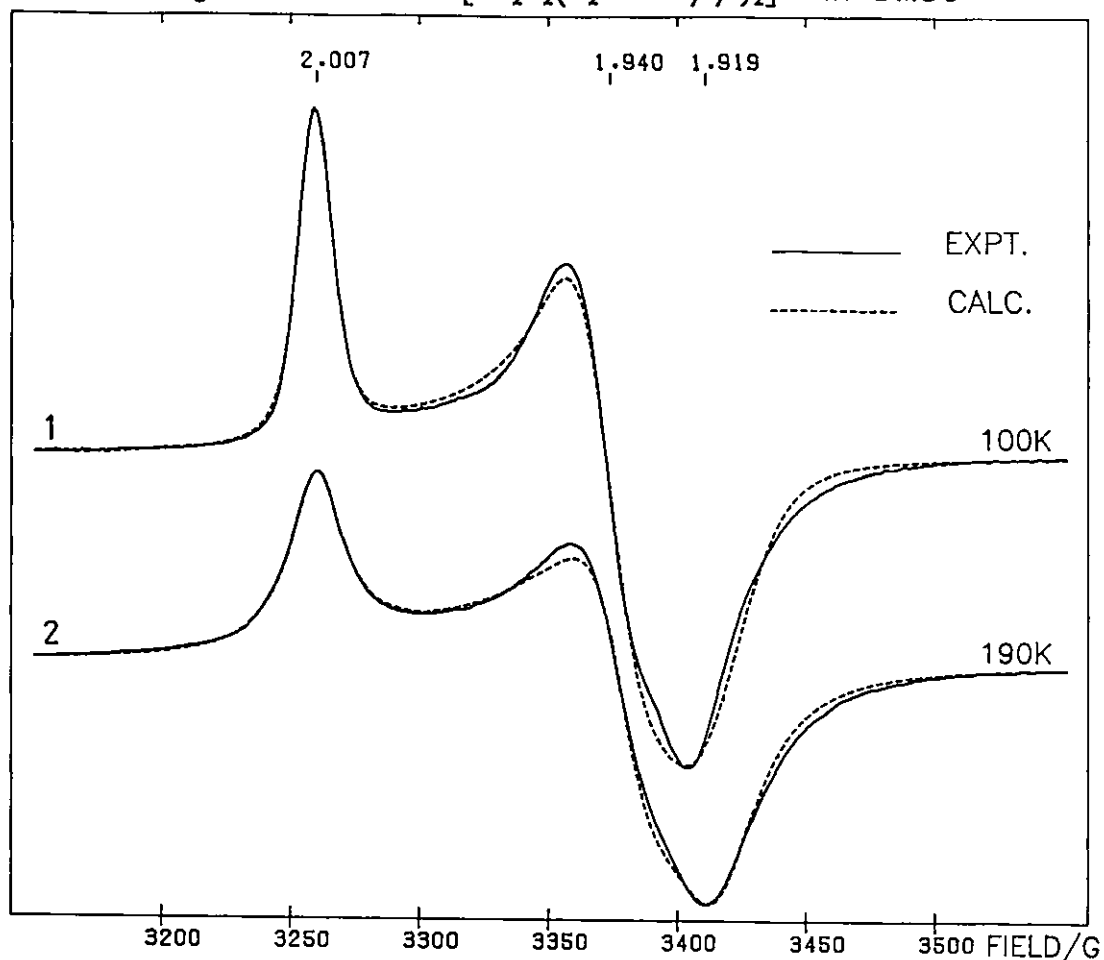
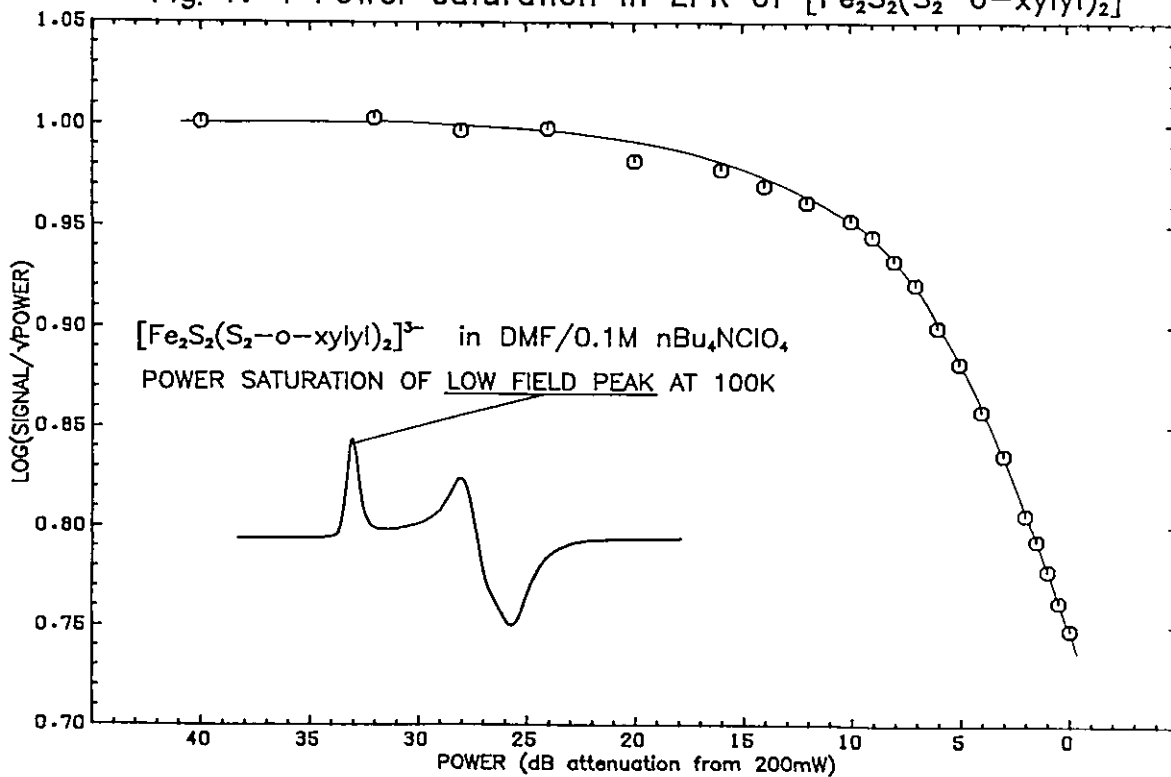
Fig. 1. 3 EPR of $[\text{Fe}_2\text{S}_2(\text{S}_2\text{-o-xylyl})_2]^{3-}$ in DMSOFig. 1. 4 Power saturation in EPR of $[\text{Fe}_2\text{S}_2(\text{S}_2\text{-o-xylyl})_2]^{3-}$ 

TABLE 1.1. EPR Parameters for $[\text{Fe}_2\text{S}_2(\text{S}_2\text{-o-xylyl})_2]^{3-}$.

DMF, 0.1 M n-Bu₄NCIO₄ (Figure 1.2.1).

Measured	2.007	1.940	1.922
Pure Gaussian (F = 1.9)	2.0064	1.939	1.919
Gaussian widths (G)	6.7	14.1	16.7
Pure Lorentzian (F = 2.5)	2.0065	1.939	1.920
Lorentzian widths (G)	6.2	11.5	14.0
Lorentz-Gaussian (F = 1.4)	2.0065	1.939	1.919
Lorentzian widths (G)	1.5	3.2	4.2
Gaussian widths (G)	5.5	12.4	14.2

DMSO (Figure 1.3)

100 K

Measured	2.008	1.940	1.923
Lorentz-Gaussian	2.0077	1.940	1.919
Lorentzian widths (G)	4.0	9.1	9.8
Gaussian widths (G)	5.8	10.2	14.2

190 K

Pure Lorentzian	2.008	1.937	1.916
Lorentzian widths (G)	12.4	18.1	20.5

F = least squares fitting parameter.

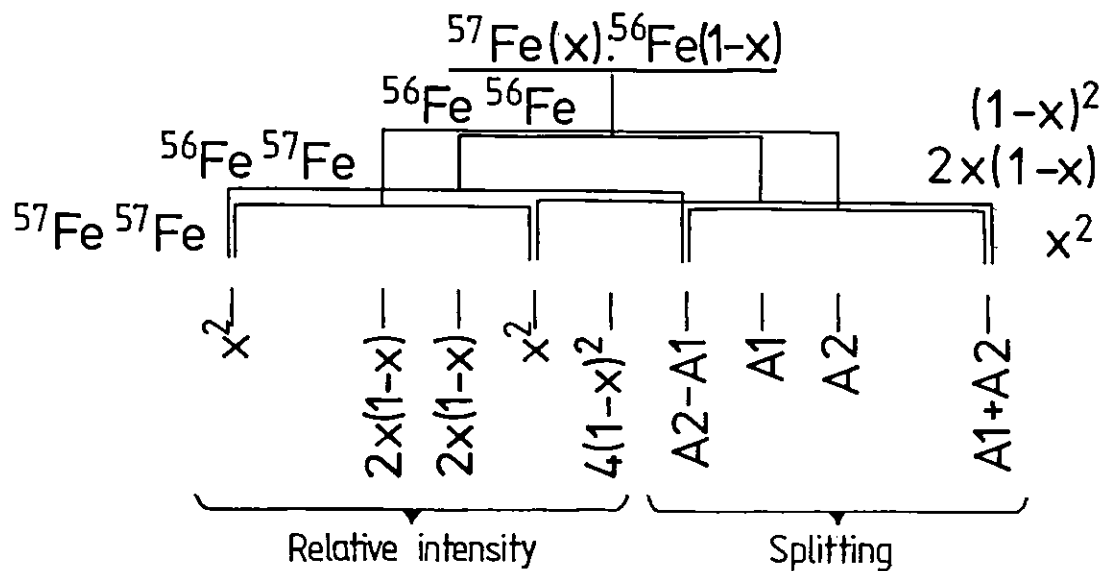
spectrum, even this simulation method also proves inadequate at high field. Details of measured and fitted parameters are given in Table 1.1.

For EPR signals obtained by chemical reduction at low temperatures in DMF, comparison of doubly-integrated intensities with a Cu(II) EDTA standard indicates 60 to 80% yield of trianion in the majority of reductions. The signal intensities of such solutions, measured at 100 K, were observed to have decayed completely after 2 to 3 minutes at 20°C. At -50°C on the other hand, solutions ca. 0.5 mM in $[\text{Fe}_2\text{S}_2(\text{S}_2\text{-o-xylyl})_2]^{3-}$ have greatly increased stability such that the EPR signal intensity measured at 100 K decreases only slightly over a period of a few hours in the strict absence of molecular oxygen. For these reasons reactions effected in DMSO led to only ca. 20% yield of trianion as they must be performed above the solvent freezing point of +18°C.

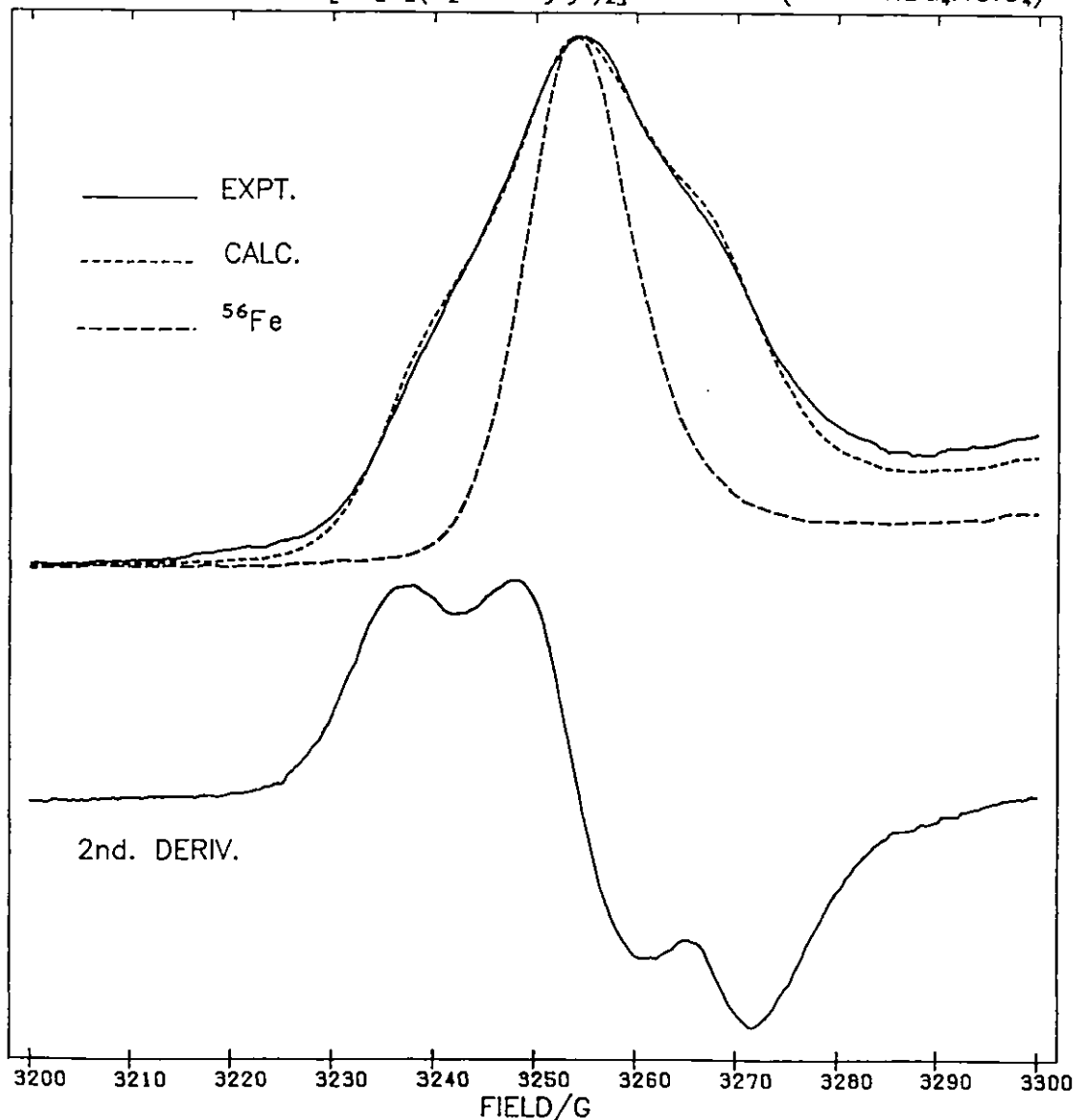
1.3.2. ^{57}Fe EPR.

^{57}Fe enriched (83%) $[\text{Fe}_2\text{S}_2(\text{S}_2\text{-o-xylyl})_2]^{2-}$ prepared on a small scale and reduced in DMF with $\text{ACN}^{\cdot-}$ gives the EPR signal shown in Figure 1.2.2. Whilst to high field only an overall broadening results from ^{57}Fe enrichment, for the low field peak side shoulders are apparent and a splitting is seen quite clearly in the second-derivative lineshape (Figure 1.2.3). With the level of isotopic enrichment employed the spectrum resulting from a spin-coupled ferric-ferrous dimer is expected to possess three component spectra. For parity of nuclear hyperfine interaction from the iron sites, the majority of the sample (69%),

Fig 1.5 ^{57}Fe hyperfine splitting at low field in the EPR of $[\text{Fe}_2\text{S}_2(\text{S}_2\text{-o-xylyl})_2]^{3-}$



83% ^{57}Fe enriched $[\text{Fe}_2\text{S}_2(\text{S}_2\text{-o-xylyl})_2]^{3-}$ in DMF(0.1M $n\text{Bu}_4\text{NClO}_4$)



containing two ^{57}Fe ions, will give rise to a 1:2:1 triplet for the low field peak.⁴⁶ The substantial proportion of mixed $^{56}\text{Fe}/^{57}\text{Fe}$ dimers (28%) will result in a splitting to a doublet and the remaining small fraction will appear similar to the unenriched spectrum. By field-shifting the spectrum for the natural abundance ^{56}Fe sample with the ^{57}Fe hyperfine splitting, and adding component spectra according to the expected statistical distribution for the three isotopic mixtures it is possible to obtain a reasonable fit to the low field peak of the ^{57}Fe enriched spectral lineshape. A least squares fitting procedure leads to an estimated hyperfine splitting of 14 G. If the splittings produced by ferric and ferrous sites are allowed to be inequivalent, values of 15.2 G and 13.5 G achieve the best fit (Figure 1.5). The splitting, assuming equivalent hyperfine interactions, is quite compatible with the 14 G obtained for Putidaredoxin⁴⁷ and spinach ferredoxin⁴⁸ by a similar method, or the 15 G found for parsley ferredoxin.⁴⁹ ENDOR measurements for several 2Fe2S proteins have indicated effective splittings of around 12-13 G and 14-15 G along the hyperfine tensor z-axis for ferrous and ferric sites respectively.^{20,50}

1.3.3. Mössbauer of $[\text{Fe}_2\text{S}_2(\text{S}_2\text{-o-xylyl})_2]^{2-}$, $^{3-}$.*

The synthesis of a ^{57}Fe enriched sample of $[\text{Fe}_2\text{S}_2(\text{S}_2\text{-o-xylyl})_2]^{2-}$ has enabled the measurement of solution Mössbauer spectra for this compound. Previously only the solid has been studied due to its limited solubility leading to very poor signal to noise ratio for solutions with natural abundance in ^{57}Fe .

* I gladly acknowledge and thank Dr. J.D. Rush and Professor C.E. Johnson (Oliver Lodge Laboratory, Liverpool University) for obtaining and parameterising the Mössbauer measurements described and discussed in this section.

1.3.3.1. Mössbauer for the Dianion.

Figure 1.6 shows low temperature spectra for a DMF solution in zero applied field and with fields of 3, 6 and 10 T applied perpendicular to the γ -ray beam. Temperature independence is demonstrated by the similarity of the zero-field spectrum obtained at 77 K to that at 4.2 K.

The Mössbauer spectra of the dianion may be characterised by 1:1 addition of two spectra having slightly different quadrupole splittings but which are otherwise identical. The absence of an observable hyperfine field is in keeping with the diamagnetism of the compound, resulting from the anti-ferromagnetic coupling between the two ferric ions.

Table 1.2 lists the parameters used to obtain best least-squares fit of spin-Hamiltonian calculated spectra to the experimental results. The

TABLE 1.2. Parameters Used to Fit Mössbauer Spectra of $[\text{Fe}_2\text{S}_2(\text{S}_2\text{-o-xylyl})_2]^{2-}$ in DMF at 4.2 K.

Perpendicular Field	Site	Isomer shift (δ) mm/s rel. Fe metal	Full Linewidth (Γ) Lorentz (mm/s)	β
0T	1	0.27	0.31	-
	2	0.27		
3T	1	0.26	0.30	0.5
	2	0.28		0.5
6T	1	0.27	0.29	0.48
	2	0.31		0.75
10T	1	0.26	0.30	0.64
	2	0.31		0.67
Generalised parameters	1	0.27	0.30	0.6
	2	0.29		

Quadrupole splitting } site 1 = 0.4
 ΔE_Q (mm/s) } site 2 = 0.57

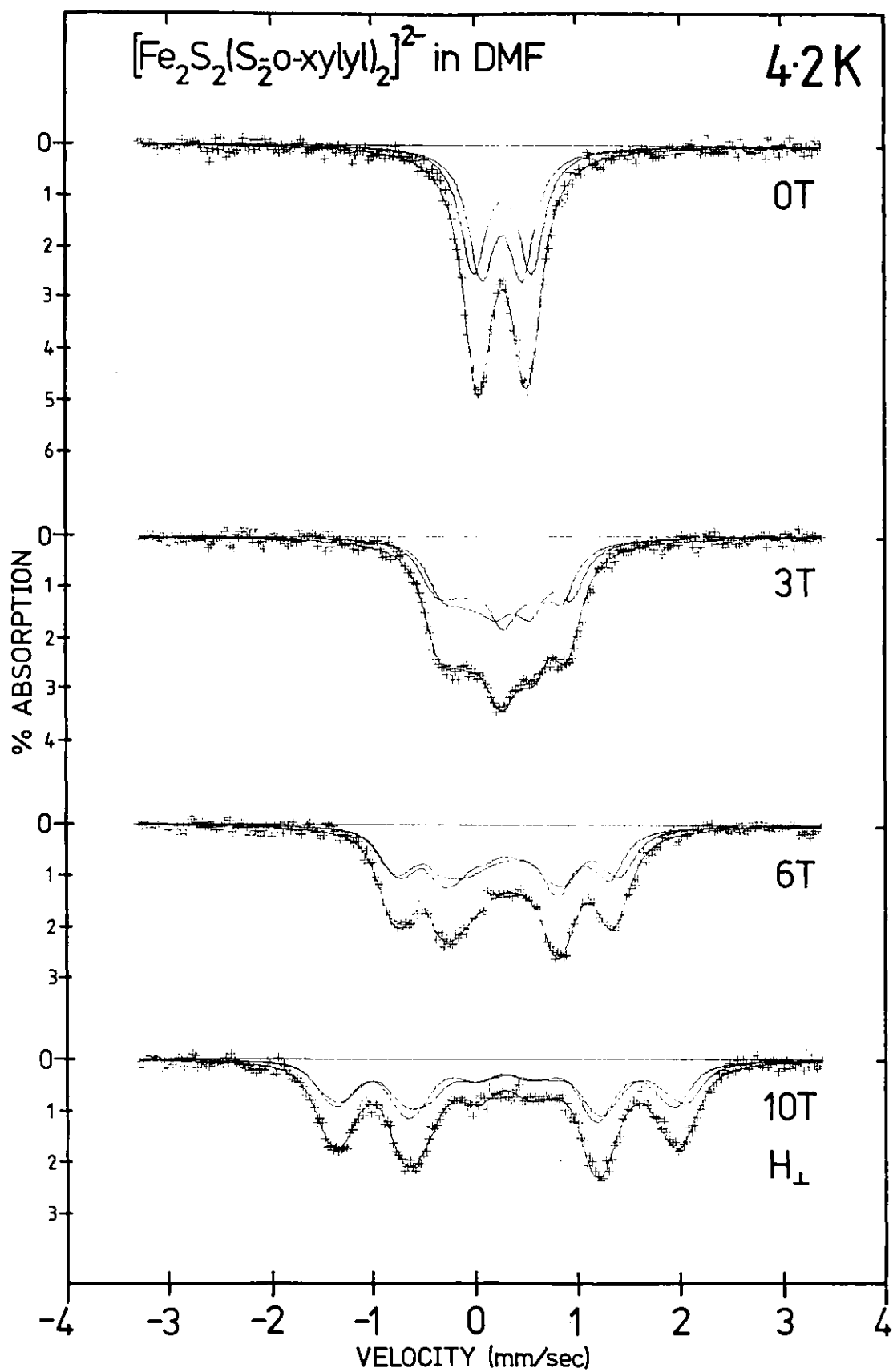


Fig 1.6 Mössbauer spectra of $[\text{Fe}_2\text{S}_2(\text{S}_2\text{-o-xylyl})_2]^{2-}$ in DMF

inequivalence in the quadrupole splittings for the two ferric sites is revealed in the zero-field spectrum in that the linewidth is rather larger than the instrumental linewidth. Oxidised-ferredoxin spectra also show slight inequivalence for the two irons. Table 1.3 collects some Mössbauer data obtained from simulation of spectra for several $2\text{Fe-Fd}_{\text{ox}}$ and also for solid $[\text{Fe}_2\text{S}_2(\text{SR})_4]^{2-}$ salts. The solution results for the model complex compare quite favourably with those for the proteins, although the quadrupole splitting is observed to be somewhat lower than in the proteins.

TABLE 1.3. Mössbauer Spectral Parameters for $2\text{Fe-Fd}_{\text{ox}}$ and $[\text{Fe}_2\text{S}_2(\text{SR})_4]^{2-}$ Salts at 4.2 K.

	δ (mm/s)	ΔE_Q (mm/s)	ξ
Adrenodoxin ⁵¹	0.285	0.622	
Euglena ⁵²	0.22	0.65	
Scenedesmus ⁵³	0.20	0.60	
Putidaredoxin ⁵⁴	0.27	0.602	0.42
Spinach ²²	0.27	0.65	0.5
Parsley ²²	0.28	0.66	0.5
Clostridial ²²	0.28	0.62	0.5
Azotobacter I ²²	0.31	0.73	0.5
Azotobacter II ²²	0.29	0.71	0.5
Synechococcus ⁵⁰	0.22	0.55 & 0.83	0.5
Halobacterium ⁵⁵	0.25 & 0.29	0.47 & 0.87	
$[\text{Et}_4\text{N}]_2[\text{Fe}_2\text{S}_2(\text{S}_2\text{-o-xylyl})_2]^{38}$	0.17	0.36	
$[\text{Et}_4\text{N}]_2[\text{Fe}_2\text{S}_2(\text{SPh})_4]^{38}$	0.17	0.32	
$\text{Et}_4\text{N}[\text{Fe}(\text{S}_2\text{-o-xylyl})_2]^{56}$	0.13	0.57	

It is interesting to note the difference between the parameters for the frozen solution spectra and those for Et_4N^+ and Ph_4As^+ salts, where there is rigorous equivalence between the two iron atoms.^{27,38} The increased quadrupole splitting may be interpreted as indicating a lowering of symmetry in frozen DMF compared to the crystalline solid. Solution Raman spectra for this anion show bands in close agreement with solid state spectra, however, the reflectance spectrum for powdered $[\text{Et}_4\text{N}]_2[\text{Fe}_2\text{S}_2(\text{S}_2\text{-o-xylyl})_2]$ shows significant differences from visible spectra recorded for solutions (Section 4). The isomer shift measured for $[\text{Fe}_2\text{S}_2(\text{S}_2\text{-o-xylyl})_2]^{2-}$ in solution is more in keeping with values obtained for $2\text{Fe-Fd}_{\text{ox}}$ than is the value obtained for the solid. Hoggins and Steinfink⁵⁷ have given empirical equations relating Fe-S bond distances and δ for tetrahedral sulphur coordination; $V = 178.2 \sum (R_i)^{-6.81}$, $\delta = 1.4 - 0.4 V$ (relative to Fe metal) where V is the valence and R_i bond length in \AA . Application of these equations to $[\text{Et}_4\text{N}]_2[\text{Fe}_4\text{S}_4(\text{SCH}_2\text{Ph})_4]$ ⁵⁸ leads to $\langle\delta\rangle = 0.345$ mm/s in excellent agreement with the observed 0.34 mm/s.⁵⁹ Using the crystal structure bond-lengths for $[\text{Et}_4\text{N}]_2[\text{Fe}_2\text{S}_2(\text{S}_2\text{-o-xylyl})_2]$, V is calculated to be 2.83 and $\delta = 0.27$ mm/s. Thus, according to the empirical bonding relationships the solid state stereochemical data indicate an isomer shift corresponding to the values found in frozen solution and in Fd_{ox} rather than in the solid.

1.3.3.2. Mössbauer for the Trianion.

Figure 1.7 compares the zero-field Mössbauer spectra for ^{57}Fe -enriched $[\text{Fe}_2\text{S}_2(\text{S}_2\text{-o-xylyl})_2]^{2-}$ in DMF with a chemically reduced sample measured in a small magnetic field, sufficient to decouple electron and nuclear

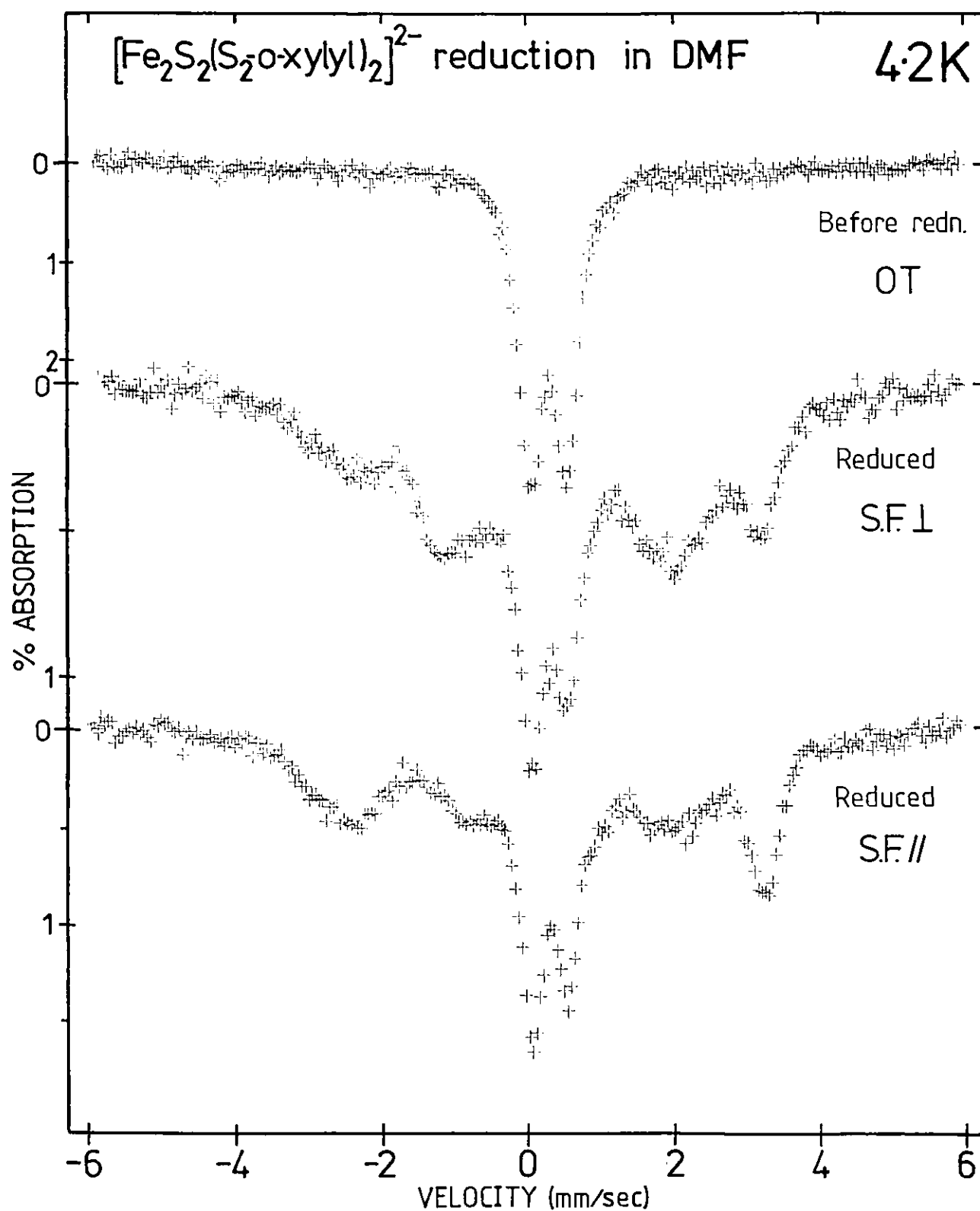
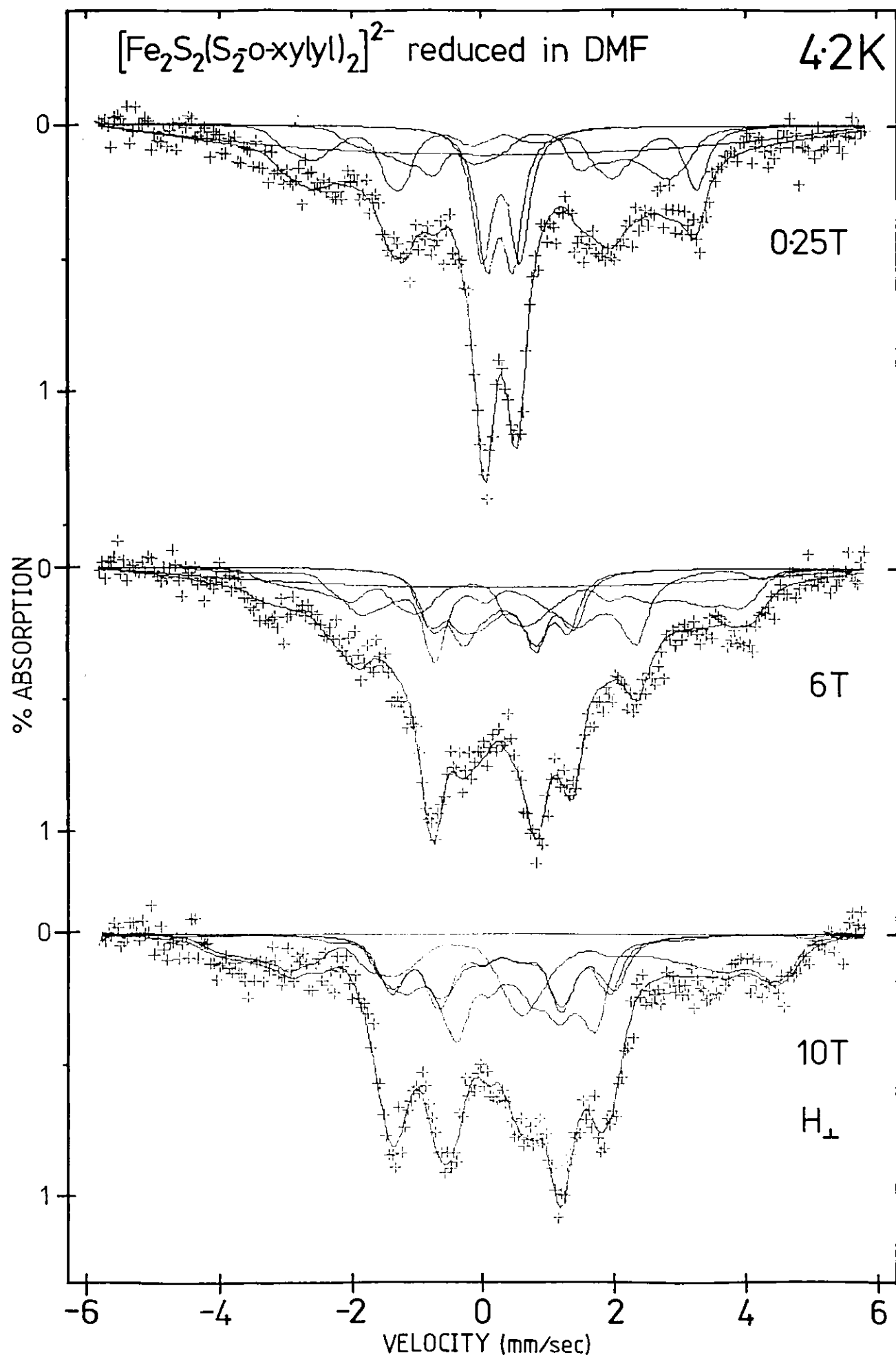


FIG. 17 Mössbauer spectra of $[\text{Fe}_2\text{S}_2(\text{S}_2\text{-o-xylyl})_2]^{2-}$ and its reduction product. (SF = Small Field).

spins, applied perpendicular and then parallel to the γ -ray beam. The latter spectra show clearly the presence of a paramagnetic species together with some dianion. The effect of applying a stronger perpendicular field of up to 10 T is shown in Figure 1.8. These spectra may be fitted quite well by a procedure involving addition of calculated spectra corresponding to an anti-ferromagnetically coupled ferric-ferrous pair, together with a proportion of the diferric species as simulated in the prereduced state. Parameters for the $[\text{Fe}_2\text{S}_2(\text{S}_2\text{-o-xylyl})_2]^{3-}$ reduced ferredoxin analogue are given in Table 1.4.

TABLE 1.4. Parameters Used to Fit Mössbauer Spectra of $[\text{Fe}_2\text{S}_2(\text{S}_2\text{-o-xylyl})_2]^{3-}$ in DMF at 4.2 K.

H_{\perp}	0.25 T		6 T		10 T		Generalised	
Site	Fe^{3+}	Fe^{2+}	Fe^{3+}	Fe^{2+}	Fe^{3+}	Fe^{2+}	Fe^{3+}	Fe^{2+}
δ (mm/s)	0.33	0.76	0.33	0.71	0.29	0.60	0.33	0.7
ΔE_Q (mm/s)	-0.8	2.8	-0.67	2.93	-0.67	3.22	-0.7	3.0
Γ_{full} (mm/s)	0.31		0.32		0.31		0.31	
\wp	0.7	0.35	0.6	0.3	0.65	0.35	0.65	0.35
A_x' (MHz)	-53.7	13.4	-58.8	12.4	-56.8	10.3	-55	11
A_y' (MHz)	-46.5	5.16	-42.3	8.26	-43.4	8.26	-45	8
A_z' (MHz)	-49.6	33.0	-49.6	39.2	-52.6	39.2	-50	39
A_x' (G)	-20.0	4.98	-21.9	4.61	-21.1	3.83	-20	4
A_y' (G)	-17.1	1.90	-15.6	3.04	-16.0	3.04	-16	3
A_z' (G)	-17.7	11.7	-17.7	14.0	-18.7	14.0	-18	14
% dianion	42%		40%		40%		40%	

FIG. 1.8 Mössbauer spectra of reduced $[\text{Fe}_2\text{S}_2(\text{S}_2\text{-o-xylyl})_2]^{2-}$.

The separation of the lines in the Mössbauer spectrum for a given site is proportional to the effective hyperfine field. The sign of the hyperfine field may be deduced by observing whether the splitting in the spectrum increases or decreases with increased applied field. Analysis of the Mössbauer spectra in Figure 1.8 in terms of the calculated lineshapes shown, demonstrates that the paramagnetic species has one site with a conventional negative hyperfine field and one with a positive hyperfine field. Disregarding the two nearly superimposed calculated lines from the dianionic species, of the remaining two lines, one has peaks which split further apart at high applied field whilst the other has somewhat sharper peaks which close together. These latter two calculated spectra may be assigned to ferrous and ferric ions respectively, antiferromagnetically coupled. Considering the case in which the coupled electron spin ($S_z = 1/2$) is aligned with the applied field, the ferric spin ($S_z = 5/2$) will also be aligned whilst the ferrous spin ($S_z = 2$) will be directed anti-parallel to the external field. Since for each ion the nuclear magnetic moment is in opposition to the hyperfine field which it experiences from the atom's electron spin, the hyperfine interaction for the ferric is observed negative, and for the ferrous positive, with respect to the external field. For the excited electronic spin-state the signs are of course reversed, but at low temperatures and large applied fields the population of the $S_z = 1/2$ state is small relative to that with $S_z = -1/2$.

Thus, the Mössbauer results for reduced $[\text{Fe}_2\text{S}_2(\text{S}_2\text{-o-xylyl})_2]^{2-}$ confirm the EPR results by demonstrating the presence of an antiferromagnetically coupled ferric-ferrous dimer. The Mössbauer behaviour is

typical of $2\text{Fe-Fd}_{\text{red}}$ proteins. Table 1.5 lists parameters derived for several proteins. Corresponding values for the reduced analogue dimer compare reasonably well with these.

TABLE 1.5. Mössbauer Spectral Parameters for $2\text{Fe Fd}_{\text{red}}$ at 4.2 K.

$2\text{Fe Fd}_{\text{red}}$	δ (mm/s)	ΔE_Q (mm/s)	η	A_x'	A_y'	A_z' (MHz)	
Putidaredoxin ⁵⁴	Fe^{3+}	+0.6		-56	-50	-43	
	Fe^{2+}	-2.7		14	21	35	
Parsley ²²	Fe^{3+}	0.25	+0.68	-0.9	-51	-46.2	-42
	Fe^{2+}	0.54	-3.00	0	11.2	14	33.6
Spinach ²²	Fe^{3+}	0.25	+0.64	-0.6	-51	-49.1	-42
	Fe^{2+}	0.54	-3.00	0	11.1	16.8	35.3
Scenedesmus ⁵³	Fe^{3+}	0.22	0.59				
	Fe^{2+}	0.56	2.57				
Synechococcus ⁵⁰	Fe^{3+}	0.15	0.60	-0.3	-51.6	-50.0	-42.0
	Fe^{2+}	0.42	-3.20	0	13.0	15.0	36.5
Halobacterium ⁵⁵ at 200 K	Fe^{3+}	0.30	0.60				
	Fe^{2+}	0.55	2.64				
Adrenodoxin ²² at 250 K	Fe^{3+}	0.28	0.81				
	Fe^{2+}	0.54	2.72				

The average values of the A tensors for the two sites in the analogue are, like those found for the proteins, considerably smaller than the value expected for an ionic iron compound. This implies a high degree of 3d electron delocalisation. Furthermore, the ferric site A tensor exhibits a far larger anisotropy than expected for an S-state ion under a crystal field approximation.

The effective hyperfine interaction along the z-axis for the ferrous site in $[\text{Fe}_2\text{S}_2(\text{S}_2\text{-o-xylyl})_2]^{3-}$ is in good agreement with the estimated splitting of ~ 14 G for the g_z EPR peak. The z-axis value for the ferric hyperfine at the electron is somewhat larger than the maximum of 15.2 G obtained from fitting the EPR assuming inequivalent sites, but is in reasonable agreement considering an estimated evaluation error of ± 1 G and the assumption necessary with regard to alignment of the \underline{g} and \underline{A} tensor axes. Bertrand and Gayda⁶⁰ have attempted to correlate principal axis $A(=3/4 \cdot A')$ tensor components for the ferrous sites of several $2\text{Fe Fd}_{\text{red}}$ with the extent of rhombic distortion at this ion as measured by $(g_y - g_x)$ (see Section 1.5.1 for a more detailed description of the distortion parameter). The z-axis value for $[\text{Fe}_2\text{S}_2(\text{S}_2\text{-o-xylyl})_2]^{3-}$ agrees well with this analysis, but the x and y axis hyperfine components are found to be rather smaller than predicted.

For Mössbauer spectra measured with magnetic fields applied parallel to the γ -ray beam there is evidence for a small amount of absorption in addition to that from dianion and trianion dimers (around +2 and -1 mm/s in the lowest spectrum of Figure 1.7). The species causing this appears paramagnetic and presumably results from decomposition or further reaction of the $[\text{Fe}_2\text{S}_2(\text{S}_2\text{-o-xylyl})_2]^{3-}$. A sample deliberately thawed and held at room temperature for several minutes showed a radically different low temperature Mössbauer spectrum, but this could not readily be interpreted in terms of any likely product, such as a tetrameric iron-sulphur cluster. Alternatively, the additional absorption in the parallel field spectra could genuinely arise from the trianion if for example, the effective field at the iron nuclei is not parallel to the applied field.

The estimate from the Mössbauer of a 6:4 ratio of trianion to dianion dimer in the sample studied falls at the low end of the percentage yield estimated from integration of EPR spectra (60 to 80%). Only two Mössbauer samples of reduced dimer have been studied in this work and the percentage yield result is in consequence less representative than that from EPR. The other Mössbauer sample showed, by visual inspection of the small-field spectra, a higher proportion of trianion but also a somewhat larger amount of the signal described above as impurity. In view of the stability of the trianion at low temperature it seems likely that a more sophisticated preparation and sample transfer technique might lead to purer trianion Mössbauer spectra.

1.3.4. Addendum.

Subsequent to the writing of this report Mascharak et al. [J. Amer. Chem. Soc., 103, 6110 (1981)] have described an EPR lineshape attributed to $[\text{Fe}_2\text{S}_2(\text{S}_2\text{-o-xylyl})_2]^{3-}$ in 7:3 v/v acetonitrile/hexamethylphosphoramide which is very similar to that presented in Figure 1.2.1, and which has comparable g-value extrema. Due to the improved solubility of the salt used by these authors the concentration of $[\text{Fe}_2\text{S}_2(\text{S}_2\text{-o-xylyl})_2]^{3-}$ attained prior to reduction was some twenty times that employed here. They have used reduction reaction times of the order 0.5 to 4.5 hrs. which are surprisingly long in view of the instability found in this work for the trianion in DMF or DMSO. Indeed, they report substantial impurities in their EPR spectra, in particular a strong feature at $g \approx 4.3$ which was not observed in the measurements in this present work. A crude calculation allowing for the different spectrometer conditions used indicates that their 80 K EPR spectrum of $[\text{Fe}_2\text{S}_2(\text{S}_2\text{-o-xylyl})_2]^{3-}$ represents less than 1% of the total iron present in the solution being measured, compared with the 60 to 80% observed here.

The major difference between the measurements reported here and those of Mascharak et al. is, however, in the Mössbauer spectra. After a 4.5 hr reduction of $[\text{Fe}_2\text{S}_2(\text{S}_2\text{-o-xylyl})_2]^{2-}$, the latter authors have assigned two quadrupole doublets having $\delta = 0.19$ mm/s, $\Delta E_Q = 0.54$ mm/s and $\delta = 0.60$ mm/s, $\Delta E_Q = 3.06$ mm/s to ferric and ferrous respectively in $[\text{Fe}_2\text{S}_2(\text{S}_2\text{-o-xylyl})_2]^{3-}$ at 4.2 K. The absence of magnetic hyperfine interaction in these spectral features implies that the electron spin on the trianion is relaxing extremely rapidly. EPR on the other hand, demonstrates that the electron spin of $[\text{Fe}_2\text{S}_2(\text{S}_2\text{-o-xylyl})_2]^{3-}$ is not

relaxing fast even at 100 K (see Section 2). Even the most rapidly relaxing reduced ferredoxins, for which the EPR spectra are substantially broadened and diminished at 100 K, show hyperfine interaction in their 4 K Mössbauer spectra. The Mössbauer spectra reported in this present work are, however, entirely compatible with the EPR measurements and compare favourably with the behaviour of reduced ferredoxins.

1.4. Reduced $[\text{Fe}_2\text{S}_2(\text{SC}_6\text{H}_4\text{Y})_4]^{2-}$, (Y = Cl, H, Me).

1.4.1. Effect of Solvent Vitrification.

Figure 1.9 shows spectra obtained for the three $[\text{Fe}_2\text{S}_2(\text{SC}_6\text{H}_4\text{Y})_4]^{2-}$ (Cl, H, Me) complexes after reduction in N-methylpyrrolidinone (NMP). The first spectrum in each group (1, 4 and 7) results from using pure dry solvent, the second (2, 5 and 8) from solutions 0.1 to 0.2 M in n-Bu₄NClO₄ frozen as transparent glasses, and the last spectrum in each group is derived from the one above following devitrification of the sample (see later). Corresponding sets of spectra for DMF solvent are given in Figure 1.10 and relevant g-values are collected in Table 1.6.

1.4.1.1. Spectral Types and Simulations.

The three basis spectral types responsible for the lineshapes in Figures 1.9 and 1.10 are exemplified in the larger scale diagram, Figure 1.11, which also shows attempted simulations. For purposes of simplifying description and discussion these three types will be referred to as (1) "N-type" (narrow), (2) "W-type" (wide) and (3) "VW-type" (very wide); the narrow-wide description referring to spectral anisotropy. Spectra for vitreous samples are best simulated assuming a Gaussian convolution lineshape. The non-vitreous samples on the other hand give spectra more closely approaching Lorentzian. This may be indicative of dipolar broadening in the latter samples due to increased magnetic concentration as a consequence of exclusion of the reduced dimer from the DMF crystal lattice. In all the spectra it proved difficult to obtain a good fit around g_x .

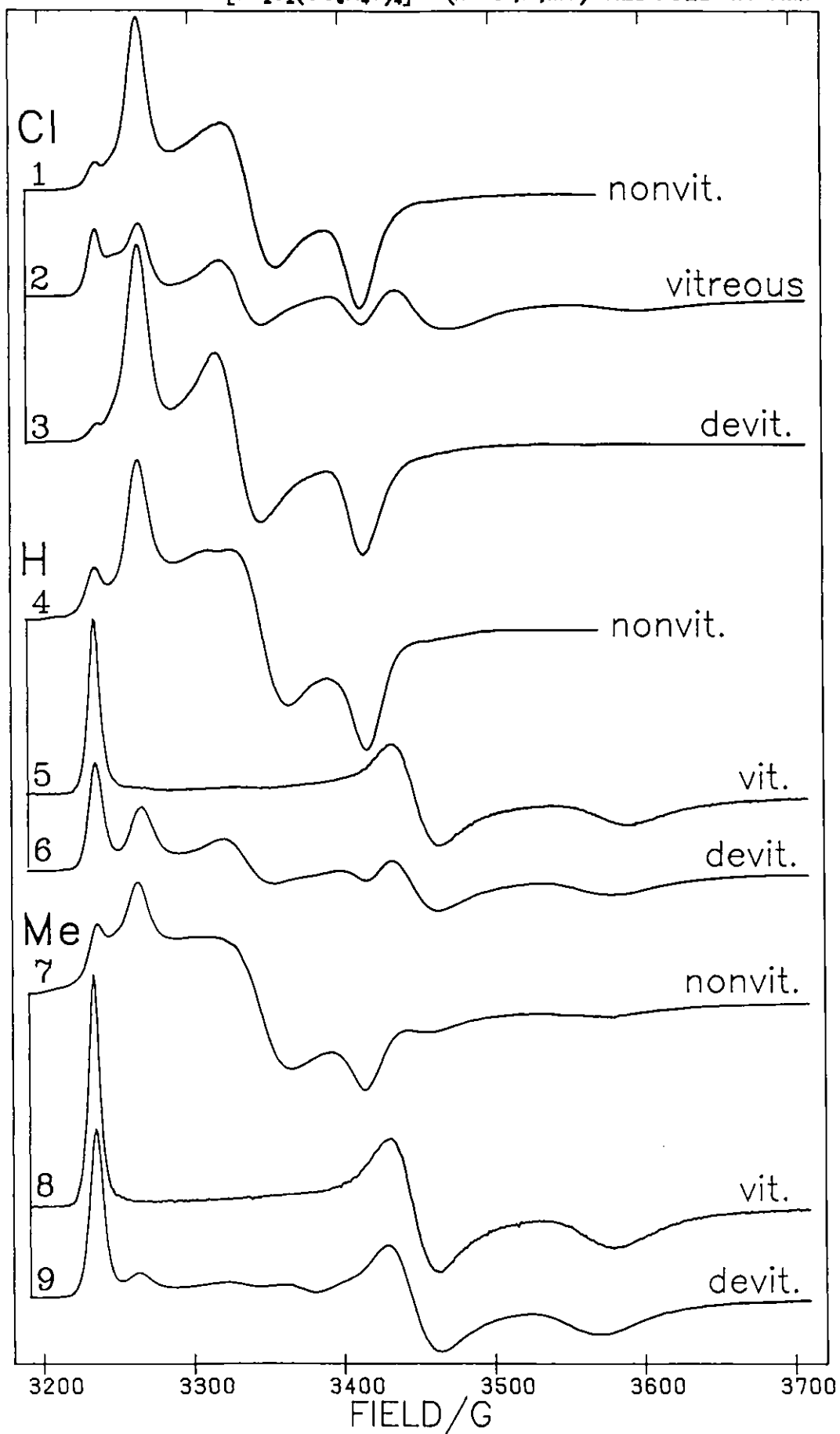
FIG. 1.9 EPR OF $[\text{Fe}_2\text{S}_2(\text{SC}_6\text{H}_4\text{Y})_4]^{2-}$ ($\text{Y}=\text{Cl}, \text{H}, \text{Me}$) REDUCED IN NMP

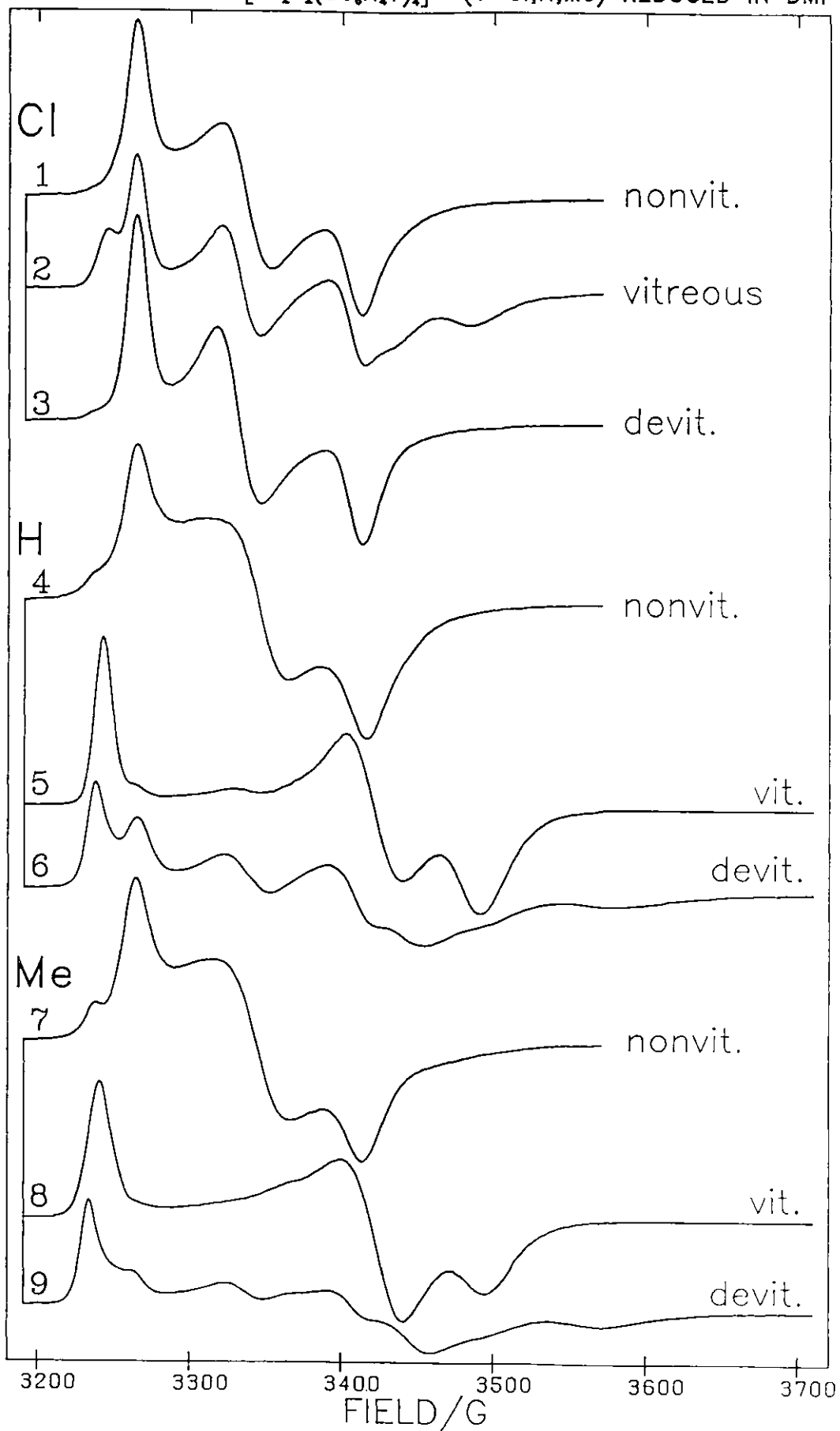
FIG. 1.10 EPR OF $[\text{Fe}_2\text{S}_2(\text{SC}_6\text{H}_4\text{Y})_4]^{2-}$ (Y=Cl,H,Me) REDUCED IN DMF

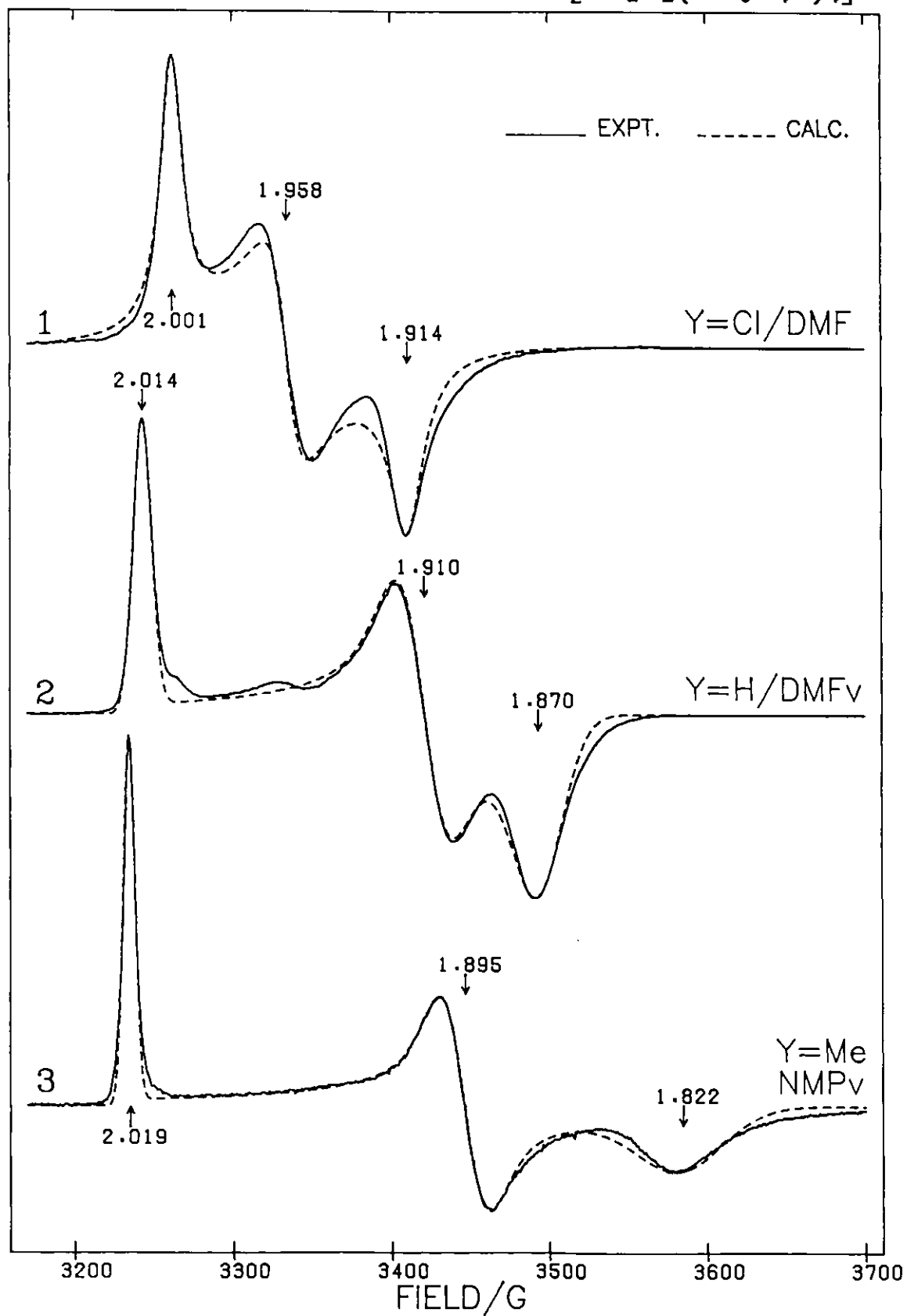
FIG. 1.11 EPR OF REDUCED $[\text{Fe}_2\text{S}_2(\text{SC}_6\text{H}_4\text{Y})_4]^{2-}$ 

TABLE 1.6. EPR Data for Reduced $[\text{Fe}_2\text{S}_2(\text{SC}_6\text{H}_4\text{Y})_4]^{2-}$.

Y	Solvent	Sec. 1 Figure		v composition		g_z	g_y	g_x	g_{av}	
				%	rest					
Cl	DMF _{nv}	10.1			100N		2.002	1.958	1.915	1.958
		11.1		g_{sim} LW			2.001	1.958	1.914	1.958
Cl	DMF _{dv}	10.3	0.1 M n-Bu ₄ NC ⁺ O ₄ ⁻	g_{sim}	100N		2.001	1.960	1.914	1.958
H	DMF _{nv}	10.4		g_{sim}	95N	W	2.001	1.954	1.913	1.956
H	DMF _{nv}	12.3	10 exs. PhSH	g_{sim}	100N		2.001	1.954	1.913	1.956
Me	DMF _{nv}	10.7			90N	W	2.002	1.954	1.914	1.957
Me	DMF _v	12.4	10 exs. TolSH, 0.1 M n-Bu ₄ NC ⁺ O ₄ ⁻		100N		2.002	1.952	1.917	1.957
Cl	NMP _{nv}	9.1		g_{sim}			2.002	1.954	1.916	1.957
					95N	VW	2.002	1.957	1.915	1.958
Cl	NMP _{dv}	9.3	0.2 M n-Bu ₄ NC ⁺ O ₄ ⁻	g_{sim}	95N	VW	2.002	1.962	1.915	1.960
H	NMP _{nv}	9.4		g_{sim}	80N	VW	2.002	1.953	1.913	1.956
Me	NMP _{nv}	9.7			70N	VW	2.001	1.954	1.914	1.956
Cl	PhCN _{nv}	12.2			100N		2.001	1.957	1.914	1.957
H	PhCN _{nv}				100N		2.001	1.952	1.911	1.955
Me	PhCN _{nv}				80N	W	2.001	1.953	1.911	1.955
Cl	DMF _v	10.2	0.1 M n-Bu ₄ NC ⁺ O ₄ ⁻		30W	N	2.013	-	1.875	-

TABLE 1.6 (cont.)

Y	Solvent	Sec. 1 Figure		~ composition		g_z	g_y	g_x	g_{av}			
				%	rest							
H	DMFv	10.5	0.1 M n-Bu ₄ NCℓO ₄	g_{sim} GW	95W	N	2.014	1.910	1.871	1.932		
		11.2					2.014	1.910	1.870	1.931		
							6.8G	16.5G	18.5G			
H	DMFdv	10.6	0.1 M n-Bu ₄ NCℓO ₄		70VW	N	2.019	~ 1.90	1.825	—		
Me	DMFv	10.8	0.1 M n-Bu ₄ NCℓO ₄		100W		2.015	1.913	1.873	1.934		
Me	DMFdv	10.9	0.1 M n-Bu ₄ NCℓO ₄		90VW	N	2.019	~ 1.90	1.831	—		
Cl	NMPv	9.2	0.2 M n-Bu ₄ NCℓO ₄		50VW	N	2.019	~ 1.90	1.817	—		
H	NMPv	9.5	0.2 M n-Bu ₄ NCℓO ₄	g_{sim}	100VW		2.019	1.895	1.820	1.911		
							2.019	1.894	1.818	1.910		
							2.020	1.895	1.824	1.913		
Me	NMPv	9.8	0.2 M n-Bu ₄ NCℓO ₄		100VW		2.019	1.895	1.822	1.912		
		11.3		g_{sim} GW			4.8G	14.7G	29.0G			
H	PhCNv		0.4 M n-Bu ₄ NCℓO ₄		60W	VW	2.011	~ 1.93	1.90	—		
H	PhCNdv		0.4 M n-Bu ₄ NCℓO ₄		70VW	N	2.019	—	1.83	—		
Me	PhCNv		0.4 M n-Bu ₄ NCℓO ₄		40W	VW	2.011	—	—	—		
Me	PhCNdv		0.4 M n-Bu ₄ NCℓO ₄		90VW	N+W	2.018	1.914	1.83	1.921		
H	DMFv	13	17% CH ₂ Cl ₂	g_{sim}	100W		2.014	1.908	1.871	1.931		
									2.013	1.908	1.870	1.930
									2.014	1.909	1.872	1.932
Me	DMFv		17% CH ₂ Cl ₂		100W		2.014	1.909	1.872	1.932		
Me	NMPv		17% CH ₂ Cl ₂		95w	N	2.019	1.894	1.821	1.911		

TABLE 1.6 (cont.)

Y	Solvent	Sec. 1 Figure		~ composition		g _z	g _y	g _x	g _{av}	
				%	rest					
H	DMFv	12.1	5% H ₂ O	100W		2.013	1.911	1.872	1.932	
Me	DMFv		2% H ₂ O	100W		2.015	1.913	1.874	1.934	
			0.1-0.2 M n-Bu ₄ NC ⁺ Cl ⁻ O ₄ + 50 exs. thiol							
H	DMFv	15.1	t-BuSH	95VW	N	2.019	1.887	1.845	1.917	
H	DMFv		EtSH	100VW		2.020	1.894	1.846	1.920	
Me	DMFv		t-BuSH	95VW	N	2.020	1.891	1.843	1.918	
Cl	NMPv		t-BuSH	100VW		2.021	1.889	1.843	1.918	
Me	NMPv		t-BuSH	100VW		2.020	1.890	1.842	1.917	
							2.020	1.888	1.841	1.916
	DMFv			[Fe ₂ S ₂ (S ₂ -o-xylyl) ₂] ³⁻ + t-BuSH	100VW		2.020	1.882	1.846	1.916
		15.2				2.020	1.882	1.845	1.916	
							4.3G	15.5G	21G	
	DMFv		[Fe ₂ S ₂ (S ₂ -o-xylyl) ₂] ³⁻ + EtSH	95VW	N	2.020	1.892	1.848	1.920	

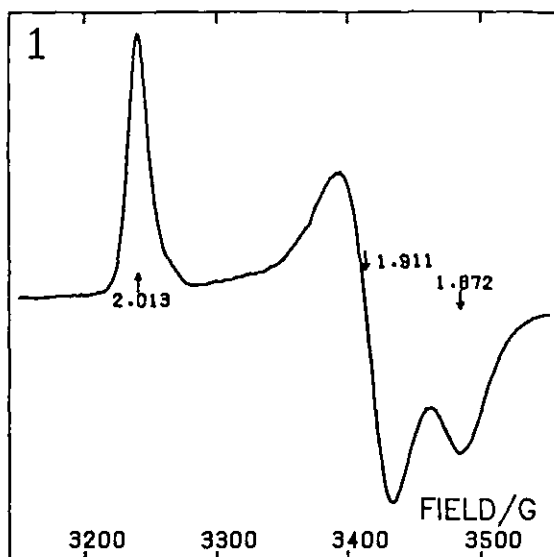
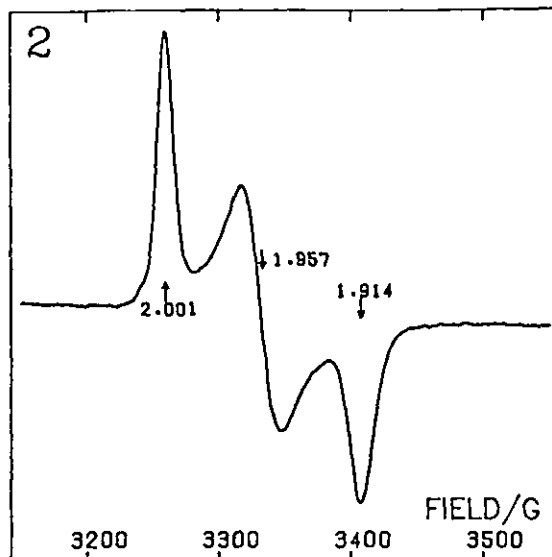
LW - Lorentzian widths, GW - Gaussian widths, N - Narrow, W - Wide, VW - Very-Wide, v - vitreous, nv - non-vitreous, dv - devitrified.

In DMF some variability in the W-type spectra for vitreous samples with $Y = H$ or Me has been observed. The two high field features shown in Figure 1.10.5 for $Y = H$ sometimes look more like those in Figure 1.10.8 for $Y = Me$, and vice versa. The experimental origin of the difference has not been traced. Both types of spectra have very similar g-values but the shape shown in Figure 1.10.5 is most easily fitted in calculations (Figure 1.11.2). Possibly, this latter lineshape represents one species and distortions in the high field part arise due to an underlying signal from another species.

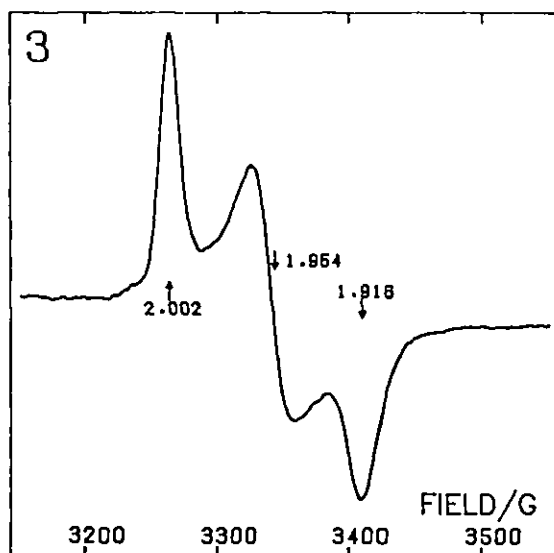
1.4.1.2. Vitreous Samples.

Vitreous samples showing increased or wholly W/VW-type signals may be produced by addition of glassifying agents other than $n\text{-Bu}_4\text{NClO}_4$. Figure 1.12.1 shows a W-type spectrum obtained in low yield ($\sim 10\%$ $S = 1/2$ per 2 Fe) following reduction of $[\text{Fe}_2\text{S}_2(\text{SPh})_4]^{2-}$ in DMF containing $\sim 2\text{M}$ H_2O (20:1, DMF: H_2O). The same complex reduced in DMF containing concentrations of CH_2Cl_2 ranging from 0 to $\sim 2\text{M}$ shows a steady change from an N-type to a W-type spectrum as the frozen solution becomes increasingly vitreous (Figure 1.13). Similar W-type signals have also been observed using DMF solvent containing toluene or methanol, though these have been less extensively studied.

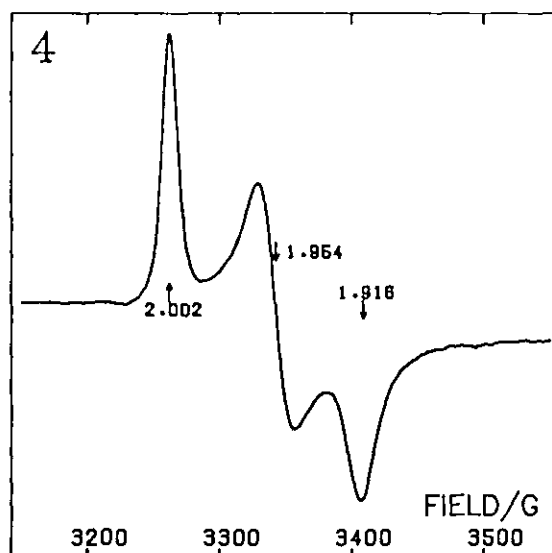
No appreciable signals were observed when reductions were performed in DMSO, MeCN, dimethyl-acetamide, aniline or CH_2Cl_2 . Visible spectral examination of DMSO and MeCN solutions subsequent to $\text{ACN}^{\cdot-}$ addition revealed 80 to 90% dimer to tetramer conversion. Reduction in PhCN (by $\text{ACN}^{\cdot-}$ in DMF) gives weak but well resolved N-type signals (Figure 1.12.2). PhCN

FIG. 1.12 EPR OF REDUCED $[\text{Fe}_2\text{S}_2(\text{SC}_6\text{H}_4\text{Y})_4]^{2-}$ (Y=Cl,H,Me)Y=H in DMF(5% H_2O)

Y=Cl in PhCN

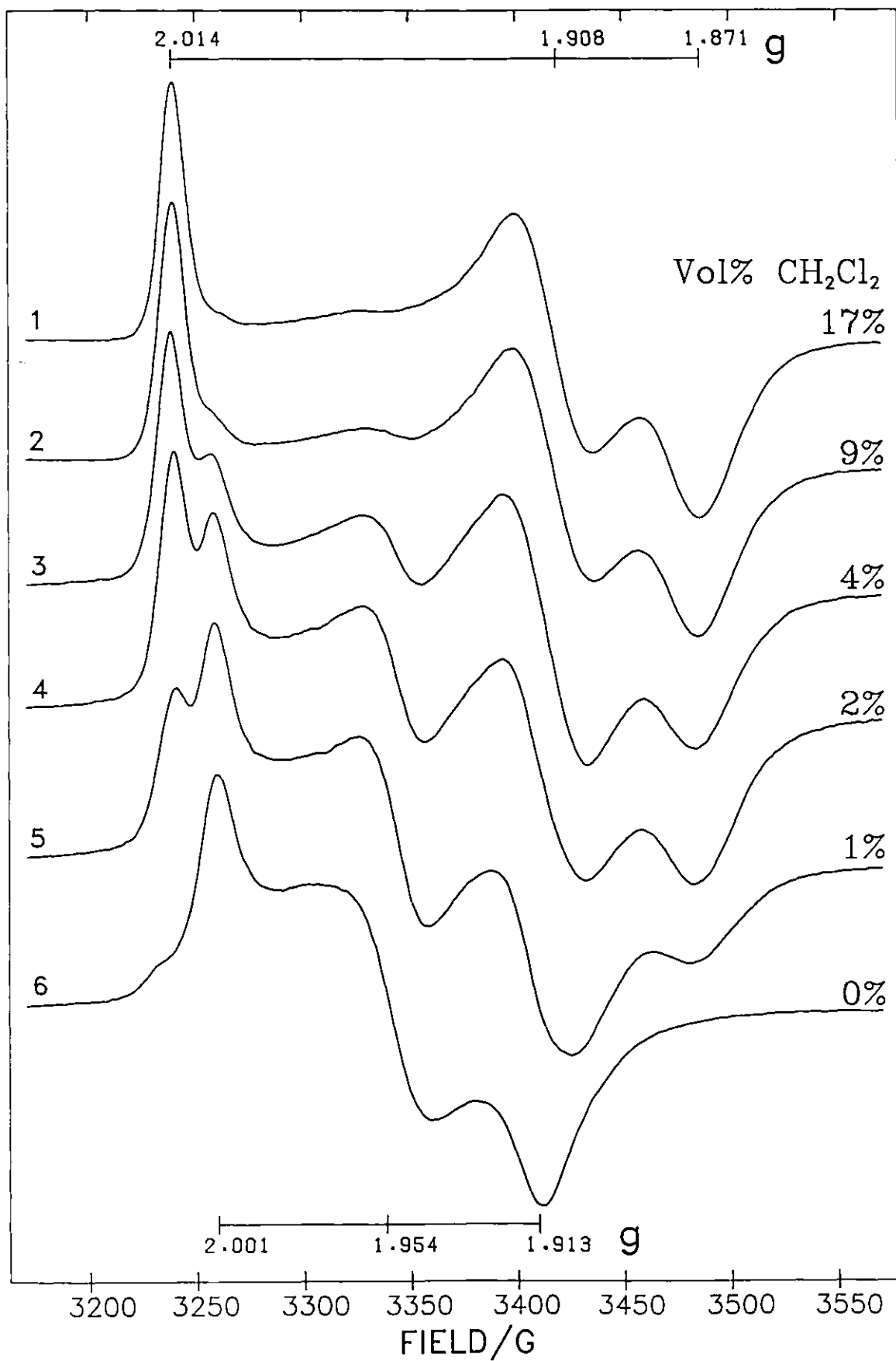


Y=H+10 exs. PhSH in DMF

Y=Me+10 exs. TolSH
in 0.1M $n\text{Bu}_4\text{NClO}_4$, DMF

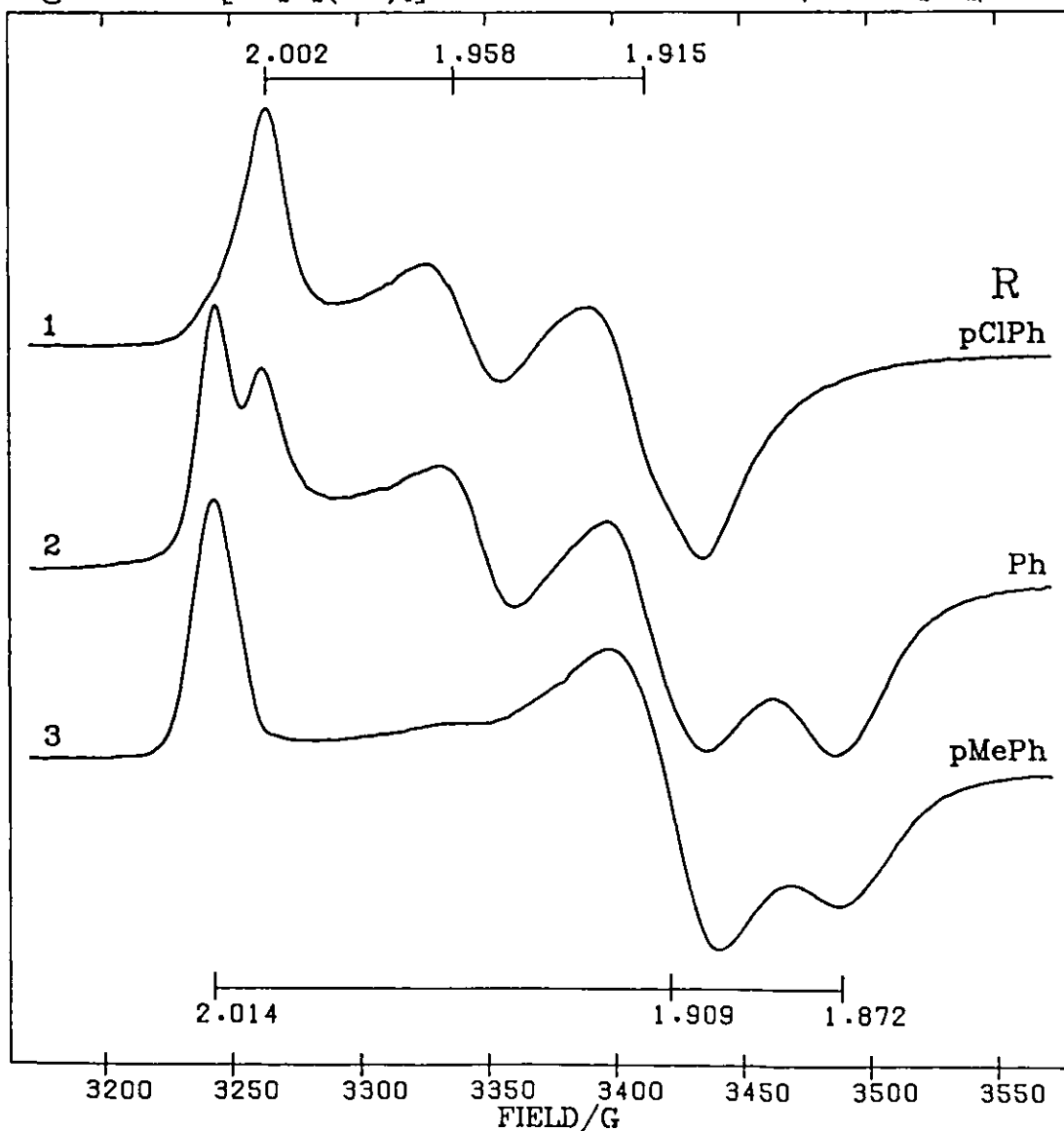
will glassify at low temperature when a considerable concentration of $n\text{-Bu}_4\text{NClO}_4$ is present (0.4 M) and resultant EPR signals are mixtures of N-type, W-type and VW-type, but extensive investigations of reductions in this solvent have not been undertaken. That the W-type and VW-type signals were not due to the DMF solvent employed for the $\text{ACN}^{\cdot-}$ was checked by using $\text{ACN}^{\cdot-}$ in PhCN, though this is an inferior solvent for general use.

Fig. 1.13 EPR of $[\text{Fe}_2\text{S}_2(\text{SPh})_4]^{2-}$ reduced in varying concentrations of $\text{CH}_2\text{Cl}_2/\text{DMF}$



Returning to Figures 1.9 and 1.10 it can be seen that the propensity to produce a W or VW-type signal on reduction increases along the series $Y = Cl, H, Me$. This is further exemplified in Figure 1.14 which shows spectra for the three complexes after reduction in DMF containing a low CH_2Cl_2 concentration. In these terms $[Fe_2S_2(S_2-o\text{-xylyl})_2]^{2-}$ must be placed at the beginning of the series since no appreciable vitrification or solvent dependency is found for the g-values observed on its reduction.

Fig. 1.14 $[Fe_2S_2(SR)_4]^{2-}$ reduced in 2% v/v CH_2Cl_2/DMF



1.4.1.3. Devitrified Samples.

Low temperature glasses, formed as a result of adding $n\text{-Bu}_4\text{NCfO}_4$ to the solvent, devitrify on warming to a few degrees below the solvent melting point, and may be maintained in this state by recooling before thawing onsets. Changes in the EPR are observed following this process, and generally occur with retention of overall doubly-integrated intensity. The simplest case is with NMP as solvent, for which a change from VW-type to the N-type signal is observed as shown in Figure 1.9. The extent of this change is dependent on the para-substituent on the thiolate ligand. For $Y = \text{Cl}$ the process goes to completion, whilst for $Y = \text{Me}$, very little change is found. Rapid thawing and refreezing of a devitrified originally glassy sample enables return to a transparent glassy state and restoration of the original lineshape, albeit with decreased signal amplitude.

With DMF as solvent, there is an additional complication. Conversion of W-type to N-type is again observed on devitrification, being total for $Y = \text{Cl}$ and only slight for $Y = \text{Me}$. For $Y = \text{H}$ or Me the majority of the rest of the signal is found, however, to be VW-type (Figure 1.10.6 and 1.10.9). The W-type signal is restored on thawing and rapidly refreezing as a glass. Devitrified samples for the three complexes having PhCN as solvent closely follow those obtained with DMF. In the case of this solvent, however, the VW-type signal already forms a considerable ($\sim 1/2$) proportion of the vitreous sample signal for $Y = \text{H}, \text{Me}$ prior to devitrification, and thus features more significantly in the devitrified spectrum.

1.4.2. Stability.

In mobile solution, reduced monodentate aryl-thiol ligated dimers are less stable than $[\text{Fe}_2\text{S}_2(\text{S}_2\text{-o-xylyl})_2]^{3-}$. Conversion to the corresponding tetramer, $[\text{Fe}_4\text{S}_4(\text{SC}_6\text{H}_4\text{Y})_4]^{2-}$, is readily seen on comparing room temperature visible absorption spectra before and after reduction. These spectral results indicate 80 to 90% dimerisation. Yields of the trianion dimer from reductions are dependent on ligand, solvent and additives. The yield obtained also varies from one reduction to another by around $\pm 10\%$ due to differences in the time taken to perform the reaction, transfer and freezing procedures. The highest yields were found for $\text{Y} = \text{H}, \text{Me}$ in NMP (50-60%) whilst the overall range averaged $\sim 20\text{-}60\%$.

1.4.3. Effect of Added Thiols.

Addition of an excess of the appropriate ligand thiol to the $[\text{Fe}_2\text{S}_2(\text{SC}_6\text{H}_4\text{Y})_4]^{2-}$ ($\text{Y} = \text{Cl}, \text{H}, \text{Me}$) solution prior to reduction has been observed to promote an increase in the proportion of N-type signal in the resulting EPR spectrum. Because the aryl thiols used readily donate their mercapto proton it was found necessary to add considerable excess of $\text{ACN}^{\dot{-}}$ in order to achieve cluster reduction. Consequent inherent difficulty in accurate estimation of the amount of $\text{ACN}^{\dot{-}}$ required for cluster reduction, together with decreased stability of the resulting reduced species, led to weaker signals. The use of an alkali mercaptide in place of thiol, whilst alleviating this difficulty, was not found to lead to the extent of the effects described below for the free thiol.

Figure 1.12.3 shows a signal resulting from reduction of $[\text{Fe}_2\text{S}_2(\text{SPh})_4]^{2-}$ in DMF containing a 10 fold excess of PhSH over the cluster concentration. The g-values are identical to those observed in the absence of thiol, however, the spectrum is better resolved, having smaller linewidth. The reduced linewidth is concomitant with the low signal intensity, indicative of increased magnetic dilution compared to the corresponding spectrum (Figure 1.10.4) where no excess thiol is present.

Rather more significantly, reduction in the presence of excess thiol, together with a glassifying agent produces a similar N-type spectrum (Figure 1.12.4). This should be compared with Figure 1.10.8 where reduction in the absence of thiol is seen to yield entirely a W-type signal for Y = Me. When only a four-fold thiol excess is used the resulting spectrum is still more than 90% N-type. Thiol promotion of the production of the N-type signal over the W or VW-type is found for both $n\text{-Bu}_4\text{CfO}_4$ and CH_2Cf_2 glassificants, for both DMF and NMP solvents and for all three compounds (Y = Cf, H, Me). The effect is also produced by benzyl mercaptan, but not by phenol. Comparable excesses of sodium mercaptide in place of thiol led to increased N-type signal for Y = Me or H on devitrifying a glassy sample, but to little or no effect on the EPR observed in the vitreous state.

When the less protic thiols, t-butyl or ethyl mercaptan are added in large excess prior to reduction, and a glassificant is also present, a new signal results (Figure 1.15.1) similar to the VW-type signal of Figure 1.11.3. This may be observed in both DMF and NMP. On

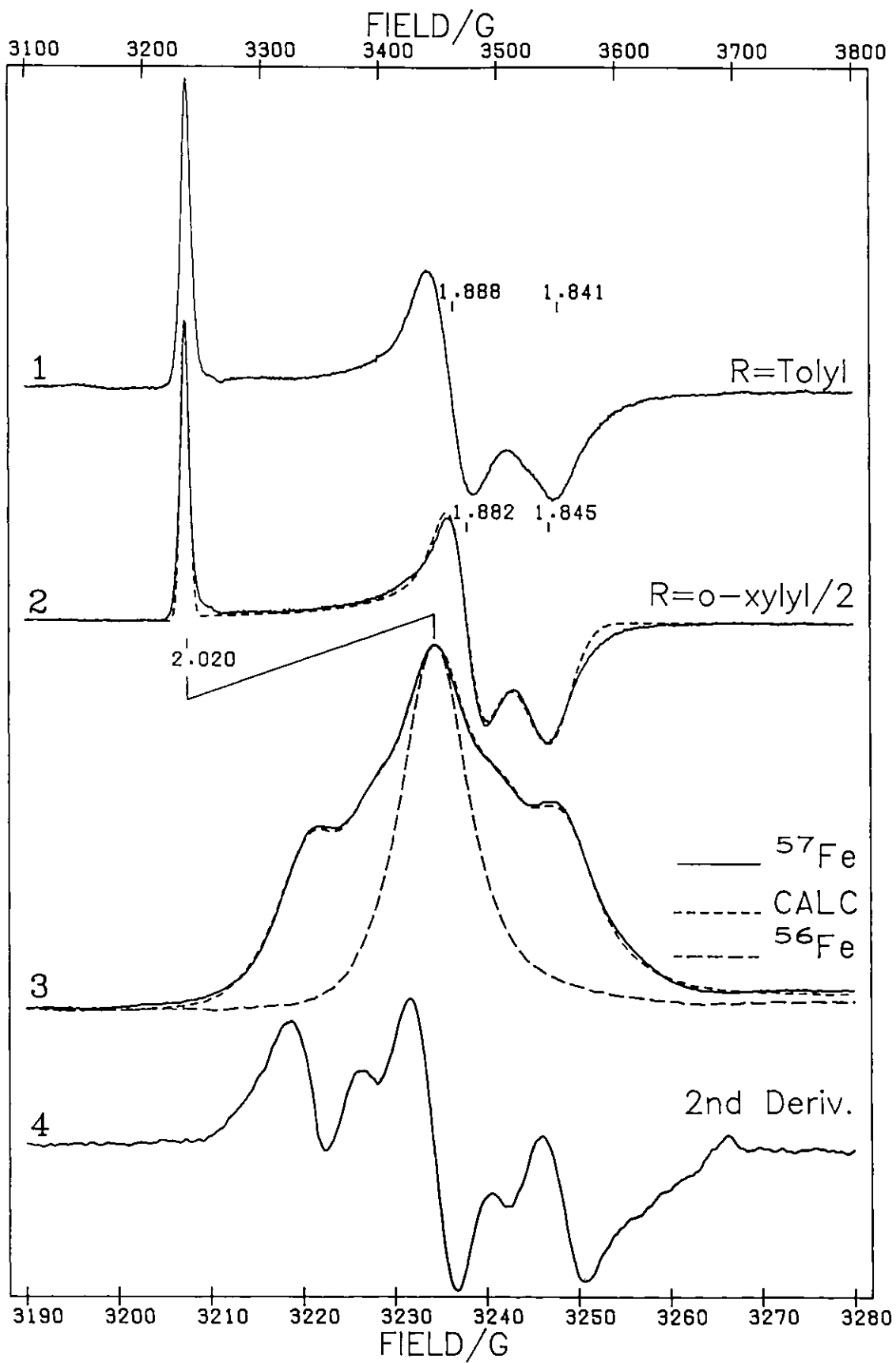


FIG. 1.15 EPR OF $[\text{Fe}_2\text{S}_2(\text{SR})_4]^{2-} + \text{tBuSH}$, AFTER REDUCTION

devitrification of such a sample, part conversion to N-type signal occurs, the extent being dependent upon the original compound (Y = Cl, H, Me). If no glassificant is present in the solvent the signal observed is predominantly N-type with a proportion of the t-BuSH signal similar in magnitude to that of the VW-type resonance in the non-vitreous sample spectra of Figure 1.9.

Similar signals of large anisotropy result from the reduction of $[\text{Fe}_2\text{S}_2(\text{S}_2\text{-o-xylyl})_2]^{2-}$ in the presence of excess t-BuSH or EtSH (Figure 1.15.2 and 1.16). A reduction performed with excess t-BuSH and 83% ^{57}Fe enriched $[\text{Fe}_2\text{S}_2(\text{S}_2\text{-o-xylyl})_2]^{2-}$ gives an EPR spectrum which has its low field peak split according to the expected statistical distribution of ^{57}Fe - ^{56}Fe in a dimer. Because the linewidth is so narrow for the lines composing this peak (half-height half width 4.3 G) the splittings for $^{57}\text{Fe}^{56}\text{Fe}$ and $^{57}\text{Fe}^{57}\text{Fe}$ (Figure 1.5) may be clearly seen. A simulation from field-shifting the natural abundance spectrum achieves quite a good fit (Figure 1.15.3), with average splitting of 14 G.

Thus it seems reasonable to assume that the Fe_2S_2 core is retained in the species giving the new signals and that the t-BuSH/EtSH act as additional ligands or substitute for one or more of the original coordinated mercaptides.

1.4.4. Summary.

1. All compounds (Y = Cl, H, Me) give spectra having very similar g-values ($2.00\frac{1}{2}$, $1.95\frac{2}{8}$, $1.91\frac{1}{5}$, type N) on reduction in pure solvents which freeze to a non-vitreous state.

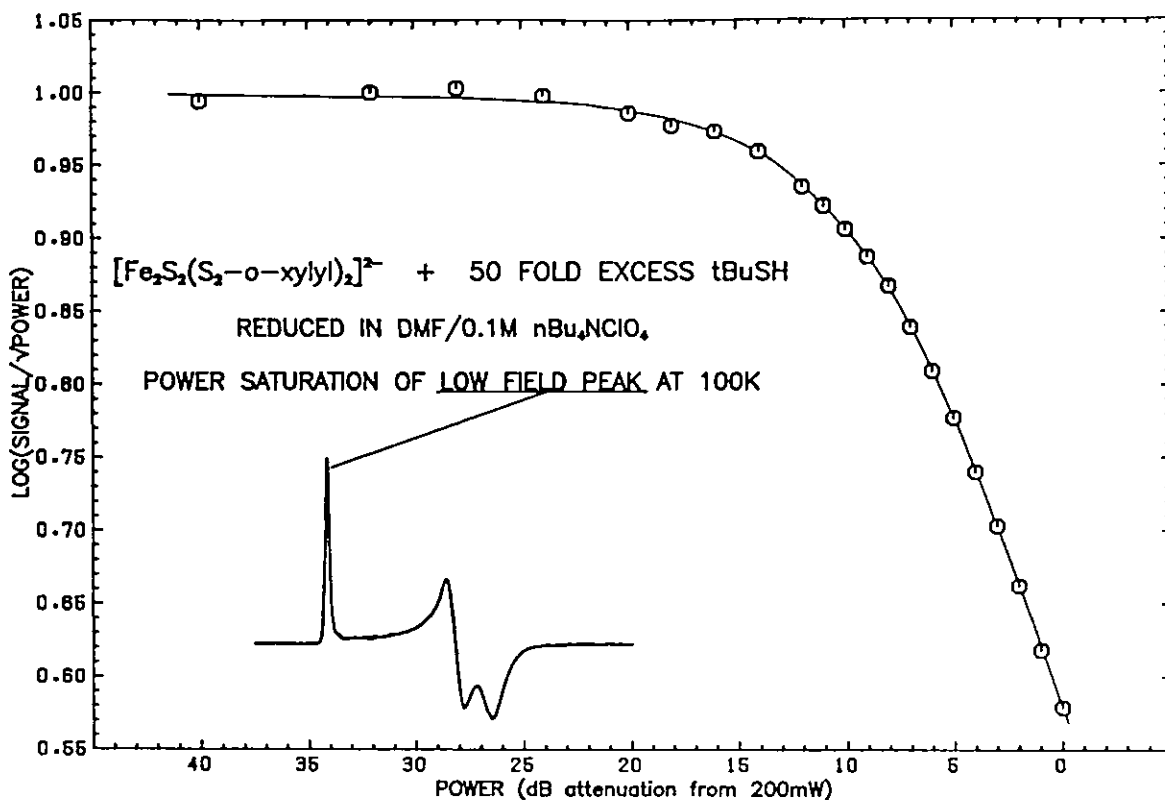


Figure 1.16. Power Saturation in the EPR signal from $[\text{Fe}_2\text{S}_2(\text{S}_2\text{-o-xylyl})_2]^{2-}$ reduced in the presence of excess t-BuSH.

2. Reduction in solvent mixtures which vitrify on freezing results in an increased proportion of a signal with solvent dependent g-values (2.01_5^3 , 1.9_{14}^{08} , 1.87_5^1 in DMF, type W; 2.0_{20}^{19} , 1.89_5^4 , 1.8_{24}^{17} in NMP, type VW).
3. Devitrification of a glassy sample leads to conversion of some W/VW-type signal to N-type. The majority of any remaining signal then appears as a VW-type resonance.
4. Formation of the W/VW-type signals is promoted in the order $Y = \text{Cl} < \text{H} < \text{Me}$.
5. Reduction in the presence of excess ligand thiol promotes formation of the N-type signal.
6. t-BuSH and EtSH added to reductions in glass forming solvent mixtures produce new signals having large anisotropy ($g = 2.0_{21}^{19}$, 1.8_{94}^{82} , 1.8_{48}^{42}).

1.5. Discussion.

1.5.1. Analysis of \underline{g} -Tensor Principal Values.

Bertrand and Gayda have given a theoretical interpretation of the \underline{g} -tensor variations in $[2\text{Fe-2S}]^{1+}$ ferredoxins.^{60,61} They consider a rhombic C_{2v} distortion in the environment of the Fe^{2+} ion, having the same geometrical character for each protein, but variable in intensity. The differences in \underline{g} , and other physical parameters, amongst the reduced ferredoxins may then be correlated with the variable mixing of certain d-orbitals consequential upon the proposed distortional differences. Expressions can be derived for the three principal \underline{g} -values in terms of a parameter θ which measures the C_{2v} symmetry-allowed mixing of the two A_1 ferrous states (E1.4-E1.6).

$$g_x(\theta) = \frac{7}{3} g_{1x} - \frac{4}{3} g_e + \frac{32\lambda_2}{3\Delta_{yz}} \sin^2 \left(\theta + \frac{\pi}{3} \right) \quad (\text{E1.4})$$

$$g_y(\theta) = \frac{7}{3} g_{1y} - \frac{4}{3} g_e + \frac{32\lambda_2}{3\Delta_{xz}} \sin^2 \left(\theta - \frac{\pi}{3} \right) \quad (\text{E1.5})$$

$$g_z(\theta, \Delta_{xy}) = \frac{7}{3} g_{1z} - \frac{4}{3} g_e + \frac{32\lambda_2}{3\Delta_{xy}} \sin^2 \theta \quad (\text{E1.6})$$

g_{1x} , g_{1y} , g_{1z} are the main components of the \underline{g}_1 -Fe(III) tensor; λ_2 is the spin-orbit coupling constant of the Fe(II) ion; and Δ_{xy} , Δ_{xz} , Δ_{yz} are the energies of the first three excited levels of Fe(II) above the groundstate. The different orbital states, in order of increasing energy are given in E1.7.

$$\begin{aligned} |\phi_0\rangle &= \cos\theta d_{z^2} + \sin\theta d_{x^2-y^2} \\ |\phi_1\rangle &= d_{xy} \\ |\phi_2\rangle, |\phi_3\rangle &= d_{xz}, d_{yz} \\ |\phi_4\rangle &= \cos\theta d_{x^2-y^2} - \sin\theta d_{z^2} \end{aligned} \quad (\text{E1.7})$$

The parameters λ_2 and g_1 are most affected by covalency, but these effects are considered to vary little amongst the different Fd. Similarly, Δ_{yz} and Δ_{xz} , having values imposed mainly by the tetrahedral part of the ligand field, are considered as constants in the analysis given by Bertrand and Gayda. With these approximations, the expressions for the principal values of the g tensor reduce to functions of θ and Δ_{xy} only (E1.4-E1.6). For small values of θ first order expansion of these equations leads to $\theta \approx -\chi$ where $\chi = (g_y - g_x)$ and to the approximate expressions (E1.8 and E1.9).

$$g_x(\chi) \sim g_0 - \Delta_{xz}\chi / (\Delta_{xz} + \Delta_{yz}) \quad (\text{E1.8})$$

$$g_y(\chi) \sim g_0 + \Delta_{yz}\chi / (\Delta_{xz} + \Delta_{yz}) \quad (\text{E1.9})$$

where

$$g_0 = \frac{7(\Delta_{yz}g_{1x} + \Delta_{xz}g_{1y}) + 48\lambda_2}{3(\Delta_{yz} + \Delta_{xz})} - \frac{4}{3}g_e \quad (\text{E1.10})$$

Experimental g -values, for several proteins, plotted against χ are shown in Figure 1.17, after Coffman and Stavens.⁶² Considering reasonable values for the six constant parameters: λ_2 (-80 cm^{-1} , reduced from the free ion value of 105 cm^{-1} by covalency); Δ_{xz}, Δ_{yz} ($6000 \text{ cm}^{-1}, 4000 \text{ cm}^{-1}$, estimated from IR spectroscopy⁶³); and g_{1x}, g_{1y}, g_{1z} ($2.015, 2.034, 2.030$), Bertrand and Gayda have obtained a fit to the experimental data using the functions E1.4-E1.6. Also plotted in Figure 1.17 are the g -values for the four complexes $[\text{Fe}_2\text{S}_2(\text{SR})_4]^{2-}$ [$2\text{R} = \text{o-xylyl}$ and $\text{R} = \text{C}_6\text{H}_4\text{Y}$ ($\text{Y} = \text{Cl}, \text{H}, \text{Me}$)], reduced in the various solvent systems. A clear distinction is demonstrated between the g -values for the $\text{S}_2\text{-o-xylyl}$ chelated complex and N-type signals in comparison with those for the W/VW-type spectra observed with vitreous

Fig. 1.17 Plot of g -values vs. $(g_y - g_x)$ for reduced model complexes and 2Fe Fd. (see Tables 1.1, 1.6, 1.7)

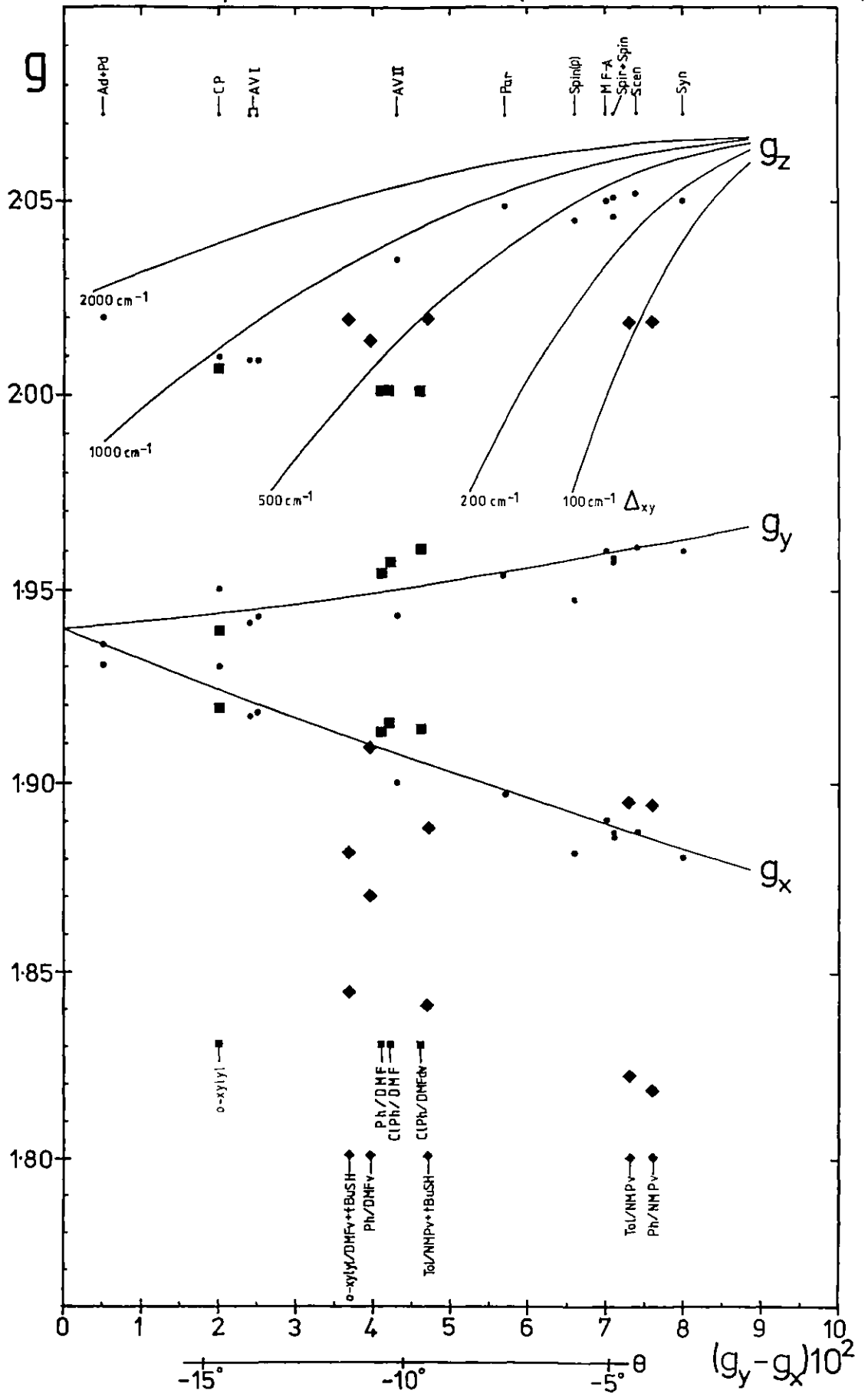


TABLE 1.7. EPR Data for Two-Iron Ferredoxins.

	Source	g_z	g_y	g_x
Ad	Adrenal glands ²⁰	2.02	1.935	1.93
Pd	<u>P. Putida</u> ²⁰	2.02	1.935	1.93
CP	<u>Clostridium pasteurianum</u> ¹⁵	2.01	1.95	1.93
AV I	<u>Azotobacter vinelandii</u> ⁶⁴ IA	2.009	1.941	1.917
AV I		2.009	1.943	1.918
AVII		2.035	1.943	~1.90
Par	Parsley ⁴⁹	2.049	1.954	1.897
Spin (p)	Spinach-powder ⁶⁵	2.045	1.947	1.881
MF-A	<u>Microcystis flos-aquae</u> ⁶⁶	2.05	1.96	1.89
Spin	Spinach ⁴⁹	2.046	1.957	1.886
Spir	<u>Spirulina maxima</u> ⁶⁰	2.051	1.958	1.887
Scen	<u>Scenedesmus</u> ⁶⁰	2.052	1.961	1.887
Syn	<u>Synechococcus lividus</u> ⁵⁰	2.05	1.96	1.88

samples. The former fit well with the experimental protein values and with the analysis of Gayda and Bertrand. Large g_z/g_{xy} anisotropy in signals for glassy samples leads on the other hand to considerable departure of g_x and g_y below that expected for the $[2Fe-2S]^{1+}$ Fd centre.

Blumberg and Peisach⁶⁷ have formerly given a less rigorous qualitative analysis of $[2Fe-2S]^{1+}$ Fd g-value trends in terms of Fe^{2+} d-orbital energies in the absence of mixing. They consider the relationship between the parameters g_z , C (El.11) and R (El.12), taking g_z as a measure of the covalency of the Fe^{3+} ion, C as indicating

$$C = (4/3)[1/(g_z - g_x) + 1/(g_z - g_y)] \quad (\text{E1.11})$$

$$R = (g_y - g_x)/(2g_z - g_y - g_x) \quad (\text{E1.12})$$

the ligand field strength and the extent of covalency at the Fe^{2+} ion and R as being sensitive to the ferrous geometrical environment. A hyperbolic relationship between g_z and C has been interpreted in terms of varying Fe_2S_6 longitudinal charge distribution. Plotting the results for the reduced synthetic models on the graphs of g_z vs. C and g_{av} vs. R in the Blumberg and Peisach paper (Figure 1 and 3, ref. 67), leads to a differentiation amongst the signal types comparable to that revealed in Figure 1.17. The W and VW-type spectra are found to lie at some considerable separation from the main $[\text{2Fe-2S}]^{1+}$ Fd trends.

On the above grounds it is believed that the signals from reduced $[\text{Fe}_2\text{S}_2(\text{S}_2\text{-o-xylyl})_2]^{2-}$ and also the N-type signals from reduced $[\text{Fe}_2\text{S}_2(\text{SC}_6\text{H}_4\text{Y})_4]^{2-}$ (Y = Cl, H, Me) result from the corresponding trianions and are genuine analogue spectra for those observed in $[\text{2Fe-2S}]^{1+}$ ferredoxins. The temperature dependence and power saturation behaviour of the signals further supports this assignment.

The range of $(g_y - g_x)$ for these signals and their small resonance field spread is consistent with changes in protein spectra produced by solvents, chaotropic anions or denaturing agents.^{68-70,62} These cause a decrease of the large x-y anisotropy found for plant two-iron ferredoxin signals. Of particular interest and relevance are the changes in signal observed by Cammack^{68,69} when employing DMSO or guanidine

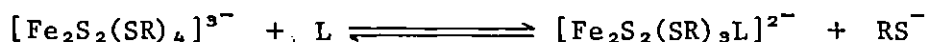
hydrochloride as denaturants. Under these conditions, where the protein is presumed unfolded to give a coordination environment more closely resembling that in the analogous model compounds, a variety of proteins produce similar spectra with g extrema in the range 1.9 to 2.0.

Blumberg and Peisach have suggested that a significant departure from the main trend of their observed relationship between g_z and C represents a change of chemical composition in the binuclear iron-sulphur cluster. This is demonstrated in their analysis by disparity in the trends for sulphur and selenium-bridged reduced ferredoxins. A comparable disparity is found for the chalcogen homologues in the analysis of Bertrand and Gayda.⁶¹ It seems likely then that the gross departure of the g -values found for the W and VW-type signals from those for the ferredoxins results from some chemical modification of the Fe_2S_6 core.

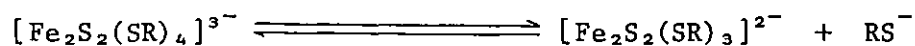
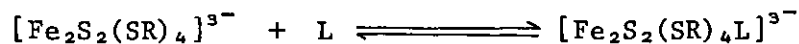
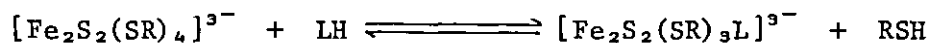
1.5.2. Further Discussion of Spectral Solvent Dependency.

The EPR data presented above for the reduced monodentate thiol-ligated dimers is insufficiently extensive to formulate a full understanding of its physico-chemical origins, but an attempt is made here to rationalise the results.

Reversible chemical modification of the reduced dimer, suggested in the last section, might involve additional coordination by, for example, solvent, and/or loss of a labile thiol ligand.



or



For reduced $[\text{Fe}_2\text{S}_2(\text{SC}_6\text{H}_4\text{Y})_4]^{2-}$ the ordering observed for the ease of formation of W or VW-type signals, as opposed to N-type, is $\text{Y} = \text{Cl} < \text{H} < \text{Me}$. This is the order of expected increasing pK_a for p- $\text{YC}_6\text{H}_4\text{SH}$ on the basis of the Y-substituent Taft parameter⁷² and of observed decreasing thiol acidity.⁷³ For $[\text{Fe}_4\text{S}_4(\text{SR})_4]^{2-}$ the ease with which coordinated thiolate (RS^-) is replaced by another ligand is found to increase with increasing pK_a of the thiol (RSH).⁷⁴⁻⁷⁶ This has been explained in terms of the affinity of RS^- for a proton or other electrophile. In the case of the reduced dimers, if the aprotic solvents DMF, NMP and PhCN are regarded as potential ligands then the origin of such a proton or other electrophile is not obvious. The efficacy of added excess thiol, as opposed to thiolate, in promoting N-type signal would seem to implicate the involvement of a proton in any considered ligand displacement process.

The S_2 -o-xylyl ligand, being an aliphatic thiol, should have a higher pK_a than the aromatic thiols and facilitated substitution would be expected in $[\text{Fe}_2\text{S}_2(\text{S}_2\text{-o-xylyl})_2]^{3-}$. No solvent dependency of the EPR

signal has been observed with this ligand and the expected increased lability must be considered offset by chelation-incurred stability (it is noted, however, that the EPR signal is modified to one of large anisotropy in the presence of excess t-BuSH).

On the assumption of a ligand displacement process for the formation of the W/VW-type signal-producing species, the reversal of the effect by introduction of excess ligand thiol would seem reasonable. That this may be achieved with such a low thiol concentration relative to that of the prospective solvent ligand is surprising. Additionally exceptional is the necessity to accept that the reverse of the thiol displacement reaction can occur in frozen solution at low temperature during a devitrification procedure, when W/VW-type signals are observed to transform wholly or partially to N-type. Whilst it is conceivable that solvent crystallisation might cause loss of a weakly bound solvent ligand it seems unlikely that thiolate replacement would then occur in view of the solid state immobilisation. Partial transformation to N-type signal has also been found following devitrification of samples containing t-BuSH and which originally gave characteristic large anisotropy spectra. It is difficult to understand why this should occur.

Visible spectra of the dimeric iron complexes, obtained prior to reduction, show no changes indicative of interaction with either solvent or added thiol.

The negative g_x & g_y shifts for the W and VW-type signals from those characteristic of the majority of ferredoxins might be a result of reduced g-values at the ferric ion. This could arise if there was

decreased Fe(III) covalency as might be expected following the replacement of a thiolate ligand by one coordinating through a nitrogenous or oxygenous donor. Thiol substitution involving t-BuSH or EtSH would not, however, be expected to lead in this case to the observed decrease in g_{av} . At first sight it also seems somewhat peculiar that DMF and NMP, which both contain the fragment $-\text{CH}_2-\text{NMe}-\text{CO}-$, should coordinate to produce such disparate g-values as those for the W-type and VW-type signals. However, observation of transformation of W-type to VW-type signal on devitrification of a glassy DMF sample would seem to indicate that the signal difference does not originate from the nature of any additional or replacement ligand so much as, for example, the number of these ligands. Thus, the W-type signal might represent further additional or replacement coordination to that present in the species giving rise to the VW-type signal. Given that the production of different signals by similar potential ligating solvents might be explained in this way then it remains somewhat exceptional that signals closely resembling these should arise in PhCN, a rather different potential ligand.

It is noted that Salmeen and Palmer⁷⁷ have suggested from PMR data that for reduced spinach ferredoxin there may be non-cysteine amino acids coordinated at the ferric ion. No corresponding proton resonances have been found in the oxidised protein.

Both the 4-methoxybenzoate O-demethylase monooxygenase from *P. Putida* (Putidamonooxin)⁷⁸ and the oxidation factor of cytochrome b-c₁ in succinate-cyt_c-reductase⁷⁹ are proteins containing [2Fe-2S] centres. EPR signals have been recorded for these proteins which have quite similar g-values to those for the VW-type signals observed for the analogue

complexes on reduction in NMP (Putidamonooxin 2.01, 1.91, 1.78 and oxidation factor 2.02, 1.90, 1.78). This is of particular interest in that both proteins form parts of enzyme complexes and may be directly involved in chemical modification processes during which additional or substitutional ligand coordination could take place.

1.6. Reduction of Selenium-Substituted Dimers.

Selenium bridged $[\text{Fe}_2\text{Se}_2(\text{SR})_4]^{2-}$ complexes are easily synthesised in a similar manner to their sulphur homologues. Additionally ligand substitution on the complex $[\text{Fe}_2\text{X}_2(\text{S}_2\text{-o-xylyl})_2]^{2-}$ ($\text{X} = \text{S}, \text{Se}$) using PhSeSePh leads to $[\text{Fe}_2\text{X}_2(\text{SePh})_4]^{2-}$. It has proven possible to observe EPR signals from all these dimer complexes subsequent to reduction with $\text{ACN}^{\cdot-}$ followed by rapid freezing.

Figure 1.18 compares spectra for $[\text{Fe}_2\text{X}_2(\text{S}_2\text{-o-xylyl})_2]^{3-}$ ($\text{X} = \text{S}, \text{Se}$). The selenium-bridged complex, like the sulphur, gives a signal with g-values which are independent of the glassification state of the frozen solvent.

Signals from reduction of complexes coordinated by monodentate chalcogenide ligands display the same solvent and vitrification dependence described in previous sections for $[\text{Fe}_2\text{S}_2(\text{SR})_4]^{2-}$. Spectra of the corresponding N-type, from non-vitreous or devitrified samples, are shown in Figure 1.19 for the series reduced- $[\text{Fe}_2\text{X}_2(\text{YPh})_4]^{2-}$ [$\text{X} = \text{S}, \text{Se}$ ($\text{Y} = \text{S}, \text{Se}$)], and g-values are collected in Table 1.8. Also given in this table are g-values obtained for vitreous DMF and NMP solvents, and Figure 1.20 shows some representative spectra.

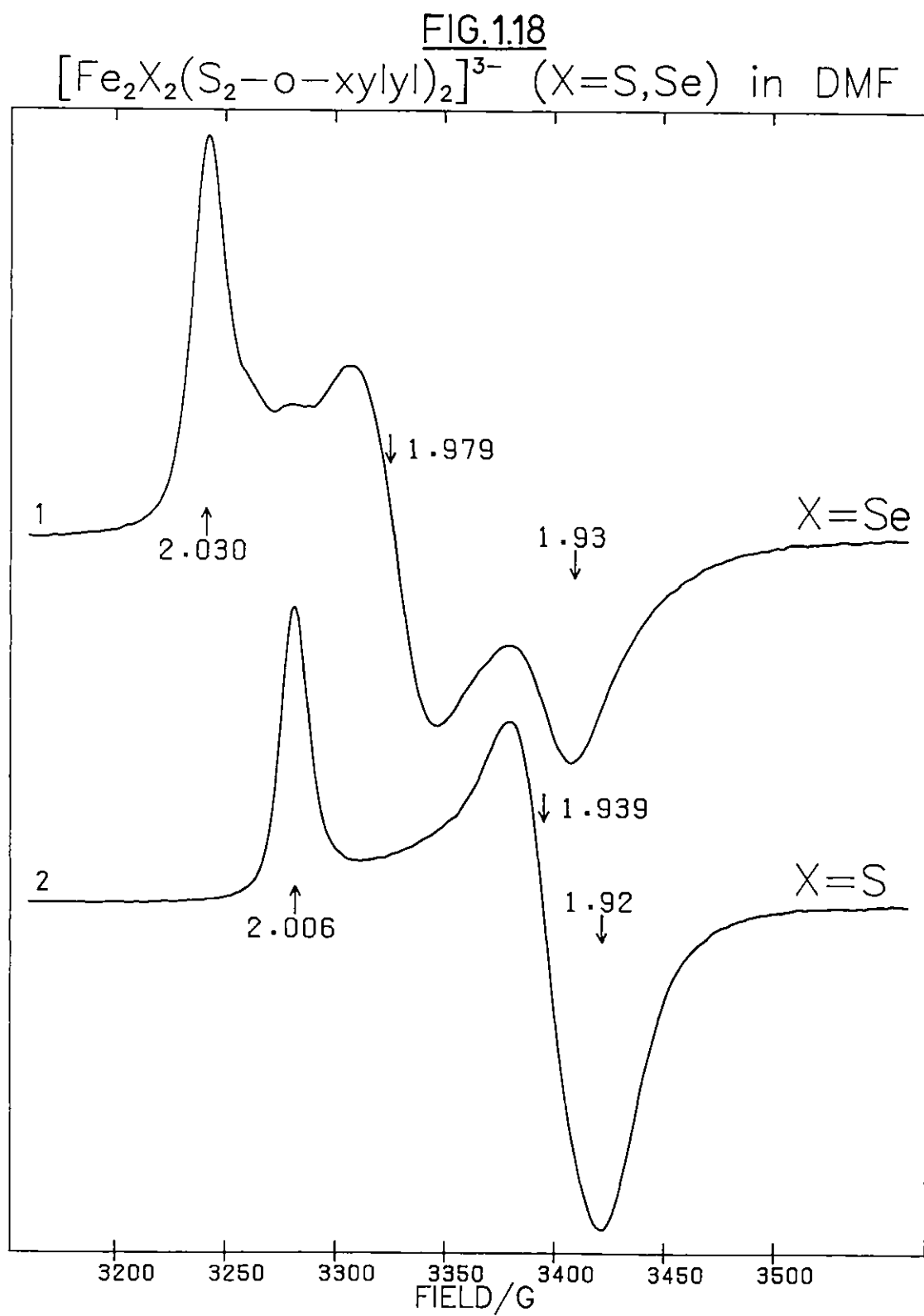


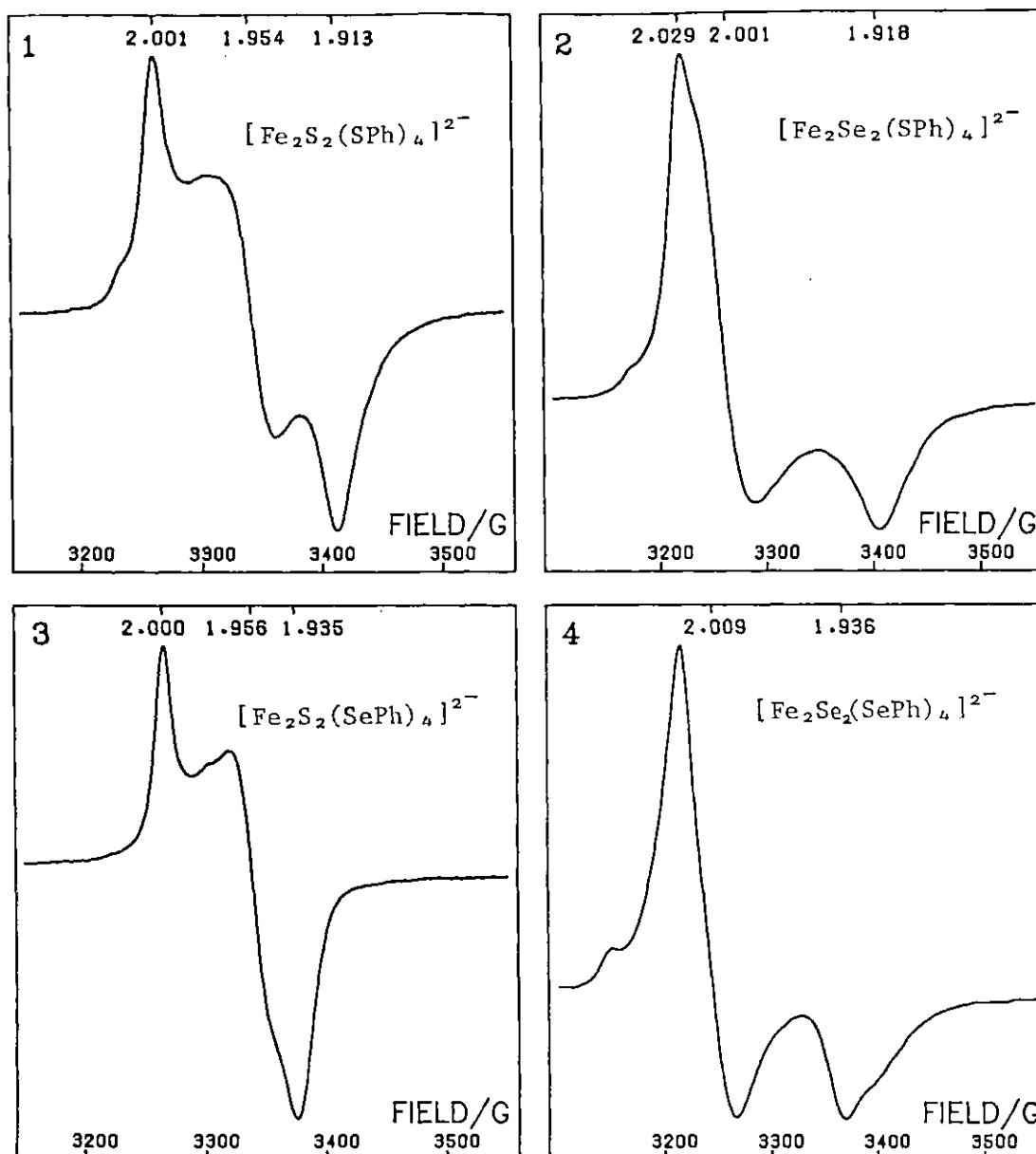
FIG. 1.19 $[\text{Fe}_2\text{X}_2(\text{YPh})_4]^{2-}$ (X,Y=S,Se) REDUCED IN DMF

Figure 1.21 displays the g-values for many of these spectra plotted against $(g_y - g_x)$. Also plotted are some measurements for proteins, together with theoretical curves from equations E1.4-E1.6, after Bertrand and Gayda⁶¹: $g_{1x} = 2.020$, $g_{1y} = 2.049$, $g_{1z} = 2.054$,⁸² $\lambda_2 = -80 \text{ cm}^{-1}$; $\Delta_{xz} = 5500 \text{ cm}^{-1}$, $\Delta_{yz} = 4450 \text{ cm}^{-1}$.⁸³ For reduced $[\text{Fe}_2\text{Se}_2(\text{S}_2\text{-o-xylyl})_2]^{2-}$ and $[\text{Fe}_2\text{Se}_2(\text{SR})_4]^{2-}$ (non-vitreous solvent) the g-values agree well with the analysis of Bertrand and Gayda considering the experimental origin

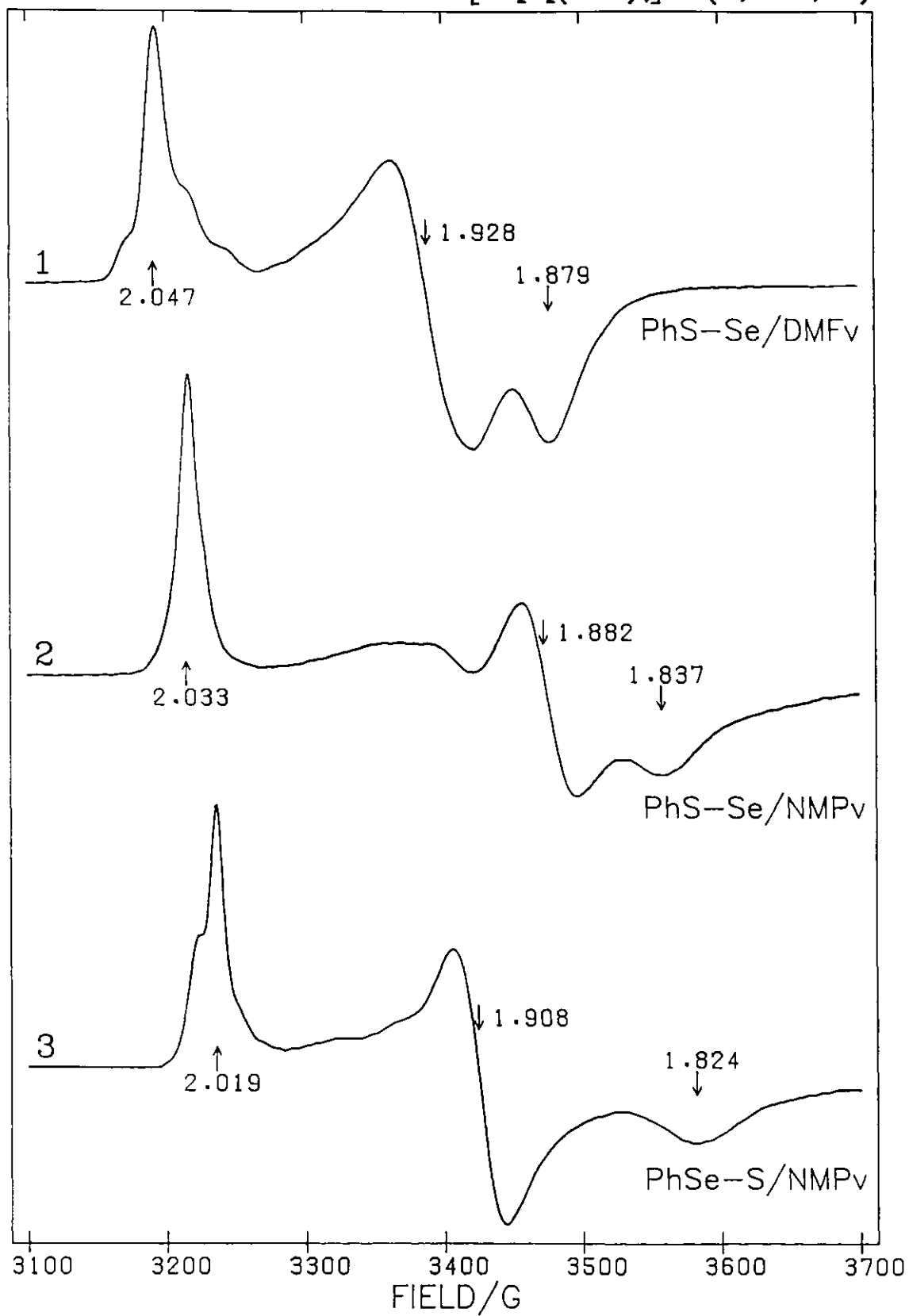
FIG. 1.20 EPR OF REDUCED $[\text{Fe}_2\text{X}_2(\text{YPh})_4]^{2-}$ ($\text{X}, \text{Y} = \text{S}, \text{Se}$)

TABLE 1.8. EPR Data for Reduced $[\text{Fe}_2\text{X}_2(\text{YR})_4]^{2-}$,
(X,Y = S, Se).

Compound			Solvent	Sec. 1 Figure	Additives	~ %	g_z	g_y	g_x	g_{av}
R	X	Y								
o-xylyl/2	Se	S	DMFv	18.1		95	2.030	1.979	1.930	1.980
o-xylyl/2	Se	S	DMFv		0.1 M n-Bu ₄ NCℓO ₄	95	2.032	1.981	1.928	1.980
Ph	Se	S	DMFv	19.2		100	2.029	2.001	1.918	1.983
Ph	Se	S	DMFv	20.1	0.2 M n-Bu ₄ NCℓO ₄	90	2.047	1.928	1.879	1.951
Ph	Se	S	DMFv		17% CH ₂ Cl ₂	90	2.048	1.929	1.880	1.952
Ph	Se	S	NMPv			95	2.030	2.004	1.917	1.984
Ph	Se	S	NMPv	20.2	0.2 M n-Bu ₄ NCℓO ₄	90	2.033	1.882	1.837	1.917
Ph	S	Se	DMPv	19.3		95	2.000	1.956	1.935	1.964
Ph	S	Se	DMFv		0.1 M n-Bu ₄ NCℓO ₄		2.025 2.017	1.917	—	—
Ph	S	Se	NMPv	20.3	0.2 M n-Bu ₄ NCℓO ₄	90	2.019	1.908	1.824	1.917
Ph	Se	Se	DMFv	19.4		90	2.009	2.009	1.936	1.985
Tolyl	Se	S	DMFv			95	2.030	1.999	1.914	1.981
Tolyl	Se	S	DMFv		0.2 M n-Bu ₄ NCℓO ₄		2.046 2.059	1.927	—	—

Fig 1.21 Plot of g -values vs. $(g_y - g_x)$ for reduced selenium derivatives of model complexes and 2Fe Fd.(Tables 1.8,1.9)

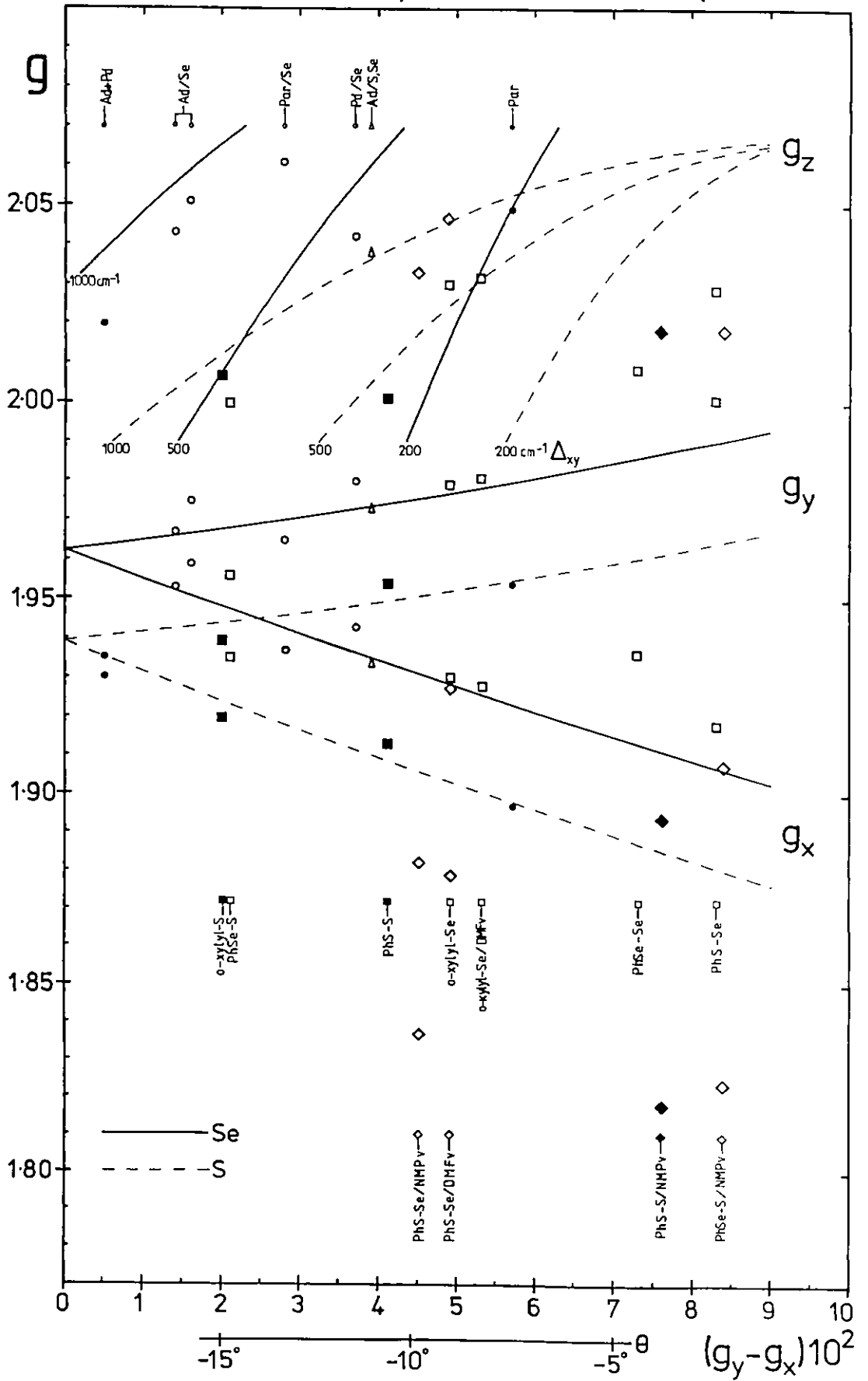


TABLE 1.9. EPR Data for Selenium-Bridged Fd_{red} .

		g_z	g_y	g_x
Ad	Adrenal glands pig ⁸⁰	2.043	1.967	1.953
	beef ⁸¹	2.051	1.975	1.959
Par	Parsley ⁴⁹	2.061	1.965	1.937
Pd	<u>P. Putida</u> ⁸⁰	2.042	1.980	1.943
Ad	Adrenal glands - beef - mixed S, Se ⁸¹	2.038	1.973	1.934

of the different parameters used in E1.4-E1.6. The g -values assumed for the ferric ion are consistent with increased covalency over that for Fe(III)S_4 . Fe(III)Se_4 shows a further positive departure of g -value from 2.0023 compared to $\text{Fe(III)S}_2\text{Se}_2$ ⁸² and consistent with this a non-vitreous sample of reduced $[\text{Fe}_2\text{Se}_2(\text{SePh})_4]^{2-}$ has g_x closer to 2.0 than in the thiophenolate-ligated homologue. Reduced $[\text{Fe}_2\text{S}_2(\text{SePh})_4]^{2-}$ on the other hand gives a signal in non-glassy frozen solvent with g_x & g_y intermediate between the values expected for sulphide and selenide bridged species. This could be indicative of intermediate ferric covalency such that the electron delocalisation is more to the bridging than to the terminal ligands.

Whilst the non-vitreous samples of reduced $[\text{Fe}_2\text{S}_2(\text{YPh})_4]^{2-}$ ($\text{Y} = \text{S}, \text{Se}$) show substantially different signals, very similar g -values are observed with glassy frozen NMP as a solvent. Vitreous NMP solutions of reduced $[\text{Fe}_2\text{Se}_2(\text{SPh})_4]^{2-}$ have on the other hand quite different

signals from these. Such results may be consistent with a large degree of ligand replacement in the vitreous samples. Results for glassy samples with DMF solvent are less clear.

As with the sulphur homologues, it seems reasonable to assign the signals for the S₂-o-xylyl-ligated dimer and non-vitreous samples containing aryl-chalcogenide ligated dimers, to trianion species resulting directly from reduction of the dianions. Such an assignment is made largely on the grounds of g-value compatibility to the Bertrand-Gayda model and because of their solvent-invariant lineshapes.

1.7. Concluding Remarks.

From the above spectroscopic evidence it is concluded that a substantial proportion of $[\text{Fe}_2\text{S}_2(\text{SR})_4]^{3-}$ may be observed following chemical reduction of $[\text{Fe}_2\text{S}_2(\text{SR})_4]^{2-}$ in solution using a fairly simple technique of reaction and product capture. As expected, these trianion species exhibit characteristics closely matching those of reduced 2Fe2S ferredoxins.

The peculiar solvent dependency of spectra for the monodentate thiol ligated complexes and the spectral changes in the presence of added thiols seem indicative of a considerably enhanced reactivity compared with the dianionic precursors. Trianionic tetramer species are also observed to have greatly increased reactivity compared with dianions.^{76,84-87} $[\text{Fe}_4\text{S}_4(\text{SPh})_4]^{3-}$ has been observed to form an adduct with carbon monoxide of undetermined structure,⁸⁵ but no differences were observed in EPR signals obtained in this present work following reductions of $[\text{Fe}_2\text{S}_2(\text{S}_2\text{-o-xylyl})_2]^{2-}$ or $[\text{Fe}_2\text{S}_2(\text{STol})_4]^{2-}$ under CO, H₂ or argon atmospheres.

With regard to reduction of $[\text{Fe}_2\text{S}_2(\text{SR})_4]^{2-}$, it has not proved possible, with the present extent of investigation, to formulate an exact rationalisation for the origin of the various spectral differences observed for a variety of solvents and additives. Certainly the changes in the EPR spectra must result from some chemical modification of the coordination at one or both irons, but the precise nature of the interactions between the dimer and solvent or added thiol have not been elucidated.

EPR proves to be a particularly useful technique in observing the reduced dimers in view of its selectivity for these species at liquid nitrogen temperatures, since precursor dianion and tetramer reaction products give no interfering signals. No other readily available spectroscopic method offers this advantage. Thus, in keeping with its considerable contribution to the discovery, isolation and characterisation of ferredoxin proteins, EPR has been found gratifyingly indispensable in detection and study of the reduced 2Fe2S model complexes.

1.8. Experimental.

Synthetic details concerning the compounds used in this section may be found in Section 6.

1.8.1. One Electron Reduction of $[\text{Fe}_2\text{X}_2(\text{YR})_4]^{2-}$ (X, Y = S, Se).

Reductions of dianionic dimers were performed anaerobically in DMF, DMSO, NMP or PhCN with sodium acenaphthylenide, generated in solution (usually DMF or NMP) from acenaphthylene reduced over 0.1 to 0.2% Na/Hg amalgam.

In a typical reduction 5 ml of a filtered solution around 0.5 to 3 mM in iron-cluster was transferred to a septum-capped Schlenk tube and further deoxygenated by several evacuation-freeze-thaw-N₂ flush cycles. An EPR sample tube or Mössbauer cell, well flushed with dinitrogen, was assembled on a stainless steel or PTFE transfer tube inserted into the Schlenk-tube septum, ready for immediate transfer of part of the cluster solution subsequent to reduction. In the cases where the solvent had a low freezing point the cluster solution was again frozen at this stage and thawed just prior to addition of reducing agent. Around 1.5-fold excess (more in cases where some oxidising additive was present) of sodium acenaphthylenide in about 100 μ l of solvent was then added to the dimer solution from a syringe, rapidly mixed by swirling the solution in the Schlenk tube, and an aliquot immediately transferred to the sample holder under pressure of N₂, where it was quickly frozen in liquid nitrogen. With experience, the whole process, from addition of reducing agent to completion of solvent solidification, could be performed in 15 to 20 seconds. The reaction is accompanied by a colour change caused by loss in intensity of low energy spectral features.

In general EPR samples were collected in a normal 10 cm tube sealed at the upper open end by a rubber septum and purged of oxygen by evacuation and flushing; where prolonged quantitative measurements or extensive thawing of a sample was to be undertaken a tube was employed which could be filled and then sealed, via a stopcock joined to the EPR tube with a graded quartz-pyrex connection. The Mössbauer cell sample

containers, of a cylindrical "pill-box" design, were loaded by tight fit insertion of a steel transfer needle into a hole drilled in the side, pre-flushed inert gas was allowed to escape through a second smaller hole bored adjacent to the inlet.

1.8.2. ^{57}Fe Enriched $[\text{Fe}_2\text{S}_2(\text{S}_2\text{-o-xylyl})_2]^{2-}$.

This was prepared from 82.94% ^{57}Fe via $[\text{Fe}(\text{S}_2\text{-o-xylyl})_2]^-$. 20 mg (0.35 mmol) of the enriched metal (AERE, Harwell) was dissolved in 0.15 ml AR CHCl_3 and 0.3 ml MeOH at 70°C over 5 hrs in a 10 ml centrifuge tube. The solution was evacuated to dryness and 210 mg (1.2 mmol) $(\text{HS})_2\text{-o-xylyl}$ thiol, 290 mg (1.8 mmol) Et_4NCl and 2.5 ml deoxygenated EtOH added. 1.6 ml of a 1.5 M NaOEt solution (2.4 mmol) was added to the above under N_2 , via a septum seal, at 0°C over 15 mins. N_2 was bubbled gently to stir the solution a further 15 mins at 0°C . Precipitated NaCl was centrifuged down and the supernatant liquid drawn off anaerobically into another centrifuge tube. The NaCl was washed with EtOH, again centrifuged down, and the washing added to the bulk solution. Oxidation of the combined product solution was accomplished by controlled ingress of atmospheric oxygen, and the precipitated red/black $\text{Et}_4\text{N}[\text{Fe}(\text{S}_2\text{-o-xylyl})_2]$ collected by centrifugation and washed well with EtOH. Conversion to $[\text{Et}_4\text{N}]_2[\text{Fe}_2\text{S}_2(\text{S}_2\text{-o-xylyl})_2]$ was accomplished in warm MeCN with NaHS as described by Cambray, et al.⁴⁵ Overall yield based on Fe metal was 87%.

1.8.3. Experimental Details for Figures.

Figure 2. $[\text{Fe}_2\text{S}_2(\text{S}_2\text{-o-xylyl})_2]^{3-}$ in 0.1 M $n\text{-Bu}_4\text{NClO}_4/\text{DMF}$.

2.1. 1.2 eq. ACN, P20, MA 1.6G, v 9.142 simulation "EPRPOW" (Gaussian) then "CONV" (Lorentzian).

2.2. 83% ^{57}Fe enriched, 2 eq ACN, P20, MA 3.2G, v 9.142.

2.3. 83% ^{57}Fe , P10, MA 4G, v 9.144.

2.4. P10, MA 2.5G, v 9.141.

Figure 3. $[\text{Fe}_2\text{S}_2(\text{S}_2\text{-o-xylyl})_2]^{3-}$ in DMSO.

3.1. 2 eq ACN, P6, MA 2.5, v 9.160; simulation - as 2.1

3.2. P6, MA 4, v 9.160; simulation - "EPRPOW" (Lorentzian).

Figure 4. The signal intensity was measured as the uncorrected height at the low field peak.

Figures 6 — 8. 0.6 mM $[\text{Fe}_2\text{S}_2(\text{S}_2\text{-o-xylyl})_2]^{2-}$ in DMF, and product of reduction with 2 eq ACN.

Figure 9. $[\text{Fe}_2\text{S}_2(\text{SC}_6\text{H}_4\text{Y})_4]^{2-}$ (Y = Cl, H, Me) reduced in NMP with 1.5 eq ACN.

Spectra in each group are normalised by integrated intensity.

Y = Cl. 9.1. P10, MA 4, v 9.149; 9.2. 0.2 M $n\text{-Bu}_4\text{NClO}_4$, P10, MA5, v 9.148;

9.3. 0.2 M $n\text{-Bu}_4\text{NClO}_4$ devit., P16, MA4, v 9.149.

Y = H. 9.4. P10, MA 2.5, v 9.147; 9.5. 0.2 M $n\text{-Bu}_4\text{NClO}_4$, P16, MA 2.5, v 9.147; 9.6. 0.2 M $n\text{-Bu}_4\text{NClO}_4$ devit., P10, MA2, v 9.147.

Y = Me. 9.7. P10, MA 3.2, v 9.146; 9.8. 0.2 M $n\text{-Bu}_4\text{NClO}_4$, P14, MA 2.5, v 9.141; 9.9. 0.2 M $n\text{-Bu}_4\text{NClO}_4$ devit., P10, MA 3.2, v 9.141.

Figure 10. $[\text{Fe}_2\text{S}_2(\text{SC}_6\text{H}_4\text{Y})_4]^{2-}$ (Y = Cl, H, Me) reduced in DMF with 1.5 eq. ACN.

Spectra in each group are normalised by integrated intensity.

Y = Cl. 10.1. P10, MA4, v 9.145; 10.2. 0.1 M n-Bu₄NClO₄, P10, MA5, v 9.144;

10.3. 0.1 M n-Bu₄NClO₄ devit., P10, MA 3.2, v 9.145.

Y = H. 10.4. P10, MA5, v 9.143; 10.5. 0.1 M n-Bu₄NClO₄, P10, MA2, v 9.143;

10.6. 0.1 M n-Bu₄NClO₄ devit., P10, MA5, v 9.143.

Y = Me. 10.7. P10, MA5, v 9.142; 10.8. 0.1 M n-Bu₄NClO₄, P10, MA5, v 9.142;

10.9. 0.1 M n-Bu₄NClO₄ devit., P10, MA5, v 9.142.

Figure 11. 11.1 as Figure 10.1; 11.2 as Figure 10.5; 11.3 as Figure 9.8.

Simulations using "EPRPOW".

Figure 12. Reduced $[\text{Fe}_2\text{S}_2(\text{SC}_6\text{H}_4\text{Y})_4]^{2-}$ (Y = Cl, H, Me).

12.1. Y = H, 1.5 eq ACN, 5% H₂O/DMF, P0, MA5, v 9.130; 12.2. Y = Cl,

1.4 eq ACN, PhCN, P10, MA5, v 9.129; 12.3. Y = H, 6 eq ACN, 10 excs PhSH,

P2, MA5, v 9.145; 12.4. Y = Me, 6 eq ACN, 10 excs TolSH, 0.1 M

n-Bu₄NClO₄, P8, MA4, v 9.140.

Figure 13. Spectra are height normalised.

1.5 eq ACN, P10, MA3.2, v 9.13 to 9.14.

Figure 14. Reduced $[\text{Fe}_2\text{S}_2(\text{SC}_6\text{H}_4\text{Y})_4]^{2-}$ (Y = Cl, H, Me) with 1.5 eq ACN.

14.1. Y = Cl, P10, MA3.2, v 9.146; 14.2. Y = H, P10, MA3.2, v 9.140;

14.3. Y = Me, P10, MA4, v 9.141.

Figure 15. $[\text{Fe}_2\text{S}_2(\text{SR})_4]^{2-}$ + 50 exs t-BuSH.

15.1. R = Toly1, 2.2 eq ACN, 0.2 M n-Bu₄NClO₄, P8, MA4, v 9.144.

15.2. R = o-xyly1/2, 1.6 eq ACN, 0.1 M n-Bu₄NClO₄, P12, MA2, v 9.149.

15.3. 83% ⁵⁷Fe enriched R = o-xyly1/2, 3 eq ACN, 0.1 M n-Bu₄NClO₄, P10, MA3.2, v 9.149.

Figure 18. $[\text{Fe}_2\text{X}_2(\text{S}_2\text{-o-xyly1})_2]^{3-}$ (X = S, Se).

18.1. X = Se, 1 eq ACN, P10, MA5, v 9.209; 18.2 X = S, 1.3 eq ACN, P10,

MA2, v 9.214.

Figure 19. $[\text{Fe}_2\text{X}_2(\text{YPh})_4]^{2-}$ (X, Y = S, Se) reduced in DMF.

19.1 X = Y = S, as Figure 10.4; 19.2 X = Se, Y = S, 2 eq ACN, P10,

MA3.2, v 9.141; 19.3 X = S, Y = Se, 1.5 eq ACN, P10, MA5, v 9.140;

19.4 X = Y = Se, 1.5 eq ACN, P10, MA5, v 9.127.

Figure 20. $[\text{Fe}_2\text{X}_2(\text{YPh})_4]^{2-}$ (X, Y = S, Se) reduced in 0.2 M $n\text{-Bu}_4\text{NClO}_4$ with 1.5 eq ACN.

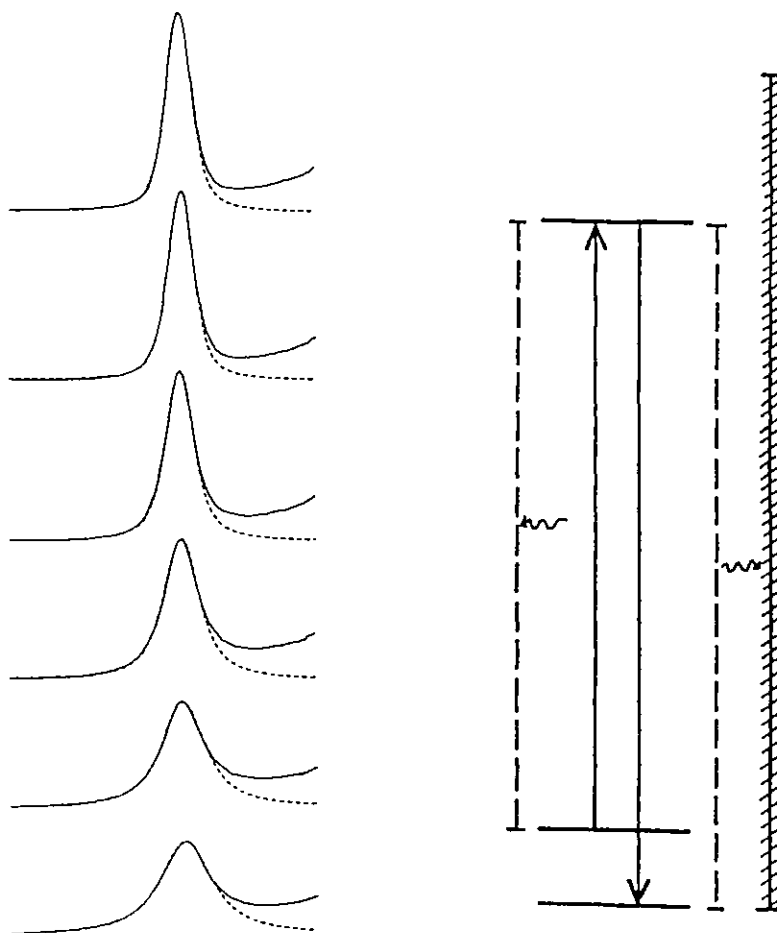
20.1 X = Se, Y = S, DMF, P10, MA4, v 9.143; 20.2 X = Se, Y = S, NMP,

P10, MA5, v 9.146; 20.3 X = S, Y = Se, NMP, P8, MA5, v 9.144.

Notes. 1) unless otherwise stated, the sample temperature is ~ 100 K

2) non-vitreous samples were often warmed after freezing to induce further crystallisation.

3) P = Power/dB attenuation from 200 mw, MA = modulation amplitude/G, v = microwave frequency/GHz, eq ACN = equivalents acenaphthylenide.

SECTION 2**SPIN-LATTICE RELAXATION
IN $[\text{Fe}_2\text{X}_2(\text{SR})_4]^{3-}$ ($\text{X} = \text{S}, \text{Se}$)**

2. SPIN-LATTICE RELAXATION IN $[\text{Fe}_2\text{X}_2(\text{SR})_4]^{3-}$ (X = S, Se).

ABSTRACT	98
2.1. <u>Introduction: Spin Lattice Relaxation in Ferredoxins.</u>	99
2.2. <u>Relaxation mechanism.</u>	100
2.3. <u>Deduction of T_1 from Homogeneous Broadening.</u>	102
2.4. <u>Spin-Lattice Relaxation in 2-Fe Synthetic Complexes.</u>	106
2.4.1. $[\text{Fe}_2\text{S}_2(\text{S}_2\text{-o-xylyl})_2]^{3-}$ in DMSO and DMF	107
2.4.2. $[\text{Fe}_2\text{Se}_2(\text{S}_2\text{-o-xylyl})_2]^{3-}$ in DMF	111
2.4.3. $[\text{Fe}_2\text{S}_2(\text{SC}_6\text{H}_4\text{Cl})_4]^{3-}$ in DMF.	113
2.5. <u>Discussion.</u>	115
2.6. <u>Conclusion.</u>	122
2.7. <u>Experimental.</u>	124

ABSTRACT

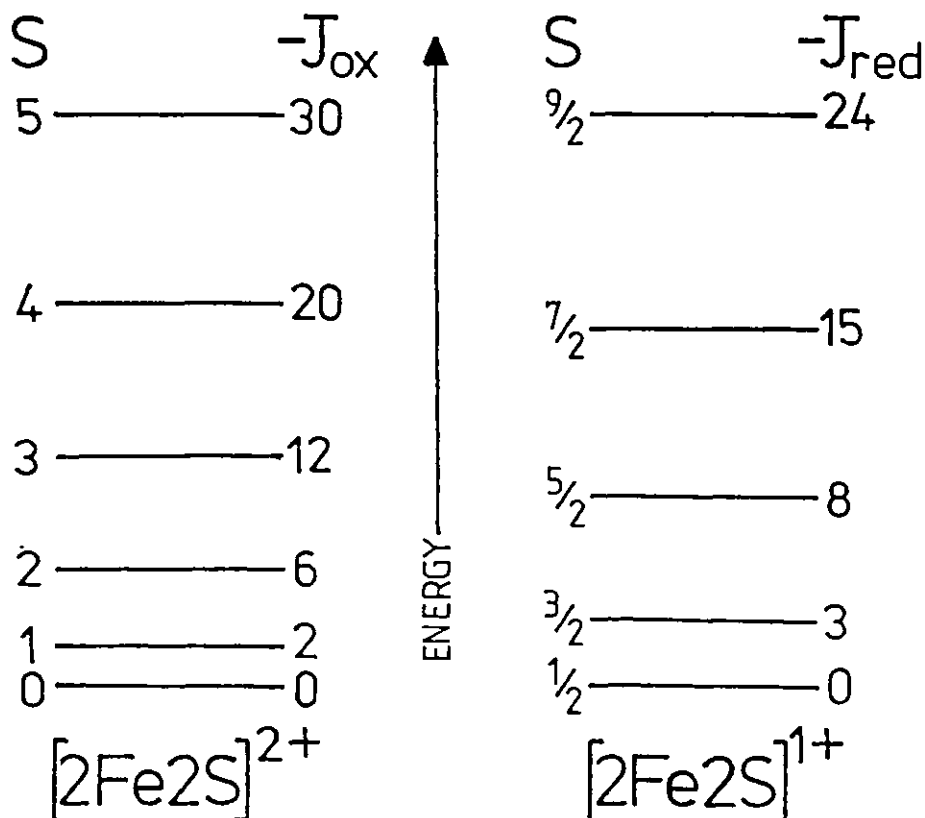
The low field peaks for the EPR spectra of $[\text{Fe}_2\text{X}_2(\text{S}_2\text{-o-xylyl})_2]^{3-}$ ($\text{X} = \text{S}, \text{Se}$) and $[\text{Fe}_2\text{S}_2(\text{SC}_6\text{H}_4\text{Cl})_4]^{3-}$ in frozen DMF and/or DMSO are analysed in terms of a convolution product between Gaussian and Lorentzian functions, over the temperature range ca. 90–200 K. The temperature-dependent component of the Lorentzian function responsible for the broadening at the higher temperatures is related to the spin-lattice relaxation time T_1 . Variation of T_1 with temperature may be fitted according to a relationship $(1/T_1) \propto T^n$ or according to a dominant Orbach relaxation mechanism involving an excited state at ΔE such that $(1/T_1) \propto \exp(\Delta E/kT)$. This last interpretation is considered more appropriate and the excited state is related to the $S = 3/2$ spin level for antiferromagnetic coupling of the irons involving exchange interactions of 300 cm^{-1} for $[\text{Fe}_2\text{S}_2(\text{S}_2\text{-o-xylyl})_2]^{3-}$, 200 cm^{-1} for $[\text{Fe}_2\text{Se}_2(\text{S}_2\text{-o-xylyl})_2]^{3-}$ and 240 cm^{-1} for $[\text{Fe}_2\text{S}_2(\text{SC}_6\text{H}_4\text{Cl})_4]^{3-}$.

2. Spin-Lattice Relaxation in $[\text{Fe}_2\text{X}_2(\text{SR})_4]^{3-}$, (X = S, Se).

2.1. Introduction: Spin-Lattice Relaxation in Ferredoxins.

The proposal of Gibson, et al.,¹⁷ that an anti-ferromagnetic interaction exists between the iron atoms in two-iron ferredoxins is well established and has been briefly described in Section 1.1 of this thesis. The manifolds of spin states resulting from this coupling are shown in Figure 2.1. for the ferric-ferric and ferrous-ferric oxidation levels. In the original description of the anti-ferromagnetic coupling model, it was suggested that the anomalous temperature dependence of the EPR observed from the ground state in Fd_{red} might be explained in terms of a resonant two-phonon relaxation process involving low lying excited states of the spin manifold.

Figure 2.1. Spin-state manifolds for antiferromagnetic coupling of two irons in ferric-ferric and ferrous-ferric oxidation levels.



2.2. Relaxation Mechanism.

For processes other than emission or spin-diffusion an excited spin must lose its energy to its surroundings (lattice) in the form of interatomic vibration. It is considered that lattice vibrations modulate the orbital moment via the ligand field, and through spin-orbit coupling this leads to an oscillatory electromagnetic field at the spin. The efficiencies of the various mechanisms by which this process occurs are dependent on the distribution of phonon energies in the sample, as determined by its temperature. The overall rate of net transfer of spin energy to the lattice is characterised by T_1 , the spin-lattice relaxation time. The variation of this parameter with temperature may be used to identify the dominant spin-lattice relaxation mechanism, provided the sample maintains thermal equilibrium with the cryostatic bath. Equation E2.1 contains terms describing the temperature dependence of the relaxation rate $1/T_1$ for three important processes which are illustrated in Figure 2.2. Detailed accounts of these may be found in references 88-90. The direct process, involving only a narrow band of phonons with energies very close to that for the spin-transitions, only makes an appreciable contribution to $1/T_1$ at the lowest temperatures. Raman processes involve pairs of phonons from anywhere in the lattice continuum, provided their energy difference coincides with that for the EPR spin system. These two-phonon relaxation mechanisms are strongly temperature dependent with exponents (n) typically equal to 7, 9 or 5. Despite having lower transition probabilities, due to involving two phonons, Raman processes dominate direct processes at higher temperature since they make use of the entire phonon-spectrum. If an

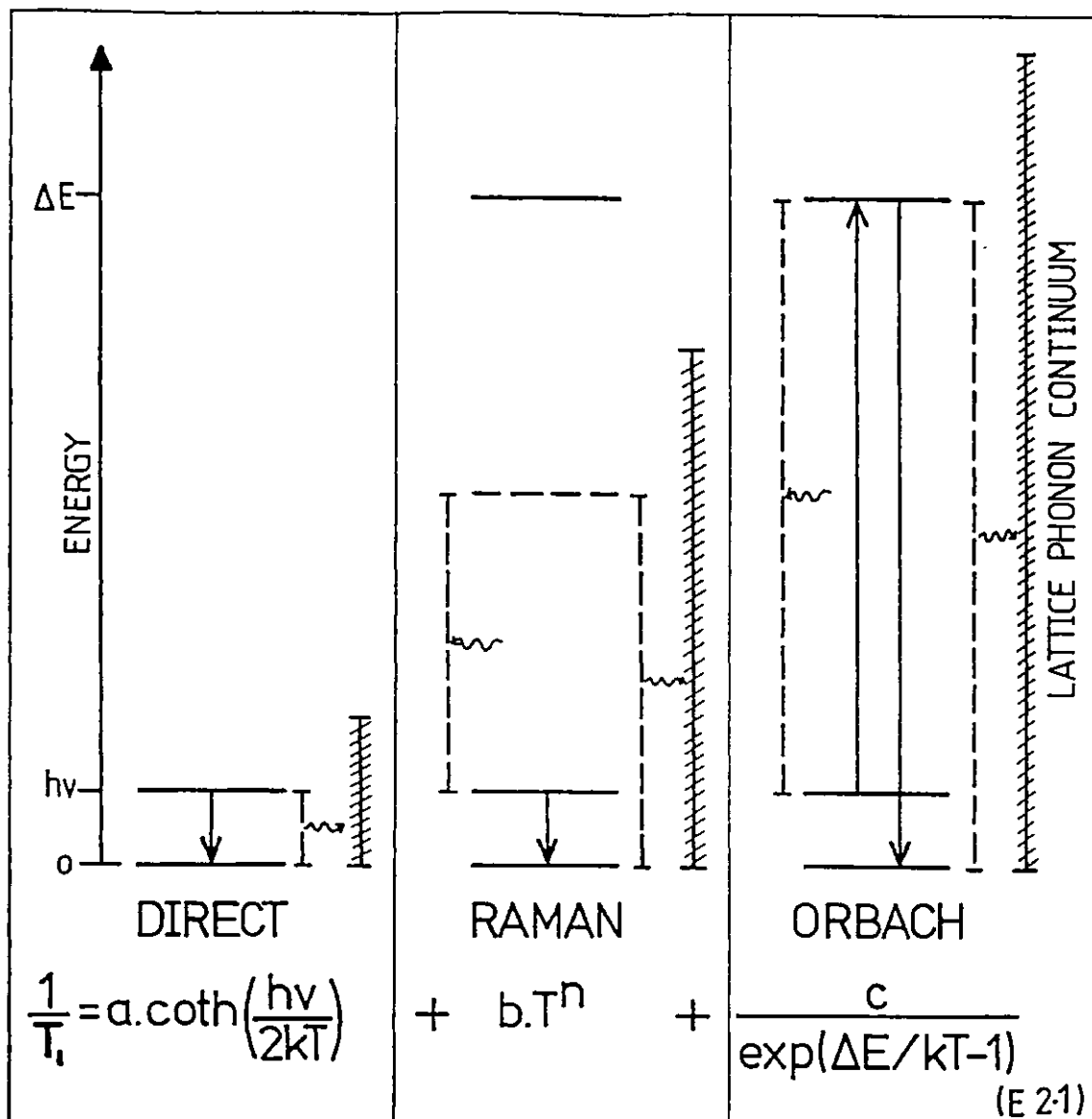


Figure 2.2. Three relaxation mechanisms of an EPR spin system and their temperature dependence.

excited state (at ΔE) lies within the phonon energy continuum it may take the place of the virtual level in the normal Raman process and the resulting resonant Orbach⁹⁰ relaxation mechanism, although involving only two narrow bands of phonon frequencies, has a greatly increased transition probability. For $\Delta E \gg kT$, the temperature dependence of the relaxation rate when an Orbach mechanism is dominant is given in equation E2.2.

$$1/T_1 = C \cdot \exp(-\Delta E/kT)$$

E2.2

For the $2\text{Fe}2\text{S}$ Fd_{red} from Spirulina maxima, Gayda et al.¹⁹ studied the temperature variation of T_1 as manifested in the changing anisotropic homogeneous broadening of the EPR lineshape. They found a good fit to E2.2 in the temperature interval 90 to 130 K with $\Delta E \approx 250 \text{ cm}^{-1}$ ($\approx 350 \text{ K}$) and interpreted this in terms of a dominant Orbach relaxation mechanism involving the first excited state from anti-ferromagnetic ferric-ferrous coupling with exchange integral $J = -83 \text{ cm}^{-1}$.

2.3. Deduction of T_1 from Homogeneous Broadening.

Shortening of the lifetime of a spin state by some relaxation process will lead to an increased uncertainty in its energy. For a group of spins (spin-packets) having otherwise identical resonance fields, this will lead to a broadening of Lorentzian shape with a width δH_L (half-width at half-height) which is directly proportional to the relaxation rate (E2.3).

$$\frac{1}{T_1} (\text{sec}^{-1}) = \frac{g\beta}{\hbar} \cdot \delta H_L (\text{Gauss}) \quad \text{E2.3}$$

If other sources of homogeneous or inhomogeneous broadening are present, or if there is resonance anisotropy, δH_L must be extracted from the experimental lineshape by some deconvolution procedure. In general then, the EPR lineshape is the convolution product of a theoretical absorption spectrum, a Gaussian inhomogeneous broadening function and the Lorentzian spin-packet lineshape as shown in Figure 2.3. The widths of the latter two broadening functions may exhibit anisotropy.

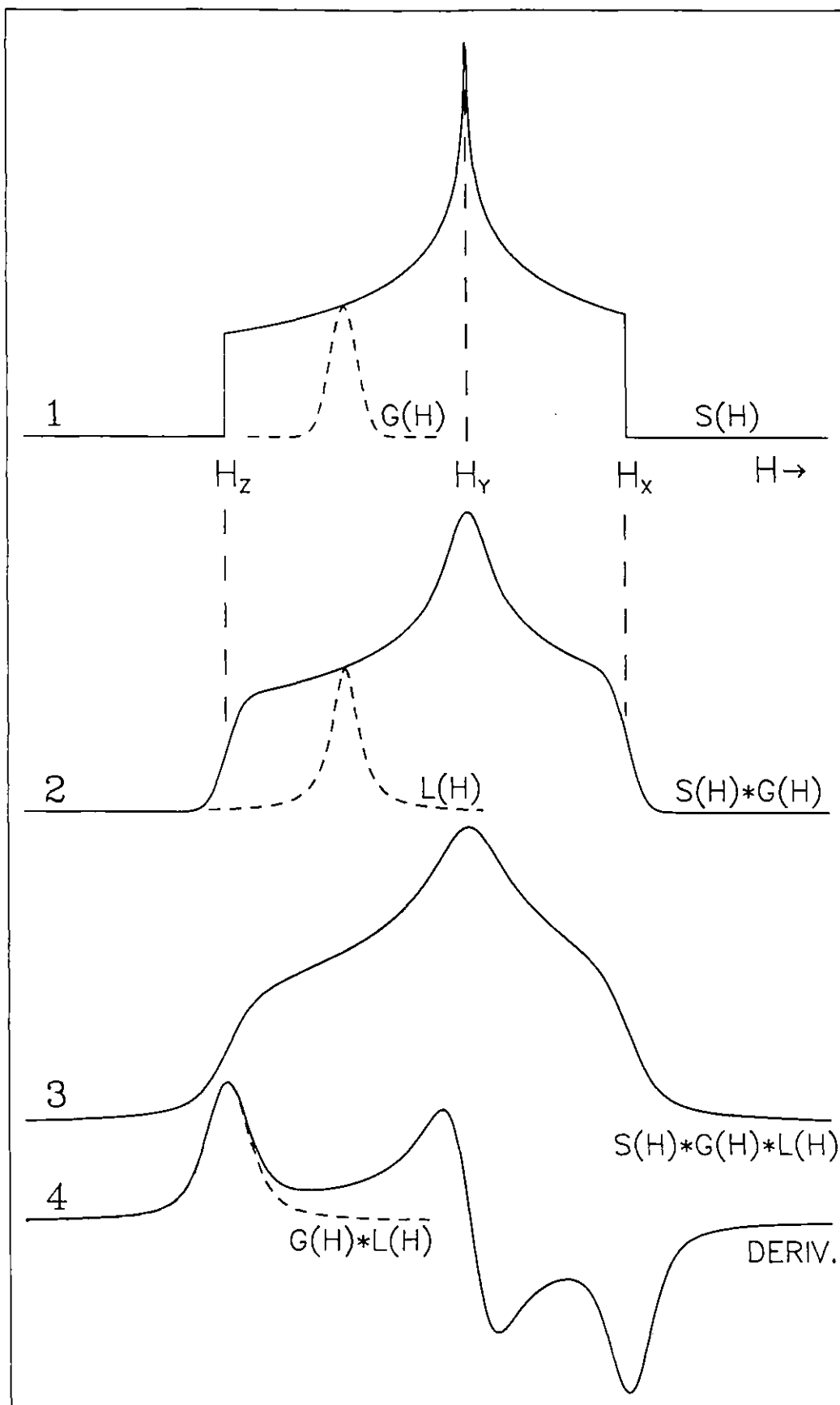


Fig. 2.3 Convolution product of theoretical EPR absorption spectrum $S(H)$ with Gaussian $G(H)$ and Lorentzian $L(H)$ functions, together with deconvolution of H_Z derivative peak by simulation with $G(H)*L(H)$ product.

Analytical expressions are available for $S = 1/2$ theoretical absorption curves⁹¹ or the curves may be derived numerically by spatial integration. Numerical convolution with Gaussian and Lorentzian functions leads to a synthesised EPR lineshape which may be fitted to that obtained experimentally. This simulation approach was the method used by Gayda et al.¹⁹ to determine T_1 at various temperatures from the lineshape of Spirulina maxima Fd_{red} . In the temperature interval studied, the Lorentzian contribution to the broadening was sufficiently greater than the Gaussian contribution to allow the use of a purely Lorentzian function. One of the main difficulties inherent in extracting δH_L by simulation, is the choice of an empirical law to describe the anisotropy of the relaxation time. If, however, one principal axis resonance lies well separated in the spectrum of interest, then the theoretical absorption curve appears like a step function at this point and this part of the broadened derivative spectrum has a shape closely approaching Gaussian-Lorentzian. Deconvolution of such a peak may then lead to an evaluation of T_1 along this axis-orientation. Bertrand et al.⁹² have made a detailed analysis of the accuracy and applicability of this method by studying synthesised spectral lineshapes. Figure 2.4 is reproduced from their work as it represents a useful summary of the results.

$\delta_L = \delta H_L / |H_{\perp} - H_{\parallel}|$, $\delta_G = \delta H_G / |H_{\perp} - H_{\parallel}|$ are Lorentzian and Gaussian widths respectively, used in the synthesis of a derivative lineshape from which a half-width, δ' , is measured for half-height at H_{\parallel} and away from H_{\perp} . For small broadening this may be taken as a Gaussian-Lorentzian convolution product, with the width of the Gaussian function given by the width of the peak when $\delta_L = 0$. Bertrand et al. then extract the

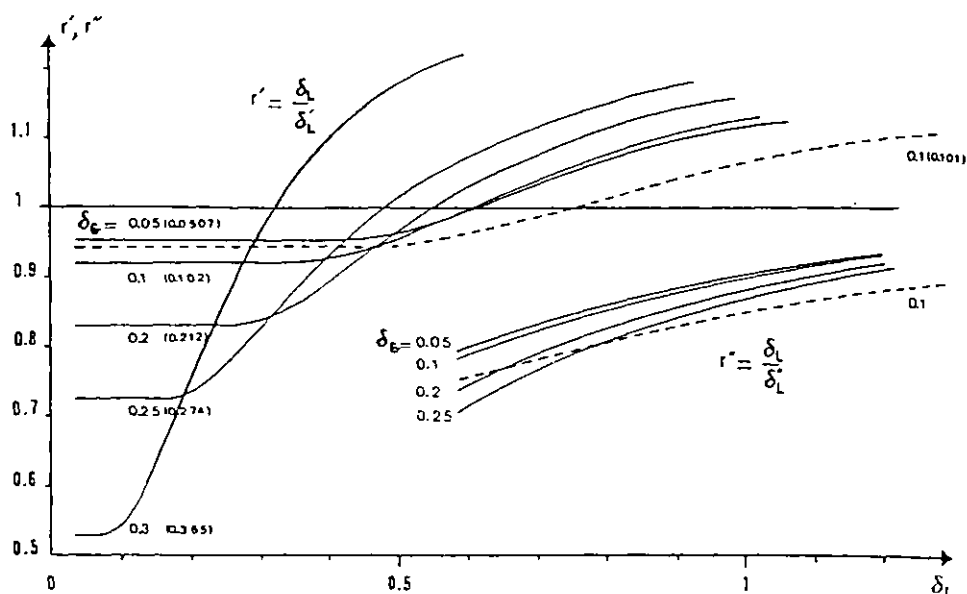


FIG. 2.4 Variations of the parameters r' and r'' upon δ_L for different values of δ_G . The values in parentheses are the half-widths of the peaks measured for $\delta_L = 0$. —, axial spectrum; ---, symmetric rhombic spectrum with $\delta_G = 0.1$. The values of r' and r'' were calculated with a precision of about 1%.⁹²

half-width δ_L' of the Lorentzian packet from δ' using Gauss-Lorentz convolution product tables.⁹³ $r' = \delta_L / \delta_L'$ is an error function for which departure from unity indicates over-estimation of the Gaussian or Lorentzian width due to incursive contributions from outside the peak. For very large broadenings the lineshape at H_{\parallel} and away from H_{\perp} , approximates a pure Lorentz derivative and the Lorentzian half-width δ_L'' is obtained as $1.236 \delta_L'$. The error function $r'' = \delta_L / \delta_L''$ tends to unity as δ_L increases. It is readily apparent from this analysis of Bertrand et al.⁹² that provided there is a reasonably well resolved spectral extremum for which $\delta_G \lesssim 0.1$, the homogeneous packet width may be measured for a single direction to better than 10% using a combination of these methods. Analysis of EPR lineshapes for Spirulina maxima Fd_{red} in this way has demonstrated dominance of the Orbach relaxation mechanism down to 50 K.⁹²

Other methods which have been used to extract δH_L from $[2Fe_2S]^{1+}$, $[4Fe_4S]^{1+}$ and $[4Fe_4S]^{3+}$ ferredoxins have involved procedures of rather dubious accuracy. The equation $\delta H^2 = \delta H_L^2 + \delta H_G^2$, where δH is the width of some spectral feature, has been used to evaluate the extent of homogeneous broadening,^{94,95} but is strictly valid only as $\delta H_L \rightarrow 0$. Another method involves simulation of broad high temperature spectra by convolution of an unbroadened low-temperature spectrum with an isotropic Lorentzian function. This ignores T_1 -anisotropy or any temperature dependency of the \underline{g} tensor and has only been applied to absorption EPR spectra, where inferior lineshape detail enables easier fits to be obtained.⁹⁵⁻⁹⁷

An additional method of measuring the energy of the first excited-state by observing the thermal depopulation of the ground-state is sometimes applicable to ferredoxin EPR spectra.⁹⁴⁻⁹⁹

2.4. Spin-Lattice Relaxation in 2Fe Synthetic Complexes.

EPR spectra have been obtained for $[Fe_2X_2(S_2\text{-o-xylyl})_2]^{3-}$ ($X = S, Se$) and $[Fe_2S_2(SC_6H_4Cl)_4]^{3-}$ in DMSO and/or DMF solvents in the temperature range ca. 90 K to 200 K. In each case the low field peak is well resolved at ca. 100 K and broadens substantially as the temperature is increased towards ca. 200 K. This Lorentzian broadening, δH_L , has been evaluated by least-squares fitting the lowest field part of the peak with a Gaussian-Lorentzian convolution function in a similar manner to Figure 2.3.4. As the function is not expected to be a good fit to the high-field side of the peak, accumulation of the squared difference between the experimental and calculated lines was terminated a little above H_z . H_z was often found to change slightly from spectrum to spectrum

and in order to attain the most accurate linewidth analysis the calculated line was in general evaluated at such a position that the crossover of its derivative superimposed the crossover of the derivative experimental lineshape.

The theoretical accuracy of the method of extraction of δH_L in the present applications is found to be better than -5% according to the analysis of Bertrand *et al.*⁹² in Figure 2.4. Since no measurements were taken for which $\delta_L > 0.3$ the error is constant over all measurements and affects only the magnitude of T_1 and not the analysis according to E2.2.

2.4.1. $[\text{Fe}_2\text{S}_2(\text{S}_2\text{-o-xylyl})_2]^{3-}$ in DMSO and DMF.

The low field peak of the $[\text{Fe}_2\text{S}_2(\text{S}_2\text{-o-xylyl})_2]^{3-}$ EPR spectrum shows only slight broadening below ca. 140 K. Above this temperature the whole signal rapidly broadens, Figure 2.5. The contribution to T_1 of the additional spin-lattice relaxation process responsible for the broadening is shown for three samples in Figure 2.6. Two of the samples are from preparations in DMSO whilst the third is for DMF as solvent. For the purpose of clarity, the points for the sample DMSO2 have halved values whilst for the DMF sample the values have been divided by four.

At 100 K the H_z peaks of the EPR spectra for the three samples were best fitted with respective Gaussian and Lorentzian half-width at half-height contributions of 5.8 G and 4.0 G for DMSO1, 5.8 G and 2.0 G for DMSO2 and 6.2 G and 2.9 G for the DMF sample. The residual Gaussian broadening of ca. 6 Gauss ($\delta_G \approx 0.05$) may result from heterogeneity in the molecular environment of the cluster ions similar to

FIG. 2.5 TEMPERATURE DEPENDENT BROADENING OF THE $[\text{Fe}_2\text{S}_2(\text{S}_2\text{-o-xylyl})_2]^{3-}$ /DMSO EPR LINESHAPE

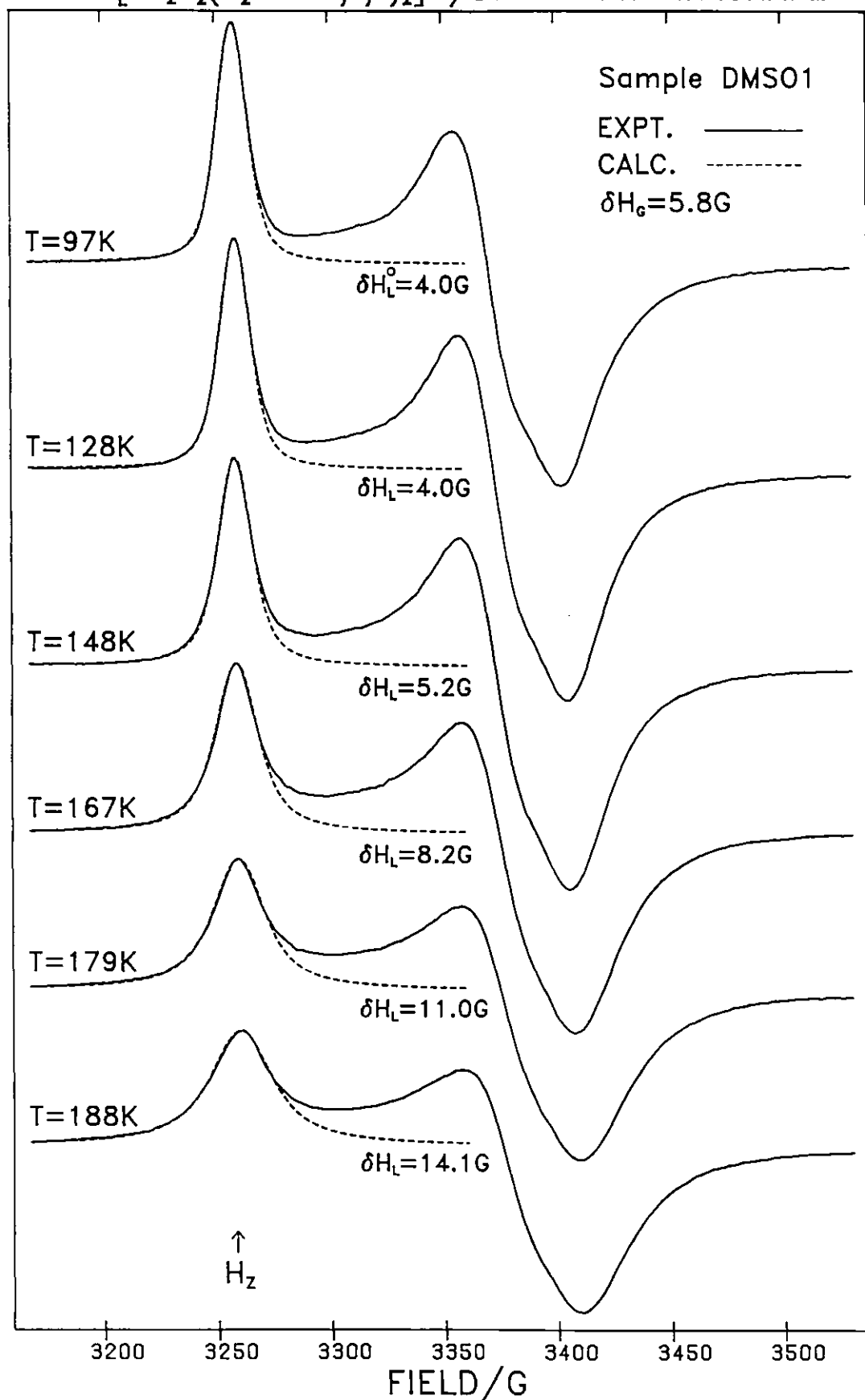
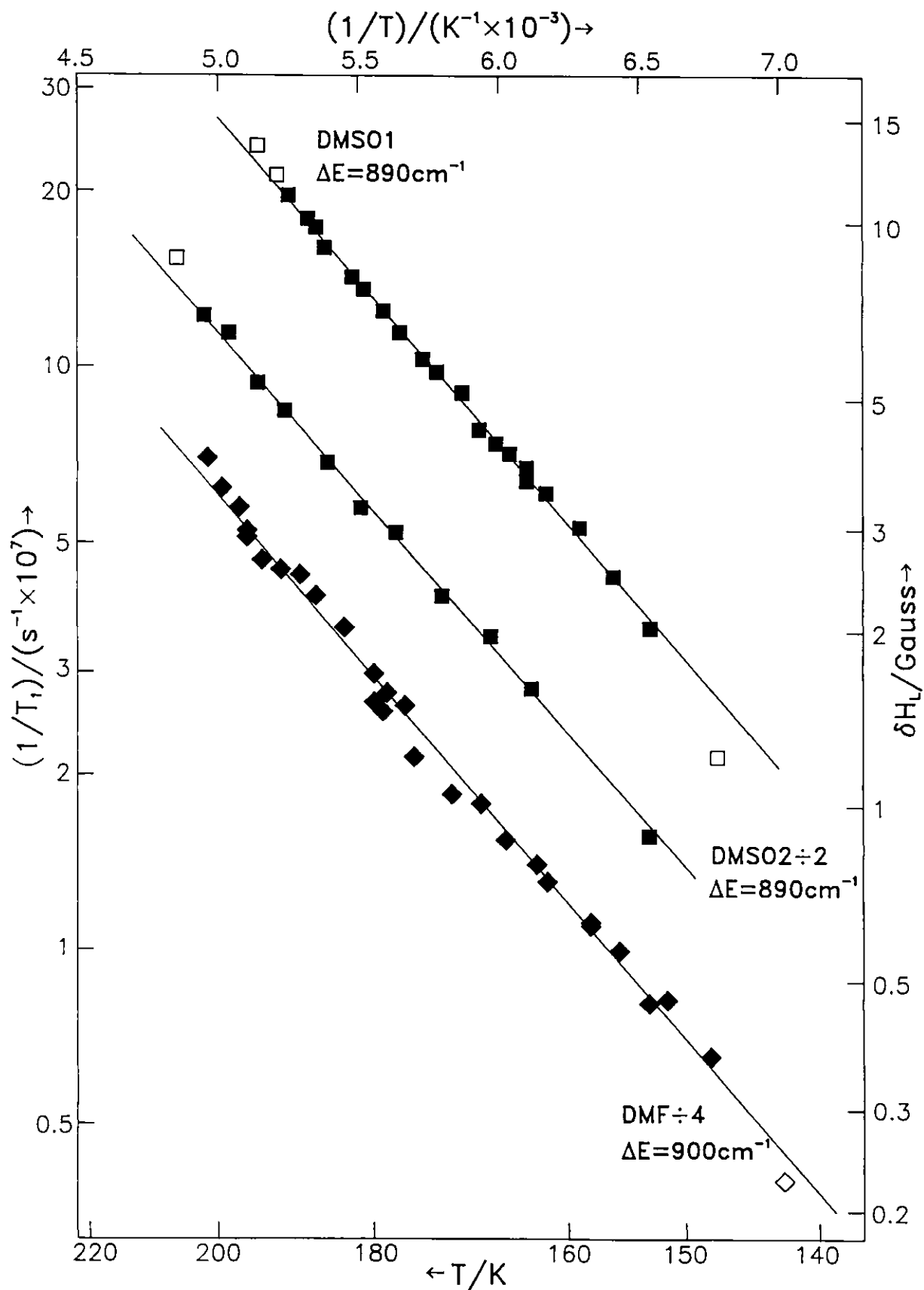


FIG. 2.6 T_1 -BROADENING WITH TEMPERATURE
 AT H_2 IN $[\text{Fe}_2\text{S}_2(\text{S}_2\text{-o-xylyl})_2]^{3-}$ EPR



that suggested for the $[2\text{Fe}-2\text{S}]^{1+}$ centres in some ferredoxins.⁶ At 36 GHz the half-height half-width of the low field peak for spectra of samples in DMF or DMSO is 22 ± 2 Gauss and is quite compatible with a Gaussian distribution in g-value of the magnitude found at X-band (9.2 GHz).

The residual low-temperature Lorentzian broadening component could originate from spin-spin relaxation enhancement. The extent of this residual homogeneous broadening is found to be significantly variable from one sample to another suggesting differences in the expectation proximities of the $[\text{Fe}_2\text{S}_2(\text{S}_2\text{-o-xylyl})_2]^{3-}$ paramagnetic ions. This latter could be caused by differences in the degree of crystallinity adopted by the solvent on freezing. Thus, the residual Lorentz width is smallest (1.5 G) when the complex is contained in a vitreous matrix (0.1 M $n\text{Bu}_4\text{NC}^+\text{O}_4^-/\text{DMF}$, Table 1.1).

The residual low temperature Lorentzian width does not present any problems to the analysis,^{90, pg. 477} and may be subtracted from the Lorentzian width determined at higher temperatures in order to investigate the temperature-dependent broadening process.

Accurate evaluation of the additional homogeneous broadening could be made only in the interval 150 K to 200 K. For temperatures below this range the broadening was too weak to be measured with sufficient accuracy. The upper limit is imposed by sensitivity conditions; also in the case of DMF, solid-state solvent changes onset above 200 K, resulting in irreversible changes in the EPR lineshape.

For the plots of $\log(1/T_1)$ against $1/T$ in Figure 2.6, linear least-squares fits have been made to the full data points according

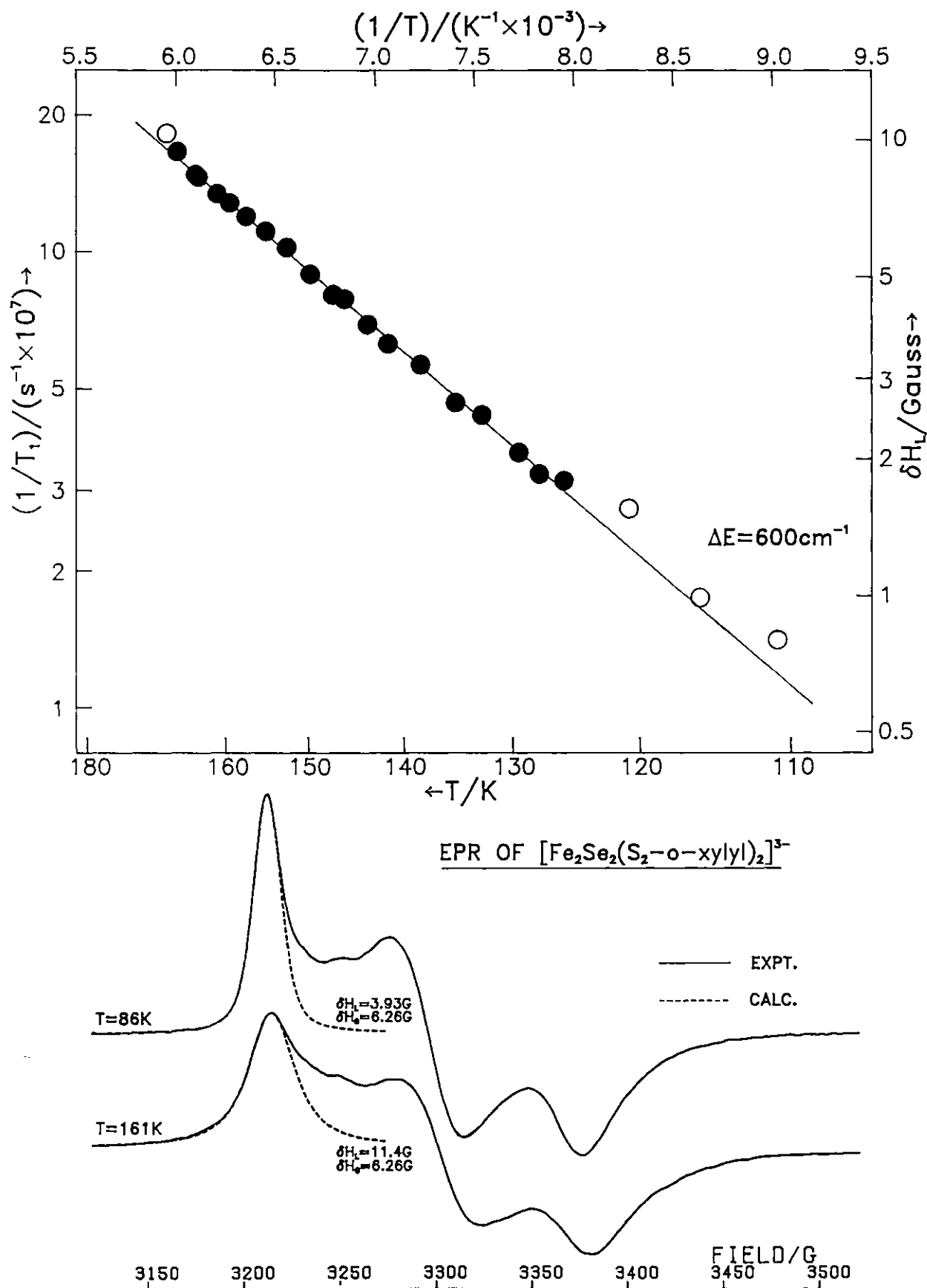
to equation E2.2. From the slopes of these linear fits the separation ΔE of the upper level involved in the proposed resonant relaxation process from the ground state is found to be 890 cm^{-1} for DMSO1, 890 cm^{-1} for DMSO2 and 900 cm^{-1} for DMF solvent (std. error of $\Delta E/\text{cm}^{-1}$, coefficient C/s^{-1} in E2.2 together with its std. error, correlation coefficient = ± 10 , $1.6 \pm 0.10 \times 10^{11}$, 0.9989 for DMSO1; ± 15 , $1.4 \pm 0.2 \times 10^{11}$, 0.9990 for DMSO2; ± 15 , $1.5 \pm 0.2 \times 10^{11}$, 0.9965 for DMF). Although the standard errors on these energies are only 1-2%, an error of $\pm 5\%$ is probably more applicable as judged by making alternative fits to the data.

Provided the temperature was not taken too high, which causes irreversible broadening, the low temperature lineshape could be reproduced on cooling together with subsequent compatible broadening as the temperature was increased a second time.

2.4.2. $[\text{Fe}_2\text{Se}_2(\text{S}_2\text{-o-xylyl})_2]^{3-}$ in DMF.

Only a single $[\text{Fe}_2\text{Se}_2(\text{S}_2\text{-o-xylyl})_2]^{3-}/\text{DMF}$ sample was studied in the temperature range 85 K to 190 K. The low field peaks in the lowest temperature spectra could be analysed in terms of a half-width at half-height Gaussian contribution of 6.3 G and a Lorentzian contribution of 3.9 G. Significant broadening onset at 110 K and could be successfully extracted in the manner described in the previous section up to ca. 170 K. Above this temperature the lineshapes were not so well formed due to depletion in intensity. Also at the highest temperatures some irreversible broadening occurred, probably due to crystalline structural changes in the solvent matrix as suggested in the previous section. Taking account of this additional Lorentzian broadening, the relaxation-broadening depicted in Figure 2.7 could be successfully reproduced in a second incrementing temperature cycle.

FIG. 2.7 T_1 -BROADENING WITH TEMPERATURE
 AT H_z IN $[\text{Fe}_2\text{Se}_2(\text{S}_2\text{-o-xylyl})_2]^{3-}$ /DMF EPR



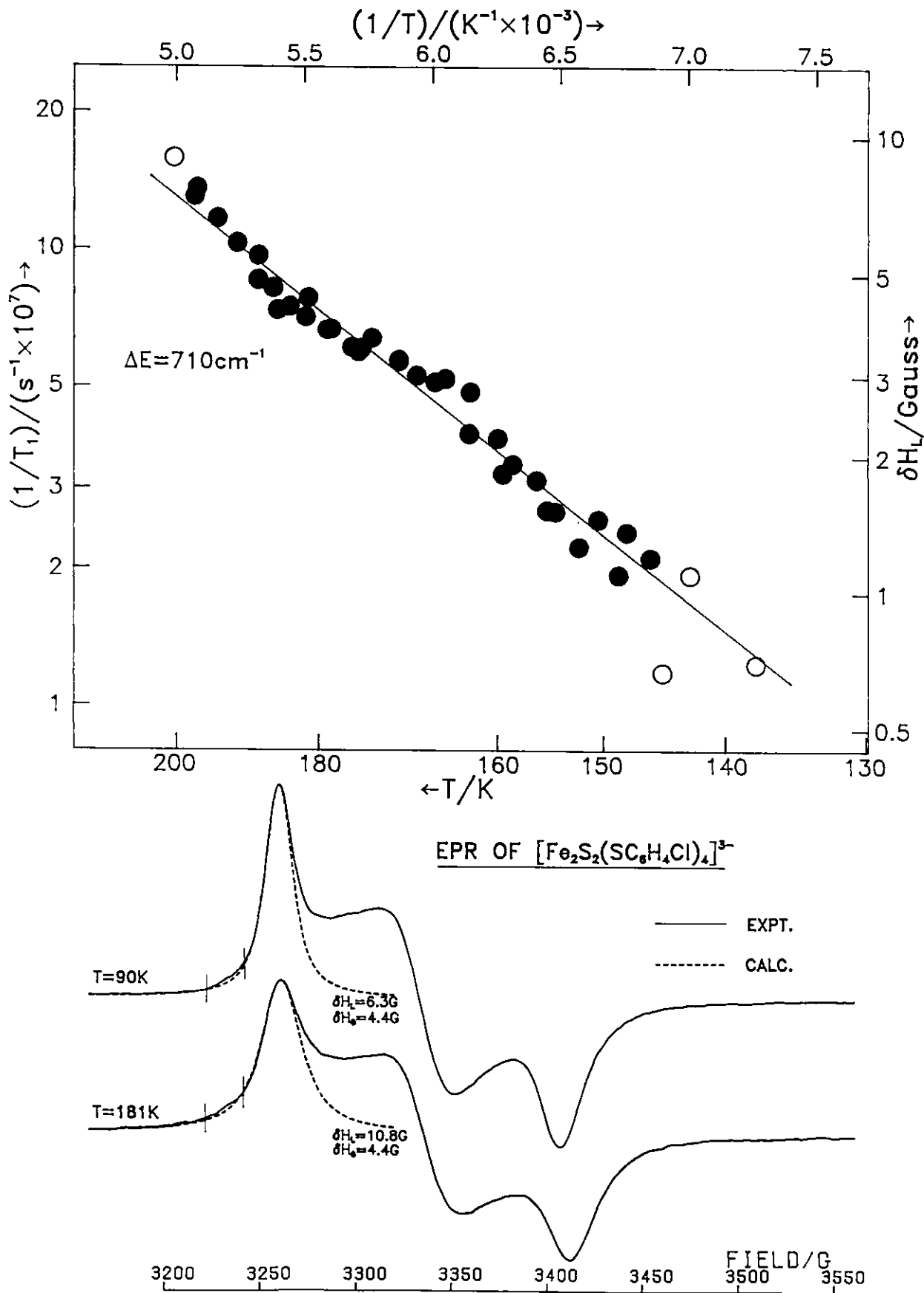
A linear least-squares fit is made to the full data points in Figure 2.7 according to equation E2.2 assuming an efficient resonant-relaxation mechanism involving an excited state at $600 \pm 30 \text{ cm}^{-1}$ above the doublet ground state. (Std. error of $\Delta E = \pm 5 \text{ cm}^{-1}$, coefficient C in E2.2 = $2.9 \pm 0.2 \times 10^{10} \text{ s}^{-1}$, correlation coefficient = 0.9992).

2.4.3. $[\text{Fe}_2\text{S}_2(\text{SC}_6\text{H}_4\text{Cl})_4]^{3-}$ in DMF.

Figure 2.8 presents data from an analysis, in the manner previously described, of the low field peak in EPR spectra from two incremental temperature cycles for $[\text{Fe}_2\text{S}_2(\text{SC}_6\text{H}_4\text{Cl})_4]^{3-}$ in DMF. After reduction and transfer to the anaerobic EPR tube the sample was frozen in an isopentane-slush bath, rather than in liquid nitrogen, in order to produce a finely crystalline DMF matrix. In this way problems with lineshape changes at high temperature, due to solvent crystalline structural reorganisation, could be mitigated.

The sample was studied from 85 K to 200 K. At the lowest temperatures the H_2 peak was found to be a product of a Gaussian function of half-height half-width 4.4 G and a Lorentzian function of half-width 6.3 G. Little broadening occurred below ca. 130 K. Extraction of the additional Lorentz broadening could be achieved between 150 K and 190 K with adequate accuracy, and the variation of these half-widths and corresponding T_1 -values with $1/T$ shown in Figure 2.8 is reasonably well fitted with a straight line according to equation E2.2 using $\Delta E = 710 \pm 70 \text{ cm}^{-1}$ (Std. error of $\Delta E = 20 \text{ cm}^{-1}$, coefficient C in E2.2 = $2.1 \pm 0.4 \times 10^{10} \text{ s}^{-1}$, correlation coefficient = 0.9858).

FIG. 2.8 T_1 -BROADENING WITH TEMPERATURE
AT H_z IN $[\text{Fe}_2\text{S}_2(\text{SC}_6\text{H}_4\text{Cl})_4]^{3-}$ /DMF EPR

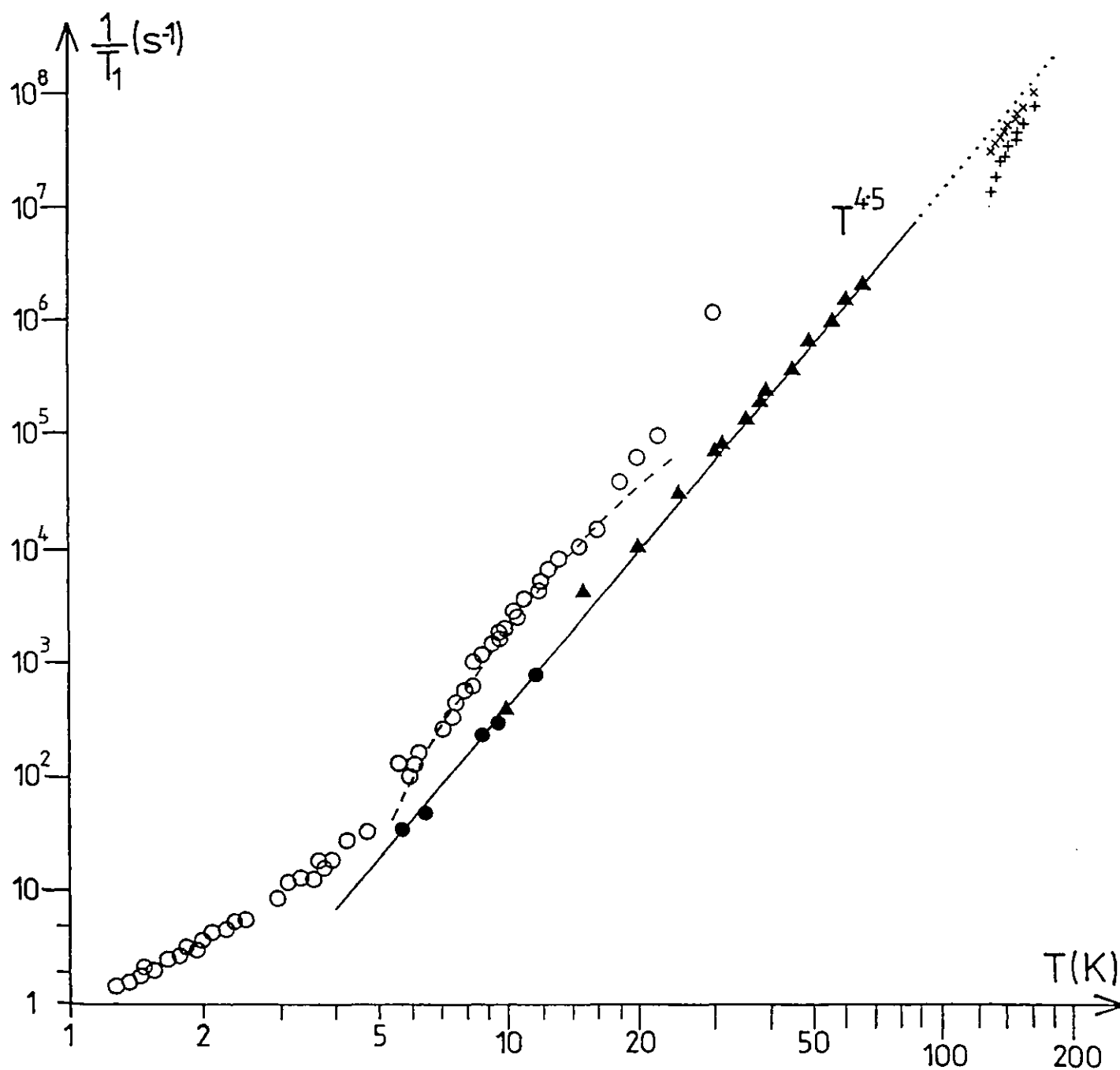


The appearance of a small impurity peak at $g = 2.013$, from the W-type signal associated with the vitreous samples (see Section 1.4), necessitated the use of a weighting function for the accumulation of the squared-difference values in order to avoid distortion of the fit to the $g = 2.002$ peak. This additional region over which squared-differences were not accumulated is shown in the simulations at the bottom of Figure 2.8.

2.5. Discussion.

The straight line fits to the five sets of data for $[\text{Fe}_2\text{X}_2(\text{S}_2\text{-o-xylyl})_2]^{3-}$ ($X = \text{S}, \text{Se}$) and $[\text{Fe}_2\text{S}_2(\text{SC}_6\text{H}_4\text{Cl})_4]^{3-}$, according to E2.2, figures 2.6-2.8, are as good as is expected for the quality of data obtained. If the same data are plotted bilogarithmically, equally convincing fits can be obtained to the data sets according to a $1/T_1 \propto T^n$ (E2.3) process where $n = 7.5 \pm 0.3$ (correlation coefficient ca. 0.998) for the three $[\text{Fe}_2\text{S}_2(\text{S}_2\text{-o-xylyl})_2]^{3-}$ samples, $n = 6.0 \pm 0.2$ (0.999) for $[\text{Fe}_2\text{Se}_2(\text{S}_2\text{-o-xylyl})_2]^{3-}$ and $n = 6.0 \pm 0.4$ (0.986) for $[\text{Fe}_2\text{S}_2(\text{SC}_6\text{H}_4\text{Cl})_4]^{3-}$. The logarithmic and inverse temperature scales show a relationship too close to linear in the 140-200 K interval to permit a clear distinction between the processes E2.2 and E2.3 to be based on the quality of fit to the data. The distinction can at present only be based on the plausibility of the relaxation mechanisms leading to the different temperature dependencies. Before discussing the results in such a context, reference is made at this point to measurements of T_1 obtained at lower temperatures.

Figure 2.9. T_1 variation with temperature for $[\text{Fe}_2\text{S}_2(\text{S}_2\text{-o-xylyl})_2]^{3-}$ in (1:1) DMSO/DMF.



● saturation pulse data

▲ continuous saturation data

× uncorrected broadening data

+ broadening data corrected by subtracting the low temperature residual Lorentz component.

○ Data for S. maxima Fd_{red} (ref. 101)

----- 2nd order Raman process with $\theta_D = 60$ K

————— $(1/T_1) = 0.013T^{4.5}$

Figure 2.9 shows T_1 data for $[\text{Fe}_2\text{S}_2(\text{S}_2\text{-o-xylyl})_2]^{3-}$ in 1:1 DMSO/DMF obtained by J.P. Gayda and P. Bertrand (Département d'Electronique, Université de Provence, Marseille)¹⁰⁰ using a continuous saturation method¹⁰¹ in the range 10-65 K and a saturating-pulse method between 6 K and 11 K. The sample was prepared by the present author. The temperature dependence of T_1 is well fitted in this overall range by the relationship $1/T_1 \propto T^{4.5}$. Such a relationship cannot be interpreted in terms of a simple Debye model. The data are, however, not dissimilar to those for the reduced 2Fe2S ferredoxin from Spirulina maxima¹⁰¹ which are also plotted for comparison in Figure 2.9.

T_1 obtained by Gayda and Bertrand from relaxation broadening at H_2 in the same $[\text{Fe}_2\text{S}_2(\text{S}_2\text{-o-xylyl})_2]^{3-}$ sample for the range 130 to 165 K is also given in this figure for comparison with the low temperature data. One set of results is shown where the entire Lorentzian component has been assumed to originate from T_1 -broadening (the mixed solvent freezes in the glassy state and so spin-spin broadening effects are probably small). A second set of results where the low temperature (~ 100 K) component has been subtracted is also given and is compatible with the results reported in this thesis, being reasonably fitted by an Orbach process involving an excited state at $770 \pm 50 \text{ cm}^{-1}$ or by a $1/T_1 \propto T^{7.5}$ law (the smaller value of ΔE for this solvent system compared with the values for pure DMSO and DMF may be a consequence of the differences in the way the solvents freeze).

One puzzling factor is that the width measurements yield T_1 relaxation times greater than the linear extrapolation of the saturation results, Figure 2.9. It could be, however, that linear extension from

the points at low temperature is not strictly correct, and that the relaxation rate due to the process dominant in this region actually curves at high temperature to lower values of $1/T_1$ than those indicated by $1/T_1 \propto T^{4.5}$. Such a curvature does occur for all Raman temperature dependencies when T becomes of the order of the Debye temperature, θ_D .

On the other hand a plot of T_1 derived from the total Lorentz width closely parallels a linear extrapolation of the low-temperature results. Thus, it is possible that the $1/T_1 \propto T^{4.5}$ law is also being observed in the high temperature region. For the $[\text{Fe}_2\text{S}_2(\text{S}_2\text{-o-xylyl})_2]^{3-}$ sample, DMSO₂, which amongst the three samples studied here has the smallest δH_L residual H_z lineshape component at 100 K, the data extend to higher temperature than for the sample of Figure 2.9, and a bilogarithmic plot of $1/T_1$, as obtained from the total uncorrected Lorentz width, against T , displays a poor linearity involving an approximate $1/T_1 \propto T^6$ relationship. The $1/T_1 \propto T^{4.5}$ parallelism of the extrapolated low temperature linewidth data for the DMSO/DMF sample studied by Gayda and Bertrand may then be adventitious.

Treating the results obtained in this present work in isolation from the low temperature data presented in Figure 2.9, a return is now made to the question of the plausibility of the T_1 temperature variation models represented by E2.2 and E2.3. The $(1/T_1) \propto T^n$ relationship of E2.3 is expected to hold for dominant Raman relaxation mechanisms with $n = 7$ and 9 respectively for first and second order processes when $T \ll \theta_D$ and with $n = 2$ when $T \gg \theta_D$. For $T \sim \theta_D$ a curvature between these two limits is anticipated. The direct process, for which $n = 1$ is predicted, and the first-order Raman process, are

in general only efficient at lower temperatures. The exponents found from bilogarithmic plots for the three 2Fe2S complexes are all too low to be associated with the value of $n = 9$ predicted for a second order Raman mechanism. Specific heat measurements in DMSO have been interpreted with two Debye temperatures, $\theta_{D1} = 130$ K and $\theta_{D2} = 265$ K,¹⁰² thus, transient bilogarithmic $(1/T_1)/T$ derivatives lower than 9 could be expected, but linearity over the range of temperatures measured would not be anticipated.

On going from a structure in which the Debye phonon spectrum is equivalent in all three dimensions to a structure of lower dimensionality the exponent n is predicted to be lower.^{103,104} Thus, a relaxation-temperature relationship of the type E2.3 with $n = 6.3$ has been considered on this basis in some hemo-proteins¹⁰³ and in a 4Fe4S ferredoxin.¹⁰⁵ This exponent is comparable with that of 6.0 found for $[\text{Fe}_2\text{Se}_2(\text{S}_2\text{-o-xylyl})_2]^{3-}$ and $[\text{Fe}_2\text{S}_2(\text{SC}_6\text{H}_4\text{Cl})_4]^{3-}$. The lowering of dimensionality for the phonon propagation in the proteins is considered to be present because of their convoluted peptide-chain structure, wherein the efficiency of vibrational transmission along the chain is greater than across adjacent chain segments. But it is difficult to see how this could apply to the bare 2Fe2S complexes in intimate contact with organic solvent.

Thus, there is no readily apparent interpretation of the results in terms of a $1/T \propto T^n$ relationship with the experimentally determined exponent values. The fact that the exponents for $[\text{Fe}_2\text{X}_2(\text{S}_2\text{-o-xylyl})_2]^{3-}$ range from 7.5 for $X = \text{S}$ to 6 for $X = \text{Se}$ is a further indication that this relationship is not applicable. If the relaxation process is more

dependent on the characteristics of the surrounding milieu (in particular θ_D) than of the iron-chalcogenide complex, as might be expected for any non-resonant Raman process, then little difference in the relaxation behaviour with temperature would be expected over the three complexes studied, and more dependence on the solvent. For an Orbach mechanism, variation in the slope for fits according to E2.2 is easily understood in terms of differences in the energies of the first excited states of the spin manifolds as determined by the coupling between the irons which may vary among the complexes.

The variation of T_1 with temperature in the region of broadening of several 2Fe2S and 4Fe4S ferredoxins has been interpreted in terms of a dominant Orbach mechanism.^{19,92,94,105-107,95-97,108} The same mechanism is reasonably expected in the 2Fe2S model complexes studied here, and as demonstrated by Figures 2.6-2.8 the T_1 data for these complexes are well fitted assuming efficient resonant-relaxation processes involving excited states ranging from 900 cm^{-1} for $[\text{Fe}_2\text{S}_2(\text{S}_2\text{-o-xylyl})_2]^{3-}$ through 710 cm^{-1} for $[\text{Fe}_2\text{S}_2(\text{SC}_6\text{H}_4\text{C}\ell)_4]^{3-}$ to 600 cm^{-1} for $[\text{Fe}_2\text{Se}_2(\text{S}_2\text{-o-xylyl})_2]^{3-}$. These energy gaps are not unreasonable for the $-3J$ splitting of the $S = 3/2$ level from the doublet ground-state in the coupled binuclear complexes, but are all well above the Debye temperatures of the organic solvents, such that the excited state cannot be in the phonon continuum. In this case efficient Orbach relaxation could not be expected. However, the vibrations of the required energy could originate from local vibrations of the ligands or of the solvent molecules. Such an origin has been suggested for an Orbach mechanism associated with some 4Fe4S ferredoxins where the excited state ranges $100\text{-}300 \text{ cm}^{-1}$ and is thus above the Debye limit

of ca. 45 cm^{-1} .^{105,107} For the dianionic forms of the complexes studied here only weak Raman or IR bands are observed in the required regions (section 4). DMF and DMSO show vibrational bands in the 600-900 cm^{-1} region which may have broad enough absorption tails to supply modes of the frequency required by the suggested Orbach process.¹⁰⁹⁻¹¹¹

A good test of the applicability of the proposed Orbach mechanism would be an independent confirmation of the excited-state to ground-state energy separations deduced. In some ferredoxins magnetic susceptibility measurements have been used to determine this energy gap.^{112,50,16} For a gap of the order of magnitude suggested by the present relaxation measurements the population of the excited state would likely be too small to give any significant deviation of magnetic behaviour from $S = 1/2$. This was found to be the case for adrenodoxin,¹¹³ for which a first excited state at ca. 800 cm^{-1} has been estimated from fitting T_1 vs. T data assuming dominant resonant relaxation.⁹⁴ This same difficulty precludes the accurate determination of the energy gap by observing the deviation of EPR signal intensity from Curie-law behaviour at higher temperatures as the ground state depopulates. This method has been applied to some ferredoxins⁹⁴⁻⁹⁸ and to $[\text{Fe}_4\text{S}_4(\text{SPh})_4]^{3-}$.⁹⁹ For the three complexes studied here a very wide scatter is seen in the data on plotting $\log(T_0 / IT - 1)$ against $1/T$ ($I =$ intensity of signal at temperature T relative to intensity at T_0 - the lowest temperature employed), and only an order of magnitude indication is obtainable for the energy separation; $\Delta E = 300$ to 1500 cm^{-1} covers all compounds. The intensity in each case does in fact drop rather more appreciably below the Curie law than expected, and indicates the excited state to have a

multiplicity relative to the ground state well in excess of the expected value of 2. This has no theoretical justification, but has been observed for all applications of this method to iron-sulphur centres⁹⁴⁻⁹⁸ [note that the multiplicity value of 4.5 is incorrectly quoted in reference 99 and should be 90 ($= e^{4.5}$)].

A third method of measuring the energy ΔE in ferredoxins using Raman has been suggested^{114,115} but is not convincing and has not been found to be applicable to the dianionic forms of the present complexes (Section 4).

2.6. Conclusion.

Assuming the broadening of the EPR signals in the range 100-200 K to result from a dominant Orbach relaxation mechanism involving the $S = 3/2$ first excited state at energy $-3J$, the derived anti-ferromagnetic coupling constants for $[\text{Fe}_2\text{S}_2(\text{S}_2\text{-o-xylyl})_2]^{3-}$ ($X = \text{S}, \text{Se}$) and $[\text{Fe}_2\text{S}_2(\text{SC}_6\text{H}_4\text{Cl})_4]^{3-}$ are collected in Table 2.1 and compared with corresponding values for some iron-sulphur proteins. The J values for the sulphur-bridged complexes are large and compare well with the value estimated for adrenodoxin.⁹⁴ A relationship between J and $(g_y - g_x)$ has been suggested whereby rhombic distortion at the ferrous ion leads to large $(g_y - g_x)$ anisotropy, as in the theoretical model of Bertrand and Gayda⁶⁰ (see also Section 1), and also to lower exchange coupling due to decreased overlap for both direct and indirect (bridging) Fe-Fe orbital interaction.⁹⁴ Thus maximal orbital overlap is expected in the undistorted axial case and adrenodoxin has a large exchange interaction. A high $|J|$ value is also expected of $[\text{Fe}_2\text{S}_2(\text{S}_2\text{-o-xylyl})_2]^{3-}$ from the

TABLE 2.1. Antiferromagnetic Coupling Parameter, J, for [2Fe-2S]^(1+,2+) Centres in Ferredoxins and Synthetic Analogues.

<u>[2Fe-2S]¹⁺</u>	<u>-J/cm⁻¹</u>		<u>Reference</u>
[Fe ₂ S ₂ (S ₂ -o-xylyl) ₂] ³⁻	300 ± 15		This
[Fe ₂ Se ₂ (S ₂ -o-xylyl) ₂] ³⁻	200 ± 10		work
[Fe ₂ S ₂ (SC ₆ H ₄ Cl) ₄] ³⁻	240 ± 20		
<u>Spirulina maxima</u>	83 ± 5		19,92
<u>Spirulina maxima</u>	98 ± 5 - 10	M	112
<u>Scenedesmus</u>	83		92
Spinach	110	M	16
<u>Synechococcus lividus</u>	98-115	M	50
Succinate dehydrogenase (S-1)	90		94
Rieske's centre	65		94
NADH:UQ ubiquinone reductase	90		94
Adrenodoxin	270		94
<u>[2Fe-2S]²⁺</u>			
[Fe ₂ S ₂ (S ₂ -o-xylyl) ₂] ²⁻	149 ± 8	M	38
<u>Spirulina maxima</u>	182 ± 20	M	112

The data were obtained from interpreting EPR-lineshape broadening in terms of an Orbach relaxation mechanism, except where marked with an "M" indicating magnetic measurement.

small ($g_y - g_x$) splitting (0.020) and a somewhat weaker interaction for $[\text{Fe}_2\text{S}_2(\text{SC}_6\text{H}_4\text{Cl})_4]^{3-}$ which has increased ($g_y - g_x$) separation (0.043). This is borne out in the results, Table 2.1. The $|J|$ values are both higher than would be anticipated from the empirical plot of $|J|$ vs. ($g_y - g_x$) for $2\text{Fe}2\text{S Fd}_{\text{red}}$ presented by Salerno et al.⁹⁴

$X\alpha$ -VB calculations for $[\text{Fe}_2\text{S}_2(\text{SH})_4]^{3-}$ predict $J \approx 80 \text{ cm}^{-1}$ using a symmetry based upon the crystal structure for $[\text{Et}_4\text{N}]_2[\text{Fe}_2\text{S}_2(\text{S}_2\text{-o-xylyl})_2]$,¹¹⁶ but the dimensions of the reduced cluster could well be different.

A preliminary study on S. maxima Fd_{red} in 80% DMSO, where the peptide chain is unfolded and the $2\text{Fe}2\text{S}$ centre exposed to the solvent, does not show appreciable broadening up to 170 K, so that large exchange interactions are also expected in this case [J-P. Gayda, personal communication].

2.7. Experimental.

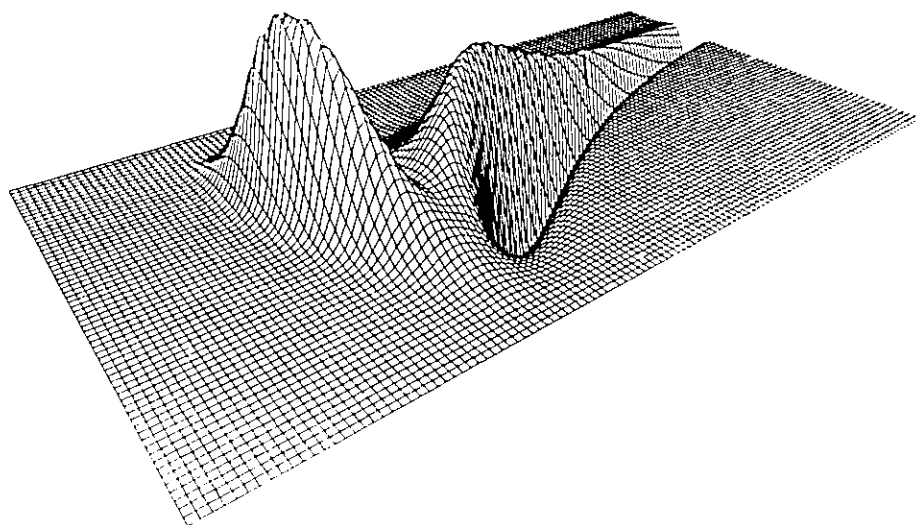
Solution samples of the trianionic dimers were obtained in the manner described in Section 1. Initial concentration of the dianion $[\text{Fe}_2\text{S}_2(\text{S}_2\text{-o-xylyl})_2]^{2-}$, prior to reduction, ranged from a maximum 3 mM in DMSO to a minimum 0.6 mM in DMF, but as reduction of the latter could be carried out at lower temperature attaining yields in the range 60 to 80% as against yields of ca. 20% in DMSO, the final concentrations of $[\text{Fe}_2\text{S}_2(\text{S}_2\text{-o-xylyl})_2]^{3-}$ were found by integrated intensity of the EPR signal to range from 0.3 to 0.6 mM. The initial concentrations of $[\text{Fe}_2\text{S}_2(\text{S}_2\text{-o-xylyl})_2]^{2-}$ and $[\text{Fe}_2\text{S}_2(\text{SC}_6\text{H}_4\text{Cl})_4]^{2-}$ in DMF were 0.84 mM and 1.2 mM respectively and ca. 20% yield of trianion was obtained in each case as judged by the intensities of the EPR signals

Within the EPR cavity samples were cooled in a nitrogen gas stream, the temperature of which was regulated to within 1 degree by a Varian variable temperature controller. The sample temperature was measured by a copper-constantan thermocouple in contact with the sample-tube, but just above the resonant-cavity. In the case of the $\{\text{Fe}_2\text{S}_2(\text{S}_2\text{-o-xylyl})_2\}^{3-}$ samples, this thermocouple was calibrated in the same position and using the same gas flow-rate against a platinum resistance of known calibration which had comparable dimensions to the solutions used and was in a similar quartz tube within the cavity dewar.

EPR spectra were collected digitally over 1000 points to a resolution of 10 bits.

SECTION 3

**COMMENTS ON THE EPR SPECTRUM
OF $[\text{Fe}(\text{S}_2\text{-o-xylyl})_2]^-$
IN FROZEN SOLUTION**



3. COMMENTS ON THE EPR SPECTRUM OF $[\text{Fe}(\text{S}_2\text{-o-xylyl})_2]^-$ IN FROZEN SOLUTION.

ABSTRACT	128
3.1. <u>Introduction: EPR in High Spin $\text{Fe}(\text{III})\text{S}_4$.</u>	129
3.2. <u>EPR of $[\text{Fe}(\text{S}_2\text{-o-xylyl})_2]^-$; Determination of λ.</u>	133
3.3. <u>EPR at Q-Band.</u>	147
3.4. <u>Determination of D.</u>	150
3.5. <u>Origin of the Sharp $g' = 4.3$ Resonance.</u>	155
3.6. <u>Conclusion.</u>	160
3.7. <u>Experimental.</u>	162

ABSTRACT

The X and Q band EPR spectra for frozen solutions of $[\text{Fe}(\text{S}_2\text{-o-xylyl})_2]^-$ are interpreted in terms of a high D value and a distribution of \underline{D} symmetries centred at $\lambda \approx 0.13$ and ranging over $\lambda \approx \pm 0.05$ in half-width. D is estimated at $2.0^{+0.8}_{-0.5} \text{ cm}^{-1}$ from an analysis of the temperature-dependent intensity variation of the feature at lowest field which has been assigned to resonance in the $S = 1/2$ Kramers doublet. Comparison of the EPR for $[\text{Fe}(\text{S}_2\text{-o-xylyl})_2]^-$ is made with spectra for rubredoxins and desulforedoxin. Several explanations are considered for the origin of a sharp feature at $g' = 4.28$ in the $[\text{Fe}(\text{S}_2\text{-o-xylyl})_2]^-$ spectra, but none is found to be entirely satisfactory.

3. Comments on the EPR Spectrum of $[\text{Fe}(\text{S}_2\text{-o-xylyl})_2]^-$ in Frozen Solution.

3.1. Introduction: EPR in High Spin Fe(III) S_4 .

$\text{S}_2\text{-o-xylyl}$ ligated iron(III) has been demonstrated spectroscopically and crystallographically closely to approach the coordination found in oxidised rubredoxin, serving as a good, albeit symmetrised, synthetic analogue.^{117,118,56} [See also Section 4.2.2.].

EPR spectra of Rd_{ox} show strong absorption centred around an effective g-value of 4.3 together with weaker derivative-maxima at $g' \sim 9.4$.¹¹⁹⁻¹²⁴ Very weak broad features are also sometimes observed at high fields ($g' \sim 1$).¹²⁵ Signals of this sort can arise from high-spin Fe(III) in a low symmetry crystal field. Whilst the sextet ground-state in high spin ferric complexes is orbitally non-degenerate, a spin-orbit coupling interaction with excited non-spherical quartet and doublet states can result in a zero-field splitting of the six ^6S spin states into three Kramers doublets. These higher interacting orbital states are sensitive to the symmetry of the local crystalline-field environment, which consequently determines the nature of the zero-field splitting.

Without considering either the actual coordination symmetry of the ligand atoms producing the crystalline field at the iron, or the exact mechanism of the spin-orbit coupling producing the zero-field splitting, it is possible to understand their effects in terms of a phenomenological spin-Hamiltonian operator which acts on the spin-state wave functions, (E3.1).

$$\hat{\mathcal{H}}_S = \beta \cdot \underline{\underline{H}} \cdot \underline{\underline{g}} \cdot \hat{\underline{\underline{S}}} + \hat{\underline{\underline{S}}} \cdot \underline{\underline{D}} \cdot \hat{\underline{\underline{S}}} \quad (\text{E3.1})$$

In this expression, the first part contains the magnetic interaction with the static field and the second the spins orientational preference.

The \underline{D} tensor is normally expressed in terms of D and λ (or $E = \lambda D$), coefficients representing the anisotropic part of the spin-orbit coupling contribution (E3.2).

$$\begin{aligned} \underline{\hat{S}} \cdot \underline{D} \cdot \underline{\hat{S}} &= D_{xx} \hat{S}_x^2 + D_{yy} \hat{S}_y^2 + D_{zz} \hat{S}_z^2 \\ &= D \left[\hat{S}_z^2 - \frac{1}{3} S(S+1) + \lambda (\hat{S}_x^2 - \hat{S}_y^2) \right] + \frac{1}{3} (D_{xx} + D_{yy} + D_{zz}) S(S+1) \\ D &= D_{zz} - (D_{xx} + D_{yy})/2, \quad \lambda = (D_{xx} - D_{yy})/2D \end{aligned} \quad (\text{E3.2})$$

All components of the ground-state are shifted equally by the last term in this equation and it is not usually included in the spin-Hamiltonian.

An Hamiltonian of the same form as E3.1 results from the dipolar spin-spin interaction between unpaired electrons. Experimentally it is not possible to separate the spin-orbit and spin-spin contributions to \underline{D} , but the latter is expected to be small for $S = 5/2$ Fe(III).¹²⁶

Additional spin-Hamiltonian terms quartic in \underline{S} with coefficients a (or $\mu = a/D$) and F are sometimes important in determining the energies of the spin states, but are not considered for the present as the quadratic terms are generally dominant.

The range of values taken by D and λ , and their significance, is dependent upon the choice of coordinate system. If the intuitive choice of D_{xx} , D_{yy} and D_{zz} axes is made such that $|D|$ is maximised and λ made positive, then λ is minimised and restricted to values from 0 to $1/3$.^{127,128} Such a system has been widely adopted and is used here. Transformation

formulae have been derived to convert D and λ to the other five reasonable definitions of axes.¹²⁹⁻¹³¹

Under the chosen axis system, when expressed in terms of D and λ , the symmetry of the \underline{D} tensor, but not necessarily that of the crystalline field, is such that $D = 0$ represents cubic; $\lambda = 0, D \neq 0$ represents axial and $0 \leq \lambda \leq 1/3$ represents rhombic symmetry. When D is small relative to the Zeeman splitting five $\Delta M_S = \pm 1$ transitions produce an EPR signal centred around $g' = 2$. When the zero-field splitting is comparable to or in excess of $h\nu$, solution of the spin-Hamiltonian (E3.1) for $S = 5/2$ to obtain the relative energies of the six spin-states, over a range of magnetic fields, makes possible an evaluation of the resonance fields for spin-state transitions. Graphs of D or λ against resonance positions for fields orientated along the \underline{D} tensor axes, or sometimes more usefully in the case of "powder spectra" for zero angular variation, provide a summary useful in the interpretation of spectra.^{132,133,127,128} For large zero-field splitting the observed EPR spectrum is mainly dependent upon λ . Figure 3.1 shows the principal-axis g' values and the energy separations for the three Kramers doublets at the extremes $\lambda = 0$ (\underline{D} axial) and $\lambda = 1/3$ (maximum \underline{D} anisotropy).

A value of λ close to $1/3$ provides an explanation for the observed resonances seen in Rd_{ox} . The strong signal around $g' = 4.3$ results from the middle Kramers doublet¹³⁴ and changes intensity with temperature in a way in keeping with an excited state. The lowest doublet gives rise to peaks at $g' \simeq 9.4$ and $g' \simeq 1$ which are weaker due to their greater anisotropy, the former being, however, more prominent at very low temperatures.¹²⁵ Resonances originating from

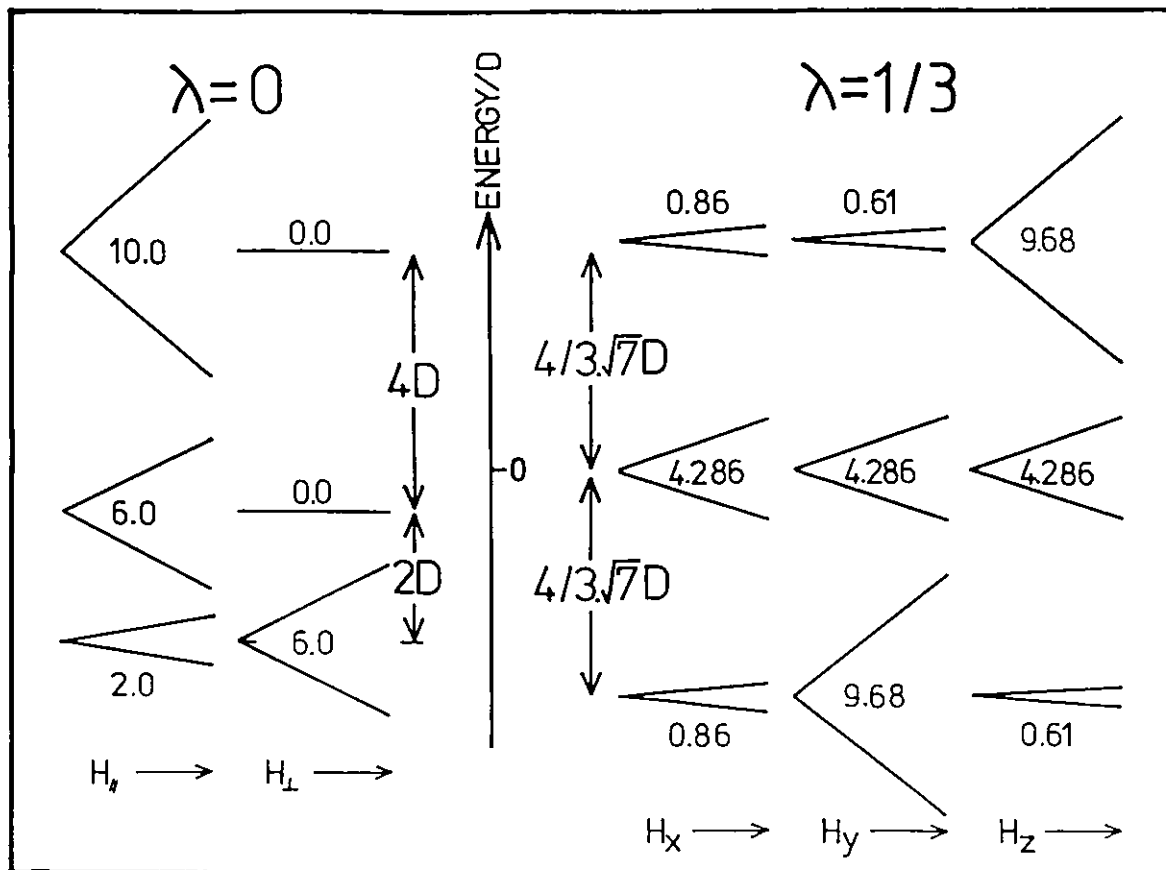


Figure 3.1. Splitting of the three Kramers doublets for $S = 5/2$ under axial ($\lambda = 0$) and fully rhombic ($\lambda = 1/3$) symmetries. The figure at each doublet represents the g value of a signal from that doublet.

the highest doublet are not generally observed in Rd_{ox} as the transition probability is low for such spin-state changes, the g' anisotropy is high and the fractional population is smaller at low temperatures than for the lower levels.

Since the resonance fields for Rd_{ox} are quite sensitive to λ , a reasonably accurate evaluation of this parameter may be made by comparison with fields predicted from solution of the spin-Hamiltonian. Peisach et al.¹²⁵ have obtained a value of 0.28 for λ in *P. oleovirans* Rd_{ox} whilst for *C. acidipurici* Rd_{ox} an EPR spectrum was observed, characteristic of $\lambda \sim 1/3$.¹³⁵ Other rubredoxins give similar or intermediate spectra and must have comparable rhombic character.

The insensitivity of the Rd_{ox} EPR to D precludes the determination of this parameter in the manner used for λ . If, however, λ is known, then an evaluation of the magnitude of the zero-field splitting leads to a direct estimation of D . The zero-field splitting may be obtained from a variable temperature study of the changing fractional population of a Kramers doublet as revealed by the varying relative intensity of part of its resonance signal. Values of $D = 1.76 \text{ cm}^{-1}$ and $D = 1.89 \text{ cm}^{-1}$ have been determined for *P. oleovarans* and *C. acidi-urici* respectively.^{125,135}

For iron coordination giving a high λ value, Blumberg and Peisach have correlated the zero-field splitting with the nature of the ligand atoms. An energy separation of $1-2 \text{ cm}^{-1}$ between lowest and middle Kramers doublets is found for ligation primarily by oxygen, whilst $5-6 \text{ cm}^{-1}$ is characteristic of a ligand system consisting mainly of sulphur atoms. A cautionary note should be added, however, exemplified in the case of the enzyme protocatechuate 3,4-dioxygenase. This shows a strong $g' = 4.3$ resonance having $\lambda = 0.29$ and has been described as primarily sulphur ligated on the grounds of its 5.39 cm^{-1} zero-field splitting.¹³⁵ Mössbauer spectra of this protein are consistent with such D and λ values, but do not support sulphur coordination.¹³⁶

3.2. EPR of $[\text{Fe}(\text{S}_2\text{-o-xylyl})_2]^-$; Determination of λ .

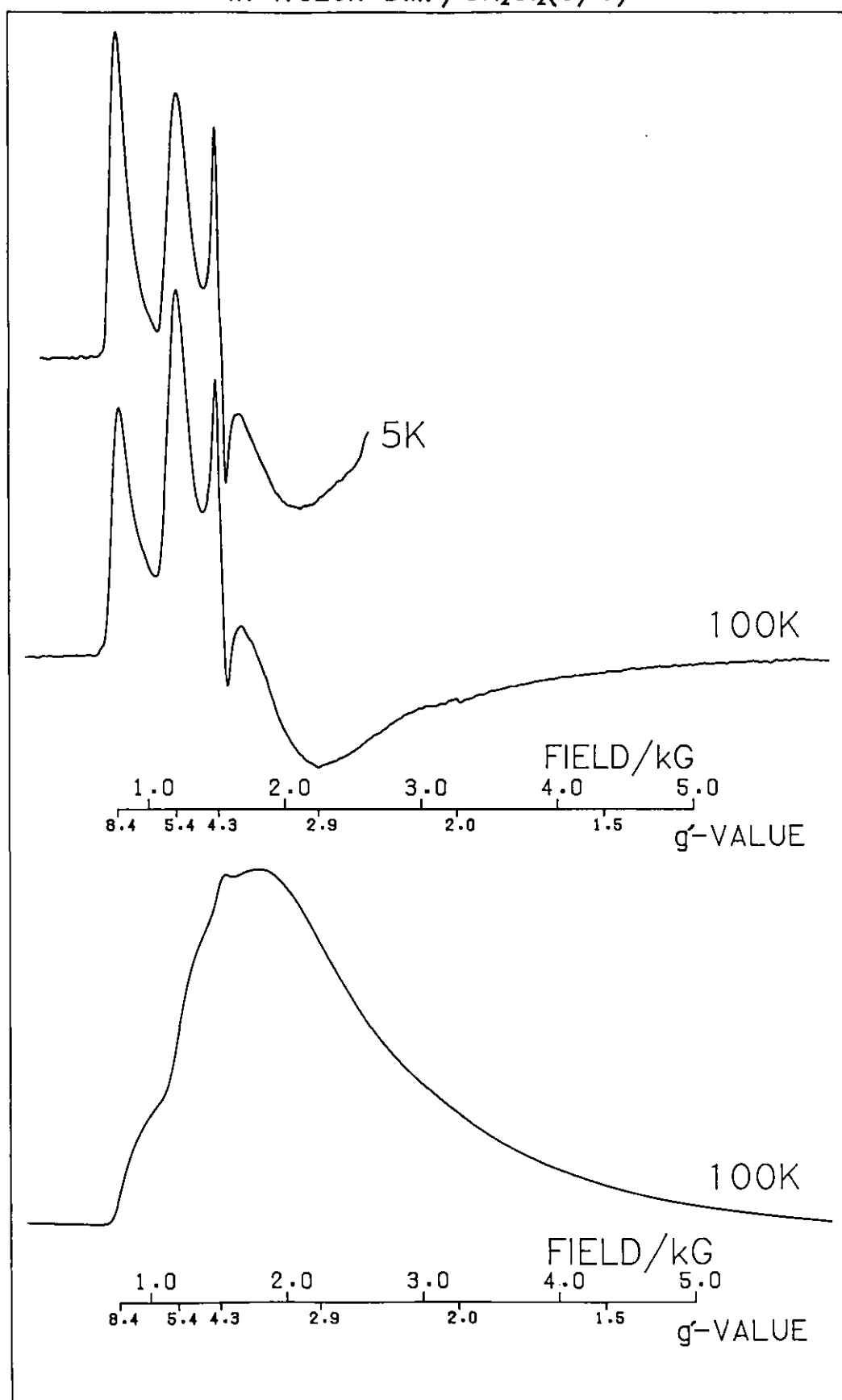
Holm, Lane and co-workers report having measured the EPR spectra of $[\text{Fe}(\text{S}_2\text{-o-xylyl})_2]^-$ in several solvent media over the temperature range 1.5 to 140 K.⁵⁶ They have described the spectra as being more complicated than those for Rd_{ox} but have given no details beyond noting the presence of a sharp $g' = 4.3$ signal thought to be indicative of fully rhombic symmetry.

Figure 3.2 shows X-band EPR measurements on a frozen 3:1 DMF/CH₂Cl₂ solution of Et₄N[Fe(S₂-o-xylyl)₂] at 100 K and 5 K. Two intense low field features are seen at $g' = 8.40$ and $g' = 5.44$, a broad trough is centred around $g' = 2.9$ and a sharp isotropic line found at $g' = 4.28$. It has been suggested that the complexity of the spectrum, in comparison to those for Rd_{ox}, might result from exchange interactions within the sample which are absent in the proteins due to greater separation of the FeS₄ centres.¹¹⁸ Whilst, as expected, it is true that for the pure solid a radically different spectrum is obtained, no major changes have been observed in the lineshape when concentrations ranging from 1 mM to 20 mM have been employed in the DMF/CH₂Cl₂ solvent system. An integrated form of the high temperature derivative spectrum is shown in the lower part of Figure 3.2 and demonstrates clearly that the sharp $g' = 4.3$ resonance is weak compared with the remainder of the signal. This isotropic line cannot then be connected with the $g' = 8.4$ peak in the way that $g' = 4.3$ and 9.4 resonances are believed to arise. In addition, on cooling from around 100 K toward around 10 K, the intensity of the sharp line is observed to increase more rapidly than predicted by a Curie-Law temperature dependence, an observation opposite to the expected behaviour for a signal arising from a middle Kramers doublet.

The intensity of this line relative to the low field features is also found to be rather solvent dependent and the signal is, for the time being, excluded from the interpretation of the rest of the spectrum on the grounds that it possibly arises from another species.

A fairly sharp change in intensity in the trough between the low field lines indicates that they probably do not arise from different orientations of the same resonance. If then the $g' = 8.4$ peak results

Fig. 3.2 X-band EPR spectra for $\text{Et}_4\text{N}[\text{Fe}(\text{S}_2\text{-o-xylyl})_2]$ in frozen $\text{DMF}/\text{CH}_2\text{Cl}_2(3/1)$



from the lowest Kramers doublet and the $g' = 5.4$ peak from the middle doublet, the two resonances must have comparable anisotropy in order to possess similar intensities. Such a situation can only arise when λ is midway between values giving axial and values giving fully rhombic \underline{D} symmetry.

The upper part of Figure 3.3 shows a plot of principal-axis resonance fields predicted from solution of the spin-Hamiltonian (E3.1) for $S = 5/2$ with $0 \leq \lambda \leq 1/3$ ($D = 2.0 \text{ cm}^{-1}$, $\nu = 9.117 \text{ GHz}$). Resonance positions of the lines at low field indicate that λ lies between 0.12 and 0.16 for $[\text{Fe}(\text{S}_2\text{-o-xylyl})_2]^-$. The broad trough around $g' = 2.9$ is considered to arise from the middle doublet along x and y orientations and from the x direction for the lowest doublet. Lines representing these resonances in Figure 3.3 intersect in the region of λ given above. The lineshape for a sample of randomly orientated molecules is expected to have a derivative form along the directions specified, however, the simulated spectrum in Figure 3.4 shows that with large linewidths a shape may result quite comparable to that observed experimentally. This calculated spectrum is the result of adding together Boltzmann-population-weighted spectra simulated for lower and middle doublets with a fictitious $S = 1/2$ spin and using g' -values from solution of the $S = 5/2$ spin-Hamiltonian (an isotropic $g' = 4.28$ line has been added in also). The resonance in the upper doublet is highly anisotropic, and the only principal-axis field position (z) in the region under consideration has very low transition probability. Linewidths for the x,z resonance field orientations of the lowest doublet and x,y orientations of the middle doublet have been varied

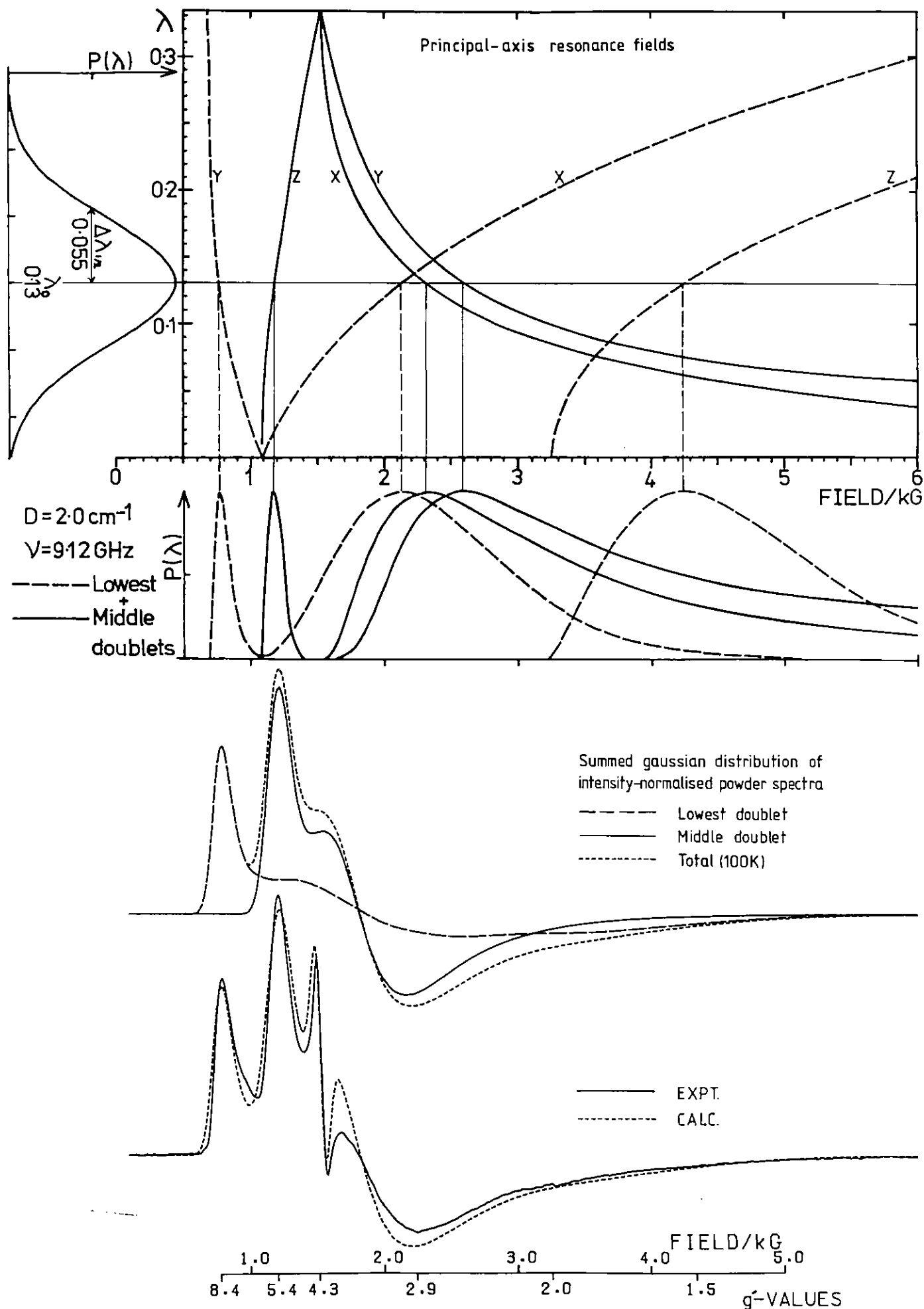


Fig 3.3 Predicted principal-axis fields for $D=2\text{cm}^{-1}$, $\nu=9.12\text{GHz}$, $\lambda=0$ to $1/3$. A simulation procedure involving a Gaussian distribution in λ is portrayed.

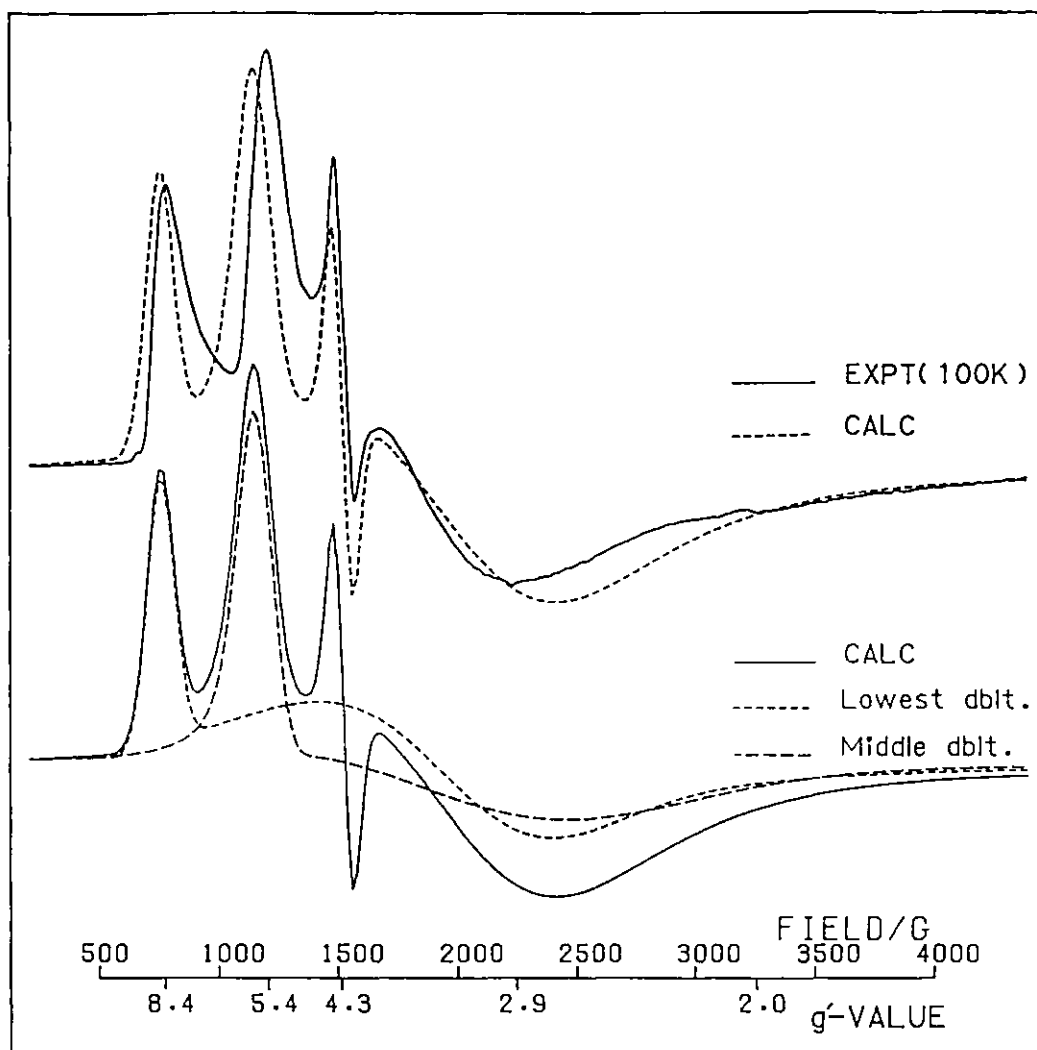


Figure 3.4. Additive powder spectra, for lowest and middle doublets resulting from fields predicted at $\lambda = 0.13$.

to least squares fit the spectral lineshape above $g' = 4$. Best overall fits result from g parameters generated with λ between 0.13 and 0.14. Outside this best fit λ range, certain of the line widths are required to be excessively large or the relative intensities of the two sharp low field peaks deviates from those experimentally observed. For close agreement to the experimental lineshape at $\lambda = 0.13$, Gaussian half-height half-widths, in order of increasing on-axis resonance field, were 65, 450, 2500 G and 74, 700, 2500 G for the lower and middle doublets respectively. A linear linewidth-anisotropy between

principal axis values has been employed. The large linewidth in the z direction for the ground state resonance, prevents resolution of any feature between 4000 and 5000 Gauss, in keeping with the observed spectrum for which only a broad tailing-off is found in this field interval.

Very anisotropic linewidths are not unexpected for this sort of compound,^{137,133} an example being NaCo[Fe(III)]ethylene-diamine-tetraacetate.4H₂O, for which single crystal linewidths vary from twelve to several hundred Gauss depending on field orientation.¹³⁸ An important linewidth contribution may arise from random variations in spin-Hamiltonian parameters for molecules in different local environments of a glassy matrix. For small variations it may be sufficient to perform a convolution of a calculated spectrum with a Gaussian broadening function in order adequately to reproduce an experimental lineshape. This is the approach used in generating Figure 3.4 and whilst the result is a reasonable fit to the observed spectrum the method can only be considered approximate. When random structural distribution produces a large fluctuation in one or more parameters, as is often the case in glasses, it has frequently proven useful in lineshape simulation calculations to vary these parameters according to a Gaussian or skewed Gaussian distribution and sum the individual component spectra resulting from the resonance equation.¹³⁹ & eg. 140-143

In the present case for $\lambda \sim 0.15$ most of the line positions are quite independent of D for values ranging from 1.0 to 3.0 cm⁻¹. However, as can be seen from Figure 3.3, when λ is centred on 0.13, but ranges by ± 0.05 , the resonances contributing to the trough at

$g' \sim 2.9$ vary over some 1000 to 2000 Gauss, whilst the two low field lines change position relatively little.

If then this is the source of the line broadening to high field, a more physically reasonable simulation model for the $[\text{Fe}(\text{S}_2\text{-o-xylyl})_2]^-$ spectrum would involve summation of calculated lineshapes resulting from a Gaussian-weighted distribution in λ . Returning to Figure 3.3, the results of performing such a calculation with 0.055 half-height half-width variation in λ centred at 0.13 can be seen in comparison to the experimental spectrum (once again an isotropic $g' = 4.3$ resonance has been added in as well). Individual component spectra for lower and middle doublets at any given value of λ were generated in a similar manner to that described above for the fixed- λ simulation of Figure 3.4. The lineshapes for the fictitious $S = 1/2$ resonances were generated by a conventional all angles (θ, ϕ) summation, the detailed equations for g and transition probability as functions of g, θ and ϕ being given in Section 6.3 (routine EPRPOW). The program "EPR"¹⁴⁴ used to generate the g' values for lowest and middle doublets, which has a more rigorous approach to transition probability, is also capable of integrating θ and ϕ for an octant using an icosahedral subdivision approximation, but could not be employed here due to its use of some two orders of magnitude more computation time for comparable orientational resolution. However, the transition probabilities for principal-axis resonances given by the equation used in "EPRPOW" ($g_x^2 + g_y^2$ along z , etc.) are seen to compare quite favourably to those from the program "EPR" (Table 3.1).

TABLE 3.1. Transition Probabilities Derived from the Programs "EPR" and "EPRPOW" Using the Parameters $\lambda = 0.13$, $D = 2.0 \text{ cm}^{-1}$ $\nu = 9.12 \text{ GHz}$ Normalised to 10 for the Largest Probability.

Transition	Field	g'	Transition Probability	
			"EPR"	"EPRPOW"
1-2 x	2129.8	3.058	9.08	9.13
1-2 y	771.4	8.444	1.47	1.45
1-2 z	4238.2	1.537	10.0	10.0
3-4 x	2309.4	2.821	4.56	4.55
3-4 y	2581.3	2.534	4.70	4.75
3-4 z	1182.5	5.509	1.79	1.78
5-6 z	653.9	9.962	0.003	-

The true g tensor was set isotropically at 2.0 for generation of the principal-axis resonance fields.¹⁴⁴ Use of values such as $g_x = 2.013$, $g_y = 2.034$ and $g_z = 2.030$ found previously for FeS_4 coordination,⁸² might be considered more appropriate, but cause a deviation from the resonance positions used here which is less than 2% at any field.

Choice of a physically reasonable linewidth anisotropy equation is difficult, as is often the case. It is still necessary to use considerably larger linewidths at higher fields for the coarse λ interval employed. If residual linewidth is considered to arise from a g' distribution, $\Delta g'$, then the resonance equation $h\nu = g'\beta H$ predicts

a field incrementing linewidth factor $\Delta H \propto \Delta g' H^2$.¹³⁸ Although it is difficult to account for the origin of an additional uniform variation in g' , the relevant linewidth-dependency relationship, $\Delta H = \Delta H_0 + \Delta H_1 \cdot H^2$, is conveniently simple and leads to a complete description of linewidth, for all component spectra, which involves only two parameters.

Having generated a file of 66 lineshapes corresponding to lower and middle doublet resonances for increments of 0.01 in the range $0.01 \leq \lambda \leq 0.33$, it was possible fairly simply to add them in many trial Gaussian-weighted λ distributions. Boltzmann distribution weighting between lower and middle doublets was made, corresponding to 100 K and a zero field splitting of 4.6 cm^{-1} (see later), and all 66 spectra were height-normalised to the inverse of their $S = 1/2$ g -corrected integrated intensities. The whole process was repeated for several different values of the linewidth coefficients and thus involved a total of four variable parameters; ΔH_0 , ΔH_1 and the λ distribution variables λ_0 and $\Delta \lambda_{\frac{1}{2}}$ (expectation and half-width respectively).

An idea of the variation in component lineshape can be obtained from Figures 3.5 and 3.6 which correspond to the parameters used for the simulation in Figure 3.3.

Figure 3.7 shows resultant spectra simulated with $\Delta \lambda_{\frac{1}{2}} = 0.05$ for $\lambda_0 = 0.11, 0.12, 0.13, 0.14, \text{ and } 0.15$, with ΔH_0 and ΔH_1 constrained to give a line-width of 60 Gauss at a field of 1000 Gauss such that the low-field peaks have reasonable widths. It can be seen that the general lineshape form is reproduced for a wide range of ΔH_0 , ΔH_1 coefficients, thus the choice of values for these parameters whilst

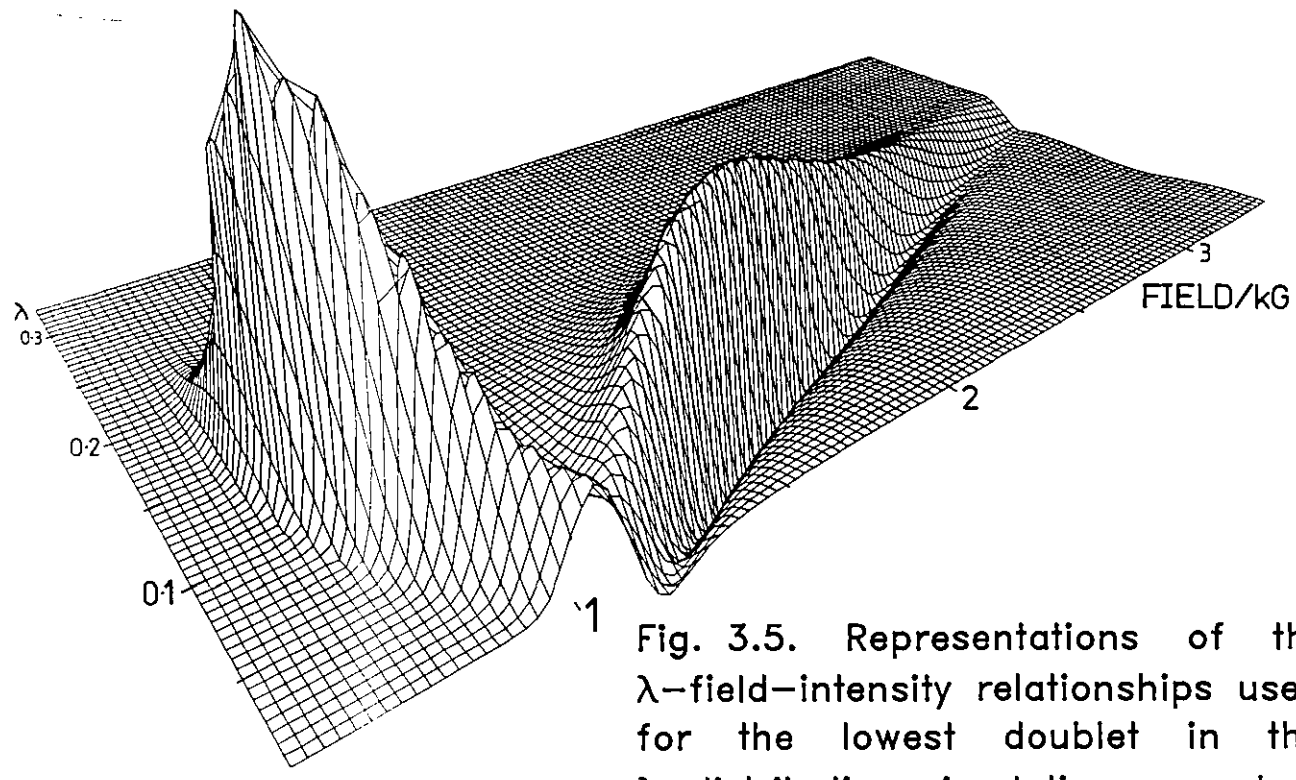
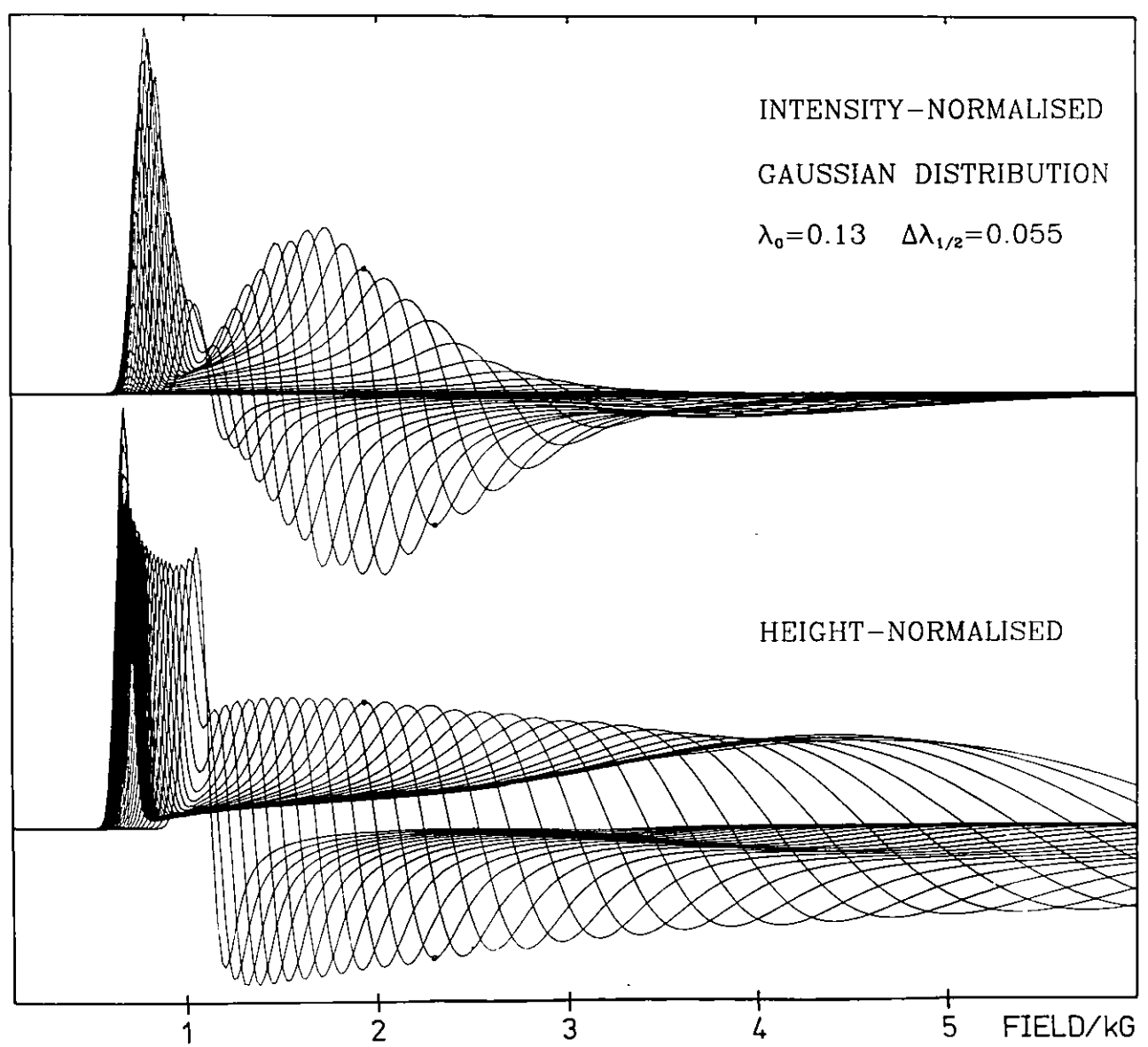


Fig. 3.5. Representations of the λ -field-intensity relationships used for the lowest doublet in the λ -distribution simulation procedure.



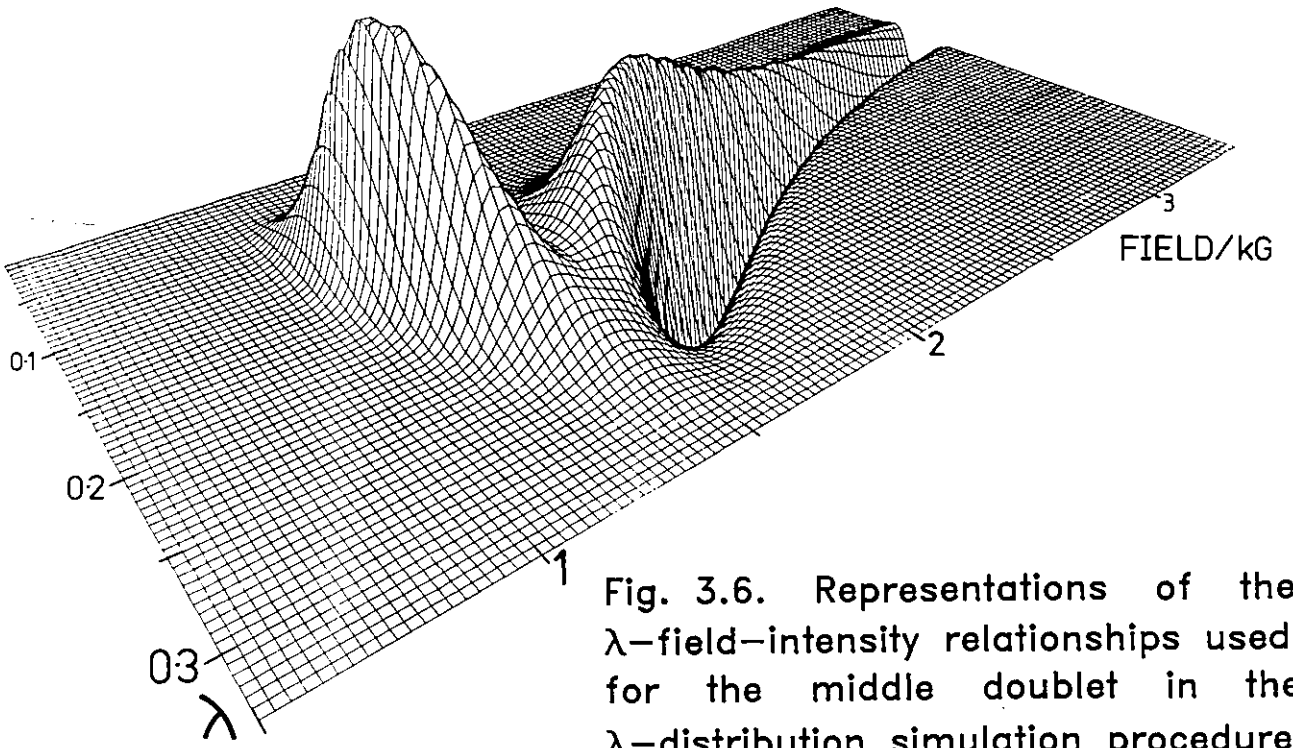
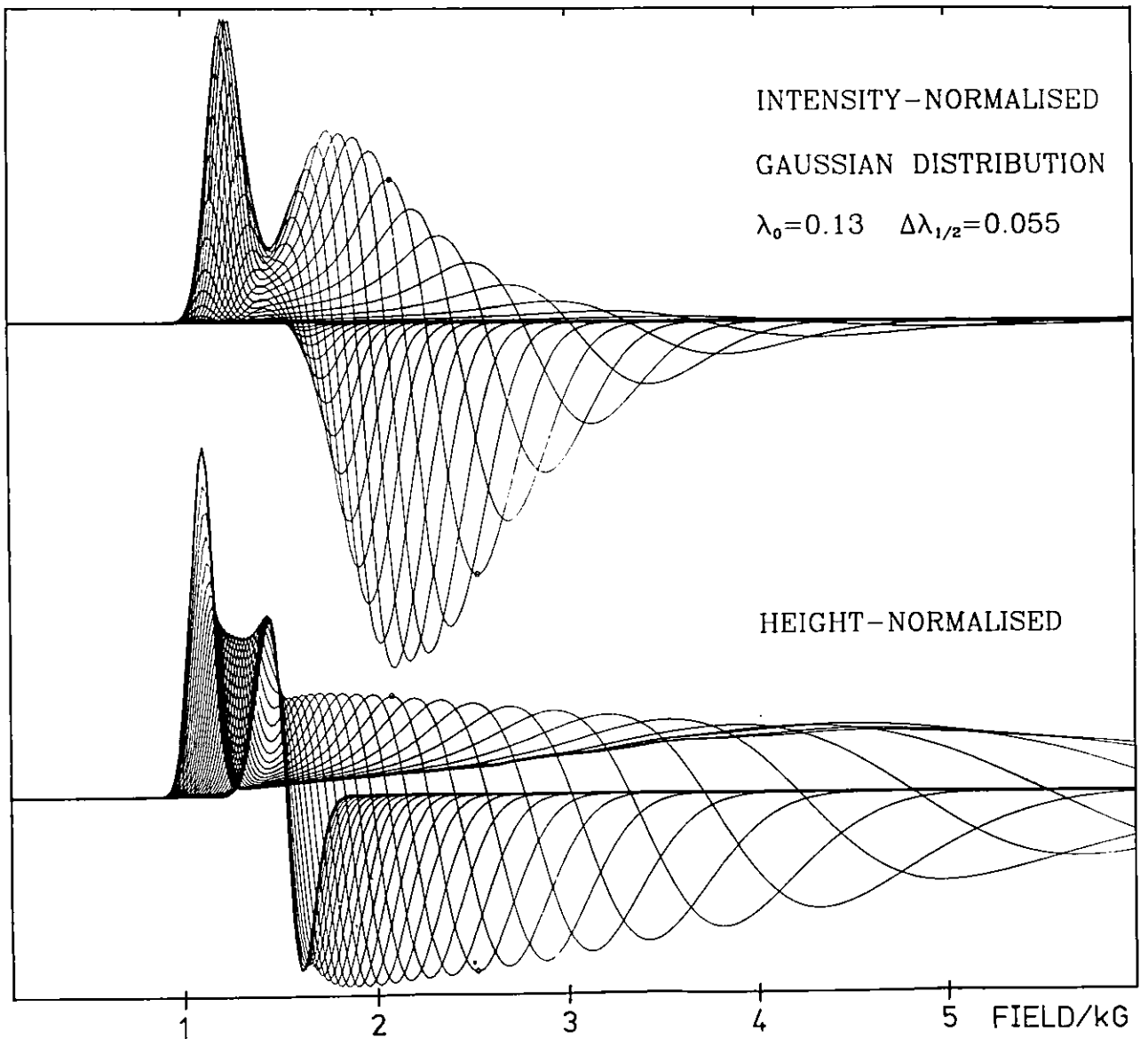


Fig. 3.6. Representations of the λ -field-intensity relationships used for the middle doublet in the λ -distribution simulation procedure.



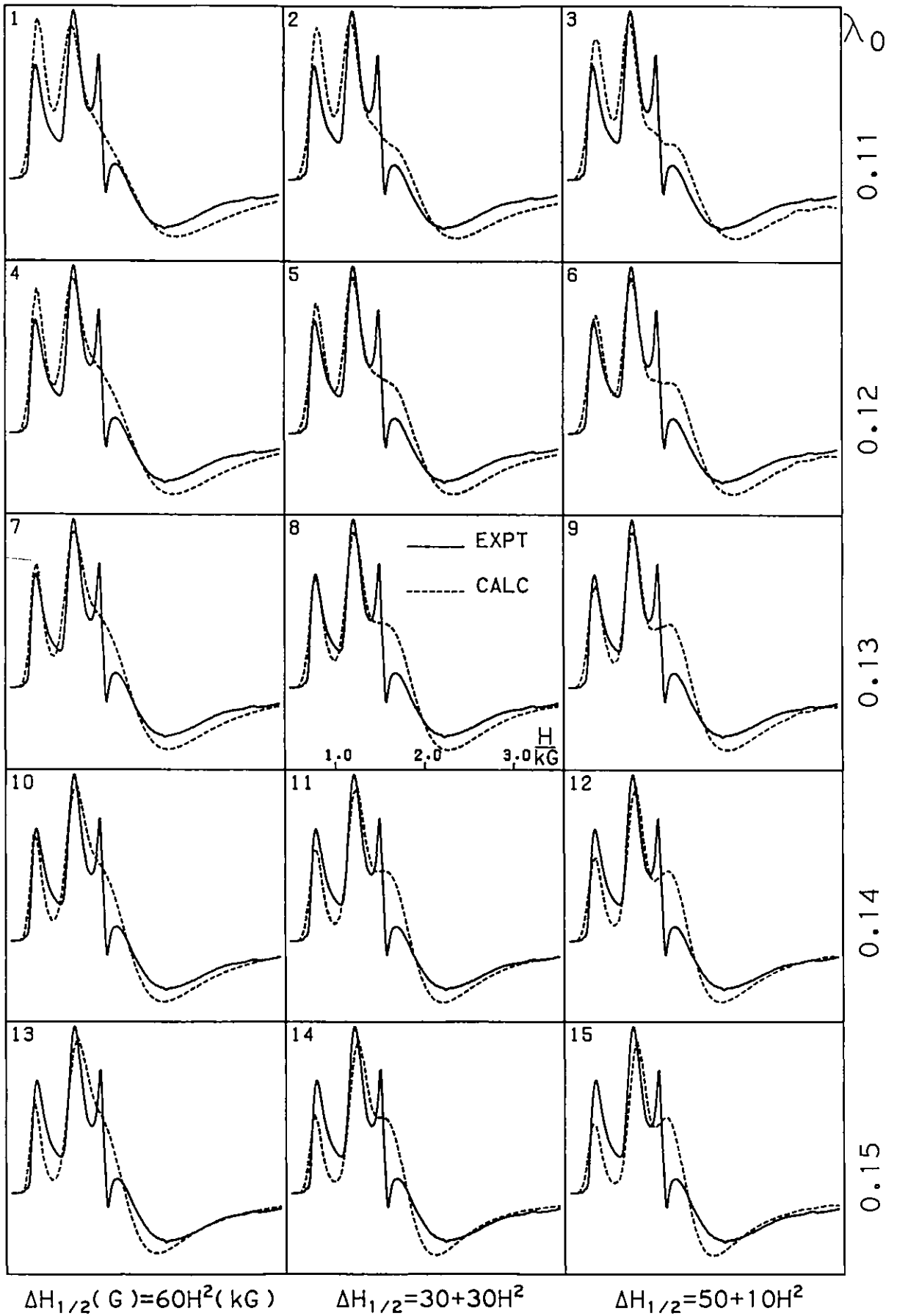


Fig 3.7 Trial simulations involving five different λ -distribution centerings ($\Delta\lambda_{1/2}=0.05$) and three linewidth formulae.

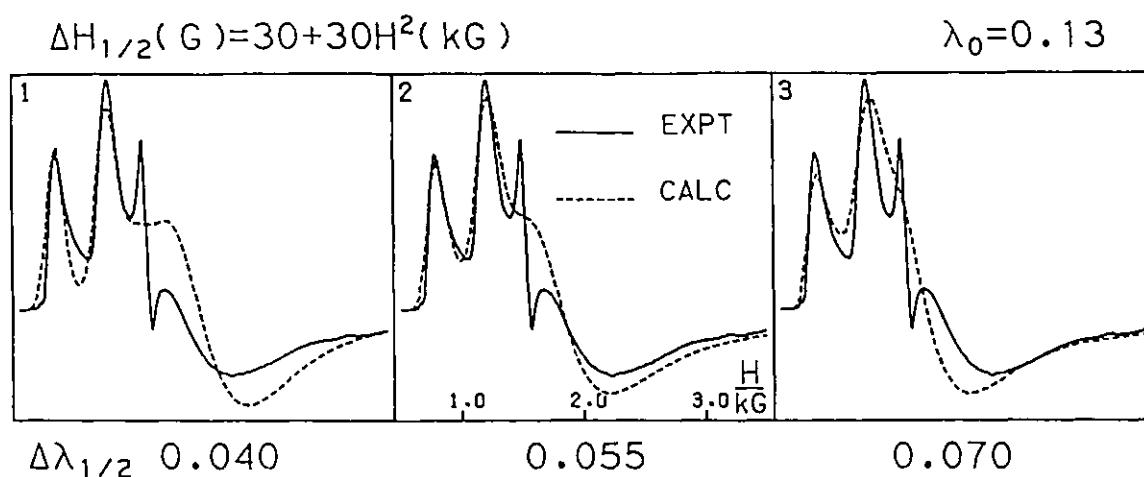


Figure 3.8. Trial simulations involving three different λ -distribution half-widths ($\lambda_0 = 0.13$).

being necessarily arbitrary is not too crucial. The fit of the calculated lines to the experimental on the other hand is seen to be a sensitive function of λ_0 , best fits being obtained for $\lambda_0 = 0.13$ - 0.14 . It was found necessary to restrict $\Delta\lambda_{\frac{1}{2}}$ to between 0.04 and 0.06 (see for example, Figure 3.8). Such a broad spread in E/D is not without precedent, a variation of ± 0.04 ¹⁴⁵ or distribution of width 0.05 ¹⁴⁶ having been proposed for example for Cr^{3+} in an aluminophosphate glass.

The closest approach to the experimental spectrum is that in Figure 3.3 where the distribution of principal-axis resonance positions resulting from the Gaussian variation in λ is also shown.

The simulation method shows that the assumption of a λ distribution as the origin of the large high-field linewidths is probably correct in that the experimental lineshape is matched quite well using greatly reduced component spectral linewidths compared with the previous fixed- λ convolution method. An attempt has been made in formulating the

simulation procedure to minimise the number of variable parameters involved and to this extent better reproduction of the experimental spectrum might be achieved using more sophisticated linewidth anisotropy or λ -distribution formulae.

Recently the EPR spectrum of desulforedoxin has been described.^{147,122} This protein, isolated from the sulphate-reducing bacterium Desulfovibrio gigas, with one iron atom and four cysteines per monomer unit has visible and Mössbauer general spectral features resembling rubredoxin, but indicative of a higher coordination symmetry at the iron. The X-band EPR spectrum shows an intense and relatively narrow peak at $g' = 7.7$, a smaller feature of similar width at $g' = 5.7$, a broad derivative line at $g' = 4.1$ and very broad minimum at $g' = 1.8$. These results have been interpreted in terms of $\lambda = 0.08$ for which resonances are predicted at $g' = 4.09, 7.70, 1.80$ and $g' = 1.87, 1.74, 5.79$, from lower and middle Kramers doublets respectively. Thus, this protein has an EPR spectrum quite different to rubredoxin, and the spectrum for $[\text{Fe}(\text{S}_2\text{-o-xylyl})_2]^-$ is intermediate between the spectra found for these two $\text{Fe}(\text{III})\text{S}_4$ proteins. The distribution of linewidths in desulforedoxin also takes a similar form to that observed here for $[\text{Fe}(\text{S}_2\text{-o-xylyl})_2]^-$.

3.3. EPR at Q-Band.

At low fields the solution Q-band (36 GHz) spectrum for $[\text{Fe}(\text{S}_2\text{-o-xylyl})_2]^-$ shows two maxima at $g' = 7.8$ and 5.3 , and a broad crossover at $g' \approx 3.0$ (Figure 3.9). No sharp isotropic resonance is observed around 6 kG. Predicted fields at Q-band for $S = 5/2$ with $D = 2.0 \text{ cm}^{-1}$ are given in Figure 3.9. Analysis of the experimental spectrum follows as for the X-band lineshape using these curves.

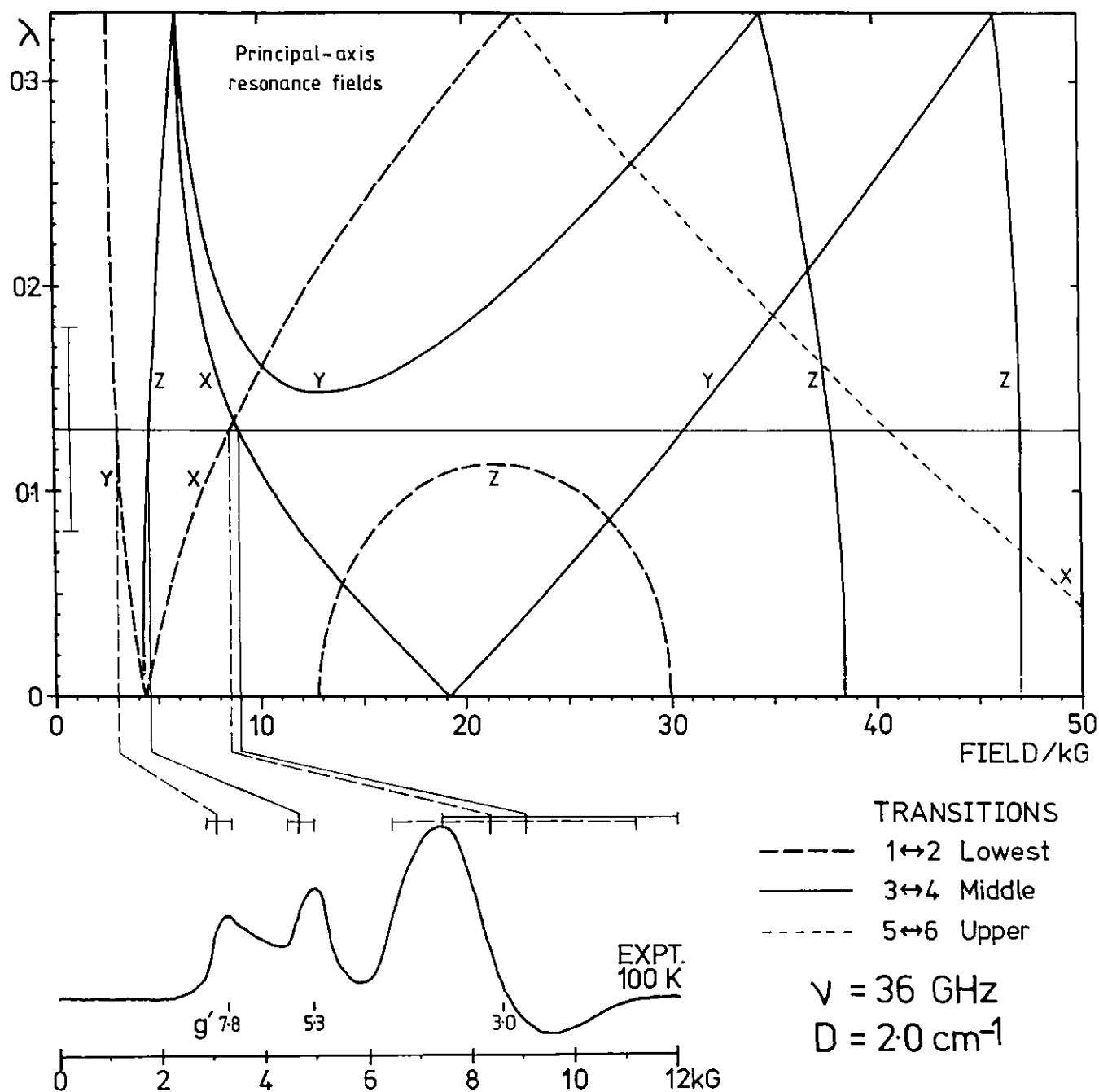


Fig. 3.9 Predicted principal-axis resonance fields for $D=2.0\text{cm}^{-1}$, $\nu=36\text{GHz}$, $\lambda=0$ to $1/3$ compared with the experimental Q-band spectrum for a frozen solution of $\text{Et}_4\text{N}[\text{Fe}(\text{S}_2\text{-o-xylyl})_2]$ in 3/1 DMF/ CH_2Cl_2

The two lowest-field lines correspond to those in the X-band spectrum and are due to respective y and z orientations for lowest and middle doublets. Resonance-fields for these transitions are relatively independent of D or λ , but the position and width of the peaks in the experimental spectrum are quite consistent with a distribution in λ centred around 0.13. The broad derivative shaped absorption at about $g' = 3$ is considered to arise mainly from the x-orientations for resonance involving the first and second pairs of energy levels. As at X-band, H vs. λ curves for these resonances are seen to cross close to $\lambda = 0.13$ (Figure 3.9). Considering the variation $\lambda = 0.13 \pm 0.05$ their Q-band resonance fields span the interval 6 to 12 kG and quite adequately account for the width of the $g' = 3$ spectral feature. It is indeed a little surprising that this feature is so well resolved compared with the X-band spectrum considering the large λ -distribution width invoked there. λ -dependency of the remaining orientations, z and y respectively, for resonance in the first and second energy level pairs, is however more complicated at the higher frequency. For a λ -distribution of the magnitude suggested in the previous section, the differences evident in the λ -H plots of Figures 3.3 and 3.9 may well account for the disparity in spectral lineshape at X and Q-band frequencies. This could only be demonstrated in detail by performing a simulation procedure for Q-band similar to that employed at X-band. In view of the complexity of the Q-band resonance positions for $\lambda = 0.13 \pm 0.05$ this would be rather more difficult to undertake. Due to local instrumentation difficulties it has not proven possible to measure the Q-band spectrum above ca. 10 kG. However, taking into account the factors of large anisotropy, appearance of a resonance along one principal direction only, or wide field variation for small

changes in λ , it is unlikely that any further peaks would be observed at fields greater than the maximum used in the present measurements.

3.4. Determination of D.

Measurement of the X-band EPR spectrum of $[\text{Fe}(\text{S}_2\text{-o-xylyl})_2]^-$ over the temperature range 5-100 K enables an estimation of the value of D. It is important to know the temperature of the sample accurately and in addition to the modified Au/Fe-Chromel thermocouple built into the cryostat beneath the sample space, two additional sensors were employed; a further similar thermocouple constructed from very fine wire was spiralled some 50 times around the sample tube and terminated in the sample just outside the EPR cavity, and a thin quartz tube containing a 3 mM aqueous solution of Cu-EDTA was frozen into the solution of $[\text{Fe}(\text{S}_2\text{-o-xylyl})_2]^-$. The temperature available from the intensity of the g_{\perp} part of the Cu^{2+} spectrum via the Boltzmann population relationship, $I \propto (1 - e^{-h\nu/kT})$, was standardised at 77.3 K to that from the Au/Fe-chromel sample thermocouple by obtaining a spectrum with the emf of the latter balanced to zero in reference to a second junction in liquid nitrogen. Under the conditions used, the Cu^{2+} lineshape is invariant and (I) was taken as the height of the derivative shaped g_{\perp} feature. Whilst over the range of application both sensors gave temperatures generally agreeing within 5%, that for the Cu^{2+} signal was considered better to represent the actual sample temperature in that it originated from the entire region of the frozen solution giving rise to the Fe(III) EPR spectra.

Denoting the zero field splitting between middle and lowest doublets by Z_1 and highest and middle doublets by Z_2 the intensity (I) of EPR spectral features relating to the lowest doublet is given by E3.3, where C is a proportionality factor reflecting instrumental conditions and the arbitrary choice of intensity measurement.

$$I = C.(1 - e^{-(h\nu/kT)}) / (1 + e^{-Z_1/kT} + e^{-(Z_1 + Z_2)/kT}) \quad (E3.3)$$

For a zero field splitting of the present magnitude there is negligible deviation of fractional doublet populations given by the denominator term in E 3.3 from the more exact expression involving Boltzmann distribution between the six spin-state energy levels at each resonance field.

In the purely axial ($\lambda = 0$) and fully rhombic ($\lambda = 1/3$) cases simple expressions are available relating Z_1 , Z_2 and D as shown in Figure 3.1. More generally, substitution for the \hat{S}_x^2 , \hat{S}_y^2 , \hat{S}_z^2 spin matrices in E3.2 and subtraction of the energy term ω from the diagonal elements leads to the secular determinant which is set equal to zero and may be reduced to equation (E3.4) with doubly degenerate solutions.

$$\begin{array}{l} | \pm 5/2 \rangle \\ | \mp 3/2 \rangle \\ | \pm 1/2 \rangle \end{array} \begin{array}{ccc} | \pm 5/2 \rangle & | \mp 3/2 \rangle & | \pm 1/2 \rangle \\ \left| \begin{array}{ccc} \frac{10}{3} - \frac{\omega}{D} & & \lambda\sqrt{10} \\ & -\frac{2}{3} - \frac{\omega}{D} & \lambda\sqrt{18} \\ \lambda\sqrt{10} & \lambda\sqrt{18} & -\frac{8}{3} - \frac{\omega}{D} \end{array} \right| & = 0 & \end{array} \quad (E3.4)$$

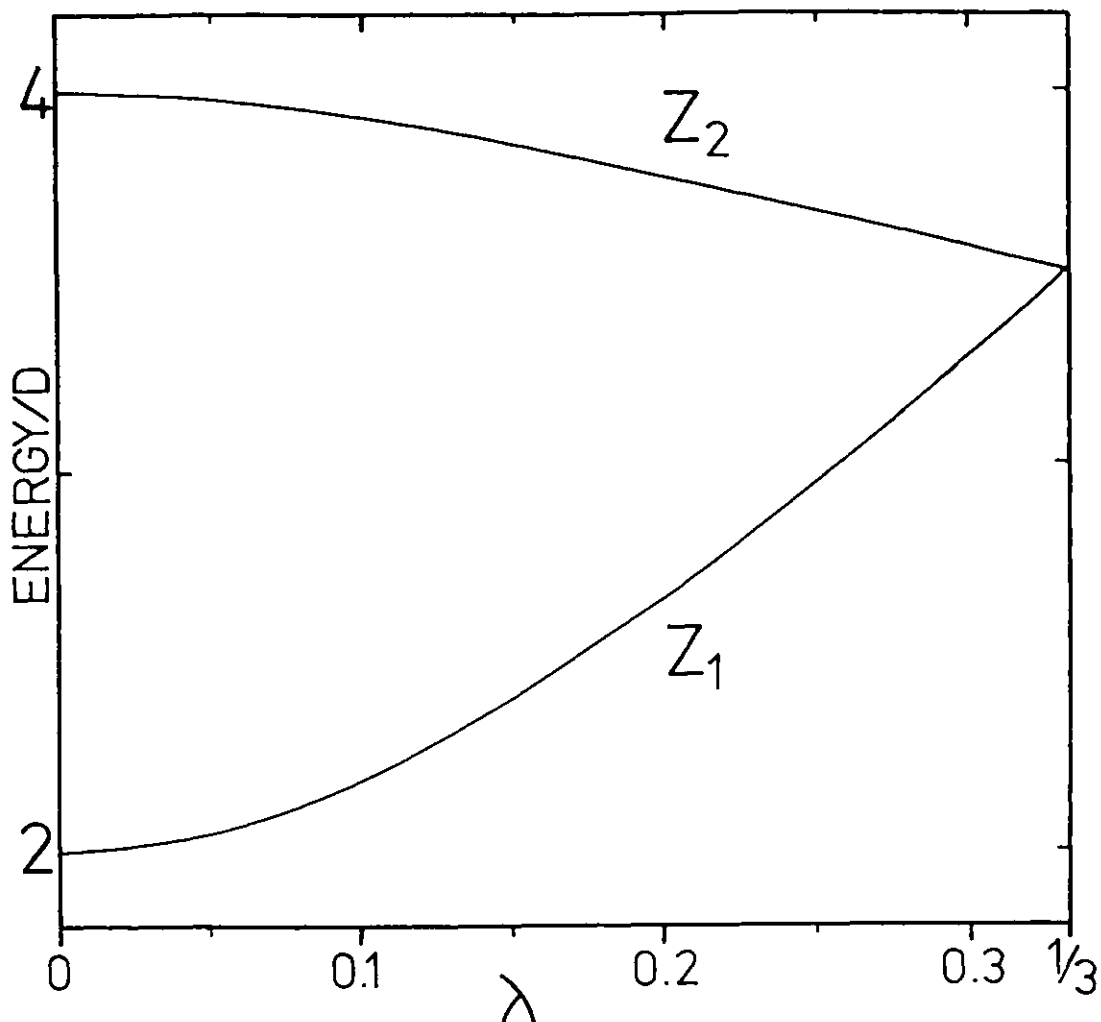


Figure 3.10. λ -Dependence of zero-field splitting between lowest and middle and between middle and upper Kramers doublets.

Expansion of this expression to a cubic in ω followed by numerical trigonometric solution yields three real degenerate spin-state relative energies, as multiples of D . The λ -dependence of the energy separations Z_1 and Z_2 for the doublets is shown in Figure 3.10. In this way it becomes possible to evaluate E3.3 in terms of the more directly useful parameters λ , D and C .

These three variables have been used in a least squares fit of equation E3.3 to the experimental data for the $g' = 8.4$ peak plotted as $I/(1 - e^{-(h\nu/kT)}) \cdot C$ against inverse temperature. The $g' = 8.4$ line has temperature invariant linewidth to low field

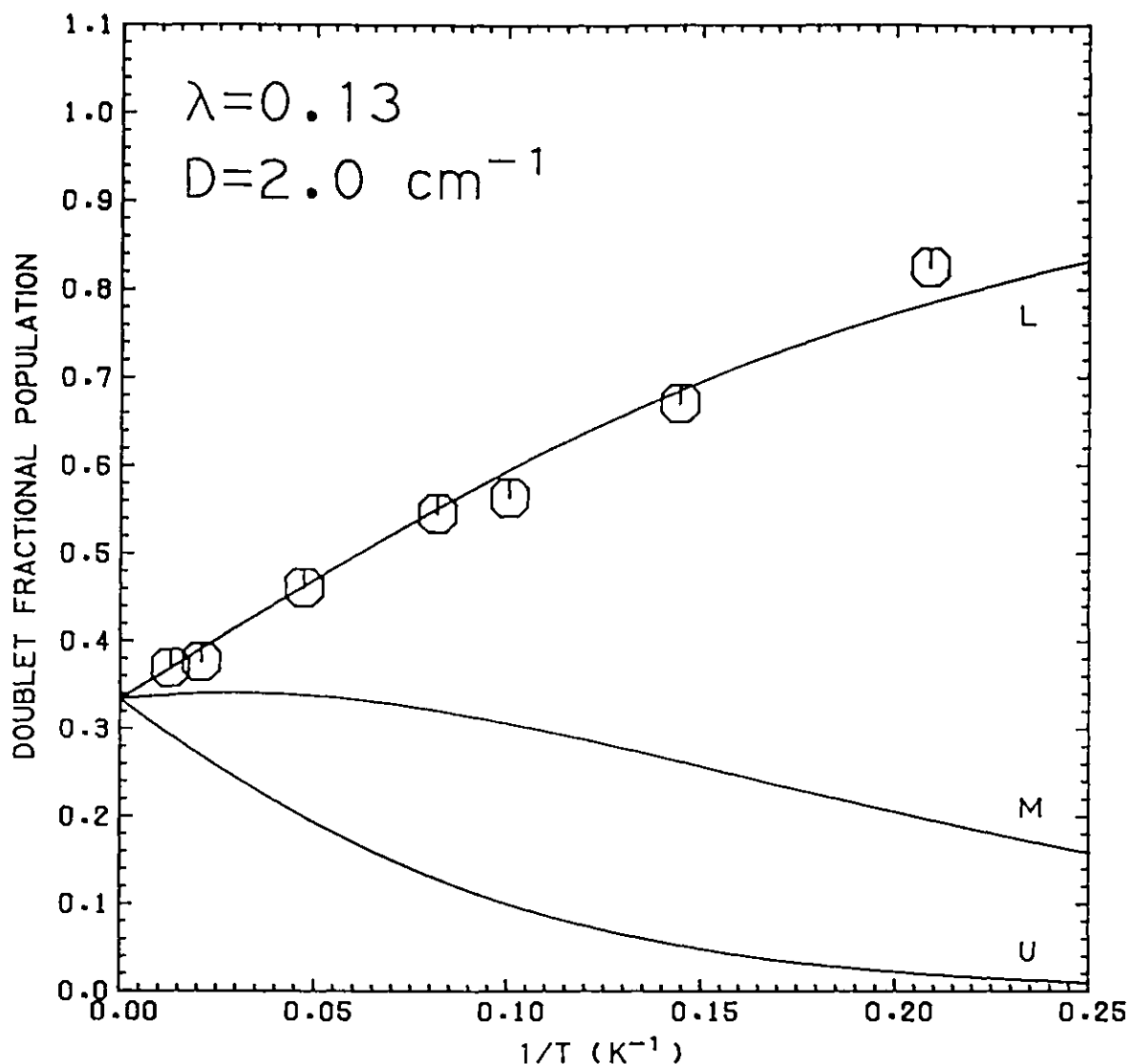


Figure 3.11. Temperature dependence of the fractional populations for the three $S = 5/2$ doublets (L = lower, M = middle, U = upper) with $D = 2.0 \text{ cm}^{-1}$ and $\lambda = 0.13$ compared with experimental normalised intensities for the $g' = 8.4$ peak of $[\text{Fe}(\text{S}_2\text{-o-xylyl})_2]^-$.

of its maximum and its height was taken directly for I. Standard deviation of the data from E3.3 is insensitive to λ over the meaningful range $0 \leq \lambda \leq 1/3$ and this parameter was removed as a variable being assigned the value 0.13 consistent with the interpretation of the resonance field positions and simulation procedures given above. The best fit with $D = 2.0 \text{ cm}^{-1}$ is shown in Figure 3.11. C has been chosen in such a way that the ordinate is the fractional population given by

the denominator of E3.3. Fitting the data for fixed values of D while still varying C shows that an accuracy of around $-0.4, +0.7$ is appropriate to D, compared with a 5% standard deviation for the best fit. In view of the λ distribution implicit in the lineshape analysis given in the previous section, the peak-intensity temperature dependence must be somewhat more complicated than the analysis undertaken. Taking into account the possible range $\lambda = 0.13 \pm 0.05$ by refitting the data for $\lambda = 0.08$ and 0.18 whilst varying D and C, leads to an increase in the estimated error such that $D = 2.0 \begin{smallmatrix} +0.8 \\ -0.5 \end{smallmatrix}$.

For the $g' = 5.4$ line the intensity temperature product appears roughly constant over the range of the present measurements, although it is more difficult accurately to assess a baseline for this peak, particularly at higher temperatures. Figure 3.11 shows that for the λ and D values quoted the fractional population of the middle Kramers doublet is expected to be fairly constant above 10 K but should drop off at lower temperatures.

From a theoretical fit of magnetisation data for $\text{Et}_4\text{N}[\text{Fe}(\text{S}_2\text{-oxylyl})_2]$, Frankel et al.¹¹⁸ have obtained a value of $D = 1.5 \text{ cm}^{-1}$ when assuming $\lambda = 1/3$. For $\lambda = 0.13$, D becomes 2.3 cm^{-1} , though this would probably be slightly lowered if Z_1 were to be reevaluated assuming this λ .

The present estimate of D is also compatible with the 1.76 and 1.89 cm^{-1} quoted for Rd_{ox} ^{125,135} and $2.2 \pm 0.3 \text{ cm}^{-1}$ obtained for desulfiredoxin from Mössbauer measurements.¹⁴⁷

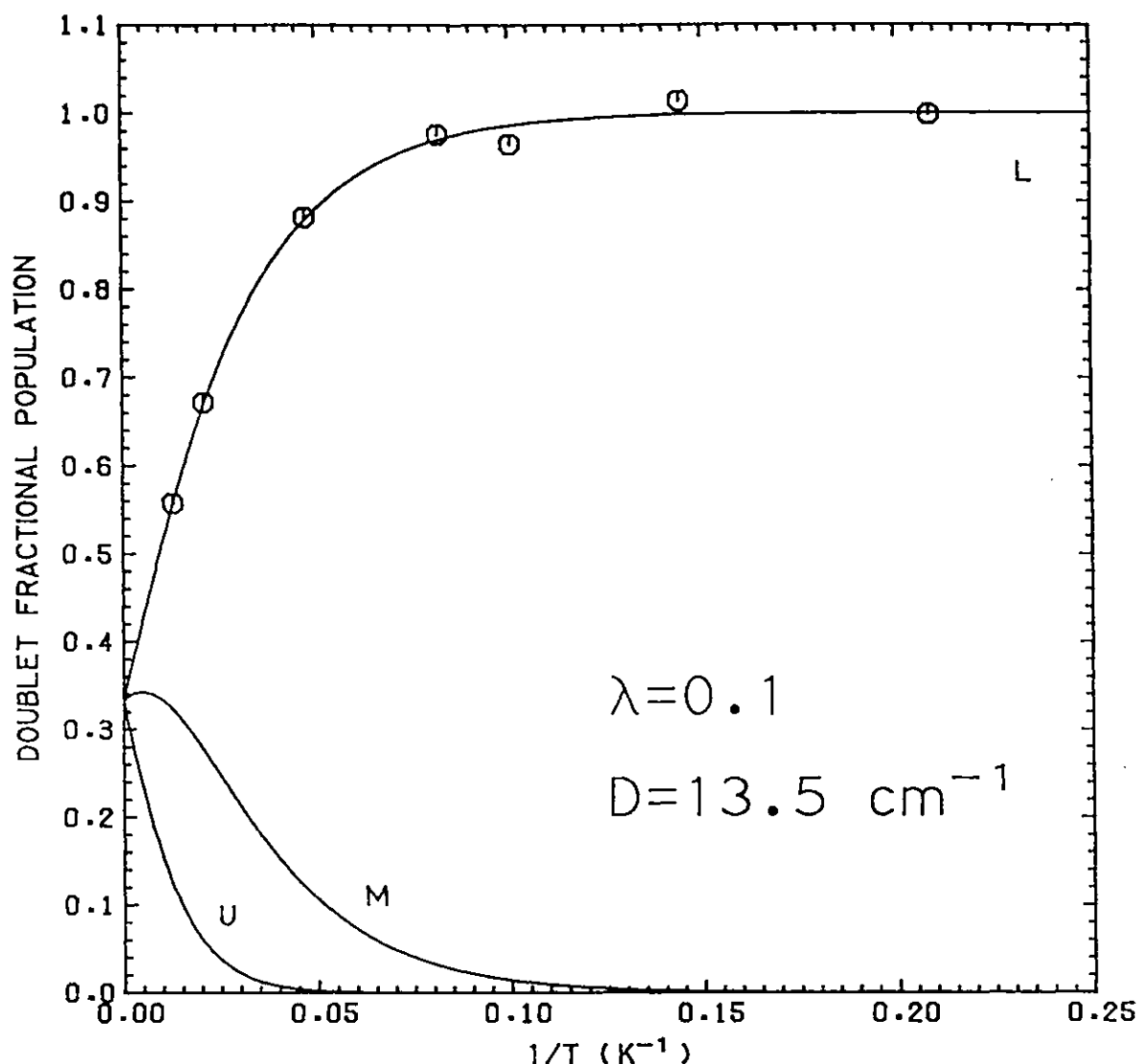


Figure 3.12. Temperature dependence of fractional doublet populations for the three $S = 5/2$ doublets with $D = 13.5 \text{ cm}^{-1}$, $\lambda = 0.1$, compared with experimental normalised intensities of the sharp $g' = 4.3$ resonance for $[\text{Fe}(\text{S}_2\text{-o-xylyl})_2]^-$.

3.5. Origin of the Sharp $g' = 4.3$ Resonance.

Figure 3.12 shows the temperature variation of the $g' = 4.3$ peak-intensity in EPR spectra for a DMF/ CH_2Cl_2 (3:1) solution of $[\text{Fe}(\text{S}_2\text{-o-xylyl})_2]^-$. Strong deviation from Curie-law behaviour is observed down to about 10 K after which the curve levels out to the expected horizontal. Using a least squares fitting procedure similar to that described for the $g' = 8.4$ peak, good agreement with the data is found for $D = 13.5 \pm 2 \text{ cm}^{-1}$, $Z_1 = 30 \pm 4 \text{ cm}^{-1}$ (curve fitting standard deviation 2%) and

with $\lambda = 0.10$, assuming the signal to arise from the lowest doublet of a Fe(III) species (Figure 3.12). Very similar zero-field splittings result when λ is constrained to any given value in the range 0 to 1/3 ($\lambda = 0$, $Z_1 = 29 \text{ cm}^{-1}$; $\lambda = 1/3$, $Z_1 = 34 \text{ cm}^{-1}$).

The ratio of the intensity at $g' = 4.3$ to that for the peak at lowest field has been found fairly constant when studying solutions prepared from different samples of the same batch of solid or from four separate $\text{Et}_4\text{N}[\text{Fe}(\text{S}_2\text{-o-xylyl})_2]$ syntheses. It would be reasonable to expect some variation in the ratio if the sharp signal arose from an impurity. On the other hand, some considerable variation in the intensity ratio is to be found on comparing spectra obtained with different solvent systems. Solvent mixtures which solidify in a vitreous state on cooling, all result in spectra similar to that described for 3:1 DMF/ CH_2Cl_2 . Some of the solvents which crystallise strongly lead to a more intense $g' = 4.3$ line, although it is difficult accurately to assess the situation when the spectrum is also broadened. One possible explanation of the line is, then, that it results from some aggregation of the iron-centres, since a strong $g' = 4.3$ line is also observed for the pure solid. The vitreous samples, however, appear quite transparent showing no signs of crystallisation likely to lead to precipitation of solid.

If the sharp line results from another species it must arise from a ground state having an excited state some 30 cm^{-1} higher in energy. This rules out a species having high λ and D and giving an isotropic $g' = 4.3$ resonance from its middle Kramers doublet, as such a signal would be thermally depopulated at low temperatures. An intermediate

spin ($S = 3/2$) Fe(III) complex with axial symmetry could give rise to a cross-over line at $g' \sim 4$ arising from a ground state doublet, and also possess a well separated higher lying doublet. Such a $g_{\perp} \sim 4$ feature would, however, be broad^{148,149} and have an asymmetric shape connected to a further peak at $g'_{\parallel} \sim 2$. Thus, this does not provide a reasonable explanation of the isotropic resonance observed.

Another potential explanation for the $g' = 4.3$ line arises from considering random variations in the spin-Hamiltonian parameters of the kind already invoked to explain the large high-field linewidths observed in the spectrum under consideration. Peterson et al.^{150,151} have analysed the situation where the distribution of principal-axis resonance fields is so large that they overlap, that is become equal. One intriguing possible consequence with reference to high-spin ferric characterised by an axial \underline{D} tensor is that resonance spectra might be dominated by a large "spike" at $g' \sim 4$, normally considered indicative of fully rhombic \underline{D} symmetry. The notion is that the $g'_{\perp} \sim 6$ and $g'_{\parallel} \sim 2$ axis-resonance positions from the lowest doublet would be spread out due to their large anisotropy and the g_{\perp} , g_{\parallel} variation, but that from a small number of molecules in the distribution having $g_{\perp} \sim g_{\parallel}$ an isotropic, and consequently strong, resonance would result midway between $g' = 2$ and $g' = 6$. In a replying letter, Jellison, et al.¹⁵² have critically described the statistical distributions assumed by Peterson et al. as hypothetical in view of their lack of attempted detailed curve fitting for simulated and experimental spectra. Griscom too has stressed the necessity of using rigorously calculated transition

schemes in assessing the correlation of distribution functions for the variables.¹⁴⁶ Can then a variation in \underline{D} tensor symmetry lead to g' isotropy? Gibson¹⁵³ and Griscom¹⁵⁴ have both briefly discussed the specifically axial case by an inspection of D/H plots^{132,133} and have concluded the absence of negative g'_{\perp} , g'_{\parallel} correlation necessary for $g' \sim 4$ spiking. Brodbeck¹⁵⁵ has presented a detailed analysis of the angular variation of g' values for $S = 5/2$, as dependent on D and E . No negative g' correlation is found for lower or upper doublets but in the case of a distribution in λ containing the value $\lambda = 1/3$, the middle doublet might give a $g' = 4.3$ "spike" even though the majority of the molecules are in an environment leading to a near axial \underline{D} tensor. A somewhat obvious conclusion consistent with the early analysis of Castner.¹³⁴

Gibson¹⁵³ has suggested that such a distribution in λ for a \underline{D} symmetry slightly lower than fully rhombic might well explain the form of the $g' = 4.3$ resonance in some Rd_{ox} , for which a sharp line is superimposed on a broad one.

For $[\text{Fe}(\text{S}_2\text{-o-xylyl})_2]^-$, where a large λ variation has been suggested to explain the overall lineshape, the identity of some middle doublet principal-axis resonance fields at $g' = 4.3$ is a distinct possibility. In detail, however, the λ -distribution simulations described in Section 3.2 do not support the production of a sharp line of the shape observed experimentally. Broader spike shaped lines at $g' = 4.3$ could be produced for certain λ -distributions but the overall fit to the rest of the spectrum would not be retained. It can be seen from Figure 3.6 that the contribution at $\lambda = 1/3$ to the simulated lineshape in Figure 3.3 is negligible.

The intensity of a $g' = 4.3$ spike produced in the manner described by Peterson et al. would be expected, having its origin in an excited state, to deviate negatively from the Curie-law unless considerable thermal variation in λ -distribution resulted in some anomalous effect. The latter is unlikely in view of the temperature invariant lineshape of the $g' = 4.3$ signal.

The isotropic resonance from the middle doublet predicted when $\lambda = 1/3$, arises at $g' = 30/7$ (4.286) and very closely approaches the $g' = 4.28$ measured for the sharp line under discussion. As previously indicated this cannot provide an explanation for the sharp line since this must come from resonance in a ground-state doublet. However, if quartic terms make a significant contribution to the spin-Hamiltonian (E 35) an isotropic $g' = 30/7$ resonance may be calculated to arise from the ground-state, as originally discussed by Kedzie et al.¹⁵⁶

$$\begin{aligned} \mathcal{H} &= \beta \cdot \underline{H} \cdot \underline{g} \cdot \hat{S} + \hat{S} \cdot \underline{D} \cdot \hat{S} \\ &+ \frac{a}{6} \cdot [(\hat{S}_x^4 + \hat{S}_y^4 + \hat{S}_z^4) - \frac{S}{5}(S+1)(3S^2 + 3S - 1)] \\ &+ \frac{F}{180} [35 \hat{S}_z^4 - 30S(S+1)\hat{S}_z^2 + 25 \hat{S}_z^2 - 6S(S+1) + 3S^2(S+1)^2] \end{aligned} \quad (\text{E3.5})$$

Several analyses have been made of the conditions necessary for an isotropic g -tensor in a high spin d^5 system,^{131,157,158} but when permutations of axis systems are taken into consideration only two independent sets of conditions corresponding to $g' = 30/7$ result, and these are adequately summarised by E3.6 given by Kedzie, et al.¹⁵⁶

$$(a \pm 3a) - F = 6D \quad (\text{E3.6})$$

The latter authors have plotted Eigen-values corresponding to these conditions showing the regions where the doublet with isotropic g' tensor is lowest in energy. It is readily apparent that in order for the isotropy relationship (E3.6) to be satisfied the magnitudes of either or both $|a|$ and $|F|$ must be equal to or greater than $|D|$. A high value of $|D|$ is indicated by the temperature dependence for the intensity of the sharp line, and it is difficult to accept that quartic spin-Hamiltonian terms could be as large as would seem to be required, since there is no literature precedent for this. The special relationship between coefficients required by E3.6 would seem to be additionally exceptional. Also the absence of any sharp-isotropic feature at $g' = 4.3$ in the Q-band $[\text{Fe}(\text{S}_2\text{-o-xylyl})_2]^-$ solution spectrum adds further to the inadequacy of this explanation for its appearance at X-band.

3.6. Conclusion.

The EPR spectrum of a solution of $[\text{Fe}(\text{S}_2\text{-o-xylyl})_2]^-$ has been analysed in terms of a high D value and \underline{D} symmetry intermediate between axial and fully rhombic with a distribution such that $\lambda_0 = 0.13 \pm 0.01$, $\Delta\lambda_{\frac{1}{2}} \sim 0.05$. From the temperature dependent intensity variation of a feature assigned to resonance in the high spin ferric lowest Kramers doublet, D has been estimated at $2.0^{+0.8}_{-0.5} \text{ cm}^{-1}$. This D value is unexceptional for sulphur ligation, but the overall \underline{D} tensor symmetry is higher than expected.

If \underline{D} and coordination symmetries are directly related via the crystal field, then the sulphur ligation in Rd_{ox} must be considered to be more aspherically distorted than in $[\text{Fe}(\text{S}_2\text{-o-xylyl})_2]^-$. It has

been suggested that such additional distortion might be protein applied leading to a metastable "entactic" state in accordance with the hypothesis of Vallee and Williams.^{159,160} However, EXAFS^{161,162} and Mössbauer¹¹⁸ investigations show the simple ferric complex to have a very similar coordination to that in Rd_{ox} . Raman spectroscopy shows the FeS_4 vibrational unit in $[Fe(S_2-o-xylyl)_2]^-$ to be of low symmetry (see Section 4).

Disparity between these results and the EPR must be resolved in terms of the relative sensitivities of the various observational techniques to the microsymmetry at the iron. In all cases, it is difficult to translate available spectroscopic differences into actual structural differences. Over all, on a somewhat empirical comparative basis, the coordination symmetry in $[Fe(S_2-o-xylyl)_2]^-$ is considered to closely approach that in Rd_{ox} but to possess less distortion from tetrahedral.

The possibility of a change in coordination of $[Fe(S_2-o-xylyl)_2]^-$ on dissolution is discounted on the basis that Raman and Mössbauer spectra are very similar to those for the solid phase. Additionally, the solution species shows no solvent dependency of its visible absorption spectrum, or indeed of its EPR spectrum beyond broadening and changes in relative intensity of the sharp $g' = 4.3$ line. It would be interesting to obtain spectra for $Et_4N[Fe(S_2-o-xylyl)_2]$ doped into a suitable host (possibly the ferrous homologue).

EPR measurements for desulfuredoxin^{147,122} are noted with interest as the iron is believed to be bound to the protein by four cysteine residues as in Rd_{ox} , yet the resonance spectrum is characteristic of an

intermediate rhombicity having $\lambda = 0.08$. An EXAFS study has been initiated to probe more deeply into the details of the iron-site geometry for this protein and the results should be instructive in understanding the disparity in the present spectroscopic results outlined above.

No firm conclusion has been reached concerning the origin of the sharp $g' = 4.28$ resonance for $[\text{Fe}(\text{S}_2\text{-o-xylyl})_2]^-$. The proximity of g' to the theoretical $g' = 30/7$ (4.286) isotropic resonances, predicted in a number of circumstances, cannot be considered accidental, although no corresponding signal is seen at Q-band.

At present $[\text{Fe}(\text{S}_2\text{-o-xylyl})_2]^-$ remains the only well-defined, isolable, synthetic mono-nuclear ferric tetra-mercapto coordinated species available and it will be interesting to see to what extent its properties extend to future $\text{Fe}(\text{III})\text{S}_4$ complexes in general.

3.6. Experimental.

3.6.1. EPR Measurements.

The $[\text{Et}_4\text{N}][\text{Fe}(\text{S}_2\text{-o-xylyl})_2]$ used for the EPR measurements was recrystallised from acetone. Solutions were filtered through a fine sintered frit prior to freezing in quartz tubes. Measurements ca. 100 K and above were made with a quartz dewar insert, employing flowing precooled nitrogen gas as refrigerant. For the temperature range 5-100 K an Oxford-Instruments ESR 10 Helium-flow cryostat with DTC-2 temperature controller was employed. The ESR-10 Au/Fe-chromel thermocouple was extended in a spiral above the He-nozzle/heater-block in order to obtain a more accurate indication of the temperature just below the sample. It was found that although the ESR-10 cryostat was capable of attaining a temperature of 2 K it could not maintain sufficient stability or a small enough thermal gradient in the sample

to allow the accurate measurement of EPR spectra below 5 K. Similar experience has been reported by other users of this cryostat.^{147,163}

3.6.2. Details of Conditions for Spectra in Figures.

Figure 3.2. At temperature 5 K, Power = 36 dB attenuation from 200 mW, Modulation = 16 G, Frequency = 9.12 GHz.
At temperature 100 K, Power = 6 dB, Modulation = 6.3 G, Frequency = 9.12 GHz.

Figure 3.3. Experimental spectrum is same as the 100 K spectrum of Figure 3.2.

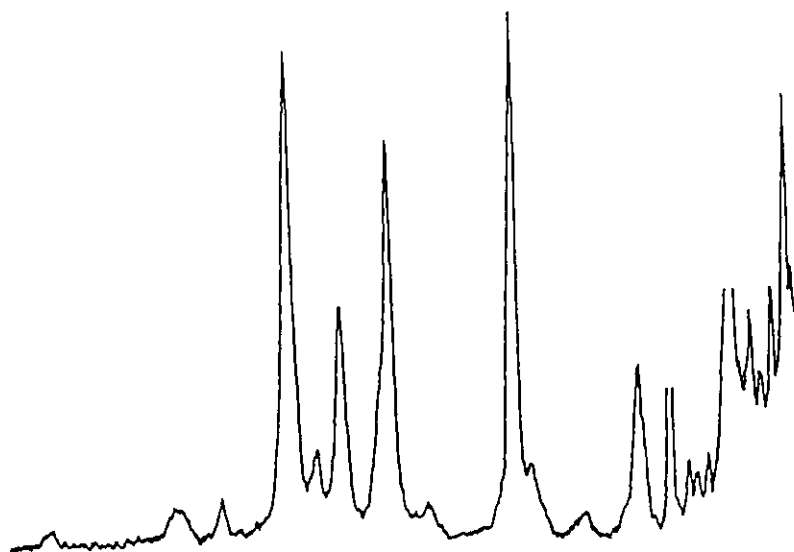
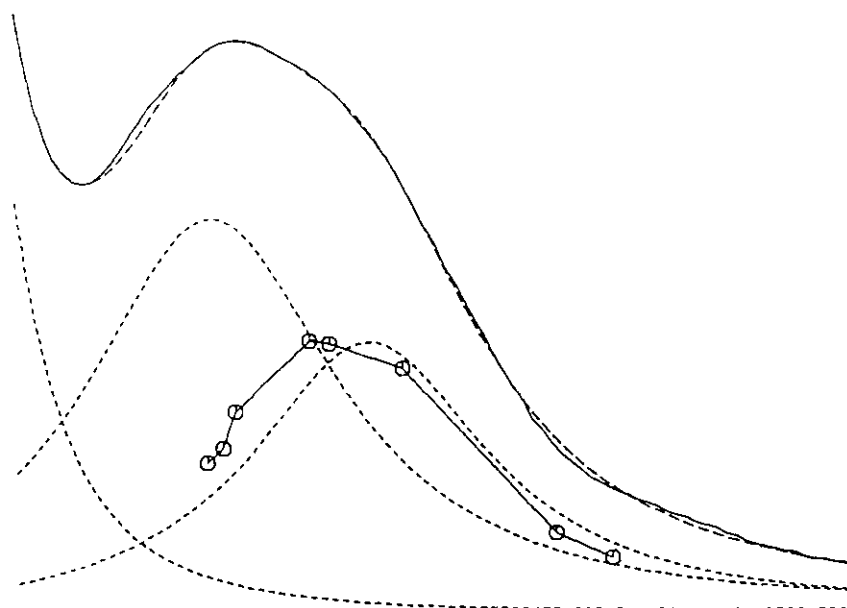
Figure 3.9. Temperature 100 K, Frequency 36 GHz.

The fractional population temperature-dependency curves of Figures 3.11 and 3.12 were calculated using the FORTRAN subroutine below:

```

SUBROUTINE EBNC(I11,I13)
C..... NUMERICAL TRIGONOMETRIC SOLUTION OF THE CUBIC :-
C      X**3 - X**2(DA+DB+DC) + X(DA*DB+DA*DC+DB*DC-DE2-DD2)
C      - (DA*DB*DC-DA*DE2-DB*DD2) = 0
C..... THIS ROUTINE FITS INTO PROGRAM SOS.
C      IT GENERATES A FRACTIONAL-POPULATION VECTOR
C      AS A FUNCTION OF A TEMPERATURE VECTOR FOR
C      THREE KRAMERS DOUBLETS FROM AN S=5/2 ION.
COMMON X(1100,5),DATA(100),IB(10)
COMMON/IN/ICOM,X1,X2,X3,X4,X5,I1,I2,I3,I4,I5
1,K1,K2,K3,K4,K5,IM,NIN,NLOOP,LOOP1,LOOP2,INU
2,ARGS(20),IARG,IS,LC,NRUN,JB(7),NSTR,ISTR(40,12)
DIMENSION FP(3)
N1=I11
N3=I13
N4=MAX0(I4,1)
N4=MIN0(N4,3)
NP=X(1100,N1)
X(1100,N3)=NP
C..... LAMBDA VALUE IN DATA(21)
XLAM=DATA(21)
C..... D VALUE IN DATA(22)
ZFS=DATA(22)/0.695116
XL=XLAM*XLAM
C..... MATRIX | DA-X      DD |
C              |          DB-X DE | = 0
C              | DD      DE  DC-X |
C..... X=ENERGY/D
DA=25.0/4.0
DB=9.0/4.0
DC=1.0/4.0
DD2=10*XL
DE2=18*XL
C..... C1,C2,C3 ARE THE ZERO-FIELD DOUBLY DEGENERATE
C      ENERGY ROOTS EXPRESSED IN UNITS OF D.
P=- (DA+DB+DC)
Q=DA*DB+DA*DC+DB*DC-DE2-DD2
R=- (DA*DB*DC-DA*DE2-DB*DD2)
SA=Q-P*P/3.0
SB=2.0*P*P*P/27.0-P*Q/3.0+R
RT=-SA*SA*SA/27.0
CTH=-SB/(2.0*SQRT(RT))
TH=ACOS(CTH)
TH1=TH/3.0
RAD=3.1415926536*120.0/180.0
TH2=TH1+RAD
TH3=TH2+RAD
RT=-SA/3.0
RT=SQRT(RT)*2.0
C1=COS(TH1)*RT-P/3.0
C2=COS(TH2)*RT-P/3.0
C3=COS(TH3)*RT-P/3.0
ZR=(C1-C3)/(C3-C2)
IF(ZFS.LT.0.0)ZR=1.0/ZR
ZR=1.0+ZR
ZFS=-ABS(ZFS)*(C3-C2)
FP(1)=1.0
DO 10 I=1,NP
C..... X(I,N1) CONTAINS A TEMPERATURE VECTOR
FP(2)=EXP(ZFS*X(I,N1))
FP(3)=FP(2)**ZR
C..... FRACTIONAL POPULATION FOR LEVEL N4
10 X(I,N3)=FP(N4)/(FP(1)+FP(2)+FP(3))
CALL SET(N3)
RETURN
END

```

SECTION 4**RESONANCE RAMAN OF
IRON-SULPHUR COMPLEXES**

4. RESONANCE RAMAN OF IRON-SULPHUR COMPLEXES.

ABSTRACT	167
4.1. <u>Introduction: RR in Iron-Sulphur Proteins.</u>	168
4.2. <u>Mononuclear Iron-Sulphur Complex; Analogue of Rubredoxins.</u>	171
4.2.1. RR in Rubredoxins.	171
4.2.2. $[\text{Fe}(\text{S}_2\text{-o-xylyl})_2]^-$ as a model for the iron-sulphur centre in Rd_{ox} .	174
4.2.3. RR spectra of $[\text{Fe}(\text{S}_2\text{-o-xylyl})_2]^-$.	175
4.2.3.1. Fe-S stretching vibrations.	176
4.2.3.2. Fe-S deformation vibrations.	180
4.2.3.3. Resonance Enhancement.	182
4.2.4. Conclusions.	182
4.3. <u>Binuclear Iron-Sulphur Complexes; Analogues of 2Fe2S Ferredoxins.</u>	184
4.3.1. RR in 2Fe Ferredoxins	184
4.3.2. RR and IR Spectra of $[\text{Fe}_2\text{S}_2(\text{SR})_4]^{2-}$.	186
4.3.3. Assignment of vibrational spectra.	191
4.3.3.1. $[\text{Fe}_2\text{X}_2(\text{S}_2\text{-o-xylyl})_2]^{2-}$ (X = S, Se).	191
4.3.3.2. $[\text{Fe}_2\text{X}_2(\text{YPh})_4]^{2-}$ (X, Y = S, Se).	205
4.3.3.3. $[\text{Fe}_2\text{X}_2(\text{STol})_4]^{2-}$ (X = S, Se), $[\text{Fe}_2\text{S}_2(\text{SC}_6\text{H}_4\text{Cl})_4]^{2-}$ and $[\text{Fe}_2\text{X}_2\text{Y}_4]^{2-}$ (X = S, Se; Y = Cl, Br).	209
4.3.4. Optical spectra and Raman resonance enhancement for the two-iron complexes.	209
4.3.5. General conclusions concerning dimer complexes.	217

4.4.	<u>Tetranuclear Iron-Sulphur Complexes; Analogues of 4Fe4S</u>	221
	<u>Proteins.</u>	
4.4.1.	RR in 4Fe4S Clusters.	221
4.4.2.	RR and IR Spectra of $[\text{Fe}_4\text{S}_4(\text{SR})_4]^{2-}$.	222
4.4.2.1.	$[\text{Fe}_4\text{X}_4(\text{YPh})_4]^{2-}$ (X, Y = S, Se).	232
4.4.2.2.	$[\text{Fe}_4\text{X}_4(\text{SBz})_4]^{2-}$ (X = S, Se).	236
4.4.2.3.	Resonance in the Raman Spectra of the 4Fe Complexes.	239
4.4.3.	General Conclusions Concerning Tetramer Complexes.	241
4.5.	<u>Experimental - Sample Preparation.</u>	245
4.5.1.	Raman Samples.	245
4.5.2.	IR Samples	247
4.5.3.	Selected Ligand Vibrations.	247
4.5.4.	Conditions and Notes Concerning Figures and Tables.	248

ABSTRACT

Resonance Raman and infrared studies are presented for 1-Fe, 2-Fe, and 4-Fe model complexes of iron-sulphur protein centres. Medium to strong resonance is observed in the Raman spectra of the complexes when exciting in the visible region, resulting in fairly good quality well-resolved spectra. Partial assignment of observed bands is made according to the normal modes expected for the three major structural types.

For $[\text{Fe}(\text{S}_2\text{-o-xylyl})_2]^-$ the FeS_4 symmetry is found to be degraded from T_d to as low as C_s . It is suggested that in rubredoxins improved Raman spectra should show evidence of a fully split nine-line spectrum.

Spectra for several $[\text{Fe}_2\text{S}_2(\text{SR})_4]^{2-}$ complexes and their selenium and halogen ligated homologues are described. Fairly extensive cross-correlation of assigned bands is possible. A deconvolution analysis of the visible electronic absorption spectra is given for several of the dimers and comparison made with low resolution excitation profiles of their totally symmetric terminal-ligand stretches. A reassessment is made of previous assignments for protein spectra.

For Raman spectra of $[4\text{Fe-4S}]^{2+}$ proteins, reassignment of some totally symmetric bands is made possible from consideration of the vibrational spectra of $[\text{Fe}_4\text{X}_4(\text{YR})_4]^{2-}$ (X, Y = S, Se) analogues.

4. RESONANCE RAMAN OF IRON-SULPHUR COMPLEXES.

4.1. INTRODUCTION: RR IN IRON-SULPHUR PROTEINS.

The resonance Raman (RR) process involves laser excitation within an electronic absorption band to produce large and selective enhancement of Raman lines which arise from vibrations of the chromophoric unit.¹⁶⁴ From the presence of intense $S \rightarrow Fe$ charge transfer absorptions throughout the visible and near-uv spectral regions of iron-sulphur proteins and analogous small inorganic complexes, the enhancement of Fe-S vibrations in RR is to be expected. Since vibrational frequencies are sensitive to geometric and bonding arrangements of localised groups of atoms in a molecule, RR is then a potentially useful technique for the observation of fine structural differences of the iron-sulphur centres. Where the RR transitions can be assigned to specific Fe-S vibrational modes it may additionally be possible, from their frequency dependent intensity enhancement, to determine the origin of the coupled electronic transition. As the inorganic model compounds are more easily well characterised, and may be to some degree subjected to structural design, a comparative analysis of RR spectra for proteins and analogues could lead to a more accurate structural and electronic definition of the iron-sulphur site in its natural environment. For multi-nuclear iron-sulphur centres the vibrational spectra are of interest for additional reasons. Firstly, the spin-lattice relaxation mechanism of the paramagnetic clusters at middle to high temperatures may involve a local vibrational mode directly¹⁰¹ or as an intermediary to the phonon bath^{105,107} (see Section 2), and Raman and IR spectra are important in establishing or invalidating this role.

TABLE 4.1. Vibrational frequencies for iron-sulphur proteins and related synthetic compounds.

Ref.	Molecule	No. Fe	Bands (cm ⁻¹)	Assignment	Raman excitation (nm)
167,168	Rubredoxin <u>Cl. pasteurianum</u>	1	368 (ρ 0.9) 314 (ρ 0.3) 150 126 (ρ 0.8)	T ₂ A ₁ T ₂ E in T _d symmetry	488.0 632.8
119,169	Rubredoxin <u>P. elsdenii</u>	1	380) 362) 320 175 w 158 75 w	A ₁ E A ₁ E A ₁ E in C _{3v} symmetry	568.2
170	Adrenodoxin	2Fe	397,297 350	core modes. terminal ligand mode	488.0
	Selena-Adrenodoxin	2Fe	355,263 350 all polarised	core modes . terminal ligand mode	488.0
114	Adrenodoxin	2Fe	390,345,288	Fe-S modes	488.0 476.2 413.1
115	Spinach Fd.	2Fe	395,330,284	Fe-S modes	488.0
171	Adrenodoxin	2Fe	344w, br	Fe-S mode	I.R.
172	<u>C. pasteurianum</u> Fd	4Fe	360,345	terminal-ligand mode	488.0
	<u>Chromatium Hipip</u>	4Fe	365,338 250 all polarised	terminal-ligand mode core mode	488.0
172	[Et ₄ N] ₂ [Fe ₄ S ₄ (SBz) ₄]	4Fe	332 275 both polarised	terminal-ligand mode core mode	448.0
173	Fe ₂ S ₂ (CO) ₆	2Fe	329(pol) 314, 267 191 (pol) 554 (pol)	Fe-S sym. str. Fe-S non-sym.mode Fe-Fe str. S-S str.	647.1 676.4
174	Fe(II)[(SPPH ₂) ₂ N] ₂	1Fe	283 205	T ₂ str. A ₁ str. in T _d symmetry	488.0

Secondly, it might be possible to observe Raman transitions involving the manifold of spin states resulting from the antiferromagnetic exchange coupled iron atoms. Such photon-spin interactions have been observed in, for example, FeF_2 ^{165,166} and have also been suggested to explain bands in RR spectra of spinach and adrenal ferredoxins.^{114,115} These bands would indicate the energy above the ground state of excited spin levels and lead to an evaluation of the magnitude of the exchange coupling between the iron atoms constituting the bridged cluster.

Whilst measurements of the vibrational properties of iron-sulphur proteins are not extensive, the frequency region where bands from Fe-S modes are expected to lie is well established. Table 4.1 summarises the Fe-S frequencies which have been observed in proteins and synthetic analogues together with some other relevant metal-ligand vibrations. Metal-sulphur stretching frequencies are found in the 480 to 210 cm^{-1} range^{175,176}; deformation frequencies are less well catalogued but those which have been described lie between 80 and 150 cm^{-1} .

The RR technique^{177, 178} and its application in biochemistry^{164,179-181} have been well reviewed.

4.2. Mononuclear Iron-Sulphur Complex; Analogue of Rubredoxins.

4.2.1. RR in Rubredoxins.

The iron-sulphur centres in rubredoxins are comprised of ferric (Rd_{ox}) or ferrous (Rd_{red}) iron approximately tetrahedrally coordinated by four cysteinyl sulphurs. Pronounced ligand field rhombicity has been detected by a number of spectroscopic measurements on both the oxidised and reduced forms.¹¹⁹ The three dimensional structure of rubredoxin from the bacterium Clostridium pasteurianum is known to a resolution of 1.2\AA from X-ray diffraction studies of Jensen and coworkers¹⁸² and the $Fe(III)S_4$ portion of the structure is shown in Figure 4.1. In the structure determination at 1.5\AA resolution, approximately the same \widehat{SFeS} angles were found but one abnormally short Fe-S(42) bond length of 2.05\AA together with remaining nearly equal lengths of 2.34 , 2.32 and 2.24\AA had indicated a distortion from tetrahedral more axial than rhombic in character.¹⁸³

Figure 4.1. Crystallographically determined structural data for the FeS_4 site in Rd from C. pasteurianum.¹⁸²

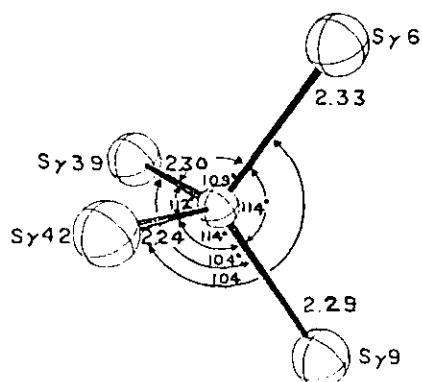


Figure 4.2. Raman spectra for Rd_{red} for C. pasteurianum with 488 nm excitation.¹⁶⁷

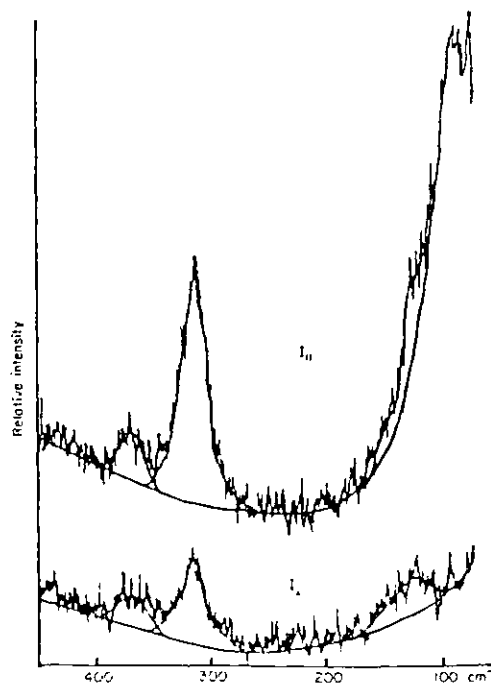


TABLE 4.2. Correlations between the point group T_d and sub-groups.

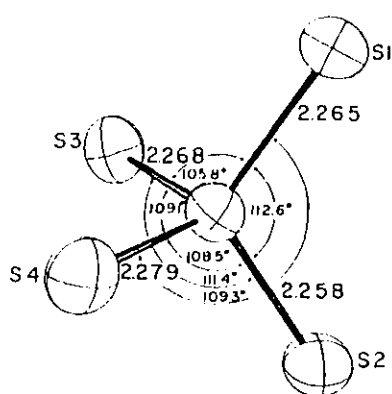
Site Group	Vibrational Symmetry			
	ν_1 (str)	ν_2 (def)	ν_3 (str)	ν_4 (def)
T_d	A_1^*	E^*	T_2	T_2
T	A^*	E^*	T	T
S_4	A^*	$A^* + B$	$B + E$	$B + E$
D_{2d}	A_1^*	$A_1^* + B_1^*$	$B_2 + E$	$B_2 + E$
C_{3v}	A_1	E	$A_1 + E$	$A_1 + E$
C_3	A	E	$A + E$	$A + E$
C_{2v}	A_1	$A_1 + A_2^*$	$A_1 + B_1 + B_2$	$A_1 + B_1 + B_2$
D_2	A^*	$2A^*$	$B_1 + B_2 + B_3$	$B_1 + B_2 + B_3$
C_2	A	2A	$A + 2B$	$A + 2B$
C_s	A'	$A' + A''$	$2A' + A''$	$2A' + A''$
C_1	A	2A	3A	3A

- (1) All vibrations are both Raman active and infrared active unless otherwise marked (* = IR inactive).
- (2) For a more detailed description of some of the normal modes of vibration see for example Nakamoto.¹⁸⁴

Table 4.2 describes the group theory predicted metal–ligand–atom vibrational selection rules for four-coordination under eleven possible symmetries. Yamamoto and coworkers have obtained a Raman spectrum of Rd_{ox} from *P. elsdeni* using 568.2 nm excitation.^{169,119} Solution RR spectra show three prominent lines at 370, 320 and 158 cm^{-1} . The 370 cm^{-1} line is split by 18 cm^{-1} and there is evidence for additional bands at 75 and

175 cm⁻¹ giving a six-line spectrum and suggesting that the effective symmetry of the FeS₄ complex is less than tetrahedral. Having regard for the X-ray diffraction structural observations for C. pasteurianum, at that time only available to 1.5Å resolution, Yamamoto et al., carried out a normal coordinate analysis for C_{3v} symmetry in keeping with a trigonal compression along one Fe-S bond. They obtained a good fit to the observed spectrum with the assignment given in Table 4.1 and by using valence force constants of 1.74 and 1.44 dynes /Å² for the one short and three long bonds respectively. The optical and EPR spectra of P. elsdeni and C. pasteurianum rubredoxins are sufficiently similar to allow the assumption that the stereochemistries of the two FeS₄ centres are essentially the same.

Long, et al.^{167,168} have measured Raman spectra for C. pasteurianum in solid phase with 632.8 nm excitation and in aqueous solution with 488 nm excitation. Figure 4.2 shows the spectrum obtained at 488 nm and has been interpreted by Long et al. as arising from an FeS₄ centre of T_d symmetry, the assignment given is described in Table 4.1. No splitting of any degenerate transitions was observed, but the non-zero depolarisation ratio for the symmetrical stretching mode was considered to indicate a distortion from tetrahedral symmetry. However, the most recent analysis to 1.2Å resolution of the X-ray diffraction results for C. pasteurianum, shown diagrammatically in Figure 4.1, indicates that five of the six \widehat{SFeS} angles of the iron-sulphur centre differ significantly from the tetrahedral value of 109.5°. The two smallest bond angles, $\widehat{S(6)FeS(42)}$ and $\widehat{S(9)FeS(39)}$, both 104°, as well as two of the three largest angles $\widehat{S(6)FeS(9)}$, 114°, and $\widehat{S(39)FeS(42)}$, 112°, are related by local approximate 2-fold axes. Analysis of the X-ray diffractions of rubredoxin from desulfovibrio vulgaris to 2Å resolution indicates \widehat{SFeS} angles in the range



	anion 1	anion 2
	Distance, Å	
Fe-S(1)	2.265 (2)	2.272 (2)
Fe-S(2)	2.258 (2)	2.252 (2)
Fe-S(3)	2.268 (2)	2.265 (2)
Fe-S(4)	2.279 (2)	2.278 (2)
	Angle, deg	
S(1)-Fe-S(2)	112.60 (8)	112.02 (8)
S(1)-Fe-S(3)	105.82 (7)	106.67 (7)
S(1)-Fe-S(4)	109.35 (7)	109.16 (7)
S(2)-Fe-S(3)	111.44 (7)	112.20 (7)
S(2)-Fe-S(4)	108.49 (7)	106.97 (7)
S(3)-Fe-S(4)	109.07 (7)	109.80 (7)

Figure 4.3. Crystallographically determined structural data for the FeS₄ sites in [Et₄N][Fe(S₂-o-xylyl)₂].^{117,56}

102-124° (precision 2-3°) and Fe-S bond lengths 2.15-2.35Å (precision 0.1Å)¹⁸⁵ suggesting considerable distortion from T_d symmetry for this protein also.

4.2.2. [Fe(S₂-o-xylyl)₂]⁻ as a model for the iron-sulphur centre in Rd_{ox}.

Ferric and ferrous complexes with the ligand o-xylyl- α,α' -dithiol are well established structurally and spectroscopically as good low molecular weight models of the iron-sulphur centre in rubredoxins.^{117,56,118} EXAFS comparisons of these anions with rubredoxins from *C. pasteurianum*¹⁶² and *P. aerogenes*¹⁶¹ reveal very similar absorption edges for corresponding oxidation states, indicating considerable stereochemical equivalence around the iron. The dimensions of the Fe(III)-S₄ group in [Fe(III)(S₂-o-xylyl)₂]⁻ are depicted in Figure 4.3. The coordination approaches T_d microsymmetry with small but definite rhombic distortions evident. Mössbauer¹¹⁸ and EPR (section 3) measurements in frozen solution indicate that upon release from a crystalline environment a non-cubic stereochemistry persists. The high-spin spherically symmetric Fe(III) ion is devoid of ligand field stabilisation effects on stereochemistry, and in the absence of perturbing

ligand or crystalline forces is expected to adopt strictly regular coordination geometry. $[\text{Fe}(\text{S}_2\text{-o-xylyl})_2]^-$ is considered to contain an essentially unconstrained Fe-S₄ unit,¹¹⁷ whose stereochemistry should closely approach that in Rd_{ox} in the absence of structural constraints imposed by the protein.

The electronic spectrum of $[\text{Fe}(\text{S}_2\text{-o-xylyl})_2]^-$ has broad principal bands at 350, 484 and 640-690 nm with extinction coefficients ranging from around 8000 to 1600 $\text{M}^{-1} \text{cm}^{-1}$. These are similar to those observed in the proteins and a strong resonant enhancement of Raman bands coupled to the electronic transitions is expected when irradiating at visible wavelengths.

4.2.3. RR spectra of $[\text{Fe}(\text{S}_2\text{-o-xylyl})_2]^-$.

Raman spectra have been obtained for $\text{Et}_4\text{N}[\text{Fe}(\text{S}_2\text{-o-xylyl})_2]$ as solid (diluted in KBr) and in acetone solution with 482.5, 530.9, 568.2 and 647.1 nm excitations. As with rubredoxin^{167,168} the samples are readily decomposed by excessive exposure to any of the above wavelengths, and besides the conventional technique of rapid sample rotation it was necessary to use low powers and, in the case of the solids, low concentrations and low temperatures in order to obtain optimal signal strength. Prolonged irradiation also results in an increasing fluorescent background. Table 4.3. lists the observed Raman and IR bands in the range up to 600cm^{-1} , and Figures 4.4 and 4.5 show examples of spectra obtained using KBr disc and acetone solution samples. The solid and solution spectra possess very similar frequency and intensity patterns indicating, as previously observed by other spectroscopic techniques,^{117,56,118} that the coordination stereochemistry is environment-independent for the two phases.

TABLE 4.3. RR and IR data for $\text{Et}_4\text{N}[\text{Fe}(\text{III})(\text{S}_2\text{-o-xylyl})_2]$

RAMAN										IR
SOLID: KBr DISC					SOLUTION: ACETONE					SOLID: POLYTHENE DISC
Band Maxima cm^{-1}	Intensities at excitation (nm)				Band Maxima cm^{-1}	ρ	Intensities at excitation (nm)			Band Maxima cm^{-1}
	482.5	530.9	568.1	647.1			482.5	568.2	647.1	
75(n)	m	m	1	-						
109	vw	w	1	w						
150	-	1	2	3	145					
160	-		1	3	160		sh	sh		
166	-	2		3						
223	0	w	-	2	222	0.3	0	2	3	
297	10	10	10	10	297	0.35	100	45	15	297vw
320	4	5	4	2	320	0.3	35	15	3	340s
350	2	1	1	4	350	0.2	10	2	5	348sh
373	1	2	1	1	375	~ 0.7	10	2	1	371m
450	w	w	vw	w						
467	1	w	w	1	467	prob. pol.	3	1	w	466m
										487w
										559mw
595		1	1	1						596m
OTHER BANDS										
93			w							394vw
280				w						418vw
487			w	w						

4.2.3.1. Fe-S Stretching Vibrations.

A simple analysis in terms of normal modes will be attempted. The most intense and polarised band at 297 cm^{-1} is assigned to the symmetrical stretching ν_1 vibration of Table 4.2. For concentrated samples the IR reveals a weak band at this frequency. Raman lines at 320 , 350 and 373 cm^{-1}

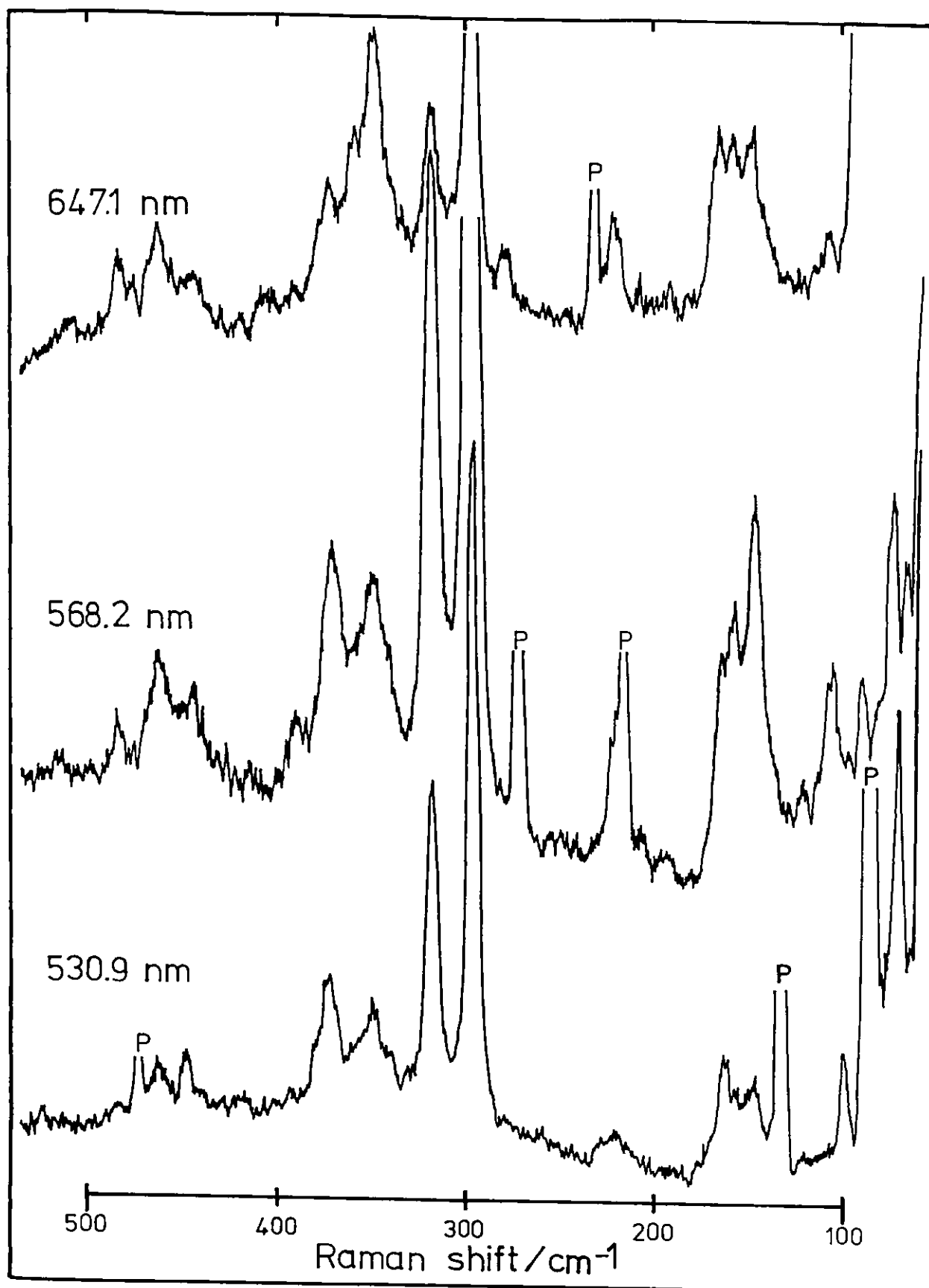


Fig 4.4 Solid-state Raman spectra for $[\text{Et}_4\text{N}][\text{Fe}(\text{S}_2\text{-o-xylyl})_2]$ with three excitation frequencies (647.1, 568.2 and 530.9 nm). P = plasma emission line.

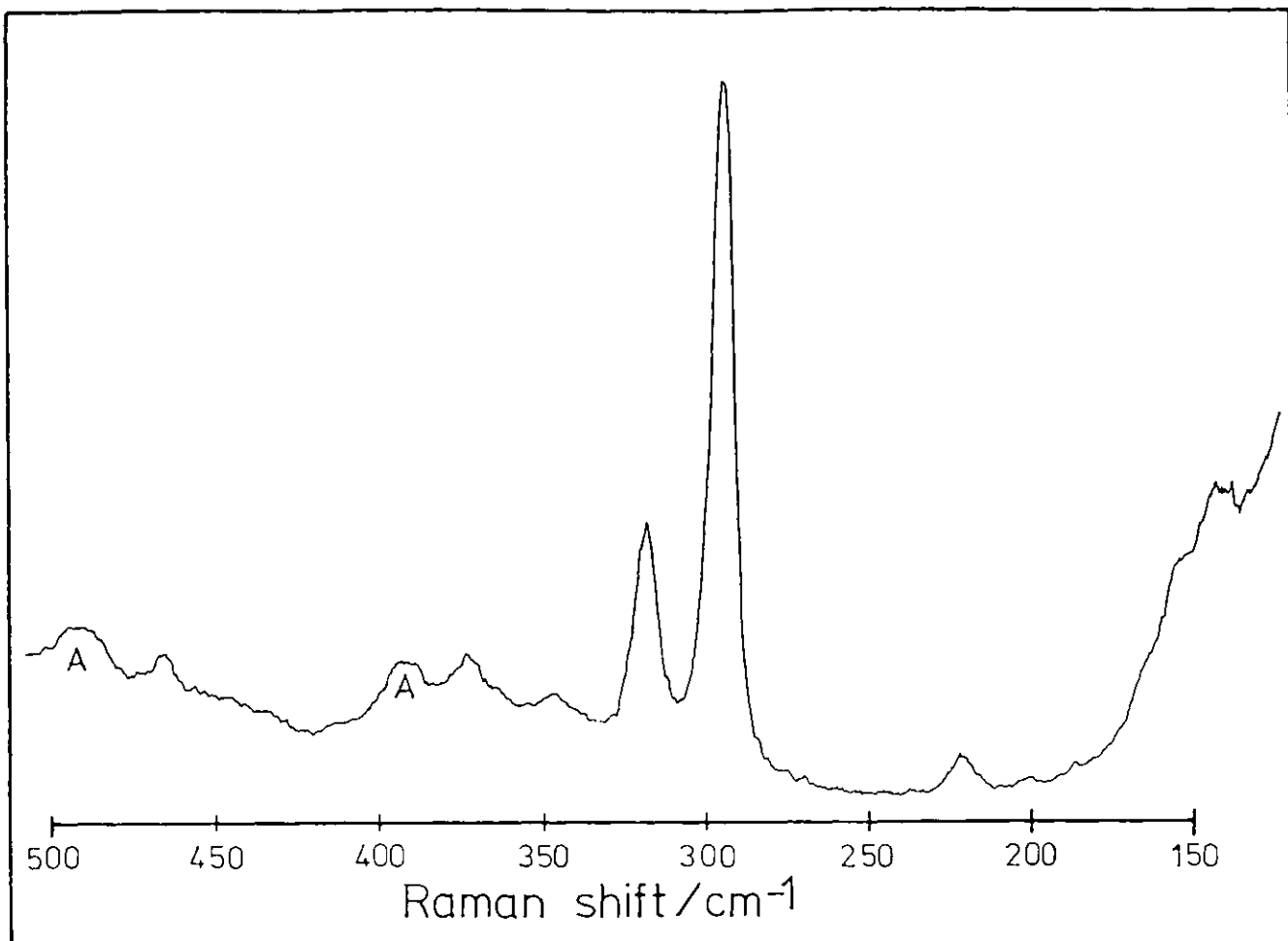


Figure 4.5. Raman spectrum for $[\text{Et}_4\text{N}][\text{Fe}(\text{S}_2\text{-o-xylyl})_2]$ in acetone with 568.2 nm excitation. A = acetone peak.

can then be assigned to the ν_3 mode triply split by degeneration of tetrahedral symmetry to C_{2v} or lower. Bands corresponding to these stretching vibrations also appear in the infrared. For the Fe-S stretching modes observed in the RR spectra of rubredoxins the most intense line also appears at lowest frequency and is similarly assigned as the vibration of highest symmetry.^{167,168,119} With a frequency of 297 cm^{-1} for ν_1 an analysis of the ratio of ν_1/ν_3 for tetrahedral metal chalcogenide anions, MX_4^{n-} , as a function of the ratio of their metal-atom and ligand-atom masses, M_m/M_x , indicates a ν_3 frequency of around 350 cm^{-1} for tetrahedrally sulphur-coordinated iron.¹⁸⁶ This value is in keeping with the range $320, 350, 373 \text{ cm}^{-1}$ observed for the triply split ν_3 mode.

Three of the stretching vibrations appear polarised in the solution spectrum, thus the iron-sulphur site symmetry must be C_s or lower. If then the remaining transition at 373 cm^{-1} is depolarised, as seems probable, the local symmetry would have to be C_s and this band can be assigned as A'' and the 320 and 350 cm^{-1} bands as A' . As in many (and probably in most) cases the totally symmetric vibrations show the largest intensities in RR spectra,¹⁷⁷ depolarised bands are often weak and it is difficult accurately to determine their depolarisation ratios. It is, of course, for precisely such peaks that accurate depolarisation data is required in order to distinguish them from polarised bands. The fact that the 373 cm^{-1} band is only weakly resonance enhanced lends a little further credence to its assignment as the asymmetric (A'') stretch. No further Fe-S stretching vibrations are expected. The weak Raman lines at 450 and 467 cm^{-1} , though just low enough in frequency to be Fe-S stretches, could possibly be bending modes about the methylene carbons, which, as chelate ring vibrations, might be subject to some resonance enhancement. This is based on the assumption that the \widehat{XYZ} angle bending frequency is roughly given by the equation $1/4[\nu(X-Y) + \nu(Y-Z)]$ [see for example, reference 184] with $\nu(\text{Ph-C})$ around 1200 cm^{-1} and $\nu(\text{C-S})$ around 650 cm^{-1} .¹¹⁰ The 595 cm^{-1} Raman line is at the frequency where a resonance enhanced overtone of the ν_1 297 cm^{-1} mode would be expected. The infrared bands at 466 , 487 , 559 and 596 cm^{-1} are also found for $[\text{Fe}_2\text{S}_2(\text{S}_2\text{-o-xylyl})_2]^{2-}$ and $[\text{Fe}_2\text{Se}_2(\text{S}_2\text{-o-xylyl})_2]^{2-}$ (Table 4.6 and section 4.3.3.1.) with a very similar frequency and intensity pattern and are attributed to vibrational modes of the chelate ring atoms; the ligand shows medium strong peaks at 450 , 547 and 594 cm^{-1} . The remaining vibrational bands below 250 cm^{-1} in the Raman spectra are associated with deformations.

4.2.3.2. Fe-S Deformation Vibrations.

For a symmetry of C_{2v} or lower, five Fe-S deformation transitions are expected. Spectral lines in the range 75 to 175 cm^{-1} have been assigned as Fe-S deformations in Rd_{ox} . The polarised band at 222 cm^{-1} seen most strongly when exciting with red light has a rather large Raman shift to be $\delta(\widehat{\text{SFeS}})$ in origin and does not correspond to anything observed in Rd_{ox} . The band might possibly be due to a $\delta(\widehat{\text{FeSC}})$ mode. The three peaks lying in the 150-166 cm^{-1} frequency interval correlate with the ν_4 (T_2) vibration in T_d symmetry which is triply split for symmetries of C_{2v} or lower. This mode has been assigned to a weak shoulder at 150 cm^{-1} in *C. pasteurianum* and to lines at 158 and 175 (weak) cm^{-1} in *P. elsdenii*. The corresponding ν_2 $\delta(\widehat{\text{SFeS}})$ vibration has been claimed to give rise to peaks at 126 and 75 cm^{-1} for these two proteins respectively.^{167,168,119} $[\text{Fe}(\text{S}_2\text{-o-xylyl})_2]^-$ shows Raman bands around 75 and 109 cm^{-1} . The presence of other small peaks and the difficulties inherent in making accurate observations in this region for $[\text{Fe}(\text{S}_2\text{-o-xylyl})_2]^-$, due to the sloping Rayleigh scattered background, the presence of strong plasmalines and of possible lattice modes, are felt to make assignment of a split ν_2 mode unjustifiable with the present quality of data. The Raman spectrum of FeCl_4^- ,^{187,188} indicates that ν_2 lines should be expected to lie around 100 cm^{-1} . Theoretical calculations of Weinstock et al.,¹⁸⁹ together with observations on chalcogenometallates indicate that ν_2 must be more intense than ν_4 in the solution Raman of tetrahedral species. This rule may, however, not apply under resonant conditions.

Table 4.4 summarises the assignment of iron-sulphur vibrational modes for $[\text{Fe}(\text{S}_2\text{-o-xylyl})_2]^-$.

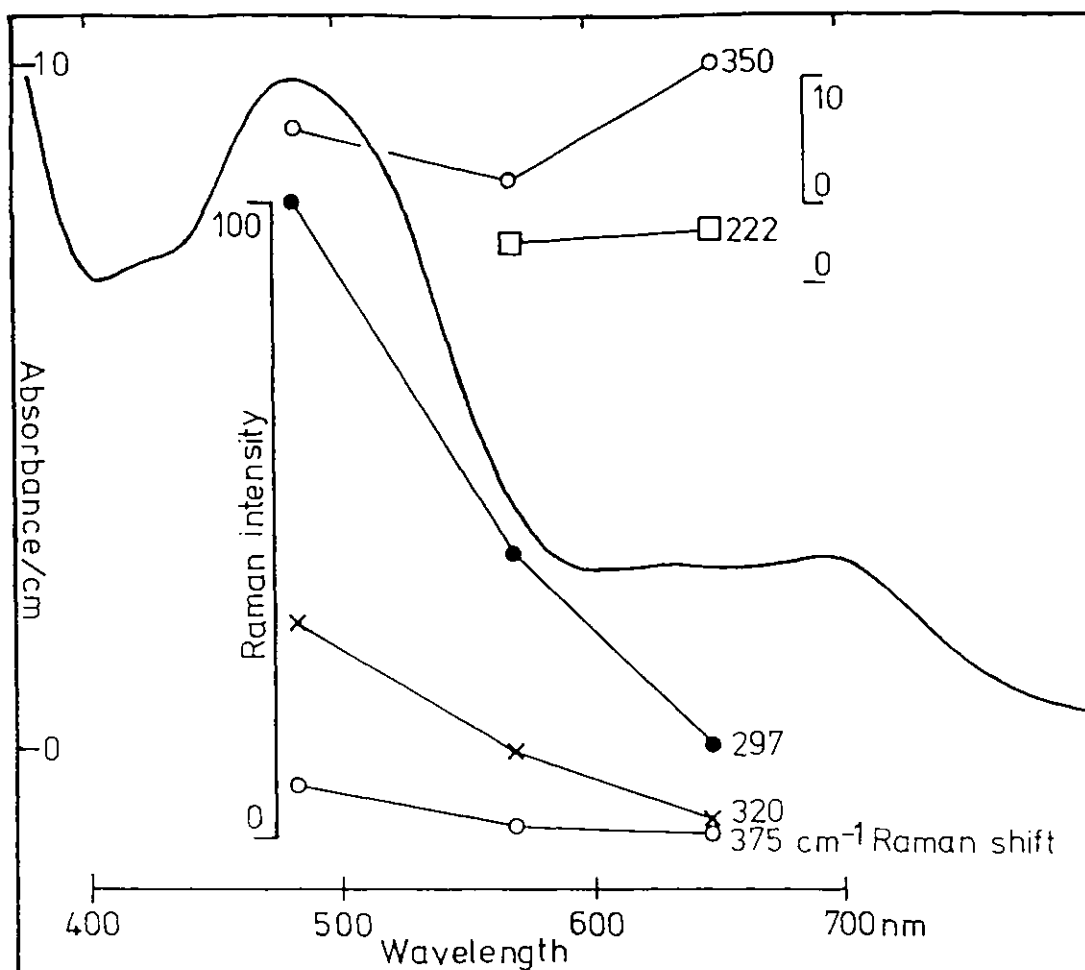


Figure 4.6. Electronic spectrum of $[\text{Fe}(\text{S}_2\text{-o-xylyl})_2]^-$ in acetone and resonance enhancement of several Raman peaks.

TABLE 4.4. RR spectrum of FeS_4 core in $[\text{Fe}(\text{S}_2\text{-o-xylyl})_2]^-$

Frequency/ cm^{-1}	Assignment		
		C_s	T_d
297	str	A'	A_1
320	str	A'	T_2
350	str	A'	
373	str	A''	
150	def	$2\text{A}' + \text{A}''$	T_2
160	def		
166	def		

4.2.3.3. Resonance Enhancement.

Although the variation in excitation frequency in this work is inadequate to obtain excitation profiles for the various resonance enhanced Raman transitions, Figure 4.6 is presented more clearly to demonstrate the intensity changes in comparison with the electronic spectrum for an acetone solution. The bands at 297, 320 and 375 cm^{-1} are clearly coupled to the 484 nm electronic transition. The peak intensities increase by an order of magnitude on going from 647.1 to 482.5 nm irradiation. The Raman peak at 222 cm^{-1} shows post-resonance with the optical absorption to lower energy. All the electronic absorption above at least 400 nm is believed to arise from S \rightarrow Fe charge transfer transitions.¹¹⁷

Taking into account the different concentrations, the 297 cm^{-1} band of $[\text{Fe}(\text{S}_2\text{-o-xylyl})_2]^-$ is around 3000 times more intense than the 787 cm^{-1} symmetric stretch of the acetone solvent, indicating that a strong resonance effect is involved.

4.2.4. Conclusions.

The analysis of the RR spectra for $[\text{Fe}(\text{S}_2\text{-o-xylyl})_2]^-$ in terms of an FeS_4 symmetry which is C_s or lower, fits well with the reported X-ray diffraction structure.⁵⁶ The situation is somewhat complicated by the existence of two independent anions in the unit cell.¹¹⁷ Figure 4.3 shows the stereochemistry of the FeS_4 portion for anion 1, and the Fe-S bond length and angles for both anions are printed alongside. It can be seen that for both anions an approximate symmetry plane exists through S(2) & S(4) and the central Fe, bisecting the $\widehat{\text{S}(1)\text{FeS}(3)}$ angle. The bond lengths Fe-S(1) and Fe-S(3) are nearly equal as are the sets of angles $\widehat{\text{S}(1)\text{FeS}(2)}$, $\widehat{\text{S}(2)\text{FeS}(3)}$ and $\widehat{\text{S}(1)\text{FeS}(4)}$, $\widehat{\text{S}(3)\text{FeS}(4)}$. The

symmetry closely approaches C_S . The RR spectra for $[\text{Fe}(\text{S}_2\text{-o-xylyl})_2]^-$ seem capable of revealing this low symmetry.

If \underline{D} and coordination symmetries are directly related via the crystal field, then the EPR analysis of $[\text{Fe}(\text{S}_2\text{-o-xylyl})_2]^-$ given in Section 3 indicates a higher symmetry than that in Rd_{ox} . In Rd_{ox} from C. pasteurianum the 1.2Å resolution analysis of the X-ray diffraction results show that the FeS_4 centre departs considerably from either C_2 or C_S .¹⁸² The vibrational results obtained in this section would suggest that the RR scattering from this protein should show characteristics of a nine-line spectrum, given adequate resolution and signal to noise ratio, and no adventitious band overlap. The spectra obtained by Long et al.^{167,168} may be of insufficient quality to show that the weak ν_3 mode is triply split and that the resulting bands are polarised (a redefinition of the baseline in the published spectra¹⁶⁷ might lead to a depolarisation ratio indicating polarisation of the Raman intensity at round 370 cm^{-1}). The results of Yamamoto et al.¹⁶⁹ come closer to agreement with a low symmetry.

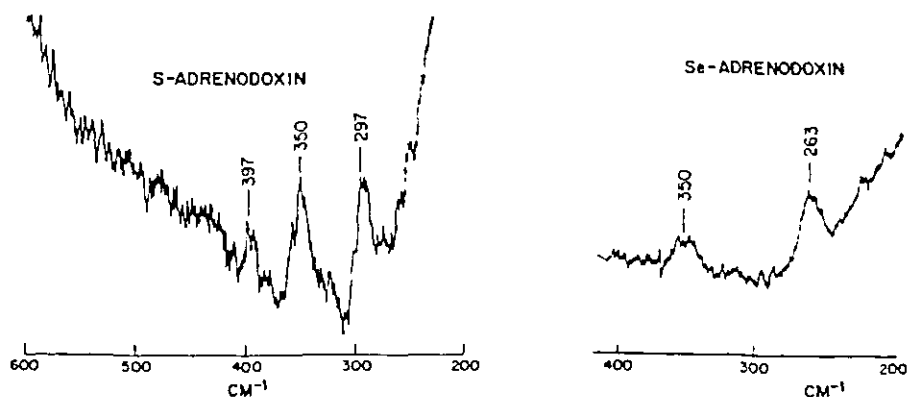
4.3. Binuclear Iron-Sulphur Complexes; Analogues of 2Fe2S Ferredoxins.

4.3.1. RR in 2Fe Ferredoxins.

Critical assessment of the physicochemical data for 2Fe ferredoxins has led to the generally accepted conclusion that the active site has the minimal composition $[\text{Fe}_2\text{S}_2(\text{SCys})_4]$ and a structure containing two antiferromagnetically coupled tetrahedrally coordinated iron atoms bridged by two sulphides.

The optical absorption spectra of oxidised proteins are adequately summarised by the following λ_{max} (nm) and ϵ (mM) data 325-333 (12-15); 410-425 (9-10); 455-470 (85-95) [see for example references 190, 191, 49, 171] and resonance enhancement of Raman spectra is expected for visible excitation wavelengths. Two RR studies of adrenodoxin have been reported.^{114,170} The technique has also been applied to the ferredoxin from spinach.¹¹⁵ The results of these studies have been summarised in Table 4.1, together with observations made on adrenodoxin absorption in the far infrared. Iron-sulphur vibrations are found in the 250 to 400 cm^{-1} region. In the Raman only polarised bands due to totally symmetric modes are sufficiently resonance enhanced to be observed above the noisy and

Figure 4.7. Raman spectra for S and Se bridged adrenodoxin with 488 nm excitation.¹⁷⁰



sloping background. The spectra of adrenodoxin and its selenium substituted derivative obtained by Tang, et al.¹⁷⁰ are reproduced in Figure 4.7. The assignment of the 397 and 297 cm^{-1} bands as due to vibrations involving the labile sulphur atoms has been made on the basis of their shift to 355 and 263 cm^{-1} when selenium is substituted as the bridging ligand. Peaks observed at 350 cm^{-1} in both sulphur and selenium adrenodoxin must then correspond to the symmetric stretch of the four terminal cysteine sulphurs.

Iron-sulphur vibrations at around the same three frequencies occur in the RR spectra of adrenal and spinach ferredoxins obtained by Blum and coworkers. Their observations for these two proteins have been made out to 3000 cm^{-1} and weak peaks distributed over this range assigned as arising from transitions within the ladder of spin-states resulting from the antiferromagnetic exchange-coupled irons. Raman scattering by so-called spin-waves in antiferromagnets such as FeF_2 is well documented and the possible mechanisms for spin-phonon interaction have been described.^{166,192} Single and multi-flip transitions from both the ground and first excited states are invoked in the interpretation of ferredoxin spectra given by Blum, et al.^{114,115} Analysis of the data in this way yields J values of $-172 \pm 16 \text{ cm}^{-1}$ and -74 cm^{-1} for oxidised and reduced spinach ferredoxin and -497 cm^{-1} for adrenodoxin. The Raman process involved has been described as resonant from an examination of the excitation wavelength dependence of the 995 cm^{-1} band intensity in adrenodoxin; this band having been assigned to a $\Delta S = 1$ transition from the ground-state.

4.3.2. RR and IR Spectra of $[\text{Fe}_2\text{S}_2(\text{SR})_4]^{2-}$.

$[\text{Fe}_2\text{S}_2(\text{S}_2\text{-o-xylyl})_2]^{2-}$ and its ligand substitution derivatives, $[\text{Fe}_2\text{S}_2(\text{SR})_4]^{2-}$ (R = Ph, pMeC₆H₄, pClC₆H₄) have been well characterised and demonstrated to be excellent model compounds for the active sites of 2Fe ferredoxins.^{27,28,38} Halide substitution products, $[\text{Fe}_2\text{S}_2\text{X}_4]^{2-}$ (X = Cl, Br, I), have also been synthesised and well characterised.^{193,194} In order to obtain a better understanding of the vibrational spectra for these iron-sulphur dimers, selenium derivatives have been prepared in this work. The ligand PhS⁻ has also been replaced by its selenium homologue, PhSe⁻, to give the crystalline salts $[\text{Et}_4\text{N}]_2[\text{Fe}_2\text{S}_2(\text{SePh})_4]$ and $[\text{Et}_4\text{N}]_2[\text{Fe}_2\text{Se}_2(\text{SePh})_4]$. RR spectra of sulphur and selenium-substituted ferredoxin analogues have been obtained in solid and, where possible, solution state; Tables 4.6-11 and Figures 4.10-14.

The starting point for analysis of these spectra is a description of the 18 fundamental modes of vibration expected for a bridged dimeric molecule, M_2X_6 , of point group D_{2h} . Figure 4.8 illustrates approximately the character of these normal modes as described by Bell and Longuet-Higgins¹⁹⁵ and used in their interpretation of vibrational spectra for diborane. It must be recognised that this description is of limited value where the masses M and X are comparable, as considerable coupling of the vibrations is then to be expected with all atoms of the vibrational unit participating significantly in each normal mode. According to the selection rules, centrosymmetric modes (those of g-character) are Raman active, 8 of the u-character vibrations are IR active and the remaining A_{1u} fundamental is inactive in D_{2h} symmetry. Since in the Fe_2S_6 centre all the bands corresponding to iron-sulphur vibrations are to be accommodated in a frequency interval of only some 400 cm^{-1} , strict adherence to the

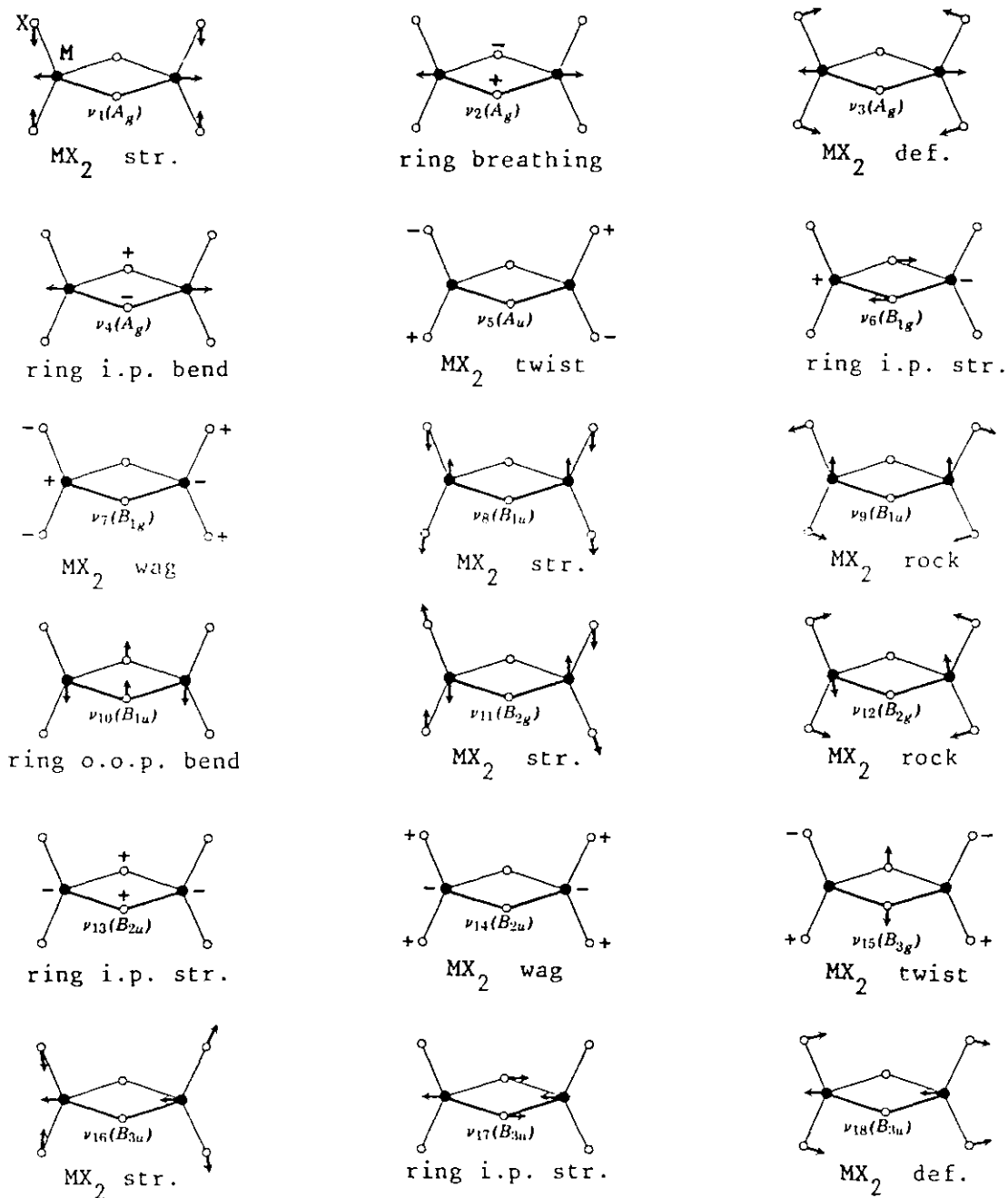


Fig. 4.8. Approximate descriptions of the normal modes of vibration for the bridged dimer M_2X_6

mutual exclusion principle is hardly to be expected in the observed spectra. Indeed, accidental coincidences or near-coincidences may be expected for vibrational modes of a similar type.

Ga_2Cl_6 , Ga_2Br_6 ,¹⁹⁶⁻¹⁹⁹ Al_2Cl_6 , Al_2Br_6 ,^{197,200,201} and more recently, Fe_2Cl_6 ²⁰²⁻²⁰⁴ have been well studied by Raman, IR and normal coordinate analyses²⁰⁵ and consequently represent useful models for the interpretation of the chalcogenide-ligated bridged diferric complexes. The following generalised rules have been used in, or deduced from, the assignment of bands in the dimeric metal halide vibrational spectra. The vibrations are divided into frequency groups:

- (a) Terminal MX_2 stretches [$\nu_1(\text{R})$, ν_8 , $\nu_{11}(\text{R})$, ν_{16}] at highest frequency with $\nu_1 \approx \nu_{16}$, $\nu_8 \approx \nu_{11}$, $\nu_{11} > \nu_1$ and $\nu_8 > \nu_{16}$. ν_1 more intense than ν_{11} in Raman.
- (b) Ring stretching [$\nu_2(\text{R})$, $\nu_6(\text{R})$, ν_{13} , ν_{17}] at somewhat lower frequency since M-X bridge linkages are usually weaker than M-X terminal links. ν_2 should be intense, whilst the antisymmetric ring-stretch ν_6 is weak or not observed.
- (c) M-M vibrations [$\nu_4(\text{R})$] in which the M-X bridge bonds are only slightly stretched but considerable change occurs in the M-M separation. Where an M-M linkage is possible the frequency and intensity of this band arising from the ν_4 mode will depend to a large degree on the strength of the interaction.
- (d) Angular motion of terminal MX_2 groups [$\nu_3(\text{R})$, ν_5 , $\nu_7(\text{R})$, ν_9 , $\nu_{12}(\text{R})$, ν_{14} , $\nu_{15}(\text{R})$, ν_{18}]. ν_3 and ν_{18} both involve changes in the $\widehat{\text{X}}_t\text{MX}_t$ angle and are expected at comparable frequencies high in this group. ν_3 should be the most intense Raman line in the region. The twisting frequency ν_5 is inactive in strict D_{2h} symmetry, and ν_{15} is likely to appear very weakly if at all.

(e) Ring out-of-plane bend (ν_{10}). This IR mode is expected to lie at very low frequency and has been assigned to a band at 24 cm^{-1} in Fe_2Cl_6 .²⁰⁴ Normal coordinate analysis predicts values of 28 and 17 cm^{-1} for Ga_2Cl_6 ¹⁹⁶ and Ga_2Br_2 ¹⁹⁹ respectively. The present observations extend down only to 250 cm^{-1} in the IR.

For Fe_2Cl_6 and Ga_2Cl_6 the first two frequency regions are around $500\text{--}400 \text{ cm}^{-1}$ and $350\text{--}250 \text{ cm}^{-1}$ (ν_6 may appear lower) respectively, the remaining deformation modes lying below 250 cm^{-1} . Adams and Churchill's extensive normal coordinate analysis for bridged M_2X_6 species indicates that whilst it is often accurate to describe stretching vibrations as terminal, there are fewer instances in which any one mode can be said to be mainly bridge-bond stretching.²⁰⁵ The use of a bridge-stretch description is, however, considered a reasonable approximation when the M:X mass ratio approaches or exceeds about 2:1. For the Fe_2S_6 core the description of the 18 modes given in Figure 4.8 is expected to be a reasonably good one, as judged by the internal coordinate potential energy distributions available for Ga_2Cl_6 and Al_2Cl_6 ,^{205,200} which have M:X ratios above and below that for Fe:S. The corresponding Al and Ga bromides show, however, extensive spreading of potential energy among internal coordinate types, and vibrational modes involving iron and selenium, having again an intermediate M:X ratio, can not be expected to achieve a good fit to the simple description used here.

X-ray crystallographic structure determinations have been described for three of the sulphur bridged iron dimers synthesised by Holm's group; $[\text{Fe}_2\text{S}_2(\text{S}_2\text{-o-xyllyl})_2]^{2-}$,²⁷ $[\text{Fe}_2\text{S}_2(\text{STol})_4]^{2-}$,²⁸ and $[\text{Fe}_2\text{S}_2\text{Cl}_4]^{2-}$,¹⁹³ Figure 4.9. Each dimer is centrosymmetric and has a symmetry degraded from D_{2h} to C_{2h} . The reason for the symmetry lowering

is different in each case. $[\text{Fe}_2\text{S}_2(\text{S}_2\text{-o-xylyl})_2]^{2-}$ has asymmetric bridge bond lengths (more rigorously terminal Fe-S distances are also slightly unequal lowering the symmetry from effective C_{2h} to C_i); in $[\text{Fe}_2\text{S}_2(\text{STol})_4]^{2-}$ there is a dihedral angle of 97° between Fe-S₂ (terminal) and Fe-S₂ (bridge) planes; $[\text{Fe}_2\text{S}_2\text{Cl}_4]^{2-}$ has asymmetric Fe-Cl bond lengths. Table 4.5. shows exaggerated skeletal diagrams of the distortions from D_{2h} . The C_2 axes of the resulting three C_{2h} symmetries are mutually perpendicular and lead to different vibrational symmetry distributions as listed in the Table. For a C_i site all Raman active modes are totally symmetric. No other non-centrosymmetric site-groups will be considered, as both the molecular point-group and the space-group have a C_i sub-group, in each of the three structures.

Since the bridge bonds are seen to be shorter than the terminal ligand bonds for each molecule depicted in Figure 4.9 any distinction of frequency regions for the respective vibrations of these bonds, as outlined above, might be expected to be lost or reversed.

Fe-Fe distances of 2.698\AA ($\text{S}_2\text{-o-xylyl}$), 2.691\AA (S-Tol) and 2.716\AA (Cl) are indicative of a stabilising metal-metal interaction and the ν_4 vibration is expected to increase in frequency as the mode takes on more stretching character with increasing bond strength.

4.3.3. Assignment of vibrational spectra.

Vibrational assignments are collected and summarised in Tables 4.12-16 at the end of each section.

4.3.3.1. $[\text{Fe}_2\text{X}_2(\text{S}_2\text{-o-xylyl})_2]^{2-}$ (X = S, Se).

Consistent with the vibrational data for $[\text{Fe}(\text{S}_2\text{-o-xylyl})_2]^-$ presented in Section 4.2.3, terminal ligand stretching modes are expected in the region $300\text{-}370\text{ cm}^{-1}$. If the polarised band at 327 cm^{-1} in the solution

TABLE 4.6. RR and IR Data for $[\text{Et}_4\text{N}]_2[\text{Fe}_2\text{X}_2(\text{S}_2\text{-o-xylyl})_2]$ (X = S, Se).

	X = S					X = Se				
	Band maxima (cm^{-1})	INTENSITY/EXCITATION				Band maxima (cm^{-1})	INTENSITY/EXCITATION			
		482.5	530.9	568.2	647.1		482.5	530.9	568.2	647.1
SOLID -RR	139	-	15	15	25	155	6sh	30	40	50
	165	15	25	15	10	165	12	35	20sh	30
	196	25	35	60	40	183		4	3	w
	224	3	4	-	-	228	25	30	20	10
	304	w, sh	4	50	10	261	20	25	15	100
	314sh	w	w	w	w	311	3	6	3	
	321	50	25	40	70	319	6			8
	348	3	w	w	2	339	9	8	6	13
	388	10	20	45	100	349	9	4	3	w, sh
						426		6	3	20
	OTHER BANDS					OTHER BANDS				
	28, 35, 44, 52, 60, 67, 75, 83, 91, 100, 108, 116, 126 (all w-m,n), 145 (w,sh), 278(w), 470(w,br), 548(w), 676(w,br), 865(w), 1230(vw), 1490(w,br)					44, 60, 67, 75, 91, 100, 108, 117, 124, 140 (all w-m,n), 520(w), 670 (vw), 865(vw).				
SOLUTION RR	160(w,sh), 198(mw,pol), 304(s at 568.2 nm, ρ 0.3), 327 (s at 482.5 nm, ρ 0.35)					150(w,sh), 160(w,sh), 226(mw,pol.), 258(vs at 647.1 nm, ρ 0.3), 299 (w,pol), 320(w), 427(w)				
IR-SELECTED BANDS	265 (vw), 274(m), 300(vw), 325(vs), 336(vs), 396(vw,sh), 410(w,sh), 415 (vs), 464(mw), 488(w), 500(w,br), 562(w), 600(m), 675(s), 752(m), 765(s), 772(m), 779(s), 861(m), 1002(s), 1058(m), 1071(m), 1172(vs), 1187(m), 1210(ms), 1222(ms), 1262(m), 1300(m), 1385(s,d1).					278(vw), 290(vw,sh), 302(mw), 320(s), 345(vw,sh), 400(w), 464(w), 488(w), 525(w,br), 562(w), 600(m), 675(s), 765(s), 772(s), 779(s), 861(m), 1002(s), 1057(m), 1071(m), 1173(s), 1187(m), 1210(m), 1222(m), 1263(w), 1301(m), 1390(s,d1).				

TABLE 4.7. RR and IR data for $[\text{Et}_4\text{N}]_2[\text{Fe}_2\text{X}_2(\text{SPh})_4]$ (X = S, Se).

	X = S					X = Se				
	Band maxima (cm^{-1})	INTENSITY/EXCITATION				Band maxima (cm^{-1})	INTENSITY/EXCITATION			
		482.5	530.9	568.2	647.1		482.5	530.9	568.2	647.1
SOLID - RR	160	3	4	3	2	140	-	-	2	3
	201	w	1	1		203	10	10	8	10
	244sh	w	w	w		235	2	3	2	-
	256	10	8	9	10	255	1	1	1	1
	320	1	w	1	3	284	1	2	2	3
	351	8	3	3		314	w	w	1	2
	387	4	2	3	8	364	3	2	1	1
	406	1	1	w		410	1	w,sh	w,sh	w,sh
	428	10	10	10	8	428	7	10	10	10
	478	1	-	1		475	w	-	1	
	510	1	w	1						
	<u>OTHER</u> 50,60,68,77,84,92,107,116,124 (all m-w, n), 985(w), 1024(w), 1082(m), 1126(w), 1473(w), 1574(m)					<u>BANDS</u> 51,60,67,75,83,92,100,108,116, 124 (all m-w,n), 996(mw), 1025(w), 1082(m), 1475(w), 1576(mw).				
SOLUTION -RR	240(w,sh), 253(m, ρ 0.3), 316(w), 354 (w, pol.), 430(vs, ρ 0.3)					190(w,sh), 206(w,sh), 250(w), 282(mw,pol.), 314(w), 429(vs, ρ 0.3)				
IR SELECTED BANDS	279(w), 305(vw,sh), 318(s), 360(vs,d1), 410(w), 424(s), 431(m), 481(s), 698(s) 745(m), 794(s), 900(w,d1), 1027(s), 1035(m) 1070(m), 1081(s), 1127(mw), 1182(s), 1303 (m), 1395(w), 1565(s,br)					<u>260(m), 313(ms), 359(s), 366(m,sh)</u> 400(w,br), 428(m), 477(ms), 690(s,d1), 738(m), 787(ms), 795(m,sh), 888(w), 1023(s), 1067(mw,sh), 1081(s), 1122(w), 1182(s), 1304(m), 1397(m), 1574(s)				

TABLE 4.8. RR and IR data for $[\text{Et}_4\text{N}]_2[\text{Fe}_2\text{X}_2(\text{SePh})_4]$ (X = S, Se).

	X = S					X = Se				
	Band maxima (cm^{-1})	INTENSITY/EXCITATION				Band maxima (cm^{-1})	INTENSITY/EXCITATION			
		482.5	530.9	568.2	647.1		482.5	530.9	568.2	647.1
SOLID - RR	123	8	6	10	2	187	10	10	10	10
	180br	1	1	1	w	217	3	6	-	8
	214	4	8	-	6	278br	w	1	1	
	242	10	9	5	5	298sh	1	1	w	1
	273	10	8	-	5	309	3	6	10	9
	306	8	10	10	10					
	384	6	2	1	2					
		<u>OTHER</u>					<u>BANDS</u>			
	74, 82, 91, 98, 108 (all m-w, n), 150(w, sh) 320(w, sh), 368(w, sh, br), 502(w, br)					40, 66, 75, 82, 91, 99, 108, 116, 124 (all m-w, n), 258(w, br), 380(w, br), 400(w, br)				
SOLUTION - RR	175(w, sh), 215-220(w, sh), 243(w, pol.), ν 270(w), ν 290(w), 310(vs, ρ 0.3)					188(w), 217(m, pol.), 242(w), 270(w), 300(w, sh), 309(vs, ρ 0.35)				
IR SELECTED BANDS	273(m), 307(w), 328(s), 408(vw), 416(s), 465(s), 665(s), 691(s), 740(obsc.), 776(m), 788(m), 1000(m, dl), 1020(s), 1066(s), 1171(s), 1182(s), 1300(ms), 1390(m), 1572(s)					274(s), 288(vw), 306(mw), 320(m) 333(w), 400(mw, br), 466(s), 665(s), 691(s), 740(obsc.), 776(mw), 789(m), 1002(m), 1020(s), 1066(s), 1172(s), 1180(s), 1300(m), 1392(m), 1572(s)				

TABLE 4.9. RR and IR Data for $[\text{Et}_4\text{N}]_2[\text{Fe}_2\text{X}_2(\text{STol})_4]$ ($\text{X} = \text{S}, \text{Se}$).

	X = S					X = Se				
	Band maxima (cm^{-1})	INTENSITY/EXCITATION				Band maxima (cm^{-1})	INTENSITY/EXCITATION			
		482.5	530.9	568.2	647.1		482.5	530.9	568.2	647.1
SOLID - RR	148	4	6	4	1	192	10	10	8	10
	215	w	2	1		218	2	3	-	1
	241	6	8	10	10	251	w	1	1	1
	320	10	10	7	3	272	2	1	-	4
	375	8	8	7	9	325	2	2	1	2
	386	w	3	6	8	387sh	w	3	5	5
	403	7	9	9	4	398	8	8	10	7
	490	w	1	1	1	630	2	2	3	3
	630	3	4	4						
		<u>OTHER</u>					<u>BANDS</u>			
	83, 92, 100, 109, 117, 125, 134 (all m-w, n), 169(w), 640(w, sh), 1085(s), 1486(m), 1595(m)					68, 76, 83, 100, 108, 117, 124, 133, 139 167 (all m-w, n), 294(w), 490(w), 590(w), 1085(s), 1487(m), 1595(m).				
SOLUTION - RR	\sim 210(w, sh), 238(mw, pol.) 305(w, pol.), 325(mw, $\rho \sim 0.3$), 378(w, sh), 384(sh)									
IR SELECTED BANDS	272(vw, br), 300(vw, br), 325(m, sh), 332(s), 374(w, sh), 382(mw), 396(s), 415(ms), 490(s) 626(ms), 783(m, br), 804(vs), 998(m), 1017(m) 1084(vs), 1172(m), 1181(m), 1300(mw, dl), 1390(m), 1590(m, br)					280(vw), 304(ms), 318(ms), 332(m), 384(vw, sh), 398(ms, dl), 490(s), 628(s), 782(m, br), 804(vs), 998(ms), 1016(m), 1084(vs), 1173(ms), 1182(mw), 1300(mw, dl), 1392(m), 1595(m)				

TABLE 4.10. RR and IR Data for $[\text{Et}_4\text{N}]_2[\text{Fe}_2\text{S}_2(\text{SC}_6\text{H}_4\text{Cl})_4]$.

SOLID-RR. Band maxima/ cm^{-1} (intensity at 482.5nm excitation): 137(2), 201(2), 221(3), 294(9), 320(2), 342(10), 368(8), 381(4), 401(4).

Other bands: 67, 75, 107, 116(all m-w,n), 273(w), 542(m), 597(w), 640(w), 1065(mw), 1090(mw), 1472(w), 1567(w).

SOLUTION-RR: 220(w,sh), 286(m, ρ 0.3), 320(w), 342(vs, ρ 0.36), 370(w,sh).

IR - SELECTED BANDS: 274(w), 293(ms), 323(ms), 345(mw), 384(s), 409(w,sh), 418(ms), 450(vw,br), 490(s), 526(w), 543(s), 782(m), 816(s), 821(s), 997(m), 1007(s), 1088(s), 1174(m), 1390(m,d1), 1565(m).

TABLE 4.11. RR and IR Data for $[\text{Et}_4\text{N}]_2[\text{Fe}_2\text{X}_2\text{Cl}_4]$ (X = S, Se) and

$[\text{Et}_4\text{N}]_2[\text{Fe}_2\text{S}_2\text{Br}_4]$.

$[\text{Fe}_2\text{S}_2\text{Cl}_4]^{2-}$

SOLID-RR. Band maxima/ cm^{-1} (intensity at 482.5nm excitation): 144(4), 178(4), 221(w), 310(2), 333(5), 358(w), 397(10), 450(w,br).

Other bands: 43, 48, 60, 67, 76, 84, 99, 108, 116, 125, 132 (all m-w,n), 507(w), 576(mw), 630(w,br), 703(w), 730(w), 796(w).

IR - SELECTED BANDS: 286(ms), 326(w,sh), 334(s), 345(vs), 416(s), 800(ms), 1008(m), 1032(m), 1182(s), 1305(m), 1368(m), 1405(m).

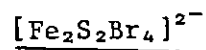
$[\text{Fe}_2\text{Se}_2\text{Cl}_4]^{2-}$

SOLID-RR. Band maxima/ cm^{-1} (intensity at 482.5nm excitation): 150 (1), 246(10), 274(1), 340(sh,w), 348(1), 397(1), 406(1), 435(1), 493(2).

Other bands: 45, 59, 68, 76, 83, 92, 100, 108, 116, 124 (all m-w,n), 538(w,br), 576(w,br), 600(w,br), 635(w), 683(w), 738(w).

IR - SELECTED BANDS: 285-295(w, may be impurity), 329(s), 342(s), 405(w), 416(w), 798(ms), 1005(m), 1030(m), 1182(s), 1305(m), 1368(m), 1402(m)

TABLE 4.11 continued.



SOLID-RR: Band maxima/cm⁻¹ (intensity at 482.5nm excitation) 124(3), 260(1), 274(2), 315(1), 393(10), 410(w,sh).

Other bands: 44,60,74,102,108 (all m-w,n), 134 (568.2nm excitation), 530(m,br,d1), 665(m), 788(m).

IR: 263(ms), 327(ms), 340(w,sh), 418(ms), 510(w,vbr).

Similar RR spectra are seen at other longer wavelength excitations.

Fig. 4.10 Solid-state Raman spectra of $[\text{Et}_4\text{N}]_2[\text{Fe}_2\text{X}_2(\text{S}_2\text{-o-xyl})_2]$ ($\text{X}=\text{S},\text{Se}$) at 530.9nm excitation

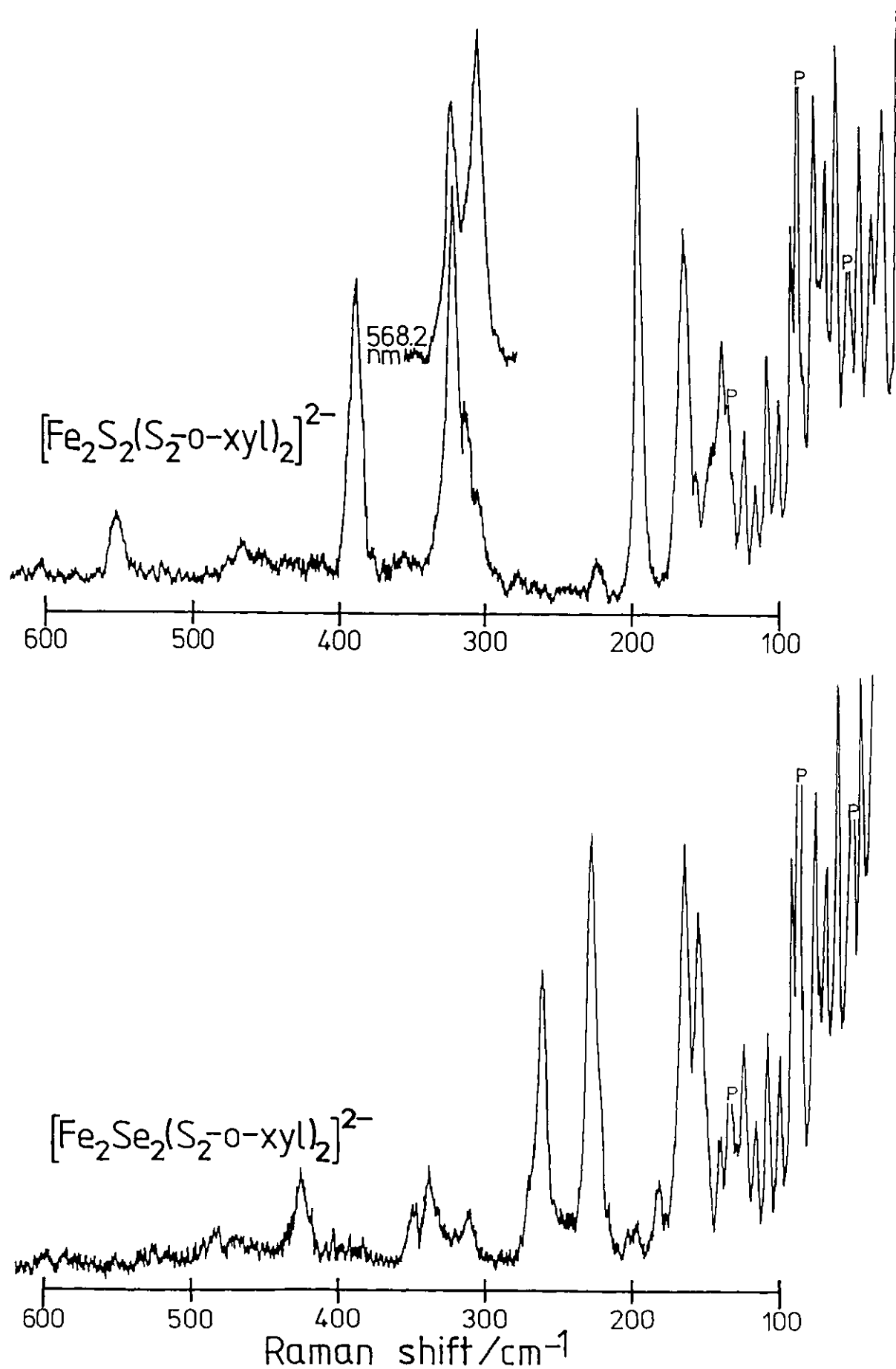


Fig. 4.11 Solid-state infra-red absorption spectra for several dimer complexes

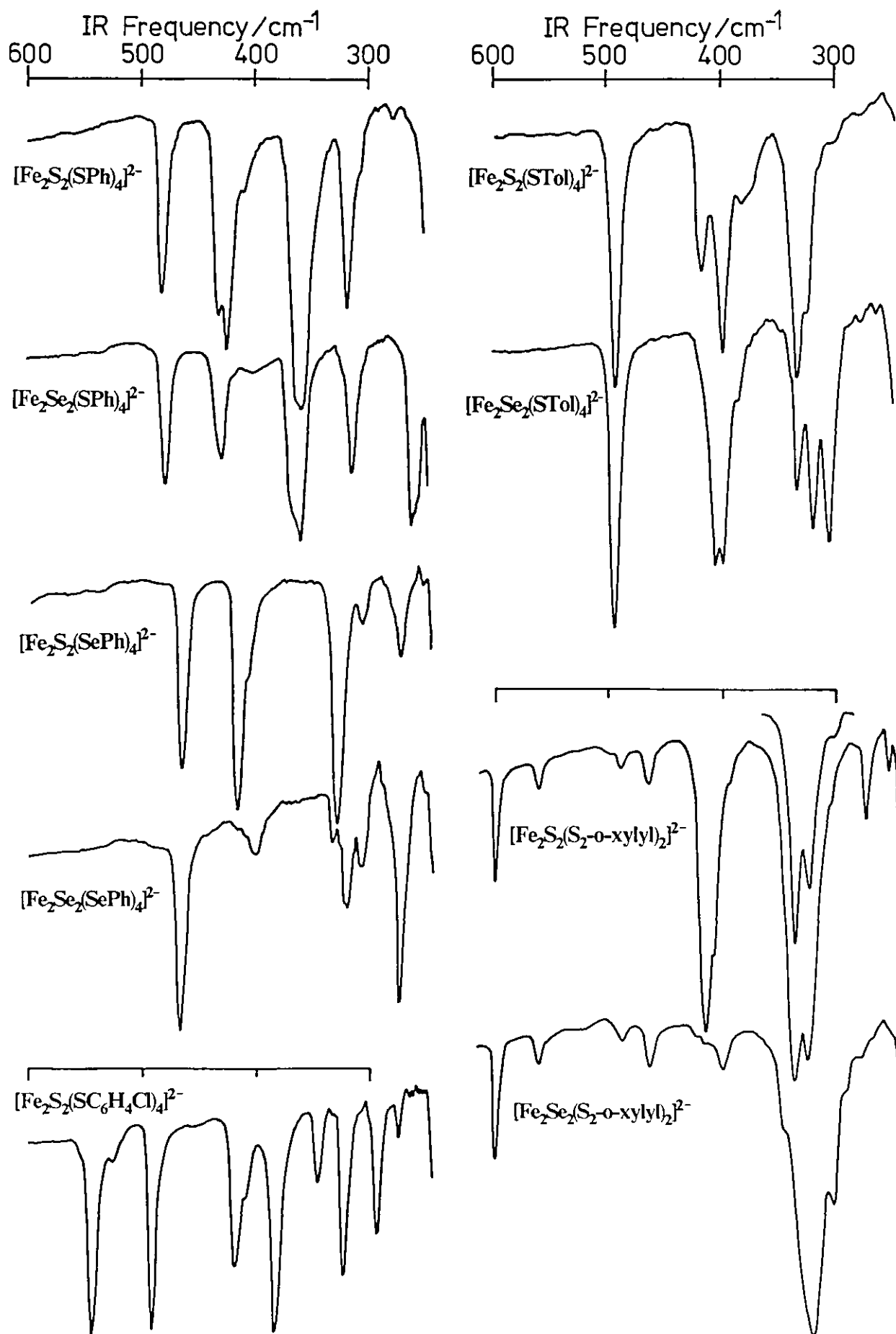


Fig. 4.12 Solid-state Raman spectra of $[\text{Et}_4\text{N}]_2[\text{Fe}_2\text{X}_2(\text{SPh})_4]$ ($\text{X}=\text{S},\text{Se}$) at 482.5nm excitation

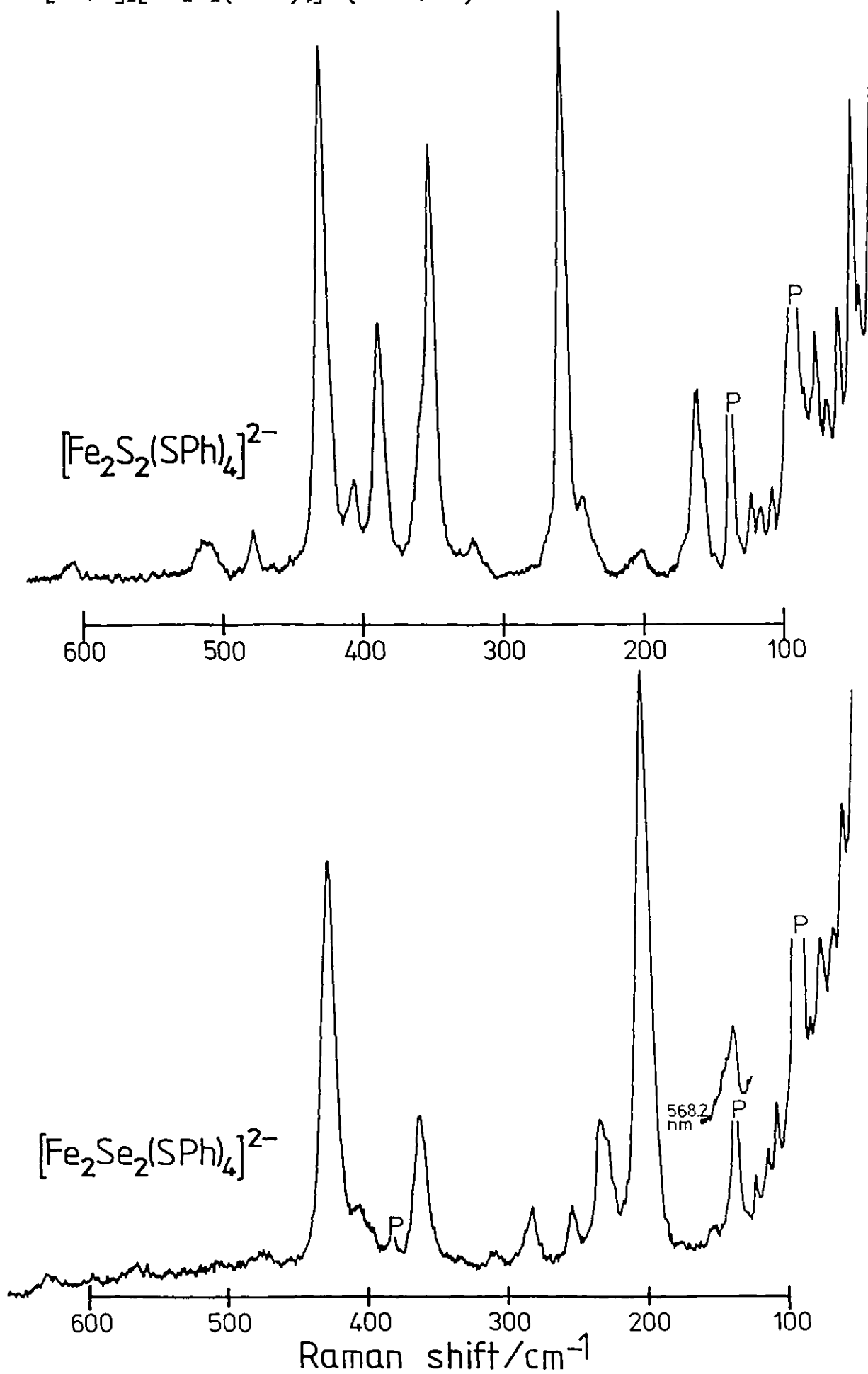


Fig. 4.13
Solid-state Raman spectra of $[\text{Et}_4\text{N}]_2[\text{Fe}_2\text{X}_2(\text{SePh})_4]$
at 482.5nm (X=S) and 530.9nm (X=Se) excitation

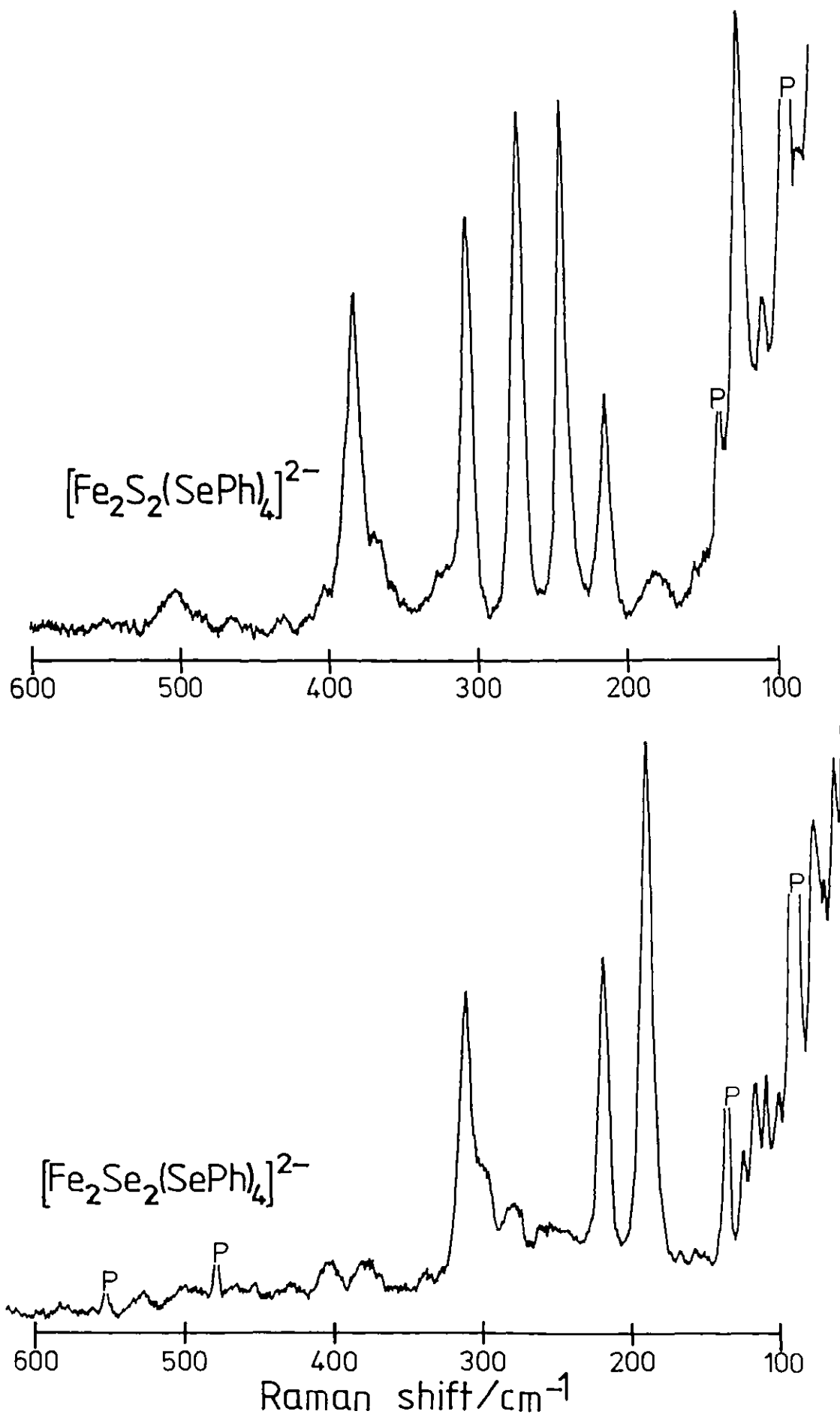
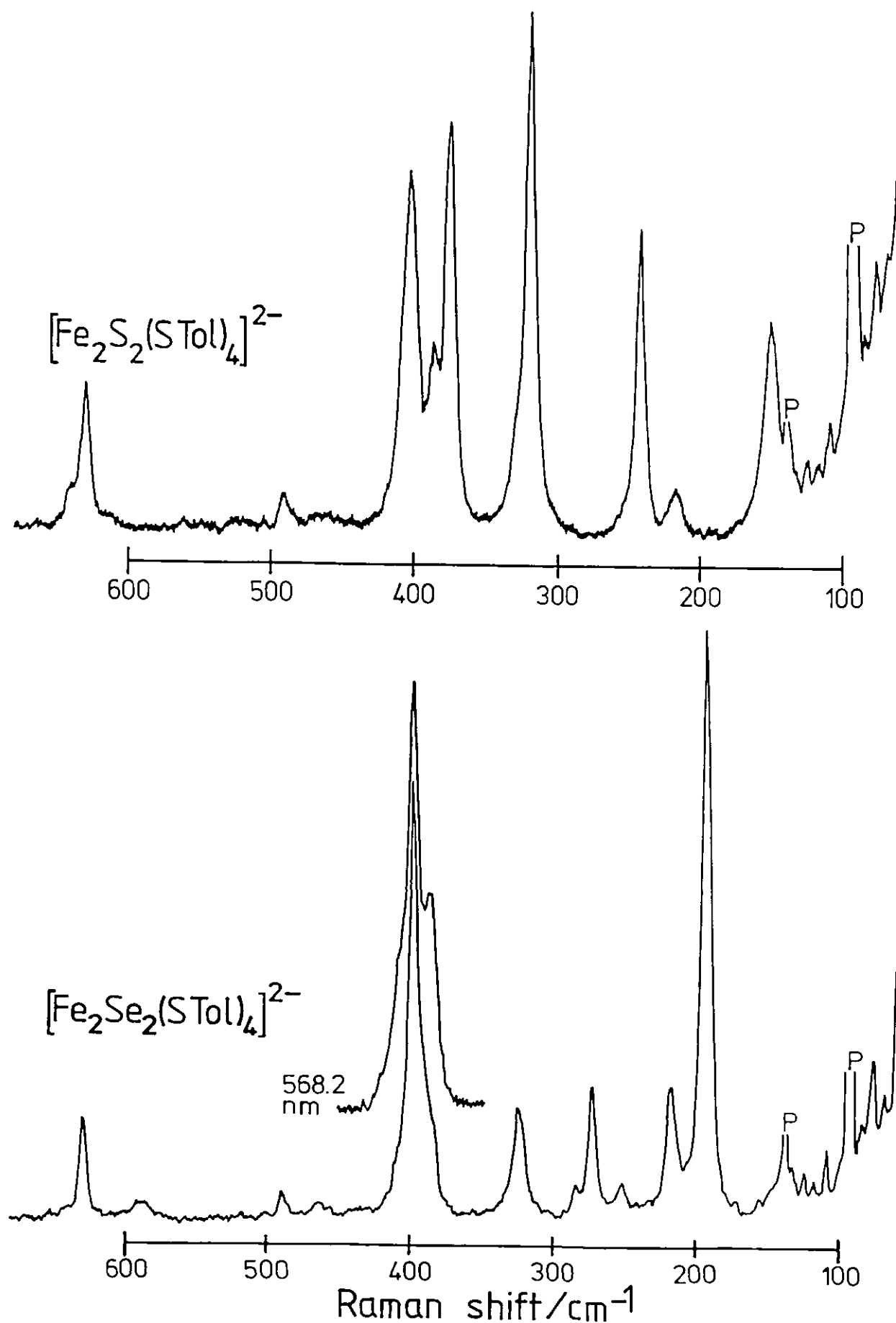


Fig. 4.14 Solid-state Raman spectra of $[\text{Et}_4\text{N}]_2[\text{Fe}_2\text{X}_2(\text{STol})_4]$ ($\text{X}=\text{S},\text{Se}$) at 482.5nm excitation



Raman spectrum of $[\text{Fe}_2\text{S}_2(\text{S}_2\text{-o-xylyl})_2]^{2-}$ corresponds to that at 321 cm^{-1} in the solid, then this latter peak, and similarly that at 304 cm^{-1} , must be due to a totally symmetric vibration. On the grounds that ν_1 and ν_{11} are the only bands reasonably expected in this region, the symmetry would have to be considered degraded to C_i even in solution. Because of the peculiar resonance effect, with the 304 cm^{-1} peak only having appreciable magnitude at 568.2 nm excitation, the relative intensities cannot be used to distinguish which fundamental should correspond to which band. As both modes are terminal it is unusual that they should show different resonance effects, and an alternative interpretation is that the 304 cm^{-1} Raman shift arises from a positive combination of 139 and 165 cm^{-1} . Intensities at these two frequencies are maximal for excitation at wavelengths relating to different parts of the solid reflectance spectrum (red and green respectively, see Figure 4.17 and Section 4.34). The excitation profiles of the 139 and 165 cm^{-1} bands intersect (Figure 4.17) close to the 568 nm krypton emission, and it is this exciting line which leads to the large resonance enhancement of the 304 cm^{-1} band. Following this line of argument, and taking ν_1 as the intense 321 cm^{-1} band it becomes necessary to assign ν_{11} to one of the weak peaks at 314 and 348 cm^{-1} or to assume coincidence with ν_1 .

Generally, $\nu_{11} > \nu_1$ & $\nu_8 > \nu_{16}$ and the strong absorptions at 325 and 336 cm^{-1} in the IR are given the designations ν_{16} and ν_8 respectively. These frequency orderings may possibly be reversed as $\nu(\text{Fe-S}_b) > \nu(\text{Fe-S}_t)$ and ν_1/ν_{16} mix in some $\nu(\text{Fe-S}_b)$ at low M:X mass ratio, whereas ν_{11}/ν_8 stay essentially pure $\nu(\text{Fe-S}_t)$.

Given no drastic structural changes on selenium substitution, ν_1 and ν_{11} should remain in the same frequency region. $[\text{Fe}_2\text{Se}_2(\text{S}_2\text{-o-xylyl})_2]^{2-}$ shows only weakly enhanced Raman lines in the $300\text{-}350\text{ cm}^{-1}$ interval. Because of the poor resolution of the four lines quoted at 311, 319, 339 and 349 cm^{-1} in Table 4.6, and their interplay of relative intensities as the excitation wavelength varies, the shifts given represent a summary for spectra obtained on different krypton lines. The surfeit of peaks presents no difficulty to making correlations with the sulphur bridged spectra, all are, however, relatively weak. In the IR the strong band at 320 cm^{-1} is thought to contain both ν_{16} and ν_8 corresponding to the 325 and 336 cm^{-1} absorptions for $[\text{Fe}_2\text{S}_2(\text{S}_2\text{-o-xylyl})_2]^{2-}$.

The intense Raman peak at 388 cm^{-1} in the spectra for the sulphur bridged molecule is not found in the selenium analogue and is firmly assigned to ν_2 , the ring breathing mode. Asymmetric ring stretches, ν_{13} and ν_{17} are proposed to give rise to the strong IR absorption around 415 cm^{-1} . If this is so it is surprising that these two vibrations should occur at around the same frequency, as whilst ν_{13} should be essentially purely bridge-bond stretching ν_{17} is expected to involve considerable $\widehat{\text{S}}_b\text{FeS}_b$ angle bending. Barring coincidence with ν_{16} or ν_8 , only the medium intensity IR band at 274 cm^{-1} remains and this would seem to be too low in energy relative to 415 cm^{-1} to be ν_{17} . Selenium substitution leads to loss of the strong 415 cm^{-1} peak and appearance of a medium strength absorption at 302 cm^{-1} , whilst in the Raman new intense lines (polarised in solution) at 228 and 261 cm^{-1} appear concomitant with the loss of the 388 cm^{-1} peak due to ν_2 . Assigning ν_2 to 261 cm^{-1} for $[\text{Fe}_2\text{Se}_2(\text{S}_2\text{-o-xylyl})_2]^{2-}$, a ratio of 0.67 for $\nu_2(\text{Se}):\nu_2(\text{S})$ results and is comparable to that of 0.64 observed on exchanging bromine for chlorine in the dimeric aluminium and gallium halides. The latter changes give ratios for $\nu_{13}(\text{Br}):\nu_{13}(\text{Cl})$ and

$\nu_{17}(\text{Br}) : \nu_{17}(\text{Cl})$ in the region 0.68 to 0.81. A shift in the IR from 415 cm^{-1} to 302 cm^{-1} for sulphur/selenium bridging in the iron complexes is then compatible with assignment of ν_{13} / ν_{17} to the absorption at 302 cm^{-1} , however, the band is rather weak to contain both modes.

The strong band at 196 cm^{-1} (polarised in solution) in $[\text{Fe}_2\text{S}_2(\text{S}_2\text{-o-xylyl})_2]^{2-}$ is assigned to ν_4 , the symmetric in-plane ring deformation. This frequency would imply a medium degree of Fe-Fe interaction, in keeping with the rather long bond length of 2.698 \AA . In $\text{Fe}_2(\text{CO})_6(\text{S}_2)$ with a shorter 2.55 \AA bond length a Raman band at 191 cm^{-1} ¹⁷³ or 195 cm^{-1} ²⁰⁶ has been described as principally $\nu(\text{Fe-Fe})$. Other iron-iron stretching frequencies in dimers fall in the region $190\text{-}280 \text{ cm}^{-1}$ depending on the degree of bonding interaction,²⁰⁷⁻²¹⁰ lower frequencies are observed where there are no bridging atoms²⁰⁷ or where no metal-metal interaction exists (e.g., in Fe_2Cl_6 $\nu_4 = 108 \text{ cm}^{-1}$ ²⁰²). In the selenium bridged homologue the 196 cm^{-1} band is absent but new features of comparable intensity appear at 155 and 228 cm^{-1} ; a decreased Raman shift would be expected.

Of the remaining unassigned peaks observed in the Raman spectrum of $[\text{Fe}_2\text{S}_2(\text{S}_2\text{-o-xylyl})_2]^{2-}$ the tentative descriptions ν_6 224 cm^{-1} , ν_3 165 cm^{-1} and ν_7 (or ν_{15}) 139 cm^{-1} are suggested.

4.3.3.2. $[\text{Fe}_2\text{X}_2(\text{YPh})_4]^{2-}$ (X, Y = S, Se).

The analysis for this set of complexes follows to some degree the arguments used in the last section. Bands of totally symmetric origin at 428 cm^{-1} in PhS-ligated dimers are assigned to ν_1 which shifts to 306 cm^{-1} in $[\text{Fe}_2\text{S}_2(\text{SePh})_4]^{2-}$ and 309 cm^{-1} in $[\text{Fe}_2\text{Se}_2(\text{SePh})_4]^{2-}$. The similar ν_{16} IR mode is thought to give rise to absorption at 431 cm^{-1} in $[\text{Fe}_2\text{S}_2(\text{SPh})_4]^{2-}$ and 428 cm^{-1} in $[\text{Fe}_2\text{Se}_2(\text{SPh})_4]^{2-}$ whilst being shifted

TABLE 4.12. $[\text{Fe}_2\text{X}_2(\text{S}_2\text{-o-xylyl})_2]^{2-}$ (X = S, Se) vibrational assignments.

<u>RR</u>	<u>X = S</u>			<u>X = Se</u>	
? ν_7 or ? ν_{15}	139	m		? ν_4	155 ms
? ν_3	165	m		? ν_3	165 m
ν_4	196 p	s			183 w
ligand?, ? ν_6	224	w			228 p m
? ν_{11} or (139+165)	304 p	m		ν_2	261 p s
	314	sh,w			311 mw
ν_1	321 p	s		?	319 mw
? ν_{11}	348	w			339 mw
ν_2	388	s		?	349 mw
					426 w
<u>IR</u>					
? ν_{17}	274	m		$\nu_{13} + ?\nu_{17}$	302 mw
(ν_{16}	325	vs		$\nu_8 + \nu_{16}$	320 s
ν_8	336	vs			400 w
$\nu_{13} + ?\nu_{17}$	415	vs			

p - polarised solution counterpart

? - possible assignment

to 273 and 274 cm^{-1} for PhSe-ligation. A double band at 360 cm^{-1} in $[\text{Fe}_2\text{S}_2(\text{SPh})_4]^{2-}$ correlates with those at 359 and 366 cm^{-1} in $[\text{Fe}_2\text{Se}_2(\text{SPh})_4]^{2-}$ and is tentatively assigned as ν_8 , split perhaps by a solid state effect. Judging by the shift ascribed to ν_{16} , for $[\text{Fe}_2\text{S}_2(\text{SePh})_4]^{2-}$ ν_8 would be shifted below the range of the present observations.

A second totally symmetric band at 351 cm^{-1} in $[\text{Fe}_2\text{S}_2(\text{SPh})_4]^{2-}$ is thought to result from ν_2 and to shift to 284 cm^{-1} when selenium is

bridging, giving $\nu_2(\text{Se}):\nu_2(\text{S}) = 0.81$. Assigning ν_2 for $[\text{Fe}_2\text{S}_2(\text{SePh})_4]^{2-}$ is less clear, but an increased frequency of 384 cm^{-1} is favoured, being absent in $[\text{Fe}_2\text{Se}_2(\text{SePh})_4]^{2-}$. Certainly the other nearest possibilities at 273 cm^{-1} or coincidence with ν_1 at 306 cm^{-1} would seem low frequencies. The remaining intense high frequency Raman line at 387 cm^{-1} in $[\text{Fe}_2\text{S}_2(\text{SPh})_4]^{2-}$ is possibly ν_{11} , occurring at 364 cm^{-1} in $[\text{Fe}_2\text{Se}_2(\text{SPh})_4]^{2-}$ and shifted to 273 cm^{-1} in $[\text{Fe}_2\text{S}_2(\text{SePh})_4]^{2-}$. Detailing $\nu_1 > \nu_{11}$ and $\nu_{16} > \nu_8$ is in contention with vibrational analyses for other M_2X_6 bridged structures. This arises from the designation of ν_1 to 428 cm^{-1} because of its low depolarisation ratio in solution. The IR active bridge stretches, ν_{13} and ν_{17} , are tentatively given to 424, 416 and 318, 328 cm^{-1} respectively in $[\text{Fe}_2\text{S}_2(\text{SPh})_4]^{2-}$, $[\text{Fe}_2\text{S}_2(\text{SePh})_4]^{2-}$. These are possibly shifted to 313 (ν_{13}) and 260 cm^{-1} (ν_{17}) in $[\text{Fe}_2\text{Se}_2(\text{SPh})_4]^{2-}$, and 320 cm^{-1} (ν_{13}) in $[\text{Fe}_2\text{Se}_2(\text{SePh})_4]^{2-}$.

The remaining intense band of totally symmetric origin observed in $[\text{Fe}_2\text{S}_2(\text{SPh})_4]^{2-}$ at 256 cm^{-1} is thought to be ν_4 , shifted considerably to 203 cm^{-1} in $[\text{Fe}_2\text{Se}_2(\text{SPh})_4]^{2-}$ and less so to 242 cm^{-1} in $[\text{Fe}_2\text{S}_2(\text{SePh})_4]^{2-}$. For the weak Fe-Fe bonding anticipated in these complexes 256 cm^{-1} is an unusually high frequency for bridge stretching, some 60 cm^{-1} higher than in $[\text{Fe}_2\text{S}_2(\text{S}_{2-0}\text{-xylyl})_2]^{2-}$. As judged by the Fe-Fe distance available for $[\text{Fe}_2\text{S}_2(\text{STol})_4]^{2-}$ the metallic bonding may well be stronger in the aromatic thiol coordinated complex, but the only way ν_4 could arise at such a large Raman shift is by mixing in some higher frequency vibration such as ν_1 .

Whilst moving ever closer to conjecture as the band frequency and intensity drops, the following designations are proffered: $\nu_3 = 160, 140, 123 \text{ cm}^{-1}$ in $[\text{Fe}_2\text{S}_2(\text{SPh})_4]^{2-}$, $[\text{Fe}_2\text{Se}_2(\text{SPh})_4]^{2-}$, $[\text{Fe}_2\text{S}_2(\text{SePh})_4]^{2-}$; $\nu_6 = 244, 235 \text{ cm}^{-1}$ in $[\text{Fe}_2\text{S}_2(\text{SPh})_4]^{2-}$, $[\text{Fe}_2\text{Se}_2(\text{SPh})_4]^{2-}$; $\nu_2, \nu_4 = 217, 187 \text{ cm}^{-1}$ in $[\text{Fe}_2\text{Se}_2(\text{SePh})_4]^{2-}$.

TABLE 4.13. $[\text{Fe}_2\text{X}_2(\text{YPh})_4]^{2-}$ (X, Y = S, Se) Vibrational Assignments.

X = Y = Se			X = Se, Y = S			X = Y = Se			X = S, Y = Se			X = Y = S			
?v ₃	160	m	→ ?v ₃	140	w	→ ?v ₄	187	s	← ?v ₃	123	s	← ?v ₃	160	m	
	201	w	→ v ₄	203	s	→ ?v ₂	217p	m		180	w		201	w	
?v ₆	244	sh,w	→ ?v ₆	235	m				ligand?	214	m		?v ₆	244	sh,w
v ₄	256p	s	→ v ₂	255	w		278	w	← v ₄	242p	s	← v ₄	256p	s	
	320	w		284p	mw				?v ₁₁	273	s	← ?v ₁₁	320	w	
v ₂	351p	m		314	w		298	w	v ₁	306p	s	← v ₂	351p	m	
?v ₁₁	387	m	→ ?v ₁₁	364	m	→ v ₁	309p	s	?v ₂	384	m	← ?v ₁₁	387	m	
	406	w		410	w								406	w	
v ₁	428p	s	→ v ₁	428p	s							← v ₁	428p	s	
	478	w		475	w								478	w	
	279	w	→ ?v ₁₇	260	m	→ v ₁₆	274	s	← v ₁₆	273	m	← ?v ₁₇	279	w	
?v ₁₇	318	s	→ ?v ₁₃	313	ms		ligand?	306	mw	ligand?	307	w		318	s
v ₈	360	vs,d1	→ v ₈	359	s	→ ?v ₁₃	320	m	← ?v ₁₇	328	s	← v ₈	360	vs,d1	
	410	w	split	366	sh,ms		333	w					410	w	
?v ₁₃	424	s		400	w,br	ligand?	400	mw,br	← ?v ₁₃	416	s	← v ₁₃	424	s	
v ₁₆	431	m	→ v ₁₆	428	m							← v ₁₆	431	m	

4.3.3.3. $[\text{Fe}_2\text{X}_2(\text{STol})_4]^{2-}$ (X = S, Se), $[\text{Fe}_2\text{S}_2(\text{SC}_6\text{H}_4\text{Cl})_4]^{2-}$ and $[\text{Fe}_2\text{X}_2\text{Y}_4]^{2-}$ (X = S, Se; Y = Cl, Br).

The reasoning behind the assignment of the vibrations for these complexes (Tables 4.14-16) follows similar lines to those used in the previous two sections and will not be treated here in detail. For $[\text{Fe}_2\text{S}_2(\text{SC}_6\text{H}_4\text{Cl})_4]^{2-}$ interpretation is difficult as there is a greater number of intense bands, in both the IR and RR spectra, than can easily be accounted for. The halogen ligated complexes, $[\text{Fe}_2\text{X}_2\text{Cl}_4]^{2-}$ (X = S, Se) and $[\text{Fe}_2\text{S}_2\text{Br}_4]^{2-}$, show a dominant feature in the Raman which has been assigned to ν_2 . The remaining weaker bands are not easily assigned. No attempt has been made to obtain solution spectra of these complexes as they are rather less stable than the thiolate coordinated dimers and additionally the strongest peak in the sulphur bridged compounds would be obscured by solvent Raman scattering. The Raman and IR results for $[\text{Fe}_2\text{S}_2\text{Cl}_4]^{2-}$ show little similarity with those for Fe_2Cl_6 .²⁰²⁻²⁰⁴ The mean Fe-Cl bridge and Fe-Cl terminal bonding lengths for the latter have recently been determined as 2.326 and 2.127 $\overset{\circ}{\text{A}}$ respectively by vapour phase electron diffraction.²¹¹ These lengths differ considerably from those for $[\text{Fe}_2\text{S}_2\text{Cl}_4]^{2-}$ (Figure 3.9) and in particular the bridge-terminal difference is reversed.

4.3.4. Optical spectra and Raman resonance enhancement for the two-iron complexes.

Figure 4.15 shows overlaid electronic spectra for $[\text{Fe}_2\text{X}_2(\text{YPh})_4]^{2-}$ (X, Y = S, Se) in DMF solution; peak positions and extinction coefficients for these and other dimeric complexes are collected in Table 4.17. Optical data has been reported previously for $[\text{Fe}_2\text{S}_2(\text{SC}_6\text{H}_4\text{Y})_4]^{2-}$ (Y = H, Cl, Me) and $[\text{Fe}_2\text{S}_2(\text{S}_2\text{-o-xylyl})_2]^{2-}$ in DMF,²⁸ and subsequent to this present work for the selenide-bridged thiolate-coordinated complexes.²⁹

TABLE 4.14. $[\text{Fe}_2\text{X}_2(\text{STol})_4]^{2-}$ (X = S, Se) vibrational assignments.

<u>RR</u>	<u>X = S</u>		<u>X = Se</u>		
? ν_3	148	m	ν_4	192	s
	215	w		218	mw
ν_4	241p	s		251	w
ν_2	320p	s	ν_2	272	mw
? ν_{11}	375	s		325	mw
ligand?, ? ν_{11}	386	m	ligand?, ? ν_{11}	387	sh, m
ν_1	403	s	ν_1	398	s
	490	w	ligand?	630	m
ligand?	630	m			
<u>IR</u>					
? ν_{17}	325	sh, m		304	ms
? ν_{17}	332	s	ν_{13}	318	ms
	374	sh, w		332	m
ν_8	382	mw	ν_8 and ν_{16}	398	ms, dl
ν_{16}	396	s			
ν_{13}	415	ms			

TABLE 4.15. $[\text{Fe}_2\text{S}_2(\text{SC}_6\text{H}_4\text{Cl})_4]^{2-}$ vibrational assignments.

	<u>RR</u>		<u>IR</u>		
	137	w	274	w	
	201	w	? ν_{17}	293	ms
? ν_4	221	mw	? ν_{17} , ? ν_8	323	ms
? ν_2 , ? ν_4	294p	s	?ligand, ν_8 ?	345	mw
	320	w	ν_{16}	384	s
? ν_2	342p	s		409	sh, w
(ν_1	368	s	ν_{13}	418	ms
ν_{11}	381	m		450	vw, br
	401	m			

TABLE 4.16. $[\text{Fe}_2\text{X}_2\text{Y}_4]^{2-}$ (X = S, Se; Y = Cl, Br) vibrational assignments.

	$[\text{Fe}_2\text{Se}_2\text{Cl}_4]^{2-}$	$[\text{Fe}_2\text{S}_2\text{Cl}_4]^{2-}$	$[\text{Fe}_2\text{S}_2\text{Br}_4]^{2-}$
<u>RR</u>			
	150 w	144 m	124 mw
ν_2	246 s ←	ν_4 178 m	260 w
	274 w	221 w	274 mw
	340 sh,w	? ν_{11} 310 mw	315 w
	348 w	ν_1 333 m	393 s
	397 w	358 w	410 sh,w
	406 w	397 s	
	435 w	450w	
	493 mw		
<u>IR</u>			
impurity?	285-95 w	286 ms	263 ms
ν_{13}	329 s ←	326 sh,vw	ν_{17} 327 ms
$\nu_8 + \nu_{16}$	342 s	334 s	340 sh,w
	405 w	345 vs	ν_{13} 418 ms
	416 w	416 s	510 m,vbr

TABLE 4.17. Electronic spectra of $[\text{Fe}_2\text{X}_2(\text{YR})_4]^{2-}$ (X, Y = S, Se).

<u>IN DMF</u>	λ/nm (ϵmM); [deconvoluted Lorentzian peaks]
$[\text{Fe}_2\text{S}_2(\text{S}_2\text{-o-xylyl})_2]^{2-}$	293, 339(16.9), 415(11.4), 455(sh), 591(5.1)
$[\text{Fe}_2\text{Se}_2(\text{S}_2\text{-o-xylyl})_2]^{2-}$	305, 346(18.8), 438(11.9), 485(sh), 628(4.9)
$[\text{Fe}_2\text{S}_2(\text{SPh})_4]^{2-}$	334(19.0), 489(11.3), \sim 540(br, sh); [480(8.5), 559(4.7)]
$[\text{Fe}_2\text{Se}_2(\text{SPh})_4]^{2-}$	342(20.4), 505(12.1); [499(9.5), 596(3.9)]
$[\text{Fe}_2\text{S}_2(\text{SePh})_4]^{2-}$	353(18.8), 500(sh), 552(11.6); [476(4.0), 564(9.9)]
$[\text{Fe}_2\text{Se}_2(\text{SePh})_4]^{2-}$	355(16.7), 540(10.4); [518(6.5), 608(5.7)]
$[\text{Fe}_2\text{S}_2(\text{STo1})_4]^{2-}$	334(20.1), 496(12.0), \sim 530(br, sh)
$[\text{Fe}_2\text{Se}_2(\text{STo1})_4]^{2-}$	341(19.5), 510(12.0)
<u>IN ACETONE</u>	
$[\text{Fe}_2\text{S}_2(\text{SPh})_4]^{2-}$	485, \sim 540(sh); [471, 551]
$[\text{Fe}_2\text{Se}_2(\text{SPh})_4]^{2-}$	500; [495, 597]
$[\text{Fe}_2\text{S}_2(\text{SePh})_4]^{2-}$	485, \sim 500(sh); [477, 563]
$[\text{Fe}_2\text{Se}_2(\text{SePh})_4]^{2-}$	\sim 530; [512, 604]
$[\text{Fe}_2\text{S}_2(\text{SC}_6\text{H}_4\text{Cl})_4]^{2-}$	476, \sim 540(sh); [480, 562]

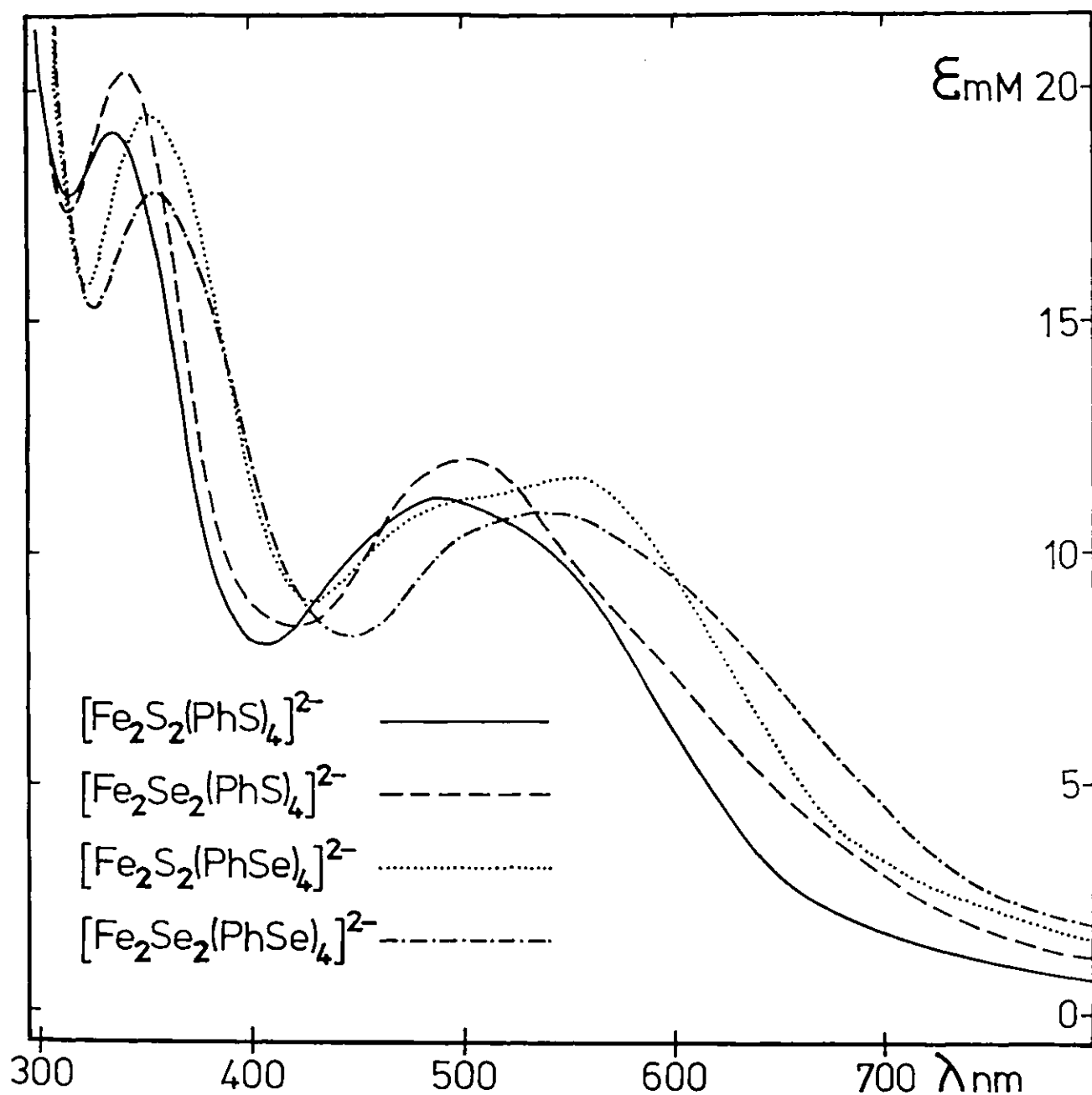


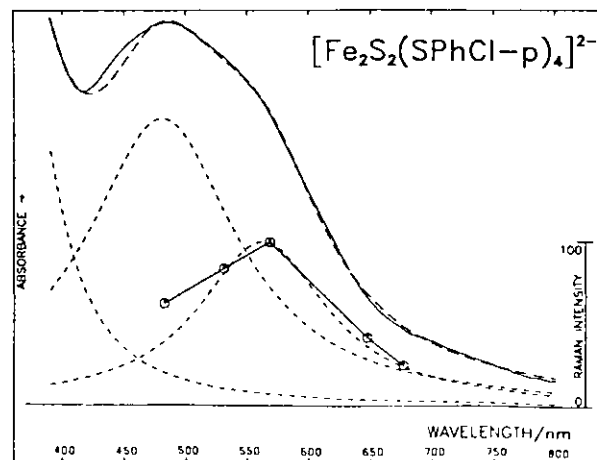
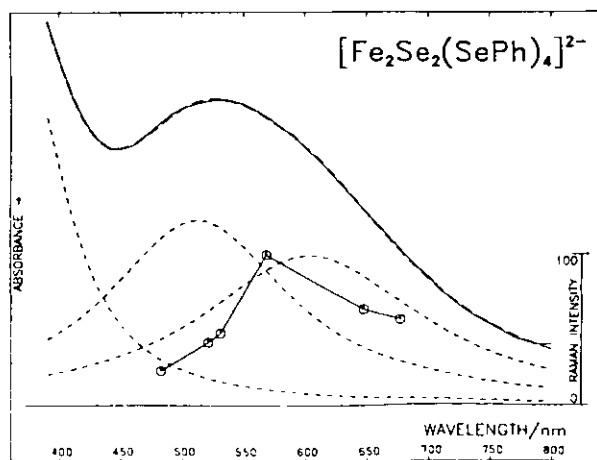
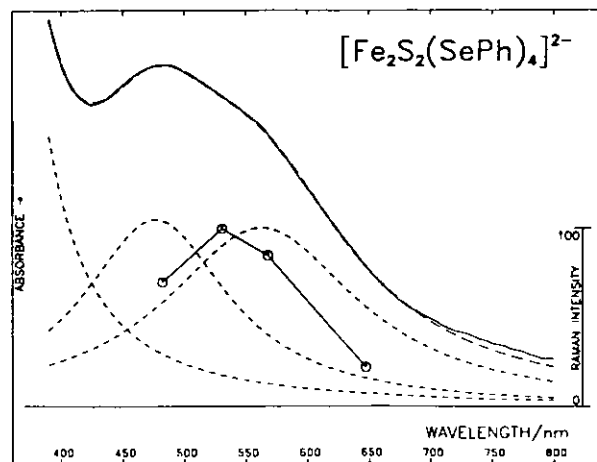
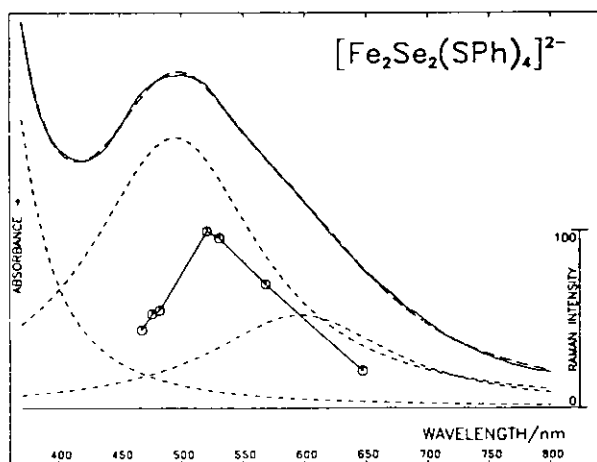
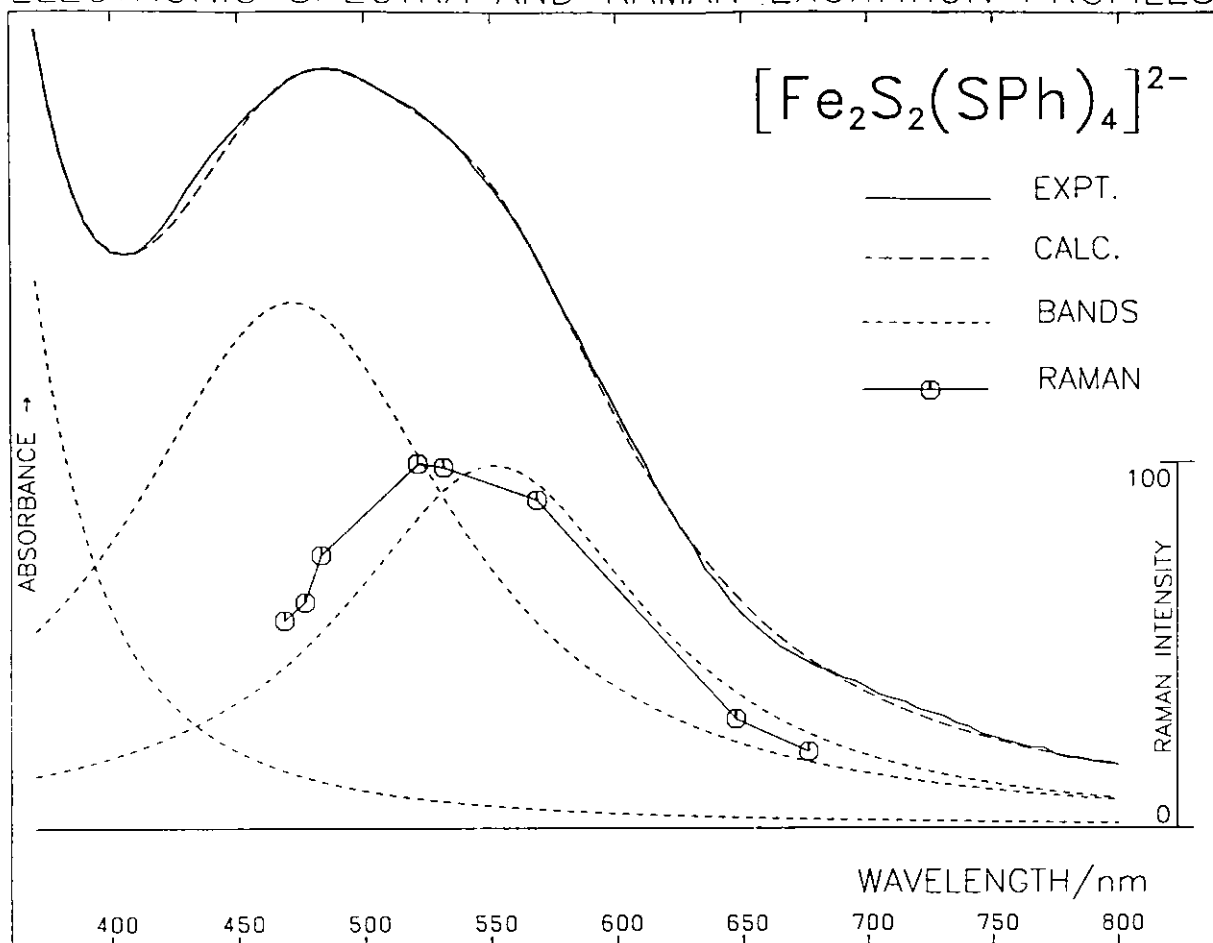
Figure 4.15. Electronic absorption spectra for $[\text{Fe}_2\text{X}_2(\text{YPh})_4]^{2-}$
(X, Y = S, Se) in DMF.

For $[\text{Fe}_2\text{X}_2(\text{YPh})_4]^{2-}$ (X, Y = S, Se) the absorption around 500–600 nm has been deconvoluted into two Lorentzian bands by a least-squares fitting procedure. All the bands above 300 nm are charge-transfer in origin and in most cases show red shifts on selenium substitution. Such shifts were also observed in the series of complexes $[\text{Fe}_4\text{X}_4(\text{YPh})_4]^{2-}$ (X, Y, = S, Se),

being greater for the PhS/PhSe ligand change than for the $\text{Fe}_4\text{S}_4/\text{Fe}_4\text{Se}_4$ core alteration²¹²; the reverse seems to be the case for the shifts in the two low energy bands of the dimeric complexes. Small red shifts resulting from replacement of coordinated sulphur by selenium, in otherwise identical complexes, have been observed for several series of compounds [see references in reference 212]. The very small change in band position produced on going from PhS- to PhSe-ligation is indicative of comparable optical electronegativities for the chalcogenides in these ligands.^{213,214} Two-iron ferredoxins reconstituted with bridging selenide, show visible band bathochromic shifts comparable to those described above for the analogue complexes.^{49,215,83,170}

Figure 4.16 shows optical spectra for five of the dimer complexes in acetone, together with Lorentzian deconvolution analyses. Raman intensities for the ν_1 assigned symmetric stretching vibrations have been plotted at Krypton emission frequencies for each complex. These are normalised using the 787 cm^{-1} acetone solvent peak as a standard. Allowing for concentration differences the ν_1 (Fe-S) modes of $[\text{Fe}_2\text{X}_2(\text{YPh})_4]^{2-}$ (X, Y, = S, Se) at full resonance range 1300 to 1600 times more intense than the 787 cm^{-1} acetone symmetric stretch, clearly indicating strong involvement of a resonance enhancement process. Considering an error of around 10% in estimation of the relative Raman intensities and an error of 10 nm or more (depending upon magnitude and width) in evaluating the deconvoluted band maxima, there appears a reasonable agreement between the peaks of the excitation profiles and of the lowest energy electronic bands. Thus, it seems that these probably arise from charge transfer involving the PhY-Fe bonds. An exception is $[\text{Fe}_2\text{Se}_2(\text{SPh})_4]^{2-}$ for which the excitation profile has a peak-value at a wavelength intermediate

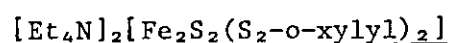
FIG 4.16 $[\text{Fe}_2\text{X}_2(\text{YR})_4]^{2-}$ ($\text{X}, \text{Y}=\text{S}, \text{Se}; \text{R}=\text{Ph}, \text{pClPh}$) IN ACETONE
ELECTRONIC SPECTRA AND RAMAN EXCITATION PROFILES



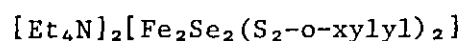
between the two deconvoluted bands, though it should be noted that for this case the simulated fit is not very good at the experimental maximum and may indicate an inadequate representation of component lineshapes leading to less accurate resolution of these underlying bands. In most of the remaining complexes the maximum Raman intensity is also observed at higher energy than the low energy deconvoluted shoulder.

Due to solvent obscuration, a study of Raman resonance enhancement for $[\text{Fe}_2\text{X}_2(\text{S}_2\text{-o-xylyl})_2]^{2-}$ ($\text{X} = \text{S}, \text{Se}$) in DMF, DMSO, or MeCN solvents is not feasible. However, an attempt has been made to correlate intensity variations of the many Raman bands observed for the solid phase with the reflectance spectra for the complexes, diluted in MgO. These electronic spectra are shown in Figure 4.17, together with Raman excitation profiles obtained relative to the symmetric NO_3^- stretch of KNO_3 added as a standard to the supporting KBr matrix. Details of band positions for these reflectance spectra, and also for $[\text{Et}_4\text{N}]_2[\text{Fe}_2\text{S}_2(\text{SPh})_4]$, are given in Table 4.18. The spectra are complex, involving many underlying bands. This is in contrast to observations for analogous tetramer compounds [see Section 4.4.2.3.]. Red shifts, comparable to those in solution, are found on going from sulphur to selenium bridging. There is a certain degree of correlation of Raman maximum intensity for several vibrational bands, with the absorption peak around 590 nm in $[\text{Fe}_2\text{S}_2(\text{S}_2\text{-o-xylyl})_2]^{2-}$.

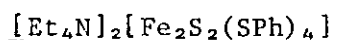
TABLE 4.18. Reflectance spectra of $[\text{Fe}_2\text{X}_2(\text{SR})_4]^{2-}$ ($\text{X} = \text{S}, \text{Se}$).



1310(w,br), \sim 850(w,br,pr), \sim 750(sh), 710, 590, \sim 470(br,pr).



1420(w,br), \sim 920(w,br,pr), \sim 790(sh), 620, \sim 450 and 480 (pr)



1450(w), \sim 900(w,pr), \sim 740(sh), 670, \sim 580, \sim 520(pr)

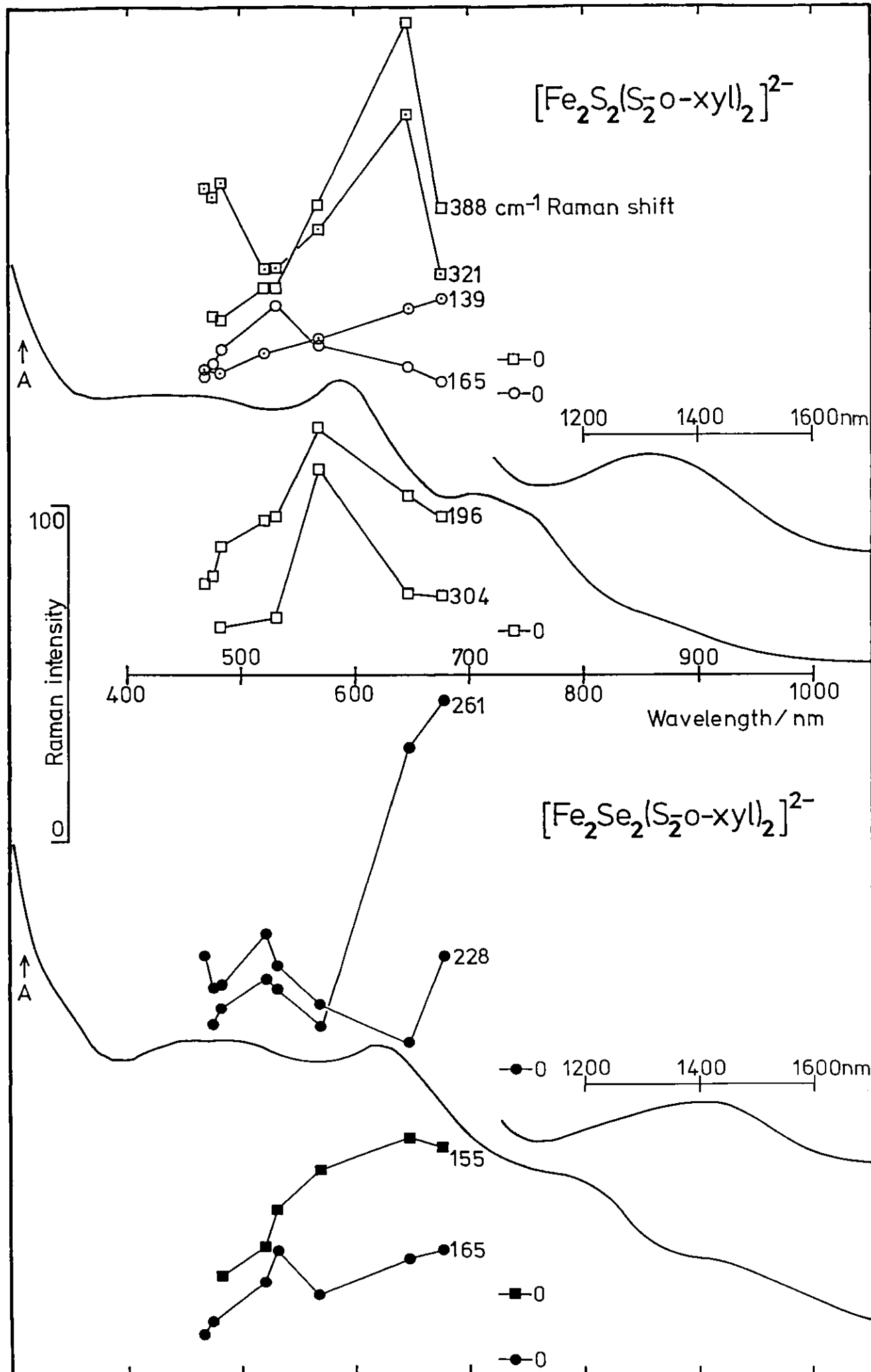


Fig. 4.17 Electronic reflectance spectra and Raman excitation profiles for $[\text{Et}_4\text{N}]_2[\text{Fe}_2\text{X}_2(\text{S}_2\text{o-xylyl})_2]$ ($\text{X}=\text{S}, \text{Se}$)

4.3.5. General Conclusions Concerning Dimer Complexes.

Table 4.19 lists by order of mode the vibrational assignments for the twelve dimer complexes studied. Comparing Fe-X vibrations for a given X-atom type, there is quite good agreement for several of the modes assigned in the different compounds. A correlation of ν_4 with Fe-Fe distance is observed for the three complexes for which dimensional structure information is available. As the Fe-Fe separation increases from 2.691\AA in $[\text{Fe}_2\text{S}_2(\text{STol})_4]^{2-}$ to 2.716\AA in $[\text{Fe}_2\text{S}_2\text{Cl}_4]^{2-}$ the frequency assigned to ν_4 decreases from 241 cm^{-1} to 178 cm^{-1} indicative of decreasing bonding interaction.

The bands observed at $330\text{--}350\text{ cm}^{-1}$ and $390\text{--}395\text{ cm}^{-1}$ in adrenal and spinach ferredoxin Raman spectra^{114,115,170} agree reasonably well with those at 321 cm^{-1} (ν_1) and 388 cm^{-1} (ν_2) for $[\text{Fe}_2\text{S}_2(\text{S}_2\text{-o-xylyl})_2]^{2-}$. For the other analogue complexes having terminal aryl thiol ligands $\nu_1 > \nu_2$, and thus the alkyl thiol chelated compound seems better to model the protein, in keeping with the cysteine coordination in the latter. The other bridge vibration observed at $284\text{--}297\text{ cm}^{-1}$ in the ferredoxins has no counterpart in the $[\text{Fe}_2\text{S}_2(\text{S}_2\text{-o-xylyl})_2]^{2-}$ Raman spectrum. For selenium bridging ν_2 has been assigned to a strong band at 261 cm^{-1} in $[\text{Fe}_2\text{S}_2(\text{S}_2\text{-o-xylyl})_2]^{2-}$, a shift of 127 cm^{-1} . There is a band in selenoadrenodoxin at 263 cm^{-1} which correlates favourably with this interpretation, but this has been tentatively described by Tang *et al.*¹⁷⁰ as shifted from 297 cm^{-1} in the native protein, a shoulder at $\sim 350\text{ cm}^{-1}$ (Se) being identified with shifting of the 397 cm^{-1} (S) peak. For the other terminal thiol ligated analogues the shift of peaks assigned as ν_2 , on going from sulphur to selenium bridging, is smaller than for

TABLE 4.19. Correlation of Vibrational Assignments for Dimer Complexes.

Dimer	ν_1	ν_2	ν_3	ν_4	ν_6	ν_8	ν_{11}	ν_{13}	ν_{16}	ν_{17}
$[\text{Fe}_2\text{S}_2(\text{S}_2\text{-o-xy1})_2]^{2-}$	321	388	165?	196	224?	336	348?	415	325	(415? 274?)
$[\text{Fe}_2\text{S}_2(\text{SPh})_4]^{2-}$	428	351	160?	256	244?	360	387?	424	431	318?
$[\text{Fe}_2\text{S}_2(\text{STol})_4]^{2-}$	403	320	148?	241		382	(375 386)	415	396	(325 332)
$[\text{Fe}_2\text{S}_2(\text{SCH}_4\text{Cl})_4]^{2-}$	(368 381)	(342? 294?)		(294? 221?)		(323? 345?)	(368 381)	418	384	(293? 323?)
$[\text{Fe}_2\text{S}_2\text{Cl}_4]^{2-}$	333	397		178		345	310?	416	345	334
$[\text{Fe}_2\text{Se}_2(\text{S}_2\text{-o-xy1})_2]^{2-}$	319?	261	165?	155?		320	349?	302	320	302?
$[\text{Fe}_2\text{Se}_2(\text{SPh})_4]^{2-}$	428	284	140?	203	235?	359- 366	364?	313	428	260?
$[\text{Fe}_2\text{Se}_2(\text{STol})_4]^{2-}$	398	272		192		398	387?	318	398	
$[\text{Fe}_2\text{Se}_2\text{Cl}_4]^{2-}$		246				342		329	342	
$[\text{Fe}_2\text{S}_2(\text{SePh})_4]^{2-}$	306	384?	123?	242			273?	416?	273	328?
$[\text{Fe}_2\text{S}_2\text{Br}_4]^{2-}$		393						418		327
$[\text{Fe}_2\text{Se}(\text{SePh})_4]^{2-}$	309	217?		187?				320?	274	

NOTES: 1. ? = possible assignment; 2. two entries at one frequency for a single compound indicate alternative possible assignments.

$[\text{Fe}_2\text{S}_2(\text{S}_2\text{-o-xylyl})_2]^{2-}$, thus it is difficult to assess from the results for the model-complexes whether the tentative assignment of Tang *et al.* is correct. However, in view of there being similarities between spectra for $[\text{Fe}_2\text{S}_2(\text{S}_2\text{-o-xylyl})_2]^{2-}$ and the proteins, assignment of ν_2 to 263 cm^{-1} in seleno-adrenodoxin is favoured here.

No attempt has been made to obtain Raman spectra for the reduced dimer species reported in Section 1. . It would be necessary to perform these measurements on frozen solutions using solvents such as DMF, DMSO, or NMP which scatter strongly in the region of interest. Gayda, *et al.*¹⁰¹ have discussed the possibility of spin-relaxation in reduced ferredoxins occurring by an Orbach process involving an Fe_2S_6 core vibrational mode, and concluded that this is unlikely in view of the similarity of Fd_{ox} Raman spectra as against the disparity of EPR temperature-dependence for the same Fe_{red} . More recently, however, Gayda *et al.*¹⁰⁷ have suggested that at high temperatures local modes could be important in determining the efficiency of the Orbach relaxation mechanism for ferredoxins, in that high frequency modes are not expected to be able to propagate through the protein. Measurements described in Section 2 for three of the analogue complexes indicate that any local mode involved in their spin-relaxation would require a frequency much higher than anticipated for $[\text{Fe}_2\text{S}_2(\text{SR})_4]^{3-}$ or observed for any of the diferric complexes.

The magnetic properties of $[\text{Fe}_2\text{S}_2(\text{S}_2\text{-o-xylyl})_2]^{2-}$ and $[\text{Fe}_2\text{S}_2\text{Cl}_4]^{2-}$ have been investigated and antiferromagnetic behaviour demonstrated with $-J = 149 \pm 8\text{ cm}^{-1}$ and 158 cm^{-1} respectively.^{38,194} For transitions from ground and first excited states to higher levels of the spin manifold

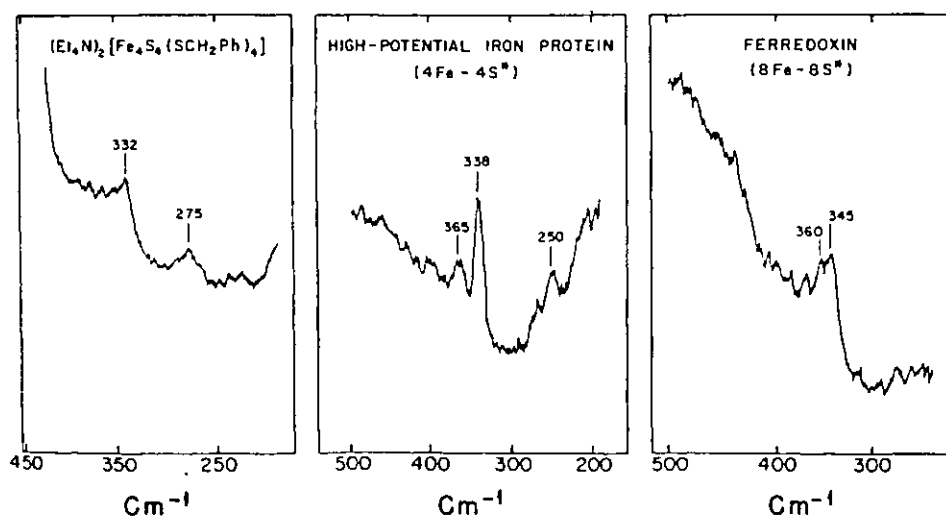
the following energies are predicted; $[\text{Fe}_2\text{S}_2(\text{S}_2\text{-o-xylyl})_2]^{2-}$ from $S = 0$, 298 ± 16 , 894 ± 48 , 1788 ± 96 , $2980 \pm 160 \text{ cm}^{-1}$; from $S = 1$, 596 ± 24 , 1490 ± 80 , $2682 \pm 140 \text{ cm}^{-1}$; $[\text{Fe}_2\text{S}_2\text{Cl}_4]^{2-}$ from $S = 0$, 316 , 948 , 1896 , 3160 cm^{-1} ; from $S = 1$, 632 , 1580 , 2844 cm^{-1} (errors on this last set are expected to be higher than quoted for the first). Although in each case a potential $S = 0 \rightarrow 1$ transition peak occurs around 300 cm^{-1} and there are weak bands at higher frequencies which correlate, within the specified error ranges, to the energies predicted from the susceptibility results, no convincing evidence is forthcoming to support the interpretation of Fd spectra given by Blum *et al.*^{114,115} This conclusion may be extended to include the Raman results for the other two-iron clusters studied; assuming the strength of their antiferromagnetic interactions to be similar.³⁸ It is difficult to eliminate cation and ligand vibrations as their intensities and frequencies in the complex and in control compounds may differ and unassigned bands are in some cases too weak, in others too numerous, to allow any confidence in fitting a 0, 2J, 6J, 12J, 20J, 30J pattern, even when allowing a generous error margin. A similar caution probably applies in judging the validity of spin-flip Raman assignments made for the proteins.

4.4. Tetranuclear Iron-Sulphur Complexes; Analogues of 4Fe4S Proteins.

4.4.1. RR in 4Fe4S clusters.

Surprisingly little investigation has been made of the vibrational properties of proteins containing 4Fe4S clusters or of their synthetic counterparts, $[\text{Fe}_4\text{S}_4(\text{SR})_4]^{2-}$, first reported almost a decade ago. The electronic spectra of these is characterised by a prominent absorption band in the 380-450 nm region, which tails off for around 100 nm to higher energy. A strong pre-resonance effect is expected for Raman active vibrations of the iron-sulphur core when exciting with the blue emission lines available on Argon/Krypton lasers. Figure 4.18 shows RR spectra obtained for $[\text{Fe}_4\text{S}_4(\text{SBz})_4]^{2-}$, Chromatium Hipip and C. pasteurianum ferredoxin by Tang et al.¹⁷² using 488.0 nm excitation. All peaks observed are polarised, those at frequencies greater than 300 cm^{-1} have been tentatively assigned to the terminal ligand breathing mode, whilst those at smaller shifts are assignable to the breathing mode of the Fe_4S_4

Figure 4.18. Raman spectra for three 4Fe-4S centres (488 nm excitation)¹⁷²



core. The appearance of two polarised bands above 300 cm^{-1} in the proteins has been interpreted as implying a lowering of symmetry below T_d .

Subsequent to this present work Holm, et al.²¹⁶ have reported that vibrational analysis of $[\text{Fe}_4\text{S}_4(\text{SPh})_4]^{n-}$ ($n = 2, 3$) is underway and that from preliminary findings $\nu_{\text{Fe-S}}$ (bridge) = 343 cm^{-1} (dianion), 341 cm^{-1} (trianion) and $\nu_{\text{Fe-S}}$ (terminal) $\approx 430\text{ cm}^{-1}$ (dianion and trianion); though the bands around 340 cm^{-1} do not arise from pure Fe-S_b stretching modes.

4.4.2. RR and IR spectra of $[\text{Fe}_4\text{S}_4(\text{SR})_4]^{2-}$.

The properties of $[\text{Fe}_4\text{S}_4(\text{SR})_4]^{n-}$ ($n = 2, 3$) have been studied in detail over the past ten years and structurally and spectroscopically the compounds demonstrated to be true analogues of the clusters present in 4Fe4S and 8Fe8S proteins. The majority of the investigations have been performed with the thiolates PhS- and BzS- as terminal ligands. RR and IR spectra for $[\text{Fe}_4\text{S}_4(\text{SPh})_4]^{2-}$, $[\text{Fe}_4\text{S}_4(\text{SBz})_4]^{2-}$ and also for the corresponding selenium bridged and PhSe- ligated species²¹² are described in Figure 4.19-22 and Tables 4.21-23.

X-ray determined crystal structures are available for $[\text{NMe}_4]_2[\text{Fe}_4\text{X}_4(\text{SPh})_4]$ ($X = \text{S}, \text{Se}$),^{58,212} and for $[\text{Et}_4\text{N}]_2[\text{Fe}_4\text{S}_4(\text{SBz})_4]$.⁷⁵ The stereochemistries of the sulphur bridged tetramers are very similar and manifest D_{2d} cluster geometry, having a compression along the unique C_2 axis. Carter²¹⁷ has made the observation that the S-S distances for the four thiolate ligands can be divided into two sets of three, forming a unique base (mean S-S $\approx 6.3\text{\AA}$) and apex (mean S-S $\approx 6.5\text{\AA}$) of a trigonally distorted tetrahedron. This distortion, taken together with the tetragonal Fe_4S_4

core distortion eliminates all symmetry elements except the mirror plane and the molecular point group is therefore C_s . The same symmetry reductions can be seen in the Fe_4S_8 core structures of $HIPIP_{red}$ and Fd_{ox} . The core S_4 approximate-tetrahedron is dimensionally larger than the Fe_4 tetrahedron which it interpenetrates. The $Fe_4Se_4S_4$ cluster is devoid of symmetry but closely approaches D_{2d} .

For an $M_4(X_b)_4(X_t)_4$ cubane structure with strict T_d symmetry thirteen normal vibrations are expected. The symmetries and selection rules, together with an approximate description for each vibration, are given in Table 4.20. Twenty-three modes result from losses in degeneracy when the cluster symmetry is degraded to D_{2d} , and the number of totally symmetric vibrations increases from three to six. The symmetry reducing distortions outlined above are not gross, particularly in the case of $[Fe_4S_4(SPh)_4]^{2-}$, and effective T_d symmetry will be assumed in describing vibrational assignments, with due allowance for departure from this where necessary.

Detailed interpretation of the IR and Raman spectra for the tetranuclear clusters is not straightforward. This is not unexpected in view of the complexity of the molecules, the comparable masses of the constituent atoms, the close spacing of the vibrational frequencies and the likely similarity of the bond force-constants.

It seems probable that the symmetry coordinate representations will be extensively mixed in the normal modes of vibration. The change in metal: ligand-atom mass ratio from above to below unity on going from sulphur to selenium ligation reduces the interpretive assistance which might otherwise be gained from a comparison of their vibrational spectra. Whilst reasonably firm assignments of the T_d A_1 modes are possible, in the absence of rigorous force field calculations, much of the rest of the brief analysis which follows must be regarded as tentative.

TABLE 4.20. Normal vibrations of $M_4(X_b)_4(X_t)_4$ in T_d and D_{2d} symmetries.

	T_d	Description	D_{2d}
ν_1	A_1	$M-X_t$ breathing.	A_1
ν_2	A_1	$M_4(X_b)_4$ in-phase breathing.	A_1
ν_3	A_1	$M_4(X_b)_4$ out-phase breathing; interior angle deformation or M-M stretch.	A_1
ν_4	E	$M_4(X_b)_4$ elongation-compression.	$A_1 + B_1$
ν_5	E	Interior angle deformation or M-M stretch.	$A_1 + B_1$
ν_6	E	$M-(X_t)$ rocking deformation.	$A_1 + B_1$
ν_7	$T_1(\text{IA})$	$M-(X_b)$ stretch.	$A_2(\text{IA}) + E(\text{IR})$
ν_8	$T_1(\text{IA})$	$M-(X_t)$ deformation.	$A_2(\text{IA}) + E(\text{IR})$
ν_9	$T_2(\text{IR})$	$M-(X_t)$ stretch.	$B_2(\text{IR}) + E(\text{IR})$
ν_{10}	$T_2(\text{IR})$	$M-(X_b)$ stretch.	$B_2(\text{IR}) + E(\text{IR})$
ν_{11}	$T_2(\text{IR})$	$M-(X_b)$ stretch.	$B_2(\text{IR}) + E(\text{IR})$
ν_{12}	$T_2(\text{IR})$	Interior angle deformation or M-M stretch.	$B_2(\text{IR}) + E(\text{IR})$
ν_{13}	$T_2(\text{IR})$	$M-(X_t)$ deformation.	$B_2(\text{IR}) + E(\text{IR})$

All modes are Raman active unless labelled inactive (IA).

Vibrational assignments are collected and summarised in Tables 4.24 and 4.25 at the ends of the next two sections.

TABLE 4.21. RR and IR Data for $[\text{Et}_4\text{N}]_2[\text{Fe}_4\text{X}_4(\text{PhS})_4]$ (X = S, Se).

	X = S		X = Se	
	Band Maxima (cm^{-1})	Intensity at 530.9 nm excitation	Band Maxima (cm^{-1})	Intensity at 530.9 nm excitation
SOLID -RR	150	w	155	2
	200	w,br	166	w,sh
	240	1	197	1,sh
	267	2	209	5
	280	2	254	2
	338	4	260	w,sh
	382	w	362	1,br
	434	10	382	vw
	431		431	10
	<u>OTHER</u>		<u>BANDS</u>	
	60,68,74,101,109,117,125, 116,172(all m-w,n),360(vw) 406(w,sh),694(w),996(mw), 1014(w),1081(m),1471(w), 1576(m),2330(w)		67,75,100,107,115,123 (all m-w,n), ~280(w,br),382(vw), 885(vw),998(mw),1025(vw), 1081(m),1240(vw),1473(w), 1576(m),2330(w)	
SOLUTION -RR	207(vw),240(vw, ~ depol.) 268(2, ρ 0.2),288(1, ρ ~ 0.7),341(4, ρ 0),432 (10, ρ 0.33)		155(w,sh),196(sh,pol.), 209(4, ρ 0.1),255(1,depol.) 270(sh,pol.),432(10, ρ 0.3)	
IR SELECTED BANDS	280(sh),286(m),338(w,sh), 348(s),358(s),377(m), 425(sh),432(m),479(m), 692(s),744(s),782(m),997 (m),1024(s),1080(s),1170(s) 1180(s),1297(m),1389(m), 1575(s)		250(w),262(w),275(w),287(m), 350(s,d1),365(sh),420(sh), 430(m),480(ms),693(s),744 (s),781(m),998(m),1024(s), 1079(s),1170(s),1180(s), 1300(m),1389(m),1575(s)	

TABLE 4.22. RR and IR Data for $[\text{Et}_4\text{N}]_2[\text{Fe}_4\text{X}_4(\text{SePh})_4]$ (X = S, Se).

	X = S		X = Se	
	Band Maxima (cm^{-1})	Intensity at 482.5 nm excitation	Band Maxima (cm^{-1})	Intensity at 482.5 nm excitation
SOLID - RR	143	2	150	w
	208	w	204	s
	229	1	215	sh
	247	1	234	s
	270	w	260	w
	288	1	278	m
	309	10	311	s
	362	w	384	vw
	384	1	405	vw
	406	1		
	468	vw		
		<u>OTHER</u>		<u>BANDS</u>
	58, 67, 64, 84, 91, 101, 107, 116, 124, 132 (all m-w, n)		108, 116, 124 (all m-w, n).	
SOLUTION -RR	228(w), 249(1, ρ 0.3), 289 (2, ρ 0), 310 (10, ρ 0.3)		204(9, ρ 0.1), 238 (1), 271(3), 311 (10, ρ 0.3)	
IR-SELECTED BANDS	297(s), 312(s), 379(s), 403(w, sh), 466(s), 667(s), 694(s), 790(s), 902(m), 1018(s), 1064(s), 1179(s), 1230(m, br), 1296(m), 1304(m), 1395(m), 1572(s)		256(mw), 275(m), 287(mw), 312(w), 466(s), 659(s), 688(s), 780(ms, br), 993(m), 1016(s), 1059(ms), 1167(s, br), 1560(ms, br)	

TABLE 4.23. RR and IR Data for $[\text{Et}_4\text{N}]_2[\text{Fe}_4\text{X}_4(\text{SBz})_4]$ (X = S, Se).

	X = S		X = Se	
	Band Maxima (cm^{-1})	Intensity at 482.5 nm excitation	Band Maxima (cm^{-1})	Intensity at 482.5 nm excitation
SOLID-RR	245	2	213	m
	268	1	236	s
	334	10	258	s
	356	6	~370	m, vbr, mlt.
	386	4	474	w
	474	1		
	OTHER BANDS 67, 75, 83, 91, 99, 107, 116, 123, 132, 140, 172 (all m-w, n), 293(w, m on 568.2 nm), 506(w), 680 (w, vbr), 1000(w)			
SOLUTION-RR	245(mw, ρ 0.7 ± 0.2), 271(w, ρ 0.7 ± 0.2), 338(s, ρ 0), 361(w)		214(s, ρ 0.1), 280 (w, ~ depol.), 378 (s, part obsc., pol).	
IR-SELECTED BANDS	332(m), 355(s), 364(w, sh), 381(m), 473(mw), 562(mw), 700(m, dl), 766(s), 778 (m), 997(s), 1024(m), 1065(m), 1170(s), 1221(m) 1389(m), 1595(s)		273(s), 282(m), 328(w), 355(s, dl), 472(ms), 560(m), 760(m), 780(m), 1000(s), 1027(m), 1066(m), 1172(s), 1198(m), 1222(m), 1367(m), 1391(s), 1598(s)	

Fig 4.19 Solid-state Raman spectra of $[\text{Et}_4\text{N}]_2[\text{Fe}_4\text{X}_4(\text{SPh})_4]$ ($\text{X}=\text{S},\text{Se}$) at 530.9nm excitation

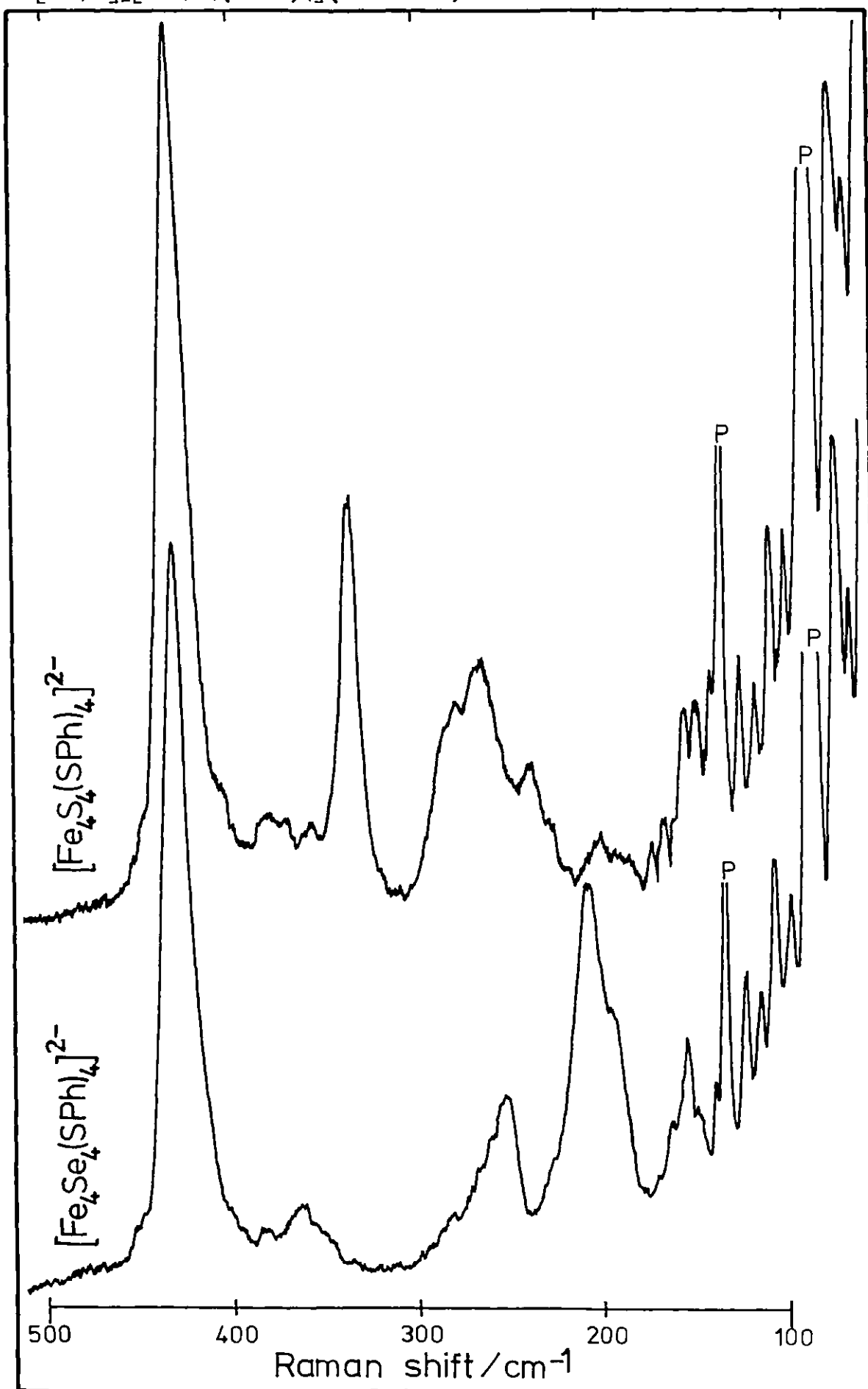


Fig. 4.20 Solid-state infra-red absorption spectra for the tetramer complexes

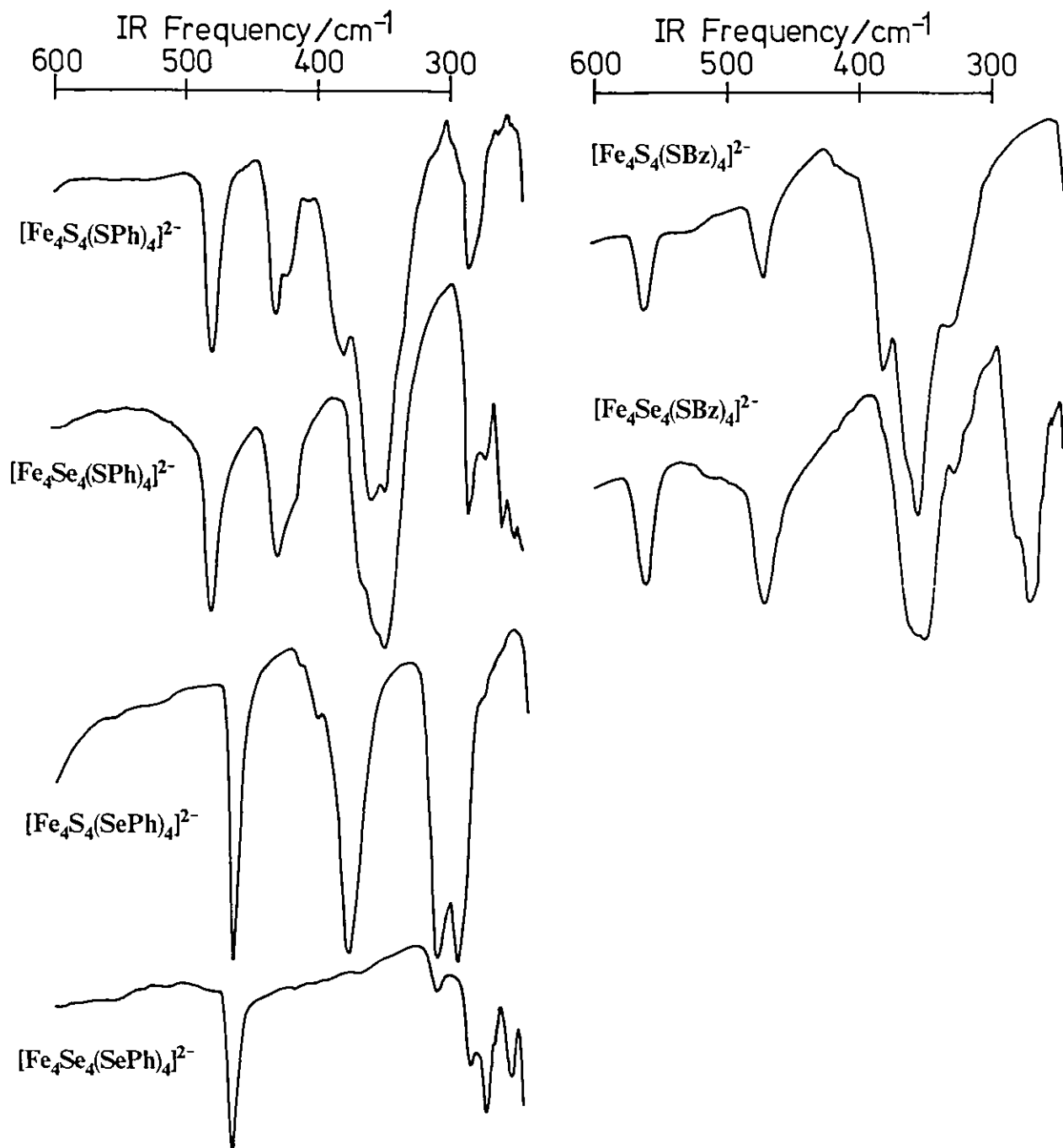


Fig 4.21 Solid-state Raman spectra of $[\text{Et}_4\text{N}]_2[\text{Fe}_4\text{X}_4(\text{SePh})_4]$ ($\text{X}=\text{S},\text{Se}$) at 482.5nm excitation

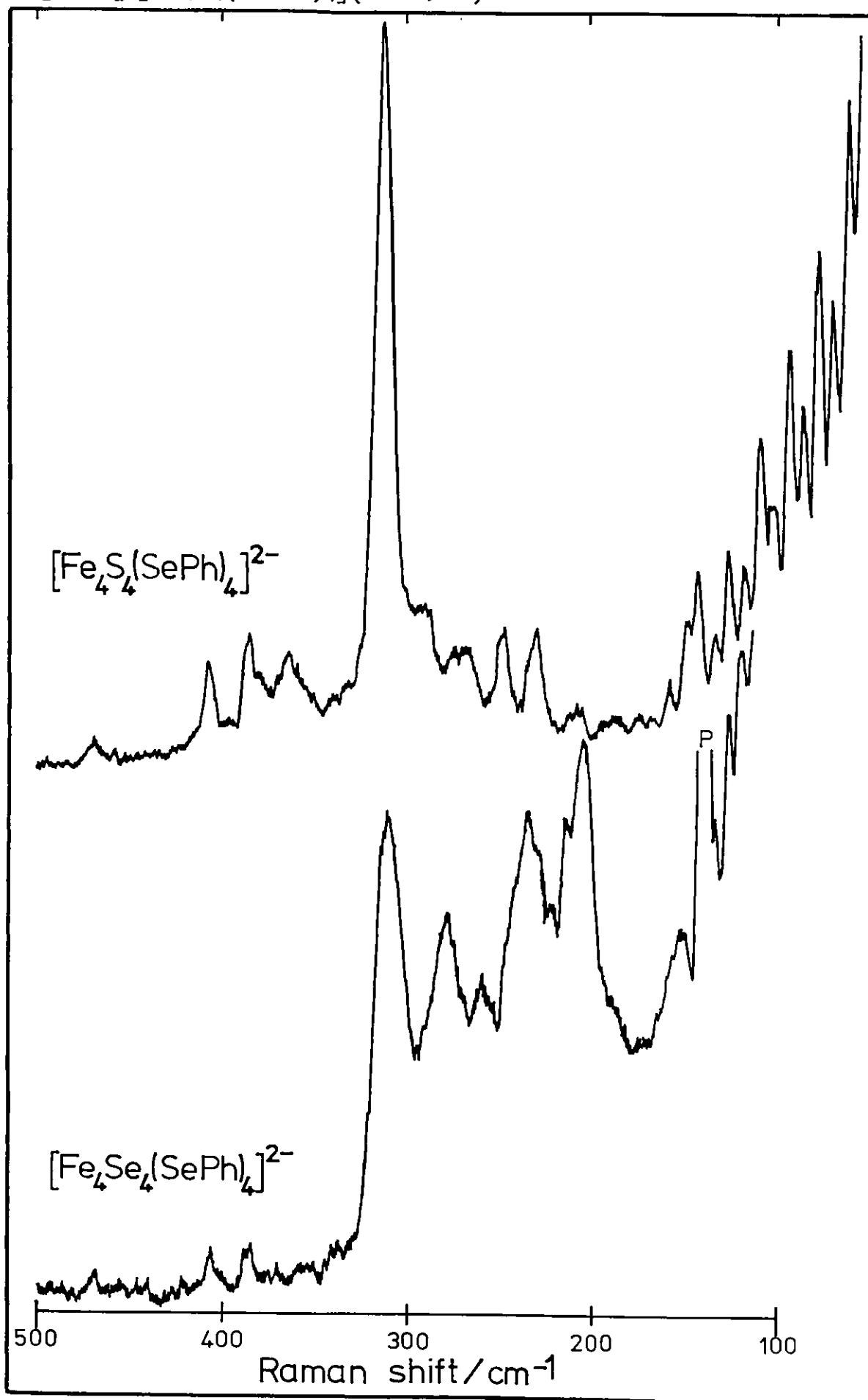
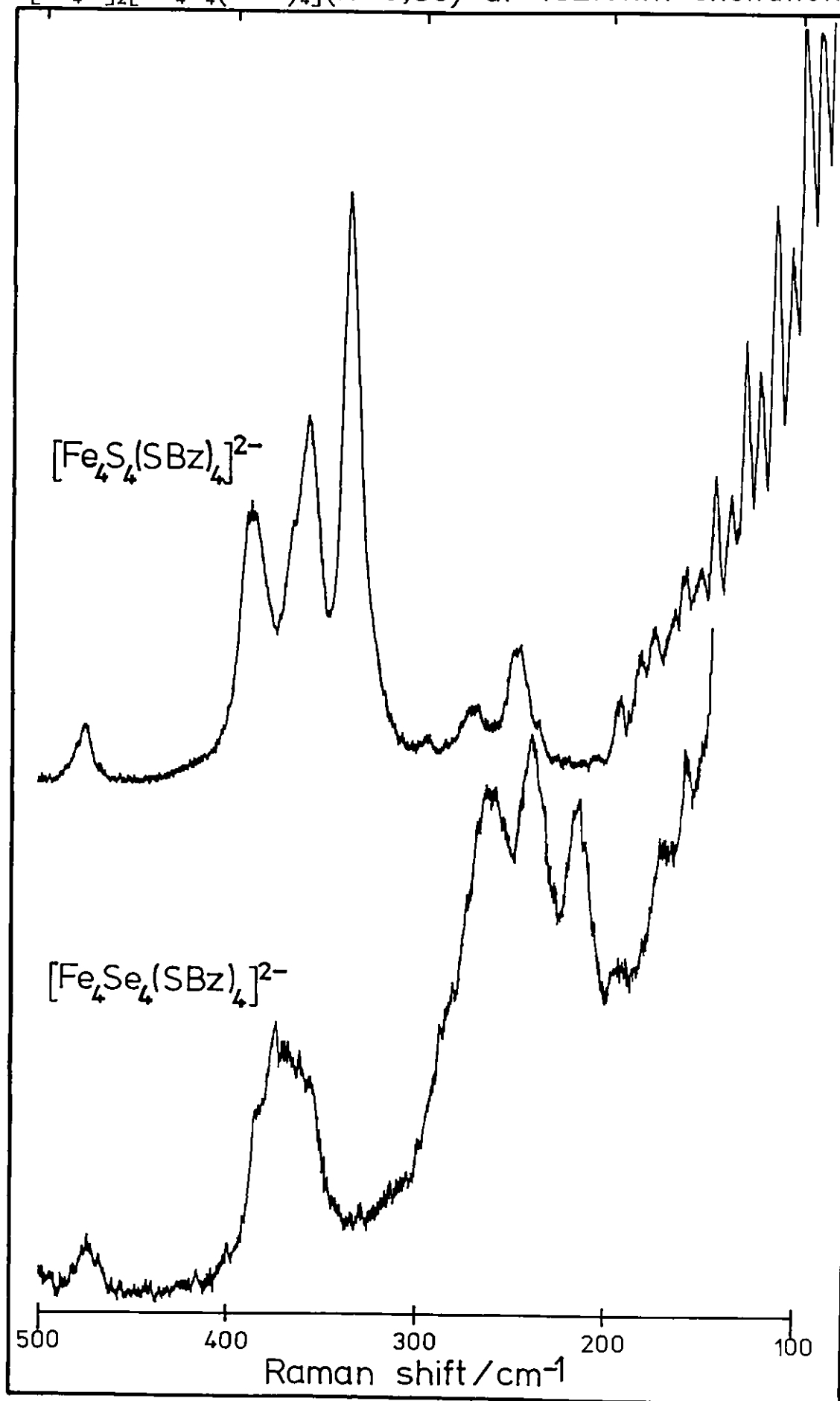


Fig 4.22 Solid-state Raman spectra of $[\text{Et}_4\text{N}]_2[\text{Fe}_4\text{X}_4(\text{SBz})_4]$ ($\text{X}=\text{S},\text{Se}$) at 482.5nm excitation



4.4.2.1. $[\text{Fe}_4\text{X}_4(\text{YPh})_4]^{2-}$ (X, Y = S, Se).

The intense Raman band at 434 cm^{-1} (polarised in solution) in $[\text{Fe}_4\text{S}_4(\text{SPh})_4]^{2-}$ has a counterpart at 431 cm^{-1} in $[\text{Fe}_4\text{Se}_4(\text{SPh})_4]^{2-}$ and is assigned to ν_1 . PhSe-ligated derivatives show corresponding peaks shifted to 309 and 311 cm^{-1} . These frequencies are comparable to those observed for the dimer species with phenylchalcogenide ligands (Section 4.3). Similarly the IR spectra for $[\text{Fe}_4\text{S}_4(\text{SPh})_4]^{2-}$ and $[\text{Fe}_4\text{Se}_4(\text{SPh})_4]^{2-}$ show bands around $420\text{--}430\text{ cm}^{-1}$; these are attributable to a splitting of the triply degenerate ν_9 terminal ligand stretch. This vibration should be weaker in the Raman and is masked by ν_1 . Using the change in ν_1 as a measure of the frequency shift accompanying PhS/PhSe substitution, either or both IR absorptions at 312 and 297 cm^{-1} in $[\text{Fe}_4\text{S}_4(\text{SePh})_4]^{2-}$ are candidates for ν_9 . Weaker bands appear around the same frequencies, 312 and 287 cm^{-1} , in the fully selenium substituted $[\text{Fe}_4\text{Se}_4(\text{SePh})_4]^{2-}$. The in-phase cube breathing mode, ν_2 , is reasonably assigned to the polarised 338 cm^{-1} Raman line for $[\text{Fe}_4\text{S}_4(\text{SPh})_4]^{2-}$, shifted to 209 cm^{-1} in $[\text{Fe}_4\text{Se}_4(\text{SPh})_4]^{2-}$. Comparably, $[\text{Re}_4\text{S}_4(\text{CN})_{12}]^{4-}$ has this A_1 mode at 335 cm^{-1} however, the frequency shift is only to 280 cm^{-1} in $[\text{Re}_4\text{Se}_4(\text{CN})_{12}]^{4-}$.²¹⁸ The $\nu_2(\text{Se}):\nu_2(\text{S})$ ratio of 0.62 for $[\text{Fe}_4\text{S}_4(\text{SPh})_4]^{2-}/[\text{Fe}_4\text{Se}_4(\text{SPh})_4]^{2-}$ is low but not in gross disagreement with values observed for the μ_2 -bridged iron dimers, which have comparable stretching frequencies. For $[\text{Fe}_4\text{S}_4(\text{SePh})_4]^{2-}$ no intense Raman shifts in excess of 309 cm^{-1} are observed and it is necessary to assign ν_2 at this frequency in coincidence with ν_1 . This is not unrealistic in view of the high intensity of this band and the mixing of ν_1 with the core breathing modes which might be expected given the relatively high mass of the terminal selenium ligand.

The remaining $T_d A_1$ vibration, ν_3 , can be described as mainly interior cluster-angle deformation or as mainly iron-iron stretching in character.²¹⁹ Although at a rather high frequency for this kind of vibration the polarised band at 267 cm^{-1} may be a feasible assignment for ν_3 . This out-of-phase breathing mode occurs at 215 cm^{-1} in $[\text{Re}_4\text{S}_4(\text{CN})_{12}]^{4-}$ ²¹⁸ and at 214 cm^{-1} in $\text{Cp}_4\text{Fe}_4(\text{CO})_4$ ²²⁰; both compounds have strong metal-metal bonding. $[\text{Pb}_4(\text{OH})_4]^{4+}$,²²¹ $\text{Tl}_4(\text{OEt})_4$ ²²² and $\text{Pt}_4(\text{Me})_{12}\text{X}_4$ ($\text{X} = \text{OH}, \text{Cl}, \text{I}$)²²³ probably possess weak metal-metal interactions, and relatively strong bands in the range 80 to 140 cm^{-1} have been assigned to ν_3 . In general, the frequency of ν_3 is expected to increase as the mode becomes more metal-metal stretching in character. The Fe-Fe distance in $[\text{Fe}_4\text{S}_4(\text{SPh})_4]^{2-}$ averages 2.736 ⁷⁵ and any bonding interaction must be weak. For a high M:X mass ratio where the $T_d A_1$ vibrational descriptions of Table 4.20 apply the terminal X-ligand atom and M_4 tetrahedra move in phase for ν_2 & ν_3 and out of phase for ν_1 and it is evident that as the M/X masses approach parity the internal coordinate variations used to describe ν_1 will no longer be dominant and will apply to some extent to the descriptions of ν_2 and ν_3 also. Approximate force constant calculations for $\text{Fe}_4(\text{CO})_4\text{Cp}_4$ ²²⁰ and the cubic $[(\text{Mo}_6\text{Cl}_8)\text{Cl}_6]^{2-}$ ²²⁴ reflect a very substantial interaction of the coordinates for ν_3 and ν_1 . A greater mixing must be expected in the case of $[\text{Fe}_4\text{S}_4(\text{SPh})_4]^{2-}$, leading to an increased frequency for ν_3 . It is on these grounds that the assignment of ν_3 to 267 cm^{-1} is considered tenable. A high value for this mode is also in keeping with Raman shifts interpreted as out-of-phase bridge breathing vibrations in some of the $[\text{Fe}_2\text{S}_2(\text{SR})_4]^{2-}$ complexes (Section 4.33).

In $[\text{Fe}_4\text{Se}_4(\text{SPh})_4]^{2-}$ a polarised line at 197 cm^{-1} is tentatively assigned to ν_3 , possibly on excessive shift from 267 cm^{-1} considering the arguments invoked above. The mode has an identical frequency in $[\text{Re}_4\text{Se}_4(\text{CN})_{12}]^{4-}$.²¹⁸ Two weak polarised bands at 247 and 288 cm^{-1} are candidates for ν_3 in $[\text{Fe}_4\text{S}_4(\text{SePh})_4]^{2-}$. More mixing of ν_1 and ν_3 might be anticipated for a higher terminal ligand-atom mass, leading to an increase in ν_3 .

An alternative assignment for ν_3 in $[\text{Fe}_4\text{S}_4(\text{SPh})_4]^{2-}$ is the weak band of unknown polarisation at the unexceptional frequency of around 200 cm^{-1} . It would then become necessary to assume that the 267 cm^{-1} line is due to ν_4 , which has a totally symmetric component in D_{2d} symmetry. The low depolarisation ratio and high relative intensity at 268 cm^{-1} do not favour this interpretation.

The $\nu_{12}(\text{T}_2)$ and $\nu_5(\text{E})$ vibrations are related to $\nu_3(\text{A}_1)$ by similarly becoming predominantly $\nu(\text{M-M})$ in character with increased tetra-metal bonding. For an isolated M_4 tetrahedron of like atoms, the frequency ratios predicted for the Raman active vibrations $\text{A}_1:\text{T}_2:\text{E}$ are $2:\sqrt{2}:1$.²²⁵ If the 200 cm^{-1} and a further weak peak at 150 cm^{-1} are tentatively ascribed to ν_{12} and ν_5 the ratios $2:1.5:1.1$ result for $[\text{Fe}_4\text{S}_4(\text{SPh})_4]^{2-}$. In view of the considerable mixing of modes which has been suggested use of this so called 'simple cluster ratio' rule might be considered unjustified, however, it has been found applicable to the low frequency vibrations of $[\text{Pb}_4(\text{OH})_4]^{4+}$ and $\text{Tl}(\text{OR})_4$ ²¹⁹ for which the weak Pb_4 , Tl_4 interactions must lead to considerable coupling with M-O stretching. The approximate fitting of the simple cluster ratio in $\text{Re}(\text{SMe})_4(\text{CO})_{12}$ ²²⁶ was considered adventitious, and this may also be the case here for $[\text{Fe}_4\text{S}_4(\text{SPh})_4]^{2-}$.

TABLE 4.24. $[\text{Fe}_4\text{X}_4(\text{YPh})_4]^{2-}$ (X, Y = S, Se) Vibrational Assignments.

X = Y = S			X = Se, Y = S			X = Y = Se			X = S, Y = Se			X = Y = S		
? ν_5	150	w		155	mw		150	w		143	mw	? ν_5	150	w
? ν_{12}	200	w,br		166	sh,w		204	p s		208	w	? ν_{12}	200	w,br
	240~dp	w		197	p sh,w		215	sh,w		229	mw		240~dp	w
ν_3	267	p mw		209	p m		234	s		247	p mw		267	mw
	280~dp	mw		254	dp mw		260	w		270	w		280~dp	mw
ν_2	338	p m		260	p sh,w		278	m		? ν_3 288	p w		338	p m
	382	w		362	w,br		311	p s		$\nu_1 + ?\nu_2$ 309	p vs		382	w
ν_1	434	p s		382	vw					362	w		434	p s
				431	p s					384	mw			
										406	mw			
	280	sh,w		250	w		256	mw		297	s		280	sh,w
	286	m		262	w		275	m		312	s		286	m
	338	sh,w		275	w		? ν_9 (287	mw		379	s		338	sh,w
	348	s		287	m		ligand? (312	w		403	sh,w		348	s
	358	s		350	s,dl								358	s
	377	m		365	sh,w								377	m
ν_9	(425	sh,m		(420	sh,m								(425	sh,m
	432	m		430	m								432	m

p - polarised solution counterpart ,

? - possible assignment

Returning to the IR spectra, increased difficulty is encountered in presenting any reasonable interpretation in terms of the simple descriptions in Table 4.20. The absorption at 377 cm^{-1} in $[\text{Fe}_4\text{S}_4(\text{SPh})_4]^{2-}$ is present also in $[\text{Fe}_4\text{S}_4(\text{SePh})_4]^{2-}$ (379 cm^{-1}), but is not seen in $[\text{Fe}_4\text{Se}_4(\text{SPh})_4]^{2-}$ (discounting a small shift to the shoulder at 365 cm^{-1}), and is presumably a stretching vibration involving the bridging chalcogenide. In $[\text{Fe}_4\text{Se}_4(\text{SPh})_4]^{2-}$ it is possibly split and shifted to $\sim 250\text{--}260\text{ cm}^{-1}$ where two partly obscured bands are observed; a frequency change in keeping with that observed for ν_2 in the Raman. All the remaining IR peaks for $[\text{Fe}_4\text{S}_4(\text{SPh})_4]^{2-}$ have close counterparts in the spectra of $[\text{Fe}_4\text{Se}_4(\text{SPh})_4]^{2-}$ but not in $[\text{Fe}_4\text{S}_4(\text{SePh})_4]^{2-}$, yet no further terminal ligand stretching vibrations are anticipated. As in T_d all the IR active modes are of the same symmetry, and also in D_{2d} the majority are E, intermixing is to be expected. No further explanation is proffered in the absence of a more quantitative analysis. It is noted that much of the broad and ill-resolved weak Raman scattering observed in the spectra of $[\text{Fe}_4\text{S}_4(\text{SPh})_4]^{2-}$ and $[\text{Fe}_4\text{Se}_4(\text{SPh})_4]^{2-}$ between 250 and 400 cm^{-1} correlates with the strong IR absorptions.

4.4.2.2. $[\text{Fe}_4\text{X}_4(\text{SBz})_4]^{2-}$ (X = S, Se).

The starting point in interpreting the Raman spectrum of $[\text{Fe}_4\text{S}_4(\text{SBz})_4]^{2-}$ is the designation of the strong band at 334 cm^{-1} (338 cm^{-1} and polarised in solution) as ν_2 , a frequency very similar to that of the corresponding transition in $[\text{Fe}_4\text{S}_4(\text{SPh})_4]^{2-}$. A similar S/Se frequency shift to that ascribed to the thiophenyl ligated tetramers is obtained for this band if it is assigned at 213 cm^{-1} (polarised in solution) in $[\text{Fe}_4\text{Se}_4(\text{SBz})_4]^{2-}$. Tang *et al.*¹⁷² in their preliminary solution spectra for $[\text{Fe}_4\text{S}_4(\text{SBz})_4]^{2-}$

(Figure 4.18) tentatively assigned a band at 332 cm^{-1} to the terminal breathing mode ν_1 and a lower frequency at 275 cm^{-1} to ν_2 . The higher frequency peaks at 356 and 386 cm^{-1} , seen in the spectra of the solid, are obscured in solution by Raman scattering around 400 cm^{-1} , ubiquitous for organic solvents. Comparison of the relative intensities of the bands between 300 and 400 cm^{-1} in $[\text{Fe}_4\text{S}_4(\text{SBz})_4]^{2-}$ with lines assigned to ν_1 and ν_2 in $[\text{Fe}_4\text{S}_4(\text{SPh})_4]^{2-}$ tends to favour the interpretation $\nu_1 = 332\text{ cm}^{-1}$, given by Tang et al. Also for $[\text{Fe}(\text{S}_2\text{-o-xylyl})_2]^{2-}$ and $[\text{Fe}_2\text{S}_2(\text{S}_2\text{-o-xylyl})_2]^{2-}$, which like $[\text{Fe}_4\text{S}_4(\text{SBz})_4]^{2-}$ possess $\text{ArCH}_2\text{S-}$ coordination, symmetric terminal ligand stretching descriptions have been attributed to lower frequencies ($300\text{-}320\text{ cm}^{-1}$) than for PhS- coordination. This may be an effect of chelation rather than of the aliphatic nature of the ligand. The frequency shift on going to selenium bridging, low intensity at 268 cm^{-1} for assignment to ν_2 and the compatibility with the corresponding $[\text{Fe}_4\text{S}_4(\text{SPh})_4]^{2-}$ mode, are felt to present a stronger argument than the points made above in defence of the assignments of Tang, et al., and the original designation $\nu_2 = 334$ is favoured. The lines at 356 and 386 cm^{-1} could then be due to ν_1 and, although either is rather intense to be a T_2 mode, to ν_9 . No polarisation data could be obtained and relative intensities are not a useful criterion for distinguishing which line could belong to which mode, as whilst the 356 cm^{-1} band is marginally bigger than that at 386 cm^{-1} with 482.2 nm excitation, the reverse is true when using 530.9 nm . Both frequencies have close counterparts in the IR, and on the grounds that the 355 cm^{-1} absorption is strong, as expected, and a better match to the Raman than the 381 cm^{-1} absorption, which is shifted on selenium substitution, ν_9 is assigned to 356 cm^{-1} (Ramán),

355 cm^{-1} (IR) and ν_1 to 386 cm^{-1} (Raman). In $[\text{Fe}_4\text{Se}_4(\text{SBz})_4]^{2-}$ the two modes appear as a broad unresolved Raman feature centred around 370 cm^{-1} and the T_2 355 cm^{-1} IR absorption is also unshifted from that in $[\text{Fe}_4\text{S}_4(\text{SBz})_4]^{2-}$ whilst being slightly more split. The analysis for the 381 cm^{-1} IR band follows that for the comparable 377 cm^{-1} feature in $[\text{Fe}_4\text{S}_4(\text{SPh})_4]^{2-}$, being described as mainly $\nu(\text{Fe}-\text{S}_p)$ and shifted to 273, 282 cm^{-1} on selenium substitution. The relative intensities at 381 cm^{-1} in $[\text{Fe}_4\text{S}_4(\text{SBz})_4]^{2-}$ and 273, 282 cm^{-1} in $[\text{Fe}_4\text{Se}_4(\text{SBz})_4]^{2-}$ would seem to imply that the former band does not contain all the absorption from ν_{10} and ν_{11} but that a further contribution lies buried in the poorly resolved envelope between 300 and 400 cm^{-1} .

Following the principles used to interpret the spectrum for $[\text{Fe}_4\text{S}_4(\text{SPh})_4]^{2-}$ the Raman lines at 268 and 245 cm^{-1} in $[\text{Fe}_4\text{S}_4(\text{SBz})_4]^{2-}$ might be considered good candidates for ν_3 . Inconsistent with this, however, a high value of the depolarisation, $\rho \approx 0.5$, is found at 245 and 271 cm^{-1} in the solution spectrum, although it is not possible to obtain an accurate estimate of ρ for these bands which are weak and on a high fluorescent background. Tang *et al.*¹⁷² consider the band they observe at 275 cm^{-1} in $[\text{Fe}_4\text{S}_4(\text{SBz})_4]^{2-}$ to be polarised; however, due to the lower laser powers necessary in their study of static samples, leading to less than optimal spectral quality, any determination of ρ is likely to be subject to a large error.

The origin of the strong Raman lines at 236 and 258 cm^{-1} in $[\text{Fe}_4\text{Se}_4(\text{SBz})_4]^{2-}$ is not understood. The weak peak at 474 cm^{-1} in both BzS-ligated tetramers could arise from a partly resonance-enhanced $\delta(\text{S}-\text{CH}_2\text{Ph})$ mode. In the IR spectrum of $[\text{Fe}_4\text{S}_4(\text{SBz})_4]^{2-}$ the medium intensity absorption at 332 cm^{-1} appears also in $[\text{Fe}_4\text{Se}_4(\text{SBz})_4]^{2-}$ at

328 cm^{-1} and could possibly be a splitting from ν_9 , though it is not seen in the Raman for $[\text{Fe}_4\text{Se}_4(\text{SBz})_4]^{2-}$ and the 338 cm^{-1} band in $[\text{Fe}_4\text{S}_4(\text{SBz})_4]^{2-}$ solution spectra has a depolarisation ratio close to zero.

TABLE 4.25. $[\text{Fe}_4\text{X}_4(\text{BzS})_4]^{2-}$ (X = S, Se) vibrational assignments.

RR	X = S		X = Se	
	245	\sim dp mw	213	p m
	268	\sim dp w	236	s
ν_2	334	p s	258	s
$?\nu_9$	356	s	ν_1 and ν_9	370
$?\nu_1$		m		
ligand	474	w		
<u>IR</u>				
	332	m	273	s
ν_9	355	s	282	m
	381	m	328	w
			355	s, dl

4.4.2.3. Resonance in the Raman Spectra of the 4Fe Complexes.

In acetone solution the following lowest energy intense bands are observed: 456 nm $[\text{Fe}_4\text{S}_4(\text{SPh})_4]^{2-}$, 463 nm $[\text{Fe}_4\text{Se}_4(\text{SPh})_4]^{2-}$, 476 nm $[\text{Fe}_4\text{S}_4(\text{SePh})_4]^{2-}$, 485 nm $[\text{Fe}_4\text{Se}_4(\text{SePh})_4]^{2-}$, 417 nm $[\text{Fe}_4\text{S}_4(\text{SBz})_4]^{2-}$ and 420 nm $[\text{Fe}_4\text{Se}_4(\text{SBz})_4]^{2-}$. Maxima at similar wavelengths have been reported in DMF.²¹² Only for $[\text{Fe}_4\text{S}_4(\text{SPh})_4]^{2-}$ has the solid reflectance been checked, and in the region of exciting wavelengths used to obtain the Raman spectra reported here this shows a single broad band centred around 500 nm. For $[\text{Fe}_4\text{S}_4(\text{SBz})_4]^{2-}$ solid state spectra at 5 K show better resolution,

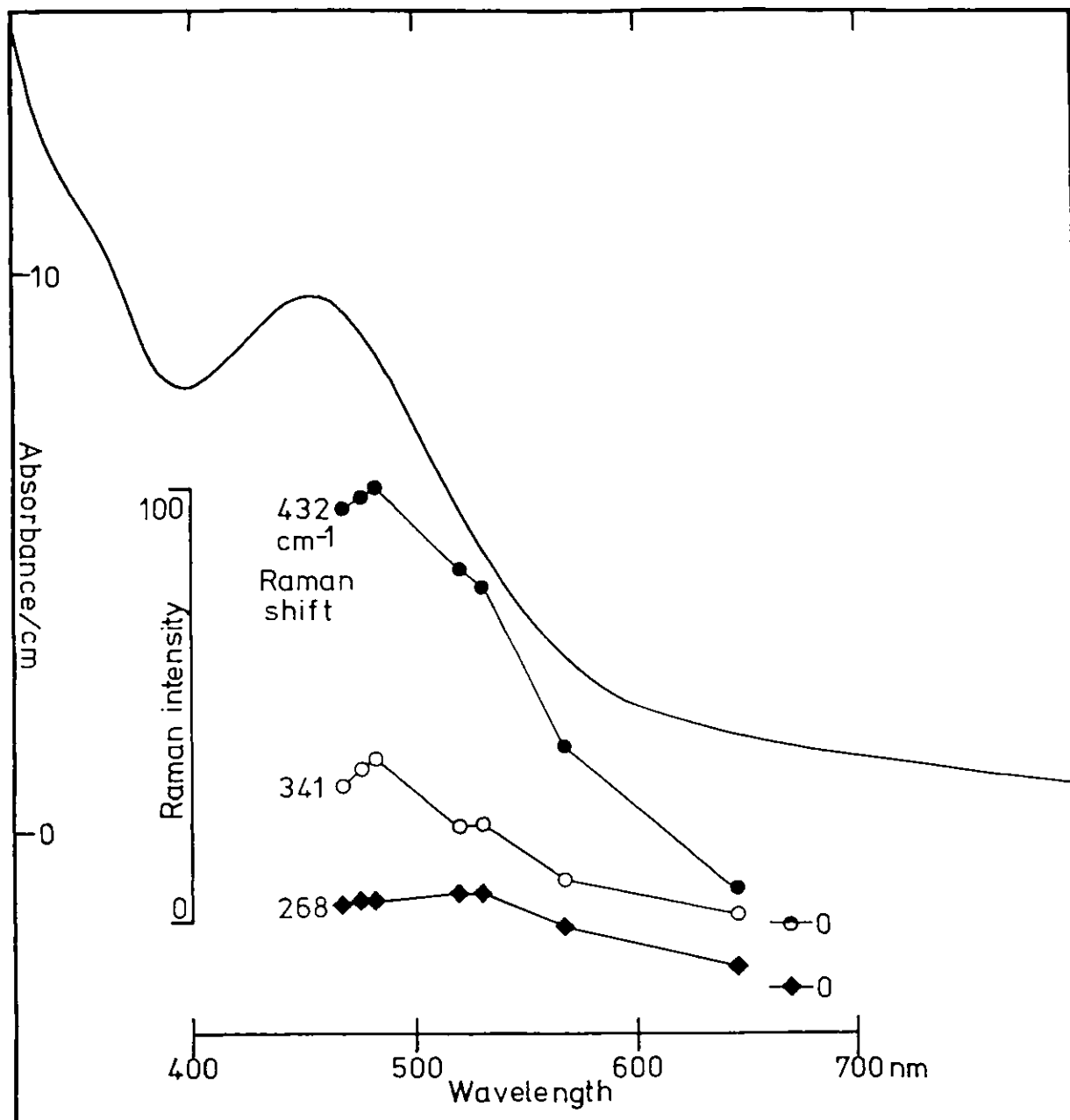


Figure 4.2.3 Electronic spectrum of $[\text{Fe}_4\text{S}_4(\text{SPh})_4]^{2-}$ in acetone and resonance enhancement of several Raman peaks.

having a narrow intense band at around 490 nm and weaker features at 600 and 800 nm.²²⁷

Figure 4.23 shows the relative variation in intensity with excitation wavelength of the three polarised bands observed for $[\text{Fe}_4\text{S}_4(\text{SPh})_4]^{2-}$ in acetone solution. Taking concentrations into account the 432 cm^{-1} peak is some 2500 times more intense than the acetone symmetric stretch at 787 cm^{-1} . Whilst the blue lines available on a Krypton laser are

separated by only a small wavelength interval, the decrease in resonance enhancement on going from 482.5 to 468.0 nm, being reproducible, is felt to be genuine. For the 432 cm^{-1} peak it is estimated that maximal intensity would be achieved at $\sim 490\text{ nm}$. The 310 and 311 cm^{-1} Raman fundamentals found for acetone solutions of PhSe-ligated tetramers show greatest resonance enhancement at wavelengths close to the 530.9 nm Krypton emission, whilst at 482.5 nm respective intensities are comparable to those at 568.2 nm . Thus, the excitation profiles for the terminal-ligand stretching modes peak at around 30 to 40 nm higher than the absorption maxima in the electronic spectra. Unlike the case of the two iron complexes, the low energy absorptions in the visible spectra of the tetramers show no evidence of any underlying band at higher wavelength.

4.4.3. General Conclusions Concerning Tetramer Complexes.

The Raman spectra for the $[4\text{Fe-4S}]^{2+}$ cluster containing proteins, Chromatium Hipip and C. Pasteurianum Fd, show similar features to those described for $[\text{Fe}_4\text{S}_4(\text{SR})_4]^{2-}$ analogues in the previous two sections. Bands at 338 and 345 cm^{-1} in the proteins correlate with those at 338 cm^{-1} in $[\text{Fe}_4\text{S}_4(\text{SPh})_4]^{2-}$ and 334 cm^{-1} (338 in solution) in $[\text{Fe}_4\text{S}_4(\text{SBz})_4]^{2-}$. The 356 and 386 cm^{-1} lines observed in $[\text{Fe}_4\text{S}_4(\text{SBz})_4]^{2-}$ compare with those at 360 and 365 cm^{-1} and possibly other weak peaks 20 to 40 cm^{-1} higher in Hipip and Fd. It is fitting that, as in the case of the $2\text{Fe}2\text{S}$ results, the Raman from the aliphatic, as opposed to aromatic, thiol ligated model complex, more closely resembles that from the protein. As already detailed the assignment of $\nu_2 = 334\text{ cm}^{-1}$ for $[\text{Fe}_4\text{S}_4(\text{SBz})_4]^{2-}$ is in contention with

$\nu_2 = 275$, $\nu_1 = 332 \text{ cm}^{-1}$ given by Tang et al.¹⁷² and this extends to the designations inferred for the proteins in the above comparisons. The appearance of a polarised band to higher frequency close to the most intense line at $\sim 340 \text{ cm}^{-1}$ is explained by these authors as resulting from a lowering of cluster symmetry from tetrahedral so as to induce totally symmetric character into an otherwise non-totally symmetric mode. The interpretation indicated by this present work is that these lines are due to ν_1 and that the low frequency polarised 250 cm^{-1} band, seen only in Hipip, is ν_3 .

The structure of $[\text{Fe}_4\text{S}_4(\text{SR})_4]^{2-}$ species in solution has been described as retaining the crystallographically observed D_{2d} distortion of the $[\text{4Fe4S}]^{2+}$ core in the solids.²²⁸ No gross structural changes are expected on dissolution and in keeping with this the Raman spectra in solid and solution show very similar peak positions (however, the Raman spectra may be insensitive to small structural changes - see below). On reduction to the trianion a considerable structural change occurs, for $[\text{Fe}_4\text{S}_4(\text{SPh})_4]^{2-/3-}$ the distortion of the cubane core changes from a compression along one of the C_2 axes into an elongation.²²⁹ Although at present no full description of the Raman for $[\text{Fe}_4\text{S}_4(\text{SPh})_4]^{2-/3-}$ has been published, Reynolds et al. make reference to preliminary work by Spiro [reference 216; see references and notes 34 to 36] in quoting $\nu_2 = 343$ and 341 cm^{-1} for the dianion and trianion respectively. They have taken this small change in frequency as indicating a weak contribution from core structural rearrangement, to the total free energy of activation for the redox process. The symmetry in $[\text{Fe}_4\text{S}_4(\text{SBz})_4]^{3-}$ is lower than tetragonal, containing six short (mean 2.302\AA) and six long (mean 2.331\AA) $\text{Fe}-\text{S}_b$ core bonds, so arranged as to afford idealised C_{2v} symmetry.²³⁰ This is evidenced in the differences of Mössbauer and magnetic properties for

solid PhS- and BzS-ligated trianions. In solution these properties become essentially coincident and similar to solid $[\text{Fe}_4\text{S}_4(\text{SPh})_4]^{3-}$.²²⁸

Preliminary Raman measurements have been made for $[\text{Et}_4\text{N}]_3[\text{Fe}_4\text{S}_4(\text{SBz})_4]$ in solid state and show bands at 235(ms), 338(s), 356(ms), 387(s). The material presents increased difficulty over $[\text{Et}_4\text{N}]_2[\text{Fe}_4\text{S}_4(\text{SBz})_4]$ with regard to air sensitivity, fluorescent background and photodecomposition. The low signal to noise ratio necessitated the use of a wide slit program resulting in poorer resolution; the quality of spectrum being similar to that for $[\text{Fe}_4\text{Se}_4(\text{SBz})_4]^{2-}$ in Figure 4.22. In view of the similarity of the above frequencies to those observed for the dianion it would seem that Raman is incapable of revealing the changes in structure accompanying reduction.

Magnetic measurements indicate a J value of $\sim 230 \text{ cm}^{-1}$ in $[\text{Fe}_4\text{S}_4(\text{SBz})_4]^{2-}$ and $[\text{Fe}_4\text{X}_4(\text{SPh})_4]^{2-}$ (X = S, Se).²²⁹ Spin-flip transitions of the sort invoked by Blum *et al.*,^{114,115} would then be anticipated from S = 0 at energies around 460, 1380, 2760 cm^{-1} and from S = 1 at energies around 920, 2300 cm^{-1} . As with the case of the dimers no satisfactory evidence for Raman scattering by such a process is forthcoming in the data obtained from tetramer samples.

ADDENDUM

Since completion of the analysis presented in this section, Spiro, et al. [J. Biol. Chem. 256, 9806 (1981) and J. Biol. Chem. 257, 2447 (1982)] have reported much improved Raman spectra for the $[4\text{Fe-4S}]^{2+}$ ferredoxin from C. pasteurianum. They observe bands at 247, 271, 295, 335, 356 and 394 cm^{-1} which correlate well with the Raman shifts at 245, 268, 293, 334, 356 and 386 cm^{-1} described in Table 4.23 for $[\text{Fe}_4\text{S}_4(\text{SBz})_4]^{2-}$. Using substitution of core sulphur by ^{34}S the authors have been able to observe shifts of $4\text{-}6\text{ cm}^{-1}$ in bands resulting from Fe_4S_4 core vibrations. In this way, they too are able to correct the assignment of ν_2 to $\sim 271\text{ cm}^{-1}$ made by Tang et al.,¹⁷² assigning this mode instead to the most intense peak in C. pasteurianum at 335 cm^{-1} . The other peaks in the spectrum have only 10-20% the intensity of this band, unlike the case for $[\text{Fe}_4\text{S}_4(\text{SBz})_4]^{2-}$ where the features at 356 and 386 cm^{-1} attain ca.50% or more of the intensity at 334 cm^{-1} . In addition the protein spectrum lies in a trough of considerable background intensity and contains additional maxima to those described above, so that the direct compatibility of the remaining band positions may not be as valid as would at first appear to be the case from the figures. The protein band at 356 cm^{-1} is assigned to a superposition of ν_1 and ν_9 and the 394 cm^{-1} band to a T_2 core mode. Although in section 4.4.2.2. ν_9 was assigned to 356 cm^{-1} in the Raman of $[\text{Fe}_4\text{S}_4(\text{SBz})_4]^{2-}$ and a T_2 core mode to 381 cm^{-1} in the IR, for the Raman band at 386 cm^{-1} an assignment as ν_1 was considered as an alternative possibility to coincidence with ν_9 at 336 cm^{-1} . Whatever the case either band seems rather intense for a single T_2 mode and a second alternative possibility is that $\nu_1 = 356\text{ cm}^{-1}$ whilst the 386 cm^{-1} band is a superposition of ν_9 and a T_2 core mode. It is peculiar that correspondingly intense T_2 modes are not observed in the Raman spectra of $[\text{Fe}_4\text{S}_4(\text{SPh})_4]^{2-}$. This probably reflects the slightly higher symmetry of the latter compared with $[\text{Fe}_4\text{S}_4(\text{SBz})_4]^{2-}$.

4.5. Experimental - Sample Preparation.

Synthetic procedures for the compounds studied in this Section are described in Section 6.

4.5.1. Raman Samples.

Solid state spectra were obtained by the spinning disk technique. The compound was placed together with about 2 to 3 times the amount of finely ground dry KBr or KCl in a ca. 2 cm diameter screw-capped septum-sealed sample bottle. This transfer operation was effected rapidly and the container purged of oxygen by evacuation and N₂-flushing via a steel needle inserted through the rubber septum at a central hole in the metal cap. A magnetic bar, with a length only slightly smaller than the internal diameter of the sample bottle, previously placed in the container, was used to grind up and mix the solids by rapid rotation on an efficient magnetic stirrer. A period of 5 to 10 minutes was usually found sufficient to give an homogeneous fine-grained powder. This could be rapidly transferred in the open to a die and pressed under vacuum at 10 tons into a 13 mm disk. Generally, a supportive backing of pure KBr and KCl was used in disk preparation. For the very air sensitive $\{Et_4N\}_3[Fe_4S_4(SBz)_4]$ the transfer to the die and pressing operations were also carried out anaerobically in a plastic bag.

Although in the form of KBr pellets the compounds were found on the whole to have greatly reduced oxygen sensitivity, they were still handled anaerobically. The spectrometer (SPEX Ramalog V) sample compartment was fitted with a small plastic bag extending from the sample spinner to the collection optics (Figure 4.24). After rapid

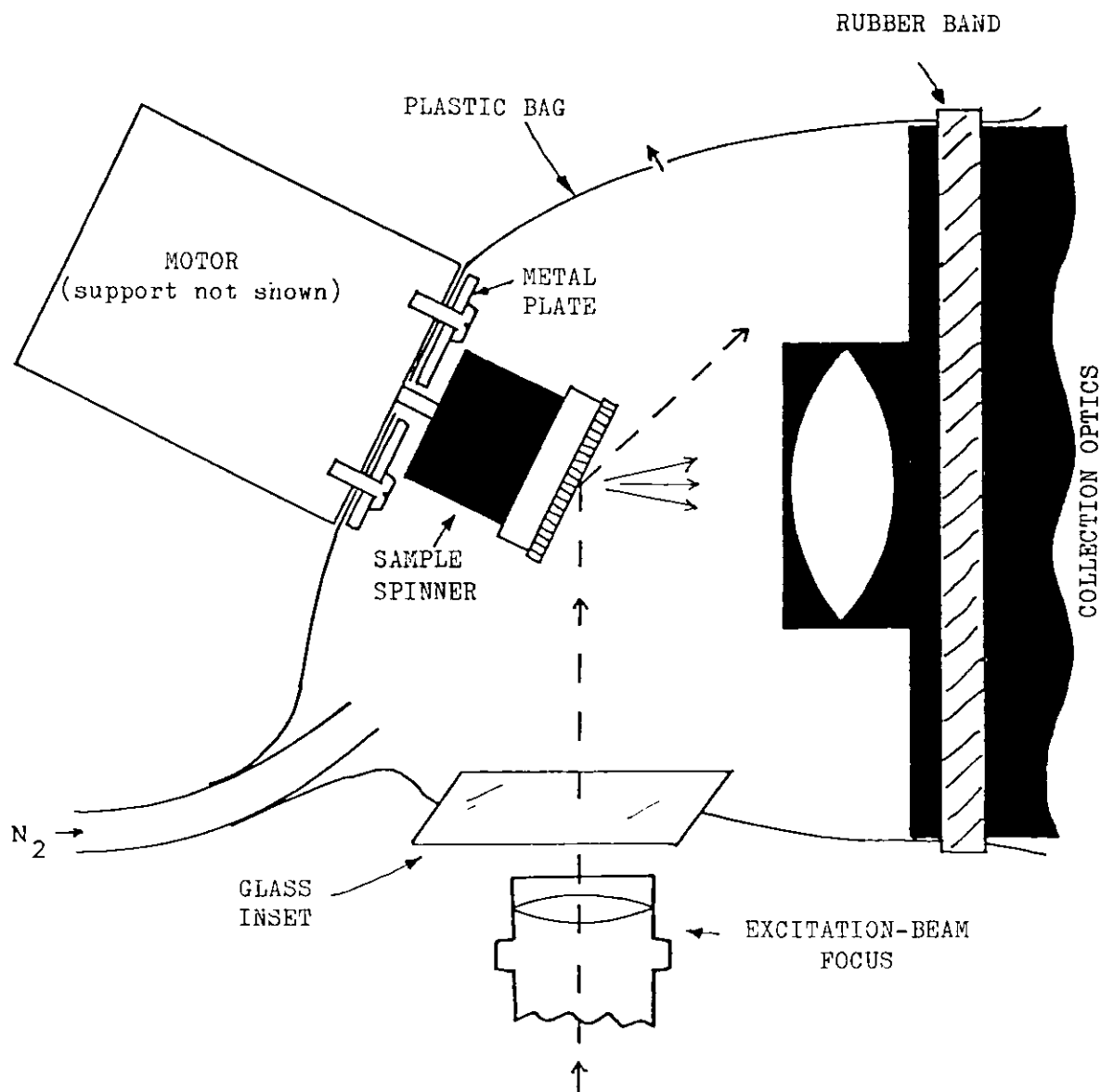


Figure 4.24. Details of Raman spectrometer (SPEX Ramalog V) sample-compartment arrangement for spinning samples in an inert atmosphere.

transfer of the disk to the holder under N_2 flow the plastic bag was fixed in place and purged of O_2 by a rapid stream of N_2 . After 5 mins the bag was sealed onto the collection optics with a rubber band and a gentle ingress of N_2 maintained. The laser beam is permitted to enter the bag via a glass microscope slide taped over a hold cut in the lower side.

Solution spectra were obtained in a 2 cm diameter rotating glass cell, of conventional design, sealed at the top with a cut-down septum.

4.5.2. IR Samples.

Samples for infrared measurements were diluted in spectroscopic polythene powder (Merck) using the magnetic stirrer technique outlined above. Longer stirring times were required to achieve good homogeneous dispersion of the complexes in the polythene. The powder was compressed at 10 tons under vacuum to give 13 mm diameter disks of approximately 0.1 mm thickness. Various concentrations and thicknesses were employed to obtain the maximum information. Measurements were made without further precautions against atmospheric oxidation of the complexes as the polythene gives excellent protection; no spectral differences were found between spectra obtained immediately (ca. 1 min) or after ca. 1 hr. Most spectra were measured within 5 to 10 mins after manufacture of the sample disk.

4.5.3. Selected Ligand Vibrations.

PhSH, Raman: 190ms, 280m, 415s, 619m, 701s, 919m, 1001vs, 1027s, 1094s, 2572s. IR: 466s, 689s, 699m, 733vs, 899m, 917m, 1023s, 1070m, 1091s, 1119ms, 1180mw, 1301mw, 1441s, 1383mw, 1479s, 1583s, 2534ms.

PhSe-SePh, Raman: 72m, 104s, 180w, 190vw, 214s, 265vw, 313s, 616w, 666w, 998s, 1022s. IR: 302mw, 400vw, 460s, 664m, 687s, 731vs, 900m, 998s, 1020s, 1062s, 1178m, 1298ms, 1380m, 1434s, 1570vs.

o-xylyl α, α' -dithiol, Raman: 75s, 108m, 130s, 230m, 332w, 518s, 593w, 670s, 769m, 789ms, 972m, 1047s. IR: 307mw, 393w, 450ms, 547ms, 594ms, 680s, 760s, 970ms, 1050ms, 1088ms, 1189m, 1248s, 1300ms, 1603m.

BzSH, Raman: 269mw, 339mw, 406vw, 474m, 559w, 622s, 682s, 762mw, 794m, 802m, 1003vs, 1032s. IR: 470m, 559m, 697vs, 758ms, 1072m, 1250ms, 1601m, 2565mw.

p-MeC₆H₄SH, Raman: 115s, 307w, 317w, 368w, 380s, 639ms, 796ms, 1098s. IR: 483s, 629mw, 800s, 914mw, 1019ms, 1099s, 1117m, 1183w, 1210m, 1307mw, 1380w, 1402m, 1494s, 1600w, 2565m.

p-ClC₆H₄SH, Raman: 115s, 305mw, 338ms, 343mw, 542w, 630mw, 741mw, 1066mw. IR: 342w, 483s, 525w, 542ms, 743m, 810vs, 1012s, 1095s, 1103s, 1178mw, 1393s, 1478s, 1570w, 2570m.

4.5.4. Conditions and Notes Concerning Figures and Tables.

TABLE 3

1. " - " indicates inability to observe band due to obscuring Rayleigh scattering or fluorescent background, plasma-tube emission line or poor signal to noise ratio (general).
2. Intensity (uncorrected peak height) ratioing is to make largest peak equal to 10 or 100 (general); correlation across excitation wavelengths for the solution is with reference to acetone internal standard 787 cm⁻¹ symmetric stretch.
3. Depolarisation ratios, ρ , are for 482.5 nm excitation, excepting 222 cm⁻¹ band - 647.1 nm excitation.
4. Solution spectra at 530.9 nm excitation are very poor quality due to large fluorescence.
5. Extra splittings to give many narrow lines in the 100-300 cm⁻¹ region together with a large intensity increase of the 103 cm⁻¹ peak have been occasionally and irreproducibly observed with 568.2 nm exctn. These are not understood.

Figure 4. IT 1.0s, TC 8s, SS $0.5 \text{ cm}^{-1}/\text{s}$, 2 Kcps FS, -150°C .

KBr disc sample.

647.1 nm exctn. ; P 100 mW , SR 5 cm^{-1}

568.2 nm exctn. ; P 100 mW , SR 6 cm^{-1}

530.9 nm exctn. ; P 50 mW , SR 4.5 cm^{-1}

Figure 5. 568.2 nm exctn. ; P 170 mW , SR 5 cm^{-1}

IT 0.5s, TC 8s, SS $0.5 \text{ cm}^{-1}/\text{s}$, FS 20 Kcps

Table 6. Correlation of intensities across solid-state RR spectra at different excitation wavelengths is with reference to the NO_3^- symmetric stretch of KNO_3 incorporated in the sample.

Figure 10. $[\text{Fe}_2\text{X}_2(\text{S}_2\text{-o-xylyl})_2]^{2-}$.

X = S 530.9 nm exctn. ; P 130 mW , SR 3 cm^{-1}

IT 1.0s, TC 10s, SS $0.25 \text{ cm}^{-1}/\text{s}$, FS 500 cps

X = Se 530.9 nm exctn. ; P 150 mW , SR 3 cm^{-1}

IT 1.0s, TC 10s, SS $0.25 \text{ cm}^{-1}/\text{s}$, FS 1 Kcps.

Figure 12. $[\text{Fe}_2\text{X}_2(\text{SPh})_4]^{2-}$ (X = S, Se).

482.5 nm exctn. ; P 50 mW , SR 2.5 cm^{-1}

IT 1.0s, TC 8s, SS $0.5 \text{ cm}^{-1}/\text{s}$

X = S FS 1 Kcps,

X = Se FS 2 Kcps

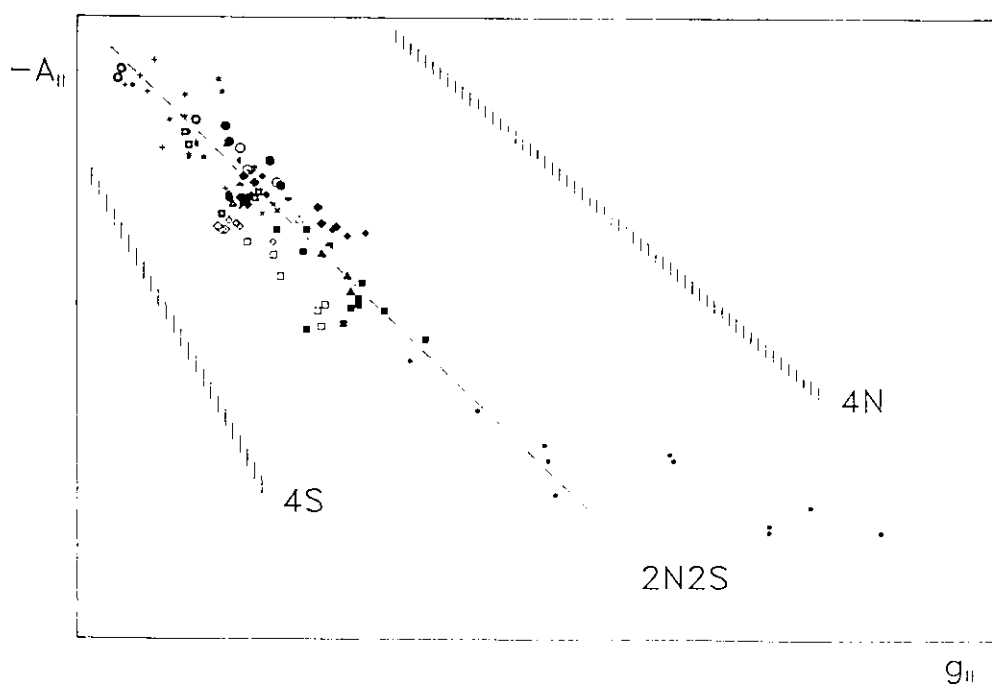
Figure 13. $[\text{Fe}_2\text{X}_2(\text{SePh})_4]^{2-}$

X = S 482.5 nm exctn. ; P 50 mW , SR 5 cm^{-1}

IT 1.0s, TC 8s, SS $0.5 \text{ cm}^{-1}/\text{s}$, FS 1 Kcps

X = Se 530.9 nm exctn. ; P 80 mW , SR 3.5 cm^{-1}

IT 1.0s, TC 8s, SS $0.5 \text{ cm}^{-1}/\text{s}$, FS 2 Kcps.

SECTION 5**TYPE 1 COPPER IN
BLUE-COPPER-PROTEINS;
 β -AMINOTHIONE MODEL COMPLEXES**

5. TYPE 1 COPPER IN BLUE-COPPER-PROTEINS; β -AMINOTHIONE MODEL COMPLEXES.

ABSTRACT	254
5.1. <u>Introduction: Proteins and Models.</u>	255
5.2. <u>Cu(II) β-Aminothione Complexes.</u>	260
5.2.1. Introduction	260
5.2.2. Synthesis of ligands	262
5.2.3. Synthesis and characterisation of Cu(II) β -aminothione complexes.	263
5.3. <u>Electronic Spectra.</u>	265
5.3.1. d-d bands	269
5.3.2. Charge-transfer bands	273
5.3.3. Electronic spectra of nickel(II) β -aminothiones.	275
5.4. <u>Electron Paramagnetic Resonance.</u>	277
5.1.4. EPR in solution	277
5.4.1.1. Lineshapes and simulation	280
5.4.1.2. g_{\parallel} vs $ A_{\parallel} $ analysis	285
5.4.2. EPR in Cu(II) doped Zn(II), Ni(II) and Cd(II) β -aminothione complexes	287
5.4.3. Discussion of EPR parameters	298
5.5. <u>Vibrational Spectra.</u>	306
5.5.1. Raman and IR spectra for Cu(RN-MeMeS) ₂ (R = Me, iBu)	306
5.5.2. Assignment	309
5.5.3. Raman assignments in blue-copper-proteins	311

5.6.	<u>Electrochemistry</u> .	315
5.6.1.	Difficulties in measurements	317
5.6.2.	Analysis of polarographic data	318
5.6.3.	Comparison of $E_{\frac{1}{2}}$ with those of other complexes	320
5.6.4.	Comparison of $E_{\frac{1}{2}}$ with blue-copper-proteins	322
5.7.	<u>Concluding Remarks and Summary.</u>	323
5.8.	<u>Experimental.</u>	324
5.8.1.	Preparation of α,β -unsaturated β -aminothione ligands and their precursors.	324
5.8.1.1.	Preparation via 1,2-dithiolium salts	324
5.8.1.2.	Preparation via β -ketoamines	325
5.8.2.	Preparation of cupric β -aminothione complexes	328
5.8.3.	Preparation of samples for spectroscopy	331
5.8.3.1.	Visible and near-IR	331
5.8.3.2.	EPR	331
5.8.3.3.	Raman	332
5.8.3.4.	Electrochemistry	332
5.8.4.	Zn(II), Ni(II) and Cd(II) complexes	332
5.8.5.	Experimental details for figures	335

The low temperature synthesis of $\text{Cu(II)N}_2\text{S}_2$ complexes incorporating N-substituted β -aminothione ligands is described. By varying the bulk of the N-substituent a systematically variable distortion in coordination geometry from square-planar toward tetrahedral may be imposed by means of steric hindrance. The resulting group of complexes represent the most extensive series of 2N2S coordinated Cu(II) currently available. They have been studied by electronic spectroscopy, EPR, resonance Raman spectroscopy and polarography, and comparisons made with corresponding properties of the type 1 centre in blue-copper-proteins.

Two intense absorption peaks are observed in the visible spectra of the complexes in the ranges ca. 600-680 nm and 470-540 nm. These are assigned as charge transfer bands and the former is correlatable with the intense 'blue' $S \rightarrow \text{Cu}$ transition found at similar wavelength in the blue-copper-proteins.

The parallel copper hyperfine splitting in the EPR spectra for frozen solution samples of the complexes varies from ca. $150 \times 10^{-4} \text{ cm}^{-1}$ down to $127 \times 10^{-4} \text{ cm}^{-1}$ as the steric bulk of the amino-substituent increases. Larger values of this parameter result for Cu(II) doped samples of the corresponding Ni(II) complexes. On the other hand $|A_{\parallel}|$ is greatly decreased in doped Zn(II) complexes, and the lowest values of ca. $100 \times 10^{-4} \text{ cm}^{-1}$ approach closely the region for blue-copper-proteins. A plot of $|A_{\parallel}|$ against g_{\parallel} for the 2N2S coordinated Cu(II) complexes shows an inverse relationship for these parameters intermediate between those for 4S and 4N coordination, which may be extrapolated to include several type 1 centres.

Solid state Raman and IR spectra are described for two of the complexes and an attempt made to assign the most intense features to fundamental vibrations of the CuN_2S_2 coordination unit.

Electrochemical measurements for a few of the complexes further establishes a role for 2N2S coordination and tetrahedral distortion in bringing about high redox potentials.

The spectroscopic and redox properties of the model complexes serve further to confirm general pseudo-tetrahedral CuN_2S_2 coordination in type 1 blue-copper-proteins.

5. Type 1 Copper in Blue-Copper-Proteins; β -Aminothione Model Complexes.

5.1. Introduction: Proteins and Models.

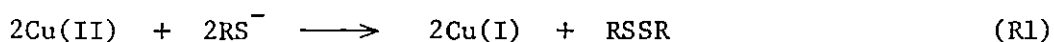
The origins of the unusual spectroscopic and redox properties found for 'Type 1' copper in blue copper-containing proteins have presented some intriguing problems in biological inorganic chemistry. Three notably anomalous properties have attracted much interest: (i) an intense absorption band near 600 nm with an extinction coefficient 10-100 times greater than found for most Cu(II) complexes; (ii) a very small copper hyperfine splitting in the EPR spectrum, $|A_{\parallel}| \approx 30-90 \times 10^{-4} \text{ cm}^{-1}$; and (iii) a redox potential appreciably higher than the aqueous Cu(II)/Cu(I) couple. ²³¹⁻²³⁵

The type 1 copper centre is found in proteins extracted from a wide variety of plants, bacteria and mammals. It occurs singly in, for example, the blue proteins azurin, plastocyanin and stellacyanin. In the larger enzymes, laccase, ceruloplasmin and ascorbate oxidase it is found in association with 'type 2' and 'type 3' copper centres, which have different, but also distinctive properties. An electron-transfer role has been established for plastocyanin and azurin and this could well be the function of the type 1 centre in many other single-copper blue proteins and in the multi-copper enzymes also.

Many physical and chemical techniques have been employed in studying type 1 centres in an attempt to elucidate the nature of the copper coordination: amino acid sequence, ²³⁶ resonance Raman, ²³⁷⁻²³⁹ protein IR, ²⁴⁰ EXAFS, ²⁴¹ EPR, ^{242,243} pulsed EPR, ²⁴⁴⁻²⁴⁶ linear electric field effect EPR, ^{247,244} ENDOR, ^{248,249} ¹³C and ¹H NMR, ²⁵⁰⁻²⁵⁸ electronic absorption, CD and MCD, ^{259-267,242} XPES, ²⁶⁸⁻²⁷⁰ electron transfer kinetics, ²⁷¹⁻²⁷⁴ nickel and cobalt substitution. ^{261,239,275-279} The picture

which has emerged as being consistent with the overall results of these extensive investigations is of a tetragonally (D_{2d}) distorted tetrahedral ligation involving a cysteinyl sulphur, two nitrogenous ligands (most probably histidine imidazole groups) and a fourth methionine, cysteine, cystine-disulphide or deprotonated peptidylamide ligand. Much effort has been directed toward the synthesis of simple copper complexes capable of mimicking the type 1 copper coordination and its unusual properties. A great diversity of ligand types and coordination stereochemistries have been employed, but no one complex has been found which represents an authentic synthetic analogue by modelling all the basic type 1 properties in combination. The particular difficulties inherent in synthesising analogues of proteins containing single metal atoms coordinated by a complex polypeptide ligand, which may impose a coordination environment, have been pointed out by Holm.¹ One problem has been the incomplete knowledge of the ligand-set in the proteins. In the specific case of poplar plastocyanin a recent X-ray crystal structure analysis (2.7 Å resolution) has established that its copper is bound with distorted tetrahedral stereochemistry (more approximately trigonal than tetrahedral elongation) to two histidyl nitrogens, a cysteinyl thiolate and a thioether sulphur from methionine.^{242,280} Similar coordination is indicated for azurin from *P. aeruginosa* by a lower resolution crystallographic study.^{281,282} It is perhaps tempting to generalise this arrangement to other type 1 copper centres. There probably is not, however, a unique structure applicable to all type 1 sites; stellacyanin, for example, contains no methionine²⁸³⁻²⁸⁶ and a cystine disulphide is a probable alternative ligand. For this reason, and in view of the insight gained from comparative studies, the synthesis and investigation of model compounds continues to be valuable in understanding the detailed geometrical and electronic structure of type 1 copper.

As has already been indicated a wide variety of copper complexes have been proposed as modelling some aspect of type 1 coordination, with equally widely varying degrees of success and applicability, and just a few of the more useful and informative will be described here. Some considerable difficulty has arisen in the formulation and interpretation of synthetic model compounds in that the three anomalous properties of the type 1 copper, listed at the beginning of this section, may have different, though interrelated, origins. In the light of the recent crystallographic analyses and subsequent more intensive investigation of the blue-proteins it appears that the intense absorption near 600 nm may be solely a result of S \rightarrow Cu(II) charge transfer^{242,259,261,263} whilst the low $|A_{||}|$ may result solely from a ligand-independent flattened-tetrahedral stereochemistry where the unpaired electron resides in an orbital which is a mixture of $3d_{xy}$ and $4p_z$.^{248,287,288} The coordination of the type 1 copper is intermediate between the square-planar arrangement of hard to soft ligands preferred by Cu(II) and the tetrahedral soft-ligand environment preferred by Cu(I); this could be responsible for the observed high redox potential. A major problem then arises in attempting to synthesise type 1 site analogues because of the instability of mercapto-copper(II) complexes due to the facile and essentially irreversible reaction (R1). Any attempt to mimic the



type 1 site must lead to further destabilisation of Cu(II) with respect to Cu(I) and promote decomposition of the complex via this reaction. In the proteins this irreversible dissociation tendency may be restricted,

Corresponding Cu(II) complexes, however, have $|A_{\parallel}| \approx 170 \times 10^{-4} \text{ cm}^{-1}$. A cupric complex similar to S1 but having one pyrazolyl group replaced by $p\text{CH}_3\text{C}_6\text{H}_4\text{S}^-$ to give a 2NS(SR) donor set, shows an even larger $|A_{\parallel}| = 187 \times 10^{-4} \text{ cm}^{-1}$.³⁰¹ On the other hand, a homologue of the ligand in S2, where the tripodal nitrogen is joined to the pyridine ring by only one carbon, complexes Cu(II) to give a lower $|A_{\parallel}| = 144 \times 10^{-4} \text{ cm}^{-1}$, but a crystal structure determination shows it to be five coordinate.³¹² A recent X-ray structural analysis for the nitrate salt of the cupric form of S2 shows this too to be five coordinate.³¹³

Several reaction products of Cu(II) with small peptides containing thiol and imidazole groups have been proposed as models for the type 1 copper site since some have $|A_{\parallel}| < 100 \times 10^{-4} \text{ cm}^{-1}$ and also medium intensity absorption around 600 nm.³¹⁴⁻³¹⁷ The reaction products are stable but have been incompletely characterised, being of unknown coordination or stereochemistry.

Patterson and Holm³¹⁸ have examined a broad series of Cu(II) complexes to identify specific ligand structural features which might give rise to Cu(II)/Cu(I) potentials in the blue-copper-protein range, but nearly all of the 37 complexes studied exhibited negative potentials with respect to SHE. However, for several cyclic and open-chain polythioether and aminothioether cupric complexes, substantially positive redox potentials have been found, comparable to those of the proteins.^{295,307,311,319} X-ray structural information for two such complexes demonstrates in one case tetragonal and in another square-pyramidal coordination.^{309,311} As certain of these complexes also show reasonably intense visible absorption around 600 nm it has been suggested that distortions from tetragonal geometry are not requisite for the generation of the spectral and redox properties which typify blue-copper-proteins.³⁰⁹ Those of this series for which EPR.

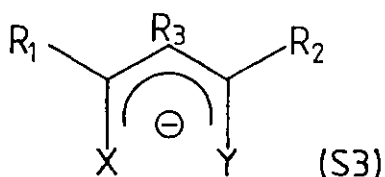
measurements have been made show $|A_{||}| > 160 \times 10^{-4} \text{ cm}^{-1}$,^{295,311} and thus this parameter at least must make tetrahedral distortion a prerequisite for complete duplication of type 1 copper properties.

In view of the confusing evidence from the large array of unrelated model complexes a more systematic approach involving the use of 2N2S coordination with variable stereochemistry would seem appropriate.

5.2. Cu(II) β -Aminothione Complexes.

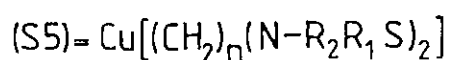
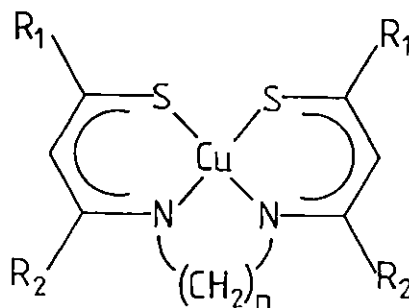
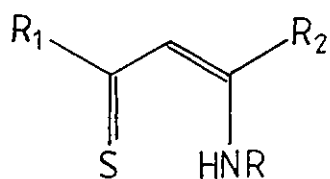
5.2.1. Introduction.

The β -difunctional ligand system (S3) (X, Y = O, S, NR, Se) has shown considerable utility in the comparative investigation of stereo-



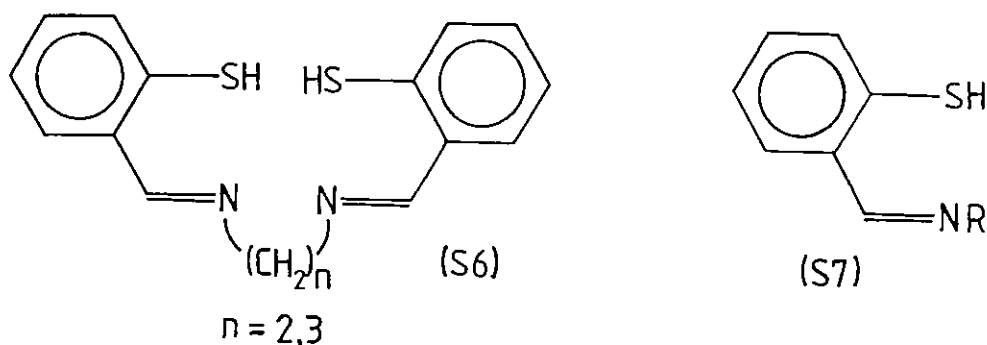
chemical and electronic properties for tetra-coordinate chelates, as dependent upon donor-atom, metal ion or ligand structure.³²⁰ For X = NR and Y = O, S, NR distortion from square-planar toward tetrahedral coordination geometry has been correlated with increased steric bulk of the R group for a number of metal ions.^{321-325,293}

Ni(II) complexes of the N-substituted β -aminothione ligands (S4) demonstrate a relatively greater stabilisation of planar stereochemistry



than do corresponding 2N2O coordinated complexes.³²² None-the-less, an increased tendency toward tetrahedral geometry is apparent as the nitrogen substituent increases in size.

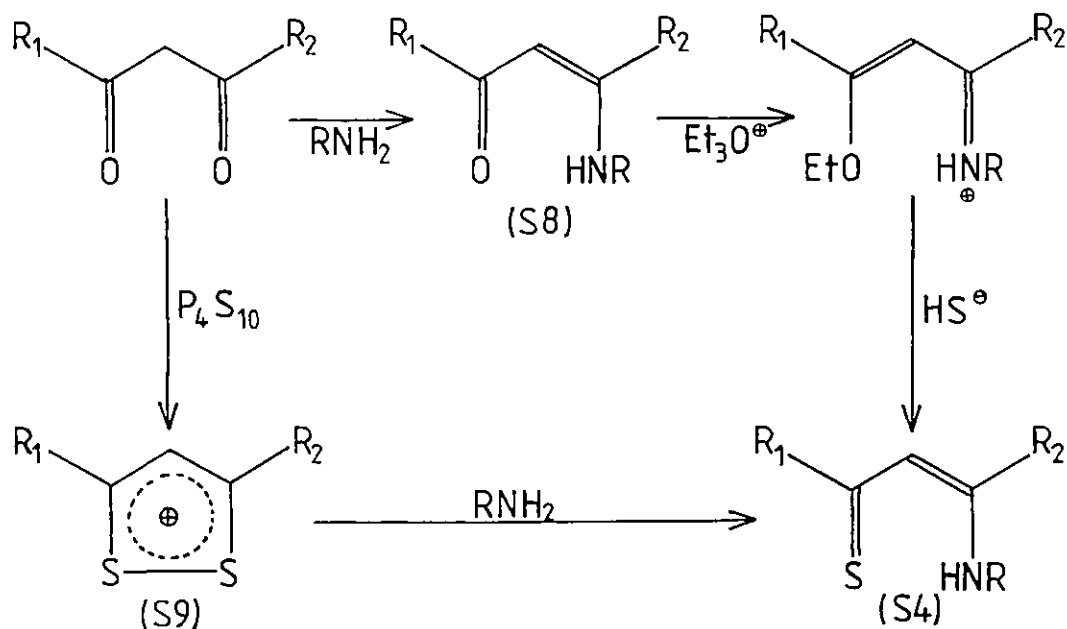
The only copper complexes reported with this type of 2N2S chelation have involved quadridentate ligands and are similar to structure (S5).³²⁶⁻³³² Comparable Cu(II) complexes of the quadridentate ligands (S6) have also been described by Corrigan *et al.*,³³³ but these authors were unable to obtain cupric complexes of the corresponding bidentate ligands (S7). The synthesis of complexes of the latter type has been reported,³³⁴ however,



attempts in this present work to obtain these have, like those of Corrigan *et al.*, failed, leading only to Cu(I) compounds. Similarly, with the bidentate β -aminothione ligands (S4) only orange coloured Cu(I) complexes are isolated from anaerobic reactions performed at room temperature, while intractable dark-brown gums result from prolonged reaction in the presence of atmospheric oxygen. If, on the other hand, the coordination of Cu(II) by these ligands is performed at low temperatures dark-green to dark-blue solutions result from which cupric complexes may be isolated.

5.2.2. Synthesis of Ligands.

Two approaches have been adopted in ligand (S4) synthesis, as originally employed by Gerlach and Holm³²²:-



The route via the β-ketoamine (S8) has been used for R₁ = R₂ = Me and R₁ = Ph, R₂ = Me, whilst the second route via the dithiolium cation (S9) has been applied to the synthesis of β-aminothione ligands having R₁ = R₂ = Ph, R₁ = R₂ = tBu, and with a different method of cation preparation,³³⁵ R₁ = Ph, R₂ = H. Only for the RN-MeMeS (i.e., RN-R₂R₁S, R₁ = R₂ = Me) ligand has extensive variation of the R group been undertaken, as the members of this series have generally higher solubilities than the phenyl-substituted homologues and involve inexpensive starting materials. Attempts to prepare tBuN-MeMeS or tBuN-tButBuS by the above procedures, were repeatedly unsuccessful.

5.2.3. Synthesis and Characterisation of Cu(II) β -Aminothione Complexes.

Cupric complexes of the β -aminothione ligands have been synthesised by mixing methanolic solutions of ligand and of cupric chloride or cupric acetate at low temperature. The resulting dark green-blue reaction solutions gave darker coloured solid on standing which could be collected by filtration at low temperature. The thermal stability of the solutions and solids formed is greatly dependent on the amino-substituent, R. Thus, for R = Me the complexation reaction may be undertaken at ca. -30°C and the isolated solid is stable for prolonged periods at ambient temperatures. For the more bulky R = iPr substituent, on the other-hand, solutions of the cupric complex must be maintained below ca. -50°C to avoid significant decomposition and the solid may be handled at room temperature for only short periods of time. An electronic effect also appears to be operative in governing the stability of the cupric complexes in that for R = p- YC_6H_4 far greater tendency towards decomposition to cuprous complexes is found when Y = H or Cl than when Y = F, Me or-OMe.

Copper complexation reactions with the β -aminothiones led to orange diamagnetic precipitates when undertaken anaerobically at room temperature. Microanalytical data for a purified complex with PhN-MeMeS demonstrates a one-to-one copper-ligand stoichiometry.

By using dilute reactant solutions and maintaining the reaction solution at ca. -70 to -80°C for several hours it has proven possible to obtain crystalline products with a number of ligands. Notably Cu(II)(iBuN-MeMeS)₂ forms dark green needles of a size sufficient to collect X-ray diffraction data, though this has not yet been achieved.

The cupric complexes are soluble in a range of polar organic solvents (DMF, THF, acetone) and their solutions are stable at low temperatures (ca. -50°C). Relative solubilities are dependent upon the R, R₁ and R₂ substituent groups.

The $\text{Cu(II)(RN-R}_2\text{R}_1\text{S)}_2$ complexes have been studied by electronic spectroscopy, EPR, Raman spectroscopy and polarography.

5.3. Electronic Spectra.

Low temperature solution visible spectra and room-temperature solid-state visible-near-IR reflectance spectra have been measured for the cupric β -aminothione complexes. Absorption band maxima and some extinction coefficients are collected in Tables 5.1 and 5.2, and Figures 5.1 and 5.2 show representative spectra. Two intense visible absorption peaks are observed in the ranges ca. 600-680 nm and ca. 470-540 nm for solutions and have close solid-state counterparts. A less intense broad

TABLE 5.1. Visible absorption band maxima of Cu(II)(RN-R₂R₁S)₂ in solution.

Ligand	Solvent	Temp./ °C	λ_{\max} /nm [ϵ /lt cm ⁻¹ mol ⁻¹]
R; R ₁ = R ₂ = Me			
Me	DMF	-60	600 [1500], 480 [2300]
	acetone	RT	610, 480
Et	THF	-50	618 [1400], 481 [1850]
	DMF	-60	613 [1450], 488 [1700]
nPr	THF	-50	610 [1400], 480 [1650]
iPr	THF	-60	679, 500-510 sh
nBu	THF	-55	612 [1400], 475 [1700]
iBu	THF	-50	603 [1400], 470 [1700]
nOct	THF	-60	612 [1400], 475 [1700]
Bz	THF	-60	605 [1500], 487 [1950]
cHx	THF	-60	678 [1400], 504 [~1000]
pMePh	THF	-55	620 br [1600], 540 br [1600]
pMeOPh	THF	-80	626 [1100], 525 pr [~1000]
pFPh	THF	-80	630 [1600], 530 [1600]
-(CH ₂) ₅ -	THF	-50	~600 br, sh, 465 pr [~1500]
EtN-PhPhS	THF	-50	618 [2100], 490 [2600]
EtN-MePhS	THF	-60	621 [2000], 491 [2350]
	DMF	-60	614 [1900], 490 [2350]
EtN-tButBuS	THF	-55	604 [1250], 528 [1350]

pr - poorly resolved; sh - shoulder; br - broad.

ELECTRONIC SPECTRA OF $\text{Cu}^{\text{II}}(\text{RN}-\text{MeMeS})_2$ IN THF OR DMF*

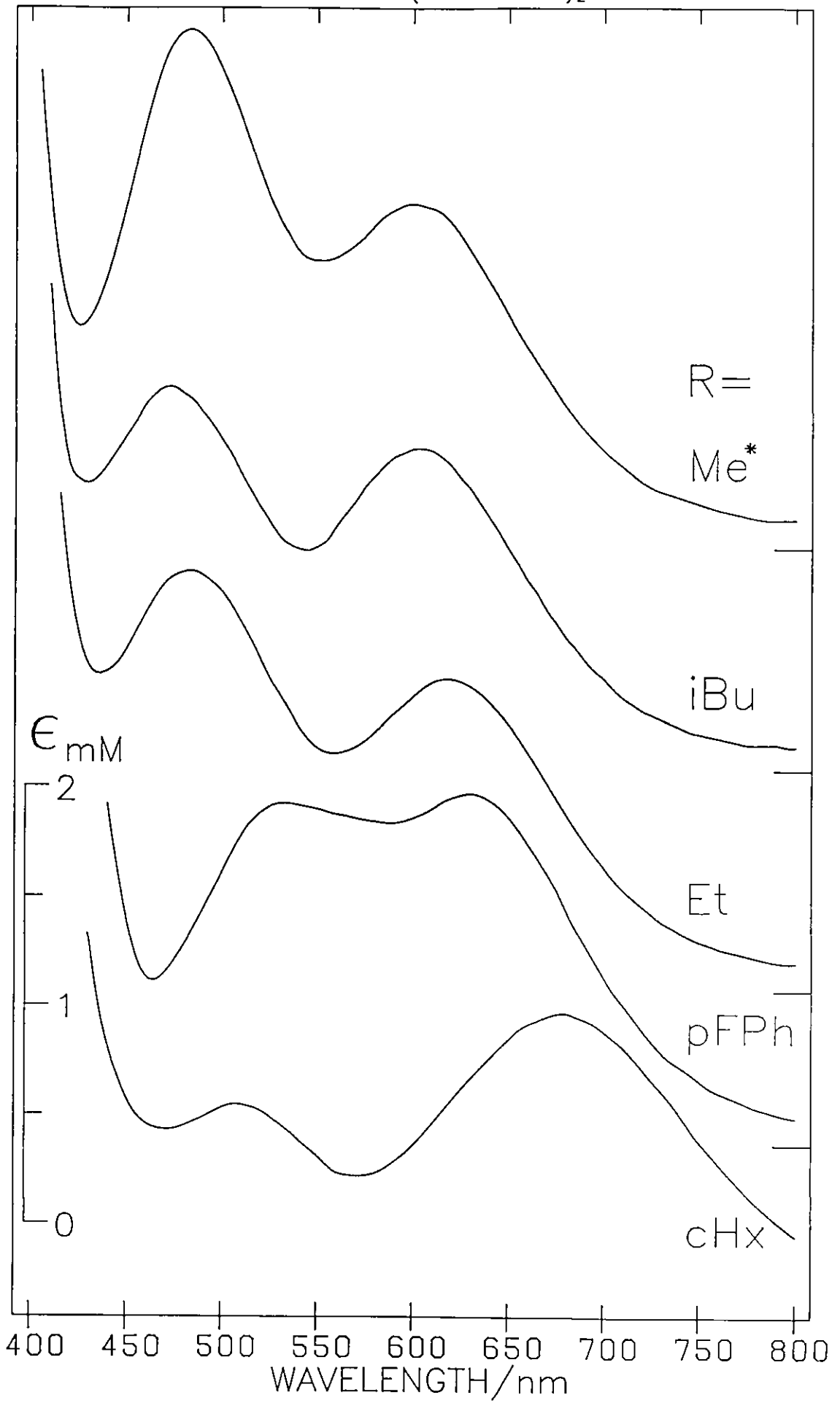


FIG. 5.2
REFLECTANCE SPECTRA OF $\text{Cu}^{II}(\text{RN}-\text{MeMeS})_2$

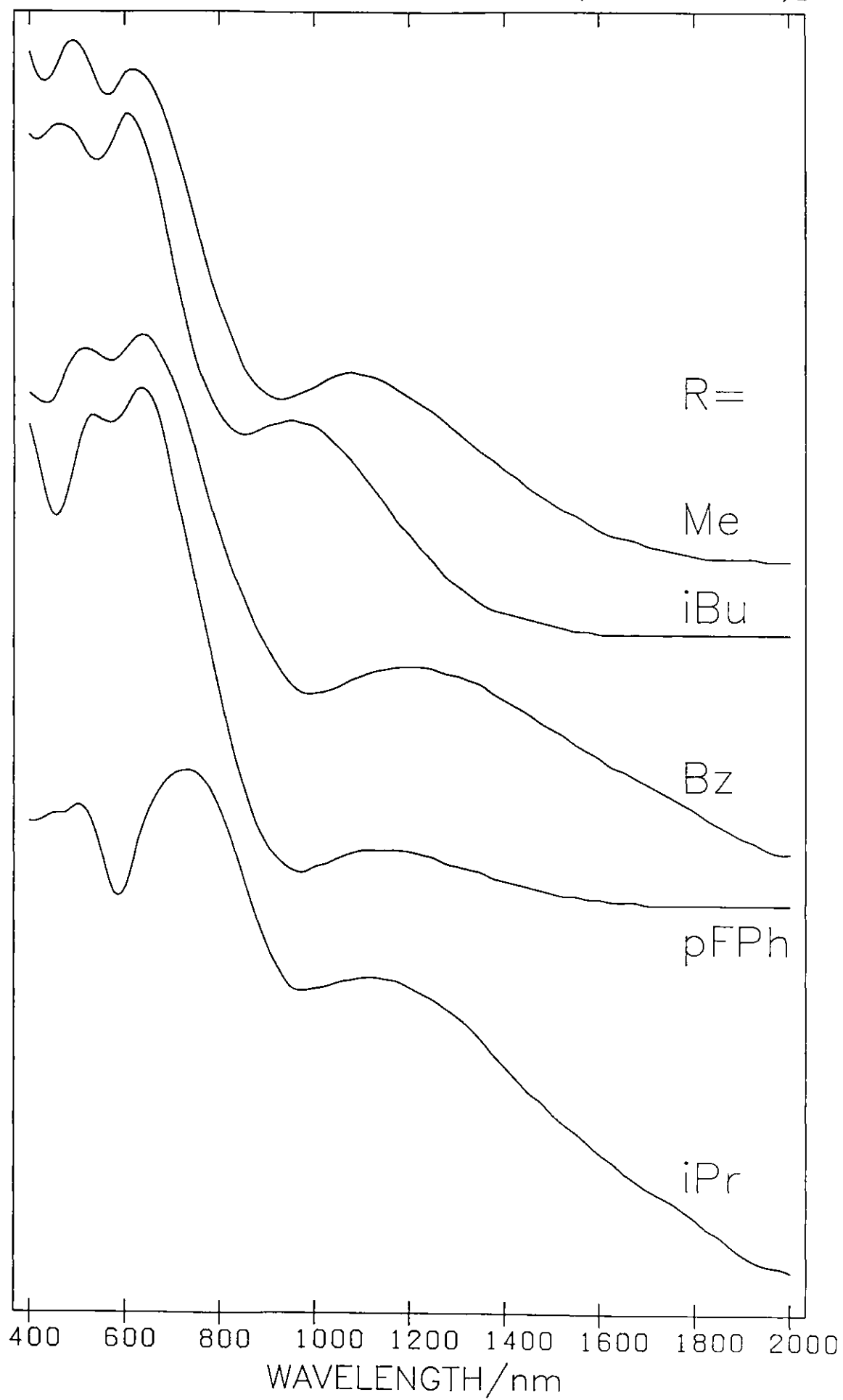


TABLE 5.2. Solid-state reflectance spectra of Cu(II)(RN-R₂R₁S)₂;
band maxima at room temperature.

Ligand	$\lambda_{\text{max}}/\text{nm}$
R, R ₁ = R ₂ = Me	
Me	1075 br, 620, 485
Et	1050 br, 615, 485
nPr	1050 br, 610, 485
iPr	1100 br, 720, 500
nBu	1000 br, 615, 475
iBu	960 br, 600, 460
nOct	980 br, 600, ~ 500
Bz	1200 br, 635, 510
cHx	960 br, 635, ~ 430
pMePh	1170 br, 630, ~ 530
pMeOPh	~1200> br. pr., 630
pFPh	1130 br, 630, 530
-(CH ₂) ₅ -	~1050 vbr. sh, 610, 490
-(CH ₂) ₆ -	~1000 vbr., 620
EtN-PhPhS	~ 1200 vbr. pr. sh., ~850vbr. pr. sh., 620, 510, 420 sh
EtN-HPhS	1130 br., 625, 505, ~ 430
EtN-tButBuS	910 br., 610, 530

feature is seen in the near IR diffuse reflectance spectra within the range 900-1200 nm. The thermal instability of the Cu(II) complexes presents some difficulty to the accurate determination of molar absorption coefficients for the solution optical bands. Dissolution of the solids must be undertaken at low temperature and the consequent reduced solubility, taken together with the opacity of the resulting

optically dense solutions, makes it difficult to ensure the complexes are completely dissolved. Dispersal of the solid could, however, be checked by low temperature filtration on a fine frit prior to spectral measurements. Decomposition of the chromophore during solution preparation and transfer to the low temperature cell, was limited as far as possible by the handling techniques employed, but the extinction coefficients measured, and reported in Table 5.1, may under-estimate the true values (see also Section 5.8.2. concerning purity of the complexes). The consistency and compatibility of the extinction coefficients quoted for the broad selection of complexes studied indicates reasonable accuracy.

The extinction coefficients of the two bands in the regions 600-680 nm and 470-540 nm indicate that they are charge-transfer in origin. The weaker low energy broad band is considered to be d-d, and possibly a composite of such transitions.

5.3.1. d-d Bands.

For the $\text{Cu(II)(RN-MePhO)}_2$ R = Me, iPr complexes with 2N2O coordination low energy broad features are observed at 625 nm and 725 nm respectively.³²⁵ The ligand field strength for 2N2S coordination is expected to be weaker, and the empirical spectrochemical series $4N \sim 4O > 2N2O > 2N2S \sim 2S2O > 4S$ has been suggested for the ligand system under consideration.³²² Thus the observed range of 900-1200 nm would seem reasonable for the lowest energy d-d transitions in the Cu(II) β -aminothione complexes

Both the position and intensity of d-d bands are expected to be dependent upon the degree of distortion, if any, from a square-planar ligand arrangement toward tetrahedral. The average energy of the d-d transitions

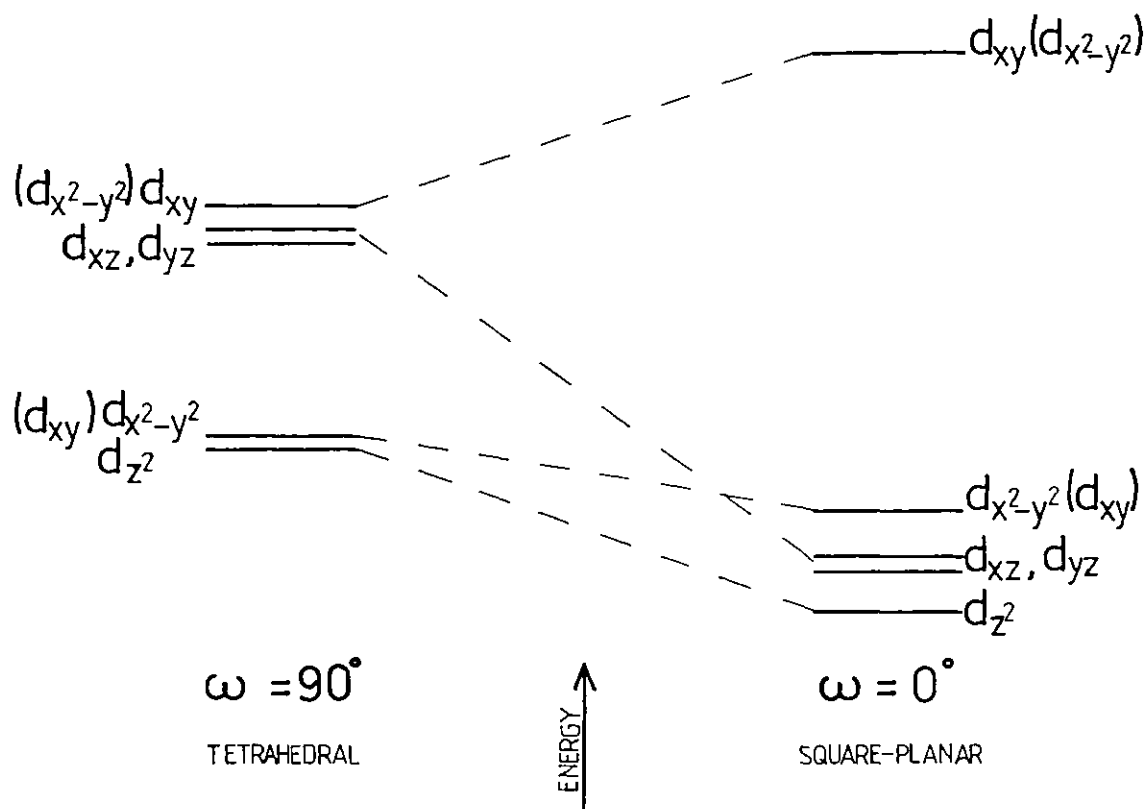


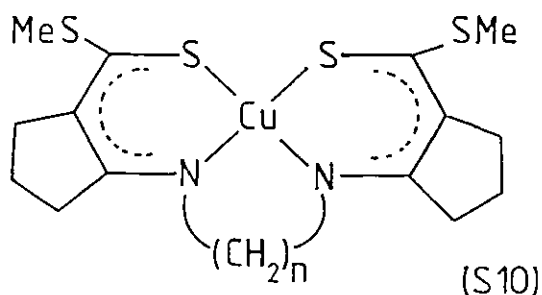
Figure 5.3. Correlation of d-orbital energies for tetrahedral and square-planar Cu(II) related by a compression along the z-axis. ω = dihedral angle between pairs of ligand atoms. The bracketed terms represent the orbitals referred to an alternative axis system.

will be largest for a square-planar chromophore and least for a regular tetrahedral chromophore, with a correlation diagram relating the two extremes as shown in Figure 5.3.

There appears, however, no correlation of the position for the near-IR absorption maximum with any expected steric bulkiness of the ligand amino R-group, or of any other spectroscopic parameter thought to be indicative of tetrahedral distortion (see later). Thus considering the bulky secondary branch-chain alkyl R-groups, the band occurs at 960 nm in the Cu(II)(CH_xN-MeMeS)₂ complex, the shortest wavelength for the RN-MeMeS series, and at 1100 nm for Cu(II)(iPrN-MeMeS)₂. The lowest

energy band maximum is found at 1200 nm for R = Bz which is not expected to be especially distorted.

Subsequent to the present investigations of bidentate- β -aminothione Cu(II) complexes Bereman *et al.* have reported investigations of the related tetradentate 2N2S coordinated complexes (S5): $R_2 = \text{Me}$, $R_1 = \text{Me}$, Ph; $n = 2, 3$ ³²⁷ and (S10): $n = 2, 3, 4$.³²⁸⁻³³⁰



For the latter complexes, crystal structures have been determined for $n = 3$ and 4 showing unexpectedly large distortion from planarity involving dihedral twist angles (ω) of 53° ($n = 3$) and 57° ($n = 4$). Accompanying the tetrahedral distortion along the series $n = 2, 3, 4$ there is a decrease in the parallel copper hyperfine splitting ($181, 160, 145 \times 10^{-4} \text{ cm}^{-1}$) and an increase in the wavelength of the lowest energy d-d band (794, 952, 1075 nm). Similar spectroscopic changes are found for the complexes of structure (S5): $R_2 = \text{Me}$; $R_1 = \text{Me}$ ($n, \lambda_{\text{max}} = 2, 719 \text{ nm}; 3, 826 \text{ nm}$); $R_1 = \text{Ph}$ ($n, \lambda_{\text{max}} = 2, 709 \text{ nm}; 3, 826 \text{ nm}$).³²⁷

The copper(II) complexes of the analogous bidentate N,S-ligands studied here show absorption at lower energies than this latter series of complexes, indicative of a more tetrahedrally distorted coordination stereochemistry. It is peculiar, however, that trends in the position of the low energy electronic bands, similar to those in the above complexes of the quadri-dentate 2N2S ligands, are not observed, as the $\text{Cu}(\text{RN}-\text{MeMeS})_2$ complexes

would be expected to show a wider range of stereochemical distortions and indeed demonstrate a broad range of absorption peak-wavelengths.

Enhancement of d-d band intensity may result for tetrahedrally distorted Cu(II) complexes from mixing with allowed 3d-4p transitions made possible by loss of centrosymmetry, or from mixing of the d-d transition with a neighbouring charge-transfer band.³³⁶ The latter mechanism is probably more applicable to the explanation of the relatively high intensities observed in the reflectance spectra of the β -aminothione complexes, though both mechanisms may be operative.

Table 5.3 lists the observed visible and near-IR absorption bands and their assignments for the proteins plastocyanin, azurin and stellacyanin. The most intense d-d bands are found ca. 850-1100 nm. Other weak near-IR absorption maxima in the proteins extend out to ca. 2000 nm.

TABLE 5.3. Electronic spectral parameters for some blue-copper-proteins and their assignments.²⁵⁹

$\lambda_{\max}/\text{nm} [\epsilon/\text{lt cm}^{-1} \text{ mol}^{-1}]$			Assignment
Plastocyanin	Azurin	Stellacyanin	
2000* $[\sim 100]$	1720* $[\sim 100]$	1900* $[\sim 100]$	d-d Cu
1070 [200]	980* $[\sim 125]$	1140 $[\sim 100]$	d-d Cu
847 [1162]		900 [565]	d-d Cu
752 [1289]	779 [686]	789 [341]	(Cys) $\pi\text{S} \rightarrow d_{xy}$ Cu [†]
606 [4364]	631 [3798]	617 [3549]	(Cys) $\sigma\text{S} \rightarrow d_{xy}$ Cu
552 [1163]	567 [504]		(Met) $\sigma\text{S} \rightarrow d_{xy}$ Cu [†]
		572 [1542]	
450 [300]	481 [198]		$\pi\text{N} \rightarrow d_{xy}$ Cu
		450 [942]	
428 $[\sim 100]$			$\pi\text{N} \rightarrow d_{xy}$ Cu

*CD band positions ; † These assignments are according to reference 259.

More recently, single crystal studies of plastocyanin indicate there to be no degeneracy in the sulphur p-orbitals and the 552 nm band is assigned as $\text{S}(\alpha\text{S} + \beta\text{p}_z) \rightarrow \text{Cu}(d_{xy})$.²⁴² This has been questioned.²⁶⁰

(The σ and π designations are carryovers from studies of octahedral complexes in which one ligand p-orbital is σ -bonded and the other two π -bonded to the metal centre.²¹³)

5.3.2. Charge-transfer bands.

The intense absorption ca. 600-630 nm in blue-copper-proteins, responsible for the blue colouration wherein is the origin of their colloquial name, has a well established assignment to a LMCT $S(\sigma) \rightarrow Cu(d_{xy})$ transition.^{259,242,262} Bands ca. 600-680 nm in the Cu(II) β -aminothione complexes are, at first sight, reasonably given a similar assignment. A correlation is noted between the position of this band and the expected bulkiness of the R-group on the ligand nitrogen. Thus the series pri-alkyl (600-620 nm) < aryl (620-630 nm) < sec-alkyl (678-679 nm) connects the increasing steric bulk of R with movement of the absorption maximum to longer wavelength. The explanation for this trend is considered to lie in the lowering of the energy of the 'hole' ground-state d_{xy} (or $d_{x^2-y^2}$) orbital (see Figure 5.3) relative to the ligand orbital as distortion from square-planar geometry is increased by steric hindrance from R. The R_1 and R_2 substituents are seen to have relatively little effect on the position of the band at ca. 600 nm for the complexes with R = Et. Construction of molecular models shows that these groups are expected to play little part in causing stereochemical distortion. An electronic effect is seen, however, in the extinction coefficients of $Cu(EtN-MePhS)_2$ and $Cu(EtN-PhPhS)_2$ which are significantly larger than for the corresponding $Cu(EtN-MeMeS)_2$ and $Cu(EtN-tButBuS)_2$ complexes. A similar intensity enhancement has been observed for phenyl substitution in the chelate ring of copper(II) N,N'-diaryl- β -iminoamines.²⁹³

It is less easy to make a categoric assignment of the LMCT bands observed in the region 470-540 nm, and indeed, determination of the origin of this absorption casts some doubt on the assignment made for the peak at ca. 600 nm. Firstly, a $N \rightarrow Cu(II)$ transition would seem an unlikely origin for the band at ca. 500 nm as the observed extinction is much higher than would be expected (see, for example, Table 5.3). It is possible, then, that the 500 nm band should be assigned as $S(\sigma) \rightarrow Cu(d_{xy})$ and the maximum at ca. 600 nm as $S(\pi) \rightarrow Cu(d_{xy})$, in contradiction to the assignment given above. Such a blue shift relative to the peaks assigned to these transitions for the blue-copper-proteins, would perhaps be indicative of a less distorted coordination geometry. In the proteins the $S(\pi) \rightarrow Cu(d_{xy})$ band is observed at a much lower intensity than that attributed to $S(\sigma) \rightarrow Cu(d_{xy})$ CT, whereas comparable intensities are observed for the two visible LMCT bands in many of the Cu(II) β -aminothione complexes. This might, however, be due to greater π -resonance delocalisation in the six membered chelate ring of the complexes compared to the $S(\pi)$ -Cu(II) overlap in the proteins. Substantial π -delocalisation has been suggested for analogous quadridentate 2N2S complexes from IR, NMR and X-ray structural data.^{326, 328, 329, 332}

An alternative explanation for the bands occurring ca. 500 nm in the model complexes is that there exists an energy difference in the two $S(\sigma)$ orbitals and that both this and the band at ca. 600 nm arise from $S(\sigma) \rightarrow Cu(d_{xy})$ transitions. Such a view might be supported by the observation that only a single intense band around 600 nm is found in the optical spectrum of $Cu(II)[HB(3,5\text{-dimethyl-1-pyrazolyl})_3](pNO_2C_6H_4S)$,^{299, 300} containing only one Cu(II)-S bond, whereas two bands of comparably high extinction are found for $Cu(II)[S(Ph)_2PNP(Ph)_2S]_2$ at 407 nm and 575 nm.²⁹⁷

If this were the case the $S(\pi) \rightarrow Cu(d_{xy})$ transition would be considered to contribute only to the substantial tailing toward longer wavelengths. An energy splitting between the two $S(\sigma)$ orbitals of the order 2500-5000 cm^{-1} would be required, and is rather difficult to justify. $S(\sigma)$ orbital splittings approaching these have, however, been suggested and justified for Cu(II) complexes having more than one sulphur-donor by Amundsen et al.³¹⁰

For some of the complexes a slight asymmetry is seen in the high energy LMCT band. This could be indicative of assignment of this band to $S(\sigma) \rightarrow Cu(d_{xy})$ with a small difference in the two $S(\sigma)$ orbital energies and assignment of the lower energy LMCT band to $S(\pi) \rightarrow Cu(d_{xy})$ as discussed previously.

Circular dichroism or resonance Raman excitation-profile measurements might resolve the question of the exact assignment of the LMCT transitions responsible for the intense visible absorption features of these complexes.

5.3.3. Electronic spectra of nickel(II) β -aminothiones.

Table 5.4 lists band positions and intensities for several Ni(II) $(RN-MeMeS)_2$ complexes in CH_2Cl_2 . All show a d-d band in the region ca. 640-700 nm. For R = aryl additional near-IR absorption ca. 1200-1600 nm is indicative of a planar-tetrahedral stereochemical equilibrium in solution.³²² The near-IR absorption is of greatest intensity for R = 2,6-dimethylphenyl, which from considerations of steric bulkiness amongst the six substituents employed, would be expected to most favour a tetrahedral coordination geometry. The LMCT bands are found at higher energy in the nickel complexes compared to the copper. Shifts from 600 and 480 nm in $Cu(MeN-MeMeS)_2$ to 442 and 350 nm in $Ni(MeN-MeMeS)_2$ are

TABLE 5.4. Electronic spectral parameters for Ni(II)(RN-MeMeS)₂ Complexes in CH₂Cl₂.

R	$\lambda_{\text{max}}/\text{nm}$ [$\epsilon/\text{lt cm}^{-1} \text{ mol}^{-1}$]
Me	640 [128], 442 [2090], 350 sh [5600], 310 [9500], 262 [24400]
nOct	650 [118], 445 sh [2100], ~390 sh, 353 sh [5200], 315 [8440], 255
Octadecyl	645 [113], 445 sh [2000], ~ 390 sh, 355 sh [5100], 314 [8700], ~260
Ph	~1500 sh, 1280 [15], 680 [240], ~450 br. sh 332 [5000], 276 [9000].
pClPh	~1500 sh, 1270 [15], 678 [250], 460 br.sh, 335 [8000], 280 [10400].
2,6-dimethylphenyl	~1550 [50], 1330 [50], 704 [304], ~450 br.sh, 360 sh [10000], 325 sh, 383 [14500]

comparable to those from 621 and 521 nm in native azurin to 439 and 392 nm in the Ni(II) derivative, and are quite compatible with the expected optical electronegativity differences for Cu(II) and Ni(II).^{261,265,213}

5.4. Electron Paramagnetic Resonance.

EPR spectra have been recorded for a wide range of the $\text{Cu(II)(RN-R}_2\text{R}_1\text{S)}_2$ complexes in mobile and frozen solution. For the RN-MeMeS ligand-series measurements have also been made on Cu(II) doped Zn(II), Ni(II) and Cd(II) complexes.

5.4.1 EPR in Solution.

For the complexes isolated as solids, toluene was used as a solvent since it forms an adequate glass when frozen and is expected to be non-coordinating. EPR parameters derived from frozen and mobile solution spectra are reported in Table 5.5. Also to be found in this table are data from spectra recorded for complexes prepared in methanol from Cu(II) and excess deprotonated ligand. This method of sample preparation has been utilised where isotopically pure ^{63}Cu was desired (e.g., 1-Naphthyl-N-MeMeS), where isolation of the solid cupric complex proved difficult or impossible (e.g., tBuN-HPhS) or merely for convenience in order to avoid the lengthy low temperature filtration and drying procedure (e.g., iPrN-tButBuS). In view of the similarity in form of the EPR spectra it is considered a reasonable assumption that the spectra recorded for reaction-solutions result from complexes with similar 2N2S coordination to those which have been isolated and for which other spectroscopic and also analytical data are available. No signals attributable to 2N2S coordination could be obtained from reactions with the ligands tBuN-PhPhS and diphenylmethyl-N-MeMeS, presumably due to the steric opposition to chelation proffered by the bulky amino-substituents.

TABLE 5.5. EPR parameters for $\text{Cu(II)(RN-R}_2\text{R}_1)_2$ in solution at 100 K.

Ligand $R_1 = R_2 = \text{Me}$		g_{\parallel}	$-A_{\parallel}$	g_{\circ}	$-A_{\circ}$	$N_{A_{\circ}}$	g_{\perp}	$-A_{\perp}$
R	Solvent							
Me	M	2.147	143					
Me	T	2.148	147	2.070	60	10	2.031	16.5
Et	T	2.146	140	2.071	59	9.5	2.034	18.5
nPr	T	2.144	142	2.070	60	10	2.033	19
iPr	T	2.166	134	2.077	55	nr	2.033	15.5
nBu	T	2.145	142	2.071	60	10	2.034	19
iBu	M	2.150	149	2.067	63	10.5	2.023	20
iBu	T	2.145	149	2.071	64	10.5	2.034	21.5
sBu	M	2.178	131	2.078	56	9	2.028	18.5
sBu	T	2.170	133	2.076	56	9	2.029	17.5
nOct	T	2.146	142	2.071	61	10	2.034	20.5
cHx	M	2.173	130	2.079	56	pr	2.032	19
cHx	T	2.165	139	2.076	56	pr	2.032	14.5
Bz	T	2.141	142	2.071	63	9.5	2.036	23.5
αMeBz	M	2.169	132	2.078	56	pr	2.033	18
1-Naphthyl	M	2.151	143	2.072	62	11.5	2.033	21.5
Ph	M	2.143	134	2.069	56	8.5	2.032	17
pMePh	T	2.139	132	2.069	55	10	2.034	16.5
pMeOPh	M	2.144	133	2.069	55	8.5	2.032	16
pMeOPh	T	2.140	132	2.069	55	8.5	2.034	16.5
pClPh	M	2.141	135	2.069	56	8	2.033	16.5
pFPh	T	2.138	133	2.068	55	pr	2.033	16
p(Me_2N)Ph	M	2.143	134	2.065	53	pr	2.026	12.5
2,6- Me_2Ph	M	2.153	128	2.077	55	11.5	2.039	18.5
EtN-MePhS	T	2.144	140	2.070	58	9.5	2.033	17
EtN-PhPhS	T	2.141	143	2.067	60	9	2.030	18.5
nBuN-PhPhS	M	2.144	154	2.066	61	9	2.027	14.5
iPrN-PhPhS	M	2.169	127	2.076	52	nr	2.030	14.5

/continued.....

TABLE 5.5.(continued).

Ligand		$g_{ }$	$-A_{ }$	g_o	$-A_o$	N_{A_o}	g_{\perp}	$-A_{\perp}$
RN-R ₂ R ₁ S	Solvent							
BzN-HPhS	M	2.144	146					
iPrN-HPhS	M	2.141	142	2.072	57	pr	2.038	14.5
tBuN-HPhS	M	2.168	127	2.083	52	nr	2.041	14.5
EtN-tButBuS	T	2.147	151	2.067	67	9.5	2.027	25
iPrN-tButBuS	M	2.157	142	2.070	65	9	2.027	26.5

KEY: Solvents: T = Toluene

nr = not resolved

M = Methanol

pr = poorly resolved

NOTES: 1) $A_{||}$, A_o and N_{A_o} in $\text{cm}^{-1} \times 10^{-4}$ (± 1).2) $\text{Cu(II)(1-Naphthyl-N-MeMeS)}_2$ $N_{A_{||}} = 12 \times 10^{-4} \text{ cm}^{-1}$ $\text{Cu(II)(2,6-dimethylphenyl-N-MeMeS)}_2$ $N_{A_{||}} = 12.5 \times 10^{-4} \text{ cm}^{-1}$

overlapping 1:2:3:2:1 $N_{A_{||}}$ structure on the lowest field feature of the latter complex indicates the presence of more than one species or conformation.

3) Frequencies range 9.21 to 9.25 GHz

No 'half-field' ($\Delta M = 2$) transitions, which are indicative of dimer formation, were observed for any of the complexes.

The measured transition fields corresponding to g_o , $|A_o|$ in mobile solution and $g_{||}$, $|A_{||}|$ in frozen solution were least-squares fitted according to the second-order equations of Kuska and Rogers³³⁷ and the resultant g and $|A|$ parameters are accurate to about ± 0.001 and $\pm 0.0001 \text{ cm}^{-1}$ respectively. g_{\perp} and $|A_{\perp}|$ were evaluated via the relationships

$g_o = (g_{\parallel} + 2g_{\perp})/3$ and $A_o = (A_{\parallel} + 2A_{\perp})/3$, neglecting any temperature dependence of g_o and A_o which is probably small with the non-coordinating solvents employed.

5.4.1.1. Lineshapes and simulation.

Figures 5.4-5.6 show a selection of spectra together with some attempted simulations. Most notable is the well resolved g_{\perp} nitrogen superhyperfine structure seen on many of the spectra. Only in the cases of $\text{Cu(II)(1-Naphthyl-N-MeMeS)}_2$ and $\text{Cu(II)(2,6-dimethylphenyl-N-MeMeS)}_2$ has well resolved superhyperfine splitting been observed on the low field g_{\parallel} features, Figure 5.5. The powder-pattern simulations, parameters for which are collected in Table 5.6, result from a Fortran program 'EPRPOW' which is more fully described in the experimental section (Sec. 6).

TABLE 5.6. EPR parameters used in simulating $^{63}\text{Cu(II)(RN-MeMeS)}_2$ solution spectra.

R =	iBu	sBu	1-Naphthyl	pMeOPh
g_x	2.019	2.022	2.018	2.013
g_y	2.041	2.043	2.050	2.040
g_z	2.150	2.178	2.153	2.144
$-A_x$	21	20	22	16
$-A_y$	21	16.5	22	18
$-A_z$	148.5	130.5	141	133
N_{A_x}	12	11	9	9.5
N_{A_y}	11	11	11	9
N_{A_z}	11	9.5	12.3	9
W_x	6	5	10	4
W_y	2.5	3.5	4	3
W_z	6	6	5	12
W-anisotropy	DC	DC	DC	L
Frequency/GHz	9.224	9.238	9.214	9.219
Figure	5.4	5.4	5.5	5.5

W = Gaussian-linewidth (half-height half-width) in gauss.

L = Linear anisotropy, DC = direction cosine anisotropy equation (Sec. 6).

\underline{A} and $N_{\underline{A}}$ are in $\text{cm}^{-1} \times 10^{-4}$.

FIG. 5.4
X-BAND EPR SPECTRA IN MeOH AT 100K

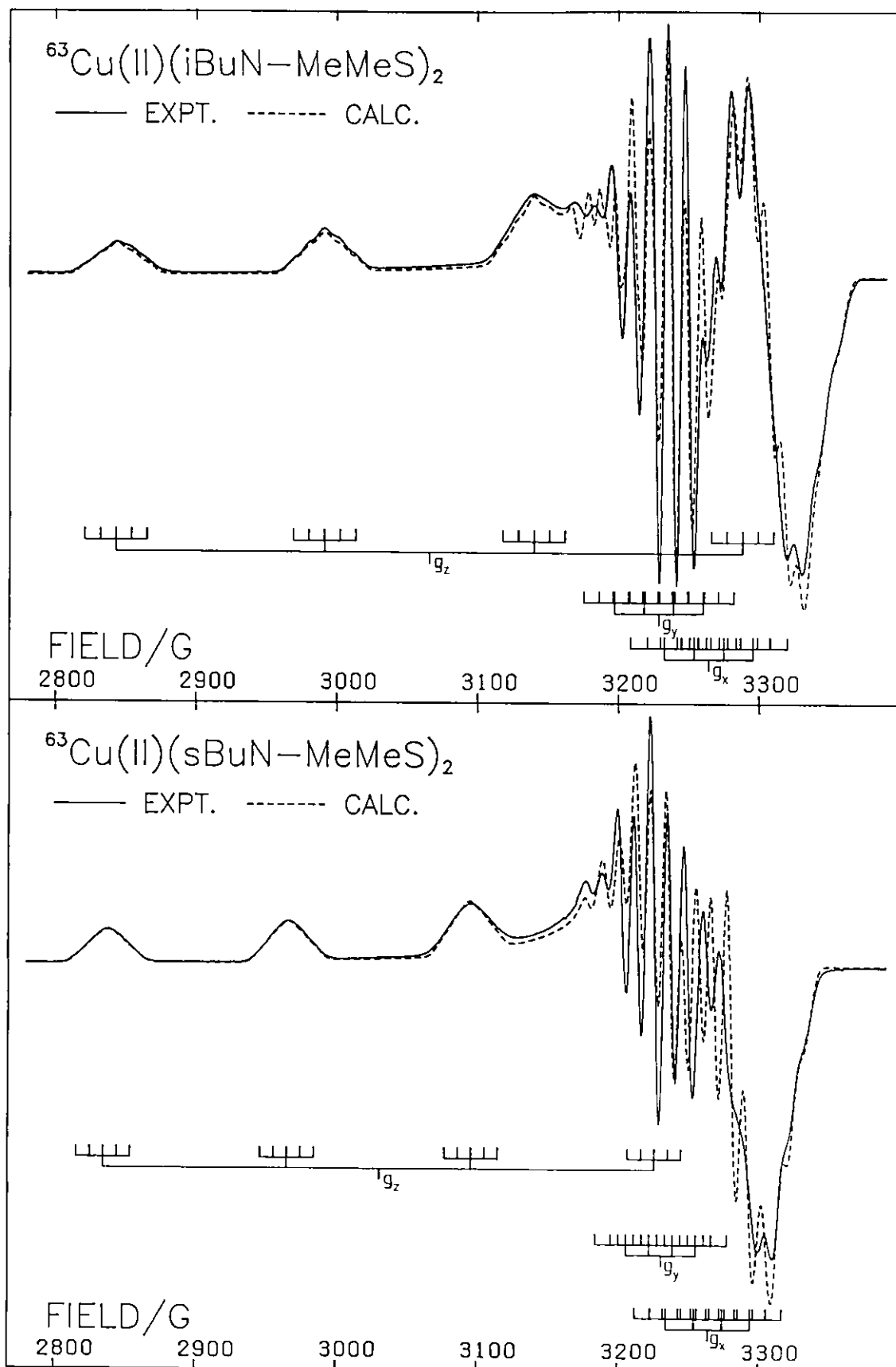


FIG. 5.5
X-BAND EPR SPECTRA IN MeOH AT 100K

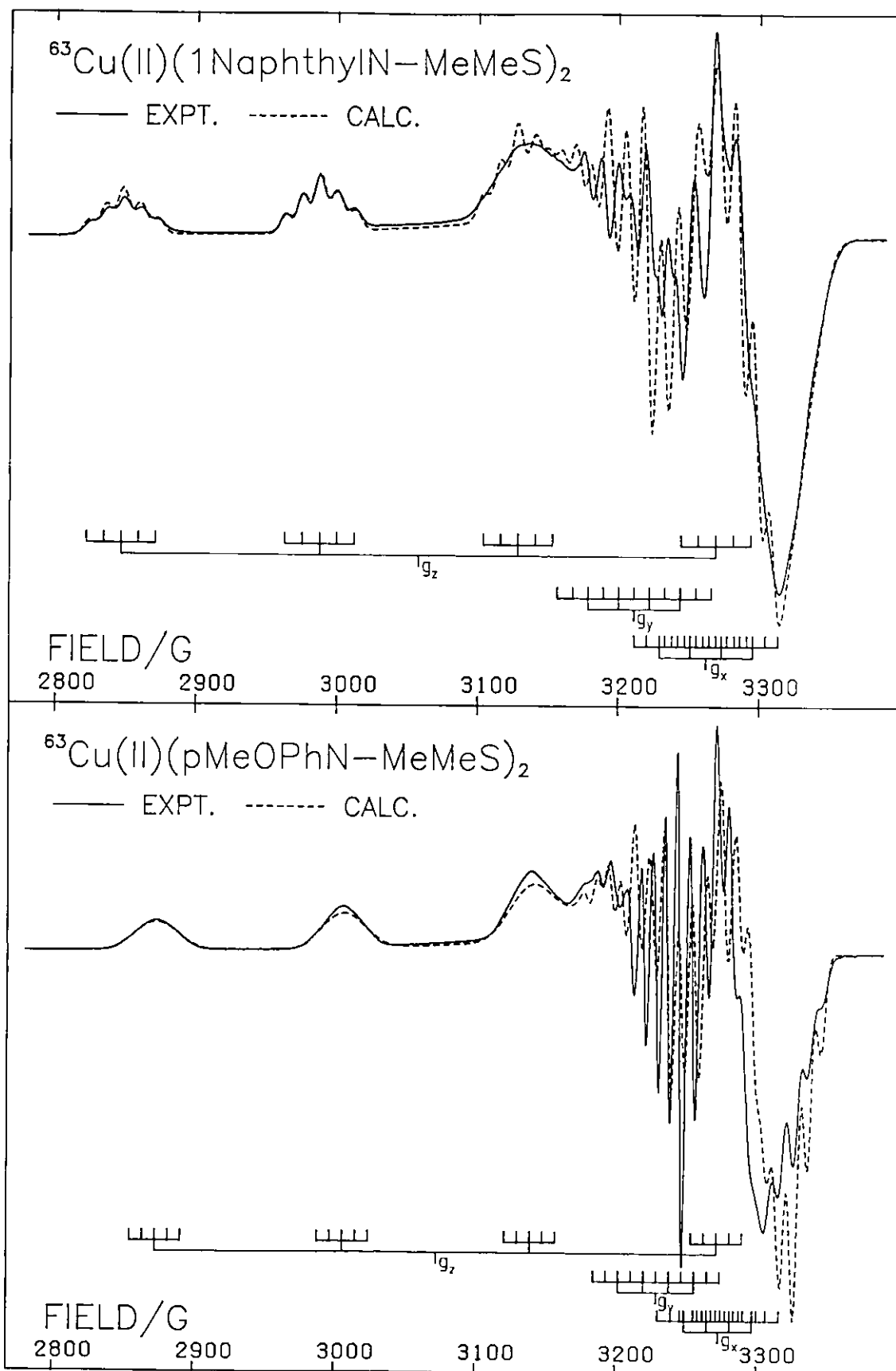
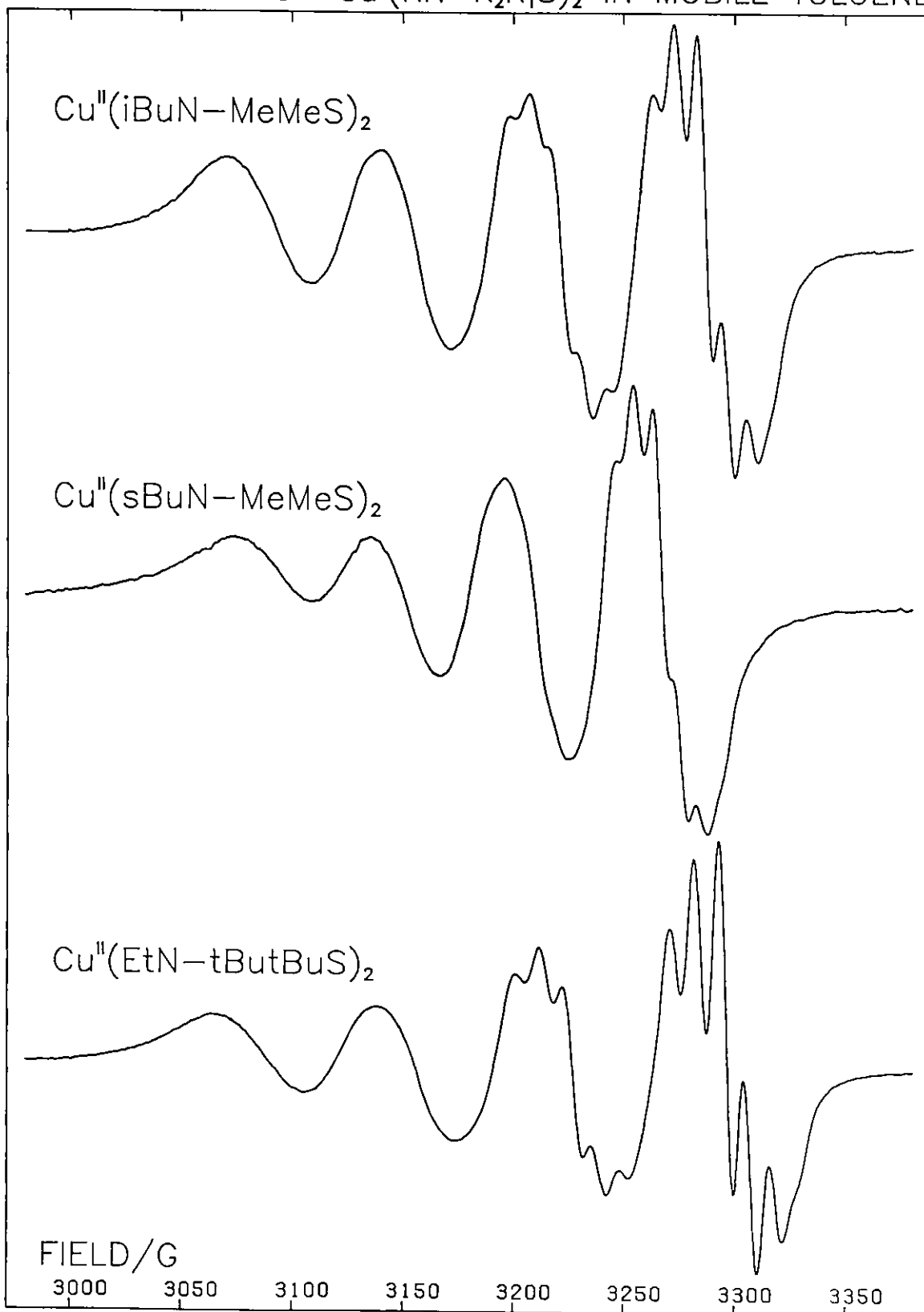


FIG. 5.6
EPR SPECTRA FOR $\text{Cu}^{II}(\text{RN}-\text{R}_2\text{R}_1\text{S})_2$ IN MOBILE TOLUENE



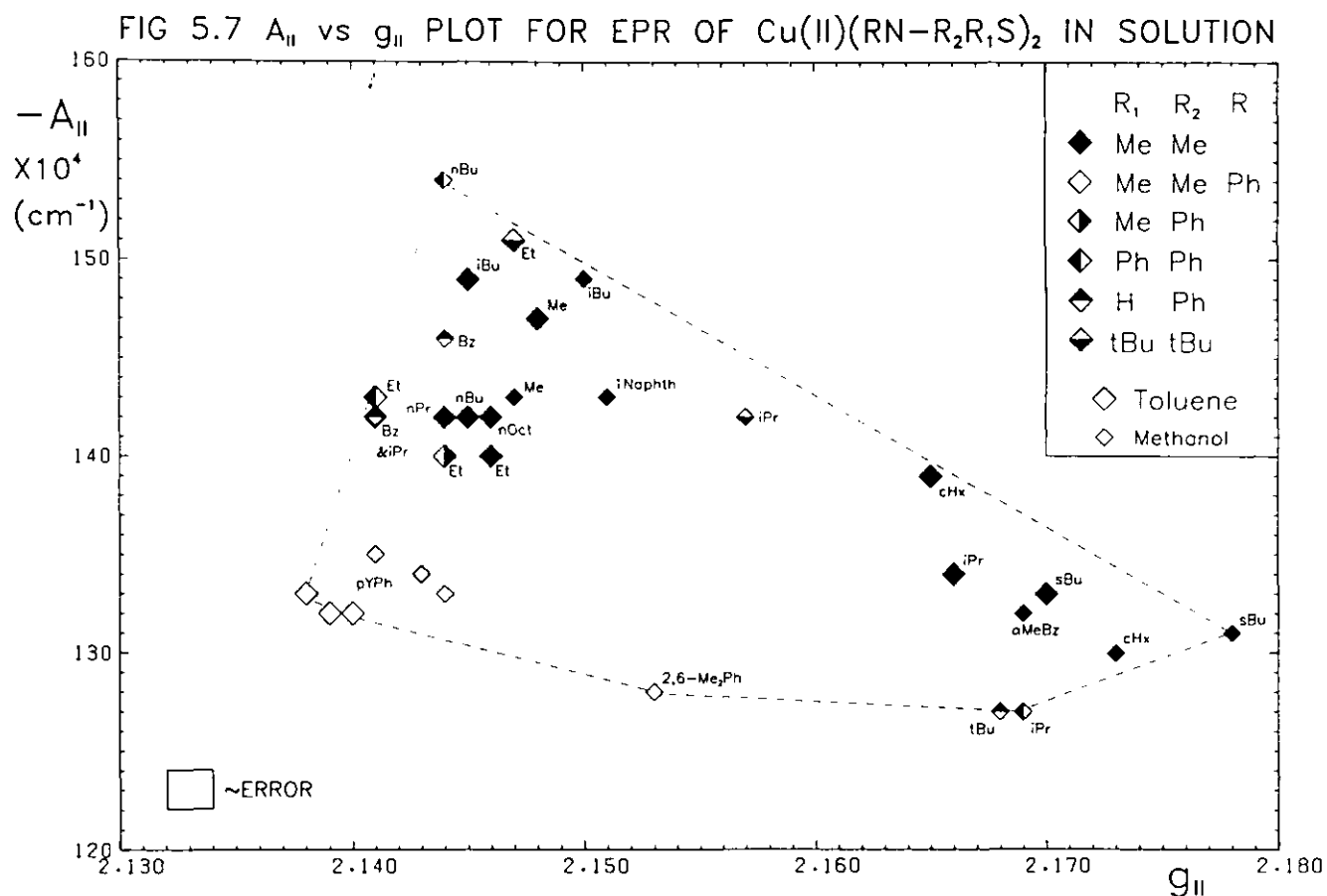
The calculation procedure employs a three-point Gauss-point angular integration method and second-order perturbation formulae for an orthorhombic spin Hamiltonian to generate line positions for the primary transitions. Weighted transition fields have been broadened with both Gaussian and Lorentzian functions, with width interpolated between three principal-axis values either linearly or by a direction cosine relationship. In some cases only limited attempts have been made to reproduce the complex superhyperfine patterns around g_{\perp} once the general form of the lineshape was attained, as the restricted capabilities of the program must be recognised. In particular, the simulation program, as written, has a simplistic approach to the orientation of the hyperfine and superhyperfine tensors. Whilst the primary hyperfine tensor may be rotated about the unique axis, any remaining hyperfine interactions must assume the principal axis system of the g -tensor. This means that for the coordination stereochemistry expected of the β -aminothione Cu(II) complexes the superhyperfine interaction will only be rigorously calculated when isotropic. It would be possible to evaluate the orientational dependence of the splitting from the two nitrogens by introducing three further parameters into the calculation to specify the relative orientations of the N_A and g tensors together with the angular relationship between the two Cu-N bonds. No attempt has been made to do this. Accurate x,y-axis parameters are not, however, required in the discussion that follows, since no attempt is made to evaluate bonding parameters in the absence of the d-d energy separations and in view of the difficulties inherent in estimating the many other unknowns. Despite the above reservations, together with the additional difficulty of adequately representing linewidth anisotropy and the neglect of quadrupole interactions, quite acceptable fits to the experimental spectra could be achieved in some cases.

Thus the simulation of the spectra in terms of superhyperfine interaction with two nitrogen nuclei, together with the observation of resolved 1:2:3:2:1 splitting on the low field g_z peaks in some cases, is strongly indicative of 2N2S coordination, which is assumed for steric reasons to be trans when projected onto the xy plane.

5.4.1.2. g_{\parallel} vs $|A_{\parallel}|$ Analysis.

Kivelson and Neiman³³⁸ first noted a correlation between Cu(II) hyperfine splitting and g_{\parallel} . Peisach and Blumberg³³⁹ constructed plots of A_{\parallel} against g_{\parallel} for a substantial range of complexes and established regions diagnostic of donor-atom coordination, overall charge and electron delocalisation. The tendency of g_{\parallel} to increase and $|A_{\parallel}|$ to decrease with an increase in the degree of tetrahedral distortion has been observed for structurally well-characterised complexes of Cu(II) with N-alkylsalicylaldehydes,^{340,341} bis(pyrazolyl)gallates²⁹¹ and dipyrromethenates,²⁹² and explicitly correlated by Addison and co-workers for complexes with pyrrole-2-carboxaldehydes²⁸⁹ and a wide range of other four-coordinate donor-sets,^{295,296} and by Symons, *et al.*³⁴² for Cu(II) doped pentacyanonitrosylferrate and tetrathiocyanatometallate salts.

$|A_{\parallel}|$ for the β -aminothione Cu(II) complexes has been plotted against g_{\parallel} in Figure 5.7. The expected anti-parallel relationship between these parameters is demonstrated by, for example, the change on going from R = Me, *i*Bu to R = *i*Pr, *s*Bu, *chx*, α MeBz in Cu(II)(RN-MeMeS)₂, the increased tetrahedral distortion in members of the latter group over the former being also manifest in their visible spectra (Sec. 5.3) and half-wave potentials (Sec. 5.6). There is, however, a wide general distribution of the points on Figure 5.7 outside an inverse correlation



of $|A_{||}|$ and $g_{||}$, particularly noticeable in the case of $R = -\text{CH}_2\text{R}'$ amino-substituents. Furthermore, a displacement toward the lower-left of the plot is observed for parameters of complexes having $R = \text{aryl}$. Thus, in addition to any stereochemical consequences, substantial electronic effects are apparent from changes in the amino and other chelate ring substituents. It must, of course, be noted that the span of $g_{||}$ and $|A_{||}|$ being considered here is not very large and detailed consideration of the interrelation of these parameters will only be given subsequent to a consideration of the wider range of values found for the Cu(II) doped, Zn(II) , Ni(II) and Cd(II) β -aminothione complexes.

5.4.2. EPR in Cu(II) doped Zn(II), Ni(II) and Cd(II) β -aminothione complexes.

Natural copper(II) or isotopically pure $^{63}\text{Cu(II)}$ has been doped at low temperature into Zn(II), Ni(II) and Cd(II) EPR-silent complexes of the RN-MeMeS ligand series. EPR parameters from features corresponding to resonance along the unique g principal-axis are listed in Tables 5.7, 5.8 and 5.9. Some representative spectra are shown in Figures 5.8 to 5.13, together with attempted simulations. Parameters used for the simulations are collected in Table 5.10.

A wide range of $|A_{\parallel}|$ values is found ($97\text{--}184 \times 10^{-4} \text{ cm}^{-1}$). Some of the spectra show excellently resolved 1:2:3:2:1 hyperfine splitting from two coordinated nitrogens. The $|^N A_{\parallel}|$ splittings range from $7\text{--}13 \times 10^{-4} \text{ cm}^{-1}$. In the case of Cu(II) doped $\text{M(II)}[(\text{CH}_2)_3(\text{N-MeMeS})_2]$ $\text{M} = \text{Zn, Cd}$ splitting is also seen at high field from two protons, 3G for $\text{M} = \text{Zn}$ (Figure 5.11) and 4G for $\text{M} = \text{Cd}$, presumably arising from the central bridging methylene group of the ligand.

Despite the reservations about the adequacy of the simulation procedure expressed in Sec. 5.4.1.1, a very good fit could be achieved for the X and Q-band spectra of Cu(II) doped $\text{Ni(II)}[(\text{CH}_2)_2(\text{N-MeMeS})_2]$, Figure 5.12 (note the stick spectra on all the simulations have no 2nd order corrections). The agreement of the sets of parameters from best-fit simulations of spectra at the two frequencies are within experimental error, Table 5.10. Simulations for other of the doped zinc complexes, Figures 5.8-10, are less acceptable and no great accuracy can be expected of the x-y parameters quoted in Table 5.10 as unique fits could not be attained in this region of the spectra; this is not unusual.³⁴³

TABLE 5.7. EPR parameters for $^{63}\text{Cu(II)}$ doped $\text{Zn(II)(RN-MeMeS)}_2$ at 100 K.

R	g_{\parallel}	$-A_{\parallel}$	$N_{A_{\parallel}}$
Me	2.177	115	10
Et	2.162	132	9
nPr	2.174	107	12-13
iPr	2.183	106	pr
nBu	2.161	125	9
iBu	2.172	102	9.5
nOct	2.176	108	pr
CHx	2.194	97	nr
Bz	2.154	132	10
α -MeBz	2.176	110	nr
1-Naphthyl	2.162	100	11
Ph	2.165	106	pr
pMePh	2.155	117	9
pMeOPh	2.153	124	9
pClPh	2.146	128	9
pFPh	2.167	108	7
2,6-Me ₂ Ph	2.166	101	12
2R = $-(\text{CH}_2)_n^-$			
n = 2 (RT)	2.130	159	12
n = 2	2.129	163	12.2
n = 3	2.139	137	10
n = 5	2.148	142	nr
n = 6	2.149	144	nr

Key: nr = not resolved, pr = poorly resolved,
RT = room temperature

Notes: 1) Frequencies in range 9.215 to 9.235 GHz
2) The low field features of R = nPr and
R = 1-Naphthyl are more complicated than
the expected $1:2:3:2:1$ $N_{A_{\parallel}}$ splitting.

TABLE 5.8. EPR parameters for Cu(II) doped Ni(II)(RN-MeMeS)₂ at 100 K.

R	g_{\parallel}	$-A_{\parallel}$	$\frac{N}{A}_{\parallel}$	Cu
Me	2.141	160	11.3	63
Et	2.140	165	10	63/65
nOct	2.152	154	10	63/65
C ₁₈ H ₃₇	2.155	146	nr	63/65
pMePh	2.144	158		63/65
pClPh	2.146	151	10.4	63
2,6-Me ₂ Ph	2.154	147	13-14	63/65
2R = -(CH ₂) _n -				
n = 2 (RT)	2.111	180.3	12	63
n = 2	2.112	183.3	12.3	63
n = 3	2.132	167	11.5	63

Frequencies range 9.22-9.23 GHz

TABLE 5.9. EPR parameters for Cu(II) doped Cd(II)(RN-MeMeS)₂ at 100 K.

R	g_{\parallel}	$-A_{\parallel}$	$\frac{N}{A}_{\parallel}$	Cu
Me	2.173	117	12	63
Et	2.166	124		63/65
nOct	2.174	112	12	63/65
pMePh	2.160	135	11.5	63
2R = -(CH ₂) ₃ -	2.142	140	10	63

Frequencies range 9.22-9.23 GHz

FIG. 5.8
EPR OF $^{63}\text{Cu}(\text{II})$ DOPED $\text{Zn}(\text{II})(\text{RN}-\text{MeMeS})_2$ AT 100K

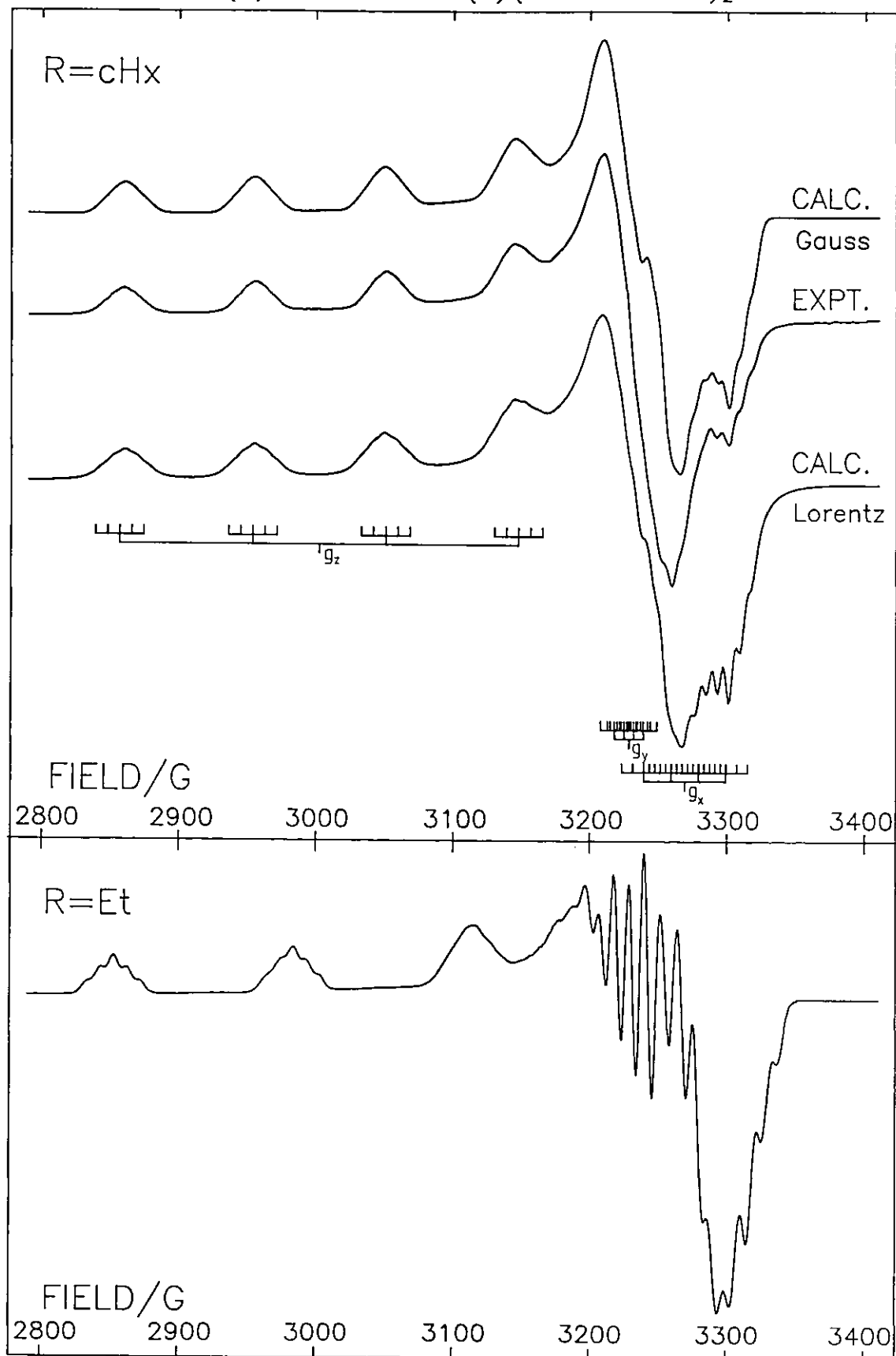


FIG. 5.9
EPR OF $^{63}\text{Cu}(\text{II})$ DOPED $\text{Zn}(\text{II})(\text{RN}-\text{MeMeS})_2$ AT 100K

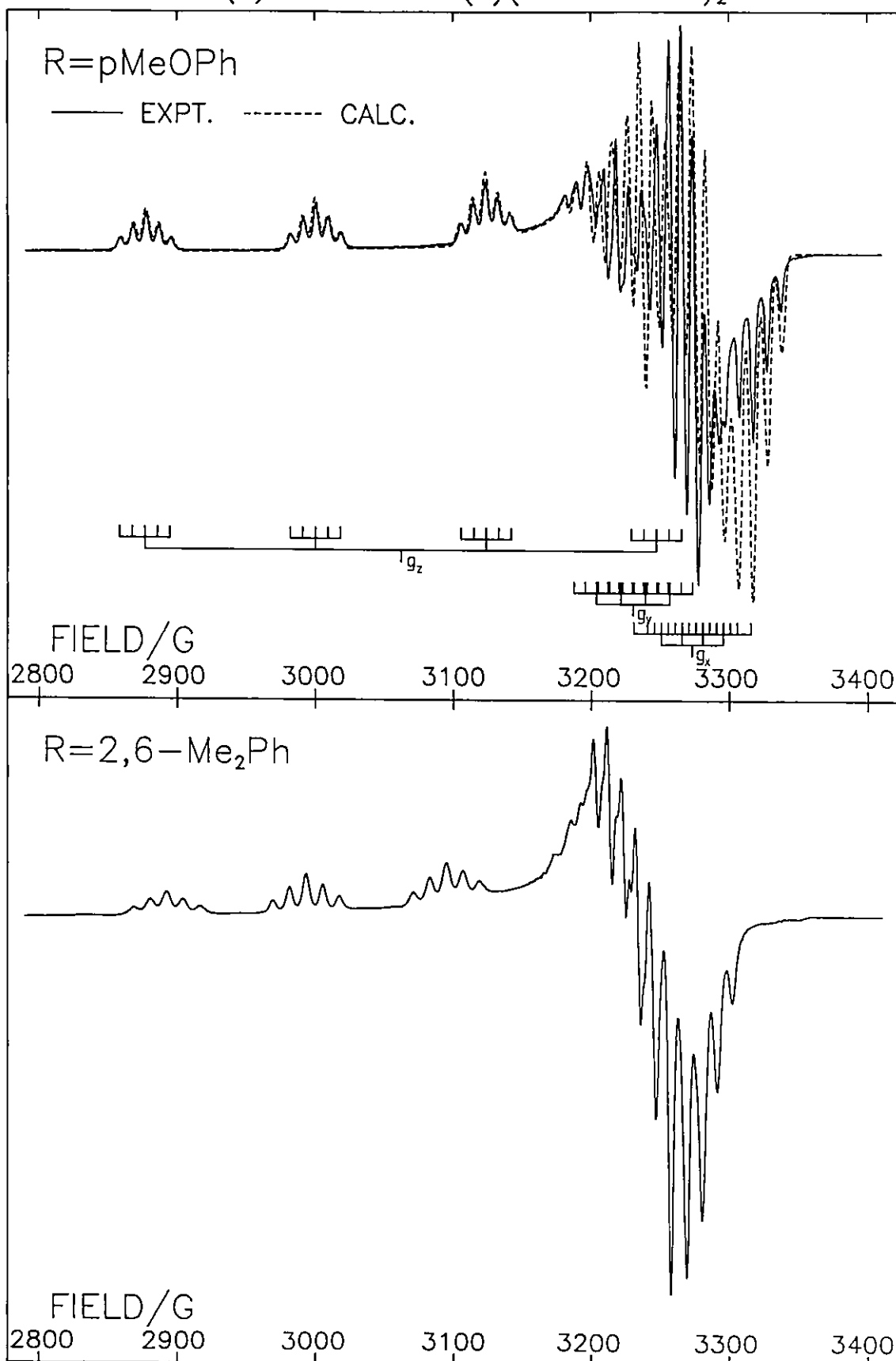


FIG. 5.10
EPR OF $^{63}\text{Cu}(\text{II})$ DOPED $\text{M}(\text{II})(\text{MeN}-\text{MeMeS})_2$ AT 100K

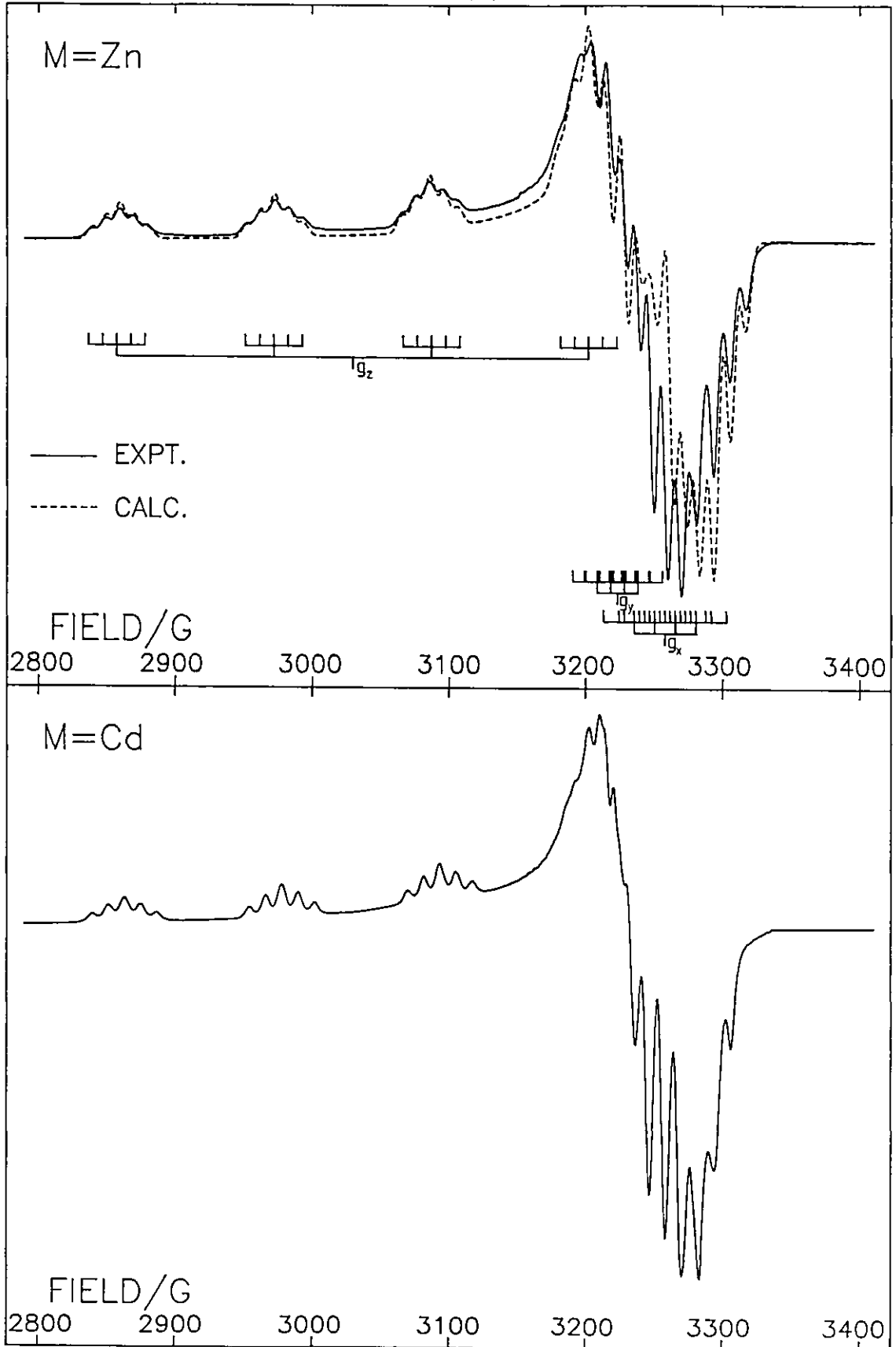


FIG. 5.11

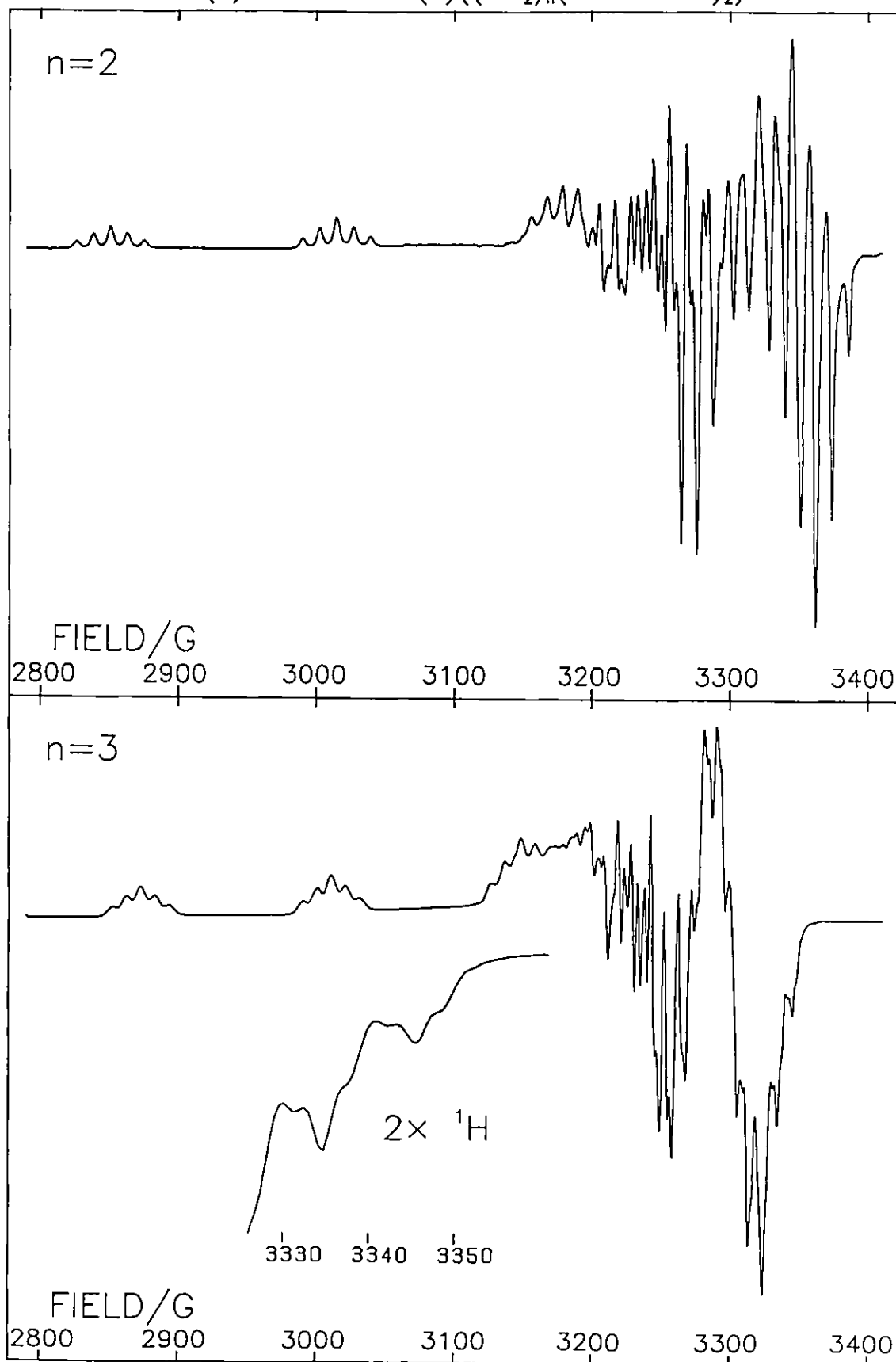
EPR OF $^{63}\text{Cu}(\text{II})$ DOPED $\text{Zn}(\text{II})((\text{CH}_2)_n(\text{N}-\text{MeMeS})_2)$ AT 100K

FIG. 5.12

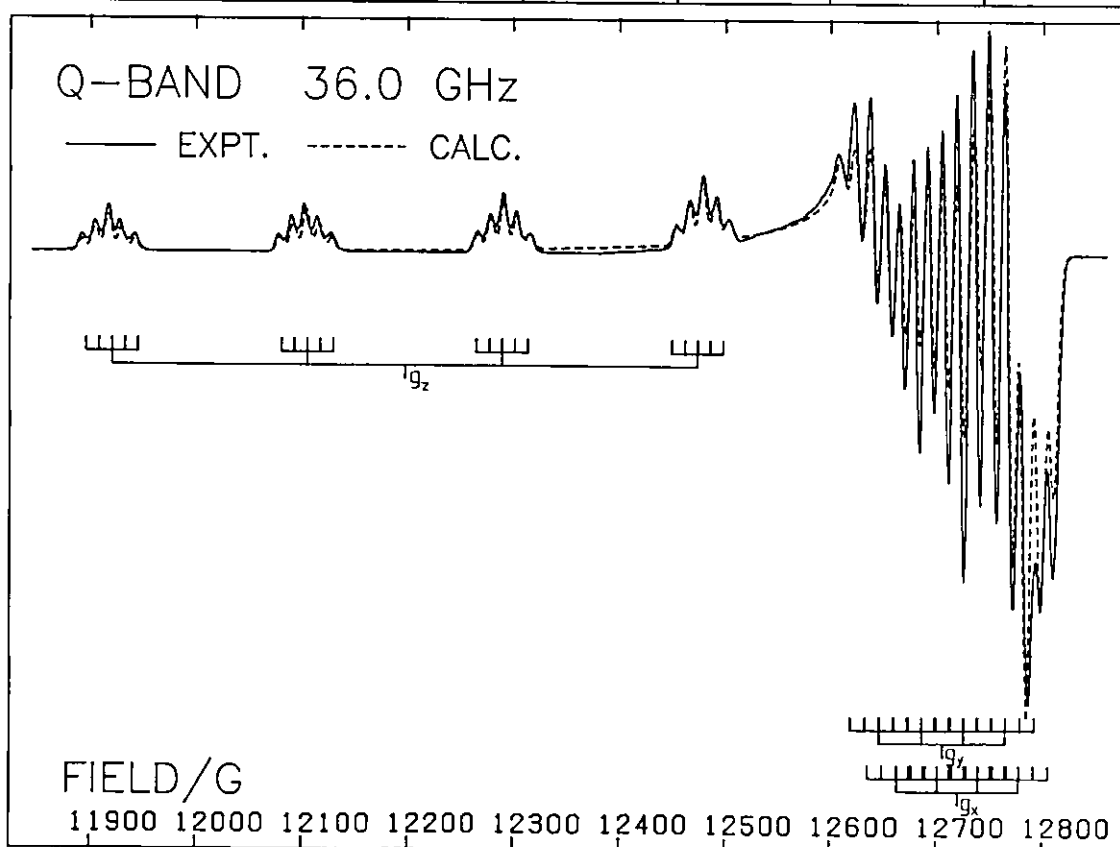
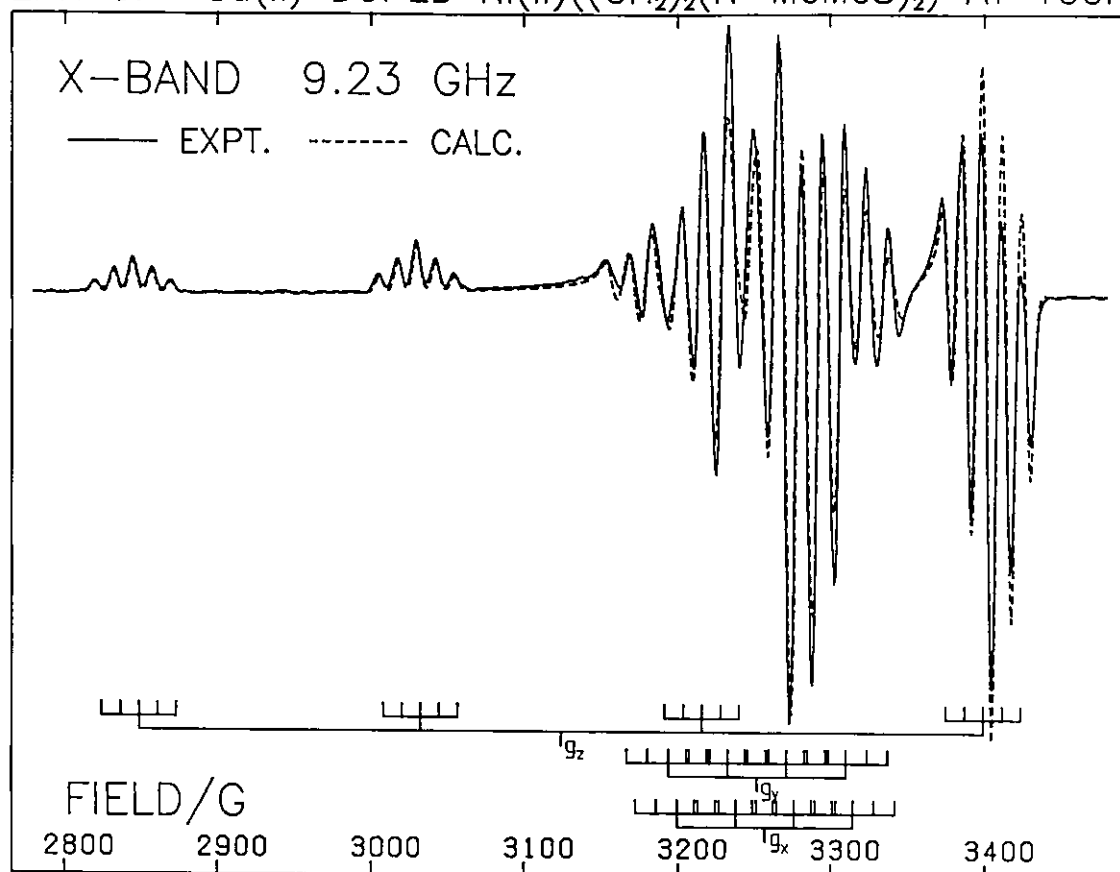
EPR OF $^{63}\text{Cu(II)}$ DOPED $\text{Ni(II)}((\text{CH}_2)_2(\text{N-MeMeS})_2)$ AT 100K

FIG. 5.13
EPR OF Cu(II) DOPED Ni(II)(RN-MeMeS)₂ AT 100K

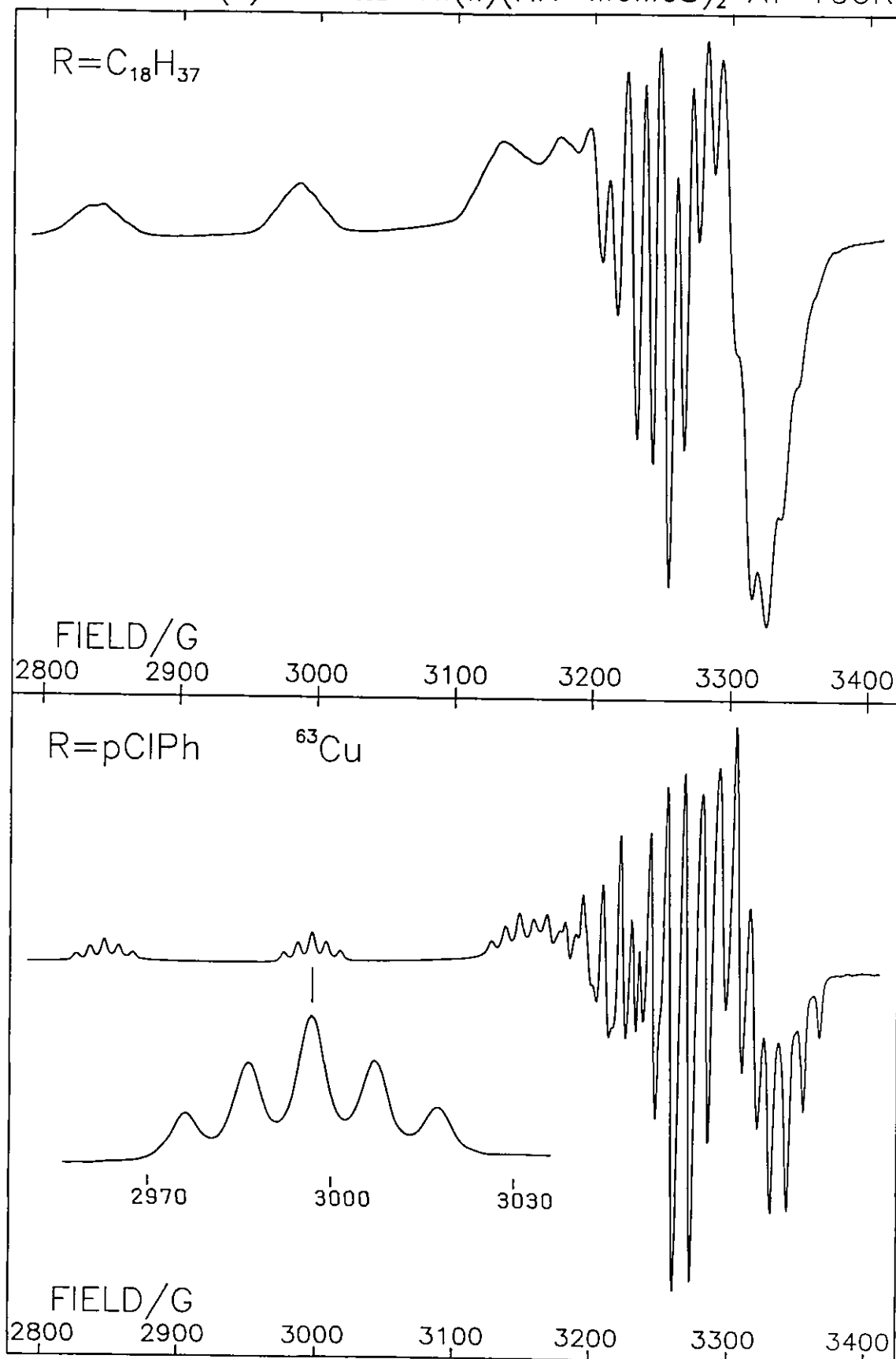
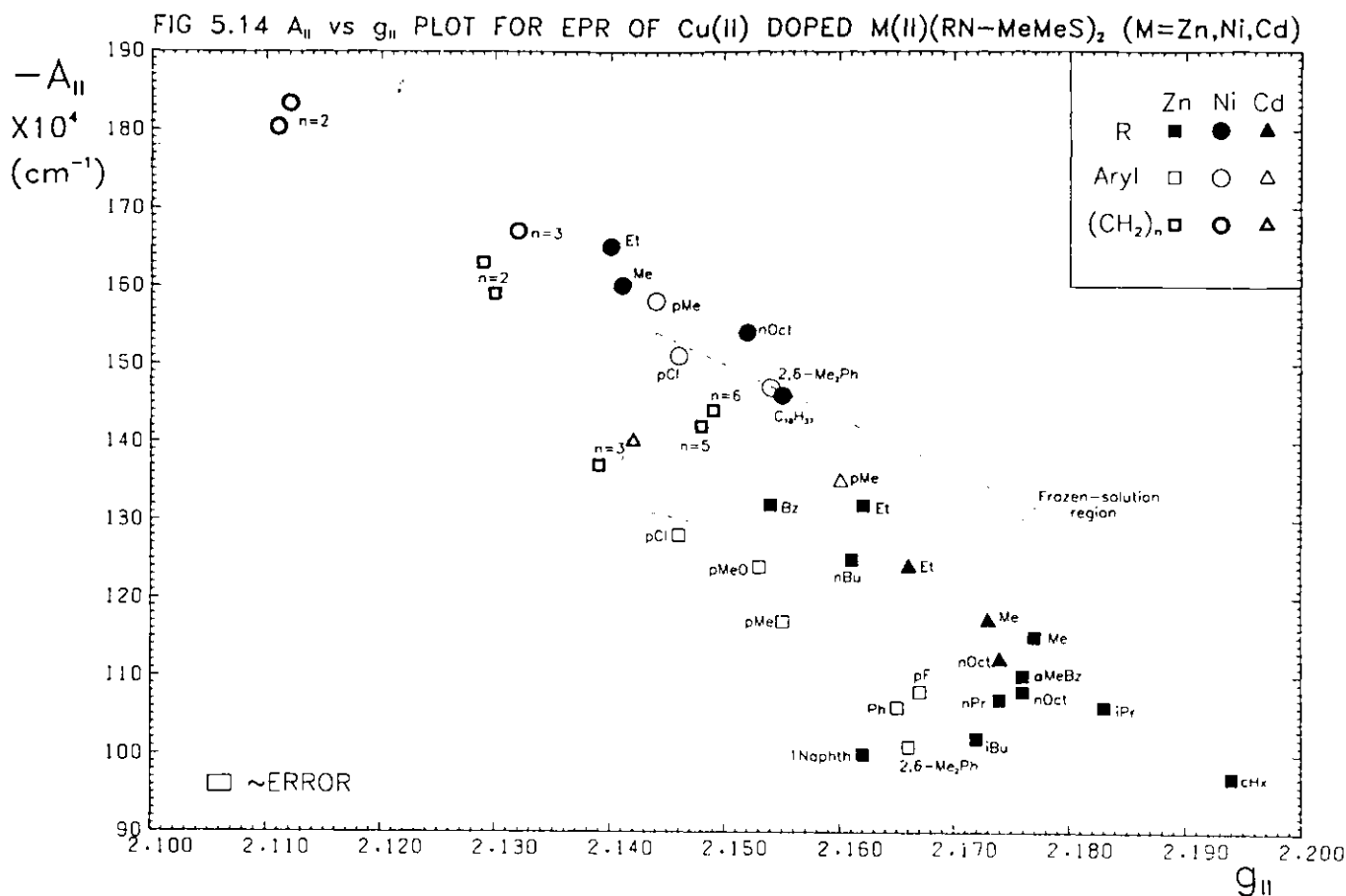


TABLE 5.10. EPR parameters used in simulating spectra of $^{63}\text{Cu(II)}$ doped M(II)(RN-MeMeS)_2 (M = Zn, Ni)

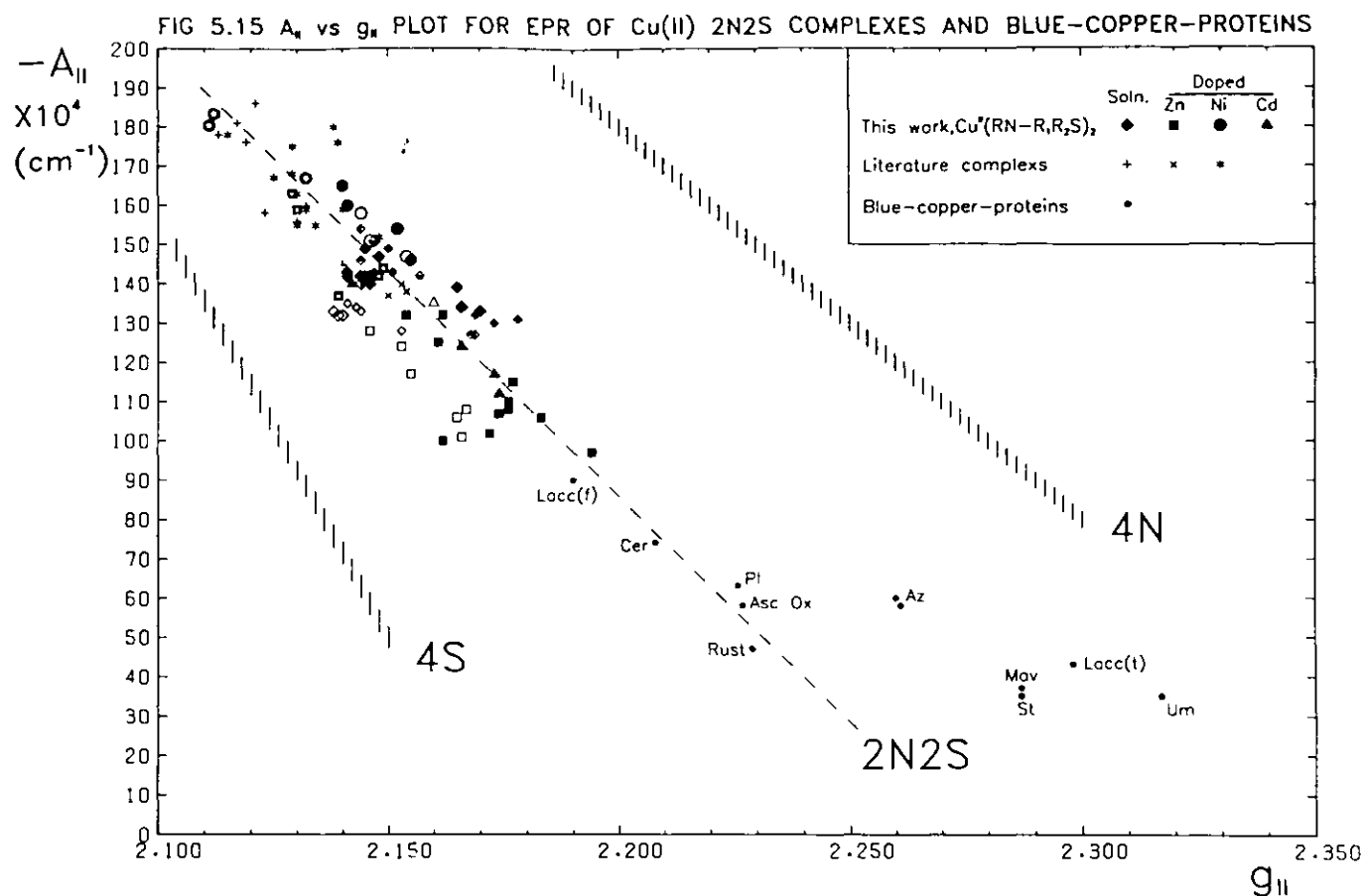
	M=Zn; R-			M=Ni; 2R=-(CH ₂) ₂ -	
	Me	pMeOPh	cHx	X-band	Q-band
g_x	2.024	2.014	2.017	2.024	2.024
g_y	2.046	2.045	2.043	2.027	2.026
g_z	2.176	2.153	2.196	2.111	2.111
$-A_x$	15	15	20	38.4	38.4
$-A_y$	10	17.8	7	38.8	39.5
$-A_z$	115	123.6	97	183.5	184.5
N_{A_x}	11.2	10	8	13.6	13.6
N_{A_y}	9	8.2	5	13.6	13.6
N_{A_z}	10.4	9.1	8.8	12.2	12.2
W_x	3.9	3.0	4.5*	4.5	5.0
W_y	3.9	2.5	7.0*	4.0	4.5
W_z	4.4	3.0	6.4*	3.0	4.0
W-anisotropy	L	L	L	DC	DC
Frequency/GHz	9.228	9.225	9.229	9.228	36.03
Figure	5.10	5.9	5.8	5.12	5.12

See footnotes to Table 5.6

*Lorentzian widths $W_x = 5$, $W_y = 8$, $W_z = 7$ Gauss.



$|A_{||}|$ values for the doped complexes are plotted against $g_{||}$ in Figure 5.14. The $|A_{||}|$, $g_{||}$ region for the solution parameters is also outlined. An approximate halving of $|A_{||}|$ is apparent on going from the Cu(II) doped Ni $[(\text{CH}_2)_2(\text{N}-\text{MeMeS})_2]$ extreme to Cu(II) doped Zn $(\text{cHxN}-\text{MeMeS})_2$, and complexes with intermediate $|A_{||}|$ values lie close to a line connecting these two complexes on the $|A_{||}|$ vs $g_{||}$ plot, albeit with a fair scatter. Other lines, connecting corresponding Ni(II)-Zn(II) and Ni(II)-Cd(II) Cu(II) doped complexes of a given specific ligand, in many cases closely parallel this trend, e.g., for R = Me, Et, nOct, $-(\text{CH}_2)_2-$ and $-(\text{CH}_2)_3-$. A steeper $|A_{||}|$ vs $g_{||}$ slope is found on going from Ni(II) to Zn(II) host when R = aryl, most notably for R = pClPh where there is a $23 \times 10^{-4} \text{ cm}^{-1}$ decrease in $|A_{||}|$ but no change in g -value.



5.4.3. Discussion of EPR parameters.

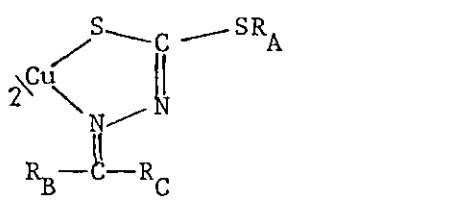
The plotting of $|A_{\parallel}|$ vs g_{\parallel} is extended in Figure 5.15 to include all the compounds previously tabulated (Tables 5.5, 5.7-5.9), other 2N2S complexes in solution or doped into Zn(II) or Ni(II) hosts (Table 5.11) and type 1 blue-copper-protein centres (Table 5.12), together with the previously established relationships between the two parameters for 4N and 4S coordination.^{289,295,296,339}

Qualitative descriptions of trends on the $|A_{\parallel}|$ vs g_{\parallel} plots have been compiled by Sakaguchi and Addison.²⁹⁵

(1) Tetrahedral distortion from square-planar causes the $(g_{\parallel}, A_{\parallel})$ point for a CuX_4 coordination centre to be shifted down and to the right.

(2) Replacement of 'hard' or class-a donor atoms by 'soft' or class-b donors tends to shift a CuX_4 centre of given geometry down and to the left.

TABLE 5.11. $g_{||}$ and $|A_{||}|$ parameters for previously reported 2N2S copper(II) complexes.

Complex	Solvent or host	ref.	$g_{ }$	$ A_{ } / \text{cm}^{-1} \times 10^{-4}$			
Cu[(CH ₂) ₂ -(N-MeMeS) ₂]	}	}	2.118	177			
Cu[(CH(CH ₃),CH ₂)-(N-MeMeS) ₂]			327	2.119	176		
Cu[(CH ₂) ₃ -(N-MeMeS) ₂]				2.130	156		
Cu[(CH ₂) ₂ -(N-MePhS) ₂]				2.113	178		
Cu[(CH ₂) ₃ -(N-MePhS) ₂]				2.123	158		
	50:50 DMF:CH ₂ Cl ₂						
Structure (S10) n = 2	}	328	2.117	181			
n = 3		329	2.132	160			
n = 4			2.140	145			
Structure (S6) n = 2	2:3 CHCl ₃ :DMF	333	2.121	186			
Cu(II)bis-(5-ethyl-2-mercapto-3-thenylidene)ethylenediamine	Ni(II)	331	2.115	178			
							
R_A	R_B	R_C					
Me	2-Naphthyl	Me	Ni(II)	}	2.130	163	
Me	mNO ₂ Ph	Me	Ni(II)		2.129	168	
Me	Ph	Me	Ni(II)		2.132	159	
Me	ptolyl	Me	Ni(II)		344	2.134	155
Me	pNO ₂ Ph	Me	Ni(II)		2.130	155	
Me	Ph	H	Ni(II)		2.138	180	
Me	H	o-tolyl	Ni(II)		2.129	175	
Me	H	m-tolyl	Ni(II)		345	2.139	176
Me	H	o-C ₆ H ₄	Ni(II)		2.125	167	

/continued

TABLE 5.11 (continued).

Complex			Solvent or host	ref.	g_{\parallel}	$ A_{\parallel} / \text{cm}^{-1} \times 10^{-4}$
R_A	R_B	R_C				
Bz	Me	Ph	Ni(II)	} 345	2.148	152
Bz	Me	ptolyl	Ni(II)		2.140	143
Bz	Me	2-naphthyl	Ni(II)		2.140	159
Me	H	o-tolyl	Zn(II)		2.150	137
Me	Me	p-tolyl	Zn(II)		2.153	140
Me	Me	Ph	Zn(II)		2.154	138

TABLE 5.12 EPR parameters for blue-copper-proteins.

Protein	ref.	g_{\parallel}	$ A_{\parallel} / \text{cm}^{-1} \times 10^{-4}$	g_{\perp}	$ A_{\perp} / \text{cm}^{-1} \times 10^{-4}$
Azurin (Az) <u>Ps. fluorescens</u>	346	2.261	58	2.052	~ 0
<u>Ps. aeruginosa</u>	"	2.260	60	2.052	~ 0
Stellacyanin (St)					
<u>R. vernicifera</u>	347	2.287	35	x 2.025 y 2.077	x 57 y 29
Plastocyanin (Pl)	348				
<u>Chenopodium album</u>		2.226	63	2.023	< 20
Umecyanin (Um)	349	2.317	35	2.05	
<u>Armoracia lapathifolia</u>					
Mavicyanin (Mv)	350	2.287	37	x 2.025 y 2.077	x 54 y 28
<u>Cucurbita pepo medullosa</u>					
Rusticyanin (Rust)	351	2.229	47	x 2.019 y 2.064	x 61 y 19
<u>Thiobacillus ferro-oxidans</u>					
Laccase					
[Lacc(t)] <u>R. vernicifera</u>	347	2.298	43	2.047	17
[Lacc(f)] <u>P. versicolor</u>	352	2.190	90	2.042	10
Ceruloplasmin (Cer) Human	353	2.208	74	2.050	
Ascorbate oxidase (Asc.ox)	} 354 355	2.27	58	x 2.036	x 5
<u>Curcubita pepo medullosa</u>				y 2.058	y 5

(3) Increasing net charge on the CuX_4 moiety, increasing ligand electron donation or increasing electron delocalisation tends to decrease g_{\parallel} and increase $|A_{\parallel}|$.

No ready general confirmation of the expected electronic effects (point 3) of substituents is forthcoming from the results on the present complexes.

Point 2 is illustrated by the intermediate position of the $g_{\parallel}, |A_{\parallel}|$ region containing the 2N2S complexes with respect to the regions established for complexes having 4N and 4S coordination. The shift to smaller g -values on going to 'softer' donor-atoms is indicative of increased delocalisation of the unpaired spin-density away from the copper nucleus, interpreted as increased covalency in the metal-ligand bonds.

The increase in g_{\parallel} and decrease in $|A_{\parallel}|$ with increasing distortion from square-planar toward tetrahedral coordination (point 1 above) has already been described for the complexes, but is now more clearly seen in Figure 5.15. Although no direct, for example crystallographic, evidence can be presented to indicate the relative degree of tetrahedral distortion in any of the β -aminothione complexes, the trends in $g_{\parallel}, |A_{\parallel}|$ do follow those expected from considering the stereochemical distortions anticipated from the steric bulk of substituents and/or structural imposition by host lattice, and have ample precedent in comparable series of complexes. Thus to reiterate, complexes having α -branched amino-substituents giving steric hinderance^{289,340,292,291,341} and/or Zn host lattices^{342,344,345} are expected more closely to approach tetrahedral coordination stereochemistries than those having α -unbranched substituents and/or Ni hosts, and the $(g_{\parallel}, |A_{\parallel}|)$ points for the former appear, in general, down and to the right of those for the latter.

X-ray crystallographic structure determinations for $\text{Zn(II)}[(\text{CH}_2)_n - (\text{N-MeMeS})_2]$, $n = 2$, and 4 demonstrate the adoption of a pseudo-tetrahedral Zn coordination geometry,^{356,357} whilst for $\text{Ni(II)}[(\text{CH}_2)_2 - (\text{N-MeMeS})_2]$ the expected square-planar geometry has been spectroscopically confirmed.³²⁶ All of the nickel complexes used as hosts are considered to be predominantly planar in solution by comparison with similar compounds,³²² although as mentioned in Sec. 5.3.3 the presence of near-IR absorption for the $R = \text{aryl}$ complexes is indicative of some tetrahedral form also, Table 5.4. Reflectance spectra of the solids did not show near-IR features, and were not helpful in determining the crystalline stereochemistry. Reflectance measurements were also made on several of the more intensely coloured Cu(II) doped Zn(RN-MeMeS)_2 complexes in an attempt to correlate electronic and EPR parameters, but no correlation of the band maxima with $|A_{\parallel}|$ or g_{\parallel} was apparent.

Solution visible and polarographic results presented in other parts of this section indicate more tetrahedrally distorted coordination geometry in the bidentate β -aminothione Cu(II) complexes than in related complexes (see Table 5.11) having quadridentate 2N2S ligands, and this is borne out in their relative positions in Figure 5.15. A similar spectroscopic and polarographic distinction between members of the dissolved bidentate β -aminothione Cu(II) complex series concerning α -branching of the amino substituent has already been pointed out in Sec. 5.4.1.2.

From the orbital magnetic contribution of g_{\parallel} to $|A_{\parallel}|$ a direct antiparallel relationship is anticipated between these two parameters, and such an explanation has been invoked to interpret the behaviour of certain series of copper(II) complexes.^{243,342} The trends in g_{\parallel} and $|A_{\parallel}|$ on passing from square-planar to tetrahedral stereochemistry may thus be qualitatively understood in similar terms; the energy separation of the electronic levels decreasing and leading to increasing g -values.

Indeed, evaluation of the orbital coupling contribution to \underline{A} , by diagonalisation of the spin-orbit coupling perturbation matrix (all order perturbation), has been considered by Bertini, *et al.*³⁵⁸ entirely sufficient to account for the copper-hyperfine and g -tensor parameters when the distortion from square-planar is not too severe. For distortions of large extent the admixture of 4p and 4s orbital character into the ground state, permitted by loss of a coordination sphere inversion centre, becomes increasingly important. The expressions for the EPR g and \underline{A} tensor parameters as obtained from 2nd order perturbation theory, after considering linear combinations of copper 3d, 4s and 4p orbitals and ligand orbitals pertinent to D_{2d} symmetry, are too complex to allow any analysis in terms of a simple direct relationship between $|A_{||}|$ and $g_{||}$ for the present series of complexes.^{287-289,359,360} Decrease in $|A_{||}|$ due to 3d-4p and 3d-4s orbital mixing was first suggested by Bates²⁸⁷ to account for the very small \underline{A} values found for the cupric complex of (α, α' -bromo)dipyrromethane. Mixing of 4p and 4s character into the ground-state is favourable where there is a tetrahedral distortion from square-planar since it leads to a lowering of energy. The spin distribution in the admixed orbital produces a magnetic field at the nucleus which is opposite in direction to that from the d_{xy} orbital and the resultant reduced field leads to a small hyperfine splitting. Sharnoff³⁵⁹ suggested that the unpaired electron in the tetrachlorocuprate anion spends 12% of its time in a 4p(Cu) orbital, in order to explain the low value of $25 \times 10^{-4} \text{ cm}^{-1}$ found for $|A_{||}|$. A 19% 4p contribution to the ground state in azurins was proposed by Brill and Bryce²⁸⁸ to account for the unusual characteristics of both EPR and electronic spectra. However, although the reduction of $|A_{||}|$ by 3d-4p and 3d-4s orbital mixing has become well established in interpreting EPR parameters from tetrahedrally distorted copper complexes,^{291,298,340,361,362} the validity of invoking

large mixing coefficients is not without dispute. On the basis of the wide variation of $|A_{||}|$ observed in cupric complexes having similar pseudo-tetrahedral structures, Bencini et al.³⁶³ have proposed that the $|A_{||}|$ values for CuCl_4^{2-} and type 1 copper-proteins are essentially due to covalency of copper-ligand interactions and large spin-orbit coupling of the ligand donor-atoms. Similarly, the unexpectedly high $|A_{||}|$ values of Cu(II) N,N'-diaryl- β -iminoamines (considering their expected degree of tetrahedral distortion from square-planar) has been cited as indicating that 3d-4p mixing may not be so dominant a factor in decreasing $|A_{||}|$ for pseudo-tetrahedral copper(II).²⁹³ It is difficult, however, to accept the view of Bencini et al.³⁶³ that covalency is important in reducing $|A_{||}|$ since in Cu(TPP), for example, the unpaired electron wave-function has a high proportion of ligand character but the copper hyperfine splitting is large and anisotropic.³⁶⁴ and refs. therein

For the present series of complexes $|A_{||}|$ falls too low to be accounted for purely by coupling of the orbital momentum with the nuclear spin and thus some additional contribution to the hyperfine splitting must be present. Drastic changes in covalency of the metal-ligand interactions are neither manifested in trends in the superhyperfine ^{14}N splittings nor anticipated in view of the constant 2N2S coordination, and the mechanism for reduction of $|A_{||}|$ proposed by Bencini, et al.³⁶³ is rejected. The lowering of $|A_{||}|$ by 4p and 4s mixing into the ground level, which has increasing effectiveness as the coordination geometry distorts more toward tetrahedral, is considered, together with the orbital contribution to $|A_{||}|$, to be a correct interpretation of the behaviour of the present compounds as depicted in Figure 5.15.

The $(g_{\parallel}, |A_{\parallel}|)$ points for many of the type 1 copper proteins are found in a region which is an extension to the trend of decreasing $|A_{\parallel}|$ with increasing g_{\parallel} for the 2N2S model complexes. Distorted tetrahedral 2N2S coordination sites have been crystallographically established for plastocyanin²⁸⁰ and azurin²⁸¹ and seem reasonable assumptions for fungal laccase, ceruloplasmin, ascorbate oxidase and rusticyanin on the basis of the results in Figure 5.15. This coordination may also be appropriate to tree laccase, stellacyanin, umcyanin and mavicyanin since although the $(g_{\parallel}, |A_{\parallel}|)$ points for these appear at some distance from the 2N2S delineator constructed in Figure 5.15, the present results give no real indication of the behaviour of the g_{\parallel} vs. $|A_{\parallel}|$ relationship at such remote values.

A large tetrahedral distortion in the copper centres of all type 1 proteins is believed to be a necessary, and probably sufficient, condition to explain their unusual copper A-tensors. The z-axis EPR parameters for Cu(II) doped Zn(II)(cHxN-MeMeS)₂ represent the closest approach to date by a 2N2S coordinated complex to those for the type 1 proteins and are quite comparable to the values observed for fungal laccase (Table 5.12).

5.5. Vibrational Spectra.5.5.1. Raman and IR spectra for Cu(RN-MeMeS)₂ (R = Me, iBu).

The thermal instability of the cupric complexes, together with their intense absorption in the visible presents some considerable difficulty to the measurement of Raman spectra. Using the technique of spinning samples at low temperature, described in Appendix B, spectra of reasonable quality have been obtained for the most stable solids, Cu(II)(MeN-MeMeS)₂ and Cu(II)(iBuN-MeMeS)₂. Band positions and relative intensities at several excitation wavelengths are reported in Tables 5.13 and 5.14 and Figure 5.16 shows some representative spectra obtained for solid

TABLE 5.13. Raman spectral parameters for Cu(II)(MeN-MeMeS)₂ at -140°C (KBr disc).

Band maxima (cm ⁻¹) and intensities vs. excitation (nm)								Ligand	
647.1		568.2		530.2		482.5			
						97	2	77	8
108	w	108	~7					112	4
		124	2					185	10
151	4	149	3	150	3	151	2	298	br,w
		167	1	166	vw			334	br,w
191	3	193	w	185	br,w	191	1	372	br,w
242	9	241	9	242	2	242	5	471	5
294	4	291	4	293	2	293	1	630	2
317	10	315	3	317	1	318	2	715	2
365	2	260	w					844	w
380	2	376	10	376	10	376	10	1023	w
395	1							1035	w
440	w							1069	w
486	4	485	3						
500	2	495	w						
		566	3						
598	4	598	w						

Other w-m bands observed on 647.1 nm at 665, 704, 802, 840, 864, 986, 1022 and 1060 cm⁻¹.

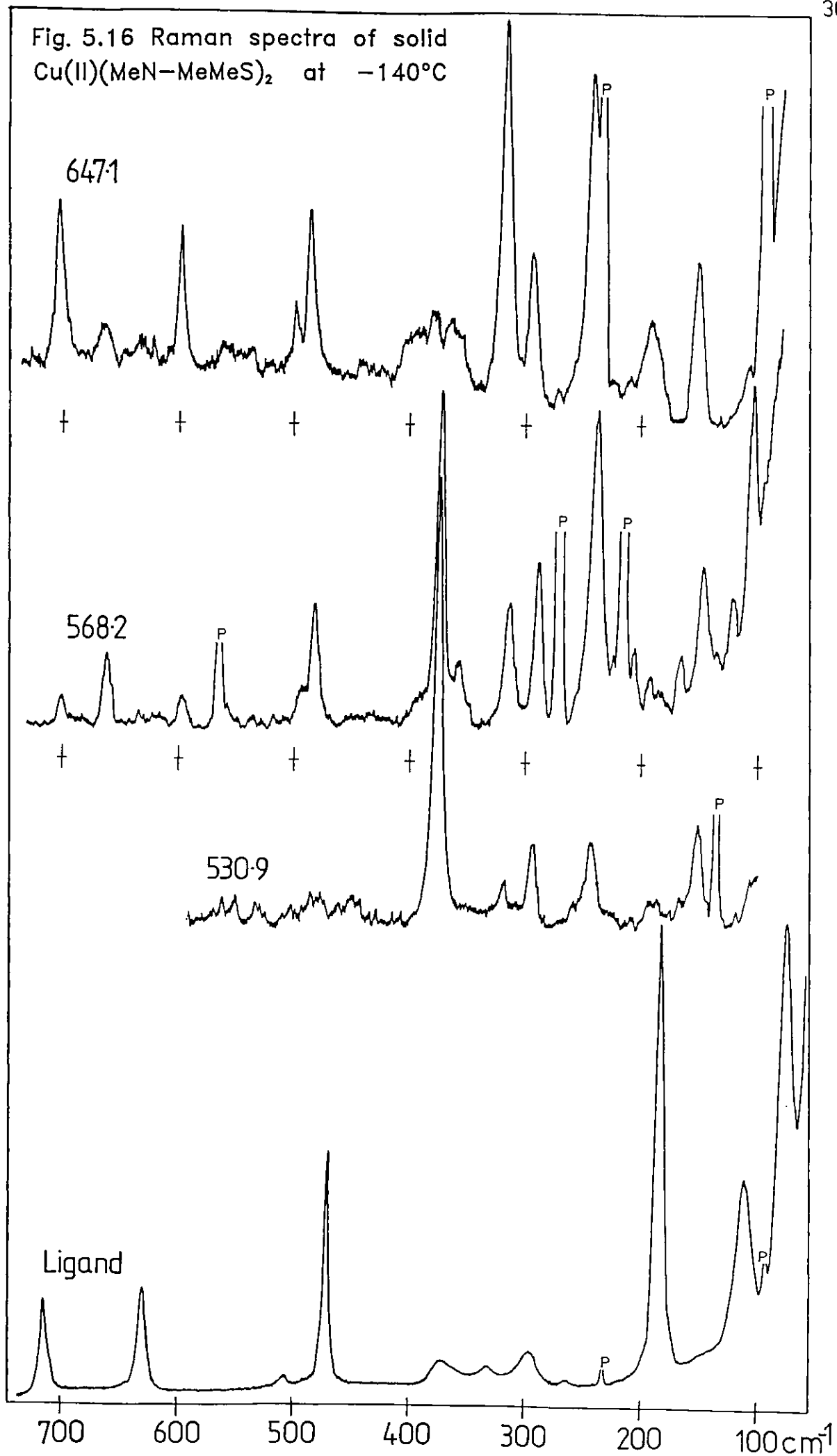
Cu(II)(MeN-MeMeS)₂ in acetone at -75°C 647.1 nm excitation: 244(m, ρ0.35), 320(m, ρ0.25), ~190(w), ~151(w). 482.5 nm excitation: ~250(w), ~380(w)

TABLE 5.14. Raman Spectral Parameters for Cu(II)(iBu-MeMeS)₂ at -140°C
(KBr disc).

Band maxima (cm ⁻¹) and intensities vs. excitation (nm)								Ligand	
647.1		568.2		530.9		482.5			
		107	10	106	1			96	7
		123	3					177	10
154	s	155	10	157	5	155	mw	290	2
		196	1					331	2
221	m	208	6	220	br,1	231	w	389	1
253	m	252	9	255	3	254	w	452	3
		290	4	286	2	286	w	476	1
300	m	300	4	300	2	300	vw	499	3
						340	w	522	1
380	mw	380	2	381	10	381	s	637	2
				476	2			717	2
485	m	485	4	488	1			814	w
514	ms	513	6	513	w			840	w
				550	w			950	w
				602	2			1025	w
				658	2			1073	2

TABLE 5.15. Low frequency IR data for Cu(II)(RN-MeMeS)₂ (R = Me, iBu).

MeN-MeMeS		iBuN-MeMeS	
Cu(II) Complex	Ligand	Cu(II) Complex	Ligand
257w		263m	
288w	300w	290m, d1	292m
317w		330w	338m
	335vw	370s, d1	
370m	371br, w		393w
~ 480sh, vw	472mw	457vw	
498m		478sh, w	477m, d1
	512m	488w	
598mw	597m	512m	510m
	628m	532ms	
663mw		600m	594s
700mw			629ms
	718s	658m	
798s	806s		



$\text{Cu}(\text{MeN-MeMeS})_2$. Measurements have also been made on an acetone solution of the latter complex and are of sufficient quality to indicate the polarisation of two bands which correlate with shifts observed for the solids. Attempts to obtain spectra for a few of the other less stable complexes were frustrated by excessive fluorescent emission leading to extremely poor signal to noise ratio. Low frequency IR spectral details for $\text{Cu}(\text{MeN-MeMeS})_2$ and $\text{Cu}(\text{iBuN-MeMeS})_2$ in polythene are given in Table 5.15.

5.5.2. Assignment.

Table 5.16 presents the group-theoretically predicted symmetries and selection rules for the normal modes of a trans-planar and a tetrahedral or tetrahedrally-distorted planar CuN_2S_2 vibrational unit. In each case

TABLE 5.16. Symmetries and selection rules for normal modes of CuN_2S_2 .

trans-planar, C_{2h}		tetrahedral, C_{2v}	
$2A_g$	$\nu(\text{R})$	$2A_1$	$\nu(\text{R+IR})$
$2A_g$	$\delta(\text{R})$	$2A_1$	$\delta(\text{R+IR})$
$1A_u$	$\delta(\text{IR})$	A_2	$\delta(\text{R})$
$1B_g$	$\delta(\text{R})$	B_1	$\nu(\text{R+IR})$
$2B_u$	$\nu(\text{IR})$	B_1	$\delta(\text{R+IR})$
$1B_u$	$\delta(\text{IR})$	B_2	$\nu(\text{R+IR})$
		B_2	$\delta(\text{R+IR})$

ν - stretch; δ - deformation

R - Raman active; IR - infrared active

two polarised Raman active stretching frequencies are anticipated. Two bands at 242 cm^{-1} and 317 cm^{-1} in $\text{Cu(II)(MeN-MeMeS)}_2$ have polarised solution counterparts at 244 cm^{-1} ($\rho \approx 0.35$) and 320 cm^{-1} ($\rho \approx 0.25$), and do not appear in the ligand spectrum. These bands are reasonably assigned as mainly metal-donor-atom stretching in character, probably predominantly $\nu(\text{Cu-S})$. The 317 cm^{-1} shift correlates with a weak IR absorption at an identical frequency and from the selection rules of Table 5.16 would tend to suggest, as expected, a departure from square-planar geometry; unless this were to be cis, which is unlikely for steric reasons.

For $\text{Cu(II)(iBuN-MeMeS)}_2$ corresponding medium-strong lines are observed in the Raman at 253 cm^{-1} and 300 cm^{-1} . The Raman bands at 376 cm^{-1} in $\text{Cu(II)(MeN-MeMeS)}_2$ and 381 cm^{-1} in $\text{Cu(II)(iBuN-MeMeS)}_2$, seen most strongly with blue-green excitation wavelengths, have no plausible strong ligand counterparts and are considered also to be metal-ligand vibrations, probably mainly $\nu(\text{Cu-N})$. An IR absorption at 370 cm^{-1} seen in both metal complexes may be due to the same mode, though a weaker absorption at a very similar frequency is also seen in the MeN-MeMeS ligand and presents an alternative explanation for the Cu(MeN-MeMeS)_2 band.

Barring coincidence, a fourth metal-ligand stretching mode is anticipated and Raman bands at 293 , 486 and 500 cm^{-1} in $\text{Cu(II)(MeN-MeMeS)}_2$ and 286 , 485 and 514 cm^{-1} in $\text{Cu(II)(iBuN-MeMeS)}_2$ would seem reasonable candidates. Correlatable absorptions at 288 , 480 , 498 cm^{-1} for Cu(MeN-MeMeS)_2 and 290 , 488 and 512 cm^{-1} (also additional candidate at 532 cm^{-1}) for Cu(iBuN-MeMeS)_2 are seen in the IR. Most have close ligand counterparts in the Raman or IR. The higher frequencies would be expected to involve considerable mixing with ligand modes due to rigidity of the chelate ring conferred by electron delocalisation, and resonance enhancement of Raman

active ligand vibrations is not unexpected. No categorical assignment is attempted here.

Looking to lower frequencies, the Raman shifts of 151 cm^{-1} and 155 cm^{-1} in $\text{Cu}(\text{MeN-MeMeS})_2$ and $\text{Cu}(\text{iBuN-MeMeS})_2$ respectively are probably primarily CuN_2S_2 deformations of totally symmetric character. The band at 191 cm^{-1} in $\text{Cu}(\text{MeN-MeMeS})_2$ is noted to have a very intense ligand counterpart at 185 cm^{-1}

The intense Raman lines at 242 , 317 and 376 cm^{-1} in $\text{Cu}(\text{MeN-MeMeS})_2$ are matched by similar intense features at 259 , 317 and 384 cm^{-1} in $\text{Ni}(\text{MeN-MeMeS})_2$.

Metal sulphur stretches have been assigned by normal-coordinate analysis to around 290 cm^{-1} and 380 cm^{-1} in metal dithioacetylacetonates³⁶⁵ but to around 250 cm^{-1} and 190 cm^{-1} in metal monothioacetylacetonates.³⁶⁶

5.5.3. Raman assignments in blue-copper-proteins.

Several papers have been published reporting or discussing Raman spectra of blue-copper-proteins.^{237-239,367-371} Table 5.17 summarises the main bands which have been observed at low frequencies. The bands have been categorised as $\nu[\text{Cu-S}(\text{Cys})]$, $\nu[\text{Cu-S}(\text{Met})]$ or $\nu(\text{Cu-N})$ according to the general concensus in the literature, and in light of the available X-ray structural information for plastocyanin and azurin. The division of the observed protein bands into these categories must, however, be regarded as tentative. Originally, the weak line $\nu 260\text{ cm}^{-1}$ was considered to be primarily $\nu[\text{Cu-S}(\text{cys})]$ but the $\nu[\text{Cu-S}(\text{Met})]$ assignment seems now to be generally preferred in view of Raman studies on cupric thioether complexes³⁶⁹ and on anion binding in ceruloplasmin.³⁶⁸ $\nu[\text{Cu-S}(\text{thiolate})]$ bands have been assigned at 375 and 427 cm^{-1} in the cis-planar copper D-penicillamine

TABLE 5.17. Raman spectral data for blue-copper-proteins.

Protein	Assigned Stretching Vibration		
	Cu-S(Met)	mainly Cu-S(Cys)	mainly Cu-N(His)
Azurin ²³⁹	262w	372	407,425
Azurin ²³⁷	260w	374	412,422,462w
Plastocyanin ²³⁷	265w	382	415,434
Plastocyanin ²³⁸	262w	379	407,426
Ceruloplasmin ²³⁸	250w	325w 350w,375	400,450w
Ceruloplasmin ²³⁷	280w	355w,375w	395,425
Ceruloplasmin Ia ³⁶⁸	270w	340w 380	415
Ceruloplasmin Ib ³⁶⁸	270w,	360,	402,415
Tree laccase ²³⁸	259w	331w 360w,383,	408,419,485w
Ascorbate oxidase ²³⁸	260w	350w,383	407,417,429,488w
Stellacyanin ²³⁸	267w	350,388	410w,424w,444w

2N2S complex.³⁷² In $\text{Cu}[\text{HB}(3,5\text{-dimethyl-1-pyrazolyl})_3](\text{pNO}_2\text{C}_6\text{H}_4\text{S})$, however, a polarised band at 276 cm^{-1} has been reasonably assigned as $\nu(\text{Cu-S})$ ²⁹⁹ and would tend to support a $\nu[\text{Cu-S(Cys)}]$ assignment for the ca. 260 cm^{-1} shift in the proteins.

Solomon et al.²⁵⁹ have estimated from the shape of the 606 nm electronic absorption band in plastocyanin that a vibrational mode of frequency $240 \pm 60 \text{ cm}^{-1}$ is coupled to the $\text{S}(\sigma) \rightarrow \text{Cu(II)}$ CT transition. Similarly, for the 617 nm absorption in stellacyanin a frequency of $290 \pm 80 \text{ cm}^{-1}$ is calculated. However, the shape of the 631 nm band in azurin indicates a vibronically coupled mode of frequency $390 \pm 150 \text{ cm}^{-1}$.

As an elongation of the Cu-S bond is expected to be the dominant distortion in the $S(\sigma) \rightarrow Cu(d_{x^2-y^2})$ excited state, the coupled vibrational frequencies should provide rough estimates of the Cu-S stretching frequencies in the proteins.

The observation of bands at 242 cm^{-1} in $Cu(II)(MeN-MeMeS)_2$ and 253 cm^{-1} in $Cu(II)(iBuN-MeMeS)_2$ assigned to predominantly $\nu(Cu-S)$, demonstrates that copper-sulphur stretching vibrations other than those for copper-thioether bonds may reasonably be expected at such low frequency. It must be recognised, however, that the β -aminothione cupric complexes may have rather different CuN_2S_2 vibrational properties from the blue-copper-proteins, in that they are expected to possess a more rigid chelating ring structure. The 242 and 253 cm^{-1} bands of the $Cu(II)-(RN-MeMeS)_2$ ($R = Me, iBu$) complexes feature amongst the most intense lines in their respective Raman spectra, and it is the weakness of the scattering ca. 260 cm^{-1} in the proteins, compared with that at higher frequencies, which most militates against assignment as $\nu[Cu-S(Cys)]$, since this mode should be most strongly coupled to the $S(\sigma) \rightarrow Cu(II)$ CT band within which the Raman excitation wavelength lies.

The high intensity of the bands assigned as predominantly $\nu(Cu-N)$ in the proteins, compared with the intensity of bands considered to be mainly $\nu[Cu-S(Cys)]$, is surprising. Attempts have been made to rationalise this observation in terms of metal-ligand orbital-overlap criteria.^{237,238} For $Cu(MeN-MeMeS)_2$ the Raman lines considered to be mainly $\nu(Cu-S)$ are only the most intense features in the spectrum when exciting with light of wavelength 647.1 nm . At shorter wavelengths, the 376 cm^{-1} feature,

thought to be mainly $\nu(\text{Cu-N})$, becomes most intense. $\nu(\text{Cu-N})$ modes, together with certain ligand modes, are expected to be resonance enhanced to some degree, when exciting within the $S(\sigma) \rightarrow \text{Cu(II)}$ CT absorption contour, due to extensive mixing with the $\nu(\text{Cu-S})$ vibration. However, unless, for example, the electronic absorption with maximum around 480 nm were considered to be $N(\sigma) \rightarrow \text{Cu(II)}$ in origin, which seems unlikely, the relative intensities of the Raman bands is, as in the proteins, difficult to understand completely.

5.6. Electrochemistry.

Initial investigative measurements have been made on the electrochemical properties of a few of the cupric β -aminothione complexes in DMF solution. Reduction processes have been studied at low temperature using a rapid-dropping-mercury-electrode (RDME), a hanging-mercury-drop-electrode (HMDE) and at stationary and rotating platinum electrodes; all referenced to an aqueous SCE via a double electrolyte junction. Table 5.18 summarises electrochemical data for $\text{Cu(II)(RN-MeMeS)}_2$ $R = \text{Me, Et, nOct, iPr}$ and also for $\text{Cu(II)[(CH}_2)_2(\text{N-MeMeS})_2]$. Figure 5.17 shows cyclic voltammograms for $\text{Cu(II)(MeN-MeMeS)}_2$ at platinum and mercury-drop electrodes.

TABLE 5.18. Electrochemical data for $\text{Cu(II)(RN-MeMeS)}_2$ ($R = \text{Me, Et, nOct, iPr}$ and $\text{en}/2$) at ca. -35°C .

R	$E_{\frac{1}{2}} \pm 0.02/\text{V}$	slope ^a /mV	ΔE^{b} /mV
Me (Hg)	-0.67		-65
Me (Pt)			-90
Et (Hg)	-0.64	-28	-80
nOct (Hg)	-0.67	-27	-80
iPr	-0.50		
en^{c} (Hg)	-1.09	-29	-60
en^{c} (Pt)			-90

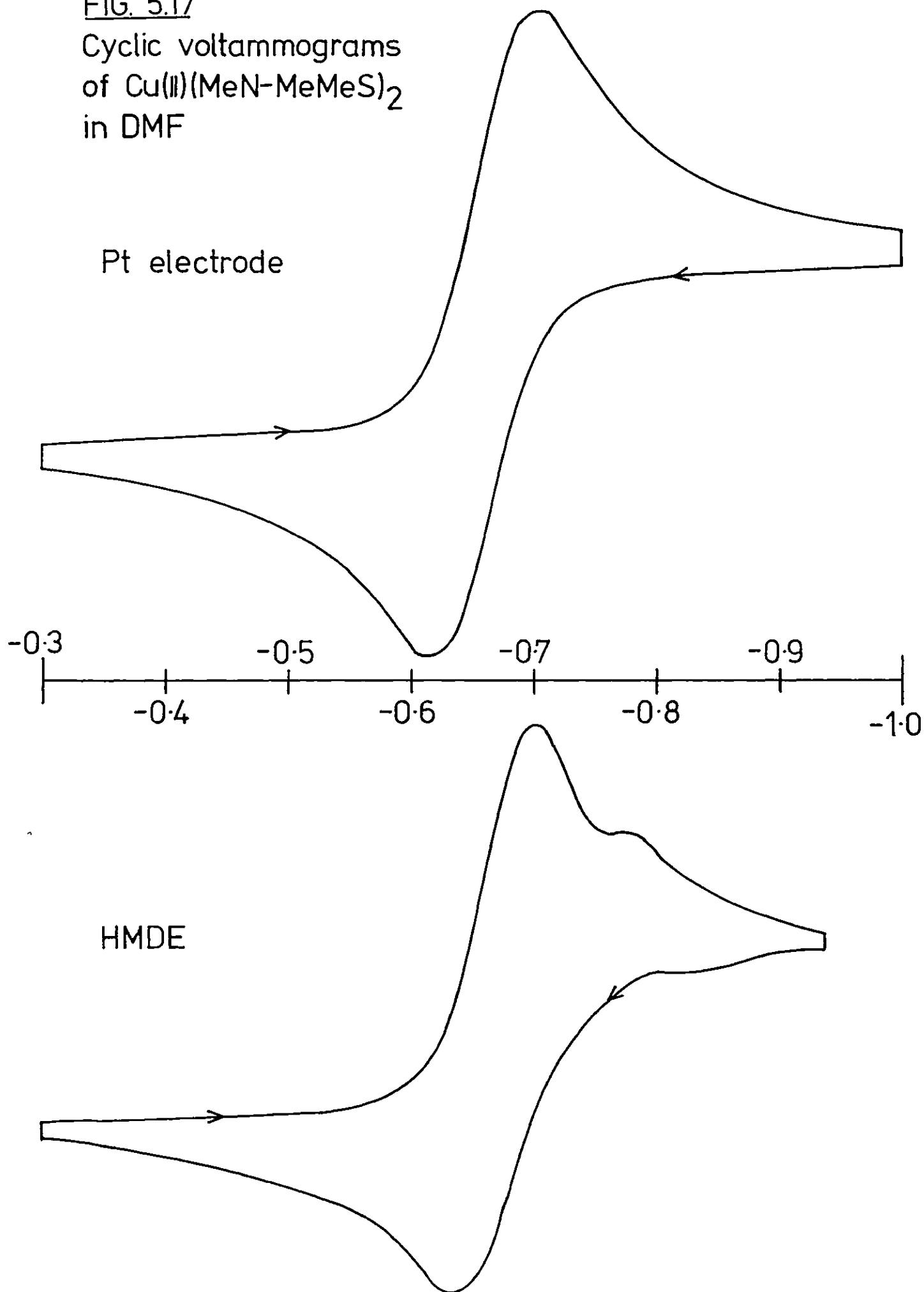
NOTES: a. E vs. $\ln[(i_d - i)/i]$ plot.

b. cathodic peak - anodic peak; 5-10 mV/s scan rate

c. measured at 20°C .

FIG. 5.17

Cyclic voltammograms
of $\text{Cu(II)(MeN-MeMeS)}_2$
in DMF



5.6.1. Difficulties in measurements.

Voltammetry of $\text{Cu}(\text{MeN-MeMeS})_2$ at platinum is complicated to some degree by electrode kinetics at the scan-rate used, as is demonstrated by the anodic peak to cathodic peak potential separation of 90 mV. At mercury the peak potential separation is 65 mV and closely approaches that expected for reversible one-electron redox processes. Quasi-reversibility of the reduction at platinum was also observed for $\text{Cu}(\text{II})[(\text{CH}_2)_2(\text{N-MeMeS})_2]$ [see also ref. 373] and further departure from reversible behaviour was found for $\text{Cu}(\text{II})(\text{nOctN-MeMeS})_2$, thus the HMDE was favoured for general use. This necessitated the use of a sample-solution temperature in excess of -40°C to avoid solidification of the electrode. Decomposition half-lives of the less stable complexes having nOct- and iPr-ligand amino-substituents, are considerably shortened above -30°C and so a temperature of ca. -35°C was maintained and electrochemical analysis performed within a short time from preparation of the electrolyte solution. Any cuprous decomposition products would be stable under the anaerobic measurement conditions and would not be expected to undergo reduction in the potential range investigated.

An additional problem encountered with the HMDE was the presence of non-Faradaic (adsorption) processes, probably exacerbated by the use of low temperatures. This may be seen in the cyclic voltammograms of $\text{Cu}(\text{MeN-MeMeS})_2$, Figure 5.17. A post reduction peak is seen on the cathodic scan. Similar but more intense peaks were observed for the other $\text{Cu}(\text{II})(\text{RN-MeMeS})_2$ complexes and are indicative of medium to strong reactant adsorption.³⁷⁴ Typical of the behaviour of such systems, where the adsorbed layer is of constant amount but the material diffusing to the electrode surface is time- and concentration-dependent, the post-peak increases in intensity, relative to the cathodic peak current, with increasing scan-rate and with dilution. The adsorption effects were thus

minimised by using solutions near saturation in the copper complex and employing low voltage sweep rates of 5-10 mV/s.

In polarographic measurements the adsorption effect manifests itself as a post-wave of constant height (i_a) 100-200 mV more negative than the wave for the diffusing complex (i_d'), such that the total diffusion current $i_d = i_d' + i_a$. Since $i_a \propto h$ (height of mercury column) whilst $i_d' \propto \sqrt{h \cdot c}$ (concentration)^{375,376} it proves possible to verify that the second wave is due to adsorption by observing the ratio of $i_a:i_d'$ as h and c are varied. The evidence for adsorption from such measurements was, however, less conclusively convincing than that from the stationary electrode voltammetry, as the estimation of i_d' involved a large degree of uncertainty due to the poor resolution of the two waves.

5.6.2. Analysis of polarographic data.

For Cu(II)(nOctN-MeMeS)₂ only a single wave was resolved, Figure 5.18, though the cyclic voltammogram reveals a post peak due to adsorption. Analysis of this polarographic wave in terms of equation E5.1³⁷⁷ is given in Figure 5.18.

$$E = E_{\frac{1}{2}} + \frac{RT}{nF} \cdot \ln[(i_d - i)/i] \quad \text{E 5.1}$$

Deviation from linearity in the $\ln[(i_d - i)/i]$ vs. E plot cathodic of ca. -0.7 V could be due to adsorption of the Cu(II)(nOctN-MeMeS)₂ on the HMDE. The slope of -27 mV approaches the theoretical -26 mV expected for a reversible one-electron redox reaction. A similar analysis for Cu(II)(EtN-MeMeS)₂, where there is a reasonably well defined post wave, using i_d' in place of i_d yields a $\ln[(i_d' - i)/i]$ vs. E slope of -28 mV.

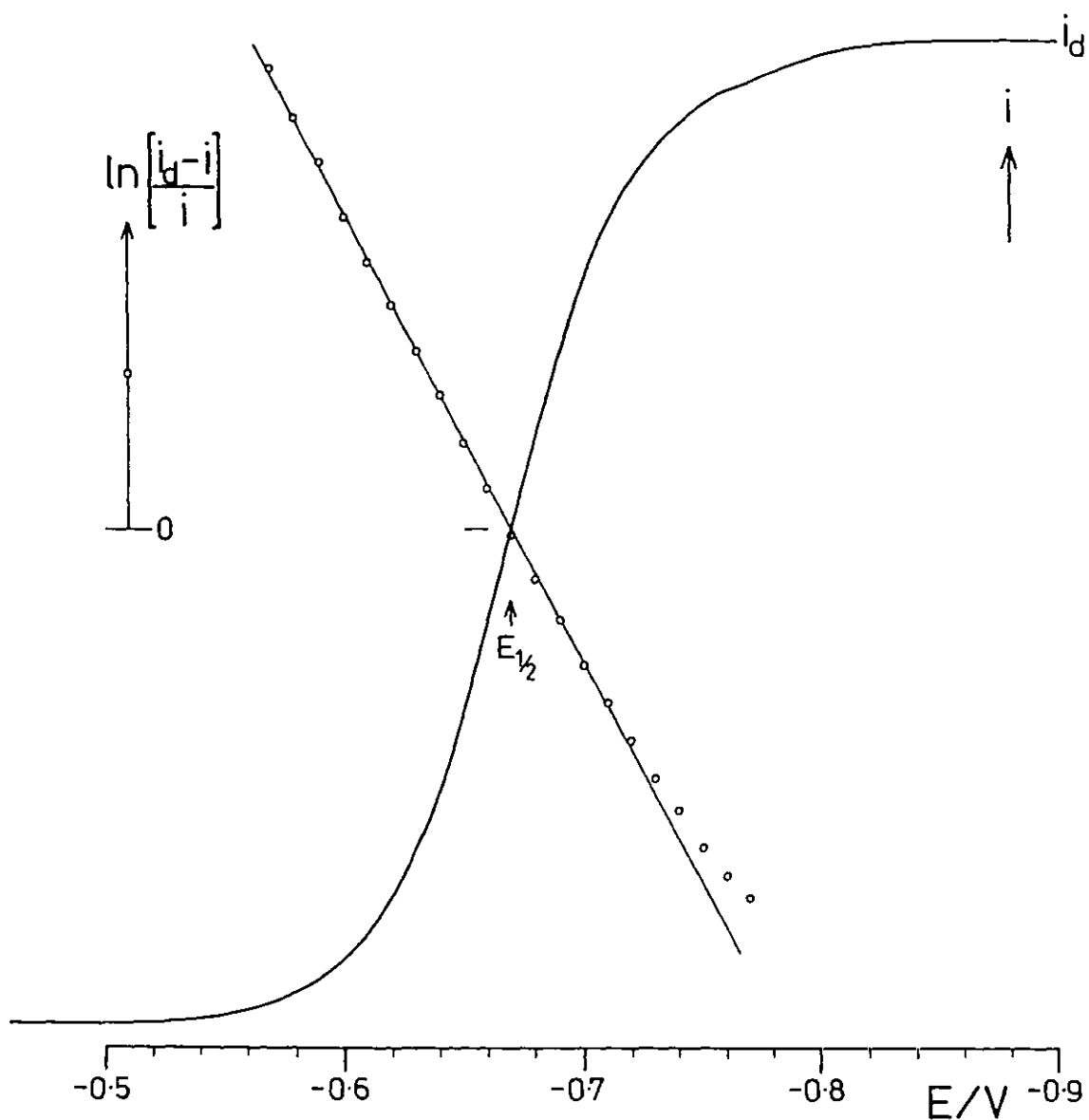


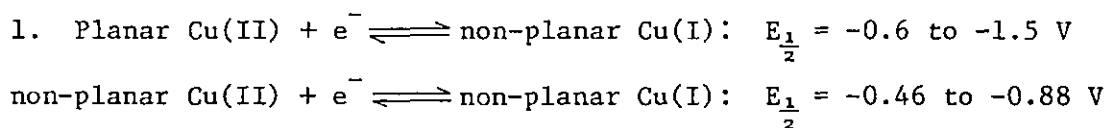
Figure 5.18. Polarogram of $\text{Cu(II)(nOctN-MeMeS)}_2$ in DMF at a RDME.

Cyclic voltammetric cathodic-anodic peak potential separations of 80 mV observed for these two complexes, indicate, on the other hand, some departure from reversibility. Thus the coefficient RT/nF in equation E5.18 may be modified by a reduced transfer coefficient.³⁷⁷

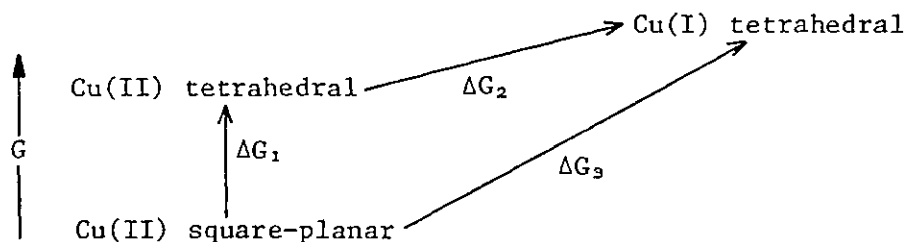
Several electrochemical studies of the $\text{Cu(II)[(CH}_2)_2(\text{N-MeMeS})_2]$ complex have been reported: (electrode, solvent, $E_{1/2}/\text{V}$, $\Delta E/\text{mV}$); Pt, MeCN, -1.09, 80³⁷⁸; Hg, DMF, -1.07, 68³¹⁸; Pt, DMA, ---, 70³⁷⁹; Hg, MeCN, -1.18, 58³⁷³. A comparable half-wave potential is found in this present work, Table 5.18.

5.6.3. Comparison of $E_{\frac{1}{2}}$ with those of other complexes.

Patterson and Holm³¹⁸ in a study of the electrochemical properties of a wide range of Cu(II) coordination environments have made the following general observations:



2. Increasing stereochemical distortion from planarity in a series of Cu(II) complexes involving a common ligand type results in progressive raising of $E_{\frac{1}{2}}$; interpreted in terms of destabilisation of the Cu(II) complex, relative to the real or hypothetical sterically unstrained planar geometry, toward the non-planar Cu(I) reduction product. Thus, in the idealised scheme:



$$\Delta G_2 < \Delta G_3$$

3. For Cu(II) complexes where only the donor atom portion of the ligand is varied the order of increasing anodic potential is 4N < 2N2O < 2N2S.

4. Increasing electron-releasing tendency in chelate-ring substituents is reflected in cathodic potential shifting of $E_{\frac{1}{2}}$, provided there are no dominating structural changes.

Some of these observations are confirmed for 2N2S coordination in the β -aminothione complexes studied. On going from $\text{Cu(II)}[(\text{CH}_2)_2(\text{N-MeMeS})_2]$, which must be considered as essentially planar, to $\text{Cu(II)}(\text{RN-MeMeS})_2$ ($\text{R} = \text{Me, Et, nOct}$) an anodic shift in $E_{\frac{1}{2}}$ of 420 to 450 mV occurs and is interpreted as resulting from a tetrahedral distortion from square-planar geometry in the latter series of complexes. The trend is extended on going to $\text{Cu(II)}(\text{iPrN-MeMeS})_2$ where the shift in $E_{\frac{1}{2}}$ from the planar reference value approaches 600 mV, in keeping with increased stereochemical distortion due to the sterically bulky iPr group. Patterson and Holm³¹⁸ observed comparable anodic $E_{\frac{1}{2}}$ shifts of 450 and 630 mV respectively in the analogous oxygen-donor β -ketoaminate complexes $\text{Cu(II)}(\text{MeN-MePhO})_2$ and $\text{Cu(II)}(\text{iPrN-MePhO})_2$, when compared to the planar reference $\text{Cu(II)}[(\text{CH}_2)_2(\text{N-MePhO})_2]$. Yokoi and Addison²⁸⁹ have correlated $E_{\frac{1}{2}}$ with g_{\parallel} in cupric pyrrole-2-carboxaldimines (4N) and salicyaldimines (2N2O) for a range of pseudo-tetrahedral coordination symmetries. For the Cu(II) β -aminothione complexes the paucity of data does not permit analysis in any detail, but the trend of increasing $E_{\frac{1}{2}}$ potential with increasing g_{\parallel} is noted in the series $\text{Cu(II)}[(\text{CH}_2)_2(\text{N-MeMeS})_2]$, $\text{Cu(II)}(\text{RN-MeMeS})_2$ ($\text{R} = \text{Me, Et, nOct}$), $\text{Cu(II)}(\text{iPrN-MeMeS})_2$. The steric bulk of the amino-substituents on the ligands appears to dominate any electronic inductive effects, as found for other series of Cu(II) Schiff-base complexes.^{289,318}

A nearly constant anodic shift of ca. 0.4 V was noted by Patterson and Holm³¹⁸ upon replacing oxygen by sulphur in complexes with otherwise identical ligands. They were unable, however, to study complexes containing both a 2N2S donor set and non-planar stereochemistry. Comparison of $\text{Cu(II)}(\text{MeN-MeMeS})_2$ with $\text{Cu(II)}(\text{MeN-MePhO})_2$ and $\text{Cu(II)}(\text{iPrN-MeMeS})_2$ with $\text{Cu(II)}(\text{iPrN-MePhO})_2$ ³¹⁸ indicates 2N2O — 2N2S anodic shifts of 290 and 280 mV respectively. An additional 80–90 mV is probably appropriate to these figures however, due to the electronic effect of the Ph chelate ring substituent for the 2N2O complexes.³¹⁸

5.6.4. Comparison of $E_{1/2}$ with blue-copper-proteins.

Redox potentials for type 1 Cu(II) in proteins vary widely from ca. 0.0 to 0.6 V²³¹ relative to the SCE. Thus, the highest potential found for the β -aminothione copper complexes (-0.5 V) falls 500 mV short of the protein range, though it is the least negative observed for this type of β -difunctional ligand system. The revealed trends of increasing redox potential with distortion from planar symmetry and with adoption of 2N2S as opposed to 2N2O or 4N coordination, must, however, be considered appropriate in view of the known and speculated type 1 coordination environments for the blue-copper-proteins. What additional factors lead to the highly facilitated reduction found for the type 1 Cu(II) centre remains to be fully investigated and understood, as does the origin of the wide difference in potentials found amongst the individual proteins which have otherwise very similar spectroscopic parameters. Rather unexpectedly, the highest potentials are found for proteins with largest $|A_{\parallel}|$ and lowest g_{\parallel} .³⁸⁰

Notable in respect of their ability to reproduce redox potentials comparable to the full range found in the proteins, are Cu(II) complexes of quadridentate and macrocyclic ligands involving thioether donors.^{295,307,311,319} The reasons for the low potentials have not been fully elucidated.

5.7. Concluding Remarks and Summary.

The complexes described in this section represent the most extensive series of 2N2S coordinated copper with systematically variable stereochemistry at present available. Spectroscopic and redox measurements on the complexes are consistent with pseudo-tetrahedral 2N2S geometry in which the degree of tetrahedral distortion is dependent upon the steric bulk of the amino-substituent. In solution the complexes show the lowest $|A_{\parallel}|$ values yet observed for this type of coordination in synthetic compounds. Constrained as impurities in Zn(II) complexes of the same ligand, z-axis EPR parameters closely approaching those found for type 1 copper proteins are observed, further supporting the belief that the coordination of the latter is near tetrahedral and predominantly, if not exclusively, 2N2S. Intense absorption bands in the visible spectra of the complexes are attributable to sulphur to copper charge transfer and are correlatable with similar features in type 1 protein spectra. The results give further evidence of the need for sulphur coordination and at least some degree of tetrahedral distortion from square-planar in order to reproduce in model compounds the intense protein 'blue' bands.

Redox potentials for the complexes deviate substantially negative of the type 1 centres, but are indicative of a role for tetrahedral distortion in bringing about high potentials.

Thus, the series of β -aminothione complexes serve to confirm some trends extrapolated from the extensive studies of other type 1 model complexes and to support the present-day understanding of the type 1 coordination site as revealed by the detailed and wide ranging investigations made during the past decade.

5.8. EXPERIMENTAL

5.8.1. Preparation of α,β -unsaturated β -aminothione ligands and their precursors.

The β -aminothione ligands were prepared by nucleophilic reactions of primary amines with 1,2-dithiolium salts ($R_1, R_2 = \text{Ph, Ph; Ph, H; tBu, tBu}$) or of hydrosulphide ion with O-alkylated β -ketoamine salts ($R_1, R_2 = \text{Me, Me; Ph, Me}$).³²² and refs. therein

5.8.1.1. Preparation via 1,2-dithiolium salts.

Phenyl-1,2-dithiolium perchlorate ($R_1, R_2 = \text{Ph, H}$) was prepared by the method of Klingsberg.³³⁵ The other two dithiolium cations were prepared by fusion of the corresponding β -diketones with excess P_4S_{10} .³⁸¹ The preparation of 2,2,6,6-tetramethyl-5-ethylamino-4-heptane dione (EtN-tButBuS) from 2,2,6,6-tetramethyl-3,5-heptanedione, which has not previously been reported, is outlined below as an example.

5 g of dipivaloylmethane and 10 g of P_4S_{10} were warmed to 120°C under N_2 . After an initial vigorous reaction the mixture was maintained at ca. 130°C for 15 mins. with occasional stirring, and then extracted by refluxing with 50 ml of ca. 2 M HCl for 1 hr. After cooling and filtering the solution was treated with excess perchloric acid and the precipitated dithiolium perchlorate salt collected and recrystallised from MeOH/Et₂O. Yield 60% white plates; Mpt. $288\text{--}290^\circ\text{C}$; Anal. calc. C 41.94; H, 6.09; S, 20.38; Cl, 11.26%. Found C, 42.18; H, 6.07; S, 20.35; Cl, 11.82%.

1 g of the above dithiolium salt and 2 ml of a 33% ethanolic solution of EtNH₂ together with 10 ml of hexane, were stirred and gently warmed for 15 mins. A small amount of charcoal was added to the yellow reaction solution which was then filtered. The solvent was removed in vacuo and

the β -aminothione product recrystallised (low temperature) from 40-60 petroleum ether. Yield, ca. 50% yellow needles; Mpt. 69-73°C; Anal. Calc. C, 68.72; H, 11.01; N, 6.17; S, 14.10. Found, C, 68.80; H, 11.21; N, 6.17; S, 14.29.

Other β -aminothione ligands were prepared by reactions of the corresponding dithiolium cation and primary amine in MeOH, Et₂O, hexane or mixtures of these solvents.

5.8.1.2. Preparation via β -ketoamines.

β -Ketoamine precursors were synthesised by refluxing component β -diketone and primary amine in Et₂O over 3Å molecular sieves. The separated Schiff's bases were treated successively with Et₃O⁺BF₄⁻ 382 in dry CH₂Cl₂ and NaSH in dry EtOH, as described by Gerlach and Holm.³²² The resulting pale yellow to deep orange solutions were filtered and solvent removed in vacuo. The crude aminothione products could generally be purified by recrystallisation from petroleum ether, Et₂O, MeOH or mixtures of these solvents. In some cases chromatography on Al₂O₃ with toluene as solvent was necessary in order to separate the products from some β -ketoamine reactant.

No conversion to thione could be achieved by this reaction method when the alkylamino-substituent had a tertiary branched α -carbon (t-butylamine, 1-adamantanylamine or 1,1,4,4-tetramethyl-1,4-butane diamine).

Compounds not subjected to elemental analyses were identified by their PMR spectra. Many of the compounds have not previously been described, and characterisation data are presented in Tables 5.19 and 5.20.

TABLE 5.19. PMR data for β -aminothione ligands - (RN-R₂R₁S).

R	δ (R ₁ =Me)	δ (R ₂ =Me)	δ (β -H)	δ (NH)	δ (R)
Me	2.51	2.08	6.16	14.0	CH ₃ 3.08(d)
Et	2.50	2.09	6.10	14.0	CH ₃ 1.35(t), CH ₂ 3.41(m)
iPr	2.47	2.10	6.01	14.2	CH ₃ 1.33(d), CH 3.92(m)
nBu	2.55	2.11	6.18	14.2	CH ₃ 0.98(t), -(CH ₂) ₂ - 1.66(m), N-CH ₂ 3.45(m).
iBu	2.55	2.11	6.25	14.3	CH ₃ 1.06(d), CH \sim 2.0(m), CH ₂ 3.30(\sim t).
sBu	2.55	2.13	6.12	14.3	CH ₃ 1.32(d), CH 3.76(m), CH ₂ -CH ₃ 1.00(t), 1.7(m).
nOctyl	2.59	2.12	6.25	14.2	CH ₃ 0.90(t), -(CH ₂) ₆ - \sim 1.3 \sim , NCH ₂ 3.49(m).
C ₁₈ H ₃₇	2.51	2.10	6.03	14.0	CH ₃ 0.90, -(CH ₂) ₁₆ - \sim 1.3, N-CH ₂ \sim 3.4(m).
cHx	2.53	2.12	6.12	14.3	-(CH ₂) ₅ - 1.5 to 1.9, CH 3.7br.
Bz	2.62	2.10	6.30	14.5	Ph 7.48, CH ₂ 4.69
α MeBz	2.57	1.97	6.16	14.6	Ph 7.37, CH ₃ 1.65(d), CH 4.89(m)
α PhBz	2.59	2.02	6.20	14.8	Ph 7.39, CH 5.96(d)
1-Naphthyl	2.73	2.00	6.50	16.0	Naphthyl \sim 7.3 to 8.2
Ph	2.50	2.05	6.24	15.6	Ph \sim 7.25
pMePh	2.61	2.10	6.32	15.7	Me 2.37, Ph 7.17(m)
pMeOPh	2.60	2.08	6.31	15.6	Me 3.83, Ph 7.05(m)
pClPh	2.64	2.12	6.36	15.7	Ph 7.33(m)
pFPh	2.64	2.12	6.41	15.6	Ph \sim 7.3
p(NMe ₂)Ph	2.59	2.08	6.29	15.5	Me 3.02, Ph 6.98
2,6-Me ₂ Ph	2.64	1.82	6.43	15.5	Me 2.23, Ph 7.25
2R=-(CH ₂) ₅ -	2.58	2.12	6.21	14.3	-(CH ₂) ₃ - 1.78(br), N-CH ₂ 3.52(d)
2R=-(CH ₂) ₆ -	2.55	2.12	6.20	14.4	-(CH ₂) ₄ - \sim 1.7(br), N-CH ₂ \sim 3.45
EtN-MePhS	Ph \sim 7.4(m)	Me 1.93	6.40	14.3	CH ₃ 1.18(t), CH ₂ 3.25(m)
iPrN-PhPhS	Ph \sim 7.5(m)	Ph \sim 7.5(m)	6.52	14.7	CH ₃ 1.28(d), CH 3.7(m)
EtN-HPhS	Ph \sim 7.6(m)	H \sim 7.6*	6.56(d)	13.9	CH ₃ 1.36(t), CH ₂ 3.48(m)
iPrN-HPhS	Ph \sim 7.5(m)	H \sim 7.5*	6.46(d)	13.8	CH ₃ 1.34(d), CH 3.66(m)
EtN-tButBuS	tBu 1.39	tBu 1.29	6.56	15.2	CH ₃ \sim 1.5(m), CH ₂ 3.77(m)
iPrN-tButBuS	tBu \sim 1.4	tBu \sim 1.4	6.48	15.4	Me \sim 1.4, CH 4.35

CDCl₃ - solvent; shifts(δ) in ppm; *hidden in Ph resonance;

Ph resonances - approximate centre of multiplet; d - doublet, t - triplet, m - multiplet.

TABLE 5.20. Elemental microanalyses for β -aminothione ligands - (RN-R₂R₁S).

R, R ₁ =R ₂ =Me		C	H	N	S	Mpt./°C
Me	C	55.77	8.58	10.84	24.81	90-91
	F	55.67	8.62	10.78	24.84	
Et	C	58.69	9.15	9.78	22.38	43-44
	F	58.87	9.27	9.77	22.59	
nPr	C	61.09	9.61	8.91	20.39	28.5-30.5
	F	61.09	9.62	8.86	20.30	
nBu	C	63.10	10.00	8.18	18.72	33-34
	F	63.00	10.18	8.32	18.91	
iBu	C	63.10	10.00	8.18	18.72	38
	F	63.46	10.17	8.23	18.77	
sBu	C	63.10	10.00	8.18	18.72	oil
	F	63.30	10.20	8.10		
nOctyl	C	68.66	11.08	6.16	14.01	30-31.5
	F	68.60	11.27	6.25	13.55	
C ₁₈ H ₃₇	C	75.13	12.34	3.81	8.73	
	F	75.99	12.74	3.87		
cHx	C	66.95	9.70	7.10	16.25	66.5-68
	F	66.94	9.83	7.09	16.22	
Bz	C	70.20	7.36	6.82	15.62	46-7
	F	70.11	7.55	6.82	15.58	
α MeBz	C	71.18	7.81	6.39	14.62	
	F	71.55	7.92	6.40	13.54	
α PhBz	C	76.82	6.81	4.98	11.39	
	F	77.06	6.83	5.07	10.96	
1-Naphthyl	C	74.65	6.26	5.80	13.28	97-98
	F	74.74	6.35	5.80	13.41	
Ph	C	69.07	6.85	7.32	16.76	61.5-63
	F	68.97	6.78	7.26	16.47	
pClPh	C	58.53	5.36	6.20	14.20	76-77
	F	58.75	5.39	6.22	14.22	
pFPh	C	63.13	5.78	6.69	15.32	32-33
	F	63.06	5.80	6.68	15.77	
2,6-Me ₂ Ph	C	71.18	7.81	6.39	14.62	76.5-78
	F	71.27	7.87	6.41	14.94	
Et-MePh	C	70.20	7.36	6.82	15.61	
	F	70.22	7.32	6.80		
tBu-PhPh	C	72.24	7.16	4.74	10.85	136-138
	F	76.96	7.16	4.81	11.07	
Et-HPh	C	69.07	6.85	7.32	16.76	
	F	68.73	6.81	7.25	17.05	
Et-tButBu	C	68.66	11.08	6.18	14.10	69-73
	F	68.80	11.21	6.17	14.29	

Other Mpts: - iPrN-MeMeS 31.5-33°C; pMePhN-MeMeS 33-35°C;
 pMeOPhN-MeMeS 50-51.5°C; EtN-PhPhS 80-81.5°C; BzN-HPhS 85-86;
 iPrN-HPhS 67.5-68.5°C; tBuN-HPhS 63-64°C.

5.8.2. Preparation of cupric β -aminothione complexes.

The concentration of ligand and the temperature and duration of reaction used in any specific preparation were dependent upon the solubility of the ligand and the stability of the product copper complex, as determined by the substituent groups R, R₁ and R₂. An exemplary preparation is outlined below.

80 ml of MeOH was carefully added to 2 mmol of ligand and 10 mmol of NaH (5 fold excess). The NaOMe generated in situ serves to deprotonate the ligand. This solution was filtered, cooled to ca. -60°C and then added to 1 mmol of $\text{CuCl}_2 \cdot 2\text{H}_2\text{O}$ in 40 ml of MeOH at the same temperature. The mixture on stirring generally developed a dark green-blue colouration. Further, sometimes prolonged, cooling to -80°C led to a dark coloured precipitate or microcrystalline solid. This could be collected by filtration at ca. -70°C and washed well with MeOH and sometimes with Et_2O . Drying was accomplished by initially sucking N_2 through the filtered solid at low temperature and then, after replacing the filtrate collection vessel with a dry one, applying a vacuum and allowing the temperature to rise gradually to room temperature. Collected solids were stored at -30°C . A cooling bath of industrial methylated spirits was used in preparations, contained in a 8 x 30 cm Dewar and refrigerated by careful addition of liquid nitrogen. Such a bath could be maintained below -70°C for up to 24 hrs, if desired, by storage in a freezer at -30°C . Solutions were handled in tubes 20-30 cm long and 3-5 cm in diameter. The filtration apparatus is shown in Figure 5.19 and may be immersed up to the B34 joint in the cooling bath.

Microanalytical data for the complexes is given in Table 5.21. Good analyses were obtained for several of the compounds, but for the less stable complexes the results are less good. The microanalysis samples were maintained at low temperature prior to weighing, but it is difficult to assess to what extent decomposition with weight change may have taken place whilst the individual samples were awaiting analysis within the automatic loading mechanism of the machine. Difficulty in attaining good microanalytical data of thermally unstable copper-thiolate complexes has been expressed by others.²⁹⁹ Where the CHN analyses are in substantial error the deviation is generally found to be negative but the C:H:N ratio is close to that expected for the ligand, this may be indicative of

Figure 5.19. Low temperature filtration apparatus.

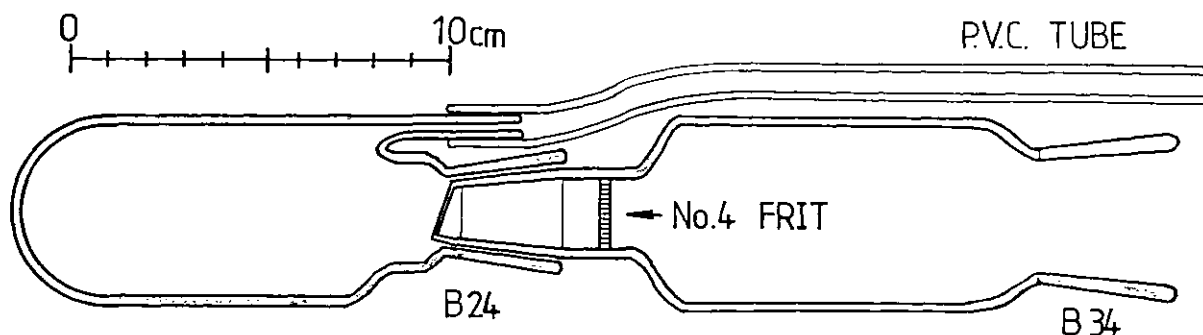
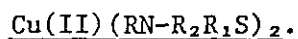


TABLE 5.21. Elemental microanalyses for cupric β -aminothione complexes

R	R ₂	R ₁		C	H	N
Me	Me	Me	C	45.04	6.30	8.76
			F	44.93	6.18	8.49
iBu	Me	Me	C	53.50	7.98	6.93
			F	53.54	8.04	6.93
Bz	Me	Me	C	61.05	5.98	5.93
			F	60.63	5.96	5.86
pMePh	Me	Me	C	61.05	5.98	5.93
			F	60.62	5.93	5.90
Et	Me	Ph	C	61.05	5.98	5.93
			F	61.03	5.97	5.84
Et	tBu	tBu	C	60.48	9.37	5.43
			F	60.40	9.25	5.29
Et	Me	Me	C	48.32	6.95	8.05
			F	46.39	6.26	7.23
nPr	Me	Me	C	51.10	7.50	7.45
			F	48.73	6.96	6.93
iPr	Me	Me	C	51.10	7.50	7.45
			F	46.18	6.93	6.57
nBu	Me	Me	C	53.50	7.98	6.93
			F	51.74	7.86	6.65
nOct	Me	Me	C	60.48	9.37	5.43
			F	56.90	8.31	5.00
cHx	Me	Me	C	57.92	7.95	6.14
			F	55.85	7.56	5.86
pFPh	Me	Me	C	55.04	4.62	5.84
			F	53.59	4.51	5.62
pMeOPh	Me	Me	C	57.18	5.60	5.56
			F	56.37	5.50	5.53
Et	Ph	Ph	C	68.48	5.41	4.70
			F	65.72	5.20	4.50
Et	H	Ph	C	59.50	5.44	6.31
			F	57.35	5.34	5.97

contamination by $\text{Cu(I)(RN-R}_2\text{R}_1\text{S)}_2$. The $\text{Cu(II)(RN-R}_2\text{R}_1\text{S)}_2$ formulae assigned to those compounds having elemental analyses in good agreement, are reasonably extended to other complexes isolated on the basis of the spectroscopic evidence (EPR in particular) presented in the previous sections.

5.8.3. Preparation of samples for spectroscopy.

5.8.3.1. Visible and near-IR.

Solution electronic spectra were measured for samples maintained at ca. -50 to -80°C in a Beckman RIIC variable temperature accessory with glass windows. The sample was sucked through the optical cell (1 mm path length, mounted on a low temperature finger within an evacuated case) via wide-bore PTFE tubing, until the tubing was well cooled and the absorption at one of the band maxima was constant.

For solid state reflectance spectra samples of pure or MgO diluted powders were applied to a supported piece of filter paper and protected by a glass microscope cover slide.

5.8.3.2. EPR.

Frozen solution EPR samples were contained in 200 x 5 mm (o.d.) quartz tubes having small holes at the end which is normally sealed. Low temperature solutions could be easily sucked into these tubes (precooled in liquid nitrogen) with a Pasteur pipette bulb, and then frozen in place and stored in liquid nitrogen.

Mobile solution samples were loaded into flat cells 0.5 x 3 x 40 mm in a similar manner and placed in the spectrometer cavity with the smallest cell dimension perpendicular to the magnetic field.

5.8.3.3. Raman.

Solids diluted in KBr and pelleted under pressure, and acetone solutions were investigated using the apparatus described in Appendix B.

5.8.3.4. Electrochemistry.

Polarographic and cyclic-voltammetric measurements in DMF with 0.1 M $n\text{Bu}_4\text{NClO}_4$ supporting electrolyte, were performed on a Beckman Electroscan 30. A three electrode configuration was employed with the platinum counter electrode partitioned by a frit from the bulk solution. The saturated calomel reference electrode was separated from the sample via a $n\text{Bu}_4\text{NClO}_4/\text{DMF}$ bridge with fumed-silica gel junction, then a $\text{Et}_4\text{NCl}/\text{H}_2\text{O}$ bridge with a frit junction, then a $\text{KCl}/\text{H}_2\text{O}$ bridge with a fibre junction. For DC polarography a Metrohm E354 drop-knocker was employed at 5-6 drops/sec.

5.8.4. Zn(II), Ni(II) and Cd(II) complexes.

The Cu(II) doped Zn(II) and Cd(II) β -aminothione complexes were prepared in a similar manner to the cupric complexes (Sec. 5.8.2.) but using zinc and cadmium acetates plus ca. 0.5 to 1.0 mole % Cu(II). For some of the complexes it was necessary to maintain the reaction solution at low temperature (ca. -80°C) for 1-2 days in order to obtain a good yield. For the quadridentate ligands having $2\text{R} = -(\text{CH}_2)_n-$ ($n = 2,3$) the reactions were performed at room temperature, as the cupric complexes are stable; where $n = 5,6$ the reactions were performed in a freezer at ca. -30°C and acetone was added to the ligand solution to prevent precipitation prior to reaction.

For the Ni(II) complexes, which are generally more soluble, preparations of pure products were carried out in MeOH at room temperature. These were then dissolved in acetone together with a little deprotonated ligand, cooled, and a methanolic Cu(II) solution added. The doped complexes formed from these solutions were collected by low temperature filtration as described for the Cu(II) complexes. Doping of the nickel complexes having $2R = -(CH_2)_n$ - $n = 2,3$ was undertaken at room temperature. For $n = 3$ a green and a brown form of the solid Ni(II) complex were collected, the EPR parameters reported in Table 5.8 were common to both forms.

Microanalytical results for these complexes are reported in Table 5.22.

TABLE 5.22. Elemental microanalyses for zinc, nickel and cadmium β -amino-
thione complexes $M(II)(RN-MeMeS)_2$.

M = Zn; R =		C	H	N	S
Me	C	44.79	6.26	8.71	
	F	45.00	6.33	8.73	
Et	C	48.06	6.91	8.01	
	F	48.05	7.01	8.04	
nPr	C	50.85	7.47	7.41	
	F	50.73	7.49	7.33	
nBu	C	53.26	7.95	6.90	
	F	53.45	8.08	6.89	
iBu	C	53.26	7.95	6.90	
	F	53.44	8.06	6.91	
nOct	C	60.27	9.34	5.41	
	F	60.25	9.50	5.50	
Bz	C	60.82	5.95	5.91	
	F	60.68	5.92	5.97	
Ph	C	59.25	5.42	6.38	14.38
	F	59.48	5.39	6.29	14.71
pFPh	C	54.83	4.60	5.81	
	F	54.38	4.63	5.71	
2R = $-(CH_2)_2-$	C	45.07	5.67	8.76	
	F	44.99	5.63	8.66	
2R = $-(CH_2)_3-$	C	46.78	6.04	8.39	
	F	47.08	6.14	8.38	
M = Ni; R =					
Me	C	45.74	6.40	8.89	
	F	45.61	6.45	8.84	
nOct	C	61.05	9.46	5.48	
	F	60.83	9.61	5.49	
C ₁₈ H ₃₇	C	69.76	11.20	3.54	
	F	70.48	11.36	3.68	
pClPh	C	52.00	4.36	5.51	
	F	52.06	4.38	5.48	
2,6-Me ₂ Ph	C	63.04	6.51	5.65	12.94
	F	63.38	6.54	5.70	12.93
2R = $-(CH_2)_2-$	C	46.03	5.79	8.95	20.48
	F	46.27	5.83	8.96	20.17
2R = $-(CH_2)_3-$	C	47.73	6.16	8.56	
	F	47.49	6.12	8.44	

/continued

TABLE 5.22 (continued.)

M = Cd; R =		C	H	N	S
Me	C	39.08	5.47	7.60	
	F	38.86	5.44	7.50	
Et	C	42.37	6.10	7.06	
	F	42.25	5.99	6.92	
C ₁₈ H ₃₇	C	55.25	8.56	4.96	
	F	55.36	8.66	4.94	
2R = -(CH ₂) ₃ -	C	41.00	5.29	7.36	
	F	40.75	5.20	7.22	

5.8.5. Experimental details for Figures.5.8.5.1. EPR.

Fig. 4. EPR of ⁶³Cu(II)(RN-MeMeS)₂ in MeOH. R = iBu; P 20, MA 2.5, RG 800
v9.224. R = sBu; P 20, MA2, RG 800, v9.238.

Fig. 5. EPR of ⁶³Cu(II)(RN-MeMeS)₂ in MeOH.

R = 1-Naphthyl; P20, MA 4, RG 800, v9.214

R = pMeOPh; P 20, MA 1.6, RG 1250, v9.219

Fig. 6. EPR in mobile toluene, temperature ca. -30°C.

Cu(II)(iBuN-MeMeS)₂; P 0, MA 1, RG 250, v9.245

Cu(II)(sBuN-MeMeS)₂; P 0, MA 1.6, RG 630, v9.247

Cu(II)(EtN-tButBuS)₂; P 0, MA 1.6, RG 400, v9.242

Fig. 8. EPR of Zn(II)[Cu(II)](RN-MeMeS)₂.

R = cHx; P 20, MA 1, RG 320, v9.229

R = Et; P 30, MA1, RG 1250, v9.228

Fig. 9. EPR of Zn(II)[Cu(II)](RN-MeMeS)₂.

R = pMeOPh; P 30, MA 0.8, RG 630, v9.225

R = 2,6-dimethylphenyl; P 20, MA 3.2, RG 1600, v9.225

Fig. 10. EPR of $M(II)[Cu(II)](RN-MeMeS)_2$.

M = Zn; P 30, MA 1, RG 630, ν 9.228.

M = Cd; P 20, MA 1.6, RG 320, ν 9.230.

Fig. 11. EPR of $Zn(II)[Cu(II)][(CH_2)_n(N-MeMeS)_2]$

n = 2; P 20, MA 0.63, RG 200, ν 9.227

n = 3; P 20, MA 0.8, RG 400, ν 9.217.

Fig. 12. EPR of $Ni(II)[Cu(II)][(CH_2)_2(N-MeMeS)_2]$

X-Band; P 30, MA 0.8, RG 500, ν 9.228.

Fig. 13. EPR of $Ni(II)[Cu(II)](RN-MeMeS)_2$.

R = $C_{18}H_{37}$, P 20, MA 2, RG 800, ν 9.227

R = pClPh, P 22, MA 0.63, RG 250, ν 9.228.

NOTES. P = Power/dB attenuation from 200 mW, MA = modulation amplitude/G,

RG = receiver gain, ν = microwave frequency/GHz.

5.8.5.2. Raman.

Fig. 16. $Cu(II)(MeN-MeMeS)_2$ at $-140^\circ C$.

647.1 nm exctn., P 200 mW, SR 6 cm^{-1} , IT 1.0s, TC 8s, SS $0.6\text{ cm}^{-1}/s$, FS 2 Kcps.

568.2 nm exctn., P 130 mW, SR 7 cm^{-1} , IT 1.0s, TC 8s, SS $0.5\text{ cm}^{-1}/s$, FS 2 Kcps.

530.9 nm exctn., 100 mW, SR 6 cm^{-1} , IT 1.0 s, TC 7s, SS $0.5\text{ cm}^{-1}/s$, FS 5 Kcps

Ligand at room temperature

647.1 nm exctn., SR 4 cm^{-1} , IT 0.5s, TC 3s, SS $0.5\text{ cm}^{-1}/s$, FS 100 Kcps.

NOTES. P on figure = plasma-emission line, FS - full scale (cps counts per sec.), IT - integration time, P - power, SR - spectral resolution, SS - scan speed, TC - time constant.

5.8.5.3. Electrochemistry.

Fig. 17. Pt electrode- scan rate = 5 mV/s at $-41^\circ C$.

HMDE - scan rate = 10 mV/s at $-38^\circ C$

Fig. 18. Scan rate 2 mV/s at $-36^\circ C$.

SECTION 6

EXPERIMENTAL

6.1.	<u>Preparative Chemistry of Iron-Sulphur Complexes.</u>	338
6.2.	<u>Instrumentation.</u>	340
6.3.	<u>"EPRPOW"; EPR Powder Simulation Program for S = 1/2.</u>	340

6. EXPERIMENTAL.

6.1. Preparative chemistry of iron-sulphur complexes.

All manipulations were carried out in an atmosphere of oxygen-free dinitrogen or argon, purified by passage through a hot tower containing BASF catalyst R3-11 and dried in a second tower of P_2O_5 supported on molecular sieves.

Solvents: MeOH, EtOH, DMSO and acetone were AR grade and not further purified; THF, Et_2O and HMPA were distilled from sodium under N_2 ; MeCN, PhCN, DMF and CH_2Cl_2 were distilled from P_2O_5 ; NMP was distilled from molecular sieves under vacuum. The solvents were freed of dissolved dioxygen by prolonged purging with N_2 and/or by repeated evacuation/gas flushing cycles whilst shaking.

$Et_4N[Fe(S_2\text{-}o\text{-xylyl})_2]$ was prepared as by Lane et al.⁵⁶ but using ethanol in place of acetonitrile, and recrystallised from hot acetone. $[Et_4N]_2[Fe_2S_2(S_2\text{-}o\text{-xylyl})_2]$ from $Et_4N[Fe(S_2\text{-}o\text{-xylyl})_2]$ as by Cambray et al.⁴⁵ $[Et_4N]_2[Fe_2Se_2(S_2\text{-}o\text{-xylyl})_2]$ as for the sulphur bridged complex, but using sodium hydroselenide³⁸³ in place of sodium hydrosulphide. $[Et_4N]_2[Fe_2X_2(SC_6H_4Y)_4]$ (X = S, Se; Y = H, Me, Cl) by ligand substitution from $[Et_4N]_2[Fe_2X_2(S_2\text{-}o\text{-xylyl})_2]$ in acetonitrile.²⁸ $[Et_4N]_2[Fe_2S_2Y_4]$ (Y = Cl, Br) as Wong et al.¹⁹³ similarly for $[Et_4N]_2[Fe_2Se_2Cl_4]$. $[Et_4N]_2[Fe_4S_4(SR)_4]$ (R = Ph, Bz) as Averill et al.⁵⁸ (see also reference 384). $[Et_4N]_2[Fe_4Se_4(SR)_4]$ (R = Ph, Bz), $[Et_4N]_2[Fe_4X_4(SePh)_4]$ (X = S, Se) as Bobrik et al.²¹² (see also reference 385). $[Et_4N]_2[Fe_4Se_4(SBz)_4]$ has a tendency to separate as an oil and is best recrystallised by slow addition of MeOH to a saturated room temperature acetonitrile solution, followed by slow cooling.

$[\text{Et}_4\text{N}][\text{Fe}_2\text{X}_2(\text{SePh})_4]$ ($\text{X} = \text{S}, \text{Se}$) were prepared in a similar manner to the PhS- ligated complexes. To a stirred slurry of around 1.5 mmol of $[\text{Et}_4\text{N}]_2[\text{Fe}_2\text{X}_2(\text{S}_2\text{-o-xylyl})_2]$ in 50 ml of acetonitrile a solution of 30 mmol of PhSeSePh ³⁸⁶ in 200 ml of acetonitrile was added. After about 15 mins the reaction mixture developed a dark purple/black colouration and was stirred overnight. Reduction of the solvent volume to around 150 ml resulted in separation of excess ligand and after filtration on Celite the crude product was precipitated with ca. 200 ml THF. Filtering again on Celite separates the product from a grey-brown filtrate, spectralexamination of which revealed the presence of a large amount of tetramer dianion $[\text{Fe}_4\text{X}_4(\text{SePh})_4]^{2-}$. The black solid collected in the Celite was dissolved out with acetonitrile at room temperature, concentrated by removal of solvent in vacuo, and recrystallised by slow addition with stirring of room-temperature THF. $\text{X} = \text{S}$ yields 40% of purple-black needles. $\text{X} = \text{Se}$ yields 25% of small purple-black crystals.

Microanalyses are given for previously unreported complexes only:-
 $[\text{Et}_4\text{N}]_2[\text{Fe}_2\text{Se}_2(\text{S}_2\text{-o-xylyl})_2]$: Calc.; C, 44.35; H, 6.51; N, 3.23. Found; C, 44.87; H, 6.54; N, 3.45. $[\text{Et}_4\text{N}]_2[\text{Fe}_2\text{Se}_2(\text{SPh})_4]$; Calc.; C, 49.69; H, 6.26; N, 2.90. Found; C, 50.03; H, 6.40; N, 2.91. $[\text{Et}_4\text{N}]_2[\text{Fe}_2\text{Se}_2(\text{STol})_4]$: Calc.; C, 51.66; H, 6.70; N, 2.74. Found: C, 51.67; H, 6.72; N, 2.88. $[\text{Et}_4\text{N}]_2[\text{Fe}_2\text{S}_2(\text{SePh})_4]$: Calc.; C, 45.43; H, 5.72; N, 2.65. Found: C, 45.11; H, 5.66; N, 2.79. $[\text{Et}_4\text{N}]_2[\text{Fe}_2\text{Se}_2(\text{SePh})_4]$: Calc.; C, 41.62; H, 5.24; N, 2.43. Found: C, 41.85; H, 5.30; N, 2.40. $[\text{Et}_4\text{N}]_2[\text{Fe}_4\text{Se}_4(\text{SBz})_4]$: Calc.; C, 40.89; H, 5.30; N, 2.17. Found: C, 40.55; H, 5.29; N, 2.33.

Subsequently Reynolds and Holm²⁹ have published details concerning preparation of the selenium bridged dimers by a different direct route.

6.2. Instrumentation.

X-band EPR measurements were made with a Varian E12 spectrometer operating at about 9.2 GHz. For low temperature measurements, samples were cooled in a stream of N₂ gas the temperature of which was regulated by a Varian variable temperature accessory. The Q-band machine has a Varian 36 GHz microwave bridge, cavity, detection electronics and field-controller, together with a Newport instruments 12 inch type-F magnet powered by a C905 rotary generator. Fields were calibrated using proton and lithium nuclear magnetic resonances.

Raman spectra were obtained using a Spex Ramalog V instrument with a cooled RCA gallium-arsenide photomultiplier and DPC-2 photon counter. A CRL-52 Krypton-ion laser was used with excitation wavelengths blue (468.0 nm, 476.2 nm, 482.5 nm), green (520.8 nm, 530.9 nm), yellow (568.2 nm) and red (647.1 nm, 676.4 nm). Plasma emission lines and CCl₄ were used to calibrate the monochromator frequency scale.

Infrared spectra were recorded using Perkin-Elmer 597 and 683 spectrometers.

NMR spectra were obtained with Perkin-Elmer R12A and R32 machines.

Electronic spectra were measured with Perkin-Elmer 551 and Cary 14 spectrophotometers.

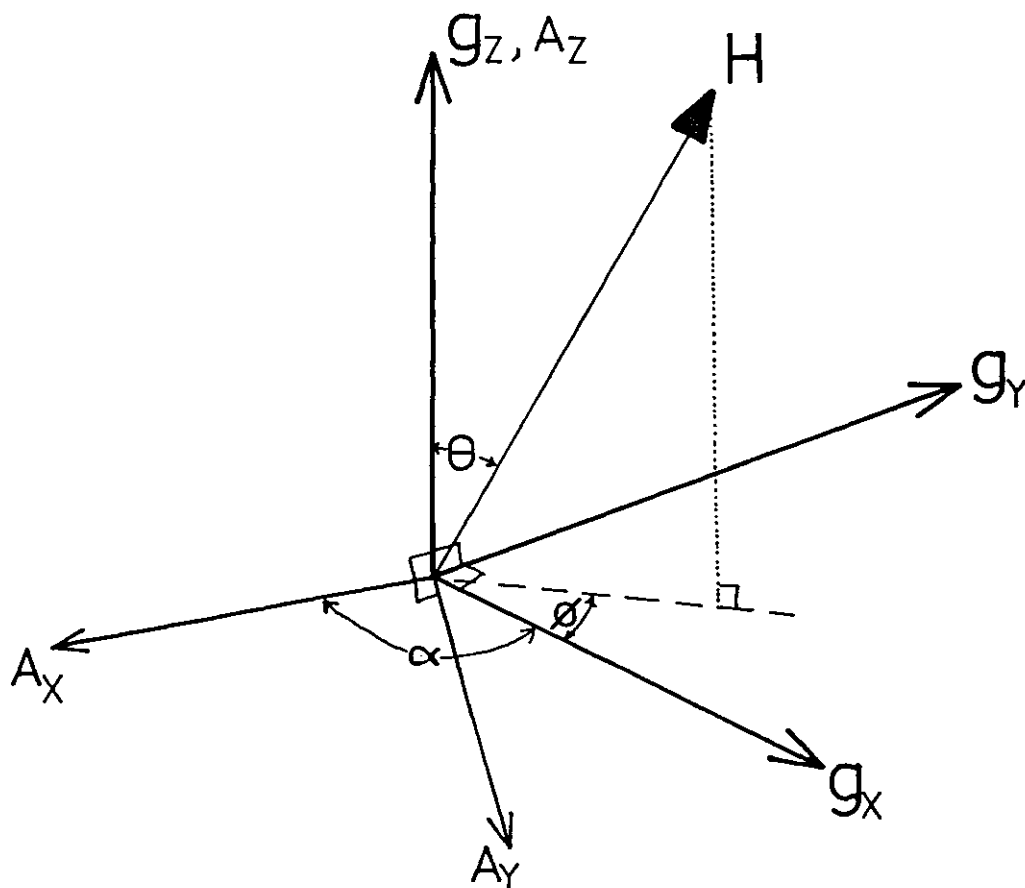
6.3. "EPRPOW"; EPR Powder Simulation Program for S = 1/2.

The following program has been employed in this work in simulating the EPR spectra of reduced [Fe₂S₂(SR)₄]²⁻ (Sec. 1) and Cu(II) β-aminothiones (Sec. 5) and in calculating component spectra for simulation of the solution spectrum of [Fe(S₂-o-xylyl)₂]⁻ (Sec. 3). The equations and methodology of the calculation are based on a program originally written by Belford and White³⁸⁷ but the algorithm has been completely re-written for faster, shorter and interactive execution. Additional linewidth and lineshape options have been incorporated.

The program is similar to that of Pilbrow and co-workers.^{343,388,389}
 The powder EPR spectrum is a summation of hyperfine (m) peaks over all θ and ϕ molecular orientations with respect to field (Figure 6.1):-

$$F(H) = \sum_{\theta} \sum_{\phi} \sum_m P(\theta, \phi) \cdot G(H, m, \theta, \phi) \cdot \sin \theta \cdot \Delta\theta \Delta\phi \quad E6.1$$

Figure 6.1. Relations between the \underline{g} and \underline{A} tensor coordinate systems
 (g_x, g_y, A_x and A_y are coplanar).



The summation is performed by a three-point Gauss-point approximation.³⁹⁰ Positions, $H(m, \theta, \phi)$ of the primary transitions are generated from second-order perturbation formulae for an orthorhombic spin Hamiltonian:

$$\hat{\mathcal{H}}_s = \beta(g_x H_x \hat{S}_x + g_y H_y \hat{S}_y + g_z H_z \hat{S}_z) + A_x \hat{S}_x \hat{I}_x + A_y \hat{S}_y \hat{I}_y + A_z \hat{S}_z \hat{I}_z$$

E6.2

\underline{g} and \underline{A} tensors are assumed coincident about the z-axis but misalignment by an angle α (see Figure 6.1) is allowed in the x-y plane (see references 388 and 389 for detailed equations on $\underline{g} - \underline{A}$ non-coincidence and second order hyperfine formulae).

Transitions are weighted by the anisotropic probability:-

$$P(\theta, \phi) = [g_x^2 g_y^2 (1 - \ell_z^2) + g_y^2 g_z^2 (1 - \ell_x^2) + g_z^2 g_x^2 (1 - \ell_y^2)] / 2g^3$$

E6.3

where $g^2 = g_x^2 \ell_x^2 + g_y^2 \ell_y^2 + g_z^2 \ell_z^2$, and the direction cosines ℓ_x, ℓ_y, ℓ_z are given by $\ell_x = \sin\theta \cos\phi, \ell_y = \sin\theta \sin\phi$ and $\ell_z = \cos\theta$. This transition probability factor differs from those originally used by White and Belford³⁸⁷ and Pilbrow and co-workers^{343, 388, 389} in having an additional g denominator, in keeping with the analysis of Aasa and Vännngård.³⁹¹

Ligand superhyperfine splitting is treated only to first order with an anisotropy equation:

$$A^2 = (A_x^2 g_x^2 \ell_x^2 + A_y^2 g_y^2 \ell_y^2 + A_z^2 g_z^2 \ell_z^2) / g^2$$

E6.4

The transitions are broadened by a Lorentzian or Gaussian function, $G(H, m, \theta, \phi)$ of anisotropic width. The form of the function used depends on whether an absorption or derivative resultant lineshape presentation is desired:-

Lorentzian: $Y = Y_{\max} \cdot \delta^2 / [\delta^2 + (H-H_0)^2]$

$$Y' = -2(H-H_0) \cdot Y^2 / \delta^2$$

Gaussian: $Y = Y_{\max} \cdot \exp[(-\ln 2)(H-H_0)^2 / \delta^2]$

$$Y' = -2(\ln 2)(H-H_0) \cdot Y / \delta^2$$

where

$$Y_{\max} = 1/\pi\delta, \quad \delta = \text{halfwidth at half-height,}$$

$$H_0 = \text{central field position of the function}$$

Mixed convolution products of these Lorentzian and Gaussian functions may be used, though this is more time consuming. To save calculation time the broadening functions are cut off where they have low intensity (default cut-offs in terms of half-height half-widths are ± 3 for Gaussian and ± 10 for Lorentzian).

Four linewidth anisotropy formulae are available. The simplest, and possibly the most useful, makes no recourse to any theory, using a linear interpolation by field between principal axis values. A second is similar but uses a parabolic interpolation formula. The third is based upon an assumption of unresolved hyperfine splitting as the main reason for broadening and uses equation E6.4 with the linewidth in place of A .^{388,389} The last is useful if a linear variation in a g -distribution, Δg , is dominant in defining the linewidth. In this case the anisotropy formula is a quadratic in H , with the three coefficients replacing the role of the principal-axis linewidth values used in the other three formulae.

The number of θ, ϕ divisions required to obtain a satisfactory computed lineshape depends on the degree of anisotropy in g and A and on the component linewidth and spectral resolution. Typically 50 θ intervals and

12 ϕ intervals were found adequate in the case of the 400 point spectrum of reduced $[\text{Fe}_2\text{S}_2(\text{SPh})_4]^{2-}$ in Figure 1.11, whilst a 180 by 15 θ, ϕ grid was used for the 600 point simulation of the $\text{Cu}(\text{II})(\text{iBuN-MeMeS})_2$ spectrum in Figure 5.4. The respective times for these two calculations on a CDC Cyber 174 were 3.2 secs. and 150 secs. The former is sufficiently low to allow least squares fitting of an experimental lineshape, but the latter is too high by around two orders of magnitude.

```

SUBROUTINE EPRPOW
C
C.....A ROUTINE TO CALCULATE AN EPR LINESHAPE
C.....USING SPATIAL INTEGRATION
C
C.....BASED ON A NUMERICAL ALGORITHM DEVELOPED
C      BY L.K.WHITE & R.L.BELFORD OF THE SCHOOL OF
C      CHEMICAL SCIENCES OF THE UNIVERSITY OF ILLINOIS.
C      COMPUTATIONAL ALGORITHM REWRITTEN AND
C      FURTHER DEVELOPED BY P.BEARDWOOD (CHEM. DEPT.,
C      IMPERIAL COLLEGE OF SCIENCE AND TECHNOLOGY).
C
      REAL LX,LY,LZ
      COMMON XI(1100),TDTL(1100),X2(2200),TLG(1100)
      1,DATA(100),ID,ID(9)
      COMMON/REFVAB/DUM(426),IDUM(28),INTO(20),INT(20,4)
      DIMENSION HG(2),AGZ(2),HL(2),AHL(2),SIG(2),SN(2)
      DIMENSION D(9),THETA(9),PHI(9)
      DIMENSION A(3,4),GG(3),HA(4),WL(3),WG(3),HM(3)
      DATA HG(2),AGZ(2),HL(2),AHL(2),SIG,SN(2)/6*1.0,-1.0/
C.....ARRAY 'DATA' CONTAINS INPUT PARAMETERS
C.....STARTING FIELD
      HS=DATA(9)
C.....ENDING FIELD
      HE=DATA(10)
C.....NUMBER OF POINTS
      NPS=DATA(11)
      DPH=(HE-HS)/FLOAT(NPS-1)
C.....FREQUENCY
      HV8=DATA(12)*714.4843012
      IF(HV8.EQ.0.0)CALL ERROR(25,2HNU,0.0)
C.....NUMBER OF PHI INTERVALS
      NN=DATA(13)
C.....NUMBER OF THETA INTERVALS
      MM=DATA(14)
C.....DERIVATIVE=0
      ND1=DATA(42)+1.0
      NDG=DATA(43)+1.0
C.....CONVOLUTION FUNCTION CUTOFFS
      CUTL=DATA(46)
      CUTG=DATA(47)
      CUTLG=DATA(48)
      IF(CUTL.EQ.0.0)CUTL=10.0
      IF(CUTG.EQ.0.0)CUTG=3.0
      IF(CUTLG.EQ.0.0)CUTLG=1.0
C.....LORENTZIAN WIDTHS
      WL(1)=DATA(24)/DPH
      WL(2)=DATA(25)/DPH
      WL(3)=DATA(26)/DPH
C.....GAUSSIAN WIDTHS
      WG(1)=DATA(27)/DPH
      WG(2)=DATA(28)/DPH
      WG(3)=DATA(29)/DPH
C.....G-TENSOR ORDERING
      GX=DATA(21)
      IF(GX.EQ.0.0)CALL ERROR(13,0,0,0)
      GY=DATA(22)
      GZ=DATA(23)
      IF(GY.GT.0.0)GO TO 255
      GY=GX
      WL(2)=WL(1)
      WG(2)=WG(1)
255 IF(GZ.GT.0.0)GO TO 256
      GZ=GX
      WL(3)=WL(1)
      WG(3)=WG(1)
C.....HTOG CONVERTS FIELDS TO G-VALUES
256 GX=HTOG(GX)
      GY=HTOG(GY)
      GZ=HTOG(GZ)
      GXX=GX*GX
      GYY=GY*GY
      GZZ=GZ*GZ
      GXXY=GXX*GY
      GYYZ=GYY*GZZ
      GZZX=GZZ*GXX
C.....CONVOLUTION FUNCTION TYPE
C.....LORGAU= 0 FOR LORENTZIAN
C.....      1 FOR GAUSSIAN
C.....      2 FOR LORENTZIAN ON GAUSSIAN
C.....      3 FOR GAUSSIAN ON LORENTZIAN
      LORGAU=DATA(41)+1.0
      GO TO(21,22,23,24)LORGAU
21 ASSIGN 401 TO IGL3
      GO TO 28
22 ASSIGN 402 TO IGL3
      GO TO 28
23 ASSIGN 403 TO IGL3
      ASSIGN 50 TO IGL4
      SI=SIG(ND1)
      GO TO 28
24 ASSIGN 404 TO IGL3
      ASSIGN 80 TO IGL4
      SI=SIG(NDG)
      GO TO 28

```



```

C.....LINEWIDTH ANISOTROPY
C.....LWFN= 0 FOR LINEAR ANISOTROPY
C.....      1 FOR PARABOLIC ANISOTROPY
C.....      2 FOR DIRECTION COSINE ANISOTROPY
C.....      4 FOR QUADRATIC ANISOTROPY
 28 LWFN=DATA(44)
C.....DIRECTION COSINE LINEWIDTH ANISOTROPY
  IF(LWFN=2)250,251,252
 251 IF(LORGAU.EQ.1)GO TO 264
  WGX=WG(1)*WG(1)*GXX
  WGY=WG(2)*WG(2)*GYY
  WGZ=WG(3)*WG(3)*GZZ
  ASSIGN 650 TO IGL1
  ASSIGN 211 TO IGL2
  IF(LORGAU.EQ.2)GO TO 29
  ASSIGN 550 TO IGL2
  GO TO 267
 254 ASSIGN 550 TO IGL1
 257 WXL=WL(1)*WL(1)*GXX
  WYL=WL(2)*WL(2)*GYY
  WZL=WL(3)*WL(3)*GZZ
  GO TO 29
C.....QUADRATIC LINEWIDTH ANISOTROPY
 252 IF(LORGAU.EQ.1)GO TO 253
  ASSIGN 640 TO IGL1
  ASSIGN 211 TO IGL2
  IF(LORGAU.EQ.2)GO TO 29
  ASSIGN 540 TO IGL2
  GO TO 29
 253 ASSIGN 540 TO IGL1
  GO TO 29
C.....LINEAR AND PARABOLIC LINEWIDTH ANISOTROPY
 250 HM(1)=HVB/GX
  HM(2)=HVB/GY
  HM(3)=HVB/GZ
  IMAX=1
  IF(HM(2).GT.HM(1))IMAX=2
  IF(HM(3).GT.HM(IMAX))IMAX=3
  IMIN=1
  IF(HM(2).LT.HM(1))IMIN=2
  IF(HM(3).LT.HM(IMIN))IMIN=3
  IMID=1
  IF(HM(2).LT.HM(IMAX).AND.HM(2).GT.HM(IMIN))IMID=2
  IF(HM(3).LT.HM(IMAX).AND.HM(3).GT.HM(IMIN))IMID=3
  HX=HM(IMAX)
  HY=HM(IMID)
  HZ=HM(IMIN)
  IF(LORGAU.EQ.1)GO TO 260
  WX=WG(IMAX)
  WY=WG(IMID)
  WZ=WG(IMIN)
  IF(LWFN.EQ.0)GO TO 261
C.....PARABOLIC
  ASSIGN 670 TO IGL1
  ASSIGN 211 TO IGL2
  CALL INTPL(HZ,HY,HX,WZ,WY,WX,CG1,CG2,CG3)
  IF(LORGAU.EQ.2)GO TO 29
  ASSIGN 570 TO IGL2
  GO TO 260
C.....LINEAR
 261 ASSIGN 660 TO IGL1
  ASSIGN 211 TO IGL2
  CALL INTPL(HX,HX,HY,WX,0.0,WY,CG1,CG2,0.0)
  CALL INTPL(HY,HY,HZ,WY,0.0,WZ,CG3,CG4,0.0)
  IF(LORGAU.EQ.2)GO TO 29
  ASSIGN 560 TO IGL2
 260 WX=WL(IMAX)
  WY=WL(IMID)
  WZ=WL(IMIN)
  IF(LWFN.EQ.0)GO TO 263
C.....PARABOLIC
  CALL INTPL(HZ,HY,HX,WZ,WY,WX,CL1,CL2,CL3)
  IF(LORGAU.EQ.1)ASSIGN 570 TO IGL1
  GO TO 29
C.....LINEAR
 263 CALL INTPL(HX,HX,HY,WX,0.0,WY,CL1,CL2,0.0)
  CALL INTPL(HY,HY,HZ,WY,0.0,WZ,CL3,CL4,0.0)
  IF(LORGAU.EQ.1)ASSIGN 560 TO IGL1
 29 IF(DATA(71).EQ.0.0)GO TO 265
C.....LINEWIDTH ANISOTROPY DRAWN INSTEAD OF SPECTRUM
  ASSIGN 309 TO IGL3
  DO 280 I=1,NPS
 280 XZ(I)=0.0
  AL=0.0
  AG=0.0
 265 IF(DATA(15).GT.0.0)GO TO 41
C.....PRIMARY-HYPERFINE PARAMETERS
  INTO(1)=1
  NHLO=1
  SPINO=0.0
  SPN=0.0
  CA=0.0
  CB=0.0
  ZG=0.0
  ASSIGN 52 TO IHYP1
  ASSIGN 52 TO IHYP2
  GO TO 46
C.....NUMBER OF HYPERFINE LINES
 41 NHLO=DATA(15)
C.....PRIMARY-HYPERFINE TENSOR
  AX=DATA(30)
  AY=DATA(31)
  AZ=DATA(32)
  IF(AY.EQ.0.0)AY=AX
  IF(AZ.EQ.0.0)AZ=AX
  AXX=AX*AX
  AYY=AY*AY
  AZZ=AZ*AZ
C.....A-TENSOR NON-COINCIDENCE ANGLE: ROTATION ABOUT Z
  ALP=DATA(40)*0.01745329252
  SALP=SIN(ALP)
  CALP=COS(ALP)
C.....SECOND-ORDER PRIMARY-HYPERFINE CONSTANTS
  TXX=AXX*CALP*CALP+AYY*SALP*SALP
  TYY=AXX*SALP*SALP+AYY*CALP*CALP
  TXY=(AXX-AYY)*CALP*SALP
  GTXX=GXX*TXX
  GTYY=GYY*TYY
  GTXY=Z.0*GX*GY*TXY
  GXYT=GX*GY*(TYY-TXX)+(GXX-GYY)*TXY
  GXYT=GXYT*GXYT
  TXXYYY=TXX*TYY-TXY*TXY
  SPINO=(DATA(15)+1.0)/2.0
  SPN=SPINO*(SPINO-1.0)
  CALL INTIN(0,NHLO)
  ASSIGN 53 TO IHYP1
  ASSIGN 53 TO IHYP2
C.....SECONDARY-HYPERFINE PARAMETERS
 46 DO 200 I=1,4
 200 IF(DATA(49+I*5).GT.0.0)GO TO 45
  DO 90 I=1,4
  HA(I)=0.0
 90 INT(I,I)=1
  NHL1=1
  NHL2=I
  NHL3=1
  NHL4=1
  SPIN1=0.0
  SPIN2=0.0
  SPIN3=0.0
  SPIN4=0.0
  GO TO 42
 45 ASSIGN 51 TO IHYP1
  NHL1=AMAX1(DATA(54),1.0)
  NHL2=AMAX1(DATA(59),1.0)
  NHL3=AMAX1(DATA(64),1.0)
  NHL4=AMAX1(DATA(69),1.0)
  SPIN1=(DATA(54)+1.0)/2.0
  SPIN2=(DATA(59)+1.0)/2.0
  SPIN3=(DATA(64)+1.0)/2.0
  SPIN4=(DATA(69)+1.0)/2.0
  ND=50
  GG(1)=GXX
  GG(2)=GYY
  GG(3)=GZZ
  DO 300 I=1,4
  IHL=DATA(ND+4)
  IF(IHL.EQ.0)GO TO 301
  CALL INTIN(I,IHL)
  DO 400 K=1,3
  A(K,I)=DATA(ND+K)*DATA(ND+K)*GG(K)
 400 IF(A(K,I).EQ.0.0)A(K,I)=A(1,I)
  GO TO 300
 301 DO 500 K=1,3
 500 A(K,I)=0.0
  INT(I,I)=1
 300 ND=ND+5
 42 NSN=1
  DO 100 I=1,1100
  TOTL(I)=0.0
  NN=MAX0(NN,3)
  MM=MAX0(MM,3)
  NN3=3*NN
  MM3=3*MM
C.....3-POINT GAUSS-POINT INTEGRATION SET UP
  IF(GX.EQ.GY.AND.GZ.EQ.GY)GO TO 89
  D(1)=0.22222222
  D(2)=1.02497166
  D(3)=0.75280612
  D(4)=0.55555555
  D(5)=0.88888888
  D(6)=D(4)
  D(7)=D(3)
  D(8)=D(2)
  D(9)=D(1)
  C1=1.570796327

```

```

C2=0.77459667
C3=1-0.28989794
C4=1+0.88989794
C5=3.141592654
SINT=C1*0.5/NN
GSINT=SINT*C2
THETA(1)=0.0
THETA(2)=SINT*C3
THETA(3)=SINT*C4
THETA(4)=SINT-GSINT
THETA(5)=SINT
THETA(6)=SINT+GSINT
THETA(7)=C1-THETA(3)
THETA(8)=C1-THETA(2)
THETA(9)=C1
SINT=SINT*2.0
IF(GX.EQ.GY.OR.GZ.EQ.GY)GO TO 82
IF(DATA(40).EQ.0.0)C5=C5*0.5
SINP=C5*0.5/MM
GSINP=SINP*C2
PHI(1)=0.0
PHI(2)=SINP*C3
PHI(3)=SINP*C4
PHI(4)=SINP-GSINP
PHI(5)=SINP
PHI(6)=SINP+GSINP
PHI(7)=C5-PHI(3)
PHI(8)=C5-PHI(2)
PHI(9)=C5
SINP=SINP*2.0
GO TO 81
89 NN3=1
D(1)=1.0
THETA(1)=0.0
SINT=0.0
NSN=2
82 MM3=1
PHI(1)=0.0
SINP=0.0
81 NN1=MAXO((NN3-3),1)
MM1=MAXO((MM3-3),1)
NPS=NPS+2
C.....LOOP FOR THETA INTEGRATION: XY-Z
DO 108 I=1,NN3
IX=MAXO((I-3),0)
IX=MINO(IX,1)
IY=MAXO((I-NN1),0)
IY=MINO(IY,1)
NPB=MOD((I+2),3)+3*(IX+IY)+1
IF=(I-1)/3
FL=FLOAT(IX-IY)*IF
TETA=THETA(NPB)+SINT*FL
CS=COS(TETA)
CS2=CS*CS
SN(1)=SIN(TETA)
SN2=SN(1)*SN(1)
DD=D(NPB)*SN(NSN)
C.....LOOP FOR PHI INTEGRATION: XY PLANE
DO 108 M=1,MM3
IX=MAXO((M-3),0)
IX=MINO(IX,1)
IY=MAXO((M-MM1),0)
IY=MINO(IY,1)
MPB=MOD((M+2),3)+3*(IX+IY)+1
IF=(M-1)/3
FL=(IX-IY)*IF
FI=PHI(MPB)+SINP*FL
CC=COS(FI)
CC2=CC*CC
SS=SIN(FI)
SS2=SS*SS
SSCC=SS*CC
C.....DIRECTION COSINES
LX=SN2*CC2
LY=SN2*SS2
LZ=CS2
GLX=GXX*LX
GLY=GYY*LY
GLZ=GZZ*LZ
G2=GLX+GLY+GLZ
G=SQRT(G2)
GB=0.4668398728*G
GGB=G*GB
C.....TRANSITION PROBABILITY
U=(GXYY*SN2+GYZZ*(SS2+CS2*CC2)+GZZX*(CC2+CS2*SS2))/(G*G2)
C.....*W*-INCLUDES INTEGRATION AND SITE WEIGHTING FACTORS
W=U*DD*D(MPB)
H=HVB/G
GO TO IHYP1(51,52,53)
C.....SECONDARY-HYPERFINE
31 DO 47 K=1,4
47 HA(K)=(SQRT(LX*A(1,K)+LY*A(2,K)+LZ*A(3,K)))/GGB
C.....SECOND-ORDER PRIMARY-HYPERFINE
53 GPERP2=GXX*CC2+GYY*SS2
AZG=TX*GLX+TY*GLY+AZZ*GLZ+GTXY*SN2*SSCC
ZZ=AZG/G2
ZG=SQRT(ZZ)/GB
APERP2=(GTXX*CC2+GTY*SS2+GTXY*SSCC)/GPERP2
ABCDEZ=SSCC*SSCC*GX*Y/(ZZ*G2*GPERP2)
AA=APERP2*AZZ/Z2
AB=TX*Y*Y/APERP2
AC=ABCDEZ*AZZ*GZZ*CSZ/(APERP2*GPERP2)
AD=GZZ*GPERP2*((APERP2-AZZ)**2)*SN2*CSZ/(ZZ*G2*G2)
AE=ABCDEZ*SN2
GBBH=GB*GB*H
CA=(AA+AB+AC)/(4*GBBH)
CB=(AD+AE)/(2*GBBH)
C.....GAUSSIAN LINEWIDTH
52 GO TO IGL1(540,550,560,570,640,650,660,670)
C.....QUADRATIC ANISOTROPY
640 AG=WG(1)+WG(2)*H+WG(3)*H*H
GO TO 600
C.....DIRECTION COSINE ANISOTROPY
650 AG=(SQRT(WGX*GLX+WGY*GLY+WGZ*GLZ))/G
GO TO 600
C.....LINEAR ANISOTROPY
660 IF(H.LT.HY)GO TO 661
AG=CG1+H*CG2
GO TO 600
661 AG=CG3+H*CG4
GO TO 600
C.....PARABOLIC ANISOTROPY
670 AG=CG1+H*(CG2+H*CG3)
600 AGI=1.0/AG
AG2(1)=AGI*AGI*0.69314718
ICOG=CUTG*AG+0.5
FCOG=ICOG
FGI=AGI*AG2(NDG)*W
C.....LORENTZIAN WIDTHS
GO TO IGL2(211,540,550,560,570)
C.....QUADRATIC ANISOTROPY
540 AL=WL(1)+WL(2)*H+WL(3)*H*H
GO TO 700
C.....DIRECTION COSINE ANISOTROPY
550 AL=(SQRT(WGL*GLX+WGL*GLY+WGL*GLZ))/G
GO TO 700
C.....LINEAR ANISOTROPY
560 IF(H.LT.HY)GO TO 561
AL=CL1+H*CL2
GO TO 700
561 AL=CL3+H*CL4
GO TO 700
C.....PARABOLIC ANISOTROPY
570 AL=CL1+H*(CL2+H*CL3)
700 AL2=AL*AL
ICOL=CUTL*AL+0.5
FCOL=ICOL
FLI=AL*W
C.....SECONDARY-HYPERFINE LOOPS
211 DO 98 I4=1,NHL4
H4=H*HA(4)*(FLOAT(I4)-SPIN4)
DO 98 I3=1,NHL3
H3=H4+HA(3)*(FLOAT(I3)-SPIN3)
DO 98 I2=1,NHL2
H2=H3+HA(2)*(FLOAT(I2)-SPIN2)
DO 98 I1=1,NHL1
H1=H2+HA(1)*(FLOAT(I1)-SPIN1)
C.....PRIMARY-HYPERFINE LOOP
DO 98 IO=1,NHLO
SPINM=FLOAT(IO)-SPINO
H0=H1-SPINM*(ZG+SPINM*(CB-CA))-CA*SPN
HSTAR=((H0-HS)/DPH)+2.0
IM=HSTAR+0.5
HF=INTO(IO)*INT(I1,1)*INT(I2,2)*INT(I3,3)*INT(I4,4)
C.....BROADENING FUNCTIONS
GO TO IGL3(401,402,403,404,309)
C.....GAUSSIAN
402 CALL LIMITS(L1,L2,ICOG,1,IM,NPS)
FG=FGI*HF
DO 20 L=L1,L2
HG(1)=HSTAR-FLOAT(L)
AHG=AG2(1)*HG(1)*HG(1)
AHG=AMINI(AHG,700.0)
20 TOTL(L)=TOTL(L)+FG*HG(NDG)/EXP(AHG)
GO TO 98
C.....LORENTZIAN
401 CALL LIMITS(L1,L2,ICOL,1,IM,NPS)
FL=FLI*HF
DO 30 L=L1,L2
HL(1)=HSTAR-FLOAT(L)
AHL(1)=AL2+HL(1)*HL(1)
TOTL(L)=TOTL(L)+FL*HL(NDL)/(AHL(1)*AHL(NDL))
GO TO 98
C.....LORENTZIAN ON GAUSSIAN
403 J1=IM-ICOG

```

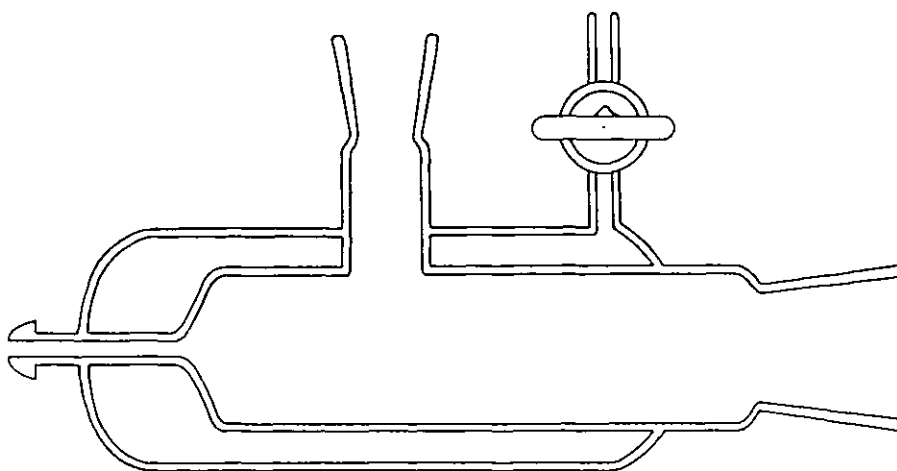
```

J2=IM+ICOG
L2=MINO(ICOL,NPS)+1
DO 40 L=1,L2
HL(1)=L-1
40 AHL(1)=ALZ+HL(1)*HL(1)
   TLG(L)=AL*HL(NDL)/(AHL(1)*AHL(NDL))
   TLG(1)=TLG(1)*0.5
   FG=FGI*HF
   HG(1)=HSTAR-FLOAT(J1)
   AHG=AGZ(1)*HG(1)*HG(1)
   AHG=AMIN1(AHG,700.0)
   TGI=FG*HG(NDG)/EXP(AHG)
   CDL1=AL*CUTLG/TGI
   DO 50 J=J1,J2
   HG(1)=HSTAR-FLOAT(J)
   AHG=AGZ(1)*HG(1)*HG(1)
   AHG=AMIN1(AHG,700.0)
   TGL=FG*HG(NDG)/EXP(AHG)
   ICOLG=AMIN1((ABS(TGL*CDL1)+0.5),FCOL)
   GO TO 306
50 CONTINUE
   GO TO 98
C.....GAUSSIAN ON LORENTZIAN
404 J1=IM-ICOL
     J2=IM+ICOL
     LZ=MINO(ICOG,NPS)+1
     FG=FGI*HF
     DO 70 L=1,L2
     HL(1)=L-1
     AHG=AGZ(1)*HG(1)*HG(1)
     AHG=AMIN1(AHG,700.0)
70   TLG(L)=FG*HG(NDG)/EXP(AHG)
     TLG(1)=TLG(1)*0.5
     HL(1)=HSTAR-FLOAT(J1)
     AHL(1)=ALZ+HL(1)*HL(1)
     TL1=AL*HL(NDL)/(AHL(1)*AHL(NDL))
     COG1=AG*CUTLG/TL1
     DO 80 J=J1,J2
     HL(1)=HSTAR-FLOAT(J)
     AHL(1)=ALZ+HL(1)*HL(1)
     TGL=AL*HL(NDL)/(AHL(1)*AHL(NDL))
     ICOLG=AMIN1((ABS(TGL*COG1)+0.5),FCOG)
     GO TO 306
80 CONTINUE
98 CONTINUE
108 CONTINUE
   GO TO 91
C.....LOOP EXTERNAL
306 CALL LIMITS(K1,K2,ICOLG,1,J,NPS)
     JI=MAX0(J,K1)
     JP=MINO(JI,(K2+ICOLG))+1
     JI=MINO(JI,K2)
     JM=MINO(J,K2)
     JM=MAX0(JM,(K1-ICOLG))-1
     DO 60 K=K1,JI
     TOTL(K)=TOTL(K)+TGL*TLG(JP-K)
     TGL=TGL*SI
     DO 61 K=JI,K2
     TOTL(K)=TOTL(K)+TGL*TLG(K-JM)
     GO TO IGL4(50,80)
C.....END OF LOOPS
91 NPS=NPS-2
   DO 900 I=1,NPS
900  TOTL(I)=TOTL(I+1)
     TOTL(1100)=NPS
     TOTL(1098)=HS
     TOTL(1099)=HE
     TOTL(1095)=1.0
C.....NORMALISE SPECTRUM
   CALL NORMAL(Z,2)
   IF(IB(6).NE.0)CALL DRAW(2,0.0,0.0,0)
   IF(DATA(71).EQ.0.0)RETURN
   DATA(71)=0.0
   DO 320 I=1,NPS
320  TOTL(I)=XZ(I)
     GO TO 81
309  TOTL(IM)=AL
     XZ(IM)=AG
     GO TO 108
   END
CHTOG
  FUNCTION HTOG(X)
  C
  C.....FIELD:G-VALUE INTERCONVERSION
  C
  C.....IF X +VE RESULT IS A G-VALUE
  C.....IF X -VE RESULT IS A FIELD
  C.....IF X<10 X IS ASSUMED TO BE A G-VALUE
  C.....IF X>10 X IS ASSUMED TO BE A FIELD
  C
  COMMON S(5500),DATA(100)
  HTOG=ABS(X)
  IF(X.LT.0.0)GO TO 1
  IF(HTOG.LE.10.0)RETURN
2  FREQ=DATA(12)
  IF(FREQ.EQ.0.0)CALL ERROR (25,4HFREQ,0.0)
  HTOG=714.484301*FREQ/HTOG
  RETURN
1  IF(HTOG.GT.10.0)RETURN
  GO TO 2
  END
CINTPL
  SUBROUTINE INTPL (XX,XY,XZ,YX,YY,YZ,C1,C2,C3)
  C
  C.....EVALUATES COEFFICIENTS OF PARABOLIC INTERPLOATION
  C.....AND EXTRAPLOATION EQUATION- Y=C1+C2X+C3X*X USING
  C.....CRAMERS RULE.
  C
  C.....X-VALUES
  VX=XX
  VY=XY
  VZ=XZ
  C.....Y-VALUES
  AX=YX
  AY=YY
  AZ=YZ
  VV=ABS((VY-VZ)*(VX-VY))
  IF(VV.LT.0.0000001)GO TO 4
  GO TO 3
4  VV=ABS(VZ-VX)
  IF(VV.LT.0.0000001)GO TO 1
  GO TO 2
1  C1=AX
  C2=0.0
  C3=0.0
  RETURN
2  DENOM=VZ-VX
  DELX=VZ*AX-AZ*VX
  DELY=AZ-AX
  C1=DELX/DENOM
  C2=DELY/DENOM
  C3=0.0
  RETURN
3  VX2=VX*VX
  VY2=VY*VY
  VZ2=VZ*VZ
  DENOM=VZ2*(VY-VX)+VY2*(VX-VZ)+VX2*(VZ-VY)
  DELX=VZ2*(AX*VY-AY*VX)+VY2*(AZ*VX-AX*VZ)+VX2*(AY*VZ-AZ*VY)
  DELY=VZ2*(AY-AX)+VY2*(AX-AZ)+VX2*(AZ-AY)
  DELZ=VZ*(AX-AY)+VY*(AZ-AX)+VX*(AY-AZ)
  C1=DELX/DENOM
  C2=DELY/DENOM
  C3=DELZ/DENOM
  RETURN
  END
CINTIN
  SUBROUTINE INTIN(I,IHL)
  C.....SET HYPERFINE PARAMETERS
  COMMON X(5500),DATA(100),IO,IG(8)
  COMMON/REFVAB/DUM(426),IDUM(28),INT(20,5)
  COMMON/IN/ICOM,X1,X2,X3,X4,X5,IDUM2(10),IM
  1,NIN,NLOOP,LOOP1,LOOP2,INU,ARGS(20),IARG,J0(10)
  2,NSTR,ISTR(40,12)
  N=I+1
  INTX=DATA(N*5+45)
  C.....INTX=0 - READ IN VALUES
  C.....INTX>0 - SET ALL VALUES TO INTX
  C.....INTX=-1 - USE PREVIOUS INPUT VALUES
  IF(INTX.EQ.-1)RETURN
  NHL=IHL
  IF(INTX.EQ.0)GO TO 1
  DO 10 K=1,NHL
10  INT(K,N)=INTX
  RETURN
1  WRITE(IO,1000)N,NHL
  1000 FORMAT(1HYPERFINE INTENSITIES FOR SET*,I3,* -ENTER*,I3,* VALUES*)
  CALL PRINT
  READ(INU,*) (INT(K,N),K=1,NHL)
  IF(EOF(INU))1.2
2  DATA(N*5+45)=-1.0
  RETURN
  END
CLIMITS
  SUBROUTINE LIMITS(L1,L2,ICO,IS,IM,IE)
  C
  C.....EVALUATES RANGE(L1 TO L2) FOR BROADENING FUNCTION.
  C.....THE FUNCTION IS CLIPPED AT THE CUTOFF(ICO) OR AT
  C.....THE START AND END POINTS(IS,IE)
  C
  L1=MAX0((IM-ICO),IS)
  L1=MINO(L1,IE)
  L2=MINO((IM+ICO),IE)
  L2=MAX0(L2,IS)
  RETURN
  END

```

APPENDICES

A	An interactive spectral manipulation program	349
B	A variable temperature cryostat for rapidly-rotating Raman samples	360



APPENDIX A

An Interactive Spectral Manipulation Program.

A.1. Introduction.

During the course of this work a program has been developed which has general utility for manipulation of spectra and related data, with particular emphasis on EPR. The overriding principle employed in designing the programs' mode of operation has been to put the maximum amount of control at the users disposal and to maintain a high level of default on the available options. The aim has been to achieve flexibility and generality in the program's applications and to maximise the speed of user/program interaction, but at the same time to ensure a simplicity of operation, with adequate error recovery, so that basic manipulations may be performed without difficulty by an infrequent user. To this end virtually all input is taken in response to a single prompt as character information (A - format) and interpreted by a routine ('SYNTAX') which defines the syntax for a command-orientated language.

A.2. Commands.

Input commands take the general form:

COMMAND: P1/P2 = P3*P4+P5 (S1) (S2)

'COMMAND' is an alpha-identifier of up to 10 characters, P1 to P5 are parameters which may be (1) signed or unsigned integer or floating point numbers (2) alpha-numeric strings up to 10 characters in length (3) alpha

identifiers from the data-set (see below). The separators $' / = * + '$ may occur in any order and thus need only be entered if their respective parameters P2-P5 are to be specified. The $':'$ separator is optional unless P1 begins with an alpha character. Further sequential parameters or long character strings may be attached to the command with the optional terminating parenthetical terms, S1 and S2.

Commands may be strung together in sentences by separating with $','$ or $','$, and are then processed sequentially. Such a sentence may form a line of input with up to 100 characters. If the operation performed by a command is to be repeated with new parameters then it is implicitly assumed following $','$ without being re-entered. The $','$ delimiter also causes retention of the parameter values P2-P5, unless they are respecified by the input.

A.3. Data-Identifiers.

A data set of 100 elements is available at any one time for use as data, switches, registers, etc. These are allotted names of up to 10 alpha—characters and may be set using the general form of the command input:

DATAID P1*P4/P2+P5

or DATAID = P3*P4/P2+P5

where the separators now take their normal mathematical meanings. Unlike the usual form of the command, if after a data entry and $','$ or $','$ the command field is left unspecified, data entry to the next element in the data set is assumed, thus allowing rapid sequential setting of blocks of adjacent elements.

A.4. Spectra.

Up to five spectra (intensities at equally spaced monotonic values of some spectroscopic variable) may be retained in central memory, each having a small updatable data-set of its own. Additional random access storage is available for 100 spectra and/or main data-sets on each of three files.

A.5. Some Examples.

A.5.1. Data identifiers;- GX, GY, GZ and NU

GX 2.001

GY = GX + 0.03

NU 9.21

GZ = 714.5 * NU/3030

A.5.2. Commands DRAW, READ, SMOOTH

DRAW 1 * 2.5 - draw spectrum 1 at 2.5 times normal intensity

READ 3/2 = 4 - read record 3 on file 2 into spectrum 4

SMOOTH 2 = 3 * 4 - smooth spectrum 2 4 times and place result in spectrum 3.

A.6. Strings.

A group of commands up to 300 characters in length may be collected together and given a new name using the command 'STRING/P2(S1)'. The string of commands between the brackets, S1, is stored and may be executed by simply naming P2 in the normal way for a command. Any parameters (P1-P5) in this string of commands may be replaced by '?' and variably specified at execution of the string-command as parenthetical arguments. A string may call another string, or indeed itself.

Example.

STRING/RASD (READ?/2, 7/3 = 2, ADD 1 = 3, 2* -1.5, SMOOTH 3, DRAW 3)

RASD (1,1), RASD (1,3)

- reads two spectra from different files, subtracts 1.5 of one from the other, smooths the result and draws it.

A.7. Editor.

The contents of character strings of this sort may be modified using a built in editor. Commands to this editor take the same form as the general command input and may thus be interspersed with any other command. The following string editor commands are available:

P	- print the string
A(S1)	- add the substring S1 to the end
C(S1)(S2)	- change all occurrences of substring S1 to S2
M	- print the string and receive modification instructions on the next line

A.8. Command File.

Any number of lines of commands may be collected into a file and input may be switched to read from this file instead of the keyboard. In this way it is possible to write a subprogram in the spectroscopic language defined by the Fortran program, and to have it executed in interpreter fashion. Movement in and modification of this file is made possible via the editor; the relevant additional commands being:


```

N P1      - move forward P1 lines
GOTO P1   - move to line P1
T         - move to top of file
B         - move to bottom of file
L(S1)     - locate first occurrence of string S1
D P1      - delete P1 lines
I P1      - insert P1 lines
SOSRUN P1*P4 - move to line P1 and execute P4 lines

```

A particularly useful feature of this command file, in connection with the screen-display, is the 'PIC' command. This, together with associated commands 'UNPIC' and 'REPIC', automatically controls the writing and reading of the command file, where plot space positional information is also stored, allowing a complex picture easily to be built-up on the screen and modified.

A.9 . Examples of Program Applications.

The following string and command files demonstrate the syntax and some of the commands outlined above. The examples are taken from the work in this thesis. Many of the figures in this manuscript have been produced entirely using the graphical capabilities of the program, e.g., Figures 0.2, 1.4, 1.9, 2.6, 3.7, 5.4, and 5.15.

Example 1.

The following set of strings were used in the fitting and plotting of the composite band analysis for $[\text{Fe}_2\text{S}_2(\text{SR})_4]^{2-}$ electronic spectra, Figure 4.16, Table 4.17.

```

$...RENAME DATA-ID ELEMENTS
$...FX-WAVELENGTH , LX-LINEWIDTH , HX-HEIGHT
$...X=A,B,C - THREE BANDS
RENAME/AXA=FA,/AXB=FB,/AXC=FC,/AYA=LA,/AYB=LB,/AYC=LC
/AZA=HA,/AZB=HB,/AZC=HC
$...CALCULATE COMPONENT BANDS, DRAW, ADD INTO ACCUMULATOR
$...AND DRAW RESULT AT END
STRING8/SS(LTYP2,ADD=3,COMPSET3/INTL=BL,GZ=FA,LZL=LA,AX=HA,CC,
GZ=FB,LZL=LB,AX=HB,CC,GZ=FC,LZL=LC,AX=HC,CC,SPEC2=3,LTYP,DRAW2)
STRING9/CC(GOFF,ISO,GON,TDATA2/SIG=AX,COMPSET2/INTL=BL,ADD2,DRAW2)
$...ITERATIVE FITTING
STRING10/RR(REFINE(FA?,FB?,FC?,LA?,LB?,LC?,HA?,HB?,HC?,
GZ=FA,LZL=LA,ISO,COMPSET2/INTL=BL,TDATA2/SIG=HA,ADD2=3
GZ=FB,LZL=LB,ISO,COMPSET2/INTL=BL,3,TDATA2/SIG=HB,ADD2,
GZ=FC,LZL=LC,ISO,COMPSET2/INTL=BL,TDATA2/SIG=HC,ADD2,SPEC2=3))
$...PRINT PEAK-WAVELENGTH,WIDTHS AND HEIGHTS
$...OF COMPONENT BANDS
STRING11/PP(PVAL/FA*3,/FB*3,/FC*3)

```

Example 2.

The command file and strings below were used in generating the simulation of the solution EPR spectrum for $[\text{Fe}(\text{S}_2\text{-o-xylyl})_2]^-$ depicted in Figure 3.3. and described in Section 3.

```

$...CALCULATION STRING
STRING12/SS(PDW,INTCOR2,AX=AX+1,STOSPEC:AX=2/3)
AX,GOFF
$...DATA FOR LOWER THEN MIDDLE DOUBLET(S=5/2)
$...AT INCREASING VALUES OF LAMBDA
GX3262.4,1132.7,1045.4,NPC40,10,SS
GX10000.0,9312.8,1086.2,NPC20,1,SS
GX3279.4,1182.9,1007.7,NPC40,10,SS
GX10000.0,8025.8,1088.2,NPC20,1,SS
GX3307.6,1237.9,973.6,NPC40,10,SS
GX10000.0,6849.7,1091.4,NPC20,1,SS
GX3347.2,1298.1,942.7,NPC40,10,SS
GX10000.0,5837.6,1095.9,NPC20,1,SS
GX3398.3,1363.7,914.8,NPC40,10,SS
GX10000.0,5009.6,1101.6,NPC20,1,SS
GX3460.9,1435.2,889.6,NPC40,10,SS
GX5760.3,4352.1,1108.4,NPC20,1,SS
GX3535.2,1512.9,866.9,NPC40,10,SS
GX4605.8,3835.4,1116.3,NPC20,1,SS
...      ...      ...
...      ...      ...
...      ETC
...      ...      ...
...      ...      ...
GX8688.5,5320.6,684.0,NPC40,10,SS

```

```

GX1642.6,1550.0,1421.1,NPC20,1,SS
GX9217.3,5648.1,681.5,NPC40,10,SS
GX1616.5,1539.7,1439.0,NPC20,1,SS
GX9798.2,5999.2,679.3,NPC40,10,SS
GX1592.2,1531.8,1457.3,NPC20,1,SS
GX10441.5,6356.6,677.2,NPC40,10,SS
GX1526.3,1569.2,1475.9,NPC20,1,SS
GX11160.2,6738.5,675.3,NPC40,10,SS
GX1547.6,1522.7,1494.8,NPC20,1,SS
GX11974.8,7139.6,673.6,NPC40,10,SS
GX1527.1,1521.1,1514.0,NPC20,1,SS
$...CALCULATE GAUSSIAN INTENSITY DISTRIBUTION
$...PLACING RESULT IN SPEC 4
STRING8/G8(RDATA2,PDATA2,PAUSE,PDATA2,GOFF,ISO,GON,PSPEC2*40=NH,SPEC4=2,RDATA1)
$...ADD LOWER THEN MIDDLE DOUBLET SPECTRA OVER THE
$...ENTIRE LAMBDA RANGE USING A GAUSSIAN DISTRIBUTION
$...OF INTENSITIES(SPEC 4),AND STORE THE TWO RESULTING SPECTRA
STRING9/AA(AX=-1,AY1,ADD=3,HE15000,CC,STORE1/2=3,AX,AY1,ADD=3,CC,STORE2/2=3)
STRING10/CC(AX=AX+2,RSPEC:AX/3=2,AY=AY+1,TDATA/AZ=AY*4,/AXC=INT*2,AXC=AZ/AXC,
ADD2+M*AXC,IF65*AX/GT,CC)
$...ADD TOGETHER LOWER AND MIDDLE DOUBLET SPECTRA
$...INCORPORATING BOLTZMANN DISTRIBUTION FACTOR 'INT'
STRING11/II(HE6000,RSPEC1/2=2,ADD2=2+M,RSPEC2/2=3,ADD3+M*INT,TDATA2/SIG=1)

```

Example 3.

This command file constructs Figure 3.11.

```

$...READ EXPERIMENTAL TEMPERATURES AND INTENSITIES
RSPEC1/2,READ2/2=2
$...PLOT AXES, EXPERIMENTAL POINTS AND CALCULATED
$...LINES FOR THE THREE DOUBLETS(S=5/2).
XAX,DECP1,YAX,PLOT1*2,EQNC,LINES*3,EQNC*2,LINES*3,EQNC*3,LINES*3
$...MARK DOUBLETS WITH IDENTIFIERS
$...NAME FOLLOWED BY ITS LOCATION WRITTEN AFTER
PIC,ANOTATE=W(L);(M);(U)
$L
$ 23.275269617204231 17.295526315789516 X
$M
$ 23.275269617204231 4.556710526315840 X
$U
$ 23.275269617204231 .810000000000073 X
$...AXIS NAMES
PIC,ANOTATE=W+90(DOUBLET FRACTIONAL POPULATION)
$DOUBLET FRACTIONAL POPULATION
$ -2.230106726881615 6.055394736842231 X
PIC,ANOTATE=W(1/T (K$+-1$=))
$1/T (K$+-1$=)
$ 10.372043810752757 -1.834736842105144 X
$...FURTHER ANNOTATION OF GRAPH
PIC,ANOTATE=W*2($4K$==0.13),=W*2(D=2.0 $2CM$=$+-1)
$4K$==0.13
$ 1.683871767742005 22.540921052631688 X
$D=2.0 $2CM$=$+-1
$ 1.683871767742005 20.557368421052729 X

```

A.10 *****
 COMMANDS AND THEIR PARAMETERS:PROGRAM SDS

CONTROL

START	INITIALISE FOR GRAPHICS VDU.
END	TERMINATE PROGRAM EXECUTION.
KMAT	INITIALISE FOR MICROFILM OR KINGMATIC PLOTTING.
FAST	ENABLE HIGH SPEED OUTPUT ON GRAPHICS VDU.
SLOW	DISABLE HIGH SPEED OUTPUT ON GRAPHICS VDU.
DATA P1=P3*P4/P2+P5	SET DATA-SET ELEMENT P1 TO (P3*P4/P2+P5).
TABLE P1=P3	USE TABLE P1 FOR CHECKING INPUT COMMANDS AND/OR(P3) DATA-IDENTIFIERS.
RENAME/P2=P3	TEMPORARILY CHANGE COMMAND-NAME OR DATA-IDENTIFIER P2 TO P3.
DOSTR P1	EXCECUTE STRING P1.
SOSRUN P1*P4	READ AND PROCESS P4 LINES OF INPUT FROM FILE 'SOSRUN' STARTING AT LINE P1.
PAUSE	TEMPORARILY DIVERT FROM 'STRING' OR 'SOSRUN' PROCESSING TO 'INPUT'.
CONT	AFTER 'PAUSE' RETURN TO ORIGINAL COMMAND/DATA STRING.
ABORT P1	AFTER 'PAUSE' ABORT ORIGINAL COMMAND STRING BY P1 LEVELS.
IF P1*P4/P2	AS FORTRAN - IF(P1.P2.P4)CONTINUE,OTHERWISE AS 'CONT'.
PIC P1/P2	INSERT INPUT STRING IN FILE 'SOSRUN'.P1&P2 GOVERN POSITION.SPECIAL CONDITIONS ARE SET UP FOR X-WIRES INPUT WHICH IS ALSO WRITTEN TO 'SOSRUN'.
UNPIC P1	REMOVE LINE P1 AND ASSOCIATED X-WIRE INPUT.
REPIC P1	REGENERATE LINE P1 AND ASSOCIATED X-WIRES INPUT.
PRINT P1	SET PRINT QUANTITY CONTROL SWITCH TO P1.

SPECTRA STORAGE FILES

READ P1/P2=P3	READ RECORD P1 ON FILE P2 INTO SPEC P3 AND MAIN DATA-SET.
RSPEC P1/P2=P3	READ RECORD P1 ON FILE P2 INTO SPEC P3.
RDATA P1/P2	READ RECORD P1 ON FILE P2 INTO MAIN DATA-SET.
STORE P1/P2=P3	STORE SPEC P3 AND MAIN DATA-SET AS RECORD P1 ON FILE P2.
STOSPEC P1/P2=P3	STORE SPEC P3 AS RECORD P1 ON FILE P2.
STODATA P1/P2	STORE MAIN DATA-SET AS RECORD P1 ON FILE P2.
CATALOG P1=P3	PRINT CATALOG OF FILE P1; P3=DUMP SUPPRESSES OUTPUT.
OPEN P1	OPEN FILE P1.
UNPACK P1/P2=P3	UNPACK 'PACK' FILE, STORING SPECTRA P1-P2(INCLUSIVE) ON FILE P3.

SPECTRAL MANIPULATION

SPEC P1=P3/P2*P4+P5	COPY SPECTRUM P3 INTO P1 FROM ELEMENT P2 TO P4 ADDING P5 TO EACH VALUE.
SPECIN P1/P2=P3*P4	MODIFY ELEMENT P2 OF SPEC P3 TO VALUE P1; P4=IN-INSERT, P4=OUT-REMOVE.
PSPEC P1/P2*P4=P3	PRINT DATA-SET OF SPEC P1,AND P4 ELEMENT-VALUES STARTING AT ELEMENT P2; P3=DUMP SUPPRESSES OUTPUT.
INTEG P1=P3*P4	INTEGRATE SPEC P1 P4 TIMES PUTTING RESULT IN SPEC P3.
DERIV P1=P3*P4	DIFFERENTIATE SPEC P1 P4 TIMES PUTTING RESULT IN SPEC P3.

SMOOTH P1=P3*P4	SMOOTH SPEC P1 P4 TIMES PUTTING RESULT IN SPEC P3.
FILTER P1=P3/P2*P4	DIGITALLY FILTER SPEC P1 P4 TIMES ACCORDING TO CONVOLUTION SHAPE SPECIFIED BY P2, PUTTING RESULT IN SPEC P3.
NOISE P1=P3*P4/P2+P5	ADD NOISE OF S/N=P4 TO SPEC P1 FROM ELEMENT P2 TO P5 PUTTING RESULT IN P3.
LEVEL P1=P3*P4/P2+P5	SUBTRACT LINEAR BASELINE (<1ST. P2 POINTS>-<LAST P2 PTS.>)*P4 FROM P1 PUTTING RESULT IN SPEC P3.
NORMAL P1=P3	NORMALISE SPEC P1 PUTTING RESULT IN SPEC P3.
ALIGN P1=P3/P2*P4+P5	INTERPOLATE SPEC P1 WITH POLYNOMIAL ORDER P4 ACCORDING TO MAIN DATA-SET OR SPEC P2 PUTTING RESULT IN SPEC P3; P5-NEW MICROWAVE FREQUENCY.
REVERSE P1=P3	REVERSE ORDER OF POINTS FOR SPEC P1 PUTTING RESULT IN SPEC P3.
ADD P1=P3/P2*P4+P5	ADD P4 TIMES SPEC P1 INTO SPEC P3 AFTER COMPARISON WITH SPEC P2; P5=M-EMPLOY 'MATCH' MODE.
EDIT=P3	EDIT SPECTRUM P3 USING X-WIRES INPUT.
EXPACT P1=P3/P2*P4+P5	EXPAND OR CONTRACT SPEC P1 AT FIELD POSITION P2 BY AMOUNT P5 PUTTING RESULT IN SPEC P3; P4- VALUE TO INSERT IN EXPANSION.
HSHIFT P1=P3/P2*P4	SHIFT SPEC P1 BY AMOUNT P4 PUTTING RESULT IN SPEC P4; P2- POLYNOMIAL INTERPOLATION ORDER.
INTCOR P1=P3	USE G-VALUES IN DATA-SET TO EVALUATE INTEGRATED-INTENSITY CORRECTION FACTOR, APPLY TO SPEC P1 AND ENTER VALUE IN DATA-SET ELEMENT P3.
TDATA P1/P2=P3*P4	SET DATA-SET ELEMENT P2 FROM DATA-SET ELEMENT P3; P1&P4=0 FOR MAIN DATA-SET OR =SPEC-NUMBER FOR SPEC DATA-SETS.
XDATA P1/P2=P3*P4	EXCHANGE DATA-SET ELEMENTS P2 AND P3; P1&P4=0 FOR MAIN DATA-SET OR =SPEC-NUMBER FOR SPEC DATA-SETS.
GRAPHICAL	

DRAW P1/P2*P4+P5	DRAW SPEC P1 IN COMPARISON TO SPEC P2, Y-SHIFTED BY P5 AND MULTIPLIED BY P4.
PLOTPT P1/P2=P3	PLOT POINT AT X=P1,Y=P2 WITH SYMBOL TYPE P3; P3=0 FOR NO SYMBOL; P3 -VE FOR NO LINE FROM LAST POINT.
AXIS P1/P2=P3*P4+P5(S1)(S2)	DRAW X-AXIS WITH START AND END VALUES DETERMINED BY MAIN DATA-SET OR BY SPEC P1 OR BY,P2&P3; P4 CONTROLS SIZE AND ORIENTATION OF MARKINGS; P5 CONTROLS NUMBERING FORMAT; S1-ALTERNATIVE AXIS NAME; S2-ALTERNATIVE MARKING POSITIONS.
MARK P1/P2=P3*P4+P5(S1)(S2)	MARK FIELD OR G-VALUE POSITION P1 WITH ARROW; P2,P3 S1 AND S2 CONTROL LABELLING; P4 CONTROLS SIZE; P5 CONTROLS Y-SHIFT.
BASELINE P1/P2	DRAW BASELINE OF SPEC P1 WITH LINETYPE P2.
BOX P1/P2=P3*P4(S1)	SET BOX P1 WITH X-Y SIDES RATIO P2 AND P3 X-BOXES BY P4 Y-BOXES; S1- FOUR SEQUENTIAL VALUES CONTROL X,Y-FRAME SIZE AND X,Y-BOX INTERNAL PLOT SPACE.
DRAWBOX P1/P2=P3*P4+P5(S1)	ESTABLISH TEMPORARY BOX STRUCTURE (PARAMETERS AS 'BOX'), AND DRAW BOX P1; P5 CONTROLS BOX NUMBERING.
GRID P1*P4/P2	DRAW GRID WITH P1 X-DIVISIONS, P4 Y-DIVISIONS AND LINETYPE P2.
ANOTATE P1/P2=P3*P4+P5(S1)	PLOT CHARACTERS IN S1 OR 'STRING' P1/P2 WITH SIZE P4 AND AT ANGLE P5; P3 GOVERNS CHARACTER SET TO BE USED.
VECTOR P1	DRAW LINES OF TYPE P1 USING X-WIRES INPUT.
OBLONG P1	DRAW OBLONG WITH LINE TYPE P1 USING X-WIRES INPUT.
ASIZE P1/P2=P3*P4	MARK OUT A(P1) PAPER SIZE ACCORDING TO FORMAT P2,P3; P4=0 FOR X-WIRES ORIGIN INPUT.
ORIGIN P1=P3/P2*P4	REDEFINE ORIGIN AT X-WIRES INPUT (OR AT X=P2,Y=P4) WITH ROTATION P1; P3=ROT FOR NO ORIGIN TRANSLATION.
MAG P1	REDEFINE MAGNIFICATION AS P1.
HARDON	ENABLE MICROFILM GENERATION.
HARDOFF	DISABLE MICROFILM GENERATION.
HARD	GENERATE MICROFILM.
GON	ENABLE GRAPHICS.
GOFF	DISABLE GRAPHICS.

CALCULATION AND CURVE FITTING

(CALCULATED SPECTRA ARE PLACED IN SPEC 2)

ISO	ISOTROPIC SPECTRUM,
KNEUB	ANISOTROPIC EPR SPECTRUM ACCORDING TO ANALYTICAL SOLUTION OF KNEUBUHL (JCP VOL.33,PG.1074(1960)).
POW	POWDER EPR SPECTRUM BY SPATIAL INTEGRATION.
CONV	CONVOLUTE SPEC 4 WITH LORENTZIAN-GAUSSIAN LINESHAPE.
CALC	USER SUPPLIED CALCULATION ROUTINE.
FUNC P1/P2=P3*P4+P5	EVALUATE RMS PER CENT DIFFERENCE FUNCTION VALUE FOR SPECTRA P1 AND P2 USING MASK IN SPEC P4; P3 AND P5 ARE SPECTRA TO RECEIVE ALIGNED SPECTRA FROM P1 AND P2.
REFINE P1/P2=P3*P4+P5(S1)	FIND MINIMUM VALUE OF 'FUNC'--LEAST SQUARES FIT,FOLLOWING EXECUTION OF STRING S1; PARAMETERS AS 'FUNC', DATA VALUES TO BE VARIED ARE SPECIFIED BY '?' WITHIN S1.

STRINGS AND EDITOR

STRING P1=P3/P2(S1)	DEFINE 'STRING' P1 WITH NAME P2 AS S1 OR AS 'STRING' P3.
PSTR P1/P2	PRINT 'STRING' P1/P2.
SEDIT P1	EDIT 'STRING' P1.
TEDIT	EDIT 'SOSRUN' FILE.

FOR FOLLOWING EDITOR COMMANDS P2=NP SUPPRESSES OUTPUT; PARENTHETICAL INPUT STRINGS MAY BE REPLACED WITH STORED 'STRINGS' BY SPECIFYING P2=S1 AND P5=S2 IN THE ABSENCE OF S1,S2,P2,P5 AN INPUT REQUEST IS PROMPTED.

A P1(S1)	ADD STRING S1 TO NEXT P1 LINES.
B	MOVE TO BOTTOM OF FILE.
C P1(S1)(S2)	LOCATE STRING S1 IN P1 LINES AND CHANGE TO S2.
D P1	DELETE P1 LINES.
I P1(S1)	INSERT P1 LINES OF STRING S1.
L P1(S1)	LOCATE STRING S1 IN P1 LINES.
M P1(S1)	MODIFY NEXT P1 LINES ACCORDING TO S1; IF S1 NOT SPECIFIED, THE LINE IS PRINTED AND MODIFICATION INSTRUCTIONS ARE RECEIVED ON NEXT LINE.
N P1	MOVE P1 LINES DOWN FILE.
P P1	PRINT P1 LINES.
T	MOVE TO TOP OF FILE.
W	PRINT SEQUENCE NUMBER OF PRESENT LINE.
GOTO P1	MOVE TO LINE P1.
LNON	ENABLE AUTO-LINE NUMBERING.
LNOFF	DISABLE AUTO-LINE NUMBERING.

TWO AXIS GRAPHS

XAX P1	SET X-AXIS ACCORDING TO VECTOR P1 AND DRAW.
YAX P1	SET Y-AXIS ACCORDING TO VECTOR P1 AND DRAW.
PLOT P1*P4/P2	PLOT POINTS X-VECTOR=P1 AGAINST Y-VECTOR=P4 USING SYMBOL P2.
LINE P1*P4	JOIN POINTS X-VECTOR=P1 PLOTTED AGAINST Y-VECTOR=P4 WITH LINE.
GRAPH P1*P4/P2	DRAW X-AXIS ACCORDING TO VECTOR P1 AND Y-AXIS ACCORDING TO VECTOR P4 PLOTTING POINTS USING SYMBOL P2 JOINED BY A LINE.
SET P1	SET MAX. AND MIN IN DATA-SET OF VECTOR P1.
ORDER P1/P2	SET ELEMENTS OF VECTOR P1 IN ASCENDING OR DESCENDING(P1 -VE) ORDER OF MAGNITUDE; VECTORS P2(EG. 235) ARE ALSO ORDERED RETAINING POSITION OF ELEMENTS RELATIVE TO P1.
EGNA P1/P2=P3	USER SUPPLIED ROUTINE USING VECTOR P1 TO GENERATE NEW VECTOR P3; IF P1=0 A VECTOR OF EQUALLY SPACED POINTS IS CREATED IN P2 AND USED TO GENERATE P3.
EGNB P1/P2=P3	AS EGNA.
EGNC P1/P2=P3	AS EGNA.

MISCELLANEOUS

SIZE P1	ON GRAPHICS VDU- SET CHARACTER SIZE P1.
SKIP P1	ON GRAPHICS VDU- SKIP P1 LINES ON SCREEN.
NEW	ON GRAPHICS VDU- CLEAR PAGE.
TITLE P1(S1)	APPLY TITLE S1 TO SPECTRUM P1 OR TO MAIN DATA-SET(P1=0).
PDATA P1=P3	PRINT FORMATTED SELECTION OF MAIN DATA-SET ELEMENT VALUES; P1 CONTROLS QUANTITY; P3=DUMP SUPPRESSES OUTPUT.
PFILE/P2	PRINT CONTENTS OF 'DUMP' FILE; IF P2=R REWIND FILE AFTERWARDS.
PVAL P1/P2=P3*P4	PRINT P4 VALUES OF MAIN DATA-SET OR SPECTRAL DATA-SET(P1>0) STARTING AT VALUE P2; P3=DUMP SUPPRESSES OUTPUT.
PF(S1)	PERMANENT FILE OPERATING-SYSTEM STATEMENT S1 EXECUTED FROM WITHIN PROGRAM.
CTIME	PRINT CENTRAL PROCESSOR SECONDS USED SINCE LOGON.
BELL	RING BELL.
XIN P1=P3	INPUT FIELD OR G-VALUE TO MAIN(P1=0) OR SPECTRAL(P1>0) DATA-SET USING X-WIRES; X-WIRES CONTROL CHARACTERS:- C=CONTINUE,D=DIFFERENCE,G=G-VALUE,E=END.
YIN P1=P3	AS XIN BUT X-WIRES INPUT IS A Y-MAGNITUDE.
HVAL P1/P2=P3	CONVERT FIELD VALUE P1/P2 TO G-VALUE AND PUT RESULT IN MAIN DATA-SET POSITION P3.
GVAL P1/P2=P3	CONVERT G-VALUE P1/P2 TO FIELD-VALUE AND PUT RESULT IN MAIN. DATA-SET POSITION P3.
COMPSET P1/P2=P3	SET COMPARISON POINTS FOR SPEC P1 OR MAIN DATA-SET(P1=0); P2=POSN,INTL,INTU; P3=BL,MAX,MIN,HS,HE OR NUMERIC FIELD.
HELP/P2	PROVIDE INFORMATION ABOUT THE PROGRAM OR ITS COMMANDS(P2).

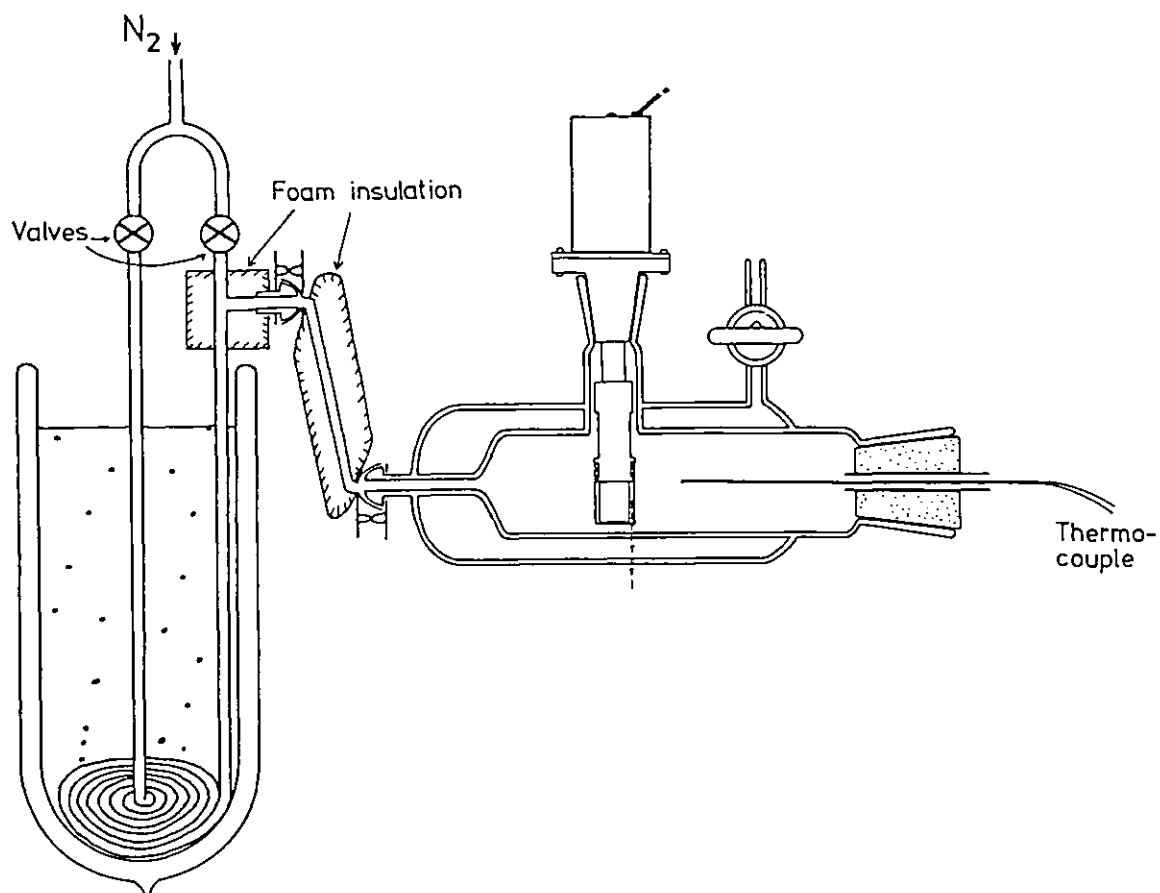
APPENDIX BA Variable Temperature Cryostat for Rapidly-Rotating Raman Samples.

For highly absorbing solid and solution Raman samples, intense local heating, which may lead to decomposition or solvent cavitation, can often be avoided by rapidly rotating the sample relative to the exciting laser beam. A device has been described which uses a rotating lens to circularly scan the laser beam across a static sample, the scattered light being collected by the same lens.³⁹² In the latter case it proves possible to study samples cryostated at low temperatures. The rotational mechanism and alignment of the optical components for this sample technique are, however, more complicated than for the conventional sample-spinning arrangement employed at ambient temperatures. A cryostat for spinning-samples is described here which is of fairly simple construction and which is easily optically aligned. Solid or solution samples may be rotated with several thousand r.p.m. at temperatures in the range ca. 100-300 K. The ability to use low temperatures may be essential when studying compounds which are not stable at room temperature, and for other samples which are very susceptible to thermal or photolytic decomposition by the laser beam, may allow the use of higher incident excitation power levels, leading to enhanced signal to noise ratio.

The main cryostat is a double surface evacuated container of Pyrex construction. Gaseous nitrogen, precooled by passage through a spiralled 5 mm copper tube immersed in liquid nitrogen refrigerant, flows continually

through the cryostat and around the sample, figure B.1. Controlled dilution of the cooled N_2 with gas at ambient temperature allows a wide range of intermediate temperatures to be selected to an accuracy of ca. 1-2 K. Solid samples are prepared as thin 13 mm alkali-halide compressed discs and held in contact with a brass heat sink by a nylon retaining cap. Liquids are contained in 15 mm o.d. cylindrical quartz cells. Both samples are spun by a small 10-20 V motor having ball-race bearings and an extended axle. The motor is supported in a B19 side-arm of the cryostat. The exciting beam enters perpendicularly

Figure B.1. Cryostat, solution sample spinner and refrigeration method.



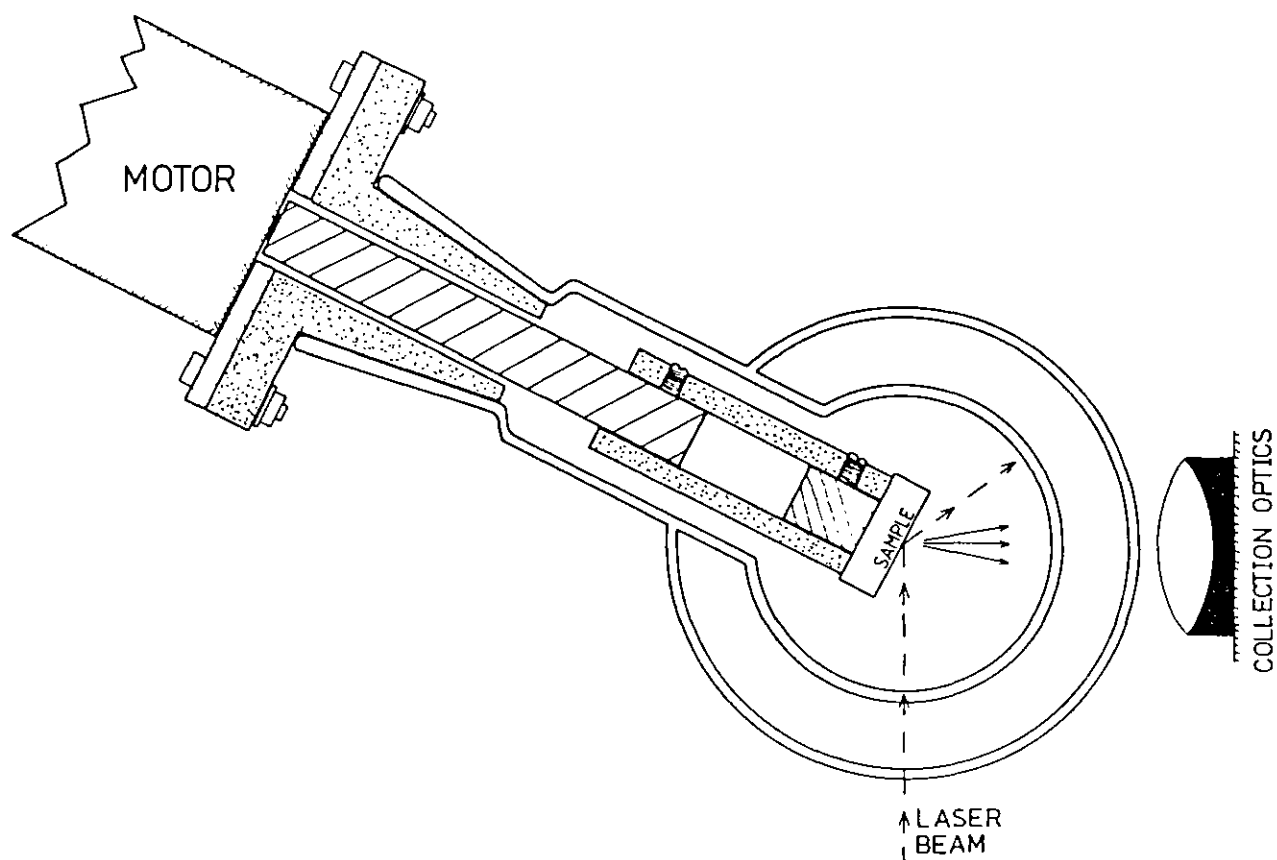


Figure B.2. Cross sectional view of cryostat and solid-sample spinner

through the side of the cryostat and Raman scattered light is collected at 90° after further transmission through the cryostat wall. The arrangement for solid samples is such that scattered light is transmitted without distortion, being perpendicular to the glass wall, since the sample is located on the axis of the cylindrical cryostat, Figure B.2.

The cryostat has been used in this work to achieve greatly improved S/N ratio in Raman spectra of the intensely absorbing $[\text{Et}_4\text{N}][\text{Fe}(\text{III})(\text{S}_2\text{-oxylyl})_2]$ and $\text{Cu}(\text{II})(\text{RN-MeMe})_2$ [R = Me, *i*Bu] solids at ca. 130 K [Sections 4.2 and 5.5, Figures 4.4 and 5.16]. For $\text{Cu}(\text{II})(\text{MeN-MeMe})_2$ in solution, where thermal instability would preclude measurements at room temperature, Raman spectra have been obtained in acetone at ca. 200 K.

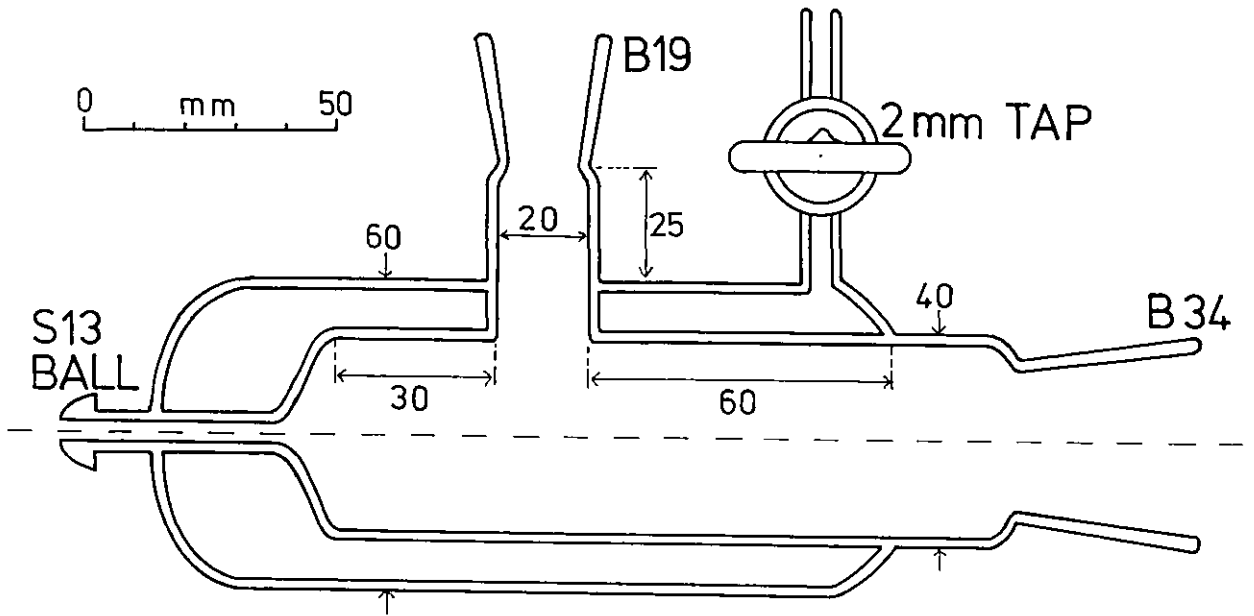


FIG. B.3 Pyrex cryostat body

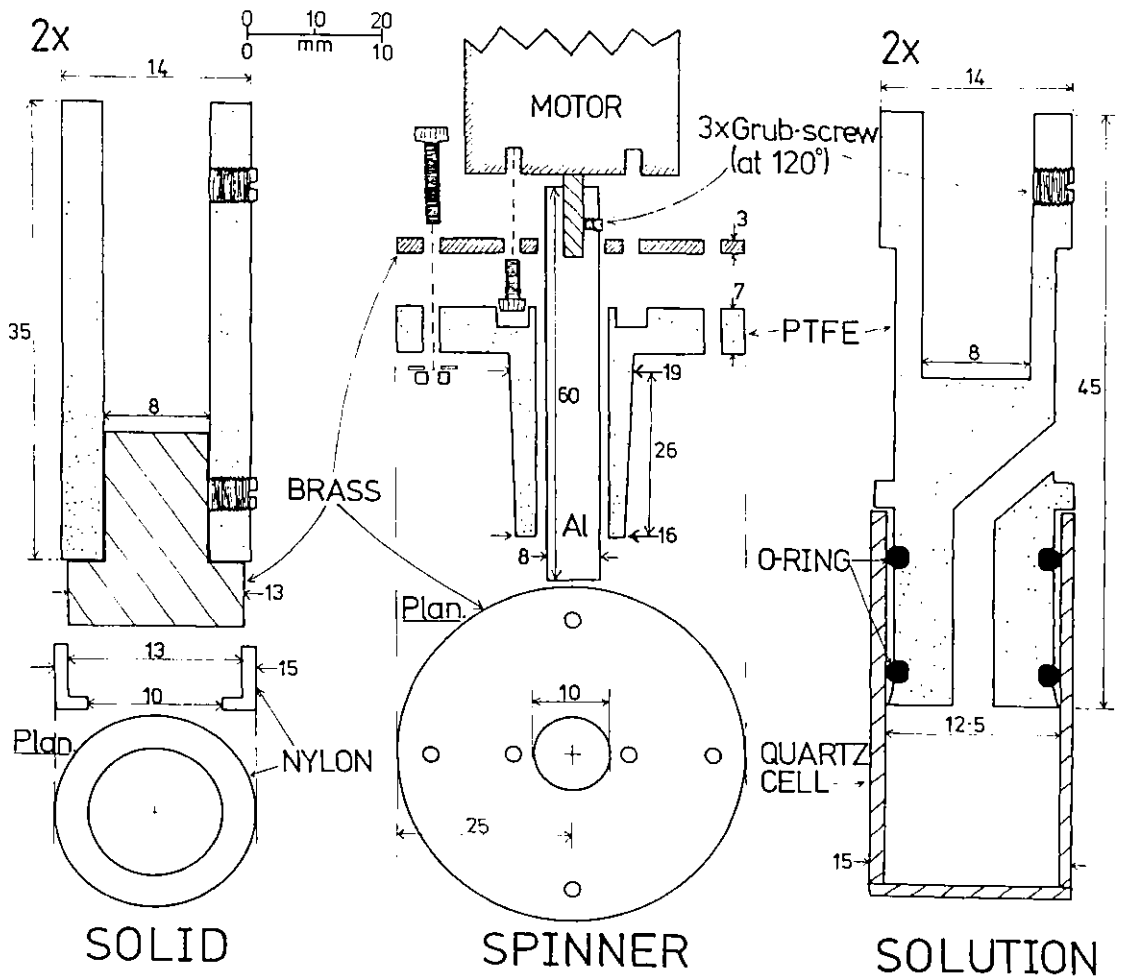


FIG. B.4 Details of the sample spinners.

REFERENCES

1. J.A. Ibers, R.H. Holm,
Science, 209, 223 (1980).
2. R. Cammack,
Nature, 286, 442 (1980).
3. Nomenclature Committee of the International Union of Biochemistry
(NC-IUB), Eur. J. Biochem., 93, 427 (1979).
Biochim. Biophys. Acta, 549, 107 (1979).
Arch. Biochem. Biophys., 195, 609 (1979).
4. "Iron-Sulfur Proteins", Vols. 1-3,
W. Lovenberg, Ed., Academic Press, New York.
5. W.H. Orme-Johnson, N.R. Orme-Johnson,
Methods in Enzymology, 53, 259 (1978).
6. R.H. Sands, W.R. Dunham,
Q. Rev. Biophysics, 7, 443 (1975).
7. R. Cammack,
J. de Phys. (Orsay, Fr.), Colloque, C6, 37, 137 (1976).
8. R. Cammack,
"Metalloproteins: Structure, Function and Clinical Aspects";
U. Weser, Ed.; Thieme Verlag; Stuttgart; pgs. 162-184. (1979).
9. G. Palmer,
The Enzymes, 12, 1 (1975).
10. W.H. Orme-Johnson,
Ann. Rev. Biochem. 42, 159 (1973).
11. R.H. Holm,
Acc. Chem. Res. 10, 427 (1977).
12. R.H. Holm, J.A. Ibers in
"Iron-Sulfur Proteins" Vol. 3; W. Lovenberg, Ed.;
Academic Press; New York, Ch. 7 (1977).
13. R.H. Holm,
Endeavor 34, 38 (1975).
14. R. Cammack, D.P.E. Dickson, C.E. Johnson in
"Iron-Sulfur Proteins", Vol. 3,
W. Lovenberg, Ed., Academic Press, New York, N.Y. (1977), Ch. 8.
15. W.H. Orme-Johnson, R.H. Sands in
"Iron-Sulfur Proteins", Vol. 2,
W. Lovenberg, Ed., Academic Press, New York, N.Y. (1973), Ch. 5.

16. G. Palmer in
" Iron-Sulfur Proteins ", Vol.2,
W. Lovenberg, Ed., Academic Press, New York, N.Y., (1973) Ch. 8.
17. J.F. Gibson, D.O. Hall, J.H.M. Thornley, F.R. Whatley,
Proc. Natl. Acad. Sci. U.S.A., 56, 987 (1966).
18. J.H.M. Thornley, J.F. Gibson, F.R. Whatley, D.O. Hall,
Biochem. Biophys. Res. Commun., 24, 877 (1966).
19. J.P. Gayda, J.F. Gibson, R. Cammack, D.O. Hall, R. Mullinger,
Biochim. Biophys. Acta, 434, 154 (1976).
20. J. Fritz, R. Anderson, J. Fee, G. Palmer, R.H. Sands, J.C.M. Tsibris,
I.C. Gunsalus, W.H. Orme-Johnson, H. Beinert,
Biochim. Biophys. Acta, 253, 110 (1971).
21. M. Bowman, L. Kevan, K. Mukai, T. Kimura,
Biochim. Biophys. Acta, 328, 244 (1973).
22. W.R. Dunham, A.J. Bearden, I.T. Salmeen, G. Palmer,
R.H. Sands, W.H. Orme-Johnson, H. Beinert,
Biochim. Biophys. Acta, 253, 134 (1971).
23. W.R. Dunham, G. Palmer, R.H. Sands, A.J. Bearden,
Biochim. Biophys. Acta, 253, 373 (1971).
24. H. Brintzinger, G. Palmer, R.H. Sands,
Proc. Natl. Acad. Sci. U.S.A. 55, 397 (1966).
25. T. Tsukihara, K. Fukuyama, H. Tahara, Y. Katsube, Y. Matsuura,
N. Tanaka, M. Kakudo, K. Wada, H. Matubara,
J. Biochem. (Tokyo) 84, 1645 (1978).
26. K. Fukuyama, T. Hase, S. Matsumoto, T. Tsukihara, Y. Katsube,
N. Tanaka, M. Kakudo, K. Wada, H. Matsubara,
Nature, 286, 522 (1980).
27. J.J. Mayerle, R.B. Frankel, R.H. Holm, J.A. Ibers,
W.D. Phillips, J.F. Weiher,
Proc. Natl. Acad. Sci. U.S.A. 70, 2429 (1973).
28. J.J. Mayerle, S.E. Denmark, B.V. DePamphilis,
J.A. Ibers, R.H. Holm,
J. Amer. Chem. Soc., 97, 1032 (1975).
29. J.G. Reynolds, R.H. Holm,
Inorg. Chem., 19, 3257 (1980).
30. R.H. Tieckelmann, B.A. Averill,
Inorg. Chim. Acta, 46, L35 (1980).
31. D. Coucouvanis, D. Swenson, P. Stremple, N.C. Baenziger,
J. Amer. Chem. Soc., 101, 3392 (1979).

32. N. Ohta, C. Kawasaki, M. Maeda, S. Tani, K. Kawasaki,
Chem. Pharm. Bull., 27, 2968 (1979).
33. Y. Sugiura, M. Kunishima, H. Tanaka, H.H. Dearman,
J. Inorg. Nucl. Chem., 37, 1511 (1975).
34. Y. Sugiura, K. Ishizu, T. Kimura, H. Tanaka,
Bioinorg. Chem., 4, 291 (1975).
35. A. Terzis, R. Rivest,
Inorg. Chem., 12, 2132 (1973).
36. C.H. Wei, L.F. Dahl,
Inorg. Chem., 4, 1 (1965).
37. K.A. Rubinson, G. Palmer,
J. Amer. Chem. Soc., 94, 8375 (1972).
38. W.O. Gillum, R.B. Frankel, S. Foner, R.H. Holm,
Inorg. Chem., 15, 1095 (1976).
39. B-K. Teo, R.G. Shulman, G.S. Brown, A.E. Meixner,
J. Amer. Chem. Soc., 101, 5624 (1979).
40. A. Röder, E. Bayer,
Angew. Chem. Int., 6, 263 (1967).
41. C.S. Yang, F.M. Huennekens,
Biochemistry, 9, 2127 (1970).
42. M. Clare, H.A.O. Hill, C.E. Johnson, R. Richards,
J.C.S. Chem. Commun., 1376 (1970).
43. B.A. Averill, J.R. Bale, W.H. Orme-Johnson,
J. Amer. Chem. Soc., 100, 3034 (1978).
44. W.O. Gillum, L.E. Mortenson, J-S. Chen, R.H. Holm,
J. Amer. Chem. Soc., 99, 584 (1977).
45. J. Cambray, R.W. Lane, A.G. Wedd, R.W. Johnson, R.H. Holm,
Inorg. Chem., 16, 2565 (1977).
46. C.E. Johnson, R. Cammack, K.K. Rao, D.O. Hall,
Biochem. Biophys. Res. Commun., 43, 564 (1971).
47. J.C.M. Tsibris, R.L. Tsai, I.C. Gunsalus, W.H. Orme-Johnson,
R.E. Hansen, H. Beinert,
Proc. Natl. Acad. Sci. U.S.A. 59, 959 (1968).
48. G. Palmer,
Biochem. Biophys. Res. Commun., 27, 315 (1967).
49. J.A. Fee, G. Palmer,
Biochim. Biophys. Acta, 245, 175 (1971).

50. R.E. Anderson, W.R. Dunham, R.H. Sands, A.J. Bearden, H.L. Crespi,
Biochim. Biophys. Acta, 408, 306 (1975).
51. R. Cammack, K.K. Rao, D.O. Hall, C.E. Johnson,
Biochem. J., 125, 849 (1971).
52. C.E. Johnson, E. Elstner, J.F. Gibson, G. Benfield,
M.C.W. Evans, D.O. Hall,
Nature, 220, 1291 (1968).
53. K.K. Rao , R. Cammack, D.O. Hall, C.E. Johnson,
Biochem. J., 122, 257 (1971).
54. E. Münck, P.G. Debrunner, J.C.M. Tsibris, I.C. Gunsalus,
Biochemistry, 11, 855 (1972).
55. M.M. Werber, E.R. Bauminger, S.G. Cohen, S. Ofer,
Biophys. Struct. Mechanism, 4, 169 (1978).
56. R.W. Lane, J.A. Ibers, R.B. Frankel, R.H. Holm,
Proc. Natl. Acad. Sci., U.S.A., 72, 2868 (1975).
57. J.T. Hoggins, H. Steinfink,
Inorg. Chem., 15, 1682 (1976).
58. B.A. Averill, T. Herskovitz, R.H. Holm, J.A. Ibers,
J. Amer. Chem. Soc., 95, 3523 (1973).
59. R.B. Frankel, B.A. Averill, R.H. Holm,
J. de Phys. (Orsay, Fr.) Colloque C6, 35, 107 (1974).
60. P. Bertrand, J.P. Gayda,
Biochim. Biophys. Acta, 579, 107 (1979).
61. P. Bertrand, J.P. Gayda,
Biochim. Biophys. Acta, 625, 337 (1980).
62. R.E. Coffman, B.W. Stavens,
Biochem. Biophys. Res. Commun., 41, 163 (1970).
63. W.A. Eaton, G. Palmer, J.A. Fee, T. Kimura, W. Lovenberg,
Proc. Natl. Acad. Sci., U.S.A., 68, 3015 (1971).
64. D.V. Dervartanian, Y.I. Shethna, H. Beinert,
Biochim. Biophys. Acta, 194, 548 (1979).
65. K. Mukai, T. Kimura , J. Helbert, L. Kevan,
Biochim. Biophys. Acta, 295, 49 (1973).
66. K.K. Rao, R.V. Smith, R. Cammack, M.C.W. Evans, D.O. Hall, C.E. Johnson,
Biochem. J., 129, 1159 (1972).

67. W.E. Blumberg, J. Peisach,
Arch. Biochem. Biophys., 162, 502 (1974).
68. R. Cammack,
Biochem. Soc. Trans., 3, 482 (1975).
69. R. Cammack, K.K. Rao, D.O. Hall,
Biochem. Biophys. Res. Commun., 44, 8 (1971).
70. L. Kerscher, D. Oesterhelt, R. Cammack, D.O. Hall,
Eur. J. Biochem., 71, 101 (1976).
71. D.H. Petering, G. Palmer,
Arch. Biochem. Biophys., 141, 456 (1970).
72. L.P. Hammett in
" Physical Organic Chemistry ", 2nd Edn.,
McGraw Hill, N.Y., (1970), pg. 356.
73. J.P. Danehy, K.N. Parameswaran,
J. Chem. Eng. Data, 13, 386 (1968).
74. G.R. Dukes, R.H. Holm,
J. Amer. Chem. Soc., 97, 528 (1975).
75. L. Que, M.A. Bobrik, J.A. Ibers, R.H. Holm,
J. Amer. Chem. Soc., 96, 4168 (1974).
76. R.W. Johnson, R.H. Holm,
J. Amer. Chem. Soc., 100, 5338 (1978).
77. I.T. Salmeen, G. Palmer,
Arch. Biochem. Biophys. 150, 767 (1972).
78. F.H. Bernhardt, E. Heymann, P.S. Traylor,
Eur. J. Biochem. 92, 209 (1978).
79. B.L. Trumpower, C.A. Edwards,
FEBS Lett. 100, 13 (1979).
80. W.H. Orme-Johnson, R.E. Hansen, H. Beinert, J.C.M. Tsibris,
R.C. Bartholomaeus, I.C. Gunsalus,
Proc. Natl. Acad. Sci. U.S.A., 60, 368 (1968).
81. K. Mukai, J.J. Huang, T. Kimura,
Biochem. Biophys. Res. Commun., 50, 105 (1973).
82. J. Schneider, B. Dischler, A. Rauber,
J. Phys. Chem. Solids, 29, 451 (1968).
83. K. Mukai, J.J. Huang, T. Kimura,
Biochim. Biophys. Acta, 336, 427 (1974).
84. R.S. McMillan, J. Renaud, J.G. Reynolds, R.H. Holm,
J. Bioinorg. Chem., 11, 213 (1979).
85. B.A. Averill, W.H. Orme-Johnson,
J. Amer. Chem. Soc., 100, 5234 (1978).

86. G. Christou, R.V. Hageman, R.H. Holm,
J. Amer. Chem. Soc., 102, 7600 (1980).
87. J.G. Reynolds, R.H. Holm,
Inorg. Chem. 20, 1873 (1981).
88. A. Abragam, B. Bleaney in
"Electron paramagnetic resonance in transition ions",
Clarendon Press, Oxford (1970).
89. K.W.H. Stevens,
Rep. Prog. Phys. 30, 189 (1967).
90. R. Orbach,
Proc. R. Soc. Lond. Ser. A, 264, 458 (1961).
91. F.K. Kneubühl,
J. Chem. Phys. 33, 1074 (1960).
92. P. Bertrand, G. Roger, J-P Gayda,
J. Magn. Reson. 40, 539 (1980).
93. D.W. Posener,
Austr. J. Phys. 12, 184 (1959).
94. J.C. Salerno, T. Ohnishi, H. Blum, J.S. Leigh,
Biochim. Biophys. Acta, 494, 191 (1977).
95. H. Blum, J.C. Salerno, P.R. Rich, T. Ohnishi,
Biochim. Biophys. Acta, 548, 139 (1979).
96. H. Blum, J.C. Salerno, M.A. Cusanovich,
Biochem. Biophys. Res. Commun., 84, 1125 (1978).
97. H. Blum, J.C. Salerno, R.C. Prince, J.S. Leigh, T. Ohnishi,
Biophysical J. 20, 23 (1977).
98. D. Sh. Burbaev, A.V. Lebanidze,
Biofizika, 24, 930 (1979).
99. G.C. Papaefthymiou, R.B. Frankel, S. Foner, E.J. Laskowski, R.H. Holm,
J. de Phys. (Orsay, Fr.) Colloque Cl, 41, 493 (1980).
100. P. Beardwood, J.F. Gibson, P. Bertrand, J.P. Gayda,
Biochim. Biophys. Acta, accepted for publication.
101. J-P. Gayda, P. Bertrand, A. Deville, C. More, G. Roger,
J.F. Gibson, R. Cammack,
Biochim. Biophys. Acta, 581, 15 (1979).
102. H.L. Clever, E.F. Westrum,
J. Phys. Chem. 74, 1309 (1970).

103. H.J. Stapleton, J.P. Aleen, C.P. Flynn, D.G. Stinson, S.R. Kurtz,
Phys. Rev. Lett, 45, 1456 (1980).
104. P. Bertrand,
These de 3e Cycle, Universite'de Provence (1977).
105. P. Bertrand, J-P. Gayda, K.K. Rao,
J. Chem. Phys., 76, 4715 (1982).
106. D.Sh. Burbaev, A.V. Lebanidze,
Biofizika, 24, 392 (1979).
107. J-P. Gayda, P. Bertrand, C. More, J. le Gall, R.C. Cammack,
Biochem. Biophys. Res. Commun., 99, 1265 (1981).
108. T. Ohnishi, H. Blum, S. Sato, K. Nakazawa, K. Hon-Nami, T. Oshima,
J. Biol. Chem., 255, 347 (1980).
109. W.D. Horrocks, F.A. Cotton,
Spectrochimica Acta, 17, 134 (1961).
110. F.R. Dollish, W.G. Fateley, F.F. Bentley in
"Characteristic Raman Frequencies of Organic Compounds",
John Wiley, New York, (1974).
111. J.W. Robinson,
"CRC Handbook of Spectroscopy", Vol. II,
CRC Press, Cleveland, Ohio (1974).
112. L. Petersson, R. Cammack, K.K. Rao,
Biochim. Biophys. Acta, 622, 18 (1980).
113. T. Kimura, A. Tasaki, H. Watari,
J. Biol. Chem., 245, 4450 (1970).
114. F. Adar, H. Blum, J.S. Leigh, T. Ohnishi, J. Salerno, T. Kimura,
FEBS Letts., 84, 214 (1977).
115. H. Blum, F. Adar, J.C. Salerno, J.S. Leigh,
Biochem. Biophys. Res. Commun., 77, 650 (1977).
116. J.G. Norman, P.B. Ryan, L. Noodleman,
J. Amer. Chem. Soc., 102, 4279 (1980).
117. R.W. Lane, J.A. Ibers, R.B. Frankel, G.C. Papaefthymiou, R.H. Holm,
J. Amer. Chem. Soc., 99, 84 (1977).
118. R.B. Frankel, G.C. Papaefthymiou, R.W. Lane, R.H. Holm,
J. de Phys. (Orsay, Fr.), Colloque C6, 37, 165 (1976).
119. W.A. Eaton, W. Lovenberg in
"Iron-Sulfur Proteins", Vol.II,
W. Lovenberg, Ed., Academic Press, New York, N.Y. (1973), Ch. 3.

120. E.T. Lode, M.J. Coon,
J. Biol. Chem., 246, 791 (1971).
121. H. Bachmayer, L.H. Piette, K.T. Yasunobu, H.R. Whiteley,
Proc. Natl. Acad. Sci. U.S.A., 57, 122 (1967).
122. I. Moura, A.V. Xavier, R. Cammack, M. Bruschi, J. Le Gall,
Biochim. Biophys. Acta, 533, 156 (1978).
123. K.K. Rao, M.C.W. Evans, R. Cammack, D.O. Hall, C.L. Thompson,
P.J. Jackson, C.E. Johnson,
Biochim. J., 129, 1063 (1972).
124. S-S. Yang, L.G. Ljungdahl, D.V. Dervartanian, G.D. Watt,
Biochim. Biophys. Acta, 590, 24 (1980).
125. J. Peisach, W.E. Blumberg, E.T. Lode, M.J. Coon,
J. Biol. Chem., 246, 5877 (1971).
126. P.S. Han, T.P. Das, M.F. Rettig,
J. Chem. Phys., 56, 3861 (1972).
127. H.H. Wickman, M.P. Klein, D.A. Shirley,
J. Chem. Phys., 42, 2113 (1965).
128. W.E. Blumberg in
" Magnetic Resonance in Biological Systems " ,
A. Ehrenberg, B.G. Malmström, T. Vännngård, Eds.,
Pergamon Press, Oxford (1967), p. 119.
129. P.L. Hall, B.R. Angel, J.P.E. Jones,
J. Magn. Reson. 15, 64 (1974).
130. C.P. Poole, H.A. Farach, W.K. Jackson,
J. Chem. Phys., 61, 2220 (1974).
131. K. Spartalian, W.T. Oosterhuis, J.B. Neilands,
J. Chem. Phys. 62, 3538 (1975).
132. R.D. Dowsing, J.F. Gibson,
J. Chem. Phys., 50, 294 (1969).
133. R. Aasa,
J. Chem. Phys., 52, 3919 (1970).
134. T. Castner, G.S. Newell, W.C. Holton, C.P. Slichter,
J. Chem. Phys. 32, 668 (1960).
135. W.E. Blumberg, J. Peisach,
Ann. N.Y. Acad. Sci., 222, 539 (1973).
136. L. Que, J.D. Lipscomb, R. Zimmermann, E. Münck,
N.R. Orme-Johnson, W.H. Orme-Johnson,
Biochim. Biophys. Acta, 452, 320 (1976).
137. D.L. Griscom, R.E. Griscom,
J. Chem. Phys., 47, 2711 (1967).

138. R. Aasa, T. Vänngård,
Arkiv. fur Kemi, 24, 331 (1965).
139. P.C. Taylor, P.J. Bray,
J. Magn. Reson. 2, 305 (1970).
140. J. Kliava, J. Purāns,
J. Magn. Reson. 40, 33 (1980).
141. H. Kawazoe, H. Hosono, H. Kokumai, J. Nishii, T. Kanazawa,
J. Non-Cryst. Solids, 40, 291 (1980).
142. D.L. Griscom, P.C. Taylor, D.A. Ware, P.J. Bray,
J. Chem. Phys., 48, 5158 (1968).
143. G.E. Peterson, C.R. Kurkjian, A. Carnevale,
Phys. Chem. Glasses, 17, 88 (1976).
144. Local program EPR-DRAW (originally ESRS¹³² re-written in FORTRAN IV
by Dr. R.D. Dowsing, Department of Computer Science, University
College of Swansea, and subsequently modified by Gordon M. Lack,
Imperial College).
145. E.I. Abdrashitova, R. Ya. Khodakovskaya, N.I. Khar'kova,
Inorg. Mat. USSR, 8, 1966 (1972).
146. D.L. Griscom,
J. Non-Cryst. Solids, 40, 211 (1980).
147. I. Moura, B.H. Huynh, R.P. Hausinger, J. Le Gall, A.V. Xavier,
E. Münck,
J. Biol. Chem., 255, 2493 (1980).
148. G.E. Chapps, S.W. McCann, H.H. Wickman, R.C. Sherwood,
J. Chem. Phys., 60, 990 (1974).
149. D. Niarchos, A. Kostikas, A. Simopoulos, D. Coucouvanis,
D. Piltingsruo, R.E. Coffman,
J. Chem. Phys., 69, 4411 (1978).
150. G.E. Peterson, C.R. Kurkjian, A. Carnevale,
Phys. Chem. Glasses, 15, 52 (1974).
151. G.E. Peterson, C.R. Kurkjian, A. Carnevale,
Phys. Chem. Glasses, 15, 59 (1974).
152. G.E. Jellison, P.J. Bray, P.C. Taylor,
Phys. Chem. Glasses, 17, 35 (1976).
153. J.F. Gibson in
"ESR and NMR of Paramagnetic Species in Biological and Related Systems",
I. Bertini, R.S. Drago, Eds., D. Reidel Publishing Co.,
Dordrecht, (1980), p. 225.

154. D.L. Griscom in
" Borate Glasses: Structure, Properties, Applications ",
L.D. Pye, V.D. Frechette, N.J. Kreidl, eds., Plenum Press,
New York (1978), p. 123.
155. C.M. Brodbeck,
J. Non-Cryst. Solids, 40, 305 (1980).
156. R.W. Kedzie, D.H. Lyons, M. Kestigian
Phys. Rev. A, 138, 918 (1965).
157. R.M. Golding, T. Singhasuwich, W.C. Tennant,
Mol. Phys., 34, 1343 (1977).
158. R.M. Golding, M. Kestigian, C.W. Tennant,
J. Phys. C., 11, 5041 (1978).
159. R.J.P. Williams,
Inorg. Chim. Acta Rev., 5, 137 (1971).
160. B.L. Vallee, R.J.P. Williams,
Proc. Natl. Acad. Sci., U.S.A., 59, 498 (1968).
161. R.G. Shulman, P. Eisenberger, B-K. Teo, B.M. Kincaid, G.S. Brown,
J. Mol. Biol. 124, 305 (1978).
162. B. Bunker, E.A. Stern,
Biophys. J., 19, 253 (1977).
163. S. Slappendel, G.A. Veldink, J.F.G. Vliegenthart,
R. Aasa, B.G. Malmström,
Biochim. Biophys. Acta, 624, 30 (1980).
164. T.G. Sprio,
Acc. Chem. Res., 7, 339 (1974).
165. P.A. Fleury, R. Loudon,
Phys. Rev., 166, 514 (1968).
166. Y.R. Shen, N. Bloembergen,
Phys. Rev., 143, 372 (1966).
167. T.V. Long, T.M. Loehr, J.R. Allkins, W. Lovenberg,
J. Amer. Chem. Soc., 93, 1809 (1971).
168. T.V. Long, T.M. Loehr,
J. Amer. Chem. Soc., 92, 6384 (1970).
169. T. Yamamoto, G. Palmer, L. Rimai, D. Gill, I. Salmeen,
Fed. Proc., Fed. Am. Soc. Exp. Biol. 33, 1372 (1974).
170. S.W. Tang, T.G. Spiro, K. Mukai, T. Kimura,
Biochem. Biophys. Res. Commun., 53, 869 (1973).
171. T. Kimura, J.J. Huang,
Arch. Biochem. Biophys. 137, 357 (1970).

172. S.W. Tang, T.G. Sprio, C. Antanaitis, T.H. Moss, R.H. Holm, T. Herskovitz, L.E. Mortensen, Biochem. Biophys. Res. Commun., 62, 1 (1975).
173. W.M. Scovell, T.G. Spiro, Inorg. Chem., 13, 304 (1974).
174. R. Czernnuszewicz, E. Maslowsky, K. Nakamoto, Inorg. Chim. Acta, 40, 199 (1980).
175. D.M. Adams in "Metal-Ligand and Related Vibrations", Edward Arnold, London (1967), Ch. 7.
176. J.R. Ferraro in "Low-Frequency Vibrations of Inorganic and Coordination Compounds", Plenum Press, New York, (1971).
177. J. Behringer, Chem. Soc. Spec. Per. Rep., Molecular Spectroscopy 3, 163 (1975).
178. R.J.H. Clark in "Advances in Infrared and Raman Spectroscopy", 1, R.J.H. Clark, R.E. Hester Ed., Heyden, London (1975), Ch. 4.
179. T.G. Sprio, T.M. Loehr, in "Advances in Infrared and Raman Spectroscopy", 1, R.J.H. Clark, R.E. Hester, Ed., Heyden, London (1975), Ch. 3.
180. P.R. Carey, Quart. Rev. Biophys. 11, 309 (1978).
181. A. Warshel, Ann. Rev. Biophys. Bioeng. 6, 273 (1977).
182. K.D. Watenpaugh, L.C. Sieker, L.H. Jensen, J. Mol. Biol. 131, 509 (1979).
183. L.H. Jensen, in "Iron-Sulfur Proteins", Vol. 2, W. Lovenberg, Ed., Academic Press, New York, N.Y. (1973), Ch. 4.
184. K. Nakamoto in "Infrared and Raman Spectra of Inorganic and Coordination Compounds", John Wiley, New York, (1978).
185. E.T. Adman, L.C. Sieker, L.H. Jensen, M. Bruschi, J. Le Gall, J. Mol. Biol. 112, 113 (1977).
186. A. Müller, K.H. Schmidt, K.H. Tytko, J. Buuwlma, F. Jellinek, Spectrochimica Acta, 28A, 381 (1972).
187. L.A. Woodward, M.J. Taylor, J. Chem. Soc., 4473, (1960).
188. J.S. Avery, C.D. Burbridge, D.M.L. Goodgame, Spectrochimica Acta, 24A, 1721 (1968).

189. N. Weinstock, H. Schulze, A. Müller,
J. Chem. Phys. 59, 5063 (1973).
190. G. Palmer, H. Brintzinger, R.W. Estabrook,
Biochemistry, 6, 1658 (1967).
191. K. Tagawa, D.I. Arnon,
Biochim. Biophys. Acta, 153, 602 (1968).
192. K.P. Sinha, N. Kumar in
"Interactions in Magnetically Ordered Solids",
Oxford University Press (1980).
193. M.A. Bobrik, K.O. Hodgson, R.H. Holm,
Inorg. Chem., 16, 1851 (1977).
194. G.B. Wong, M.A. Bobrik, R.H. Holm,
Inorg. Chem., 17, 578 (1978).
195. R.P. Bell, H.C. Longuet-Higgins,
Proc. R. Soc. London, 183(A), 357 (1945).
196. I.R. Beattie, T. Gilson, P. Cocking,
J. Chem. Soc. (A), 702, (1967).
197. I.R. Beattie, J.R. Horder,
J. Chem. Soc. (A), 2655 (1969).
198. A. Balls, A.J. Downs, N.N. Greenwood, B.P. Straughan,
J. Chem. Soc., Faraday Trans., 521 (1966).
199. I.R. Beattie, T. Gilson, G.A. Ozin,
J. Chem. Soc. (A), 813, (1968).
200. V.A. Maroni, D.M. Gruen, R.L. McBeth, E.J. Cairns,
Spectrochimica Acta, 26A, 418 (1970).
201. S.J. Cyvin, O. Törset,
Rev. Chim. Miner., 9, 179 (1972).
202. A. Givan, A. Loewenschuss,
J. Raman Spectroscopy, 6, 84 (1977).
203. A. Loewenschuss, A. Givan,
Ber. Bunsenges. Phys. Chem., 82, 75 (1978).
204. R.A. Frey, R.D. Werder, Hs. H. Günthard,
J. Mol. Spectroscopy 35, 260 (1970).
205. D.M. Adams, R.G. Churchill,
J. Chem. Soc. (A), 697 (1970).
206. S.F.A. Kettle, P.L. Stanghellini,
Inorg. Chem., 16, 753 (1977).
207. S. Onaka, D.F. Shriver,
Inorg. Chem., 15, 915 (1976).

208. I.S. Butler, S. Kishner, K.R. Plowman,
J. Mol. Struct. **43**, 9 (1978).
209. G.J. Kubas, T.G. Spiro,
Inorg. Chem., **12**, 1797 (1973).
210. C.D. Cooper, S. Onaka, D.F. Shriver, L. Daniels, R.L. Hance,
B. Hutchinson, R. Shipley,
Inorg. Chim. Acta, **24**, L92 (1977).
211. M. Hargittai, J. Tremmel, I. Hargittai,
J. Chem. Soc., (Dalton), **87** (1980).
212. M.A. Bobrik, E.J. Laskowski, R.W. Johnson, W.O. Gillum,
J.M. Berg, K.O. Hodgson, R.H. Holm,
Inorg. Chem., **17**, 1402 (1978).
213. C.K. Jørgensen,
Prog. Inorg. Chem., **12**, 101 (1970).
214. C.K. Jørgensen,
Inorg. Chim. Acta Rev. **2**, 65 (1968).
215. J.C.M. Tsibris, M.J. Nantvedt, I.C. Gunsalus,
Biochem. Biophys. Res. Commun., **30**, 323 (1968).
216. J.G. Reynolds, C.L. Coyle, R.H. Holm,
J. Amer. Chem. Soc., **102**, 4350 (1980).
217. C.W. Carter,
J. Biol. Chem., **252**, 7802 (1977).
218. W.P. Griffith, P.M. Kiernan, B.P. O'Hare,
J. Mol. Struct. **46**, 307 (1978).
219. P.A. Bulliner, T.G. Spiro,
Spectrochimica Acta **26A**, 1641 (1970).
220. A. Terzis, T.G. Spiro,
J.C.S. Chem. Commun., 1160 (1970).
221. V.A. Maroni, T.G. Spiro,
Inorg. Chem., **7**, 188 (1968).
222. V.A. Maroni, T.G. Spiro,
Inorg. Chem., **7**, 193 (1968).
223. P.A. Bulliner, V.A. Maroni, T.G. Spiro,
Inorg. Chem., **9**, 1887 (1970).
224. D. Hartley, M.J. Ware,
J.C.S. Chem. Commun., 912 (1967)
225. T.G. Spiro,
Prog. Inorg. Chem., **11**, 1, (1970).
226. E.W. Abel, P.J. Hendra, R.A.N. McLean, M.M. Qurashi,
Inorg. Chim. Acta **3**, 77 (1969).

227. R.H. Holm, B.A. Averill, T. Herskovitz, R.B. Frankel, H.B. Gray, O. Siiman, F.J. Grunthaner, J. Amer. Chem. Soc., 96, 2644 (1974).
228. E.J. Laskowski, J.G. Reynolds, R.B. Frankel, S. Foner, G.C. Papaefthymiou, R.H. Holm, J. Amer. Chem. Soc., 101, 6562 (1979).
229. E.J. Laskowski, R.B. Frankel, W.O. Gillum, G.C. Papaefthymiou, J. Renaud, J.A. Ibers, R.H. Holm, J. Amer. Chem. Soc., 100, 5322 (1978).
230. J.M. Berg, K.O. Hodgson, R.H. Holm, J. Amer. Chem. Soc., 101, 4586 (1979).
231. J.A. Fee, Structure Bonding, 23, 1 (1975)
232. H. Beinert, Coord. Chem. Rev., 33, 55 (1980).
233. B.G. Malmström, L.E. Andréason, B. Reinhammer, The Enzymes, 12, 507 (1975).
234. R. Malkin, B.G. Malmström, Adv. Enzymol. 33, 177 (1970).
235. H.B. Gray, E.I. Solomon in "Copper Proteins", T. Spiro ed., Wiley, New York (1981), pg. 1.
236. G. McLendon, A.E. Martell, J. Inorg. Nucl. Chem., 39, 191 (1977).
237. V. Miskowski, S-P.W. Tang, T.G. Spiro, E. Shapiro, T.H. Moss, Biochemistry 14, 1244 (1975).
238. O. Siiman, N.M. Young, P.R. Carey, J. Amer. Chem. Soc., 98, 744 (1976).
239. N.S. Ferris, W.H. Woodruff, D.L. Tennent, D.R. McMillin, Biochem. Biophys. Res. Commun., 88, 288 (1979).
240. J.W. Hare, E.I. Solomon, H.B. Gray, J. Amer. Chem. Soc., 98, 3205 (1976).
241. T.D. Tullius, P. Frank, K.O. Hodgson, Proc. Natl. Acad. Sci., U.S.A., 75, 4069 (1978).
242. K.W. Penfield, R.R. Gay, R.S. Himmelwright, N.C. Eickman, V.A. Norris, H.C. Freeman, E.I. Solomon, J. Amer. Chem. Soc., 103, 4382 (1981).
243. T. Vänngård in "Biological Applications of Electron Spin Resonance", H.M. Swartz, J.R. Bolton, D.C. Borg, Eds., Wiley, New York, (1972), Ch. 9.

244. B. Mondovi, M.T. Graziani, W.B. Mims, R. Oltzik, J. Peisach, Biochemistry, 16, 4198 (1977).
245. W.B. Mims, J. Peisach, J. Biol. Chem., 254, 4321 (1979).
246. L. Avigliano, J.L. Davis, M.T. Graziani, A. Marchesini, W.B. Mims, B. Mondovi, J. Peisach, FEBS Letts., 136, 80 (1981).
247. J. Peisach, W.B. Mims, Eur. J. Biochem. 84, 207 (1978).
248. J.E. Roberts, T.G. Brown, B.M. Hoffman, J. Peisach, J. Amer. Chem. Soc., 102, 825 (1980).
249. G.H. Rist, J.S. Hyde, T. Vänngård, Proc. Natl. Acad. Sci., U.S.A., 67, 79 (1970).
250. H.A.O. Hill, W.K. Lee, J. Inorg. Biochem., 11, 101 (1979).
251. H.A.O. Hill, B.E. Smith, J. Inorg. Biochem., 11, 79 (1979).
252. H.C. Freeman, V.A. Norris, J.A.M. Ramshaw, P.E. Wright, FEBS Lett., 86, 131 (1978).
253. E.L. Ulrich, J.L. Markley, Coord. Chem. Rev., 27, 109 (1978).
254. J.L. Markley, E.L. Ulrich, S.P. Berg, D.W. Krogman, Biochemistry, 14, 4428 (1975).
255. K. Ugurbil, R. Bersohn, Biochemistry, 16, 3016 (1977).
256. K. Ugurbil, R.S. Norton, A. Allerhand, R. Bersohn, Biochemistry, 16, 886 (1977).
257. J.L. Markley, E.L. Ulrich, D.W. Krogman, Biochem. Biophys. Res. Commun., 78, 106 (1977).
258. H.A.O. Hill, J.C. Leer, B.E. Smith, C.B. Storm, R.P. Ambler, Biochem. Biophys. Res. Commun., 70, 331 (1976).
259. E.I. Solomon, J.W. Hare, D.M. Dooley, J.H. Dawson, P.J. Stephens, H.B. Gray, J. Amer. Chem. Soc., 102, 168 (1980).
260. D.R. McMillin, M.C. Morris, Proc. Natl. Acad. Sci., U.S.A., 78, 6567 (1981).

261. D.L. Tennent, D.R. McMillin,
J. Amer. Chem. Soc., 101, 2307 (1979).
262. D.M. Dooley, J.H. Dawson, P.J. Stephens, H.B. Gray,
Biochemistry, 20, 2024 (1981).
263. E.I. Solomon, J.W. Hare, H.B. Gray,
Proc. Natl. Acad. Sci., U.S.A., 73, 1389 (1976).
264. N. Noyer, F.W. Putnam,
Biochemistry, 20, 3536 (1981).
265. V. Lum, H.B. Gray,
Isr. J. Chem. 21, 23 (1981).
266. D.M. Dooley, J. Rawlings, J.H. Dawson, P.J. Stephens,
L.E. Andréason, B.G. Malström, H.B. Gray,
J. Amer. Chem. Soc., 101, 5038 (1979).
267. J.H. Dawson, D.M. Dooley, R. Clark, P.J. Stephens, H.B. Gray,
J. Amer. Chem. Soc., 101, 5046 (1979).
268. U. Weser, M. Younes, H-J. Hartmann, S. Zienau,
FEBS Letts., 97, 311 (1979).
269. E.I. Solomon, P.J. Clendening, H.B. Gray, F.J. Grunthaner,
J. Amer. Chem. Soc., 97, 3878 (1975).
270. J. Peeling, B.G. Haslett, I.M. Evans, D.T. Clark, D. Boulter,
J. Amer. Chem. Soc., 99, 1025 (1977).
271. J.M. Wiesenfeld, E.P. Ippen, A. Corin, R. Bersohn,
J. Amer. Chem. Soc., 102, 7256 (1980).
272. D. Cummins, H.B. Gray,
J. Amer. Chem. Soc., 99, 5158 (1977).
273. J.V. McArdle, C.L. Coyle, H.B. Gray, G.S. Yoneda, R.A. Holwerda,
J. Amer. Chem. Soc., 99, 2483 (1977).
274. R.C. Rosenberg, S. Wherland, R.A. Holwerda, H.B. Gray,
J. Amer. Chem. Soc., 98, 6364 (1976).
275. D.R. McMillin, R.C. Rosenberg, H.B. Gray,
Proc. Natl. Acad. Sci., U.S.A., 71, 4760 (1974).
276. D.R. McMillin, R.A. Holwerda, H.B. Gray,
Proc. Natl. Acad. Sci., U.S.A., 71, 1339 (1974).
277. E.I. Solomon, R-H. Wang, D.R. McMillin, H.B. Gray,
Biochem. Biophys., Res. Commun., 69, 1039 (1976).
278. H.A.O. Hill, B.E. Smith, C.B. Storm, R.P. Ambler,
Biochem. Biophys. Res. Commun., 70, 783 (1976).

279. D.R. McMillin,
Bioinorg. Chem., 8, 179 (1978).
280. P.M. Colman, H.C. Freman, J.M. Guss, M. Murata, V.A. Norris,
J.A.M. Ramshaw, M.P. Venkatappa,
Nature, 272, 319 (1978).
281. E.T. Adman, R.E. Stenkamp, L.C. Sieker, L.H. Jensen,
J. Mol. Biol. 123, 35 (1978).
282. E.T. Adman, L.H. Jensen,
Israeli. J. Chem. 21, 8 (1981).
283. J. Peisach, W.E. Levine, W.E. Blumberg,
J. Biol. Chem., 242, 2847 (1967).
284. C. Bergman, E-K. Gandvik, P.O. Nyman, L. Strid,
Biochem. Biophys. Res. Commun., 77, 1052 (1977).
285. T.T. Wang, N.M. Young,
Biochem. Biophys. Res. Commun., 74, 119 (1977).
286. M. Lundeen,
Inorg. Chim. Acta, 56, 149 (1981).
287. C.A. Bates, W.S. Moore, K.J. Standley, K.W.H. Stevens,
Proc. Phys. Soc., 79, 73 (1962).
288. A.S. Brill, G.F. Bryce,
J. Chem. Phys., 48, 4398 (1968).
289. H. Yokoi, A.W. Addison,
Inorg. Chem., 16, 1341 (1977).
290. D.C. Gould, A. Ehrenberg,
Eur. J. Biochem., 5, 451 (1968).
291. F.G. Herring, D.J. Patmore, A. Storr,
J. Chem. Soc. (Dalton) 711 (1975).
292. Y. Murakami, Y. Matsuda, K. Sakata,
Inorg. Chem., 10, 1734 (1971).
293. Y. Nishida, N. Oishi, S. Kida,
Inorg. Chim. Acta, 32, 7 (1979).
294. D. Attanasio, A.A.G. Tomlinson, L. Alagna,
J.C.S. Chem. Commun., 618, (1977).
295. U. Sakaguchi, A.W. Addison,
J. Chem. Soc., (Dalton), 600 (1979).
296. U. Sakaguchi, A.W. Addison,
J. Amer. Chem. Soc., 99, 5189 (1977).

297. R.D. Bereman, F.T. Wang, J. Najdzionek, D.M. Braitsch,
J. Amer. Chem. Soc., 98, 7266 (1976).
298. R.A. Palmer, W.C. Tennant, M.F. Dix, A.D. Rae,
J. Chem. Soc. (Dalton), 2345 (1976).
299. J.S. Thompson, T.J. Marks, J.A. Ibers,
J. Amer. Chem. Soc., 101, 4180 (1979).
300. J.S. Thompson, T.J. Marks, J.A. Ibers,
Proc. Natl. Acad. Sci., U.S.A., 74, 3114 (1977).
301. J.S. Thompson, J.L. Zitzmann, T.J. Marks, J.A. Ibers,
Inorg. Chim. Acta, 46, L101 (1980).
302. Y. Agnus, R. Louis, R. Weiss,
J.C.S. Chem. Commun., 867 (1980).
303. J.M. Downes, J. Whelan, B. Bosnich,
Inorg. Chem., 20, 1081 (1981).
304. A. Dobry-Duclaux, P. Périchon,
J. Chim. Phys. Phys-Chim. Biol. 73, 1058 (1976).
305. J.V. Dagdigian, C.A. Reed,
Inorg. Chem., 18, 2624 (1979).
306. K.D. Karlin, P.L. Dahlstrom, M.L. Stanford, J. Zubieta,
J.C.S. Chem. Commun., 465 (1979).
307. E.R. Dockal, T.E. Jones, W.F. Sokol, R.J. Engerer, D.B. Rorabacher,
L.A. Ochrymowycz,
J. Amer. Chem. Soc., 98, 4322 (1976).
308. T.E. Jones, D.B. Rorabacher, L.D. Ochrymowycz,
J. Amer. Chem. Soc., 97, 7485 (1975).
309. M.D. Glick, D.P. Gavel, L.L. Diaddario, D.B. Rorabacher,
Inorg. Chem., 15, 1190 (1976).
310. A.R. Amundsen, J. Whelan, B. Bosnich,
J. Amer. Chem. Soc., 99, 6730 (1977).
311. G.R. Brubaker, J.N. Brown, M.K. Yoo, R.A. Kinsey, T.M. Kutchan,
E.A. Mottel,
Inorg. Chem., 18, 299 (1979).
312. K.D. Karlin, P.L. Dahlstrom, J.R. Hyde, J. Zubieta,
J.C.S. Chem. Commun., 906 (1980).
313. K.D. Karlin, P.L. Dahlstrom, J. Zubieta,
Trans. Met. Chem., 6, 314, (1981).
314. Y. Hirayama, Y. Sugiura,
Biochem. Biophys. Res. Commun., 86, 40 (1979).
315. Y. Sugiura, Y. Hirayama, H. Tanaka, K. Ishizu,
J. Amer. Chem. Soc., 97, 5577 (1975).

316. Y. Sugiura,
Inorg. Chem., 17, 2176 (1978).
317. Y. Sugiura, Y. Hirayama,
J. Amer. Chem. Soc., 99, 1581 (1977).
318. G.S. Patterson, R.H. Holm,
Bioinorganic Chem., 4, 257 (1975).
319. M.A. Augustin, J.K. Yandell, A.W. Addison, K.D. Karlin,
Inorg. Chim. Acta, 55, L35 (1981).
320. R.H. Holm, M.J. O'Connor,
Prog. Inorg. Chem., 14, 241 (1971).
321. G.W. Everett, R.H. Holm,
J. Amer. Chem. Soc., 87, 2117 (1965).
322. D.H. Gerlach, R.H. Holm,
J. Amer. Chem. Soc., 91, 3457 (1969).
323. S.S. Eaton, R.H. Holm,
Inorg. Chem., 10, 1446 (1971).
324. S.G. McGreachin,
Can. J. Chem., 46, 1903 (1968).
325. D.H. Gerlach, R.H. Holm,
Inorg. Chem., 9, 588 (1970).
326. P.R. Blum, R.M.C. Wei, S.C. Cummings,
Inorg. Chem., 13, 450 (1974).
327. G.D. Shields, S. Christiano, R.D. Bereman,
J. Inorg. Nucl. Chem., 40, 1953 (1978).
328. R.D. Bereman, M.R. Churchill, G. Shields,
Inorg. Chem., 18, 3117 (1979).
329. R.D. Bereman, G.D. Shields, J. Bordner, J.R. Dorfman,
Inorg. Chem., 20, 2165 (1981).
330. R.D. Bereman, J.R. Dorfmann, J. Bordner, D.P. Rillema,
P. McCarthy, G.D. Shields,
J. Inorg. Biochem., 16, 47 (1982).
331. I.V. Miroshnichenko, Y.L. Gol'dfarb, V.P. Litvinov, E.G. Ostapenko,
G.M. Larin, M.E. Dyatkina, V.A. Kolosov,
Russ. J. Inorg. Chem., 19, 1164 (1974).
332. S.K. Mondal, D.S. Joardar, K. Nag,
Inorg. Chem., 17, 191 (1978).
333. M.F. Corrigan, K.S. Murray, B.O. West, J.R. Pilbrow,
Aust. J. Chem., 30, 2455 (1977).

334. L.P. Olekhovich, V.P. Kurbatov, O.A. Osipov, L.S. Minkina, V.I. Minkin,
J. Gen. Chem., USSR, 38, 2512 (1968).
335. E. Klingsberg,
J. Amer. Chem. Soc., 83, 2934 (1961).
336. B.J. Hathaway, D.E. Billing,
Coord. Chem. Rev., 5, 143 (1970).
337. H.A. Kuska, M.T. Rogers in
" Radical Ions ", E.T. Kaiser, L. Kevan, eds., (1968), pg. 596.
338. D. Kivelson, R. Neiman,
J. Chem. Phys., 35, 149 (1961).
339. J. Peisach, W.E. Blumberg,
Arch. Biochem. Biophys., 165, 691, (1974).
340. H. Yokoi,
Bull. Chem. Soc., Japan, 47, 3037 (1974).
341. R.C. Rosenberg, C.A. Root, P.K. Bernstein, H.B. Gray,
J. Amer. Chem. Soc., 97, 2092 (1975).
342. M.R. Symons, D.X. West, J.G. Wilkinson,
J. Chem. Soc. (Dalton), 1696 (1975).
343. T.D. Smith, J.R. Pilbrow ,
Coord. Chem. Rev., 13, 173 (1974).
344. T. Oniki,
Bull. Chem. Soc. Japan, 51, 2551 (1978).
345. T. Oniki,
Bull. Chem. Soc., Japan, 52, 2584 (1979).
346. A.S. Brill, G.F. Bryce, H.J. Maria,
Biochim. Biophys. Acta, 154, 342 (1968).
347. B.G. Malmström, B. Reinhammar, T. Vänngård,
Biochim. Biophys. Acta, 205, 48 (1970).
348. W.E. Blumberg, J. Peisach,
Biochim. Biophys. Acta, 126, 269 (1966).
349. T. Stigbrand, B.G. Malmström, T. Vänngård,
FEBS Letts. 12, 260 (1971).
350. A. Marchesini, M. Minelli, H. Merkle, P.M.H. Kroneck,
Eur. J. Biochem., 101, 77 (1979).
351. J.C. Cox, R. Aasa, B.G. Malmström,
FEBS Letts, 93, 157 (1978).
352. B.G. Malmström, B. Reinhammar, T. Vänngård,
Biochim. Biophys. Acta, 156, 67 (1968).

353. L.E. Andréasson, T. Vänngård,
Biochim. Biophys. Acta 200, 247 (1970).
354. J. Deinum, B. Reinhammar, A. Marchesini,
FEBS Letts., 42, 241 (1974).
355. A. Marchesini, P.M.H. Kroneck,
Eur. J. Biochem., 101, 65 (1979).
356. R. Cini, A. Cinquantini, P. Orioli, M. Sabat,
Inorg. Chim. Acta, 41, 151 (1980).
357. M.J.E. Hewlins,
J. Chem. Soc. (Dalton), 429 (1975).
358. I. Bertini, G. Canti, R. Grassi, A. Scozzafava,
Inorg. Chem., 19, 2198 (1980).
359. M. Sharnöff,
J. Chem. Phys., 42, 3383 (1965).
360. J.I. Zink, R.S. Drago,
J. Amer. Chem. Soc., 94, 4550 (1972).
361. V.G. Krishnan,
J. Chem. Phys., 68, 660 (1978).
362. J. Choisnet, D. Cornet, J-F. Hemidy, N. Nguyen, Y. Dat,
J. Solid State Chem., 40, 161 (1981).
363. A. Bencini, D. Gatteschi, C. Zanchini,
J. Amer. Chem. Soc., 102, 5234 (1980).
364. R. Sheahan, B. Hathaway,
J. Chem. Soc. (Dalton), 17 (1979).
365. O. Siimann, J. Fresco,
Inorg. Chem., 8, 1846 (1969).
366. O. Siimann, D.D. Titus, C.D. Cowman, J. Fresco, H.B. Gray,
J. Amer. Chem. Soc., 96, 2353 (1974).
367. O. Siimann, N.M. Young, P.F. Carey,
J. Amer. Chem. Soc., 96, 5583 (1974).
368. L. Tosi, A. Garnier, M. Herve, M. Steinbuch,
Biochem. Biophys. Res. Commun., 65, 100 (1975).
369. N.S. Ferris, W.H. Woodruff, D.B. Rorabacher, T.E. Jones,
L.A. Ochrymowycz,
J. Amer. Chem. Soc., 100, 5939 (1978).
370. L. Tosi, A. Garnier,
Biochim. Biophys. Res. Commun., 91, 1273 (1979).

371. L. Tosi, A. Garnier,
J. Chem. Soc. (Dalton), 53 (1978).
372. O. Siimann, P.R. Carey,
J. Inorg. Biochem., 12, 353 (1980).
373. A. Cinquantini, R. Cini, R. Seeber, P. Zanello,
J. Electroanal. Chem., 121, 301 (1981).
374. R.H. Wopschall, I. Shain,
Anal. Chem., 39, 1514 (1967).
375. I.M. Kolthoff, J.J. Lingane,
in "Polarography"
Interscience (John Wiley), New York, Vol. 1 (1952).
376. R. Brdicka,
Coll. Czech. Commun., 12, 522 (1947).
377. D.T. Sawyer, J.I. Roberts in
"Experimental Electrochemistry for Chemists",
John Wiley, New York (1974).
378. W.R. Pangratz, F.L. Urbach, P.R. Blum, S.C. Cummings,
Inorg. Nucl. Chem. Letts., 9, 1141 (1973).
379. A. Kotočová, J. Šima,
Inorg. Chim. Acta, 40, 115 (1980).
380. L. Morpurgo, L. Calabrese, A. Desideri, G. Rotilio,
Biochem. J., 193, 639 (1981).
381. H. Behringer, A. Grimm,
Ann. 682, 188 (1965).
382. H. Meerwein,
Org. Synth., 46, 113 (1966).
383. D.L. Klayman, T.S. Griffin,
J. Amer. Chem. Soc., 95, 197 (1973).
384. G. Christou, C.D. Garner,
J. Chem. Soc., (Dalton) 1093 (1979).
385. G. Christou, B. Ridge, H.N. Rydon,
J. Chem. Soc., (Dalton) 1423 (1978).
386. D.G. Foster in
Org. Synth. Coll. Vol. 3, 771 (1955).
387. L.K. White, R.L. Belford,
J. Amer. Chem. Soc., 98, 4428 (1976).
388. A.D. Toy, S.H.H. Chaston, J.R. Pilbrow, T.D. Smith,
Inorg. Chem., 10, 2219 (1971).
389. J.R. Pilbrow, M.E. Winfield,
Mol. Phys. 25, 1073 (1973).

390. H. Margenau, G.M. Murphy, in
" The Mathematics of Physics and Chemistry ",
Van Nostrand, New York (1956), pg. 479.
391. R. Aasa, T. Vänngård,
J. Magn. Reson. 19, 308 (1975).
392. N. Zimmerer, W. Kiefer,
Appl. Spectros. 28, 279 (1974).

Like one, that on a lonesome road
Both walk in fear and dread,
And having once turned round, walks on,
And turns no more his head;
Because he knows a fightful fiend
Both close behind him tread.